

DIFFRACTION AND SCATTERING OF X-RAY AND SYNCHROTRON RADIATION

Formation of Photoelectron Holograms of Crystals Excited by Synchrotron Radiation

V. L. Nosik

Center of Technological Innovations Crystal Growth, Russian Academy of Sciences,
Leninskii pr. 59, Moscow, 117333 Russia

Received June 15, 2001

Abstract—The theoretical aspects of formation of photoelectron beams excited by the ultraviolet synchrotron radiation incident onto a crystal are considered. It is shown that the change in the energy of the monochromatized synchrotron radiation incident onto a hematite crystal results in the change of the number of reflections participating in the hologram formation. © 2002 MAIK “Nauka/Interperiodica”.

INTRODUCTION

The development of nanotechnology resulted in the creation of various structural methods of visualizing atomic structures which are based on the use of short-wavelength radiation (neutrons, electrons, X-ray and synchrotron radiation, etc.). The term *atomic holography* coined by Gabor in 1948 [1] describes the method of the three-dimensional reconstruction of atomic structures due to positive interference of the strong reference and weak object waves [2]. Later, the terms *atomic holography* or the *Fourier-transformation without a lens* became widely used because of the well-known optical analogy.

However, the principle of image formation was known long ago, e.g., as Kikuchi lines (in X-ray and electron diffraction), X-ray standing waves in multi-beam diffraction, Kossel lines, etc. [3, 4].

Lately, most of the published articles on this subject considered electron holography [5–7]. It was shown that, for high-energy electrons, the Cowley–Moody calculations [8] yield images whose main features are the same as those of the experimental images [4]. However, strong scattering of secondary electrons considerably distorts the signal, which, in turn, hinders image processing.

At the same time, some schemes for studying photo- and Auger electrons, elastically scattered X-ray radiation, fluorescence, etc. were created [9].

Below, we consider the theoretical aspects of one of the new methods—positional-sensitive photoelectron spectroscopy—where excitation is caused by beams of soft synchrotron radiation. In fact, this method is a modern modification of photoelectron spectroscopy with angular resolution [10], which has been widely used for a long time to determine the band structure of electrons.

SPECIMEN

The specimen was an orthorhombic hematite α - Fe_2O_3 crystal with the unit-cell parameter $a = 5.42 \text{ \AA}$ and $\alpha = 55.17^\circ$ cut out in such a way that the hexagonal c -axis was normal to the entrance surface (Fig. 1). This crystal was selected because of the characteristic magnetic structure of the outer electron shells and its simple atomic structure.

It is well known that the outer electrons of an iron atom ($3d^64s^2$) obey the inequality $E_{4s} < E_{3d}$, which explains the incomplete filling of the d -shell. It is interesting to analyze the distributions of both collective $3d$ -electrons (magnetic structure) and $4s$ -electrons (positions of individual atoms) in these crystals. Below, we consider only the photoeffect of $4s$ -electrons.

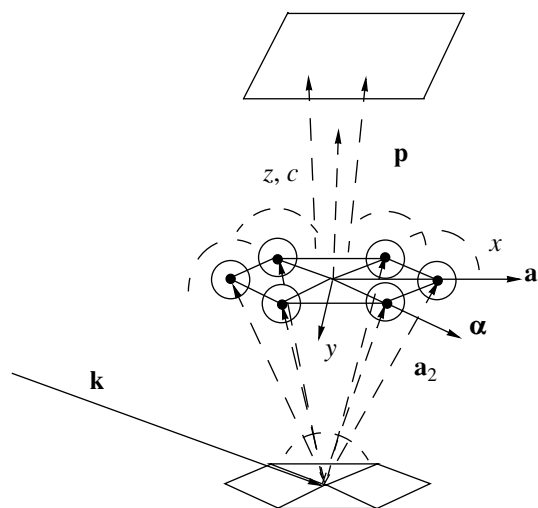


Fig. 1. Geometry of scattering from an oriented hematite crystal.

THEORY

Within the framework of perturbation theory [11], absorption of a photon with the potential vector \mathbf{A} , the wave vector \mathbf{Q} , and the frequency ω (in the dipole approximation $\exp(iQa) \approx 1$, $V = 1$),

$$\mathbf{A} = \sqrt{\frac{2\pi}{\omega}} \mathbf{e} \exp(-i\omega t) \quad (1)$$

results in electron transition (with a certain probability) from the initial state ψ_{4s} localized at the atom \mathbf{R}_i to one of the delocalized states,

$$\begin{aligned} \psi_i(\mathbf{r} - \mathbf{R}_i, t) &= \psi_{4s}(\mathbf{r} - \mathbf{R}_i) + \psi_i^0, \\ \psi_i^0 &= \int d^3 p \exp(i\mathbf{p}\mathbf{r}) U_i B(\mathbf{p}, t), \end{aligned} \quad (2)$$

where the state of the photoelectron is described by the integral over the plane waves $\exp(i\mathbf{p}\mathbf{r})$, whereas the pulse p is measured in units \hbar .

It should be emphasized that the calculation of the matrix element U_i of the transition

$$U_i = -i \sqrt{\frac{2\pi}{\omega}} \frac{\hbar}{m} \int \psi_{4s}(\mathbf{r} - \mathbf{R}_i) (\mathbf{e}\nabla) \exp(-i\mathbf{p}\mathbf{r}) d^3 r \quad (3)$$

results in the appearance of the phase factor

$$U_i = \mathbf{e}\mathbf{p}D(p) \exp(i\mathbf{p}\mathbf{R}_i), \quad (4)$$

where \mathbf{e} is the polarization vector of the incident synchrotron radiation (SR), and \mathbf{p} , the wave vector of the photoelectron.

The coefficient $D(p)$ is independent of the direction of the vector \mathbf{p} because of the spherical symmetry of the wave function ψ_{4s} . Thus, in the hydrogen-like approximation we have

$$\begin{aligned} \psi_{4s} &= \frac{\exp(i\phi)}{4\sqrt{4\pi}} Z^{3/2} \\ &\times \exp(-\xi r) \left(1 - 3\xi r + 2\xi^2 r^2 - \frac{1}{3}\xi^3 r^3 \right), \end{aligned} \quad (5)$$

where $\xi = Z/4a_B$, Z is the charge of the iron nucleus, the distances are measured in atomic units $a_B = \hbar^2/me^2 = 0.529 \text{ \AA}$, and ϕ is an arbitrary phase of the wave function. Differentiating the well-known expression

$$\int d^3 r \frac{\exp(-\lambda r + i\mathbf{p}\mathbf{r})}{r} = \frac{4\pi}{p^2 + \lambda^2} \quad (6)$$

with respect to λ , we arrive at the cumbersome but rigorous expression for the function $D(p)$,

$$D(p) \sim \exp(i\phi) \frac{1}{p^2 + \xi^2} (\xi + \dots). \quad (7)$$

Taking into account the high degree of monochromatization of the incident synchrotron radiation, we assume the pulse p and the coefficient $D(p)$ to be constant.

The coefficient $B(p, t)$ determines the dependence of the scattered radiation on time

$$B(p, t) = \frac{\exp i(\hbar\omega - E_{4s} - p^2/2m) - 1}{\hbar\omega - E_{4s} - p^2/2m}. \quad (8)$$

When SR action on the atom is prolonged, the coefficient $B(p, t)$ is simplified to the form

$$\begin{aligned} \lim_{t \rightarrow \infty} |B(p, t)|^2 &= \frac{2\pi t}{\hbar} \delta\left(\frac{p^2}{2m} - k^2\right) \\ &= \frac{2\pi t m}{\hbar} (\delta(p_z - k_z) + \delta(p_z + k_z)) \end{aligned} \quad (9)$$

and has the nonzero value only if the law of energy conservation is obeyed. We used the following notation:

$$k^2 = \hbar\omega + E_{4s}, \quad k_z = \sqrt{2mk^2 - p_z^2}, \quad (10)$$

where \mathbf{p}_t and p_z are the components of the pulse vector lying in the plane of the crystal surface and normal to it, respectively.

Since the photoeffect is an inelastic process, no interference between the waves of the primary photoelectrons emitted by various atoms is possible, which can readily be seen if one takes into account the arbitrary phase factors before the wave functions of the core electrons. The holographic effects can be explained if one takes into account the interference between the primary photoelectron radiation and the elastically scattered secondary photoelectron waves. The electron flux through the unit area J recorded by a two-dimensional detector (the surface normal \mathbf{n}) is determined as

$$J = \frac{\hbar}{im} (\psi^* (\mathbf{n}\nabla)\psi - \psi (\mathbf{n}\nabla)\psi^*). \quad (11)$$

Using expression (2) and ignoring photoelectron scattering, we arrive at the following expression for intensity, which has no term containing information on the structure,

$$J_0 \Delta S = \Delta S \frac{\hbar}{m} \sum_i \int d^3 p (\mathbf{n}\mathbf{p}) |U_i|^2 |B(p, t)|^2 \tau_i(p), \quad (12)$$

where $\tau_i(p)$ takes into account inelastic scattering and absorption of photoelectrons prior to their detection, and ΔS is the area of the detector pixel.

Now, take into account the scattering of the primary photoelectron wave propagating from the i th and scattered by the j th atoms with the scattering field $\phi(\mathbf{r})$ using perturbation theory (the kinematical or the Born approximation). The secondary wave generated by this atom is the convolution

$$\psi_{ij}^s(\mathbf{R}_0) = -\int d^3 r G(\mathbf{R}) \phi(\mathbf{r}_j + \mathbf{r}) \psi_i^0(\mathbf{r}_j + \mathbf{r}, t), \quad (13)$$

where $\mathbf{R} = \mathbf{R}_0 - \mathbf{r}_j - \mathbf{r}$. Expanding the wave function of the primary photoelectrons, (2), and the Green's function into the Fourier series

$$G(R) = \frac{1}{4\pi} \frac{\exp(ikR)}{R} = \int d^3q \frac{\exp(i\mathbf{q}\mathbf{r})}{q^2 - k^2}, \quad (14)$$

$$k^2 = p^2/2m,$$

we arrive at the following expression for the secondary wave:

$$\psi_{ij}^s(\mathbf{R}_0) = \int d^3p U_i B(p, t) \int \frac{d^3q}{q^2 - k^2} \times \exp(i\mathbf{q}\mathbf{R}_0) \exp(i(\mathbf{p} - \mathbf{q})\mathbf{r}_j) 4\pi f(\mathbf{p} - \mathbf{q}), \quad (15)$$

obtained based on the definition of the structure factor [12]

$$f(\mathbf{p} - \mathbf{q}) = \int d^3r \varphi(\mathbf{r}) \exp(i(\mathbf{p} - \mathbf{q})\mathbf{r}). \quad (16)$$

Assuming that the atom is spherically symmetric, we obtain the atomic factor in the form

$$f(\mathbf{s}) = \frac{2me^2 Z - f_p(s)}{\hbar^2 s^2}, \quad (17)$$

where the term proportional to the number of protons, Z , corresponds to scattering from the nucleus and the term $f_p(s)$, to scattering by the electron shells of the atoms. With an increase in s , the atomic-scattering factor rapidly decreases. Its absolute value equals $F(0) = 4.74\kappa$, $F(h_1) \approx 3\kappa\dots$, where $\kappa = 2.393 \times 10^{-8}$ cm [12]. The limitations of this approximation are considered in detail elsewhere [12]. The total wave function of the secondary electrons is the sum over all the i atoms in the s atomic waves $\mathbf{r}_j = Z_s \mathbf{e}_z - \mathbf{R}_i^s$, where \mathbf{e}_z is the unit vector normal to the crystal surface, Z_s is the depth of the location of the s th plane, and R_i^s is the coordinate of the i th atom in the s th plane.

The ideal surface structure of a hematite crystal is characterized by two vectors of the direct lattice, \mathbf{a}_1 and \mathbf{a}_2 (Fig. 1). Now, let the x -axis lie along the \mathbf{a}_1 vector. Then, the vectors of the two-dimensional direct and reciprocal lattices ($\mathbf{h}_{1,2}$) take the form

$$\mathbf{a}_1 = a(1, 0, 0), \quad \mathbf{a}_2 = a(\cos\alpha, \sin\alpha, 0),$$

$$\mathbf{h}_1 = \frac{2\pi}{a}(1, -\cot\alpha, 0), \quad \mathbf{h}_2 = \frac{2\pi}{a}(0, 1/\sin\alpha, 0). \quad (18)$$

Using the two-dimensional variant of the well-known summation rule,

$$\sum_i \exp(i(\mathbf{p}_t - \mathbf{q}_t)\mathbf{R}_i^s) = \frac{4\pi^2}{a^2} \sum_{j,k} \delta(\mathbf{p}_t - \mathbf{q}_t - \mathbf{H}_{jk}), \quad (19)$$

$$\mathbf{H}_{jk} = j\mathbf{h}_1 + k\mathbf{h}_2,$$

we can represent the wave function of photoelectrons scattered by all the atoms in the form

$$\psi_i^s(\mathbf{R}_0) = \sum_{jk} \exp(-i\mathbf{H}_{jk}\mathbf{R}_0) \times \int d^3p U_i B(p, t) \exp(i\mathbf{p}_t\mathbf{R}_0) F_{jk}(\mathbf{p}, R_0^z), \quad (20)$$

where

$$F_{jk}(\mathbf{p}; R_0^z) = \frac{4\pi^2}{a^2} \int dq_z \frac{\tau(p_z - q_z)}{q_z^2 + (\mathbf{p}_t - \mathbf{H}_{jk})^2 - k^2} \times \exp(i(q_z - p_z)R_0^z) f(\mathbf{H}_{jk}, p_z - q_z).$$

The function $\tau(p_z - q_z)$ describes the effective decrease of the contributions from deeply located atomic planes

$$\tau(p_z - q_z) = \sum_s \exp\left(-i(p_z - q_z)Z_s - \frac{Z_s}{L}\right), \quad (21)$$

where L is the free path, which for electrons with the energy ranging within 10–1000 eV is almost constant and equals several interatomic distances, and $L \approx 10$ Å. Thus, only several upper atomic planes actively participate in the signal formation.

With due regard for elastic scattering, the flux of electrons from the i th atom is the sum of the primary and the scattered waves [see (11) and (12)]

$$I_e \approx \Delta S \frac{\hbar}{m} \sum_i \int d^3p (\mathbf{n}\mathbf{p}) |U_i|^2 |B(p, t)|^2 |M(\mathbf{R}_0; \mathbf{p})|^2, \quad (22)$$

where

$$M(\mathbf{R}_0; \mathbf{p}) = 1 + \sum_{jk} \exp(-i\mathbf{H}_{jk}\mathbf{R}_0) F_{jk}(\mathbf{p}).$$

With due regard for the law of energy conservation, (9), integration of (22) over p_z yields

$$I_e \approx 2\pi t \sum_i \int d\mathbf{p}_t |U_i|^2 |M(\mathbf{R}_0; \mathbf{p}, k_z)|^2. \quad (23)$$

The above expression can be considered as the sum of three terms. The first term corresponds to the signal of the primary photoelectrons, (12), the second one, to the interference of the signals of the primary and scattered photoelectrons,

$$I_e^{0s} \approx 4\pi t \sum_i \int d\mathbf{p}_t |U_i(\mathbf{p}_t, k_z)|^2 \times \text{Re} \left\{ \sum_{jk} \exp(-i\mathbf{H}_{jk}\mathbf{R}_0) F_{jk}(\mathbf{p}_t, k_z; R_0^z) \right\}, \quad (24)$$

Reflections in order of their appearance

No.	\mathbf{H}	γ	Value of γ , eV	$\delta\varepsilon_{jk}$, eV
1	\mathbf{H}_{11}	$\sqrt{2(1 - \cos\alpha)}$	0.927	6.502
2	$\mathbf{h}_1, \mathbf{h}_2$	1	1	7.566
3	$\mathbf{H}_{21}, \mathbf{H}_{12}$	$\sqrt{5 - 4\cos\alpha}$	1.649	20.573
4	$\mathbf{H}_{1,-1}$	$\sqrt{2(1 + \cos\alpha)}$	1.77	23.704
5	\mathbf{H}_{22}	$2\sqrt{2(1 - \cos\alpha)}$	1.854	26.007

and the third one (which is almost always very small except for the region of the multibeam diffraction), to the interference of the secondary electrons.

Below, we consider only term (24), which is responsible for the formation of the holographic image of the crystal. It is convenient to represent this term in the form of a Fourier spectrum

$$I_e^{0s} \sim \text{Re} \left\{ \sum_{jk} \exp(-i\mathbf{H}_{jk}\mathbf{R}_0) g_{jk}(k) \right\}. \quad (25)$$

The contributions of individual harmonics depend on the parameters of the two-dimensional crystal lattice and the photon energy (k) in a complicated way,

$$g_{jk}(k) = \int_{|\mathbf{p}_t| < k} d\mathbf{p}_t |U_i(\mathbf{p}_t, k_z)|^2 F_{jk}(\mathbf{p}_t, k_z; R_0^z). \quad (26)$$

It should be indicated once more that the intensity of the holographic signal is proportional to the atomic scattering factor (and not to its squared value as in conventional scattering) because of the interference between the primary and the elastically scattered secondary waves.

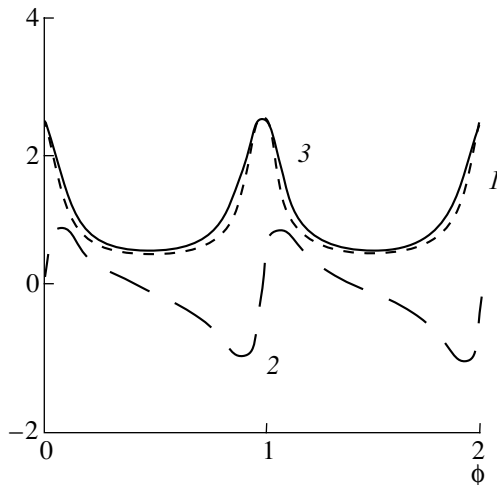


Fig. 2. (1) The real and (2) the imaginary parts of the function $\tau(\phi)$ and (3) its modulus as functions of $\phi = (p_z - q_z)a$.

With an increase in the energy of the synchrotron-radiation quantum, the wavelength of a photoelectron increases, which results in the excitation of the first reflections with the minimum \mathbf{H}_{jk} values. The threshold value of the energy providing the excitation of a given reflection is determined by the following expression:

$$\delta\varepsilon_{jk} = \hbar\omega_{jk} - E_{4s} = \frac{(\hbar\mathbf{H}_{jk})^2}{2m} \approx 7.566\gamma^2, \quad (27)$$

where $\gamma = H_{ika} \sin\alpha/2\pi$. The table indicates the calculated values of several reciprocal-lattice vectors and the corresponding energies of the synchrotron radiation.

It should be indicated that electrons from other levels (e.g., $3d$) are excited at much higher SR energies and, therefore, this contribution can be ignored.

Thus, for an iron atom, the difference in the energies of the $3d$ and $4s$ levels in the hydrogen-like approximation is about 500 eV ($E_{4s} = -574.6$ and $E_{3d} = -1021.5$ eV). At the same time, standard SR monochromators (e.g., multilayer or segmented mirrors [13]) possess the energy resolution

$$E/\delta E \approx 10^3,$$

sufficient for the formation of an SR beam with the energy width $\delta E \approx 0.5$ eV.

The structure of the photoelectron beam emitted by the crystal is determined by the ratio between the coefficients $g_{jk}(k)$ before individual harmonics, so the main problem is reduced to their correct calculation.

Ignoring the lattice relaxation near the surface ($a = \text{const}$), we arrive at the absorption coefficient in the form

$$\tau(p_z - q_z) \approx (1 - \exp(-(i(p_z - q_z) + 1/L)a))^{-1}. \quad (28)$$

This coefficient attains its maximum value,

$$C = \frac{1}{1 - \exp(-a/L)} \quad (29)$$

at $\phi = (p_z - q_z)a = 2\pi m$. The plots of the real and the imaginary parts of the function $\tau(\phi)$ and also of its modulus are shown in Fig. 2. In the limiting case of a large absorption length

$$\tau(p_z - q_z) \approx \frac{2\pi}{a} \sum_l \delta(p_z - q_z - H_l), \quad (30)$$

the integration over q_z in Eq. (20) presents no difficulties

$$F_{jk}^0(\mathbf{p}, R_0^z) = \frac{8\pi^2}{a^3} \sum_l \frac{f(\mathbf{H}_{jk}, 0)}{(p_z - H_l)^2 + (\mathbf{p}_t - \mathbf{H}_{jk})^2 - k^2}. \quad (31)$$

With due regard for the law of energy conservation ($p_z^2 + \mathbf{p}_t^2 = k^2$), the latter equation starts converging

with the approach to the Laue point of the given jk th reflection ($l = 0$),

$$(\mathbf{p}_l^L)^2 = (\mathbf{p}_l^L - \mathbf{H}_{jk})^2, \quad (32)$$

because Eq. (2) was obtained within the framework of perturbation theory (the Born approximation) invalid in the vicinity of the Laue point.

In this case, it would be expedient to use the two-beam Green's function obtained from the system of equations for dynamical diffraction as the basis for constructing the solution. However, this approach would considerably complicate the calculation of the photoelectron signal, because the well-known Green's functions can be used only within a narrow angular region in the vicinity of the Bragg angle, whereas the integration should be made within much wider limits. Nevertheless, if one uses approximation (30), the contribution to the intensity from an arbitrary harmonic equals

$$g_{jk}^0(k) = \frac{8\pi^3}{a^3} \int_{|p_l| < k} d\mathbf{p}_l |U_l(p_l, k_z)|^2 \frac{1}{(\mathbf{p}_l - \mathbf{H}_{jk})^2 - \mathbf{p}_l^2} f(\mathbf{H}_{jk}, 0), \quad (33)$$

and the integrand acquires a pole as soon as a region in the reciprocal space is formed in which Laue condition (32) is fulfilled. Such a region can be formed only if some photoelectrons have pulses exceeding half of the reciprocal lattice vector, $2p_l > H$.

The analytical expressions for the coefficients $g_{jk}^0(k)$ can be obtained in the approximation taking into account the finite free path (28). As is shown in the Appendix, the first term of the asymptotic series for the coefficient (27) in the far wave zone has the form

$$g_{10}(k) \sim \mu(k) \frac{e_x^2}{(R_0^z)^{5/2}} \exp(i\sqrt{H(2k-H)}R_0^z), \quad (34)$$

where

$$\mu(k) = -D(k) \frac{28\pi^3}{a^2} \tau(0) f(H, 0) \frac{k^{3/2}}{2H^{3/4} (2k-H)^{1/4}}. \quad (35)$$

For further calculations, it is convenient to represent the contribution from an individual harmonic to a hologram as a product of the amplitude ($G_{jk}(k) = |g_{jk}(k)|$) and the phase terms

$$I_e^{0s} \sim \sum_{jk} \cos(\mathbf{H}_{jk} \mathbf{R}_0 + \sqrt{H_{jk}(2k-H_{jk})} R_0^z) G_{jk}(k). \quad (36)$$

We should like to emphasize the importance of the use of monochromatic synchrotron radiation. If it were not used the holographic signal would be suppressed by the destructive interference of the waves excited by photons with various energies k .

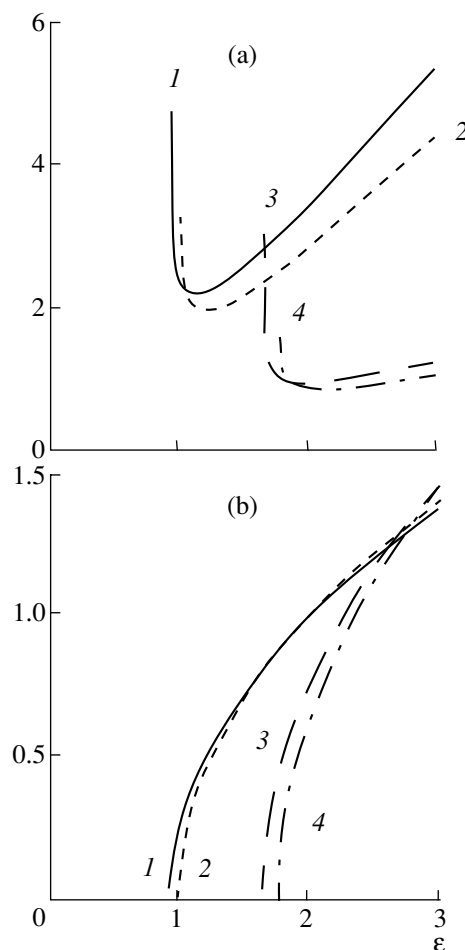


Fig. 3. (a) Modulus of G_{jk} and (b) the phase factor $\sqrt{H_{jk}(2k-H_{jk})}$ as functions of $\epsilon = 2k/h$ for the coefficients before the first four harmonics.

Figure 3 shows the amplitude G_{jk} and the phase term $\sqrt{H_{jk}(2k-H_{jk})}$ as functions of $\epsilon = 2k/h$ for the first four harmonics. The curve number corresponds to the reflection number in the table. A reflection can take an active part in the formation of the hologram only if $\epsilon > \gamma_i = 2H_i/h$ (see table).

Figure 4 shows a number of holographic images for different energies of an SR beam calculated by formulas (34) and (36). Each of the holograms formed upon the first one corresponds to the SR energy slightly exceeding the threshold energy $\epsilon_i = 2k/h = \gamma_i + 0.05$, $i = 1-4$.

Upon the attainment of the threshold photon energy, the number of reflections increases in a jumpwise manner (see table): \mathbf{H}_{11} (Fig. 4a); $\mathbf{H}_{11}, \mathbf{h}_1$ (Fig. 4b); $\mathbf{H}_{11}, \mathbf{h}_1, \mathbf{H}_{21},$ and \mathbf{H}_{12} (Fig. 4c) and $\mathbf{H}_{11}, \mathbf{h}_1, \mathbf{H}_{21}, \mathbf{H}_{12},$ and $\mathbf{H}_{1,-1}$ (Fig. 4d). It was assumed that the wave vector of the synchrotron radiation and the surface normal formed an angle of 45° and that it was projected onto

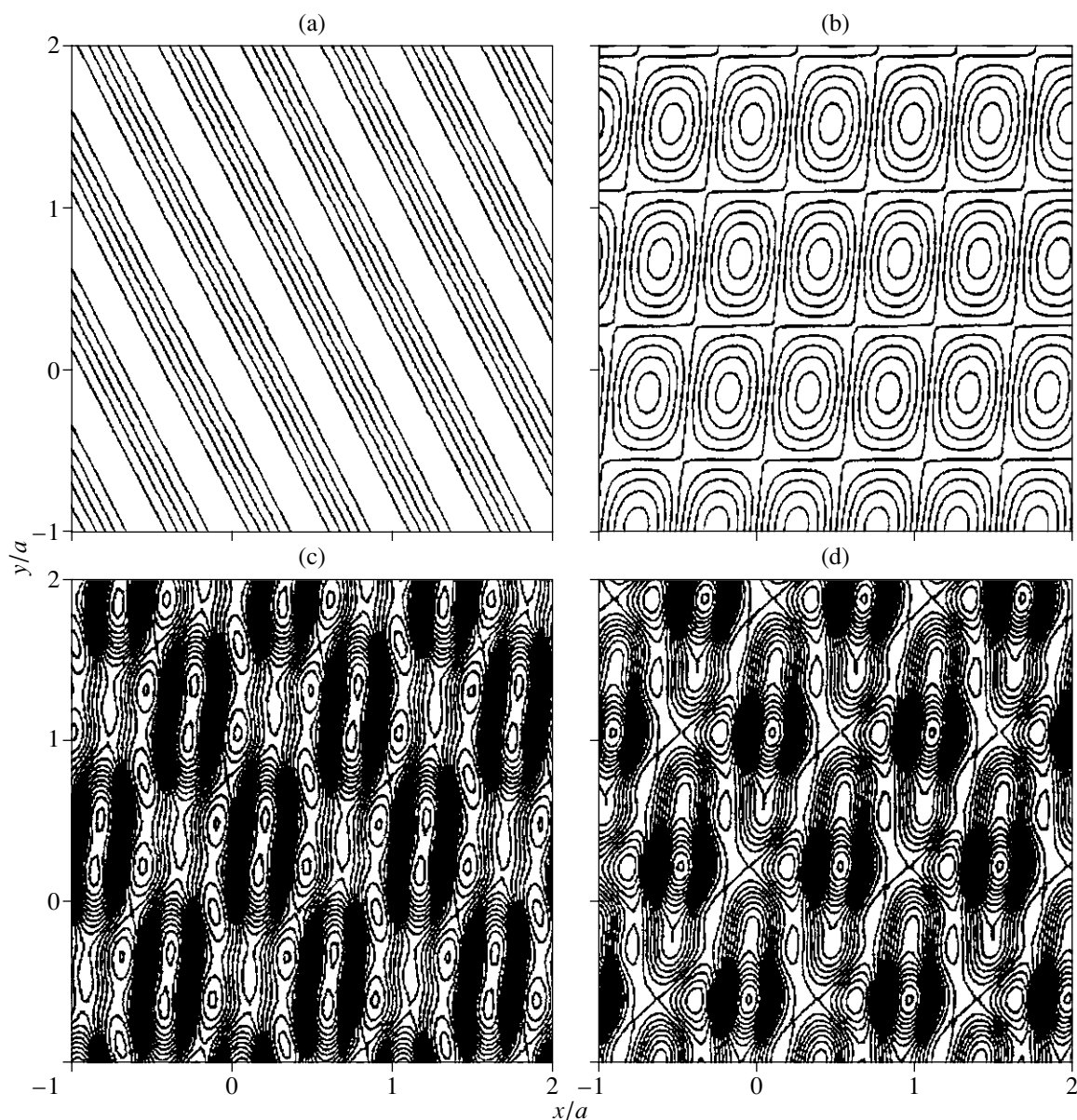


Fig. 4. Calculated holographic images at different energies of the synchrotron radiation.

the surface along the direction of the vector \mathbf{a}_1 , whereas the crystal–detector distance was equal to $R_0^z = 10^5 a$. The polarization vector of the synchrotron radiation is $\mathbf{e} = \frac{1}{\sqrt{2}}(1, 0, -1)$. The polarization of the synchrotron radiation prevents the harmonic corresponding to vector \mathbf{h}_2 from participating in the hologram formation.

Usually, the SR used in the experiments is both monochromatized and linearly polarized. Rotating the specimen around the beam, it is possible to vary the contribution of each harmonic \mathbf{H} because of the change of the factor $(\mathbf{eH})^2/H^2$.

When considering the experimental schemes, one has to take into account the finite dimensions of both specimen and incident beam. As a result, the diffracted photoelectron beams corresponding to different diffraction vectors diverge in the space, and the interference pattern is formed only in the region of their intersection. However, considering only the problem of the precise determination of the lattice parameter along a certain crystallographic direction, one can examine only the “striped” hologram formed from only one reflection (Fig. 4a).

Moreover, the record of complicated holograms is rather time-consuming, even if powerful SR sources and position-sensitive detectors are used.

CONCLUSION

In terms of physics, all the holographic methods are based on the well-known phenomenon of interference of the primary wave and the waves elastically scattered by ordered atoms in a crystal. In practice, atomic holography can be used for extracting structural information in the case of relatively weak scattering.

Most probably, photoelectron beams cannot compete with the modern technologies used in optics and fiber optics to transfer information. However, we believe that the use of photoelectrons in scientific experiments is promising because of the extremely high sensitivity of low-energy electron beams transmitted by crystalline objects to their structures. Moreover, in recent decades, we have seen the rapid development of efficient methods for electron beam control (enlargement, focusing, etc.) and the transformation of electron images into corresponding analogous and digital optical images, which gives us hope for the further successful development of combined holographic methods.

The small escape depth of photoelectrons allows one to record a signal from the subsurface region, where the lattice is often rather distorted by relaxation and surface reconstruction. While the method of X-ray standing waves allows the determination of distances with an accuracy of 0.1% of the interplanar spacing along the surface normal, the photoelectron hologram allows the determination of the lattice periodicity in the surface plane.

Photoelectron holography can be used not only in studies of crystal structures, but also in studies of objects with dimensions not exceeding several nanometers. If one places any noncrystalline object or an object possessing lattice parameters different from those of the crystal, the hologram preserves its periodic structure, but the region coated by this object is considerably shadowed. This can be efficiently used for visualizing the structures of complex objects such as Langmuir–Blodgett films and films of other organic materials.

Thus, the main advantages of photoelectron holography in the case of photoelectron excitation by SR beams are:

—the possibility of analyzing the distribution of electrons of a certain level because of high coherency and monochromaticity of highly polarized SR beams;

—the dependence of the number of reflections forming holograms on the energy of an SR beam;

—the possibility of determining the structure of crystal surfaces.

APPENDIX

CALCULATION OF CONTRIBUTIONS FROM INDIVIDUAL HARMONICS

In fact, this Appendix deals with the calculation of integral (27). As an example, consider the coefficient before the harmonic with \mathbf{H}_{10} .

The integrand in the expression for $F_{jk}(\mathbf{p}_t, k_z; R_0^z)$

$$F_{10}(\mathbf{p}_t, k_z; R_0^z) = \frac{4\pi^2}{a^2} \int dq_z \frac{\tau(k_z - q_z) f(\mathbf{H}, k_z - q_z)}{q_z^2 + (\mathbf{p}_t - \mathbf{H})^2 - k^2} \exp(i(q_z - k_z)R_0^z) \quad (\text{A.1})$$

includes with the pole points $q_z^{1,2} = \pm \kappa$, $\kappa = \sqrt{k^2 - (\mathbf{p}_t - \mathbf{H})^2}$ formed due to the singularities of the Green's function and $q_z^{3,4} = k_z \pm H$ associated with the form of the atomic scattering factor. Formally, the last two points arise because of scattering from a single atom accompanying the U-processes and thus have no physical meaning.

Also, one has necessarily to take into account the contribution from the function τ . One can readily see that one of the best approximations of this function in the vicinity of the maximum ($q_z \approx k_z$) is

$$\tau(q_z - k_z) = \frac{1}{1 - \exp(2\pi i(q_z - k_z)a - 0.5)} \approx \tau_m - \frac{0.15i}{a(q_z - k_z - i0.08/a)}, \quad (\text{A.2})$$

where $\tau_m = 0.622$ is the minimum value of the initial function. In this approximation, the function τ acquires a pole, $q_z^5 = k_z + i0.08/a$.

Integration upon the closure of the integration contour with respect to q_z around the poles q_z^1 and q_z^5 yields

$$F_{10}(\mathbf{p}_t, k_z; R_0^z) = \frac{8\pi^3 i}{a^2 \kappa} \left\{ \exp(-i(k_z - \kappa)R_0^z) \times \tau(k_z - \kappa) \frac{f(\mathbf{H}, \kappa - q_z)}{2\kappa} - \frac{0.15i}{a} \exp(-0.08R_0^z/a) \times \frac{f(\mathbf{H}, i0.08/a)}{(k_z + i0.08/a)^2 + (\mathbf{p}_t - \mathbf{H})^2 - k^2} \right\}. \quad (\text{A.3})$$

Obviously, the exponential factor before the second term in (A.3) levels its contribution, because the detector–crystal distance usually exceeds the interatomic distance by several orders of magnitude.

Below, we consider only the contribution from the pole point of the Green's function. Since the value k is

fixed, some factors in Eq. (26) can be taken outside the integral

$$g_{10}(k) = D(k)^2 \int_0^k dp_x \int_{-p^*}^{p^*} dp_y \exp(-ibR_0^z) \Gamma(p_x, p_y), \quad (\text{A.4})$$

$$\Gamma(p_x, p_y) = \frac{4\pi^3 i}{a^2 \kappa} (e_x p_x + e_y p_y + e_z k_z)^2 \tau(b) f(\mathbf{H}, \kappa - q_z),$$

where $p^* = \sqrt{k^2 - p_x^2}$, $b = k_z - \kappa$. It should be indicated that, formally, the limits of integration with respect to $p_{x,y}$ range from minus to plus infinity, but, in fact, they are limited to a circle of radius k beyond which the function $k_z - \kappa$ becomes complex.

The expression

$$\begin{aligned} b &= k_z - \kappa \\ &= \sqrt{k^2 - p_x^2 - p_y^2} - \sqrt{k^2 - (p_x - H)^2 - p_y^2} \end{aligned} \quad (\text{A.5})$$

can go to zero at the Laue point ($2p_x^* = H$) if $2k > H$. The first and second derivatives of b with respect to p^x also go to zero at the same point, which does not allow the use of the saddle-point method to calculate an integral with a high value of the phase factor ($R_0^z \rightarrow \infty$). However, a high value of the phase factor allows one to represent the integrals as expansions in the degrees of $(R_0^z)^{-N}$,

$$\begin{aligned} I &= \int_{-p^*}^{p^*} dp_y \exp(-ibR_0^z) \Gamma(p_y) \\ &= \sum_{k=0}^N (iR_0^z)^{-k-1} \left\{ \frac{-1}{b'(p_y)} \frac{d}{dp_y} \right\}^k \frac{\Gamma(p_y)}{b'(p_y)} \\ &\quad \times \exp(-ibR_0^z) \Big|_{-p^*}^{p^*} + o(R_0^{-N}). \end{aligned} \quad (\text{A.6})$$

Here, we limit our consideration to the first nonvanishing term of this series ($\sim R_0^{-2}$), although, in order to increase the accuracy, one has to take into account the following terms [14]. The calculations with the use of the first term of the expansion yield zero because of

$$\lim_{p_y \rightarrow p^*} \frac{1}{p^* b'(p_y)} = 0$$

and, therefore, one has to take into account the second term as well

$$\begin{aligned} I &\approx \frac{1}{(R_0^z)^2 p^* a^2 b^*} \frac{32\pi^3 i}{a^2 b^*} \tau(b^*) f(H, b^*) (\Gamma_1 + \Gamma_2) \\ &\quad \times \exp(ib^* R_0^z), \end{aligned} \quad (\text{A.7})$$

where

$$\begin{aligned} b^* &\equiv b(p_x, p^*) = \sqrt{H(2p_x - H)}, \\ \Gamma_1 &= e_x^2 p_x^2 / p^*, \quad \Gamma_2 = e_y^2 p^*. \end{aligned} \quad (\text{A.8})$$

One can readily see that the integration of the expression containing Γ_2 with respect to dp_x yields zero. At the same time, the integral of Γ_1 diverges with an approach of p_x to k . Using the Erdélyi lemma [14], this integral with the diverging integrand can be evaluated by the expression

$$\int_0^a x^{\beta-1} f(x) \exp(i\lambda x^\alpha) dx \sim \sum_{k=0}^{\infty} a_k \lambda^{\frac{k+\beta}{\alpha}} \quad (\text{A.9})$$

at $\lambda \rightarrow \infty$, where

$$a_k = \frac{f^{(k)}(0)}{k! \alpha} \Gamma\left(\frac{k+\beta}{\alpha}\right) \exp\left(\frac{i\pi(k+\beta)}{2\alpha}\right). \quad (\text{A.10})$$

Using an indefinite integral, we substitute the expression

$$\frac{1}{b^*} \exp(ib^* R_0^z) = i \int \exp(ib^* R_0^z) dR_0^z$$

into expression (A.7).

The major contribution to the integral with respect to p_x

$$g_{10}(k) = -iD(k)^2 \frac{16\pi^3 i}{a^2} \frac{e_x^2}{(R_0^z)^2} \quad (\text{A.11})$$

$$\times \int_0^k dR_0^z \int dp_x \frac{p_x^2}{p^*} \tau(b^*) f(H, b^*) \exp(ib^* R_0^z)$$

comes from the region $p_x \sim k$, where $\beta = 1/2$ and $\alpha = 1$,

$$f \sim \frac{k^{3/2}}{\sqrt{2}} \tau(0) f(\mathbf{H}, 0) \exp(i\sqrt{H(2k-H)} R_0^z) \exp(i\lambda p_x), \quad (\text{A.12})$$

$$\lambda = \frac{2\sqrt{HR_0^z}}{\sqrt{2k-H}}.$$

Thus, the first term of expansion (A.9) yields the following expression for the coefficient before the harmonic:

$$\begin{aligned} g_{10}(k) &\sim -\frac{e_x^2}{(R_0^z)^2} D(k)^2 \frac{8\pi^3}{a^2} k^{3/2} \tau(0) f(\mathbf{H}, 0) \\ &\quad \times \left\{ \frac{2k-H}{16H} \right\}^{1/4} L(R_0^z, 2k-H), \end{aligned} \quad (\text{A.13})$$

where

$$L(R_0^z, 2k - H) = \int dR_0^z \frac{1}{\sqrt{R_0^z}} \exp(i\sqrt{H(2k - H)}R_0^z).$$

At $2k - H \neq 0$, let the infinite integral determining L can be represented as an expansion in degrees of $(R_0^z)^{-k-1/2}$. The first term of this expansion yields

$$L(R_0^z, 2k - H) \sim \frac{1}{\sqrt{H(2k - H)}R_0^z} \exp(i\sqrt{H(2k - H)}R_0^z). \quad (\text{A.14})$$

Finally, we have

$$g_{10}(k) \sim \mu(k) \frac{e_x^2}{(R_0^z)^{5/2}} \exp(i\sqrt{H(2k - H)}R_0^z), \quad (\text{A.15})$$

where

$$\mu(k) = -D(k) \frac{28\pi^3}{a^2} \tau(0) f(\mathbf{H}, 0) \frac{k^{3/2}}{2H^{3/4} (2k - H)^{1/4}}. \quad (\text{A.16})$$

Obviously, if the Laue condition ($2k > H$) is not fulfilled, $g_{10}(k)$ decreases with an increase in the crystal-detector distance R_0^z . If the Laue condition is met at least in a part of the space, the coefficient decreases proportionally to

$$(2k - H)^{-1/4}$$

with an increase in the photon energy.

Formally, the divergence of the result obtained at $2k = H$ is associated with the form of the Green's function used.

The contribution from the given reflection is maximal, if the polarization vector of the incident radiation is parallel to the reciprocal-lattice vector ($e_x = (\mathbf{eH})/H = 1$).

One should pay attention to an unusual dependence of the signal intensity on the detector-object distance, $(R_0^z)^{-5/2}$. For comparison, for a point source the signal intensity is $I \sim (R_0^z)^{-2}$.

REFERENCES

1. D. Gabor, *Nature* **161**, 777 (1948).
2. E. Wolf, *Opt. Commun.* **1**, 153 (1969).
3. J. M. Cowley, *Diffraction Physics* (Elsevier, New York, 1975; Mir, Moscow, 1979).
4. A. L. Danishevskii and F. N. Chukhovskii, *Kristallografiya* **27**, 668 (1982) [*Sov. Phys. Crystallogr.* **27**, 401 (1982)].
5. J. J. Barton, *Phys. Rev. Lett.* **61**, 1356 (1988).
6. D. K. Saldin, G. R. Harp, B. L. Chen, and B. P. Tonner, *Phys. Rev. B* **44**, 2480 (1991).
7. L. J. Terminello, J. J. Barton, and D. A. Lapiano-Smith, *Phys. Rev. Lett.* **70**, 599 (1993).
8. J. M. Cowley and A. F. Moodie, *Acta Crystallogr.* **10**, 609 (1957).
9. B. Adams, D. V. Novikov, T. Hiort, and G. Materlik, *Phys. Rev. B* **57**, 7526 (1998).
10. B. Feuerbacher and B. Fitton, in *Electron Spectroscopy for Surface Analysis*, Ed. by H. Ibach (Springer-Verlag, Berlin, 1977), p. 151.
11. S. Flugge, *Practical Quantum Mechanics* (Springer-Verlag, Berlin, 1971; Mir, Moscow, 1974).
12. B. K. Vainshtein, *Structure Analysis by Electron Diffraction* (Akad. Nauk SSSR, Moscow, 1956; Pergamon, Oxford, 1964).
13. A. V. Vinogradov, *Mirror X-ray Optics* (Mashinostroenie, Leningrad, 1989).
14. M. V. Fedoryuk, *Asymptotics: Integrals and Series* (Nauka, Moscow, 1987).

Translated by L. Man

DIFFRACTION AND SCATTERING OF X-RAY AND SYNCHROTRON RADIATION

X-ray Focusing by Bent Crystals in Bragg Backscattering

T. Tchen

Lomonosov Academy of Fine Chemical Technology,
pr. Vernadskogo 86, Moscow, 117571 Russia
e-mail: docent65@mtu-ten.ru, ttchen@e-mail.ru

Received July 27, 2001

Abstract—Focusing of a spherical X-ray wave in Bragg backscattering from weakly and strongly bent crystals is considered theoretically. The analytical formula describing the dimensions of the diffraction backscattering region is obtained. It is shown that, along with the well-known Johann scheme, the use of the backscattering scheme allows one to increase the aperture ratio of the crystal optics by two to three orders of magnitude. The spectral characteristics of bent crystals providing diffraction backscattering ($\theta = \pi/2$) are discussed. It is shown that the spectral resolution can attain a value of the order of 10^{-11} . © 2002 MAIK “Nauka/Interperiodica”.

Backscattering of the X-ray radiation occurring at the diffraction angle $\theta \cong \pi/2$ has some specific features that distinguish it from conventional diffraction at $\theta < \pi/2$. The width of the dynamic curve of the Bragg reflection equals $2\Delta\theta = 2|\chi_{hr}|^{1/2} \sim 10^{-2}\text{--}10^{-3}$ [1–4], which allows an increase in the aperture ratio of an optical device by two to three orders of magnitude. The use of bent crystals focusing an X-ray beam in one or two dimensions allows an increase in the aperture ratio of several orders of magnitude. Moreover, as was shown in [5], backscattering also provides the minimization of the geometrical aberration of the diffracted beam. The well-known Johann focusing scheme [6] in which both radiation source and detector are located on the Rowland circle is widely used also because of its high aperture ratio. Johann focusing was repeatedly studied [7–11]. The best possibilities for obtaining a high aperture ratio are provided by the Johann and the backscattering schemes. Theoretically, the upper limit of the aperture ratio in both schemes is attained with the aid of biaxially bent crystals. The results obtained in [5] show that the aperture ratio of a biaxially bent X-ray lens is proportional to

$$\Omega = 4 \sin \theta x_{\text{eff}} y_{\text{eff}} / L_0^2,$$

where

$$x_{\text{eff}} = L_0 \Delta\theta / |\sin \theta - L_0 / R_x|, \\ y_{\text{eff}} = L_0 \left| 2\Delta\theta \cos \theta / (\sin \theta - L_0 (1 + \sin^2 \theta) / R_y) \right|^{1/2}, \quad (1)$$

$\Delta\theta$ is the halfwidth of the Bragg reflection curve, L_0 is the distance between the source of a spherical X-ray wave and the crystal, and R_x and R_y are the curvature radii of the crystal in the meridional and the sagittal planes, respectively. The formula for x_{eff} was obtained under the assumption that $L_0 \neq R_x \sin \theta$. It is seen from Eq. (1) that at $\theta \neq \pi/2$, the beam divergence in the sag-

ittal plane can exceed the divergence in the meridional plane by two to three orders of magnitude because $y_{\text{eff}} \sim (\Delta\theta)^{1/2} \sim |\chi_{hr}|^{1/2}$. For backscattering, the substitution of $\cos \theta \sim \theta$ into Eq. (1) yields $y_{\text{eff}} \sim \Delta\theta \leq |\chi_{hr}|^{1/2}$. An additional increase in the aperture ratio can be attained by biaxial bending of the crystal with the curvature radii $R_x \sim R_y$.

Below, we consider one-dimensional focusing of a spherically divergent X-ray beam in its backscattering by weakly or strongly bent crystals. The crystals are assumed to be bent in the meridional plane. The results obtained can readily be extended to biaxial bending by using the theory of two-dimensional focusing developed in our earlier work [12]. The multibeam effects accompanying backscattering [13] are ignored.

REGION OF DIFFRACTION REFLECTION IN BACKSCATTERING

In this section, the Bragg diffraction reflection of a spherical X-ray wave by a bent crystal is considered in the geometrical-optical approach of radiation propagation. Earlier [5], we considered in a similar way the Bragg diffraction of an X-ray beam reflected from a biaxially bent crystal [5] at the diffraction angles $\theta \neq \pi/2$.

Let a spherical X-ray wave from a point source S be incident onto a cylindrically bent crystal at the Bragg angle θ . Upon diffraction from the crystal, the X-ray radiation is focused into a line normal to the diffraction scattering plane intersecting this plane at the point S' . The scheme of focusing of an X-ray beam reflected in the backward direction by uniaxially bent crystal is shown in Fig. 1.

For the sake of simplicity, we limit our consideration to the symmetric diffraction. At the Bragg angles $\theta \neq \pi/2$, the size x_{eff} of the region on the crystal surface where the diffracted beam is within the boundary of the

region of total reflection is the solution of the quadratic equation

$$\begin{aligned} \Delta\theta = & | -x_{\text{eff}}/R_x + x_{\text{eff}} \sin\theta/L_0 \\ & - x_{\text{eff}}^2(2\sin^2\theta - 1)/2R_x L_0 \cos\theta \\ & - x_{\text{eff}}^2 \sin\theta \cos\theta/L_0^2 + x_{\text{eff}}^2 \sin\theta/2R_x^2 \cos\theta \\ & + x_{\text{eff}}^2 \sin^2\theta(\sin\theta - L_0/R_x)/2L_0^2 \cos\theta|. \end{aligned} \quad (2)$$

If $L_0 \neq R_x \sin\theta$, the spherical aberration can be ignored and the terms proportional to x^2 in Eq. (2) can be rejected. Then Eq. (2) yields an equation linear with respect to x_{eff} which, in turn, yields Eq. (1).

For the Johann scheme, Eq. (2) yields

$$\begin{aligned} x_{\text{eff, Johann}} = & R_x(2\Delta\theta \tan\theta)^{1/2}, \\ L_0 = & R_x \sin\theta, \quad \theta \neq \pi/2. \end{aligned} \quad (3)$$

Here, $\Delta\theta = |\chi_{hr}|/\sin 2\theta$ is the angular halfwidth of the region of total reflection (the Bragg reflection curve), χ_{hr} is the real part of the Fourier-component of X-ray polarizability, and R_x is the curvature radius of the crystal in the meridional plane (the diffraction reflection plane).

In backscattering, x_{eff} and $\Delta\theta$ are related as

$$\begin{aligned} \Delta\theta_{\pi/2} = & x_{\text{eff}}[(1/R_x)^2 + (1/L_0)^2 + (2/R_x L_0) \\ & + x_{\text{eff}}^2(1/2R_x^2 L_0^2 - 1/R_x^3 L_0 - 3/4L_0^4 - 3/4R_x^4)]^{1/2}. \end{aligned} \quad (4)$$

If a plane wave is incident onto a crystal ($L_0 \gg R_x$), Eq. (4) yields the angular halfwidth of the reflection curve in the form

$$\Delta\theta_{\pi/2} = x_{\text{eff}}(1 - 3x_{\text{eff}}^2/4R_x^2)^{1/2}/R_x. \quad (5)$$

It follows from (5) that if $x_{\text{eff}} \ll R_x$, then the size of the diffraction-reflection region in the reflection of the plane wave in the backward direction ($\theta \cong \pi/2$) is

$$x_{\text{eff}} \approx R_x \Delta\theta_{\pi/2} \cong R_x |\chi_{hr}|^{1/2}. \quad (6)$$

If a source of the spherical wave is located at a distance $L_0 = R_x$ from the crystal, Eq. (4) yields

$$\Delta\theta_{\pi/2} = 2x_{\text{eff}}(1 - x_{\text{eff}}^2/2R_x^2)/R_x. \quad (7)$$

Taking into account that $x_{\text{eff}}/R_x \ll 1$, we obtain from Eq. (7)

$$x_{\text{eff}} \approx R_x |\chi_{hr}|^{1/2}/2. \quad (8)$$

Expressions (3), (6), and (8) show that the Johann and the backscattering schemes provide the gain in the aperture ratio exceeding by two to three orders of magnitude the gain provided by all the other focusing schemes. It should also be indicated that, when deriving Eq. (4), we took into account only the terms up to the

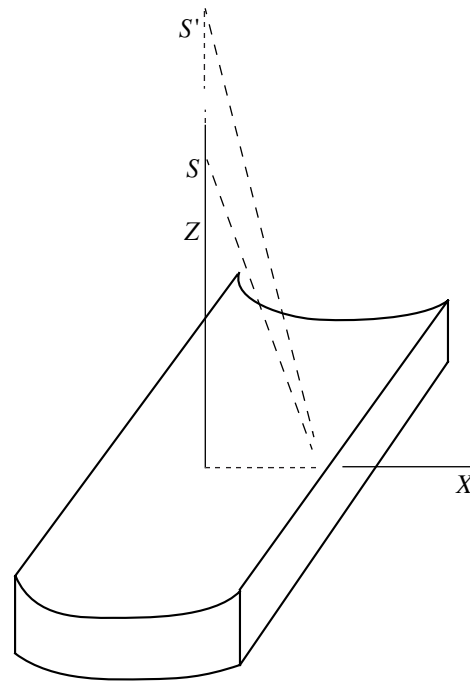


Fig. 1. Principal scheme for the focusing of a spherical back-scattered wave by a cylindrically bent crystal. S is a point source and S' is its image.

fourth order with respect to x . Moreover, we also assumed that $x_{\text{eff}}/R_x \ll 1$.

FOCUSING OF SPHERICAL AND PLANE WAVES IN BACKSCATTERING FROM A WEAKLY BENT CRYSTAL

Consider a crystal weakly bent in the meridional plane so that the dimensionless bending parameter $|v| \gg 1$ (see, e.g., [12]). In the dynamical focusing of a spherical X-ray wave by a weakly bent crystal, the intensity in the focus is distributed by the law

$$\begin{aligned} I_h(\xi_p) = & |E_h(\xi_p)|^2 \sim |J_1(\pi\Delta\xi_p^{-1}\xi_p)/\pi\Delta\xi_p^{-1}\xi_p|^2, \\ L_0 \neq & R_x \sin\theta, \end{aligned} \quad (9)$$

where ξ_p is the coordinate of the point of the source image in the transverse direction, J_1 is the first-order Bessel function of the real argument, and $\Delta\xi_p$ is the diffraction broadening of the focus.

Equation (9) was obtained under the assumption that the phase of an incident spherical wave is expanded into a series in powers of x/L_0 (up to the second-order terms). The use of the parabolic expansion of the wave phase at $L_0 \neq R_x \sin\theta$ signifies that the spherical aberration is ignored. However, in the Johann scheme, one has also to take into account the terms $\sim x^3$, which results in the redistribution of the intensity in the form of the squared modulus of the Airy function [14].

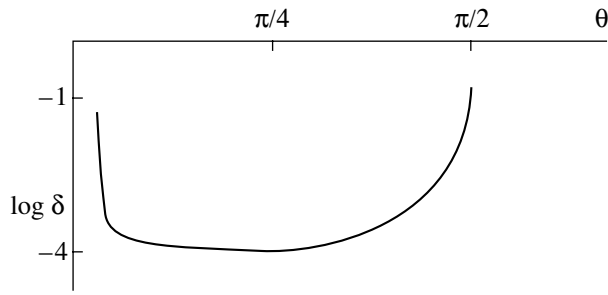


Fig. 2. Logarithm of the shift δ as a function of the diffraction angle θ . Si (111), $\lambda = 1.55 \text{ \AA}$ ($\theta = 14.31^\circ$), $\chi_{or} = -1.533 \times 10^{-5}$, $\chi_{hr} = -7.992 \times 10^{-6}$, $T/R_z = 10^{-4}$.

According to [12], the diffraction broadening of the focus in Eq. (9) is

$$\Delta\xi_p = |1 - L_h/R_x \sin\theta| \Lambda \cos\theta, \quad (10)$$

$$L_h \neq R_x \sin\theta,$$

where L_h is the crystal-image distance, $\Lambda = \lambda \sin\theta / (|C| |\chi_{hr}|)$ is the extinction length in the symmetric case, λ is the wavelength of the incident radiation, and $C = \pm 1$ (for $\theta = \pi/2$) is the polarization factor.

In the backscattering of a spherical wave, the diffraction broadening of the focus is $\Delta\xi_p \leq |1 - L_h/R_x| \Lambda (|\chi_{hr}| + |\Delta\lambda/\lambda|)^{1/2}$, where $\Delta\lambda/\lambda$ takes into account the nonchromaticity of the incident wave.

The source-crystal, L_0 , and the crystal-image, L_h , distances for a point source satisfy the modified equation of an X-ray lens [11],

$$\frac{1}{L_0} + \frac{1}{L_h} = 2[(1 + \chi_{or}/2 \sin^2\theta)/(1 + T/2R_z)]/R_x \sin\theta, \quad (11)$$

where T is the crystal thickness and R_z is determined by the components of the inverse elastic-modulus tensor [11]. The corrections in the right-hand side of Eq. (11) take into account the radiation refracted by the crystal-vacuum interface and the change in the interplanar spacing in the crystal depth. These corrections give, in fact, very small ($\sim 10^{-5}$ – 10^{-4}) contributions and, therefore, can be ignored in most of the cases of practical interest.

If a plane wave is reflected from a crystal, the diffraction broadening of the focus equals $\Delta\xi_p = \Lambda \cos\theta/2$. In backscattering, $\cos\theta \approx \cos(\pi/2) + \sin\theta\Delta\theta \approx \Delta\theta \leq (|\chi_{hr}| + |\Delta\lambda/\lambda|)^{1/2}$, i.e., the diffraction broadening of the focus equals

$$\Delta\xi_p \leq \lambda (|\chi_{hr}| + |\Delta\lambda/\lambda|)^{1/2} / 2 |C| |\chi_{hr}|. \quad (12)$$

If an incident wave is highly monochromatic ($|\Delta\lambda/\lambda| \ll |\chi_{hr}|$), Eq. (12) yields $\Delta\xi_p \leq \lambda/2 |C| |\chi_{hr}|^{1/2}$. In the reflection of the MoK α radiation from the Si(444) plane, the focus size equals $\Delta\xi_p \approx 0.037 \mu\text{m}$.

ANGULAR SHIFT OF THE BRAGG MAXIMUM IN BACKSCATTERING FROM A BENT CRYSTAL

It is well known [15] that, because of refraction, the Bragg angles in a vacuum and in a crystal are different. The shift of the Bragg angle equals $\chi_{or}/\sin 2\theta$. In the Bragg reflection from a bent crystal, crystal bending gives rise to an additional shift of the maximum of the reflection curve [11]. This shift is essential in two limiting instances: at $\theta \rightarrow 0$ and $\theta \rightarrow \pi/2$ (Fig. 2). In the case of the backscattering we are interested in, the angular shift equals

$$\delta \cong (T/R_z - \chi_{or})/2 |\chi_{hr}|^{1/2}. \quad (13)$$

At the same values of T , χ_{or} , and χ_{hr} as in [11], we obtain from formula (13) that $\delta \leq 10^{-2}$ – 10^{-1} ; in other words, the shift exceeds the width of the reflection curve. To decrease the shift of the Bragg angle, one has to use thin crystals with a thickness satisfying the conditions $T \approx R_z \chi_{or}$, whence it follows that, for bent crystals, the shift can be less than for a plane crystal.

It is seen from (13) that this shift becomes essential if $T/R_z \geq 10^{-4}$ and its order of magnitude considerably differs from that of χ_{or} or else for thin crystals where $T/R_z \ll \chi_{or}$.

FOCUSING SPECTROMETER IN BACKSCATTERING FROM A WEAKLY BENT CRYSTAL

Consider the spectral properties of a weakly bent crystal at $\theta = \pi/2$. The linear dispersion D_ξ is

$$D_\xi = d\xi_p/d\lambda \cong (L_0 - L_h)d\theta/d\lambda. \quad (14)$$

Using (10), we obtain for the spectral resolution

$$\begin{aligned} d\lambda/\lambda &= \Delta\xi_p \cos\theta / (L_0 - L_h) \sin\theta \\ &\cong |1 - L_h/R_x \sin\theta| \lambda (\Delta\theta)^2 / |C| |\chi_{hr}| (L_0 - L_h) \sin\theta \\ &\cong |1 - L_h/R_x| \lambda / |C| (L_0 - L_h), \\ &L_0 \neq L_h. \end{aligned} \quad (15)$$

Diffraction reflection is coherent for the sources with the angular dimensions $\varphi \approx a/L_0 < \lambda/x_{\text{eff}}$. Therefore, Eq. (15) is valid for the sources of the size $a \leq L_0/x_{\text{eff}}$. If $a > L_0\lambda/x_{\text{eff}}$, the quantity $\Delta\xi_p$ in Eq. (15) should be replaced by $\Delta\xi_p + L_0\lambda/x_{\text{eff}}$.

At $L_h \ll R_x \sin\theta$, the spectral resolution described by Eq. (15) is dependent on the Bragg angle θ and $d\lambda(\theta)/\lambda \sim f(\theta) = (1 + \cos 2\theta)/2 \sin\theta$ and decreases with an increase in θ (Fig. 3). Under the assumption that $L_0 \gg R_x$, we arrive at the following theoretical estimate of the spectral resolution for a plane incident wave:

$$d\lambda/\lambda \sim \lambda/2 |C| L_0. \quad (16)$$

The theoretical limit of the spectral resolution (16) in backscattering of the CuK_α radiation ($\lambda = 1.54 \text{ \AA}$) from a bent silicon crystal with the curvature radius $R_x = 1 \text{ m}$ and $L_0 = 10 \text{ m}$ attains the value of $d\lambda/\lambda \sim 10^{-11}$. This estimate is better by three orders of magnitude than for a Johann–Hamós focusing spectrometer [12].

It should be noted that the spectral resolution described by (16) is independent of χ_{hr} and is the same for both (σ and π) polarizations of the X-ray radiations.

The degree of the monochromaticity of the back-scattered wave equals

$$\Delta\lambda/\lambda \leq \cot\theta\Delta\theta \equiv (\Delta\theta)^2 \leq \chi_{hr}. \quad (17)$$

Estimate (17) for $\Delta\lambda/\lambda$ can also be obtained under the assumption that the coherency length is $L_{\text{coh}} = \lambda^2/\Delta\lambda \geq \Lambda = \lambda/|C||\chi_{hr}|$.

FOCUSING OF X-RAY WAVE BY AN ELASTIC MOSAIC CRYSTAL

Consider an elastic mosaic crystal in which the parameter obeys the condition $|\nu| \ll 1$ (a strongly bent crystal). The bending parameter in backscattering equals

$$|\nu| \approx \pi^2 \chi_{hr}/16\lambda^2|B| \quad (18)$$

and, for the crystals with the deformation gradient $B \geq 10^{14} \text{ m}^{-2}$, the condition $|\nu| \ll 1$ is satisfied at $\chi_{hr} \sim 10^{-6}$ and $\lambda \geq 1 \text{ \AA}$.

The amplitude reflection coefficient of a plane-wave harmonic from a thick (semi-infinite) crystal is

$$R(k) = i\sigma_h(i\pi/8B)^{1/2} \exp(t_0^2/2) \{1 - \Phi(-t_0/2^{1/2})\}, \quad (19)$$

where

$$\sigma_h = C\pi\chi_{hr}/\lambda \sin 2\theta \geq \pi(\chi_{hr})^{1/2}/2\lambda \quad (\theta \equiv \pi/2),$$

$$t_0 = (-i/4B)^{1/2}k, \quad k \leq 2\pi\Delta\theta/\lambda,$$

$$\Phi(t) = 2(\pi)^{-1/2} \int_0^t \exp(-x^2) dx$$

is the probability integral.

Putting $t_0/2^{1/2} \equiv \pi$ in Eq. (19), we can determine the optimum size of L_{eff} for a strongly bent crystal along the X-axis,

$$L_{\text{eff}} \equiv 2L_0\Delta\theta \equiv 2L_0(2|B|)^{1/2}\lambda. \quad (20)$$

The intensity distribution in the focus is determined by the integral over the plane-wave harmonics

$$I_h(\xi_p) = |E_h(\xi_p)|^2$$

$$= \left| G \int_{-\infty}^{+\infty} R(k) \exp\{-ik^2\lambda(\alpha_0^{-1} + \alpha_h^{-1})/4\pi\} \times \exp\{ik\xi_p/(L_h/R_x - 1)\} dk \right|^2, \quad (21)$$

where the geometric coefficient G depends on α_0 , α_h , L_0 and L_h , $\alpha_0 = 1/L_0 - 1/R_x$, $\alpha_h = 1/L_h - 1/R_x$, and $L_{0,h} \neq R_x$.

The geometrical condition of focusing by a thick strongly bent crystal has the form

$$\lambda(1/\alpha_0 + 1/\alpha_h)/2\pi + 1/4|B| = 0. \quad (22)$$

It is seen from Eq. (22) that the conditions of focusing by strongly and weakly bent crystals are different. At the deformation gradient $B \geq 10^{14} \text{ m}^{-2}$ and $R_x \leq 0.1 \text{ m}$, the source should be very close to the crystal surface. At $L_0 = 1 \text{ cm}$ and $\lambda = 1.54 \text{ \AA}$, an X-ray wave dynamically scattered in the crystal bulk is focused at a distance of $L_h = -1.2499984 \text{ cm}$ from the crystal.

With due regard for Eq. (22), we obtain the following equation for the intensity described by Eq. (21):

$$I_h(\xi_p) = G^2 \pi^3 |\chi_{hr}| (32\lambda^2|B|)^{-1} \times \left| \int_{-\infty}^{+\infty} \exp\{ik\xi_p/(L_h/R_x - 1)\} dk \right|^2. \quad (23)$$

At the finite integration limits (from $-k_{\text{eff}}$ to $+k_{\text{eff}} \equiv 2\pi X/\lambda L_0$, where X is the size of the region illuminated by an incident beam), the integral in Eq. (23) is not a

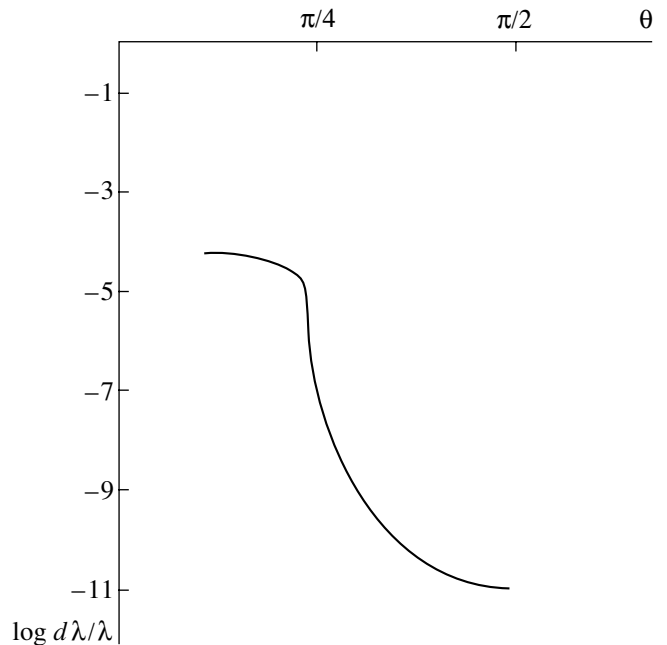


Fig. 3. Logarithm of the spectral resolution described by Eq. (15) as a function of the angle θ : $a < L_0\lambda/x_{\text{eff}}$, $L_h \ll R_x \sin\theta$, $R_x = 1 \text{ m}$, and $L_0 = 2 \text{ m}$. Si (444), $|\chi_{hr}| = 0.94 \times 10^{-6}$.

δ -like integral any more. Thus, finally, we arrive at

$$I_h(\xi_p) = G^2 \pi^3 |\chi_{hr}| (8\lambda^2 |B|)^{-1} \\ \times |\sin(\xi_p k_{\text{eff}} / (L_h/R_x - 1)) / (\xi_p / (L_h/R_x - 1))|^2, \quad (24) \\ L_h \neq R_x.$$

The main intensity maximum in the focus is

$$I_h(0) = \pi^5 |\chi_{hr}| X^2 L_0^2 G^2 / 2\lambda^4 |B|.$$

The angular halfwidth of the maximum determining the diffraction size of the focus is

$$\Delta\xi_p \approx \lambda |(L_h/R_x - 1)| L_0 / 2X. \quad (25)$$

Equation (23) at $L_0 = 1$, $L_h = 10^{-3}$, $X = 10^{-2}$, $R_x = 0.1$ m, and $\lambda = 1.54$ Å yields $\Delta\xi_p \sim 10^{-8}$ m. The focus width is dependent on the deformation gradient B and is proportional to $|\alpha B - 1|$, where α is determined by the focusing geometry and the radiation characteristics. The height of the intensity peak given by Eq. (24) is inversely proportional to B .

Now, consider a crystal of a finite thickness $T < \Lambda$. The amplitude reflection coefficient is equal to

$$R(k) = -i(i)^{1/2} (q/4a) (\pi/2B)^{1/2} \tan\theta [\Phi(-t_1/2^{1/2}) \\ - \Phi(-t_0/2^{1/2})] \exp(-t_0^2/2),$$

where $q = \pi Ca \chi_h (\lambda \sin\theta)^{-1}$ is the coefficient of reflection from an atomic plane, a is the interplanar spacing, and $t_1 = t_0 + 4T \cot\theta (-iB)^{1/2}$. In backscattering, $\cot\theta \approx \Delta\theta \leq |\chi_{hr}|^{1/2}$, i.e., is less by two to three orders of magnitude than at $\theta < \pi/2$. Assuming that $T < \pi/4\lambda B$, we can expand the difference between the probability integrals into the Taylor series. Limiting the consideration to the first derivative of the function $\Phi(t)$, we have

$$\Phi(-t_1/2^{1/2}) - \Phi(-t_0/2^{1/2}) \\ \approx -2(\pi)^{-1/2} \exp(-t_0^2/2) (t_1 - t_0) / 2^{1/2}. \quad (26)$$

Then the amplitude reflection coefficient has the form

$$R(k) = iq \exp(-t_0^2) T / a. \quad (27)$$

The intensity $I_h(\xi_p)$ in the vicinity of the focus is determined from Eq. (21) by substituting there Eq. (27). The intensity ratio for thin ($T < \Lambda$) and thick ($T \gg \Lambda$) crystals is

$$I_{h, T < \Lambda} / I_{h, T \gg \Lambda} \sim 32 |B| |\chi_{hr}| T^2 / \pi \quad (28)$$

and, at T at $\chi_{hr} \sim 10^{-6}$, $|B| \geq 4 \times 10^{14} \text{ m}^{-2}$, and $T \sim 10 \mu\text{m}$, equals $T \sim 0.4$.

Expression (28) allows the estimation of an admissible crystal thickness at the given χ_{hr} and B

$$T < \pi / (32 |B| |\chi_{hr}|)^{1/2} < \Lambda.$$

To increase the intensity at the focus, one has to use a weakly bent and not a strongly bent crystal. The intensity ratio is estimated as

$$I_{h, \text{weak}} / I_{h, \text{strong}} \sim 8 |B| / \pi k_{\text{eff}}^2, \quad (29)$$

and, it follows from (29) that, at $\lambda = 1.54$ Å, $X = 10^{-4}$, $L_0 = 0.4$, and $|B| = 4 \times 10^{14} \text{ m}^{-2}$, we have

$$I_{h, \text{weak}} / I_{h, \text{strong}} \sim 10.$$

Obviously, all the results obtained in this study are also valid for thermal neutrons with a wavelength of $\lambda \sim 1$ Å.

CONCLUSIONS

Thus, we have obtained for the first time an analytical expression for the size of the region of diffraction reflection on the crystal surface in backscattering. It follows from this expression that the aperture ratio of the crystal optics in Bragg backscattering essentially (by two to three orders of magnitude) increases in comparison with the aperture ratio attained in other focusing schemes and becomes comparable with the aperture in the Johann scheme. The advantage of the backscattering scheme is the minimum aberrations of the reflected beam. The analysis of the spectral characteristics of the diffracted beam in backscattering showed that, theoretically, it is possible to attain a resolution as high as $d\lambda/\lambda \sim 10^{-11}$. Moreover, we also showed that weakly bent crystals provide higher intensity at the focus than strongly bent ones. According to (29), the intensity ratio for these crystals is proportional to the deformation gradient B .

REFERENCES

1. K. Kohra and M. Matsushita, *Z. Naturforsch. A* **27**, 484 (1972).
2. O. Brummer, H. R. Hoche, and J. Nieber, *Phys. Status Solidi A* **53**, 565 (1979).
3. A. Caticha and S. Caticha-Ellis, *Phys. Rev. B* **25**, 971 (1982).
4. V. I. Kushnir and É. V. Suvorov, *Pis'ma Zh. Éksp. Teor. Fiz.* **44**, 205 (1986) [*JETP Lett.* **44**, 262 (1986)].
5. T. Tchen, V. A. Bushuev, and R. N. Kuz'min, *Zh. Tekh. Fiz.* **60** (10), 60 (1990) [*Sov. Phys. Tech. Phys.* **35**, 1148 (1990)].
6. H. H. Johann, *Z. Phys.* **69** (3-4), 185 (1931).
7. K. T. Gabrielyan, F. N. Chukhovskii, and Z. G. Pinsker, *Zh. Tekh. Fiz.* **50** (1), 3 (1980) [*Sov. Phys. Tech. Phys.* **25**, 1 (1980)].
8. F. N. Chukhovskii, *Metallofizika* **3** (5), 3 (1981).
9. D. B. Wittry and S. Sun, *J. Appl. Phys.* **67**, 1633 (1990).
10. W. Z. Chang and D. B. Wittry, *J. Appl. Phys.* **74**, 2999 (1993).
11. F. N. Chukhovskii, W. Z. Chang, and E. Forster, *J. Appl. Phys.* **77**, 1843 (1995).
12. K. T. Gabrielyan, F. N. Chukhovskii, and D. I. Piskunov, *Zh. Éksp. Teor. Fiz.* **96** (3), 834 (1989) [*Sov. Phys. JETP* **69**, 474 (1989)].
13. V. G. Kon, I. V. Kon, and É. A. Manykin, *Zh. Éksp. Teor. Fiz.* **116** (3), 940 (1999) [*JETP* **89**, 500 (1999)].
14. T. Tchen, *Pis'ma Zh. Tekh. Fiz.* **27** (21), 1 (2001) [*Tech. Phys. Lett.* **27**, 889 (2001)].
15. Z. G. Pinsker, *X-ray Crystal Optics* (Nauka, Moscow, 1982).

Translated by L. Man

THEORY OF CRYSTAL STRUCTURES

Quasi-Two-Dimensional Crystalline Clusters on a Sphere: Method of Topological Description

A. M. Livshits and Yu. E. Lozovik

Institute of Spectroscopy, Russian Academy of Sciences, Troitsk, Moscow oblast, 142092 Russia

e-mail: lozovik@isan.troitsk.ru

Received February 2, 2000; in final form, September 4, 2001

Abstract—The formation of a “quasicrystal” on a closed surface has been considered for the Thomson problem on the arrangement with the lowest energy of N Coulomb charges on a sphere. The stable and metastable states of the system of charges with the charge number $N = 2–100$ and the symmetry groups of the corresponding configurations have been determined. The structure and possible structural transitions between the system states are described in terms of the introduced notion of a closed quasi-two-dimensional triangular lattice with topological defects. The graph of lattice defects is defined. A method for classifying the system in terms of the charge and the arrangement of topological defects in the lattice is suggested and extended to the case of an arbitrary lattice. The use of the model is considered on various physical examples, in particular, on a closed hexagonal lattice with disclinations in fullerenes. © 2002 MAIK “Nauka/Interperiodica”.

INTRODUCTION

Recently, we have seen an ever increasing interest in mesoscopic systems and clusters [1, 2]. A large number of real electron and semiconductor mesoscopic systems is described by the model of repulsing particles in two- and three-dimensional confining potentials [3–8]. One also uses various repulsive (Coulomb, dipole, logarithmic, etc.) potentials. All the known mesoscopic systems described by such models show the following common features: (1) formation of a shell structure in the equilibrium state and (2) the “orientational melting of shells” during heating, i.e., the loss of the orientational order of neighboring shells reducing to the rotation of the “frozen” shells with respect to one another and then, with a further increase of the temperature, the loss of the radial order and the destruction of the shell structure. Thus, we arrive at the notion of the “solid” and “liquid” states of a cluster. Of course, this notion can be applied to mesoscopic systems only conditionally, e.g., because of the existence of essential “heterophase fluctuations” [9] associated with the jump of the system from the global potential-energy minima into the local ones. Since a cluster consists of a limited number of particles, it possesses no translation invariance, which, in turn, can result in the appearance of fivefold symmetry axes. In this article, we attempt to rigorously describe the structure of a mesoscopic cluster in the solid state.

Considering the cluster structures, we can single out a class of clusters that can be represented by quasi-two-dimensional (quasi-2D) closed lattices. A closed lattice is a lattice that can be inscribed into a simply connected closed two-dimensional surface with the unavoidable formation of some topological defects. The model of a

closed hexagonal lattice with topological defects can be used to describe fullerenes and other carbon clusters C_n having more complicated structures. Carbon clusters of various dimensions have already been obtained experimentally [10–13]. A closed triangular lattice can be formed during crystallization of a cluster of repulsing particles on a closed surface or in a confining potential. In the latter case, a structure of concentric shells can be formed [4], with each shell being represented by a closed triangular lattice. Because of the topological properties of a closed surface, any quasi-two-dimensional lattice always has some topological defects (disclinations), with the total topological charge M of all the defects in each type of the closed lattice being constant. In particular, in a closed triangular lattice, $M_r = +12$. Since the total topological charge of the defects is fixed, it is possible to describe the lattice by enumerating all its defects (the so-called lattice index) [14]. Below, we fully characterize a closed lattice by a “graph of defects” or a d -graph defining the charges of defects and their mutual arrangement. The “distances” between the defects are introduced in a way used in the theory of graphs.

We consider the problem of the structure of closed lattices on an example of the Thomson problem [15–17] of the optimum arrangement of point charges on a sphere, in which the Coulomb energy of the charges, $E(N) = \sum_{i>j}^N (|\mathbf{r}_i - \mathbf{r}_j|)^{-1}$, is minimized. The model describes a number of real physical systems, in particular, a system of ions or bubbles with electrons in a liquid helium cluster, the rarefied system of electrons (or holes) in a spherical “point” in a semiconductor, and a system of ions in a three-dimensional trap (3D-trap) with the potential drastically increasing in the vicinity

of the boundary. Indeed, according to the Earnshaw theorem, the equilibrium charges in a three-dimensional potential well are located on the surface. Because of the medium polarization, the charges, ions, or bubbles with electrons in a spherical helium cluster are in the effective confining potential $U^{ext}(r)$. The shape of this potential is similar to that of a potential well with rounded-off edges in the center of a cluster $U^{ext}(r)|_0 \sim \xi r^2$ and in the vicinity of the surface $U^{ext}(r)|_1 \sim \xi(r-1)^{-1}$, where $\xi \approx 0.03$. In the zero approximation, the potential $U^{ext}(r)$ degenerates into a rectangular potential well. A similar effective potential is also formed for a three-dimensional charged semiconductor or semimetal quantum dot. The classical mode of a quantum dot is characteristic of the parameter range, where the characteristic thermal length of the de Broglie wave of electrons, $\lambda \sim \hbar/\sqrt{mkT}$, is significantly less than the average distance between electrons.

To construct a unique closed triangular lattice of charges, we use the edges of a convex polygon constructed on the charges–vertices. Usually, such a polygon has only triangular faces, because, as a rule, the configurations with nontriangular faces are unstable. This is confirmed by the following symmetric configurations of the charges: a cube with $N = 8$, a dodecahedron with $N = 20$, and a “buck ball” with $N = 60$.

There is an alternative method of describing the equilibrium structures of point charges on a sphere. The configuration of the charges on a sphere can be represented by a system of coaxial rings of charges [15, 18, 19]. In this case, the structural changes occurring with an increase of N correspond to the gradual filling of the rings. This approach is justified only for a small number of charges, $N \sim 20$, whereas at large N values, the approach suggested in this article seems to be preferable.

There is a large class of variational problems [20] topologically close to the Thomson problem (e.g., the Tammes [21] problem on the determination of the configuration of N particles on a sphere such that the minimum angular distance between the particles would be maximal). It should be indicated that at $12 \leq N \leq 100$, the Thomson and the Tammes problems usually have different solutions.

CALCULATION FOR THE THOMSON PROBLEM

The energy minima were determined by the gradient descent method [22], which for our system is written in the following way [16]:

$$\mathbf{r}_i \longrightarrow \mathbf{r}'_i = (\mathbf{r}_i + \gamma \mathbf{F}_i)/|\mathbf{r}_i + \gamma \mathbf{F}_i|,$$

where \mathbf{F}_i is the force acting onto the i th particle. Of all the configurations determined, we select the local and the global (possessing the minimum energy) minima.

The equilibrium configurations obtained for the Thomson problem are listed in Table 1. At $N \leq 90$, we also indicate the solutions of the Tammes problem (the data from [23] at $N \leq 12$ and the data from [24] at $13 \leq N \leq 90$).

The configuration energies are obtained with an accuracy considerably higher than in [17, 19, 25, 26], which is of great importance for the selection of the global minimum from a large number of local ones (which often possess only slightly different energies) at charge numbers $N \sim 100$. This, in turn, provides the determination of some other configuration characteristics with a considerably higher accuracy. Some of the data obtained agree quite well with the data indicated by Edmundson [25], who analyzed all possible configurations for the Thomson problem at charge numbers $N \leq 60$ and $N = 72, 92, 100$. The configurations we determined at $N = 55, 56$, and 92 differ from those obtained in [25] and correspond to lower minima. The discrepancies in the Föppl indices for the configurations at $N = 19$ and 43 are insignificant and are explained by the higher accuracy of our calculations. The symmetry data, the Föppl indices, and other characteristics of equilibrium configurations (except for energy) at charge numbers in the range $60 < N < 100$ are obtained in our study for the first time. Earlier [16, 17, 27, 28], energies at charge numbers $N \leq 100$ were calculated with different accuracies. It was also indicated that a convex polyhedron built on the charges–vertices usually has 12 vertices–pentamers and $(N - 12)$ vertices–hexamers [17, 25, 26]. Altshuller *et al.* [17] obtained the list of configurations at $13 \leq N \leq 100$ which contradicts the above statement. The results obtained in the present study considerably differ from the data indicated by Altshuller (cf. Table 1 in [17] and Table 2 in the present article).

In 1957, Leech showed [29] that the solution of the variational problem of the search for the minimum of $U(N, n) = \sum_{p \neq q}^N r_{pq}^{-n}$ at $N = 2-6, 12$ is independent of the exponent n ($n = 1, 2, \dots, \infty$) [29]. It should be indicated that at all the other N values, the solutions of the Thomson ($n = 1$) and the Tammes ($n = \infty$) problems do not coincide (see Table 1). In particular, the Thomson problem has many more symmetric solutions. The only global energy minimum for the Thomson problem in the range of N under consideration having no symmetry elements is found at $N = 61$.

The configurations at $N = 25, 33, 47$, and 79 correspond to the symmetry group C_{1h} and, thus, have no rotational symmetry axis. Therefore, in order to write the Föppl indices for these configurations (Table 1), we had to use the direction normal to the symmetry plane. Thus, the Föppl index of the configuration at $N = 79$ is written as follows: $1^{32}, 2, 11, 2, 1^{32}$. In this case, the convex polyhedron constructed on the charges–vertices has a tetragonal face which is normal to the symmetry plane. It should also be indicated that the number of

Table 1. Equilibrium configurations of the system of N charges ($N = 2-100$) on the surface of a sphere

N	MR	G	δ	Energy	L	Föppl	G'	δ'
2	0	$D_{\infty h}$	180.00000	0.50000000	–	2	$D_{\infty h}$	180.00000
3	0	D_{3h}	120.00000	1.73205081	–	1, 2	D_{3h}	120.00000
4	0	T_d	109.47122	3.67423461	$4Tr$	1, 3	T_d	109.47122
5	0	D_{3h}	90.00000	6.47469149	$2Tr3T$	1, 3, 1	D_{3h}, C_{4v}	90.00000
6	0	O_h	90.00000	9.98528137	$6T$	1, 4, 1	O_h	90.00000
7	0	D_{5h}	72.00000	14.45297741	$5Tr2P$	1, 5, 1	C_{3v}	77.86954
8	0	D_{4d}	71.69415	19.67528786	$8P2F$	4^2	D_{4d}	74.85849
9	0	D_{3h}	69.18975	25.75998653	$3T6P$	3^3	D_{3h}	70.52878
10	0	D_{4d}	64.99562	32.71694946	$2T8P$	1, 4^2 , 1	C_{2v}	66.14682
11	0.001202	C_{2v}	58.53956	40.59645051	$2T8P$	1, 2, 4, 2^2	C_{5v}	63.43495
12	0	Y_h	63.43495	49.16525306	$12P$	1, 5^2 , 1	I_h	63.43495
13	0.000678	C_{2v}	52.31692	58.85323061	$T10P$	1, 2^2 , 4, 2^2	C_{4v}	57.13670
14	0	D_{6d}	52.86609	69.30636330	$12P$	1, 6^2 , 1	D_{2d}	55.67057
15	0	D_3	49.22487	80.67024411	$12P$	3^5	C_3, C_1	53.65785
16	0	T	48.93621	92.91165530	$12P$	1, 3^5	D_{4d}	52.24440
17	0	D_{5h}	50.10802	106.05040483	$12P$	1, 5^3 , 1	C_{2v}	51.09033
18	0	D_{4d}	47.53440	120.08446745	$2T8P$	1, 4^4 , 1	C_2	49.55666
19	0.000007	C_{2v}	44.90970	135.08946756	$F10P$	1, 4, 2, 4, 2^2 , 4	C_{1h}	47.69191
20	0	D_{3h}	46.09330	150.88156833	$12P$	1, 3^2 , 6, 3^2 , 1	D_{3h}	47.43104
21	0.000067	C_{2v}	44.32038	167.64162240	$T10P$	1, 2^2 , 4, 2^2 , 4, 2^2	C_1	45.61322
22	0	T_d	43.30201	185.28753615	$12P$	1, 3^2 , 6, 3^3	C_1	44.74016
23	0	D_3	41.48111	203.93019066	$12P$	1, 3^7 , 1	C_1	43.70996
24	0	O	42.06529	223.34707405	$6F$	4^6	O	43.69077
25	0.000041	C_{1h}	39.60981	243.81276030	$F10P$	1^{10} , 5, 1^{10}	C_3	41.63446
26	0.000074	C_2	38.74214	265.13332632	$12P$	2^{13}	C_{1h}	41.03766
27	0	D_{5h}	39.94028	287.30261503	$12P$	1, 5^5 , 1	C_{2v}	40.67760
28	0	T	37.82374	310.49154236	$12P$	1, 3^9	C_1	39.35514
29	0	D_3	36.39129	334.63443992	$12P$	1, 3^9 , 1	C_1	38.71365
30	0	D_2	36.94228	359.60394590	$12P$	1, 2^{14} , 1	D_3	38.59712
31	0.000103	C_{3v}	36.37311	385.53083806	$12P$	1, 3^2 , 6, 3^2 , 6, 3^2	C_5	37.70983
32	0	I_h	37.37736	412.26127465	$12P$	1, 5^6 , 1	D_3	37.47521
33	0.000132	C_{1h}	33.69955	440.20405745	$F11PH$	1^{13} , 7, 1^{13}	C_3	36.25455
34	0	D_2	33.27343	468.90485328	$12P$	1, 2^{16} , 1	C_2	35.80778
35	0.000012	C_2	33.10029	498.56987249	$12P$	1, 4, 2^{15}	C_1	35.31846
36	0	D_2	33.22727	529.12240838	$12P$	2^{18}	D_2	35.18973
37	0	D_{5h}	32.33243	560.61888773	$12P$	1, 5^7 , 1	C_{1h}	34.42241
38	0	D_{6d}	33.23648	593.03850357	$12P$	1, 6^6 , 1	D_{6d}	34.25066
39	0	D_{3h}	32.05295	626.38900902	$12P$	3^2 , 6, 3, 9, 3, 6, 3^2	C_1	33.48905
40	0	T_d	31.91635	660.67527883	$12P$	1, 3^2 , 6, 3^2 , 6, 3, 6, 3^2	C_3	33.15836
41	0	D_{3h}	31.52783	695.91674434	$12P$	1, 3^2 , 6, 3, 9, 3, 6, 3^2 , 1	C_1	32.72909
42	0	D_{5h}	31.24474	732.07810754	$12P$	1, 5^3 , 10, 5^3 , 1	D_5	32.50639
43	0.000009	C_{2v}	30.86664	769.19084646	$13P$	1, 2, 4, 2, 4^2 , 2^2 , 4^3 , 2, 4, 2^2	C_1	32.08447
44	0	O_h	31.25761	807.17426308	$6F$	4^3 , 8, 4, 8, 4^3	C_2	31.98342
45	0	D_3	30.20718	846.18840106	$12P$	3^{15}	C_1	31.32308
46	0	T	29.79025	886.16711364	$12P$	1, 3^{15}	C_2	30.95916
47	0.000053	C_{1h}	28.78730	927.05927068	$F10P$	1^{20} , 7, 1^{20}	C_1	30.78182
48	0	O	29.68964	968.71345534	$6F$	4^{12}	O	30.76279
49	0.000031	C_3	28.38659	1011.55718265	$12P$	1, 3^{16}	C_2	29.92358
50	0	D_{6d}	28.71140	1055.18231473	$12P$	1, 6^8 , 1	D_6	29.75296

Table 1. (Contd.)

<i>N</i>	MR	<i>G</i>	δ	Energy	<i>L</i>	Föppl	<i>G'</i>	δ'
51	0	D_3	28.16539	1099.81929032	12 <i>P</i>	3^{17}	C_1	29.36159
52	0.000009	C_3	27.66987	1145.41896432	12 <i>P</i>	$1, 3^{17}$	T	29.19476
53	0.000005	C_{2v}	27.13694	1191.92229042	3 <i>F6P</i>	$1, 4, 2, 4^2, 2, 4^2, 2^2, 4^4, 2^2, 4$	C_1	28.81390
54	0.000003	C_2	27.02959	1239.36147473	12 <i>P</i>	2^{27}	C_1	28.71692
55	0.000007	C_2	26.61507	1287.77272078	12 <i>P</i>	$1, 2^{27}$	C_1	28.26279
56	0	D_2	26.68290	1337.09494528	12 <i>P</i>	2^{38}	D_2	28.14805
57	0	D_3	26.70241	1387.38322925	12 <i>P</i>	3^{19}	C_3	27.82668
58	0	D_2	26.15523	1438.61825064	12 <i>P</i>	$1, 2^{11}, 4, 2^2, 4, 2^{11}, 1$	C_1	27.55485
59	0.000003	C_2	26.17024	1490.77333528	14 <i>P2H</i>	$1, 2^{29}$	C_1	27.39498
60	0	D_3	25.95762	1543.83040098	12 <i>P</i>	3^{20}	C_2	27.19283
61	0.000018	C_1	25.39167	1597.94183020	12 <i>P</i>	1^{61}	C_1	26.87233
62	0	D_5	25.87987	1652.90940990	12 <i>P</i>	$1, 5^{12}, 1$	C_1	26.68343
63	0	D_3	25.25672	1708.87968150	12 <i>P</i>	3^{21}	D_3	26.48692
64	0	D_2	24.92001	1765.80257793	12 <i>P</i>	2^{32}	C_1	26.23504
65	0.000006	C_2	24.52673	1823.66796026	12 <i>P</i>	$1, 2^{32}$	C_2	26.06983
66	0.000012	C_2	24.76463	1882.44152531	12 <i>P</i>	2^{33}	D_3	25.94744
67	0	D_5	24.72726	1942.12270041	12 <i>P</i>	$1, 5^{13}, 1$	C_2	25.68398
68	0	D_2	24.43292	2002.87470175	12 <i>P</i>	2^{34}	C_2	25.46062
69	0	D_3	24.13651	2064.53348323	12 <i>P</i>	3^{23}	C_1	25.33223
70	0	D_{2d}	24.29073	2127.10090155	4 <i>F4P</i>	$1, 2, 4, 2, 4^2, 2, 4^8, 2, 4^2, 2, 4, 2, 1$	C_1	25.17092
71	0.000018	C_2	23.80257	2190.64990643	14 <i>P2H</i>	$1, 2^{28}, 4, 2^5$	C_1	24.98791
72	0	I	24.49170	2255.00119097	12 <i>P</i>	$1, 5^{14}, 1$	D_3	24.92649
73	0.000022	C_2	22.81041	2320.63388375	12 <i>P</i>	$1, 2^{36}$	C_1	24.55376
74	0.000009	C_2	22.96584	2387.07298184	12 <i>P</i>	2^{37}	C_1	24.42088
75	0	D_3	22.73643	2454.36968904	12 <i>P</i>	3^{25}	C_1	24.30172
76	0.000012	C_2	22.88571	2522.67487184	12 <i>P</i>	2^{38}	C_1	24.11969
77	0	D_5	23.28614	2591.85015235	12 <i>P</i>	$1, 5^{15}, 1$	C_1	23.99585
78	0	T_h	23.42634	2662.04647457	12 <i>P</i>	3^{26}	D_3	23.93102
79	0.000009	C_{1h}	22.63614	2733.24835748	11 <i>P1PH</i>	$1^{32}, 2, 11, 2, 1^{23}$	C_1	23.62399
80	0	D_{4d}	22.77835	2805.35587598	2 <i>F8P</i>	$4^3, 8, 4^2, 8, 4^2, 8, 4^2, 8, 4^3$	D_2	23.54352
81	0.000002	C_2	21.89175	2878.52282966	12 <i>P</i>	$1, 2^{40}$	C_1	23.34764
82	0	D_2	22.20594	2952.56967529	12 <i>P</i>	$1, 2^{40}, 1$	C_1	23.19261
83	0.000004	C_2	21.64623	3027.52848892	14 <i>P2H</i>	$1, 2^{41}$	C_1	23.08300
84	0.000005	C_2	21.51267	3103.46512443	12 <i>P</i>	$1, 2^{41}, 1$	D_3	23.05173
85	0.000005	C_2	21.49758	3180.36144294	12 <i>P</i>	$1, 2^{42}$	C_1	22.77869
86	0.000016	C_2	21.52160	3258.21160571	12 <i>P</i>	2^{43}	C_1	22.67437
87	0.000009	C_2	21.45649	3337.00075001	12 <i>P</i>	$1, 2^{17}, 4, 2^{24}$	D_3	22.54666
88	0	D_2	21.48559	3416.72019676	12 <i>P</i>	2^{44}	T	22.46788
89	0.000001	C_2	21.18220	3497.43901862	12 <i>P</i>	$1, 2^{44}$	C_1	22.31660
90	0	D_3	21.23028	3579.09122272	12 <i>P</i>	3^{30}	D_3	22.15402
91	0	C_2	21.10466	3661.71369932	12 <i>P</i>	$1, 2^{45}$		
92	0	D_2	21.02582	3745.29163624	12 <i>P</i>	2^{46}		
93	0.000002	C_2	20.75075	3829.84433842	12 <i>P</i>	$1, 2^{46}$		
94	0	D_2	20.95187	3915.30926962	12 <i>P</i>	$1, 2^{46}, 1$		
95	0.000001	C_2	20.71121	4001.77167557	12 <i>P</i>	$1, 2^{47}$		
96	0	C_2	20.68657	4089.15401006	12 <i>P</i>	$2^{12}, 4, 2^{34}$		
97	0.000001	C_2	20.44961	4177.53359962	12 <i>P</i>	$1, 2^{48}$		
98	0.000001	C_2	20.42160	4266.72246416	12 <i>P</i>	2^{49}		
99	0.000002	C_2	20.28450	4357.13916313	12 <i>P</i>	$1, 2^{33}, 4, 2^{14}$		
100	0	T	20.29660	4448.35063433	12 <i>P</i>	$1, 3^{33}$		

Note: MR is the dipole moment of the system, *G* is the symmetry group (in Schönflies notation), δ is the minimum angular distance between the charges (in degrees), *L* is the index of the closed lattice, Föppl indicates the Föppl index, Energy indicates the total Coulomb energy of the system, *G'* is the symmetry group used in the solution of the Tammes problem, and δ' is the minimum angular distance between the particles in the Tammes problem.

charges located in the symmetry plane in all cases with symmetry C_{1h} is described by a simple number—5, 7, 7, or 11.

It was indicated earlier that, usually, the configurations with tetragonal faces are unstable. In particular, it is well known that a cube does not correspond to the minimum energy in the Thomson problem. We determined three configurations having cubic symmetry (at $N = 24, 44, 48$) and possessing tetragonal (in this case, square) faces. The same configurations are also indicated in [25] but, surprisingly, are not indicated in the later study [17]. The configuration at $N = 70$ is described by the symmetry group D_{2d} and has four tetragonal faces. Two of three fourfold rotation reflection axes pass through the centers of the tetragonal faces, whereas the third rotation reflection axis transforms these four faces into one another.

Configurations possessing higher symmetries can have higher energies than the low-symmetric ones. Thus, at $N = 42$, the local minimum ($E = 732.15182672$) has the symmetry I_h , whereas the global minimum has a lower symmetry D_{5h} . Table 3 lists the local minima of the system of point charges on a sphere at $N = 92$. Of nineteen configurations listed in Table 3, the minimum possessing the highest symmetry I_h is also characterized by the highest energy.

DISCUSSION OF RESULTS

One of the most well-known approaches to the description of the charge distribution on a sphere is that from the classical study performed by Thomson [15], who considered that the structures consisted of a small number of charges. According to Thomson, the charges form coaxial rings on a sphere, whereas the structural changes occurring with an increase in the charge number N in the system correspond to the gradual addition of charges to different rings (Fig. 1). A consistent formal description within the framework of the “ring approach” was developed by Föppl [30]. The axis of the coaxial rings is taken to be that of the highest symmetry, whereas the particles are considered to be located on one ring only if they all are located in the same plane normal to this axis. This approach is quite justified with a small number of charges because the rings of charges are well distinguishable. With an increase in the charge number N , increasingly less information on the real charge configuration can be extracted from the Föppl index. Thus, various local minima are often described by the same indices (see Table 3). The notion of rings itself no longer has any sense because the distances between the rings can be several times less than the distances between the charges in the individual rings. Nevertheless, the Föppl indices can successfully be used for solving a number of problems.

Since the charges in the Thomson problem are located on a sphere, one can always construct a convex polyhedron on charges–vertices if $N \geq 4$. Thus, another

Table 2. Exceptions from the rule defining the number of vertices–pentamers and vertices–hexamers in a convex polyhedron constructed on the charges–vertices at $12 \leq N \leq 100$

N	N_4	N_5	N_6	N_7	Q
13	1	10	2		
18	2	8	8		
19		14	5		1
21	1	10	10		
24		24			6
25		14	11		1
33		15	17	1	1
44		24	20		6
47		14	33		1
48		24	24		6
53		18	35		3
59		14	43	2	
70		20	50		4
71		14	55	2	
79		15	63	1	1
80		16	64		2
83		14	67	2	

Note: N is the number of charges; $N_4, N_5, N_6,$ and N_7 are the numbers of vertices incident to 4, 5, 6, and 7 edges, respectively; and Q is the number of tetragonal faces.

natural method used to describe the configurations is the consideration of the characteristics of this polyhedron. Below, we study such characteristics for a polyhedron uniquely determining the structures of all the configurations.

In fact, a convex polyhedron constructed on charges–vertices is the implementation of the idea of a closed two-dimensional triangular lattice with topological defects. The concept of a closed lattice with topological defects can be used to describe structures of various systems, including fullerenes and a large number of clusters consisting of repulsing particles in confining potentials. It is well known that, for the repulsive potentials $U \sim r^{-n}$ ($n = 1, 3, 4, \dots$), a triangular lattice is stable in the plane and possesses the minimum energy as compared with the energies of the lattices of all the other types [31, 32]—square, hexagonal, etc. Thus, one can expect that the triangular lattice would also be stable in the region $\langle r_{ij} \rangle \ll R$ on a curved surface, where R is the curvature radius of the surface and $\langle r_{ij} \rangle$ is the average distance between the particles. However, if the lattice is considered on the whole sphere surface, i.e., if the surface is closed, it possesses a number of specific features based on the topological differences between a sphere (a closed simply connected surface) and a plane.

In order to construct the lattice on a sphere, one can use several methods, in particular, the slightly modified

Table 3. The Thomson problem: local minima at number of charges $N = 92$

G	Föppl	Energy
D_2	2^{46}	3745.29163624
C_2	2^{46}	3745.32218333
C_2	2^{46}	3745.32555284
C_2	2^{46}	3745.33860835
C_1	1^{92}	3745.36351633
D_5	$1, 5^{18}, 1$	3745.36772048
C_1	1^{92}	3745.38100894
C_1	1^{92}	3745.38177220
C_2	2^{46}	3745.38212625
C_1	1^{92}	3745.38297241
C_1	1^{92}	3745.38930839
C_1	1^{92}	3745.38943469
C_2	$1, 2^{10}, 4, 2^{11}, 4, 2^{20}, 1$	3745.39152813
C_1	1^{92}	3745.39598792
C_2	2^{46}	3745.41663888
C_{1h}	$1^{31}, 2, 1^7, 12, 1^7, 2, 1^{31}$	3745.48063056
C_1	1^{92}	3745.48989730
C_1	1^{92}	3745.50315699
I_h	$1, 5^3, 10, 5^2, 10^2, 5^2, 10, 5^3, 1$	3745.61873913

Note: For notation see Table 1.

Voronoi method for constructing lattices on curved 2D-surfaces. As will be shown later, the method used for the construction does not affect the basic properties of the closed lattice. Here, we construct the lattice using the edges of a convex polyhedron with the vertices occupied by charges.

LATTICE DEFECTS

Consider defects of a plane lattice (for details, see, e.g., [33]) which can have two types of defects—dislocations and disclinations. Disclinations break the symmetry of the directions of the vectors connecting the

closest equivalent particles. If a plane lattice possesses a symmetry axis of the n th order, then, in moving around the disclination core having the charge m , the phase ϕ is changed by a value of $\delta\phi = 2\pi m/n$. Thus, a particle surrounded by five and not six closest neighbors (a pentamer) in the plane triangular lattice is a core of a disclination with the charge $m = +1$, a particle with four nearest neighbors, a core of disclination with the charge $m = +2$, etc. (Figs. 2a, 2b).

Consider the equilibrium and the quasi-equilibrium configurations of charges on the sphere surface (at all $N \geq 4$) as quasi-two-dimensional closed triangular lattices with topological defects. A closed lattice is understood as a lattice inscribed into any closed simply connected surface (not necessarily convex). Hereafter, we use the following notation for defects: a pentamer is a P -disclination ($m = +1$), a tetramer is a T -disclination ($m = +2$), a trimer is a Tr -disclination ($m = +3$), and a heptamer is an H -disclination ($m = -1$). In terms of topology, a tetragonal face is also a disclination ($m = +2$), which differs from a conventional disclination only by the absence of a particle in the disclination core (the face center) (Fig. 3a). Hereafter, we call such a defect of the closed triangular lattice a “focus” or an F -disclination. Formally, defects of this type can be excluded from the lattice. With this aim, one has to add an arbitrarily chosen edge to each tetragonal face. As a result, the modified lattice acquires two P -disclinations in the neighboring vertices instead of each of the F -disclinations, whereas the total topological charge remains unchanged (Fig. 3b). Nevertheless, we preserve here the notation of an F -disclination because it is very convenient (see below) for describing the structure of a closed lattice, in particular, the lattice symmetry. Figure 4 shows some charge configurations characterized by tetragonal faces.

BASIC PROPERTY OF A CLOSED LATTICE

In a macroscopic plane lattice, the formation of disclination is low probably because of the high energy of arising elastic deformations. A quasi-two-dimensional closed lattice always contains disclinations with the

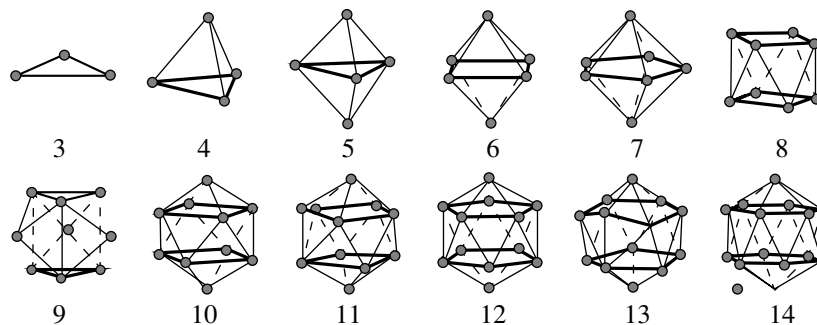


Fig. 1. Ring structures at $N = 3$ –14. The distorted ring structure at $N = 13$: $\{1, (6), (5), 1\}$.

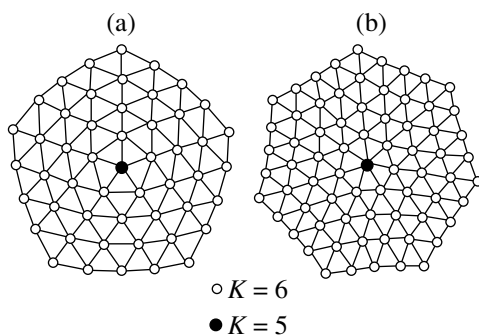


Fig. 2. Disclinations in a plane triangular lattice $\delta\phi = 2\pi m/6$: (a) the disclination with $m = +1$ and a wedge $\delta\phi = +2\pi/6$ cut out from the lattice; (b) the disclination with $m = -1$ and a wedge $\delta\phi = -2\pi/6$ inserted into the lattice.

total topological charge of M defects defined as

$$M = (N_{+1} - N_{-1}) + 2(N_{+2} - N_{-2}) + 3(N_{+3} - N_{-3}) + \dots$$

being constant and independent of the number of particles and of the method of lattice construction (where N_i is the number of disclinations in the lattice with the topological charge $m = i$). In particular, in a close triangular lattice

$$M_{tr} = 12,$$

in a closed hexagonal lattice, $M_{hex} = 12$, and in a closed square lattice $M_q = 8$. Consider the proof for a closed triangular lattice. The numbers of faces, vertices, and edges of a convex polyhedron, F , V , and E , respectively, are related by the Euler relationship $V + F - E = 2$. Three edges are incident to each face of a closed triangular lattice with each edge being tangential to two faces. Performing summation over the faces, we have $3F = 2E$. Every vertex of a closed triangular lattice is incident to six edges. If a vertex is a disclination with the charge $m = +1$, this vertex is incident to five edges (i.e., one edge less). If the disclination charge is $m = -1$, the vertex is incident to seven edges (one edge more), etc. Upon summing up all the vertices of the triangular lattice with disclinations, with due regard for the fact that each edge was summed up twice, we obtain $6V - M_{tr} = 2E$. Now, expressing M_{tr} from the above formulas, we arrive at the sought equation.

LATTICE INDEX

The lattice index is introduced to describe the types of defects in the lattice and their numbers. The examples of such indices are $12P$, $2T8P$, and $4F$. The number before the defect symbol indicates the number of defects of the given type in the lattice. Thus, index $12P$ signifies that the lattice contains 12 P -disclinations, while index $2T8P$ indicates that the lattice has 2 T - and 8 P -disclinations, and so on. A PH -dipole is considered as one defect—a dislocation ($m = 0$). The FH -complex formed in the systems with $N = 33$ and 79 can also be considered as one complex defect ($m = +1$). As

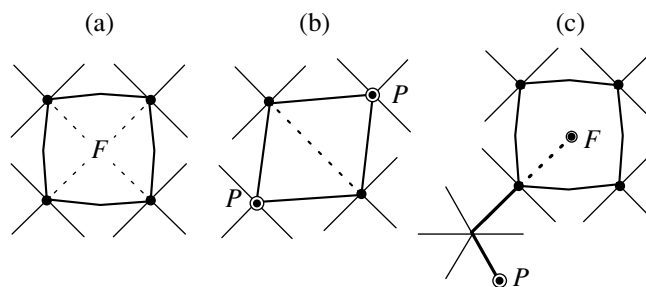


Fig. 3. F -disclination in a triangular lattice: (a) formation of an F -disclination ($m = +2$); (b) decomposition of an F -disclination into two P -disclinations; and (c) the virtual addition of a particle to the core of each F -disclination in the construction of the d graph. The distance L_{PF} between two disclinations equals three.

is seen from Table 1, most structure defects are of the $12P$ type. Then, we can also introduce the characteristics reflecting the arrangement of defects in a closed lattice.

STRUCTURE OF A CLOSED LATTICE. GRAPH OF LATTICE DEFECTS

The topology of a closed lattice is reflected by its graph G or a graph of edges of a convex polyhedron constructed on the charges located on a sphere. The symmetry of the charge configuration described by the point symmetry group is either lower or the same as the symmetry of the graph of a closed lattice constructed for the given configuration. This relationship is fulfilled for a closed lattice of an arbitrary structure including the lattice containing F -disclinations. If one were to construct a closed lattice by excluding F -disclinations and adding arbitrarily an edge to each tetragonal face of the polyhedron, one would arrive at a situation where the symmetry of the configuration would be higher than the symmetry of the corresponding graph, which would be very inconvenient for the classification.

Now, determine the distance $d(u, v)$ between two vertices, u and v , of the closed lattice as a length of the shortest simple chain connecting these vertices. Now, construct the graph of defects (the d -graph) in the following way. Take the vertices of the closed lattice (disclinations) as the vertices of the d -graph. Connect these vertices—disclinations by edges and bring each edge into correspondence with the distance between the corresponding defects. Constructing the d -graph for a structure containing F -disclinations, we can virtually add a particle into the core of each F -disclination (Fig. 3c).

Since the distance between any two vertices is determined uniquely, it is obvious that, for the given configuration of the charges forming the closed lattice, the d -graph can also be constructed uniquely. The opposite question of whether the graph of defects determines the structure of the closed lattice uniquely or nonuniquely is less trivial. We compared the d -graphs of all the local minima determined and established that, in the range of

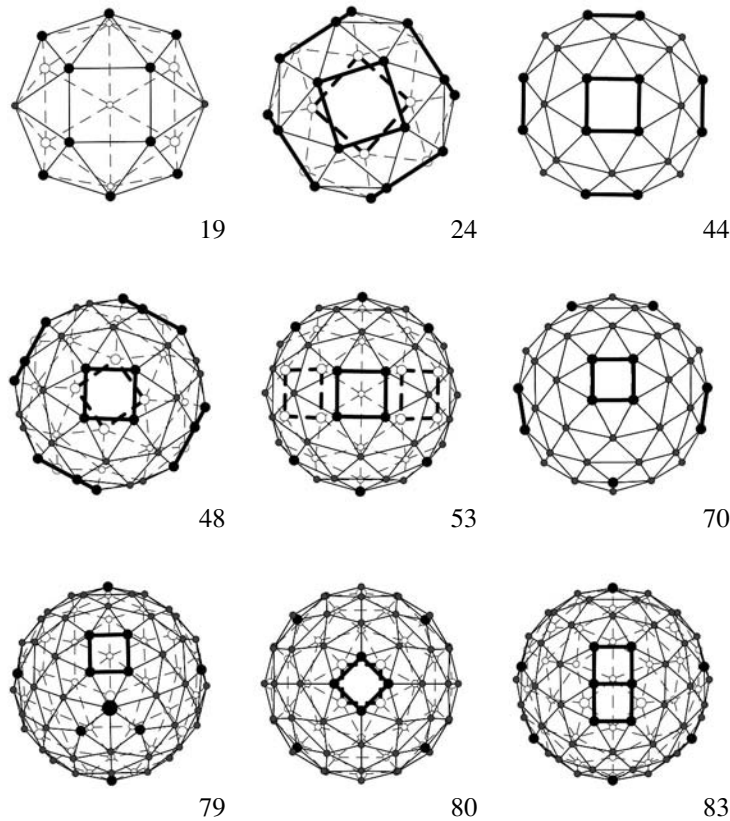


Fig. 4. Structures containing F -disclinations at $N = 19, 24, 44, 48, 53, 70, 79, 80, 83$. At $N = 83$, the local minimum $E = 3027.558629$ (the point group C_{1h}) is seen. The remaining figures show the configurations corresponding to the global minima of the systems.

N values $4 \leq N \leq 100$, the d -graph uniquely determines the structure of the closed lattice.

To a graph of polyhedron edges there corresponds the symmetric matrix A of dimensions $N \times N$; then, $a_{ij} = 1$ if the vertices i and j are connected by an edge, and $a_{ij} = 0$ if they are not connected. The graph of defects can be written with the aid of the symmetric d -matrix ($k \times k$), where k is the number of defects in the structure. To the nondiagonal matrix elements there correspond the pairs of distances between the disclinations. Now, write the symbols of the defects on the diagonal of the d -matrix. Since all the charges are equivalent, the operation of defect permutation in the d -matrix does not change the structure of the d -graph and the closed lattice. The permutation of the K and L defects is defined as

$$[d_{ij}]' = \text{swap}_{K,L}[d_{ij}]: \begin{cases} d'_{KK} = d_{LL} \\ d'_{LL} = d_{KK} \\ d'_{KL} = d'_{LK} = d_{KL} \\ d'_{iL} = d'_{Li} = d_{iK} \quad (i \neq L, K) \\ d'_{iK} = d'_{Ki} = d_{iL} \quad (i \neq L, K) \\ d'_{ij} = d_{ij} \quad (i, j \neq L, K). \end{cases} \quad (1)$$

The matrix of defects has an infinite number of invariants of the form

$$I(n, m) = \sum_{i,j} V_i(n) V_j(m),$$

where $V_i(n) = \sum_{j \neq i} d_{ij}^n$. The numbers n and m are arbitrary real numbers. One can also introduce a number of quantitative characteristics which are the functions of the d -matrix, e.g., the average distance between the defects in the lattice

$$M = \frac{2}{k(k-1)} \sum_{i>j} d_{ij}$$

and the dispersion of these distances

$$D = \frac{2}{k(k-1)} \sum_{i>j} d_{ij}^2 - M^2,$$

where k is the number of defects. In the systems containing different types of defects, one can also introduce the average distance and dispersion for defects of each type separately, e.g., M_{PP} and M_{FF} .

Figure 5 shows the matrices of defects for two different local energy minima in the Thomson problem at $N = 92$. The local minima (the second and third rows in Table 3, respectively) are described by the same Föpl indices and the same symmetry groups. At the same

(a)

P	5	3	6	4	6	6	7	4	3	6	3
5	P	6	5	3	6	3	3	8	5	7	3
3	6	P	3	3	6	8	6	4	5	4	5
6	5	3	P	3	5	6	3	5	8	3	7
4	3	3	3	P	7	6	4	7	6	6	4
6	6	6	5	7	P	3	4	3	4	3	6
6	3	8	6	6	3	P	3	5	4	5	4
7	3	6	3	4	4	3	P	6	7	4	6
4	8	4	5	7	3	5	6	P	3	3	6
3	5	5	8	6	4	4	7	3	P	6	3
6	7	4	3	6	3	5	4	3	6	P	8
3	3	5	7	4	6	4	6	6	3	8	P

(b)

P	5	7	7	4	5	6	4	3	3	3	6
5	P	5	3	5	8	6	6	3	7	3	3
7	5	P	3	6	3	3	4	7	6	6	3
7	3	3	P	4	6	3	7	4	7	6	4
4	5	6	4	P	5	3	7	3	3	6	7
5	8	3	6	5	P	3	3	7	3	6	5
6	6	3	3	3	3	P	6	5	4	8	6
4	6	4	7	7	3	6	P	7	4	3	3
3	3	7	4	3	7	5	7	P	5	4	6
3	7	6	7	3	3	4	4	5	P	5	7
3	3	6	6	6	6	8	3	4	5	P	3
6	3	3	4	7	5	6	3	6	7	3	P

Fig. 5. The d -matrices of two “similar” minima in the Thomson problem: (a) the d -matrix of the local minimum at $N = 92$ (the symmetry C_2 , the Föppl index 2^{46}); (b) the d -matrix of another local minimum at $N = 92$ (the symmetry C_2 , the Föppl index 2^{46}).

time, their d -matrices are different and cannot be reduced to one another.

Since the interaction potential between the charges is not used in the construction of the graph of a closed lattice, the formalism of the d -graph and the d -matrix can be used not only for writing and comparing different local and global minima (the solutions of the Thomson and other close problems) but also for comparing the solutions of various problems.

HEXAGONAL LATTICE

A model of a closed hexagonal lattice can be used to describe fullerene structures. A graph of a closed hexagonal lattice is dual with respect to the graph of a closed triangular lattice in which the centers of disclinations in the closed hexagonal lattice are faces and not vertices. Thus, to a closed hexagonal lattice of fullerene C_{60} there corresponds the closed triangular lattice of the local minimum ($N = 32$, I_h) in the system of Coulomb charges on a sphere.

CONCLUSION

The notion of a quasi-two-dimensional closed triangular lattice is introduced to describe the structure of

charges on the surface of a sphere. It is shown that the triangular lattice on a closed simply connected surface includes topological defects—disclinations—of different charges, with the total topological charge of defects, $M = 12$, being constant and independent of the charge and location of individual defects. The equilibrium and nonequilibrium configurations are considered at charge numbers in the range $N = 2-100$. The methods for classification and compact description of the structures are suggested. A graph of defects or a d -graph of the lattice is defined and used to describe the mutual location and charge of defects in the lattice. Thus, the description of the crystal structure of N charges on a closed surface is reduced to determining the d -graph or the d -matrix of the lattice, $k \times k$, where the number of defects in the lattice k is limited. In particular, in the Thomson problem, for most of the configurations we obtain $k = 12$.

The model of Coulomb charges on the surface of a sphere describes a number of physical systems, including the 3D-system of ions in a trap with an abrupt confining potential, a system of electrons in a semiconductor 3D-quantum dot, a multicharge bubble with an electron in liquid helium (in the classical limit), and a system of ions in a helium cluster retained by image forces.

At present, a large number of various objects are known and experimentally observed that are characterized by one common property: From the topological standpoint, these systems can be considered as sets of points distributed over the sphere surface. Such objects are clusters consisting of particles interacting according to different (Coulomb, dipole laws) laws, atomic clusters, multiatomic molecules, fullerenes, spherical viruses, etc. It is suggested that such structures be considered within the unified approach as quasi-two-dimensional closed lattices with topological defects of various charges. The structure of the lattice and the character of the defects in it are determined by various mechanisms, e.g., by valence (in fullerenes and other atomic and molecular clusters), mutual charge repulsion resulting in the formation of a triangular lattice, etc. For each type of closed lattice, the total charge of all the disclinations is an invariant. Thus, in the closed triangular lattice and in the closed hexagonal lattice (fullerenes), the total charge of all the defects is $M = 12$. However, in the former case, disclinations are vertices—nonhexamers, whereas in fullerenes, disclinations are nonhexagonal faces. A number of systems, e.g., ions in traps and multishell carbon clusters (“onions”), can be considered to be systems of concentric closed lattices. The development of nanotechnology allows one to expect the creation of new substances with molecular structures in the form closed lattices.

REFERENCES

1. *Proceedings of VIII International Symposium on Small Particles and Inorganic Clusters, ISSSPIG 8*, Copenhagen, Denmark, July 6, 1996.

2. *Proceedings of the Conference "Mesoscopic and Strongly Correlated Electron Systems," Chernogolovka, 1997*, Usp. Fiz. Nauk **168** (2), 135 (1998) [Phys. Usp. **41**, 127 (1998)].
3. Yu. E. Lozovik, Usp. Fiz. Nauk **153**, 356 (1987) [Sov. Phys. Usp. **30**, 912 (1987)].
4. Yu. E. Lozovik and V. A. Mandelshtam, Phys. Lett. A **165**, 469 (1992).
5. V. M. Bedanov and F. M. Peeters, Phys. Rev. B **49**, 2667 (1994).
6. V. Schweigert and F. M. Peeters, Phys. Rev. B **51**, 7700 (1995).
7. Yu. E. Lozovik and E. A. Rakoch, Phys. Rev. B **57**, 1214 (1998).
8. A. I. Belousov and Yu. E. Lozovik, Pis'ma Zh. Éksp. Teor. Fiz. **68**, 817 (1998) [JETP Lett. **68**, 858 (1998)].
9. A. I. Belousov and Yu. E. Lozovik, Eur. Phys. J. D **8**, 251 (2000).
10. H. W. Kroto, J. R. Heath, S. C. O'Brien, *et al.*, Nature **318**, 162 (1985).
11. A. V. Eletskii and B. M. Smirnov, Usp. Fiz. Nauk **163** (4), 33 (1993) [Phys. Usp. **36**, 202 (1993)].
12. A. V. Eletskii and B. M. Smirnov, Usp. Fiz. Nauk **165**, 977 (1995) [Phys. Usp. **38**, 935 (1995)].
13. Yu. E. Lozovik and A. M. Popov, Usp. Fiz. Nauk **167**, 751 (1997) [Phys. Usp. **40**, 717 (1997)].
14. A. M. Livshits and Yu. E. Lozovik, Chem. Phys. Lett. **314**, 577 (1999).
15. J. J. Thomson, Philos. Mag. **7**, 237 (1904).
16. T. Erber and G. M. Hockney, J. Phys. A **24**, L1369 (1991).
17. E. L. Altshuler, T. J. Williams, E. R. Ratner, *et al.*, Phys. Rev. Lett. **72**, 2671 (1994).
18. H. A. Munera, Nature **320**, 597 (1986).
19. L. T. Wille, Nature **324**, 46 (1986).
20. T. W. Melnyk, O. Knop, and W. R. Smith, Can. J. Chem. **55**, 1745 (1977).
21. P. M. L. Tammes, Recl. Trav. Bot. Neerl. **27**, 1 (1930).
22. A. A. Samarskiĭ and A. A. Gulin, *Numerical Methods* (Nauka, Moscow, 1989).
23. A. L. Mackay, J. L. Finney, and K. Gotoh, Acta Crystallogr., Sect. A: Cryst. Phys., Diffr., Theor. Gen. Crystallogr. **A33**, 98 (1977).
24. D. A. Kottwitz, Acta Crystallogr., Sect. A: Found. Crystallogr. **A47**, 158 (1991).
25. J. R. Edmundson, Acta Crystallogr., Sect. A: Found. Crystallogr. **A48**, 60 (1992).
26. J. R. Edmundson, Acta Crystallogr., Sect. A: Found. Crystallogr. **A49**, 648 (1993).
27. T. Erber and G. M. Hockney, Phys. Rev. Lett. **74**, 1482 (1995).
28. E. L. Altshuler, T. J. Williams, E. R. Ratner, *et al.*, Phys. Rev. Lett. **74**, 1483 (1995).
29. J. Leech, Math. Gazette **41**, 81 (1957).
30. L. Föppl, J. Reine Angew. Math. **141**, 251 (1912).
31. L. Bonsall and A. A. Maradudin, Phys. Rev. B **15**, 1959 (1977).
32. G. Meissner and A. Flamming, Phys. Lett. A **57A**, 277 (1976).
33. V. A. Likhachev and R. Yu. Khaĭrov, *An Introduction to the Theory of Disclination* (Leningr. Gos. Univ., Leningrad, 1975).

Translated by L. Man

**THEORY OF CRYSTAL
STRUCTURES**

Penrose Mosaic as a Quasistochastic Tree-Graph Lattice

V. V. Yudin, T. A. Pisarenko, E. A. Lyubchenko,
O. A. Chudnova, and Yu. A. Karygina

Far East State University, Vladivostok, 690600 Russia

e-mail: yudin@ifit.phys.dvgu.ru

Received June 30, 2000

Abstract—The Penrose mosaic as the minimum representative of quasicrystals is discussed in terms of generalized planar lattice models. The role of these models is played by Cayley’s tree graphs which, in the general case, are characterized by quasi-random branching. A three-level golden alphabet is defined, and a Penrose mosaic is synthesized with the aid of its highest level. The algebras of the suggested grammar are formulated in an explicit form. It is shown that the statistics of a Penrose mosaic at the level of golden rhombuses belongs to the class of Zipf–Mandelbrot distributions. The algorithm for mapping a Penrose mosaic into Cayley’s tree graphs based on the $[2q \times 2p]$ alphabet is also formulated. The problem of the entropy percolation for quasistochastic Cayley’s trees of Penrose mosaics is solved. The entropy percolation of these trees is characterized by an obvious minimum periodicity and, on average, by the invariance principle of the golden entropy. © 2002 MAIK “Nauka/Interperiodica”.

INTRODUCTION

Almost fifteen years ago, the Shechtman group studied the rapidly cooled $\text{Al}_{86}\text{Mn}_{14}$ alloy and obtained unique objects which did not belong to metallic glasses [1]. The diffraction patterns of these objects had ten spots related by a fivefold rotation axis forbidden in crystallography. Later, these objects were called quasicrystals. In an attempt to interpret the “pentasymmetry” of these diffraction patterns, the Penrose model was used [2, 3]. Somewhat later, a family of mosaics corresponding to forbidden symmetries of higher orders was also studied [4–6].

The symmetries characteristic of quasicrystals were also observed in studies of nonlinear dynamic systems [7], and it was shown that the destruction of the separatrix structure of the phase space caused by the ε -perturbation results in the formation of a stochastic web with a symmetry characteristic of quasicrystals. As follows from [7], a stochastic web is generated by recurrent two-dimensional mapping with twisting. By the end of the 1990s, a specific niche including a wide class of quasicrystal objects had been formed. Thus, it was shown that the processes of structure relaxation and decomposition of the amorphous state in metallic glasses resulted in the precipitation of star-shaped grains [8, 9].

Consider a Penrose mosaic as the minimum and universal representative of the class of quasicrystals. Below, we use the linguistic approach and interpret a Penrose mosaic as a text written in a certain language. However, we reduce the linguistic approach to the level of statistical linguistics, where we use the frequency of the occurrence of various symbols forming an alphabet and, thus, also rank statistics. A characteristic feature of

our consideration is the transition to the “quartet alphabet” at the level of golden (g) rhombuses with due regard for the types of possible contacts—the vertex and the edge neighborhoods of g -rhombuses.

The creation of the grammar is rather difficult [10], but we can simplify it and avoid the identification of the grammar type by considering a Penrose mosaic in a new tree-graph representation based on the quartet alphabet, which is equivalent to the algorithm for constructing a Penrose mosaic itself—a typical grammatical function [10].

Percolation on Cayley’s trees for a Penrose mosaic can be interpreted as a Markovian shift in the tree hierarchies, which is reflected in the probabilistic and entropy measures. This type of percolation is related to the semigroup class. Generally speaking, percolation can occur along two directions: center \rightleftharpoons periphery. The existence of two opposite semigroup percolation flows can result in a nonzero defect in percolation on Cayley’s trees. In this case, we arrive at irreversible tree graphs. It is possible to introduce the criterion of quasicrystallinity on Penrose mosaics in terms of entropy functionals. Thus, we arrive at the theoretical-probabilistic and entropy manifestations of the “golden characteristics” of the Penrose mosaic.

STATISTICS OF A PENROSE MOSAIC AT THE LEVEL OF A QUARTET RHOMBUS-BASED ALPHABET

Various Penrose mosaics are formed by golden rhombuses (g -rhombuses) of only two types, consisting, in turn, of two golden (g) triangles (Figs. 1a, 1c) sharing the golden sides. The existence of the level of

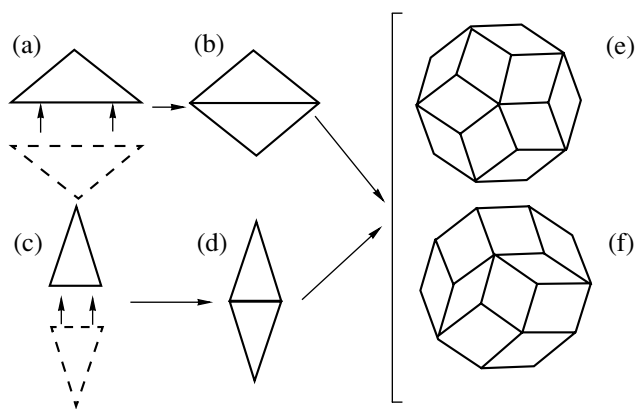


Fig. 1. Three-level alphabet of a Penrose mosaic.

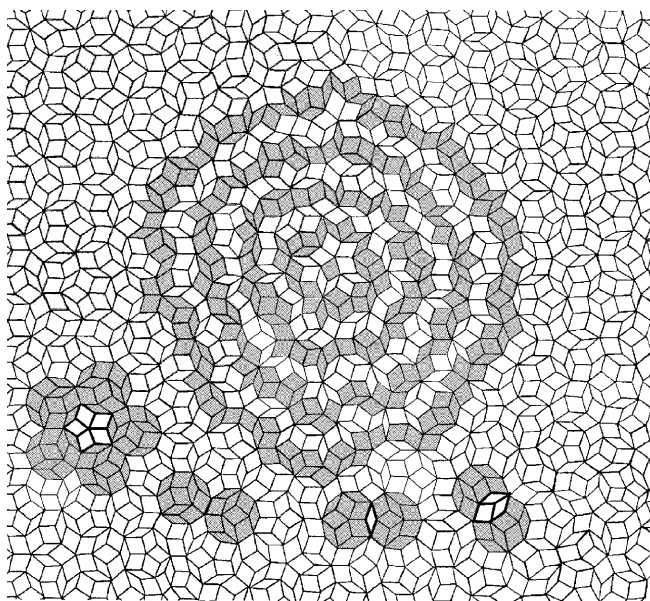


Fig. 2. Penrose mosaic. One can see elements of alphabet III, the types of intersections, and several coordination spheres.

g -triangles and, later, of g -rhombuses (Figs. 1b, 1d), indicates the hierarchical nature of the alphabet of the Penrose mosaic. Now, formulate a hypothesis which states that the synthesis of a mosaic is simplified if an alphabet of a higher rank based on blocks (sentences) of g -rhombuses is used. Possibly, the grammar of the hierarchical alphabet and Penrose tiling would be less complicated and artificial that at the level of g -rhombuses [3, 11].

To construct a dual g -basis of Penrose tiling of level III, we have to apply the following algebraic rules of linguistics II:

A “block” or a sentence of level III is chosen as a pair of convex ten-vertex polygons composed in the dual basis of g -rhombuses.

The number of g -rhombuses in the sentences of level III is $5 + 5$ (“acute” + “obtuse”) rhombuses, with both components being equally probable.

A pair of ten-vertex polygons is constructed from g -rhombuses by applying the join operation (without intersection) along a nonspecific (unit) side.

One of the compound ten-vertex polygons possesses a fivefold rotation axis, whereas the other is characterized by dorsal symmetry with a “pentacoordination” point. The role of a nucleus is played by an obtuse g -rhomb.

A three-level binary golden alphabet, level III, and their fragments are illustrated by Fig. 1. Using level III, we synthesized a Penrose mosaic shown in Fig. 2 with a rather simple grammar III. The algebra of the grammar for alphabet III is as follows:

—a fragment shown in Fig. 1e is a star-shaped ten-vertex polygon that has no contacts with other similar polygons;

—a joint with a simple intersection of the motifs in Figs. 1e and 1f is allowed with the intersection being an acute g -rhombus;

—a pair joint of dorsal ten-vertex polygons occurs with the intersection in the form of two acute and one obtuse g -rhombuses;

—the maximum coordination number of the motif surrounded by dorsal ten-vertex polygons shown in Fig. 1e is five;

—five joint dorsal fragments can form a pentasymmetry point (but not a fragment shown in Fig. 1e) with five complex intersections.

Now, complement the mosaic representation with the probabilistic consideration based on alphabet II. Along with the objects (a pair of g -rhombuses), we also take into account the contact type (adjacency neighborhood), i.e., the coordination. The Penrose mosaic has both the vertex and the edge contacts of g -rhombuses. Below, we write matrix (1) (Fig. 2) of the probability to encounter the letters “rhombuses-type of the contact” averaged over the whole Penrose mosaic. In fact, we deal here with the quartet alphabet “rhombus (q)—coordination type (p),” [$2q \times 2p$], with the matrix

	v	c	
α_1	0.4285	0.1905	$P(\alpha_1/v \vee c) = P_0(\alpha_1) = 0.619,$
α_2	0.261	0.120	$P(\alpha_2/v \vee c) = P_0(\alpha_2) = 0.381$ (1)

where α_1 is an obtuse g -rhombus, α_2 is an acute g -rhombus, c is an edge contact, and v is a vertex contact. It is seen that the sums of the rows of matrix (1) coincide with the golden ratio and its complement. The estimate of the Vajda entropy yields $H_V[P(\alpha_1/v \vee c); P(\alpha_2/v \vee c)] = 0.472 = H_{\text{gold}}$. The corresponding structurization factor equals $\eta_2 = 5.6\%$, and therefore the statistics of g -rhombuses is stochastic for about 94.4%. In this

sense, the Penrose mosaic is an almost noise stochastic parquet at the level of alphabet II.

The asymptotic probabilistic vectors of the M -chain can be conveniently mapped into a two-level binary probabilistic tree (Fig. 3). The first level of the tree indicates a division into two g -rhombuses with golden probabilities, which results in $H_{\text{gold}}(2) = 0.472$. At the second level, two more types of contact—the vertex and the edge ones—are added, which results in the formation of the quartet $[2q \times p]$ alphabet. Considering Fig. 3, we can see that the golden ratio of the first-level probability is preserved at the second level in the form of the double relationship

$$\frac{\alpha_1}{\alpha_2} = \frac{\alpha_1^v / \alpha_1^c}{\alpha_2^v / \alpha_2^c} = 0.618 \vee 1.618.$$

Then, the tree in Fig. 3 should be recognized as a golden tree on the whole. The estimate of the Vajda entropy, $H(4) = 0.6688 = H_{\text{gold}}(4)$, should also be recognized as a golden one in the quartet alphabet. The structural index in the $[2q \times 2p]$ alphabet, $\eta_4 = 10.66\%.$, indicates a higher order level of the Penrose mosaic in the quartet alphabet. Obviously, the stochastic component of the Penrose-mosaic organization in this alphabet is about 90%. Compared to the binary alphabet, the quartet alphabet $[2q \times 2p]$, remaining golden as earlier, provides a higher organization of the Penrose mosaic.

As is seen from Eq. (1), it is possible to order all four conditional probabilities by the degree of their decrease on the matrix $[2q \times 2p]$. In fact, this signifies the transition to the consideration of rank statistics. Consider the problem of identifying rank statistics using the a priori hyperbolicity hypothesis, $p(r) \approx C/(r^\gamma)$. Obviously, $\ln p(r) \equiv -s[p(r)] \equiv N[p(r)] = \ln C - \gamma \ln r = S_c - \gamma S(r)$; in other words, either the positive or the negative entropy of the distribution is proportional to the rank entropy.

Figure 4 shows the result of the statistical identification of both initial and asymptotic distributions of the quartet alphabet. The quality of the verification of the hyperbolicity hypothesis (Fig. 4) is quite satisfactory, $\gamma_0 = 0.87$, $\gamma_\infty = 1.05$, and $\bar{\gamma} = 0.96$. Thus, a Penrose mosaic obeys the Zipf–Mandelbrot statistics. Moreover, $P_0(\alpha_1/v \vee c) = P_\infty(\alpha_1/v \vee c)$ and $P_0(\alpha_2/v \vee c) = P_\infty(\alpha_2/v \vee c) \Rightarrow \{P_{\text{gold}}; \bar{P}_{\text{gold}}\}$, which indicates the invariance of these “golden frequencies” also in the problem of eigenvalues of the M -matrix.

It is well-known that the mechanism of generation of hyperbolic statistics in linguistics, economics, and sociology is the consequence of the competition assumed to be absent in the collectives with the normal (Gaussian) statistics. Figure 2 illustrates the mechanism of hyperbolicity of the quartet g -rhombus alphabet of a mosaic. Choosing an arbitrary g -rhombus as a percolation center, we can construct the coordination

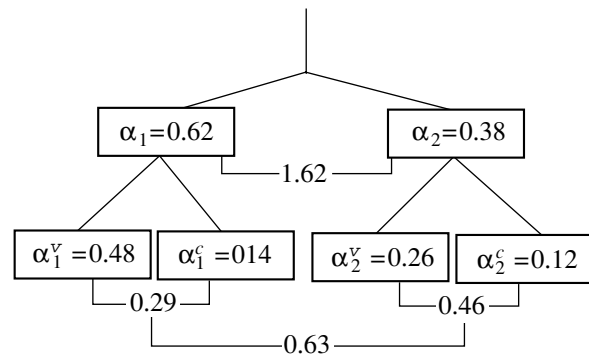


Fig. 3. Two-level binary tree of asymptotic two- and four-dimensional probabilistic vectors of a Penrose mosaic.

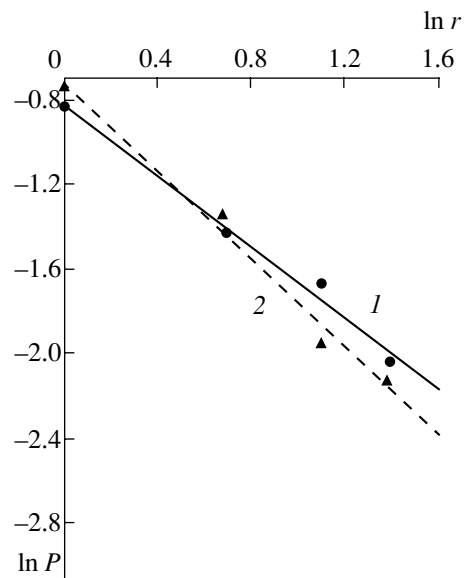


Fig. 4. Statistical identification of (1) the initial and (2) the asymptotic distributions of the quartet alphabet.

fronts, which, in the global sense, are characterized by the maximum convexity (in the discrete representation). Now, consider some specific features of the construction of coordination fronts.

The existence of edge contacts cannot provide the continuity of coordination fronts. The number of edge contacts does not exceed two.

On average, the number of possible topological vertex contacts between the rhombuses is four, i.e., exceeds the number of topological edge contacts.

As is seen from Fig. 2, the continuity and the maximum convexity of coordination fronts provide vertex contacts with a considerable statistical advantage over edge ones,

$$P(v/\alpha_1 \vee \alpha_2) = 68\%; \quad P(c/\alpha_1 \vee \alpha_2) = 32\%,$$

which reflects the golden nature of a Penrose mosaic.

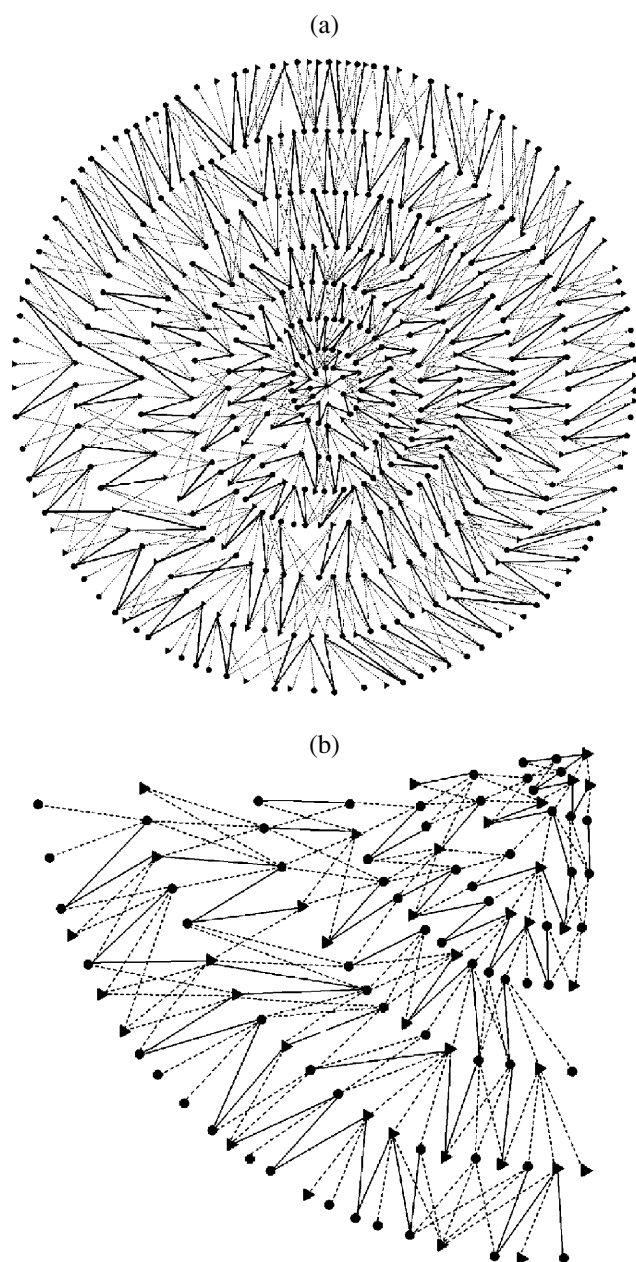


Fig. 5. Cayley's tree of (a) a Penrose mosaic and (b) its enlarged fragment. An obtuse g -rhombus on a Cayley's tree of a Penrose mosaic is depicted by a circle, an acute g -rhombus, by a triangle.

Using the Zipf linguistic interpretation, we see that an edge contact is more “expensive” (words of higher ranks), whereas a vertex contact is “cheaper” and, therefore, is encountered much more often (in our case, by a factor of 2.13). These opposite tendencies result in an “asymptotic compromise” reflected in the $[2q \times 2p]$ matrices. Thus, in terms of the Zipf–Mandelbrot law, a Penrose parquet has typical linguistic characteristics. To some extent, a Penrose mosaic (Fig. 2) can be considered as a two-dimensional text of polar geometry.

MAPPING OF A PENROSE MOSAIC INTO QUASISTOCHASTIC CAYLEY'S TREES AND ENTROPY PERCOLATION

The conventional coordinate representation of a Penrose mosaic is insufficient because a researcher can reveal only the objective coordinate component (g -rhombuses) of the quasicrystal order. We believe that the essence of cellular net structures and mosaics (including Penrose mosaics) is reflected by another component—a pulse one (see the $[2q \times 2p]$ -matrices). The pulse component is understood as the simplest adjacency pair ratio or the coordination between any two contacting pairs of golden rhombuses in a mosaic.

Such a representation (adequate for the $[2q \times 2p]$ matrix) can be conveniently considered in graph structures of a special form. We mean here the adjacency tree graphs [12] constructed by a certain algorithm. The closest analogues of such graphs are Bethe trees [13] generalized in the form of Cayley's trees. The tree representation is the most complete one, because it allows one to reveal in explicit form all the coordination relationships without the loss of the objective component [14–16]. The algorithm for constructing Cayley's tree graphs for cellular structures of the general type (such as net structures of mesodeflects in quartz glasses) and the properties of Cayley's trees are described elsewhere [14–16]. Here, we should like to emphasize that, in the general case, the degree of branching of the bushes of Cayley's trees is a random quantity. However, neither reflection in the tree topology nor some order and organization of Cayley's trees can be forbidden. Cayley's trees of such type are called quasistochastic. Cayley's trees of a Penrose mosaic are related to this class.

Now, apply the theory of graph enumeration to these Cayley's supertrees of a Penrose mosaic (Fig. 5) [12, 17]. However, the theory of graph enumeration usually considers decomposition of Cayley's trees into elementary bush subgraphs ignoring the types of vertices and bonds. In our case, this simplified approach is useless. We introduce a new type of an enumerative polynomial composed not of bushes but of elementary symbols of the $[2q \times 2p]$ alphabet. These enumerative polynomials for Cayley's trees of a Penrose mosaic are arranged according to the Zipf–Mandelbrot statistics (see the previous Section). Thus, these enumerative polynomials have the fixed rank $l = 4$. It is natural to normalize this rank enumerative polynomial and, thus, to obtain the probabilistic enumerative polynomials in the form

$$\Pi_i(x) = \sum_{l=1}^4 \mu_i(l)x^l, \quad (2)$$

where $x \in [2q \times 2p]$; $l = 1, 2, 3, 4$ are the ranks of branches in the Zipf–Mandelbrot sense; $\mu_i(l)$ are the probabilistic weights of the l th rank in the $[2q \times 2p]$ alphabet; and i is the number of the hierarchical level on Cayley's trees of a Penrose mosaic. Figures 6a and 6c

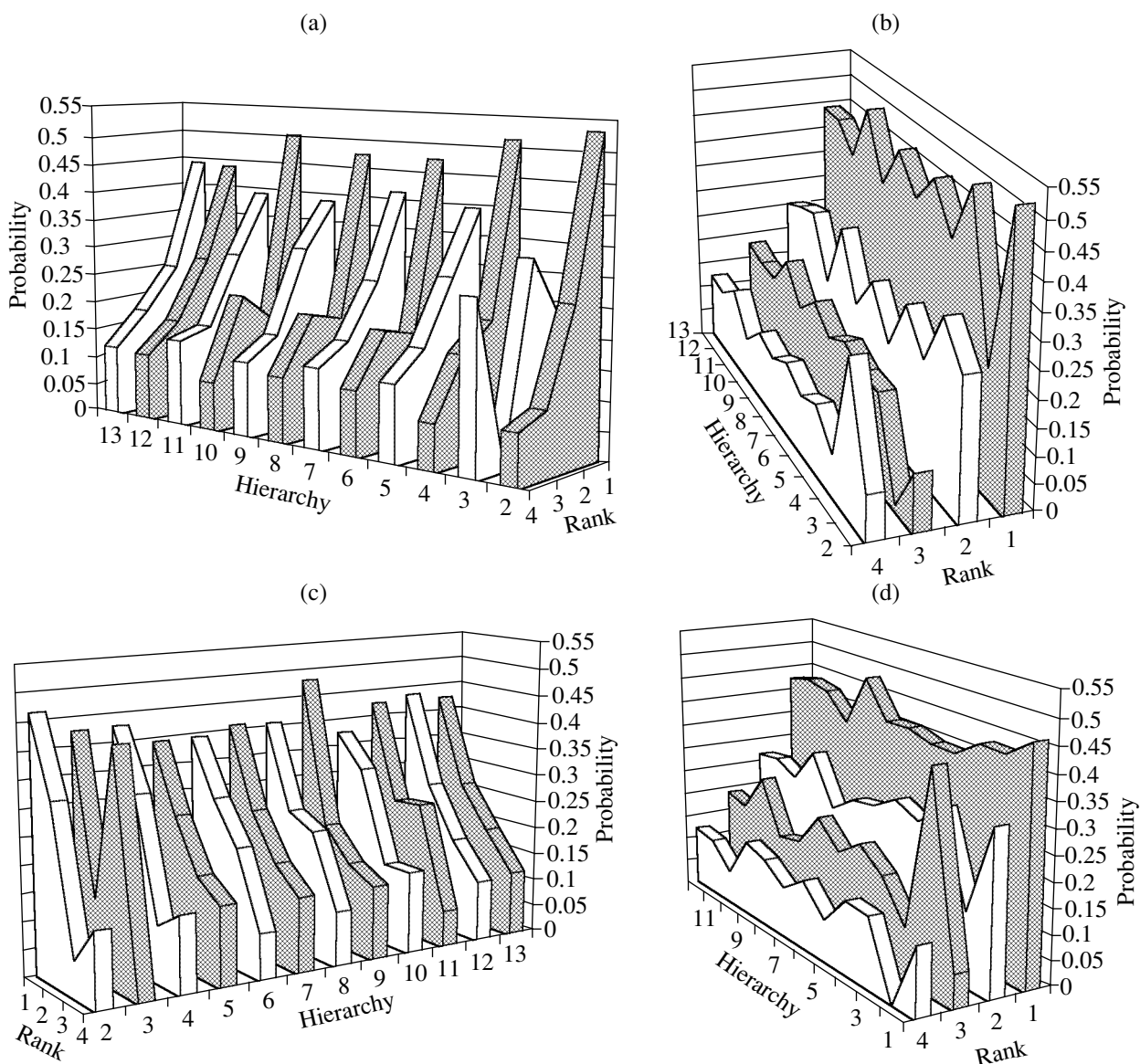


Fig. 6. Dynamics of the (a, c) rank probabilistic enumerative polynomials and (b, d) rank probabilistic dynamics over the levels of a Cayley's tree of a Penrose mosaic along the percolation directions center \rightarrow periphery; (a, b) direct and (c, d) inverse flows.

and Figures 6b and 6d show the hierarchical dynamics of the rank statistics and the partial (rank) dynamics, Eq. (2). One can readily see the obvious periodic nature of these polygons, which indicates the quasicrystal nature of a Penrose mosaic.

Compare qualitatively the hierarchical dynamics of the rank polynomials (Figs. 6a, 6c) along the percolation directions center–periphery. The alternation of decreasing and mode polygons is more clearly seen in the direct flow (Fig. 6a). The variation of the mode structure of polygons is seen in Fig. 6a more clearly than in Fig. 6c. The reflection from the ∞ -horizon results in a more homogeneous percolation structure of polygons (Fig. 6c). Comparing Figs. 6b and 6d, we see that the partial (rank) percolation over the hierarchical levels of Cayley's trees of a Penrose mosaic in the

reverse flow is somewhat smoothened. The essentially stochastic nature of the wavelike flow of the probabilistic measures is seen in all the representations in Fig. 6, which indicates the prevalence of the stochastic component over the determined percolation component of Cayley's trees of a Penrose mosaic. This qualitative analysis of the polygon percolation shows that it is necessary to convolute this detailed information into a certain functional so that it could reflect both the noiselike and the structured components in the ordering of Cayley's trees of a Penrose mosaic.

Now, consider the tree percolation of the probabilistic measures of the mosaic at the functional level. In particular, consider the entropy functional set at the probabilistic enumerative polynomial (2) of each hierarchy level. The entropy functional was chosen in

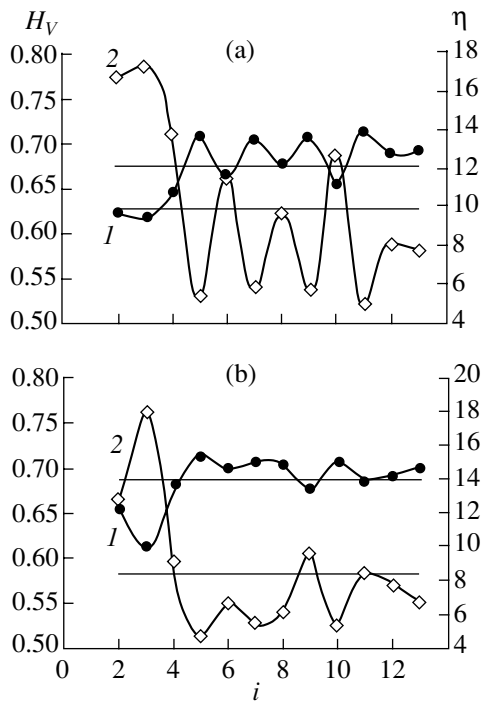


Fig. 7. (1) Percolation entropy and (2) structural coefficient over the hierarchical levels of Cayley’s tree of a Penrose mosaic: (a) direct ($H_V = 0.6749 \pm 4.13\%$, $\eta = 9.99\%$, $\delta_{\eta} = 37.14\%$) and (b) reverse ($H_V = 0.6867 \pm 2.66\%$, $\eta = 8.44\%$, $\delta_{\eta} = 31.56\%$) flows.

Vajda form:

$$H_V(i) = \sum_l \mu_i(l)[1 - \mu_i(l)], \tag{3}$$

$$\eta_V(i) = 1 - \frac{H_V[\mu_i(l)]}{\sup H_V[\mu_i(l)]}. \tag{4}$$

Thus, the entropy introduced here possesses the properties of nonnegativity, nonlinearity, and connectivity and obeys the additivity principle. The upper estimate of the asymptotic Vajda entropy equals unity, whereas the Shannon measure converges. The Vajda entropy corresponds to the chosen scheme with β -distributions, which is well-known in the theory of Brownian motion. Equation (4) can be interpreted as the structural coefficient of the percolation process in terms of entropy. If $H_V[\bar{\mu}_i^{k_i}(l)] \Rightarrow \max H_V[\bar{\mu}_i^{k_i}(l)] \eta_V(i) \Rightarrow 0$, the entropy of the i th hierarchy is purely stochastic (100% noise component). If $H_V[\bar{\mu}_i^{k_i}(l)] \Rightarrow 0$, then $\eta_V(i) \Rightarrow 1$ (is fully determined). Obviously, in real situations, the stochastic and the determined percolation components are mixed.

We should like to make an important methodological remark on the percolation problem. Usually, one considers percolation of a certain physical “agent” in the lattice whose vertices or bonds are affected by certain noise factors. We search for the percolation thresh-

old in the problem of vertices or bonds to establish the relation between this threshold and the lattice symmetry.

The percolation problem considered here is quite different in at least two aspects. First, the noiselike factor is included into the quasistochastic topology of Cayley’s trees of a Penrose mosaic (Fig. 6) and, thus, cannot be considered as an external factor. A random quantity in our problem is not only bush branching of Cayley’s trees of a Penrose mosaic, but also the bases (vertices) of the bushes. It is clear that the internal nature of the stochastics in our case is much more complicated than in the classical percolation problem.

Second, percolation in lattices is understood as a certain generalized flow also of an external nature. The carriers of this flow can be charges, masses, densities, concentrations, etc., but they all belong to the class of measures. In our case, these are polygons and statistics given by Eq. (2) and, later, also entropy functionals given by Eqs. (3) and (4). Therefore, one can consider the probabilistic entropy-like flows in Cayley’s trees of a Penrose mosaic. Again, these measures are essentially internal and, therefore, the problem of probabilistic entropy percolation is a problem of self-identification of the quasistochastic topology of Cayley’s trees of a Penrose mosaic.

Calculations by Eqs. (3) and (4) for Cayley’s trees of a Penrose mosaic are illustrated in Fig. 7, where the entropy percolation over the hierarchical levels of Cayley’s trees of a Penrose mosaic is of the wave type. Estimation of the entropy percolation by Eqs. (3) and (4) (Fig. 7) yields the minimum period consisting, on average, of two hierarchical levels. According to Figs. 7a and 7b, the quasiperiodic entropy oscillations are preserved in both direct and reverse flows, but are more pronounced in the former one. Although the average values calculated by Eq. (4) in both cases differ by 1%, the individual values of these curves can differ by 7%. The pronounced differences in η -values (Fig. 7) indicate the statistical importance of the quasiperiodicity of the percolation entropy flows in Cayley’s trees of a Penrose mosaic. In terms of thermodynamics, the reverse flow is “cooler” than the direct one. One has to pay attention to the average entropies given by Eq. (3), which almost coincide in both cases in Figs. 7a and 7b, whence follows the conclusion that, on average, the direct and reverse flows in Cayley’s trees of a Penrose mosaic are equivalent in terms of the entropy functional. The variations in entropy with respect to the average value are also essential and are from three to four percent. Comparing the stochastic and the determined levels in Figs. 7a and 7b, we see that the direct flow has a 10%-ordered component, whereas the reverse one, an 8.4%-ordered component. Thus, the reverse flow (Fig. 7b) is more stochastic than the direct one, which is the “payment” for reflection from the ∞ -horizon and can be considered as a certain analogue of the second law of thermodynamics.

Another no less important result is obtained by comparing the entropy characteristics (see the previous section) for a quartet alphabet and the percolation entropy averaged over the hierarchies of Cayley's trees of a Penrose mosaic. In fact, both entropies are practically identical. Thus, the percolation of the entropy measures on Cayley's trees for a Penrose mosaic obeys the ergodicity principle extended to Cayley's tree graphs. Moreover, on average, the probability and the entropy percolations on Cayley's trees of a Penrose mosaic can be characterized in terms of a certain entropy invariant, which corresponds to the golden entropy at the level of the quartet alphabet.

CONCLUSION

It is suggested that Penrose mosaics be considered using a quartet alphabet $[2q \times 2p]$, whose elements are g -rhombuses (vertex or edge types of contact). In a broader sense, a Penrose mosaic obeys the hierarchical three-level alphabet—a pair of golden triangles and rhombuses, a pair of ten-vertex polygons composed by $5 + 5$ obtuse and acute rhombuses possessing fivefold axis, and a point of pentacoordination (the dorsal symmetry). It is the grammar of the three-level alphabet that allows the simplest construction of a Penrose mosaic.

The hierarchical alphabet, in particular at levels I and II, should be complemented with probabilistic analysis. One can see the important role played by the golden nature of the alphabet of a Penrose mosaic at both levels. A Penrose mosaic has an invariant (a double ratio at level II) of the probabilities of an asymptotic quartet vector. We also introduced into consideration the entropy functionals in alphabets I and II generated by the golden relationships, so that a Penrose mosaic can be considered as a parquet in the alphabet $[2q \times 2p]$ synthesized with the aim of preserving the golden entropy.

It is proven in terms of rank statistics in the alphabet $[2q \times 2p]$ that, on the whole, Zipf–Mandelbrot distribution is valid for a Penrose mosaic. The mechanism of the generation of hyperbolic statistics is considered as the competition between the expensive edge and the cheap vertex contacts in the construction of convex coordination fronts. The results obtained allow the interpretation of a Penrose mosaic on the basis of a linguistic model and, thus, as a linguistic structure or a text with a two-dimensional polar geometry. The complete representation of a Penrose mosaic in quasistochastic Cayley's trees is constructed with the aid of the $[2q \times 2p]$ alphabet which, along with the objective component (g -rhombuses), takes into account the coordination and adjacency of the vertex and edge contacts. Growing and collapsing Cayley's trees are discussed, where the coordination translation is considered as a Markovian r -shift. A Cayley's tree of a Penrose mosaic is, in fact, a simplicial complex with ultrametrics. In terms of crystallography, a Cayley's tree of a Penrose mosaic is a generalized quasistochastic tree lattice.

The (internal) percolation problem for Cayley's trees of a Penrose mosaic is solved in terms of entropy functionals for enumerating rank polynomials. Cayley's trees of a Penrose mosaic are characterized by a wave flow in both center \rightleftharpoons directions with a minimum period equal to two hierarchical levels of Cayley's trees of a Penrose mosaic hierarchy. The percolation entropy is characterized by a periodic flow with $\sim 90\%$ -stochasticity and, thus, with $\sim 10\%$ order. This is an important quasicrystal aspect of a Penrose mosaic. On average, percolation entropy is equivalent to the golden entropy of a Penrose mosaic in the $[2q \times 2p]$ alphabet, which indicates the ergodicity of the tree percolation. On average, the Markovian shift on Cayley's trees of a Penrose mosaic is characterized by a golden-entropy invariant.

REFERENCES

1. D. Shechtman, I. Blech, D. Gratias, *et al.*, *Phys. Rev. Lett.* **53**, 1951 (1984).
2. M. Gardner, *Sci. Am.* **236**, 110 (1977).
3. D. R. Nelson, *Sci. Am.* **255** (2), 32 (1986); P. W. Stephens and A. I. Goldman, *Sci. Am.* **264** (4), 24 (1991).
4. D. Gratias, *Recherche* **178**, 788 (1986); *Usp. Fiz. Nauk* **156** (2), 347 (1988).
5. A. I. Lazarev and G. A. Domrachev, *Kristallografiya* **39**, 811 (1994) [*Crystallogr. Rep.* **39**, 733 (1994)].
6. A. I. Lazarev, A. Yu. Sukhanov, and G. A. Domrachev, *Kristallografiya* **41**, 798 (1996) [*Crystallogr. Rep.* **41**, 756 (1996)].
7. G. M. Zaslavskii, R. Z. Sagdeev, D. A. Usikov, and A. A. Chernikov, *Usp. Fiz. Nauk* **156** (2), 193 (1988) [*Sov. Phys. Usp.* **31**, 887 (1988)].
8. V. V. Yudin, *Doctoral Dissertation in Physics and Mathematics* (Vladivostok, 1987).
9. V. V. Lapatin and Yu. F. Ivanov, *Pis'ma Zh. Éksp. Teor. Fiz.* **50** (11), 466 (1989) [*JETP Lett.* **50**, 499 (1989)].
10. V. A. Malyshev, *Usp. Mat. Nauk* **53** (2), 107 (1998).
11. A. M. Bratkovskii, Yu. A. Danilov, and G. I. Kuznetsov, *Fiz. Met. Metalloved.* **68** (6), 1045 (1989).
12. A. A. Zykov, *Foundations of Graph Theory* (Nauka, Moscow, 1987).
13. J. M. Ziman, *Models of Disorder: the Theoretical Physics of Homogeneously Disordered Systems* (Cambridge Univ. Press, Cambridge, 1979; Mir, Moscow, 1982).
14. V. V. Yudin, T. A. Pisarenko, E. A. Lyubchenko, and E. G. Savchuk, *Kristallografiya* **44**, 413 (1999) [*Crystallogr. Rep.* **44**, 373 (1999)].
15. E. A. Lyubchenko, *Candidate's Dissertation in Physics and Mathematics* (Vladivostok, 1999).
16. T. A. Pisarenko, *Candidate's Dissertation in Physics and Mathematics* (Vladivostok, 2000).
17. F. Harary, in *Applied Combinatorial Mathematics*, Ed. by E. F. Bechenbach (Wiley, New York, 1964; Mir, Moscow, 1968).

Translated by L. Man

STRUCTURE OF INORGANIC COMPOUNDS

Crystal Structure of Zirconium-Rich Seidozerite

D. Yu. Pushcharovskii*, M. Pasero**, S. Merlino**, N. V. Vladykin***,
N. V. Zubkova*, and E. R. Gobechiya*

* Faculty of Geology, Moscow State University, Vorob'evy gory, Moscow, 119899 Russia

** Department of Earth Sciences, University of Pisa, Pisa, 56126 Italy

*** Vinogradov Institute of Geochemistry, Siberian Division, Russian Academy of Sciences,
ul. Favorskogo 1a, Irkutsk, 664033 Russia

Received August 21, 2001

Abstract—The crystal structure of seidozerite was refined (a Siemens P4 diffractometer, MoK α radiation, 1180 independent reflections, anisotropic refinement, $R = 0.053$). The monoclinic unit-cell parameters are $a = 5.627(1)$ Å, $b = 7.134(1)$ Å, $c = 18.590(4)$ Å, $\beta = 102.68(1)^\circ$, sp. gr. $P2/c$, $Z = 4$. The structural formula, $\text{Na}_{1.6}\text{Ca}_{0.275}\text{Mn}_{0.425}\text{Ti}_{0.575}\text{Zr}_{0.925}[\text{Si}_2\text{O}_7]\text{OF}$, agrees well with the results of the electron probe analysis. Seidozerite is demonstrated to belong to the meroplesiotype polysomatic series including the structures of more than 30 titano- and zirconosilicates. © 2002 MAIK “Nauka/Interperiodica”.

INTRODUCTION

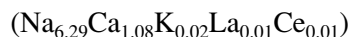
The zirconosilicate seidozerite was discovered by E.I. Semenov in 1958 in the Lovozero alkaline massif [1]. This mineral belongs to a rather large group of (Zr,Ti)-silicates, whose structures contain three-layer heteropolyhedral stacks denoted by HOH , where O is the central layer consisting of octahedra, and H are the outer layers formed by Si-tetrahedra and octahedra of highly charged Zr or Ti cations. In 1964, A.M. Portnov described the second specimen of seidozerite from North Baikal [2]. The crystal structures of the specimens from both deposits were studied by the photographic method [3, 4]. However, the high R factors (0.166 and 0.207 for the $h0l$ and $0kl$ reflections, respectively) obtained in the pioneering study [3] and the high, although slightly improved, R factors (0.146 for the non-zero $0kl$, $1kl$, and $2kl$ reflections and 0.100 for the non-zero $h0l$, $h1l$, and $h2l$ reflections) obtained in the more recent investigation [4] cast some doubt upon the characteristics of the cation distribution in the seidozerite structure.

Recently, seidozerite crystals were also discovered in another region of the Burpala massif (North Baikal). They are characterized by an higher ZrO $_2$ content (28.18–30.17 wt %) compared to those in the specimens from the Burpala and Lovozero massifs studied earlier (19.6–23.15 and 23.14 wt %, respectively). The high ZrO $_2$ content in the new seidozerite specimen, the availability of single crystals suitable for X-ray diffraction analysis, and the present-day possibilities of the instruments have stimulated interest in the refinement of the seidozerite structure.

EXPERIMENTAL

The seidozerite crystals were found in an alkaline pegmatitic body 1 m in thickness and 10 m in length located in the southwestern region of the Burpala alkaline massif, whose area and age were evaluated at 150 km 2 and 330 Ma, respectively. Seidozerite occurs as elongated crystals crosscutting earlier catapleiite isolations and intergrowing with grains of nepheline and feldspar.

According to the results of the electron probe analysis performed for three crystals, the average chemical compositions of the major components of seidozerite are as follows (wt %): SiO $_2$, 29.39; ZrO $_2$, 29.20; TiO $_2$, 13.03; Al $_2$ O $_3$, 0.26; MnO, 5.76; CaO, 3.81; FeO, 1.90; MgO, 0.32; Na $_2$ O, 12.26; K $_2$ O, 0.05; Nb $_2$ O $_5$, 0.68; La $_2$ O $_3$, 0.11; Ce $_2$ O $_3$, 0.15; and F, 3.06; the sum is 99.98. This composition corresponds to the following chemical formula of seidozerite describing the cation contents (with respect to 36 anions, namely, O $^{2-}$ and F $^-$):



A crystal of dimensions 0.08 × 0.08 × 0.1 mm 3 was selected under a microscope and was used for the qualitative electron probe analysis (a Philips PW 515 xl 30 microprobe, the accelerating voltage was 20 kV; the current intensity was 9 nA; and the diameter of the electron beam was 5 μm). The results of the analysis confirmed the presence of the above-mentioned cations in the mineral. The X-ray diffraction data were collected from the same crystal on an automated Siemens P4 diffractometer. The crystallographic characteristics and the details of the X-ray diffraction study and structure refinement are given in Table 1.

Table 1. Crystallographic characteristics and details of X-ray diffraction study

Formula	$\text{Na}_{1.6}\text{Ca}_{0.275}\text{Mn}_{0.425}\text{Zr}_{0.925}\text{Ti}_{0.575}[\text{Si}_2\text{O}_7]\text{OF}$
Unit-cell parameters, Å	$a = 5.627(1)$, $b = 7.134(1)$, $c = 18.590(4)$ $\beta = 102.68(1)^\circ$ $P2/c$; 4
Sp. gr.; Z	
Unit-cell volume V , Å ³	728.06(3)
Calculated density ρ , g/cm ³	3.574
Absorption coefficient μ , mm ⁻¹	3.34
Molecular weight	391.8
F_{000}	746.0
Diffractometer	Siemens P4
Wavelength, Å	0.71069
Maximum value of the 2θ angle, deg	60.01
Total number of reflections	3291
Total number of independent reflections	2122
Number of independent reflections with $ F > 4\sigma(F)$	1180
R_{int} , %	7.81
Number of parameters in the refinement	138
R_F upon isotropic refinement	0.081
R_F upon anisotropic refinement	0.053
$wR(F^2)$	0.145
GOF	0.990
$\Delta\rho_{\text{max}}$, e/Å ³	1.09
$\Delta\rho_{\text{min}}$, e/Å ³	-1.27

Table 2. Distribution of the cations over the positions in the seidozerite structure

Position	Content according to study [3]	Content according to study [4]	The present study	Electron content	Electron content taking into account the real occupancy	Average cation-anion distance	Sum of ionic radii
Zr	$\text{Zr}_{0.75}\text{Ti}_{0.25}$	$\text{Zr}_{0.7}(\text{Mn}, \text{Fe})_{0.3}$	$\text{Zr}_{0.8}\text{Ti}_{0.2}$	36.24	36.40	2.127	2.057
Ti	Ti	$\text{Ti}_{0.39}\text{Fe}_{0.11}$	$\text{Ti}_{0.35}\text{Zr}_{0.125}$	24.86	25.40	1.994	1.928
Mn	Mn(Mg)	$\text{Ca}_{0.42}\text{Mn}_{0.08}$	$\text{Mn}_{0.29}\text{Na}_{0.125}\text{Ti}_{0.025}$	18.35	18.35	2.265	2.153
Na(1)	Na	$\text{Na}_{0.78}\text{Ca}_{0.22}$	$\text{Na}_{0.965}\text{Ca}_{0.035}$	11	11.31	2.568	2.540
Na(2)	Na	Na	$\text{Na}_{0.43}\text{Ca}_{0.07}$	12.28	12.28	2.498	2.534
Ca	Na	Na	$\text{Ca}_{0.170}\text{Mn}_{0.135}\text{Na}_{0.080}$	15.28	15.31	2.394	2.300

Note: The cation content in the unit cell is $\text{Na}_{6.3}\text{Ca}_{1.1}(\text{Mn}, \text{Fe})_{1.7}\text{Zr}_{3.8}\text{Ti}_{2.6}$ according to the data of the electron probe analysis and $\text{Na}_{6.4}\text{Ca}_{1.1}(\text{Mn}, \text{Fe})_{1.7}\text{Zr}_{3.7}\text{Ti}_{2.3}$, according to the results of X-ray diffraction study.

The unit-cell parameters were determined by the least-squares method based on the angular parameters of 40 reflections in the range $8^\circ \leq 2\theta \leq 27^\circ$. The absorption correction was applied using the ψ scanning procedure. The structure was refined within the space group $P2/c$ starting from the atomic coordinates determined earlier [4]. Initially, the structure was refined isotropically to $R = 0.081$ for 1180 reflections with $|F| > 4\sigma(F)$ using the SHELX97 program package [5]. At

subsequent stages, the electron contents of six cationic positions were refined, and the anisotropic thermal parameters were included, which made it possible to reduce the $R(F)$ factor to 0.053. The distribution of the cations over six nonequivalent positions was established based on the refinement of their electron contents, the correspondence between the structural formula and the data of electron probe analysis, the electroneutrality of the chemical formula, the valence

Table 3. Coordinates, thermal parameters, multiplicities (Q), and occupancies (q) for the basis atoms

Atom*	x/a	y/b	z/c	Q	q	$U_{eq}^{**}, \text{\AA}^2 \times 100$
Zr	0.2004(1)	0.1193 (1)	0.07342(4)	1	1	0.97(2)
Ti	0.0	0.1153(3)	0.25	0.5	0.475	1.14(3)
Mn	0.5	0.3566(4)	0.25	0.5	0.440	1.74(6)
Na(1)	0.2051(6)	0.6157(5)	0.0695(1)	1	1	1.13(5)
Na(2)	0.0	0.6149(8)	0.25	0.5	0.5	2.18(9)
Ca	0.5	0.8656(7)	0.25	0.5	0.385	3.32(8)
Si(1)	0.7273(4)	0.3872(4)	0.1046(1)	1	1	1.00(4)
Si(2)	0.7217(4)	0.8422(3)	0.1049(1)	1	1	0.99(4)
O(1)	0.738(1)	0.6135(8)	0.1096(3)	1	1	2.3(1)
O(2)	0.451(1)	0.3264(9)	0.0680(3)	1	1	2.1(1)
O(3)	0.440(1)	0.9015(9)	0.0763(3)	1	1	2.0(1)
O(4)	0.927(1)	0.3267(9)	0.0586(3)	1	1	1.6(1)
O(5)	0.904(1)	0.9073(8)	0.0518(3)	1	1	1.4(1)
O(6)	0.797(1)	0.3154(8)	0.1900(3)	1	1	1.6(1)
O(7)	0.817(1)	0.9141(9)	0.1888(3)	1	1	1.7(1)
O(8)	0.240(1)	0.124(1)	0.1849(3)	1	1	1.9(1)
F	0.301(1)	0.600(1)	0.1922(3)	1	1	3.9(2)

* The cation contents of the positions correspond to those presented in Table 2.

** The U_{eq} values are calculated based on anisotropic thermal displacements of the atoms.

balance, and the fact that the average interatomic distances should be approximately equal to the sum of the ionic radii of the cations and anions in the correspond-

Table 4. Interatomic distances (\AA)

Zr–O(8) 2.035(5)	Na(1)–F 2.229(6)	Ca–F 2.340(8)
–O(3) 2.051(6)	–O(4) 2.370(6)	–F' 2.340(8)
–O(2) 2.061(6)	–O(3) 2.419(7)	–O(7) 2.345(6)
–O(4)' 2.110(6)	–O(2) 2.488(7)	–O(7)' 2.345(6)
–O(5) 2.223(6)	–O(4)' 2.570(7)	–O(8) 2.497(7)
–O(5)' 2.281(5)	–O(5)' 2.659(7)	–O(8)' 2.497(7)
Average, 2.127	–O(1) 2.886(7)	Average, 2.394
	–O(1)' 2.925(7)	
Mn–F 2.209(8)	Average, 2.568	Ti–O(7) 1.974(6)
–F' 2.209(8)		–O(7)' 1.974(6)
–O(6) 2.225(6)	Na(2)–F 2.200(5)	–O(8) 2.002(5)
–O(6)' 2.225(6)	–F' 2.200(5)	–O(8)' 2.002(5)
–O(8) 2.361(7)	–O(7) 2.529(8)	–O(6) 2.007(6)
–O(8)' 2.361(7)	–O(7)' 2.529(8)	–O(6)' 2.007(6)
Average, 2.265	–O(6) 2.560(8)	Average, 1.994
	–O(6)' 2.560(8)	
	–O(1) 2.702(6)	
	–O(1)' 2.702(6)	
	Average, 2.498	

ing polyhedra. The resulting distribution (Table 2) differs from the distributions found earlier [3, 4] and is supported by the lowest R factor. The structural formula $2(\text{Na,Ca})\{(\text{Na,Ca})(\text{Ca,Mn,Na},\square)(\text{Mn,Na,Ti},\square)(\text{Ti,Zr},\square)[(\text{Zr,Ti})\text{Si}_2\text{O}_7]\text{OF}\}$ (the content of the H layer is enclosed in brackets, and the content of the HOH stack is enclosed in braces; $Z = 4$) agrees well with the results of electron probe analysis. The distribution of the cations presented in Table 2 should be considered as the optimum compromise between the experimental results of chemical and X-ray analysis. Conceivably, there are insignificant variations in the cation contents in particular polyhedra, which are, apparently, responsible for the higher values of U_{eq} for the cations located in the Ca position compared to U_{eq} for the Na(1) and Na(2) positions.

The final coordinates of the basis atoms and their thermal parameters are given in Table 3. The interatomic distances are listed in Table 4. The valence balance was calculated according to Brese and O'Keeffe [6], and the results are presented in Table 5. The Si(1)–O and Si(2)–O bond lengths are (1.610(6)–1.632(6) and 1.612(6)–1.637(6) \AA , respectively with average values 1.618 and 1.626 \AA , respectively) close to the standard values and are therefore not given in Table 4. The projection of the structure (the ATOMS program [7]) is shown in the figure.

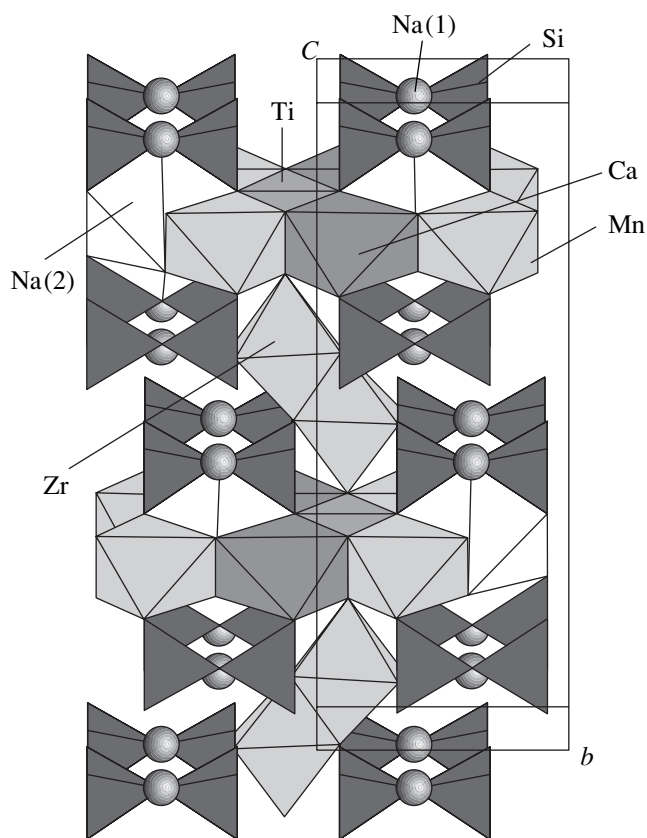
RESULTS AND DISCUSSION

The crystal structure of seidozerite is based on the *HOH* bafertsite-like stacks parallel to the (001) plane [8]. The *O* octahedral layer is composed of $(\text{Ti,Zr})\text{O}_6^-$, $(\text{Mn,Na,Ti})\text{O}_6^-$, and (Ca,Mn,Na) -octahedra and the eight-vertex $\text{Na}(2)$ -polyhedra. All the cationic positions within the octahedra of the *O* layer are only partly occupied.

On the contrary, the $(\text{Zr,Ti})\text{O}_6^-$ -octahedra, which are involved in the heteropolyhedral *H* layers together with the Si_2O_7 diortho groups, are completely occupied. The *HOH* stacks in seidozerite are directly linked to each other via edges shared by the adjacent $(\text{Zr,Ti})\text{O}_6^-$ -octahedra belonging to different stacks. Hence, the seidozerite structure can be described as a mixed framework, whose cavities located between the adjacent *HOH* stacks are occupied by the $\text{Na}(1)$ cations occupied in the eight-vertex polyhedra.

The valence balance cannot be calculated with a high degree of accuracy because of the above-mentioned cationic disordering. However, the results presented in Table 5 allow the unambiguous identification of the positions occupied by the F atoms or the OH groups. The O anions in the O(8) position and the F anions belong to the *O* layer, but they are not involved in the Si-tetrahedra.

The modular structures of more than 20 titanosilicates containing the bafertsite-like *HOH* stacks analogous to those found in seidozerite have been considered earlier [8–11]. The crystal structures of some of these minerals are still unknown, and they were assigned to the bafertsite-like group based on the comparison of the unit-cell parameters and the data on their compositions. The correctness of the application of the modular concept to the prediction of unknown structures has already been confirmed in the studies of minerals such as delindeite, perraultite, betalomonsovite, and some varieties of lamprophyllite, whose structures were established more recently. These structures were surveyed in most detail in [11].



Seidozerite structure projected onto the (100) plane.

All titanosilicates of this series have close unit-cell parameters ($a \sim 5.5 \text{ \AA}$, $b \sim 7 \text{ \AA}$) typical of the bafertsite-like *HOH* stacks. The space between these stacks, like that in layered silicates, can involve isolated atoms or atomic groups as well as the fragments of other mineral types. The latter statement is exemplified by the structures of quadruphite and polyphite [12], which contain nacaphite [13] fragments between the layers. The interlayer content (according to Belov's evocative

Table 5. Calculated valence balance

Anion, cation	O(1)	O(2)	O(3)	O(4)	O(5)	O(6)	O(7)	O(8)	F
Zr		0.675	0.694	0.592	0.436 0.373			0.724	
Ti						0.624	0.682	0.632	
Mn						0.274		0.190	0.220
Na(1)	0.053 0.048	0.156	0.188	0.214 0.125	0.098				0.225
Na(2)	0.094					0.138	0.151		0.262
Ca							0.229	0.152	0.170
Si(1)	1.016	1.030		1.039		0.979			
Si(2)	0.968		1.033		0.965		1.019		
Σ	2.179	1.861	1.915	1.970	1.872	2.015	2.081	1.698	0.877

expression, the “pie filling”) determines the c parameter, which increases as the filling becomes more complex. The thickness of the HOH stacks is $\sim 9\text{--}10$ Å. In the structures where the interlayer space is occupied only by isolated atoms, the c -parameter is $\sim n \times 10$ Å, where n is the number of the HOH stacks. The c parameter in seidozerite (18.590 Å) indicates that its unit cell contains two symmetrically equivalent HOH stacks perpendicular to the [001] axis. In the seidozerite structure, the HOH stacks are linked via the shared edges of the Zr-octahedra, and $d(001)/n$ has the minimum value (9.068 Å) of all minerals of this series. In the polyphite structure characterized by a large interlayer space, $d(001)/n$, on the contrary, reaches 26.49 Å. Within the framework of the classification of homologous and polysomatic series proposed recently [14], seidozerite, like all bafertisite-like minerals, belongs to the meroplesiotype series. This series is referred to as a merotype series because one fragment, namely, the HOH stack, is common to all the members of this series, whereas the second fragment located between the layers is individual for each mineral of this series. At the same time, the bafertisite-like polysomatic series should be considered as a plesiotype series because the HOH stacks differ from each other not only in composition but also in topology. Earlier, it has been established that these structural differences can be seen from the fact that the “octahedral” cations within the H layers can adopt different coordination numbers (either 6 or 5). Similar to delindeite studied recently, seidozerite exemplifies the plesiotype character of the HOH layers associated with the change in the coordination of the cations not only in the H layers but also in the O layers. Thus, the Na cations involved in the O layers in the delindeite and seidozerite structures are located in seven- and eight-vertex polyhedra, respectively, rather than in octahedra.

ACKNOWLEDGMENTS

This study was supported by the Russian Foundation for Basic Research (project nos. 00-05-65399, 00-15-96633, and 01-05-97243-r2001, Baikal) and by

the program “Russian Universities.” S. Merlino and M. Pasero acknowledge the support of the MURST project (“Structural Imperfections in Minerals: Microstructure, Modular Aspects, and Structure Modulation”). D.Yu. Pushcharovskii acknowledges the support of the Russian–Italian Scientific Cooperation program (project no. 62).

REFERENCES

1. E. I. Semenov, M. E. Kazakova, and V. I. Simonov, *Zap. Vseross. Mineral. O–va.* **87** (5), 590 (1958).
2. A. M. Portnov, *Dokl. Akad. Nauk SSSR* **156** (2), 338 (1964).
3. V. I. Simonov and N. V. Belov, *Kristallografiya* **4** (2), 163 (1959) [*Sov. Phys. Crystallogr.* **4**, 146 (1960)].
4. S. M. Skshat and V. I. Simonov, *Kristallografiya* **10** (5), 591 (1965) [*Sov. Phys. Crystallogr.* **10**, 505 (1965)].
5. G. M. Sheldrick, *SHELX97: Program for the Solution and Refinement of Crystal Structures* (Madison, 1997).
6. N. E. Brese and M. O’Keeffe, *Acta Crystallogr., Sect. B: Struct. Sci.* **B47**, 192 (1991).
7. E. Dowty, *Atoms 3.2: A Computer Program for Displaying Atomic Structures* (Kingsport, TN 37663, 1995).
8. G. Ferraris, *Modular Aspects of Minerals / EMU Notes in Mineralogy* **1**, 275 (1997).
9. Yu. K. Egorov-Tismenko, *Kristallografiya* **43**, 306 (1998) [*Crystallogr. Rep.* **43**, 271 (1998)].
10. C. C. Christiansen, E. Makovicky, and O. N. Johnsen, *Neues Jahrb. Mineral., Abh.* **175**, 153 (1999).
11. G. Ferraris, G. Ivaldi, D. Yu. Pushcharovsky, *et al.*, *Can. Mineral.* **39** (5), 1306 (2001).
12. A. P. Khomyakov, G. N. Nechelyustov, E. V. Sokolova, and G. I. Dorokhova, *Zap. Vseross. Mineral. O–va.* **121** (3), 105 (1992).
13. E. V. Sokolova, Yu. K. Egorov-Tismenko, and A. P. Khomyakov, *Dokl. Akad. Nauk SSSR* **304** (3), 610 (1989) [*Sov. Phys. Dokl.* **34**, 9 (1989)].
14. E. Makovicky, *Modular Aspects of Minerals/EMU Notes in Mineralogy* **1**, 315 (1997).

Translated by T. Safonova

STRUCTURE
OF INORGANIC COMPOUNDS

Ba_{1-x}R_xF_{2+x} Phases (R = Gd–Lu) with Distorted Fluorite-type Structure—Products of Crystallization of Incongruent Melts in the BaF₂–RF₃ Systems.

I. Ba_{0.75}R_{0.25}F_{2.25} Crystals (Synthesis and Some Characteristics)

B. P. Sobolev*, **A. M. Golubev****, **E. A. Krivandina***, **M. O. Marychev*****, **E. V. Chuprunov*****,
X. Alcobe****, **S. Gali******, **L. Pascual*******, **R.-M. Rojas*******, and **P. Herrero*******

* *Shubnikov Institute of Crystallography, Russian Academy of Sciences,
Leninskii pr. 59, Moscow, 117333 Russia*

e-mail: sobolevb@crossovers.com

*** *Nizhni Novgorod State University, pr. Gagarina 23, Nizhni Novgorod, 630600 Russia*

**** *Universidad de Barcelona, Barcelona, Spain*

***** *Instituto de Ciencia de Materiales, Madrid, Spain*

Received June 28, 2001

Abstract—The transparent monolithic crystal rods grown by crystallization of the incongruent Ba_{0.75}R_{0.25}F_{2.25} melts (R = Gd–Yb) are shown to be heterogeneous: the larger part of the crystal volume has a distorted fluorite-type cubic lattice, while the smaller part retains an undistorted cubic structure. The distortions were recorded by the methods of X-ray powder and electron diffraction and crystal optics. Two types of chemical heterogeneity of Ba_{0.75}R_{0.25}F_{2.25} crystals are considered as possible sources of distortions: (1) a macroheterogeneous (at a level of 1 mm) distribution of RF₃ over the crystal-rod diameter (a cellular substructure) and (2) a microheterogeneous (cluster) structure with the nanometer dispersion typical of nanostructured materials. © 2002 MAIK “Nauka/Interperiodica”.

INTRODUCTION

The $M_{1-x}R_xF_{2+x}$ phases ($M = \text{Ca, Sr, Ba, Cd, and Pb}$; R is one of 16 rare earth elements) with the defect CaF₂-type structure are characterized by pronounced nonstoichiometry ($0 < x < 0.5$). The changes in the crystal composition give rise to changes in the “defect structure” and crystal properties over a wide range. The $M_{1-x}R_xF_{2+x}$ crystals are multicomponent materials that can substitute single-component crystals (CaF₂, BaF₂, etc.), whose commercial application is very limited.

It is commonly believed that all the $M_{1-x}R_xF_{2+x}$ phases are crystallized from melts as *cubic* crystals, sp. gr. $Fm\bar{3}m$ with the fluorite-type (defect) structure. However, what are the reasons to believe it and how justified is this opinion?

This opinion is based on two types of data. First, these are the data obtained from the study of the phase diagrams of the MF₂–RF₃ systems. To study the phase equilibria in the subsolidus, a mixture of powdered components is annealed until the attainment of the equilibrium state. Then the samples are quenched and their phase composition is studied by the X-ray diffraction method. At rather high temperatures, numerous $M_{1-x}R_xF_{2+x}$ phases showed no distortions in cubic

structure. The phase diagrams and the composition studied by the X-ray diffraction method are reviewed in [1, 2] and described in a number of original publications.

It is shown that the equilibrium $M_{1-x}R_xF_{2+x}$ phases are cubic, but the crystals of the same composition grown from melt under nonequilibrium conditions are not necessarily cubic.

The second source of information on the system (cubic) of the $M_{1-x}R_xF_{2+x}$ phases is the study of their structures performed mainly on nonequilibrium samples. The standard methods fail to reveal the distortions of the fluorite unit cell, which are seen from the splitting of reflections.

Thus, the structural studies of $M_{1-x}R_xF_{2+x}$ crystals grown from melts cannot show that they are cubic either.

The only fact that can be stated is that crystallization from a melt provides the formation of the most pronounced disordered phases, i.e., nonstoichiometric fluorite cubic $M_{1-x}R_xF_{2+x}$ phases.

Thus, the opinion that the $M_{1-x}R_xF_{2+x}$ phases crystallized from melts are cubic fluorite-type phases follows more from general considerations and traditional concepts than from experimental facts.

The history of the studies of $M_{1-x}R_xF_{2+x}$ crystals includes a case where “obvious” and generally accepted concepts were disproved several years later. We mean here the widespread recognition of the theoretical model suggested by Goldschmidt to describe the isomorphism of Ca^{2+} and R^{3+} in CaF_2 [3]. According to this model, the superstoichiometric F^{1-} -ions occupy the centers of large cubic voids. The logics and the apparent uniqueness of this model (there are no other large voids) allowed the model to survive from 1926 to 1969, when, finally, experimental structural studies of $Ca_{0.61}Ce_{0.39}F_{2.39}$ [4] and $Ca_{0.9}Y_{0.1}F_{2.1}$ [5] crystals were undertaken and proved that the model was erroneous.

The story of the isomorphism model is analogous to the story discussed in the present paper and both stories are closely related. Beginning with the structural studies of 1969–1970, $Ca_{1-x}R_xF_{2+x}$ crystals were considered to be cubic, which was never verified experimentally not only for these crystals but also for other MF_2 -based phases. However, as we have already showed, this statement is true only for the equilibrium compositions.

In fact, the growth of $M_{1-x}R_xF_{2+x}$ crystals is a non-equilibrium process. The $M_{1-x}R_xF_{2+x}$ phases for most of x values are melted incongruently. The growth of crystals of these phases is accompanied by the formation of two types of macroheterogeneities in the R^{3+} distribution—axial and radial (the so-called cellular substructure). Generally, the composition changes monotonically along the growth direction of the crystalline rod, being a background against which the radial inhomogeneity is developed.

In $M_{1-x}R_xF_{2+x}$ crystals, the elements of the substructure (the cells and their boundaries) have a millimeter scale. The variations in their composition give rise to lattice-parameter gradients resulting in mechanical stresses and, in turn, in the optical anisotropy of the crystals. The optical anisotropy occasionally observed in $M_{1-x}R_xF_{2+x}$ crystal rods has not been studied and was attributed to residual thermal stresses that could not lead to considerable lattice distortions.

On the scale of crystal structures, fluorite-type $M_{1-x}R_xF_{2+x}$ phases should be considered as microinhomogeneous. Superclusters of defects and their associates with nanometer linear dimensions are enriched with R^{3+} , whereas their composition is essentially different from the MF_2 matrix of these clusters.

The aim of the present work is to establish whether the inhomogeneities of the chemical composition of the products formed in the nonequilibrium crystallization of incongruent $Ba_{0.75}R_{0.25}F_{2.25}$ melts (where $R = Gd, Tb, Dy, Er, Tm, Yb,$ and Lu) affect the structural and crystalloptical characteristics of these crystals.

SAMPLES

In the MF_2 – RF_3 systems ($M = Ca, Sr, Ba, Cd,$ and Pb ; R is a rare-earth element), we revealed 80 phases of the composition $M_{1-x}R_xF_{2+x}$. These phases are divided into five families depending on the number of MF_2 -cations. If the effect of the heterogeneity of $M_{1-x}R_xF_{2+x}$ crystals is seen in the X-ray powder diffraction patterns, they should be most pronounced for the phases of the $Ba_{1-x}R_xF_{2+x}$ family. We studied the phases with $R = Gd$ – Lu possessing the maximum difference in M^{2+} and R^{3+} sizes (among all $M_{1-x}R_xF_{2+x}$ phases) and a pronounced dependence of the lattice parameter on the composition, which is a favorable condition for the observation of the distortions of a cubic lattice.

The $Ba_{0.75}R_{0.25}F_{2.25}$ compositions were chosen from the homogeneity region of the $Ba_{1-x}R_xF_{2+x}$ phases because such an isoconcentration “cut” of the RE series provides an opportunity to study a new type of cation ordering discovered in $Ba_{0.8}Yb_{0.2}F_{2.2}$ [6] along with phases containing other rare-earth elements. The complete ordering of Ba^{2+} and rare-earth elements, accompanied by a change in the sp. gr. $Fm\bar{3}m$ to sp. gr. $Pm\bar{3}m$ is attained for the composition $Ba_{0.75}R_{0.25}F_{2.25}$.

We selected the samples in two ways. The samples obtained from the mixture of small pieces taken from different portions of the crystal rod allowed us to reveal the maximum fluctuations in the composition, because all types of inhomogeneities (axial and radial) and, hence, all types of the distortions of the cubic lattice in the crystal bulk were apparent.

The samples, obtained by grinding monolithic crystal blocks, allowed us to extract information on the local changes in the composition and the related distortions of the crystal lattice. Hereafter, these samples are called *monoblocks* and denoted as **M**. The monoblock dimension along the growth axis (typically, 2–4 mm) did not exceed ~10% of the rod length, and, therefore, the axial inhomogeneity could be neglected.

EXPERIMENTAL

The crystals were grown by the Bridgman method in an apparatus with a graphite heater. The BaF_2 charge consisted of the pieces of single crystals containing about 0.012 wt % of oxygen. The RF_3 reagents had a purity of 99.90–99.99%; they were purified of oxygen by the method described in [7] by keeping the melts overheated by 100–150°C in a fluorinating atmosphere of the products of polytetrafluoroethylene (Teflon) pyrolysis for 2–4 h up to the attainment of 0.005–0.060 wt % of oxygen.

A graphite crucible with up to seven cells filled with the charge was placed into the growth chamber first evacuated to 10^{-2} mm Hg and then filled with He. The fluorinating atmosphere was created by the products of Teflon pyrolysis. The velocity of the crucible lowering

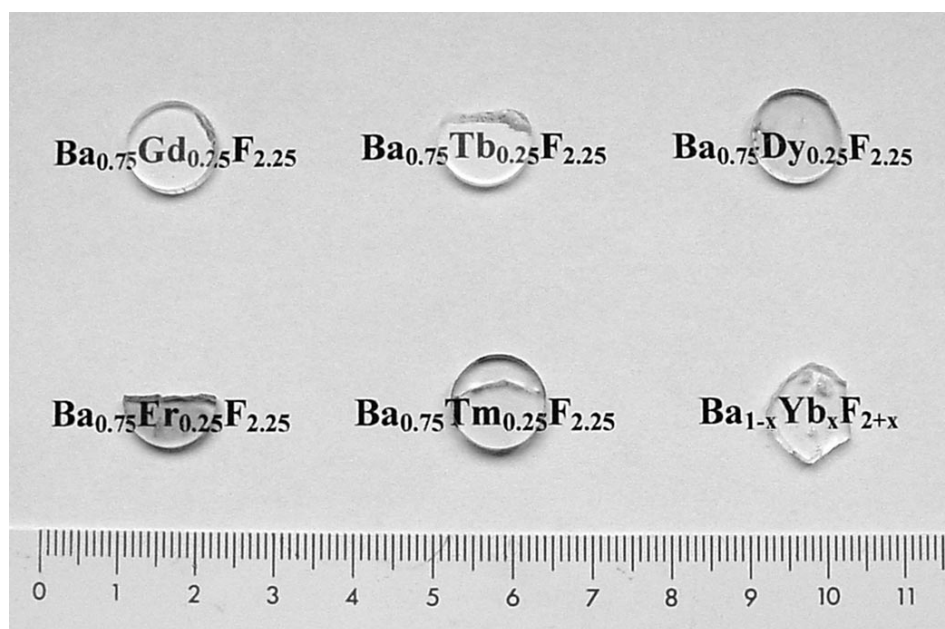


Fig. 1. The shape of Ba_{1-x}R_xF_{2+x} crystals.

was 4.9 ± 0.8 mm/h. The cooling rate upon crystallization was 100–150°C/h. The crystal rods were 35–40 mm in length and 10–12 mm in diameter. For the spectroscopic studies, the crystals were doped with 0.01 wt % of Ce³⁺, Nd³⁺, Pr³⁺, or Er³⁺. In the text, the concentrations of these rare-earth elements are indicated together with the concentration of the main RE element up to an RF₃ concentration of 25 mol %. In the figures, the true compositions are indicated.

The crystals were annealed either wrapped in Ni foil or in capillaries placed into a sealed Ni-container. The fluorinating atmosphere was created by the products of polytetrafluoroethylene pyrolysis. We showed that this technique provides conditions that practically exclude pyrohydrolysis. The crystals were annealed for 14 days at 900°C and for 32 days at 750°C. In the first case, the container was quenched by cooling at a rate of 200–300°C/min from the annealing temperature to 400–500°C; in the second case, at a cooling rate of 200–300°C/s.

The cellular substructure of the crystals was studied in the transmitted light of an He–Ne laser and in the polarized light in a MIN-8 microscope. The samples for these observations (disks with a thickness of ~2 mm) were cut out from the crystal rods normally to the growth axis and then were polished (Fig. 1).

The chemical composition of the crystals was estimated by the dependence of the unit-cell parameters of Ba_{1-x}R_xF_{2+x} on the RF₃ content [8] obtained for cubic phases brought into equilibrium by annealing. For the Ba_{1-x}R_xF_{2+x} crystals (where the weak distortions of the CaF₂-type lattice are not removed by annealing), the

chemical composition was estimated using the parameter of the pseudocubic unit cell a_{pfl} calculated using unsplit fluorite reflections. This seems to be admissible because the change in the molar volumes of the cubic M_{1-x}R_xF_{2+x} phases and the molar volumes of ordered phases lie practically on the same straight line [9].

If the distortions of the cubic fluorite-type lattice were essential, we used the parameter equal to the cube root of the volume of the distorted unit cell, which is, of course, a very rough estimate. (The compositions are given in mol % or, in formulas, in molar fractions (x) of RF₃.)

The phase composition of the crystals was studied on the following X-ray powder diffractometers: Siemens D-500 (CuK_{α1,2}-radiation), INEL (CuK_{α1}-radiation), and HZG-4 (CuK_{α1,2}-radiation). The experiments on an INEL diffractometer were performed on small samples (~0.1 mm in diameter and 3–4 mm in height); under certain conditions, this can yield essentially different results from those obtained on other diffractometers where 0.1–0.3 g of the material is used. The crystals were grinded under acetone in an agate mortar. The information on reflection broadening and splitting was obtained from profile analysis using the PeakFit.v4 program and the approximating Pearson VII function.

EXPERIMENTAL RESULTS

The X-ray diffraction study of as grown Ba_{1-x}R_xF_{2+x} crystals (R = Gd–Lu) revealed strong composition-dependent distortions of the fluorite lattice. Below, we qualitatively compare diffraction patterns

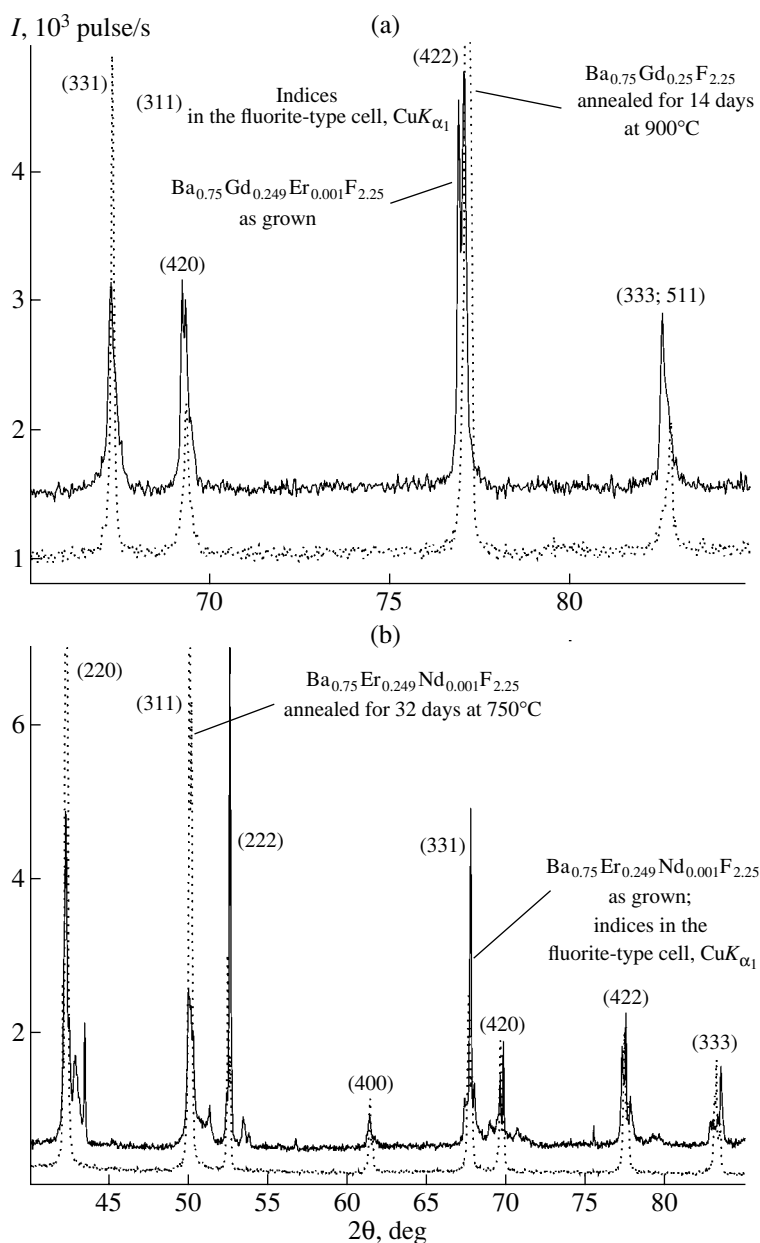


Fig. 2. A fragment of the X-ray diffraction patterns from (a) an as grown $\text{Ba}_{0.75}\text{Gd}_{0.25}\text{F}_{2.25}$ crystal and the same crystal annealed for 14 days at 900°C and (b) an as grown $\text{Ba}_{0.75}\text{Er}_{0.249}\text{Nd}_{0.001}\text{F}_{2.25}$ crystal and the same crystal annealed for 32 days at 750°C .

from distorted and undistorted (cubic) samples. We also confirmed the sample distortions by their study in polarized light. The determination of the phase composition and indexing of the X-ray diffraction patterns are the subject of a separate study.

The X-ray diffraction patterns of as grown $\text{Ba}_{0.75}\text{Gd}_{0.25}\text{F}_{2.25}$ crystals have broadened and split “fluorite” reflections (Fig. 2a). Diffraction patterns of as grown and annealed crystals are shown by solid lines; the diffraction patterns of the same crystals upon annealing, by dashed lines. The unit-cell parameter of a

pseudofluorite unit cell determined from single unbroadened 220 and 222 reflections is $a_{pfl} = 6.0632 \text{ \AA}$ (This corresponds to 24.05% GdF_3 .)

It is evident that, upon annealing, the 420 and 422 reflections are not split any more. However, profile analysis shows that some earlier unbroadened reflections become broadened upon annealing. Fourteen-day annealing at 900°C only partly removed crystal distortions. The parameter a_{pfl} (this corresponds to 25.1% GdF_3) determined with the use of the 331 reflection is $a_{pfl} = 6.0573 \text{ \AA}$.

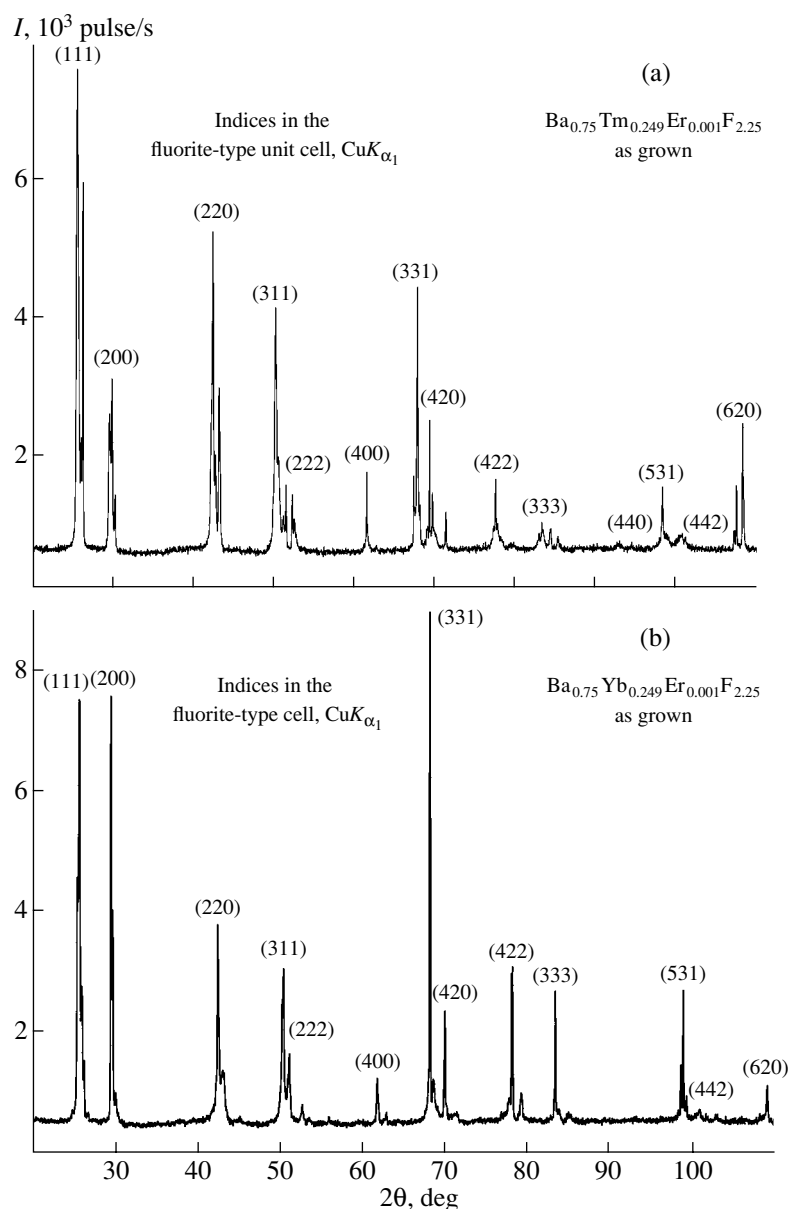


Fig. 3. X-ray diffraction patterns from (a) an as grown Ba_{0.75}Tm_{0.25}F_{2.25} crystal and (b) an as grown Ba_{0.75}Yb_{0.25}F_{2.25} crystal.

It is well known that the attainment of equilibrium during the annealing of crystals grown from a melt occurs more slowly than in crystals obtained by solid phase synthesis from components. The kinetics of the transition of as grown crystals into equilibrium cubic phases at high temperatures should be studied separately.

The Ba_{0.75}Tb_{0.25}F_{2.25} crystals are less distorted than the Ba_{0.75}Gd_{0.25}F_{2.25} ones. Only the fluorite reflection, 400, is split; the 311, 331, 422, and some other reflections are broadened. The 220, 222, 420, 333 + 511, and 442 reflections are unsplit and unbroadened. The unit-cell parameter a_{pfl} (27.3% TbF₃) determined from

unsplit and unbroadened 440 and 422 reflections is $a_{pfl} = 6.0304 \text{ \AA}$.

The Ba_{0.75}Dy_{0.25}F_{2.25} crystals showed minor distortions; the 400, 331, 440, 531, and 422 reflections are broadened. The unit-cell parameter a_{pfl} (27.1% DyF₃) determined from the broadened 620 reflection is $a_{pfl} = 6.0292 \text{ \AA}$, while those determined from unbroadened 333 and 422 reflections are $a_{pfl} = 6.0498 \text{ \AA}$ (23.9%) and $a_{pfl} = 6.0269 \text{ \AA}$ (27.5%), respectively. The considerable difference in the a_{pfl} values determined from different reflections (see Discussion) does not allow their averaging.

The Ba_{0.75}Er_{0.25}F_{2.25} crystals grown from a melt have a considerably distorted fluorite-type lattice (Fig. 2b).

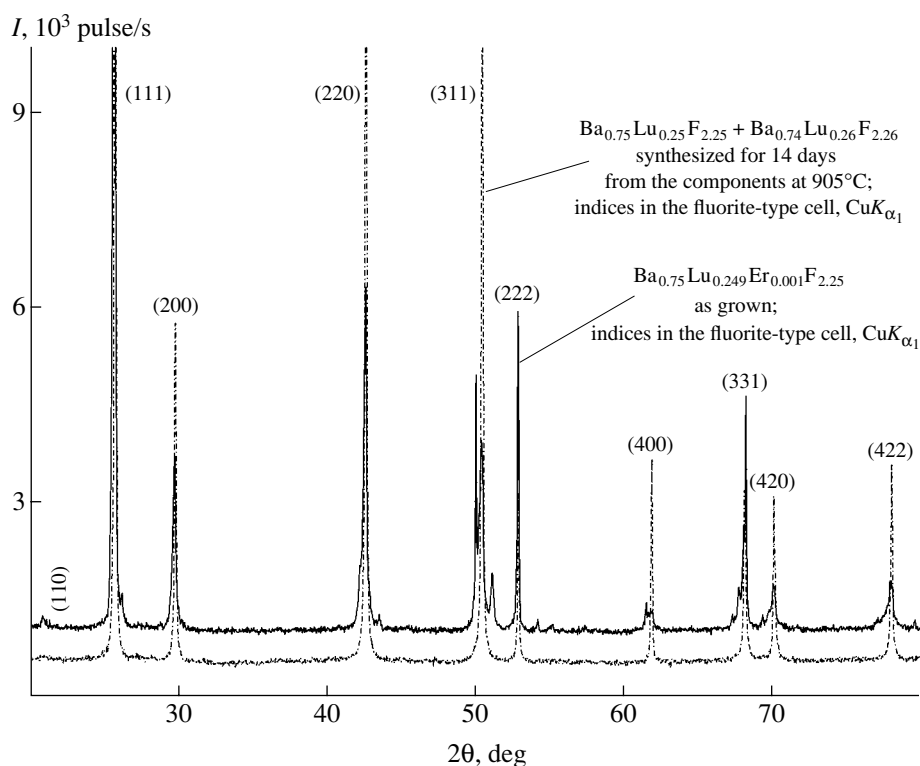


Fig. 4. Comparison of the X-ray diffraction patterns from (a) an as grown $\text{Ba}_{0.75}\text{Lu}_{0.25}\text{F}_{2.25}$ crystal and (b) the mixture of the $\text{Ba}_{0.75}\text{Lu}_{0.25}\text{F}_{2.25}$ and $\text{Ba}_{0.74}\text{Lu}_{0.26}\text{F}_{2.26}$ phases (solid-phase synthesis).

Assuming the existence of two cubic phases with different unit-cell parameters in as grown $\text{Ba}_{0.75}\text{Er}_{0.25}\text{F}_{2.25}$ crystals is inconsistent with the experimental fact—the presence in the diffraction pattern of unsplit reflections such as broadened 400 (Fig. 2b) and unbroadened 620 reflections (24.3% ErF_3), which yields $a_{\text{pfl}} = 6.0315 \text{ \AA}$.

The $\text{Ba}_{0.75}\text{Tm}_{0.25}\text{F}_{2.25}$ crystals are characterized by the most pronounced distortions. Fig. 3a shows the X-ray diffraction pattern (obtained on an INEL diffractometer) from the mixture cut out from different parts of the rod, which shows all the types of inhomogeneities and distortions. No superstructure reflections are observed at small angles (with 2θ up to 2°). Here, the suggestion that there is a mixture of cubic phases with different parameters is ruled out by the presence of unsplit reflections. The weakly broadened 400 and 620 reflections (25.7% TmF_3) yield $a_{\text{pfl}} = 6.0174 \text{ \AA}$.

The $\text{Ba}_{0.75}\text{Yb}_{0.25}\text{F}_{2.25}$ crystals show strong lattice distortions. The X-ray diffraction pattern (an INEL diffractometer) from the powder prepared from a mixture of small transparent pieces of the crystal rod is shown in Fig. 3b. At the angles $2\theta < 20^\circ$, no superstructure reflections were observed, whereas outside this region there were superstructure reflections. The suggestion that there is a mixture of several cubic phases is inconsistent with the presence of unsplit reflections. Using the 333 + 511 reflection, we obtain $a_{\text{pfl}} = 6.0137 \text{ \AA}$ (25.5% YbF_3).

No monolithic crystal rod with the composition $\text{Ba}_{0.75}\text{Lu}_{0.25}\text{F}_{2.25}$, is formed—it decomposes into small 1- to 3-mm-large pieces, which are reminiscent of the result of a polymorphic transition. Thus, in this instance, samples were prepared from a mixture of small pieces of different parts of the rod.

Figure 4 shows X-ray diffraction patterns of as grown $\text{Ba}_{0.75}\text{Lu}_{0.25}\text{F}_{2.25}$ crystals and the mixture of the phases of close compositions obtained by solid phase synthesis. The diffraction pattern from the sample of an as grown crystal showed some distorted fluorite reflections. At small angles, a weak reflection forbidden by sp. gr. $Fm\bar{3}m$ is formed. The simulation of the X-ray powder diffraction pattern under the assumption that all Ba^{2+} ions are located in the face centers (100% occupancy) shows a possible transition with the change of the symmetry $Fm\bar{3}m \rightarrow Pm\bar{3}m$ with the preservation of the lattice parameter and appearance of weak reflections, one of which corresponds to the experimentally observed 110 reflection.

The 14-day-long solid phase synthesis from the components at 905°C yielded a cubic fluorite-type phase (Fig. 4). The X-ray powder diffraction pattern was obtained from the mixture of $\text{Ba}_{0.75}\text{Lu}_{0.25}\text{F}_{2.25}$ and $\text{Ba}_{0.74}\text{Lu}_{0.26}\text{F}_{2.26}$ in approximately equal quantities. At larger angles, a doubling of reflections was observed. The use of the 620 reflection yielded the phase compo-

sitions 25.1 and 25.9% LuF₃, i.e., the compositions close to nominal compositions, which demonstrates a high resolution of the diffractometer with a difference in the composition of only 1 mol %.

DISCUSSION

The composition fluctuations in the Ba_{0.75}R_{0.25}F_{2.25} rods containing rare-earth elements from the second half of the series under consideration lead to the distortions in fluorite-type cubic lattices revealed from the corresponding X-ray powder diffraction patterns. Because the BaF₂-RF₃ systems are characterized by ordering processes with the formation of phases with structures derived from the fluorite type, we compare their X-ray diffraction characteristics with those of Ba_{0.75}R_{0.25}F_{2.25}.

1. Differences between Ba_{1-x}R_xF_{2+x} Phases with the Distorted Fluorite-type Lattice and Well-Known Ordered Phases

Two types of phases were separated in the BaF₂-RF₃ ($R = \text{Gd-Lu}$) systems within the range 0–50 mol % RF₃ (with the exception of the composition Ba_{0.625}Er_{0.375}F_{2.375}).

1.1. Cubic nonstoichiometric fluorite-type Ba_{1-x}R_xF_{2+x} phases are formed in the systems containing all the rare elements listed above (the isothermal cuts were studied in the range from 814 to 1067°C). At the peritectic temperatures, the homogeneity regions of the Ba_{1-x}R_xF_{2+x} phases lie within 42–31 mol % GdF₃ and LuF₃, respectively, and are crystallized (solid phase synthesis) in the sp. gr. $Fm\bar{3}m$ with the parameters of the fluorite-type unit cell ranging from 5.952 to 6.200 Å.

1.2. Ordered phases with a structure derived from the fluorite type are characterized by an increased unit-cell volume (in comparison with that of MF₂) and superstructure reflections in their diffraction patterns. To show that we deal here with a new family of the Ba_{0.75}R_{0.25}F_{2.25} phases, we briefly consider the known ordered phases in the BaF₂-RF₃ systems.

The (*t'*) Ba₂RF₇ ($R = \text{Dy-Lu, Y}$) phases with tetragonal CaF₂-type distortion and superstructure reflections were obtained by seven-day annealing at 400°C of the cubic Ba_{0.67}R_{0.33}F_{2.33} phases synthesized at 1000–1100°C [10, 11].

The tetragonally distorted (*t''*) Ba_{8+δ}R_{6-δ}F_{34-δ} phases were discovered in [11] and described for $R = \text{Sm, Gd, and Tb}$ in [8]. These phases are formed from the trigonal (*rhα'*) phases with an increase in temperature. Depending on the rare-earth element, their homogeneity regions range from 42 to 51 mol % RF₃. The symmetry of these phases considerably deviates from

cubic; their diffraction patterns show superstructure reflections and increased unit-cell parameters.

The (*rhα'*) Ba_{8+δ}R_{6-δ}F_{34-δ} phases are described in [12, 13] as the phases with the composition 7BaF₂ · 5TmF₃ (41.7 mol % TmF₃). These are found for $R = \text{Sm, Gd-Lu, and Y}$ in [14] and attributed the composition Ba₄R₃F₁₇ (42.86 mol % RF₃). Similar phases with $R = \text{Ce-Nd and Eu}$ were obtained in [15, 16]. The structure of Ba₄Y₃F₁₇ and Ba₄Yb₃F₁₇ crystals was studied in [17].

Thus, in the BaF₂-RF₃ systems ($R = \text{Gd-Lu}$), two types of fluorite-like phases were observed in the composition range 0–50 mol % RF₃—cubic phases with the “fluorite” (small) parameter and ordered phases with increased parameters and superstructure reflections on the diffraction patterns. The X-ray diffraction patterns for the typical representatives of these phases are shown in Figs. 5a and 5b. The cubic Ba_{0.75}Lu_{0.25}F_{2.25} phase (Fig. 5a) with the fluorite-type lattice was obtained from the components by the solid phase reaction. The Sr₂TmF₇ phase (an analogue of the Ba₂RF₇ phases, Fig. 5b) is an example of ordered phases providing the formation of weak superstructure reflections.

1.3. The phase with a distorted fluorite-type lattice without superstructure reflections on the diffraction pattern was observed and studied on the only representative (*t''*) Ba₅Er₃F₁₉ = Ba₁₀Er₆F₃₈ = Ba_{0.625}Er_{0.375}F_{2.375} (different forms of the representation of its composition in the literature). It has a tetragonally distorted fluorite structure [8] studied in [18, 19]; sp. gr. $I4/mmm$, $a = 4.199(1)$ Å, $c = 5.986(1)$ Å, $z = 4$ (for the composition Ba_{0.625}Er_{0.375}F_{2.375}). The symmetry considerably deviates from cubic; the transition from the tetragonal to the pseudocubic unit cell results in the unit-cell parameter $a = 4.199\sqrt{2} = 5.938$ Å, which differs by 0.048 Å from the “fluorite” *c*-parameter.

A new type of Ba_{0.75}R_{0.25}F_{2.25} phase with a distorted fluorite lattice providing no formation of superstructure reflections is represented by the Ba_{0.75}Lu_{0.25}F_{2.25} phase in Fig. 5c. This type differs from the ordered phases discussed in section 1.2 by the absence of weak superstructure reflections on the diffraction patterns. These phases differ from Ba₅Er₃F₁₉ (forming no superstructure reflections either) in composition and metastability. The Ba₅Er₃F₁₉ compound, a member of the M_nF_{2n+6} homologous series ($n = 14$), has a definite composition, whereas Ba_{0.75}R_{0.25}F_{2.25} is considered only as points in the series of solid solutions.

The above experimental data lead to the following conclusions: (1) The inhomogeneous chemical composition of as grown Ba_{0.75}R_{0.25}F_{2.25} rods and the corresponding distortions of the cubic fluorite lattice are recorded on the X-ray powder diffraction patterns as split fluorite reflections. (2) The metastable Ba_{0.75}R_{0.25}F_{2.25} ($R = \text{Gd-Lu}$) phases with the distorted fluorite lattice have no analogues among the known

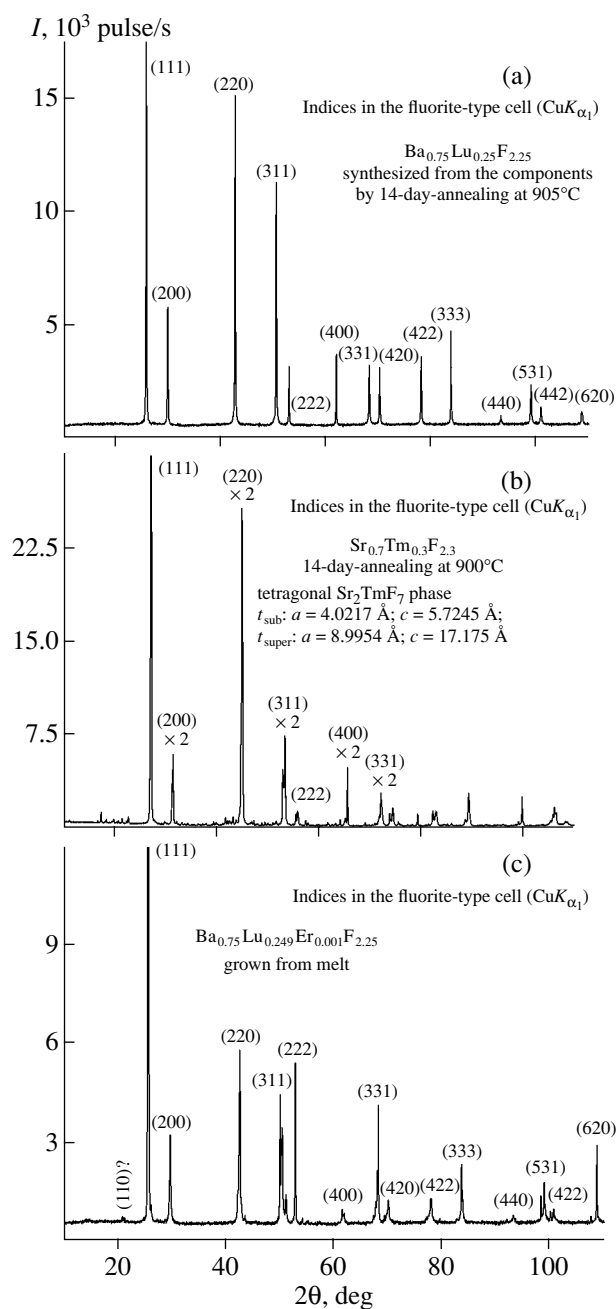


Fig. 5. X-ray diffraction patterns from three phases with a fluorite-type structure in the $\text{BaF}_2\text{-RF}_3$ systems: (a) cubic $\text{Ba}_{0.75}\text{Lu}_{0.25}\text{F}_{2.25}$ solid solution, (b) ordered tetragonally distorted Sr_2TmF_7 phase with a superstructure (an analogue of Ba_2TmF_7), and (c) a new type of phase with a distorted fluorite-type lattice having no superstructure.

equilibrium phases formed in $\text{BaF}_2\text{-RF}_3$ systems. (3) New phases are formed in the process of nonequilibrium crystallization of incongruent melts. During annealing, these phases often acquire the equilibrium state with a cubic fluorite lattice (at rather high temperatures). We failed to observe the complete transition into the equilibrium state. (4) The phase composition

and type of lattice distortion require a further more detailed study.

2. Macroinhomogeneity of As Grown $\text{Ba}_{1-x}\text{R}_x\text{F}_{2+x}$ Phases

We believe that distortions of the fluorite lattice are associated with the chemical inhomogeneity of $M_{1-x}\text{R}_x\text{F}_{2+x}$ phases resulting from the incongruent melting of the phases of this composition. The $M_{1-x}\text{R}_x\text{F}_{2+x}$ crystals exhibit two types of macroscopic inhomogeneity in the distribution of the RF_3 component—axial and radial (cellular substructure) distributions. The contribution of axial heterogeneity can be compensated by selecting appropriate samples with a small dimension along the growth axis.

As was shown above, the identification of the X-ray diffraction patterns is hampered by their complex form and the phase composition. The heterogeneity and the anisotropy inherent in some parts of the $\text{Ba}_{0.75}\text{R}_{0.25}\text{F}_{2.25}$ rod were confirmed by crystalloptical studies.

The micrographs of the cellular substructure of samples presented in Fig. 1 are shown in Fig. 6. The cell shape is better seen on the shadow pattern obtained in the transmitted light. The refractive-index gradients range within $10^{-4}\text{-}10^{-2}\text{ mm}^{-1}$.

In crossed polarizers, the same parts of the rods show the regions with weak birefringence ($2.5 \times 10^{-5}\text{-}5 \times 10^{-6}$), whereas some other parts of the rod are isotropic. The observations made at another rotation angle of the microscope stage showed that the largest part of the rod is anisotropic (to a different extent) while the fraction of isotropic parts is small. The average linear dimensions of inhomogeneities vary from 0.2 to 0.7 mm in different samples.

These observations are quite consistent with the X-ray diffraction data for the phases with low-symmetry distortions of the fluorite lattice in mixtures containing cubic phases. The morphology of the cells is different, which is quite understandable because various $\text{Ba}_{0.75}\text{R}_{0.25}\text{F}_{2.25}$ phases have different coefficients of impurity (R^{3+}) distribution. The honeycomb-like cellular substructure dominates, but, in some instances, the elongated columnar substructure with the cell axes normal to the growth axis is also observed. The morphological analysis is an individual problem that is beyond the scope of the present paper. The mechanism of formation of a cellular substructure in $M_{1-x}\text{R}_x\text{F}_{2+x}$ phases and the methods used to stabilize the planar growth front were discussed elsewhere [20–22]. Systematic morphological studies were made only for the $\text{Sr}_{1-x}\text{R}_x\text{F}_{2+x}$ family. The morphology of the $\text{Ba}_{1-x}\text{R}_x\text{F}_{2+x}$ and $\text{Ca}_{1-x}\text{R}_x\text{F}_{2+x}$ families has not been studied as yet.

The cell boundaries on the shadow patterns are due to light focusing and are not real boundaries between the volume parts (grains). At the same time, the shape

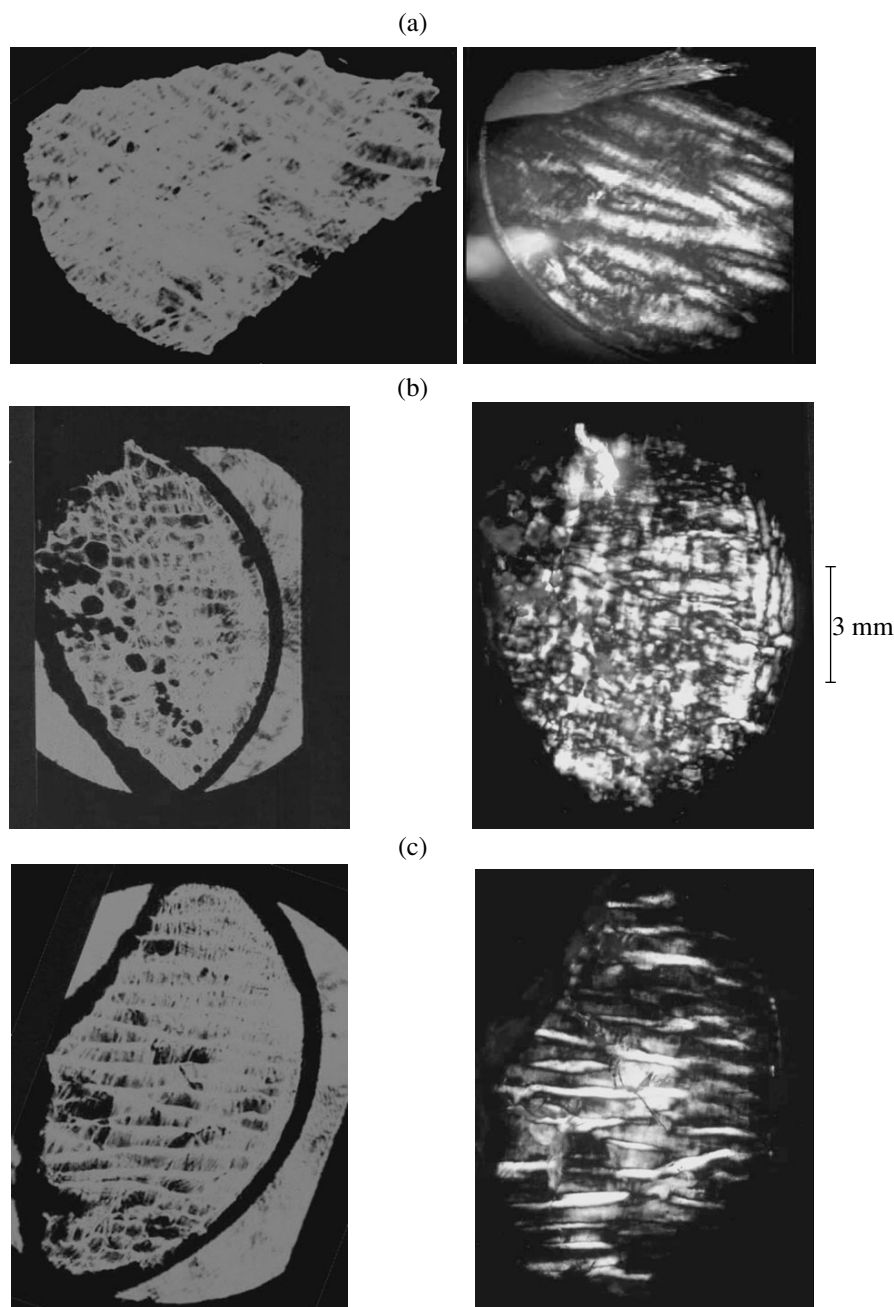


Fig. 6. Cellular substructure (radial inhomogeneity of the composition) in the crystal rods in the transmitted (left column) and in the polarized (between crossed polarizers) light: (a) Ba_{0.75}Tb_{0.249}Er_{0.001}F_{2.25}, (b) Ba_{0.75}Tm_{0.249}Er_{0.001}F_{2.25}, and (c) Ba_{0.75}Yb_{0.249}Er_{0.001}F_{2.25}.

of these boundaries reflects the regular character of the change of the refractive index in the rod bulk. Far from the point of solid-solution saturation, the boundary is the same solid solution as in the crystal bulk. Between different parts of the rod, the gradients of the refractive index and other parameters are observed, but no phase boundary is formed. Macroscopically, the rod consists of only one phase but is not equilibrium. It consists of mutually penetrating crystallites of different chemical composition (in the general case, coherent at the level

of the crystal lattice). On the whole, the rod remains monolithic (Fig. 1).

There is no direct relation between the shadow pattern and the image of the same area obtained in crossed polarizers, because these images are formed due to variations of different quantities (refractive index and birefringence). However, the similar character of morphology (cellular or striated structure) is identical for both images, which is especially clear for striated struc-

tures in Figs. 6a and 6c. The relation between the cellular substructure and the distortions of the crystal structure should be studied separately.

The concentration gradients of R^{3+} in the cellular $Ba_{1-x}R_xF_{2+x}$ crystals were not studied. They can be estimated indirectly from the X-ray diffraction pattern from the mixture of the pieces of different parts of the $Ba_{1-x}Yb_xF_{2+x}$ rod. Assuming that the mixture consists of two cubic "phases" (a rather rough approximation, as is seen from Fig. 6c and other figures), the lattice parameters show that there are volumes with a YbF_3 concentration of 13.7 and 16.5 mol %. We believe that this difference approximately corresponds to the maximum difference in the concentrations of the impurity component in various parts of the rod.

Since the cellular substructure (a typical morphological feature of the products of crystallization of the $Ba_{1-x}R_xF_{2+x}$ melts) manifests itself in the distortions of the cubic lattice, it is not improbable that this phenomenon is characteristic of the $M_{1-x}R_xF_{2+x}$ phases crystallized in MF_2 - RF_3 systems ($M = Ca, Sr, Ba, Cd,$ and Pb and $R = Sc, Y, La,$ and Lu). For $Ba_{1-x}R_xF_{2+x}$ phases, this phenomenon is the most pronounced because of the maximum difference in the Ba^{2+} and R^{3+} sizes and pronounced fluctuations of the lattice parameters.

As grown $Ba_{1-x}R_xF_{2+x}$ rods are of a dual nature. These are monolithic formations showing no signs of the second phase or the phase boundaries. However, the X-ray diffraction patterns and the known crystalloptical data allow one to consider these rods as a mixture of phases with different parameters of undistorted or distorted fluorite lattices. However, this interpretation is inconsistent with an incomplete set of fluorite reflections for one of the phases, whereas the mixture of two isostructural and compositionally close phases should have a complete set of reflections for each of the phases. It might be associated with a relatively small fraction of the cubic phase (according to the above crystalloptical data).

The X-ray diffraction pattern of a $Ba_{0.75}Lu_{0.25}F_{2.25}$ powder is fairly well indexed on the assumption of monoclinic distortion of the fcc lattice (except for several weak reflections). Only the existence of these additional reflections does not allow one to index these diffraction data as a single phase. There is more than one phase in this powder, which is also confirmed by images obtained in polarized light.

The observations in polarized light (Fig. 6) lead to the model of a nonequilibrium multiphase mixture of coherent phases with an undistorted fluorite lattice and a distorted optically anisotropic interlayer, which removes the stresses caused by the lattice mismatch in the cubic regions in the rod.

Thus, at the present level of our understanding of $Ba_{0.75}R_{0.25}F_{2.25}$ phases, their phase composition and the character of distortion of their fluorite-type lattice are

determined ambiguously and should be studied in more detail to construct a model consistent with all the experimental data.

3. Microinhomogeneity of $Ba_{1-x}R_xF_{2+x}$ Phases

The conclusion on the heterogeneity of $Ba_{1-x}R_xF_{2+x}$ and other $M_{1-x}R_xF_{2+x}$ phases at the microlevel was made based on the data on their "defect" structure. In these phases, the clusters of defects rather than M^{2+} and R^{3+} ions are isomorphously replaced. These clusters include all types of defects: highly charged R^{3+} ions, interstitial F^{1-} ions, and anionic vacancies. The high concentration of R^{3+} ions in clusters allows the crystal matrix to preserve the structure and composition close to those of MF_2 . At a microlevel, the $M_{1-x}R_xF_{2+x}$ crystals have two chemically different components—an R^{3+} -enriched and R^{3+} -depleted.

Hereafter, we propose to call the type of isomorphism with space filling [3] "block isomorphism." This isomorphism concerns large blocks (hundreds and thousands of \AA^3 -large volumes) with a close geometry and crystal structure but possessing different chemical compositions instead of isomorphism of ions. The discussion of block isomorphism in $M_{1-x}R_xF_{2+x}$ phases is beyond the scope of this paper.

Recently, heterogeneity at a level of inclusions with a size up to ten parameters of the fluorite unit cell was observed in $Ba_{1-x}La_xF_{2+x}$ by the method of diffuse neutron scattering [23, 24]. These large inclusions of cluster associates can play the role of nuclei of a new phase. However, these crystals also exhibit no phase boundaries and light scattering from the second phase.

Even in the case of elementary $[R_6F_{36}]$ clusters and $\{M_8[R_6F_{68}]\}$ superclusters, the blocks that can be isomorphously replaced have linear dimensions of the order of nanometers, while their aggregates have dimensions of tens of nanometers. Therefore, $M_{1-x}R_xF_{2+x}$ phases can be classified as nanostructured materials. The coherence of the nanophase and the matrix (in the general case, the crystal planes of the nanophase are continuously transformed into the matrix planes) separate the $M_{1-x}R_xF_{2+x}$ crystals into an individual class of nanophase materials having no analogues among the known nanostructured materials [25]. The justification of this classification and its consequences require special discussion.

Since the nanophase and MF_2 matrix are coherent, the chemically microheterogeneous $M_{1-x}R_xF_{2+x}$ crystals behave as single crystals irrespective of neutron, electron, or X-ray radiation.

Electron diffraction from as grown $Ba_{0.8}Lu_{0.2}F_{2.2}$ [26] crystals provides different patterns for different grains of the rod (Fig. 7). These differences have noth-

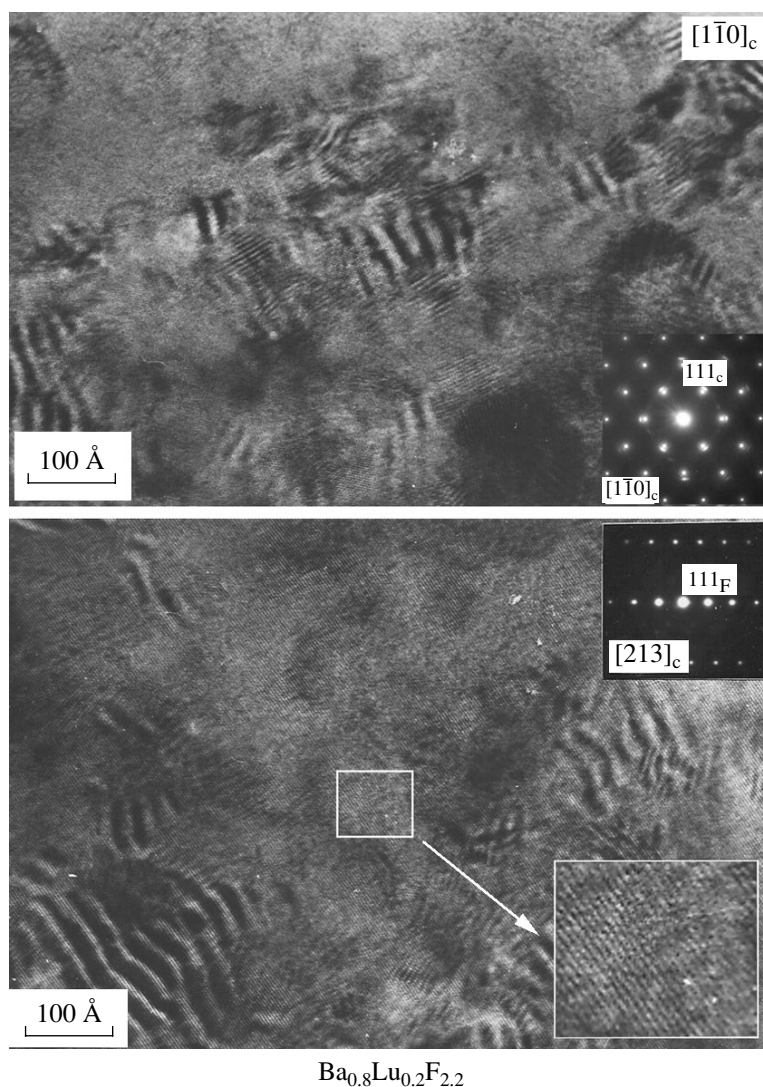


Fig. 7. Image of the crystal lattice (top) and the corresponding electron diffraction pattern (bottom) of the crystal rod of the nominal (with respect to charge) composition Ba_{0.8}Lu_{0.2}F_{2.2}.

ing to do with the decomposition of the sample under an electron beam.

The moiré patterns observed in high-resolution electron micrographs (Fig. 7) are characteristic not only of BaF₂-based Ba_{1-x}R_xF_{2+x} phases but also of nonstoichiometric fluorites. The moiré fringes can be formed because of the presence of two (or more) phases with different lattice parameters.

At the coherent conjugation of the cubic fluorite-type phases with different lattice parameters, elastic stresses contribute to lattice distortion and ordering of the clusters of defects. For solid solutions of metals, the theoretical concepts of the decisive role of the deformational interactions in the formation of a microheterogeneous system of periodically alternating regions (domains) have been quite well developed ([27], etc.). The deformation-type interactions of the replacing atoms were shown to be especially important in sub-

stitutional solid solutions, one variety of which is M_{1-x}R_xF_{2+x} phases.

CONCLUSION

The inhomogeneities in the chemical composition of nonequilibrium products of crystallization of incongruent Ba_{0.75}R_{0.25}F_{2.25} melts (*R* = Gd–Lu) at the micro- and macrolevels are revealed from their structural and crystalloptical characteristics. The distortions of cubic fluorite-type lattice in individual Ba_{0.75}R_{0.25}F_{2.25} metastable phases will be the subject of further detailed studies.

ACKNOWLEDGMENTS

The authors are grateful to L.S. Garashina and V.A. Stasyuk for their help in preparing some experi-

mental samples and to V.N. Molchanov and L.P. Otroshchenko for useful discussions.

The work was supported by the International Association for Promotion of Cooperation of the Former Soviet Union (INTAS), project no. 97-32045, and the Russian Foundation for Basic Research, project no. 99-02-18067.

REFERENCES

1. B. P. Sobolev, *Butll. Soc. Catalana Cienc. Fis., Quim. Mat.* **12** (2), 275 (1991).
2. B. P. Sobolev, *The Rare Earth Trifluorides*, Part 1: *High-Temperature Chemistry of Rare Earth Trifluorides* (Institut d'Estudis Catalans, Barcelona, 2000).
3. V. M. Goldschmidt, T. Barth, G. Lunde, and W. Zachariasen, *Geochemische Verteilungsgesetze der Elemente VII*, in *Skrifter udgitt av det Norske Videnskaps-Akademi i Oslo, I, Matematik-Naturvidenskapelig Klasse* (Oslo, 1926), Vol. 1, no. 2, p. 1.
4. V. B. Aleksandrov and L. S. Garashina, *Dokl. Akad. Nauk SSSR* **189** (2), 307 (1969) [*Sov. Phys. Dokl.* **14**, 1040 (1970)].
5. A. K. Cheetham, B. E. F. Fender, and D. Steele, *Solid State Commun.* **8** (3), 171 (1970).
6. B. A. Maksimov, Yu. B. Gubina, E. L. Belokoneva, *et al.*, in *Proceedings of the 1st National Conference on Crystal Chemistry, Chernogolovka, 1998*, Part I, p. 133.
7. G. G. Glavin and Yu. A. Karpov, *Zavod. Lab.* **30** (3), 306 (1964).
8. B. P. Sobolev and N. L. Tkachenko, *J. Less-Common Met.* **85** (2), 155 (1982).
9. O. Greis, Inaugural-Dissertation Thesis (Univ. Freiburg, West Germany, 1976).
10. O. Greis and M. Kieser, *Rev. Chim. Miner.* **16** (6), 520 (1979).
11. M. Kieser and O. Greis, *J. Less-Common Met.* **71** (1), 63 (1980).
12. B. P. Sobolev, N. L. Tkachenko, V. S. Sidorov, *et al.*, in *Proceedings of the 5th All-Union Conference on Crystal Growth, Tbilisi, 1977*, Vol. 2, p. 25.
13. B. P. Sobolev, L. S. Garashina, and V. B. Alexandrov, in *Proceedings of the 3rd International Congress on Crystal Growth, Marseilles, 1971*, p. 168.
14. N. L. Tkachenko, L. S. Garashina, O. E. Izotova, *et al.*, *J. Solid State Chem.* **8** (3), 213 (1973).
15. M. Kieser and O. Greis, *Z. Anorg. Allg. Chem.* **469**, 164 (1980).
16. O. Greis and M. Kieser, *J. Less-Common Met.* **75** (1), 119 (1980).
17. B. A. Maksimov, Kh. Solans, A. P. Dudka, *et al.*, *Kristallografiya* **41**, 51 (1996) [*Crystallogr. Rep.* **41**, 50 (1996)].
18. A. M. Golubev and B. P. Sobolev, in *Proceedings of the 7th All-Union Symposium on Chemistry of Inorganic Fluorides, Leninabad, 1984* (Nauka, Moscow, 1984), p. 112.
19. A. M. Golubev, B. P. Sobolev, and V. I. Simonov, *Kristallografiya* **30**, 314 (1985) [*Sov. Phys. Crystallogr.* **30**, 181 (1985)].
20. T. M. Turkina, P. P. Fedorov, and B. P. Sobolev, *Kristallografiya* **31**, 146 (1986) [*Sov. Phys. Crystallogr.* **31**, 83 (1986)].
21. P. P. Fedorov, T. M. Turkina, V. A. Meleshina, and B. P. Sobolev, in *Growth of Crystals* (Consultants Bureau, New York, 1988), Vol. 17, p. 165.
22. P. P. Fedorov, T. M. Turkina, and B. P. Sobolev, *Butll. Soc. Cat. Cien.* **13** (1), 259 (1992).
23. F. Kadlec, F. Moussa, P. Simon, and B. P. Sobolev, *Solid State Ionics* **119** (1-4), 131 (1999).
24. F. Kadlec, F. Moussa, P. Simon, and B. P. Sobolev, *Mater. Sci. Eng.* **57** (3), 234 (1999).
25. H. Gleiter, *Acta Mater.* **48**, 1 (2000).
26. R. Muñoz, R. Rojas, B. P. Sobolev, and P. Herrero, in *Proceeding 29th Reunión Bienal Society Española de Microscopia Electrónica, Murcia, 1999*, p. 317.
27. A. G. Khachaturyan, *The Theory of Phase Transformations and the Structure of Solids Solutions* (Nauka, Moscow, 1974), p. 384.

Translated by A. Zolot'ko

STRUCTURE
OF INORGANIC COMPOUNDS

Atomic Structure of $(\text{Sr}_{0.50}\text{Ba}_{0.50})\text{Nb}_2\text{O}_6$ Single Crystals in the Series of $(\text{Sr}_x\text{Ba}_{1-x})\text{Nb}_2\text{O}_6$ Compounds

T. S. Chernaya*, T. R. Volk*, I. A. Verin*, L. I. Ivleva**, and V. I. Simonov*

* *Shubnikov Institute of Crystallography, Russian Academy of Sciences,
Leninskiĭ pr. 59, Moscow, 117333 Russia*

e-mail: chert@ns.crys.ras.ru

** *Institute of General Physics, Russian Academy of Sciences,
ul. Vavilova 38, Moscow, 117942 Russia*

Received May 23, 2001

Abstract—Czochralski grown $(\text{Sr}_{0.50}\text{Ba}_{0.50})\text{Nb}_2\text{O}_6$ single crystals have been studied by the method of precision X-ray diffraction analysis. The structural characteristics of $(\text{Sr}_x\text{Ba}_{1-x})\text{Nb}_2\text{O}_6$ compounds with $x = 0.33, 0.50, 0.61,$ and 0.75 were analyzed. The distributions of the Sr and Ba atoms over the crystallographic positions are considered depending on their concentration. The establishment of the mechanisms of isomorphous replacements in these solid solutions allows the variation, within certain limits, of crystal properties by changing the Ba/Sr ratio. © 2002 MAIK “Nauka/Interperiodica”.

The solid solutions of the composition $(\text{Sr}_x\text{Ba}_{1-x})\text{Nb}_2\text{O}_6$ have attracted the continuing interest of researchers because of their electro-optical and nonlinear-optical properties [1–4]. Precision X-ray diffraction studies of these single crystals provide information on mechanisms of isomorphous replacements on the atomic scale in these compounds, whereas simultaneous investigations of their properties enable one to establish a correlation between their structures and properties, which is important for the transition from the phenomenological description of their crystal properties to the corresponding microscopic theory. These data are also very important for materials science because they provide targeted syntheses of these crystals and the modification of already existing crystals instead of the use of the trial-and-error approach.

The X-ray diffraction study of $(\text{Sr}_{0.50}\text{Ba}_{0.50})\text{Nb}_2\text{O}_6$ single crystals completes the systematic investigation of the structures of $(\text{Sr}_x\text{Ba}_{1-x})\text{Nb}_2\text{O}_6$ compounds with x ranging from 0.25 to 0.75. The results of our previous studies of $(\text{Sr}_{0.33}\text{Ba}_{0.67})\text{Nb}_2\text{O}_6$ [5], $(\text{Sr}_{0.61}\text{Ba}_{0.39})\text{Nb}_2\text{O}_6$ [6], and $(\text{Sr}_{0.75}\text{Ba}_{0.25})\text{Nb}_2\text{O}_6$ [7] solid solutions and the results obtained in the present investigation allow a reliable comparative analysis of the characteristic features of the atomic structures of these compounds and their physical properties.

The $(\text{Sr}_{0.50}\text{Ba}_{0.50})\text{Nb}_2\text{O}_6$ single crystals were grown by the Czochralski method. The X-ray diffraction data were collected on a CAD-4F Enraf-Nonius diffractometer (MoK_α radiation, ω scan, within the complete sphere of the reciprocal space, $\sin\theta/\lambda \leq 1.2 \text{ \AA}^{-1}$) from a spherical sample 0.30 mm in diameter. A total of 17 300 reflections with $I \geq 3\sigma(I)$ were measured. The

analysis of the collected X-ray data set confirmed the tetragonal symmetry of the crystal. The unit-cell parameters are $a = 12.461(2) \text{ \AA}$, $c = 3.9475(3) \text{ \AA}$. The X-ray diffraction symmetry, $4/mmmP\bar{1}b$, corresponds to three space groups— $P4/mbm$, $P\bar{4}b2$, and $P4bm$. Using the $(\text{Sr},\text{Ba})\text{Nb}_2\text{O}_6$ structures studied earlier as an analogy and taking into account their physical properties, we examined and confirmed the acentric space group, $P4bm$. Averaging symmetrically equivalent reflections, we arrived at 2035 independent structure factors. The R -factor of averaging was 2.4%. All the computations were carried out by the PROMETHEUS program package [8]. The structure model was refined by the full-matrix least-squares method. The difficulties associated with pronounced correlations between the structural parameters (occupancies of the positions, thermal parameters) were overcome by step-by-step scanning. The final R -factor was 3.0% and $R_w = 2.6\%$. The structure parameters are given in the table.

The atomic structure of the title compound shown in Fig. 1 consists of sharing oxygen vertices $[\text{NbO}_6]$ -octahedra forming a three-dimensional framework. This framework has three types of channels along the four-fold axis. The narrowest channels are empty. The medium-sized channels are filled with Sr atoms with a probability of 72.0%. The broad channels are statistically occupied by Ba and Sr atoms. In the $(\text{Ba}_{0.27}\text{Sr}_{0.75}\text{Nb}_2\text{O}_{5.78})$ [9] crystal structure, the Ba and Sr atoms occupy one position with a probability of 85%. In the crystal structures studied in this paper, the Ba and Sr atomic positions are split, and the distribution of strontium atoms correlates with the characteris-

Coordinates and thermal parameters of the basis atoms in the $(\text{Sr}_{0.50}\text{Ba}_{0.50})\text{Nb}_2\text{O}_6$ structure

Atom	Position multiplicity	Occupancy, %	Symmetry of the position	x/a	y/b	z/c	$B_{\text{eq}}, \text{\AA}^2$
Nb(1)	2	100	mm	0.0	0.5	0.0	0.63
Nb(2)	8	100	1	0.0743(1)	0.2113(1)	-0.0141(7)	0.75
Sr(1)	2	72.0(3)	4	0.0	0.0	0.4791(8)	0.69
Sr(2)	8	13.1(3)	1	0.1509(5)	0.6852(9)	0.5044(19)	1.79
Ba	4	62.3(3)	m	0.1727(1)	0.6727(1)	0.4745(7)	1.39
O(1)	8	100	1	0.3436(2)	0.0061(2)	-0.0441(24)	2.52
O(2)	8	100	1	0.1391(3)	0.0689(2)	-0.0497(22)	2.40
O(3)	4	100	m	0.2825(2)	0.7825(2)	-0.0452(22)	2.41
O(4)	4	50	m	0.0114(8)	0.5114(8)	0.4566(24)	3.37
O(5a)	8	50	1	0.3058(5)	0.4054(6)	0.4541(22)	1.32
O(5b)	8	50	1	0.2859(6)	0.4438(7)	0.4512(18)	1.73

tics of ferroelectric phase transitions observed in these crystals. The splitting of the statistically occupied barium and strontium positions is illustrated by Fig. 1. In the $(\text{Sr}_{0.33}\text{Ba}_{0.67})\text{Nb}_2\text{O}_6$ crystal [5] with the lowest strontium concentration, all Sr atoms are located in the medium-sized channels, whereas the broad channels are occupied by barium atoms alone. When writing the chemical formulas with due regard for the occupancies of the crystallographic positions, one has to take into account also the position multiplicities indicated in the table and the fact that the unit cell contains five formula

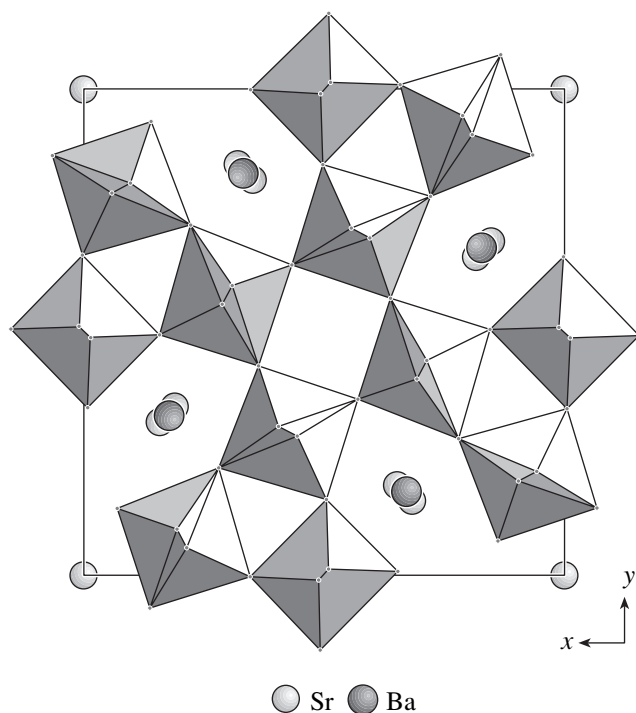


Fig. 1. The $(\text{Sr}_{0.50}\text{Ba}_{0.50})\text{Nb}_2\text{O}_6$ structure projected onto the ab plane.

units of the composition $(\text{Sr}_x\text{Ba}_{1-x})\text{Nb}_2\text{O}_6$. For the compounds with $x = 0.33, 0.50, 0.61$, or 0.75 studied in this work, the occupancies of the medium-sized channels by strontium atoms vary only slightly (70.5, 72.0, 72.5, and 71.5%, respectively). The barium atoms in the broad channels are always located in positions with multiplicities of four in mirror planes m . If the broad channels are statistically occupied by both barium and strontium atoms, the Sr atoms are displaced from the symmetry planes m toward the general positions with the multiplicity 8 [6], and the Sr–Ba distances are 0.335, 0.305, and 0.262 \AA in the compounds with $x = 0.50, 0.61$, and 0.75 , respectively. Taking into account the position multiplicities, the occupancies of the broad channels by barium atoms were determined as 84.0, 62.3, 48.7, and 30.9%, and the occupancies by strontium atoms, as 0.0, 26.2, 40.4, and 57.2% for the compounds with $x = 0.33, 0.50, 0.61$, and 0.75 , respectively, with the total occupancy being almost unchanged (84.0, 88.5, 89.1, and 88.1%, respectively). At $x < 0.25$ or $x > 0.75$, crystallization yields phases with structures different from those considered above. The phase we are interested in requires the filling of the medium-sized channels (the position on the fourfold symmetry axis with the multiplicity 2) with strontium atoms for 71–72%. This occupancy is provided by the presence of at least 25 at. % of strontium in the compound. At higher concentrations of strontium in solid solutions, strontium replaces barium in the broad channels (as was mentioned above, strontium atoms are displaced from the plane m), whereas its amount in the medium-sized channels remains virtually unchanged. The total occupancy of the broad channels remains almost constant (~88%). The optically perfect crystals of these compounds were obtained from the melt of the congruent composition with $x = 0.61$. In terms of the structure, the latter crystals are characterized by the occupancy of the broad channels by Ba and Sr atoms in a ratio close

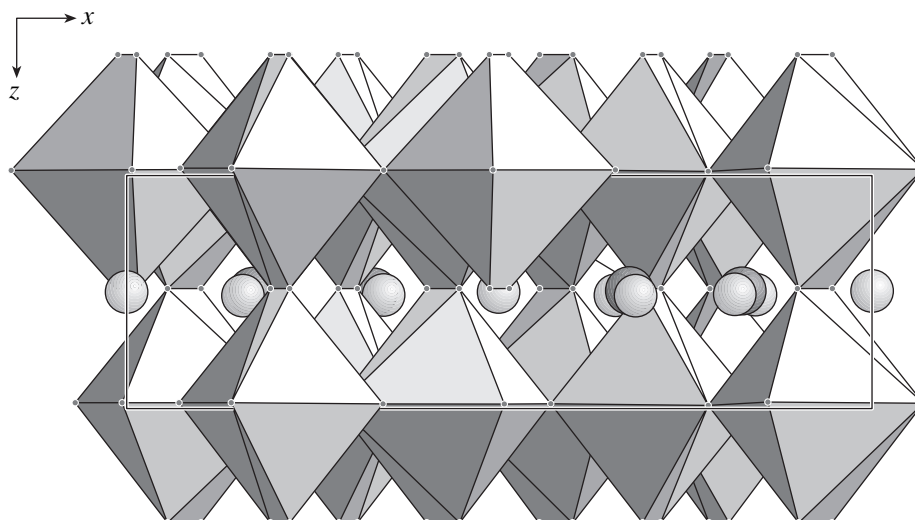


Fig. 2. The $(\text{Sr}_{0.50}\text{Ba}_{0.50})\text{Nb}_2\text{O}_6$ structure projected onto the ac plane. For notation, see Fig. 1.

to 1 : 1. Our results show that the occupancies of broad channels by Ba and Sr atoms are 48.7 and 40.4%, respectively.

It is seen from Fig. 2 that Sr and Ba ions are located at the same height along the c -axis, whereas Nb-octahedra are above and below the planes of their location at distances of $c/2$. The characteristic feature of Nb-octahedra is the location of oxygen atoms in the fixed equatorial positions in all the structures studied, whereas the apical oxygen atoms located in the planes of Sr and Ba atoms are statistically disordered over two positions with a probability of 0.5. In the compound with $x = 0.50$, these positions are spaced by the distances of 0.407 and 0.521 Å for Nb(1) and Nb(2), respectively. The distances between the split positions increase monotonically with an increase in the strontium content. Thus, these distances are 0.388 and 0.510 Å in the compound with $x = 0.33$, whereas the corresponding distances in the compound with $x = 0.75$ are 0.561 and 0.635 Å. In other words, the planes statistically occupied by Sr and Ba atoms also contain statistically arranged apical oxygen atoms of the Nb-octahedra.

The structure of $[\text{NbO}_6]$ -octahedra is essential for the optical properties of these crystals. In all structures of the series under consideration, a Nb(1)-octahedron has the crystallographic symmetry mm , whereas a Nb(2)-octahedron is in the general position. All Nb-octahedra are aligned along the c -axis and form $-\text{O}(4)-\text{Nb}(1)-\text{O}(4)-\text{Nb}(1)-$ and $-\text{O}(5)-\text{Nb}(2)-\text{O}(6)-\text{Nb}(2)-$ chains. As was mentioned above, the bridging oxygen atoms of the chains statistically occupy two positions. As a result, the octahedra “oscillate” about the c -axis of the crystal. The structure of Nb-octahedra can be described by scheme 1–4–1 showing the existence of one short (strong) Nb–O bond, four intermediate Nb–O bonds, and one elongated Nb–O bond, always being

located in the *trans* position with respect to the strong bond. It is these pairs of the shortest and the longest bonds that are approximately parallel to the c -axis. In the $(\text{Sr}_{0.50}\text{Ba}_{0.50})\text{Nb}_2\text{O}_6$ structure, the Nb(1)–O bond lengths are 1.814 (short bonds), 1.958 (four intermediate bonds), and 2.155 Å (long bond). A Nb(2)-octahedron has short (1.878 and 1.852 Å bonds with each one occurring with a probability of 0.5), four intermediate (1.932, 1.955, 2.000, and 2.000 Å) bonds, and elongated (2.123 and 2.125 Å) bonds. In the compounds with $x = 0.33, 0.50, 0.61,$ and 0.75 , the average values of the short Nb–O bonds are 1.845, 1.840, 1.863, and 1.933 Å, respectively; the average values of the intermediate bonds range within 1.961–1.970 Å; and the elongated Nb–O bond are 2.158, 2.135, 2.108, and 2.048 Å, respectively. Earlier, it was shown [7] that the refractive index and some other optical characteristics correlate with the asymmetry of Nb-octahedra expressed as the difference between the short and the long Nb–O bonds. The degree of the distortion of $[\text{NbO}_6]$ -octahedra from an ideal centrosymmetric octahedron depends on the isomorphous replacements. With a decrease in the Sr content, the structure is ordered: the Ba and Sr positions are split, and the NbO_6 -octahedra forming the framework become more distorted (acentric). It can be assumed that this structural ordering is responsible for both the dependence of the relaxation properties on the composition and the less diffuse phase transition. The filling of the tetragonal channels with strontium atoms is virtually independent of the composition, which governs only the statistical filling of the channels with barium and strontium atoms [7]. Thus, the properties of $(\text{Sr},\text{Ba})\text{Nb}_2\text{O}_6$ crystals can be changed by varying the Sr/Ba ratio in these structures.

ACKNOWLEDGMENTS

This study was supported by the Federal Program on Support of Prominent Scientists and Leading Scientific Schools, project no. 00-15-96633 and by the Russian Foundation for Basic Research, project no. 00-02-16624.

REFERENCES

1. L. I. Ivleva and Yu. S. Kuz'minov, Preprint No. 93, FIAN (Lebedev Institute of Physics, Academy of Sciences of USSR, Moscow, 1977), p. 14.
2. M. E. Lines and A. M. Glass, *Principles and Applications of Ferroelectrics and Related Materials* (Oxford Univ. Press, Oxford, 1977; Mir, Moscow, 1981).
3. L. E. Cross, *Ferroelectrics* **76**, 241 (1987).
4. M. P. Trubelja, E. Ryba, and D. K. Smith, *J. Mater. Sci.* **31**, 1435 (1996).
5. A. E. Andreïchuk, L. M. Dorozhkin, Yu. S. Kuz'minov, *et al.*, *Kristallografiya* **29**, 1094 (1984) [*Sov. Phys. Crystallogr.* **29**, 641 (1984)].
6. T. S. Chernaya, B. A. Maksimov, I. A. Verin, *et al.*, *Kristallografiya* **42**, 421 (1997) [*Crystallogr. Rep.* **42**, 375 (1997)].
7. T. S. Chernaya, B. A. Maksimov, T. R. Volk, *et al.*, *Fiz. Tverd. Tela (St. Petersburg)* **42**, 1668 (2000) [*Phys. Solid State* **42**, 1716 (2000)].
8. U. Zuker, K. Perenthaler, W. F. Kuhs, *et al.*, *J. Appl. Crystallogr.* **16**, 358 (1983).
9. P. B. Jamison, S. C. Abrahams, and J. L. Bernstein, *J. Chem. Phys.* **42**, 5048 (1968).

Translated by T. Safonova

**STRUCTURE
OF INORGANIC COMPOUNDS**

Synthesis and Crystal Structure of New Carbonate $\text{NaPb}_2(\text{CO}_3)_2(\text{OH})$

E. L. Belokoneva, A. G. Al'-Ama, O. V. Dimitrova,
V. S. Kurazhkovskaya, and S. Yu. Stefanovich

Faculty of Geology, Moscow State University, Vorob'evy gory, Moscow, 119899 Russia

e-mail: elbel@geol.msu.ru

Received June 7, 2001

Abstract—Crystals of a new lead carbonate, $\text{NaPb}_2(\text{CO}_3)_2(\text{OH})$, sp. gr. $P\bar{3}1c$, were prepared by hydrothermal synthesis. The crystal structure was established by the heavy-atom method without knowing the exact chemical formula of the compound. The polar structure of the carbonate and the distortion of the pseudosymmetry described by the supergroup $P\bar{3}1c$ are caused by the acentric arrangement of the oxygen atoms providing the satisfactory coordination of Pb and Na atoms. The bonds between a hydroxyl group and two crystallographically independent Pb atoms are directed along the c -axis and have different lengths. The study of the carbonate by the second harmonic generation method in a temperature range of 20–250°C revealed the nonlinear optical properties comparable with the similar properties of quartz. The comparison of the structure of the new carbonate with a number of carbonates demonstrated that the new compound is structurally similar to ewaldite $\text{BaCa}(\text{CO}_3)_2$, diorthosilicate $\text{NaBa}_3[\text{Si}_2\text{O}_7](\text{OH})$, and $\text{Ba}[\text{AlSiO}_4]_2$ containing a double silicon–oxygen layer.
© 2002 MAIK “Nauka/Interperiodica”.

INTRODUCTION

Carbonates belong to one of the most important classes of inorganic compounds containing planar $[\text{CO}_3]^{2-}$ anions as the major structural unit. Natural and synthetic Ca, Mg, Fe, Mn, Na, Ba, Zn, and Cu carbonates are the most widespread and well-known compounds of this type [1]. Lead carbonates are rather rare and are found in nature as minerals such as phosgenite $\text{Pb}_2(\text{CO}_3)\text{Cl}_2$, cerussite PbCO_3 , and hydrocerussite $\text{PbCO}_3 \cdot \text{PbO}(\text{H}_2\text{O})_2$. Due to the high electron polarizability of Pb^{2+} ions explained by their specific electronic structure, the constituent oxides of lead carbonates have a dipole structure and possess piezo- and pyroelectric and nonlinear-optical properties. Hence, the preparation and the study of polar compounds in the carbonate systems involving lead are of interest in terms of both crystal chemistry and materials science.

EXPERIMENTAL

Synthesis of Single Crystals and Their Preliminary Diagnostics

Single crystals were synthesized when studying the phase formation in the $\text{Na}_2\text{CO}_3\text{--PbO--B}_2\text{O}_3\text{--H}_2\text{O}$ system. The experiments were carried out in 5 to 6-cm³-large standard fluoroplastic-lined autoclaves at ~70 atm and 270–280°C. The lower temperature limit was dictated by the kinetics of hydrothermal reactions, whereas the upper one was determined by the apparatus used. The experiments were carried out for 18–20 days to bring the reactions to completion. The coefficient of

autoclave filling was chosen so as to maintain a constant pressure. Colorless transparent hexagonal single crystals of sizes up to ~1 mm had a habit ranging from tabular to isometric. The crystals had perfect cleavage along the (001)-plane.

No analogues of the X-ray diffraction powder pattern (a DRON-UM1 diffractometer, Co radiation, 40 kV, 25 mA) were found in the PDF data base, which indicated that we synthesized a new compound. The composition of the crystals was determined by qualitative X-ray spectral analysis on a CAMSCAN 4DV scanning electron microscope equipped with a LINK attachment for the energy-dispersive analysis at the Department of Petrography of the Faculty of Geology of Moscow State University. This investigation confirmed the presence of Na and Pb atoms in the sample. Thus, with due regard for the composition of the initial system, the new compound could be related either to carbonates or borates.

IR Spectroscopy

The IR spectrum of a liquid sample obtained as a neat thin film between KBr supporting plates was measured on a Specord-75 IR spectrophotometer in the frequency ranges 1800–400 and 3800–3000 cm⁻¹ (Fig. 1). The IR spectrum has stretching vibration bands of the carbonate ion. Thus, the intense band at 1432 cm⁻¹ corresponds to the asymmetric stretching vibration ν_3 , the weak band at 1055 cm⁻¹ belongs to the symmetric stretching vibration ν_1 , and the bands at 847 and

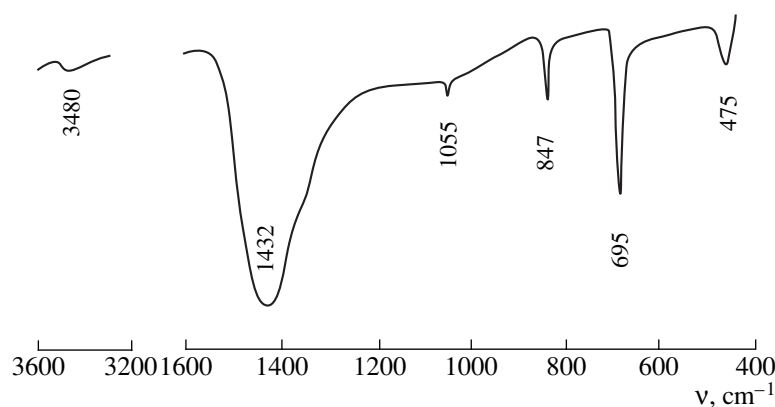


Fig. 1. IR spectrum of $\text{NaPb}_2(\text{CO}_3)_2(\text{OH})$.

695 cm^{-1} are attributed to the out-of-plane and in-plane deformation vibrations ν_2 and ν_4 , respectively. By analogy with the spectrum of cerussite PbCO_3 [2], the band at 475 cm^{-1} was assigned to lattice vibrations. The vibration band of the hydroxyl group is observed at 3480 cm^{-1} . The degeneration of the ν_3 and ν_4 vibrations is indicative of the positional symmetry with a threefold axis for a CO_3 ion. The presence of the stretching vibration ν_1 shows that the symmetry group of a CO_3 ion contains neither the inversion center nor twofold axes perpendicular to the threefold axis. Thus, the carbonate ion has the positional symmetry C_3 . The superposition of the resonance vibrations of all the CO_3 ions in the unit cell does not change the number of the bands in the spectrum. Consequently, the crystal structure may belong to the symmetry class C_3 or C_3v .

Table 1. Crystallographic data for $\text{NaPb}_2(\text{CO}_3)_2(\text{OH})$ and details of X-ray diffraction study

Molecular formula	$\text{HC}_2\text{O}_7\text{NaPb}_2$
Sp. gr.	$P31c$
a , Å	5.268(4)
c , Å	13.48(1)
V , Å ³	324.0(7)
ρ_{calc} , g/cm ³	5.877(9)
μ , cm ⁻¹	512.1(1)
Refinement mode	$F(hkl)$
Weighting scheme	$w = 1/[(\sigma(F))^2 + 0.0010F^2]$
Number of parameters in the refinement	21
2θ (deg) and $\sin\theta/\lambda_{\text{max}}$	93.55 and 1.025
Number of reflections with $F > 4\sigma(F)$	851
$R(F)$, R_w	0.0445, 0.0472
S	1.080
Reduction coefficient	0.685(4)

Single-Crystal X-ray Diffraction Analysis

The symmetry of the Laue patterns obtained from a large ($0.6 \times 0.3 \times 0.15\text{ mm}$) transparent tabular single crystal oriented normally to the incident beam showed that the crystal belongs to the diffraction class $\bar{3}1m$. The X-ray data were collected from a small isometric ($0.125 \times 0.125 \times 0.15\text{ mm}$) well-faceted crystal providing the formation of high-quality reflections in the Laue diffraction patterns. The parameters of the triclinic unit cell were determined and refined on a Syntex P1 diffractometer (Table 1). The three-dimensional set of intensities I_{hkl} were collected within the independent region of the reciprocal space in accordance with the diffraction class. The intensities were processed and converted into F_{hkl}^2 using the PROFIT program [3]. All the subsequent calculations were carried out with the use of the CSD program package. The observed systematic absences of the hhl reflections with $l = 2n$ indicated the space group $P31c-C_{3v}^4$. The interatomic vectors of the Patterson function P_{uvw} showed that the heavy Pb atoms occupy special positions on the threefold axes spaced by the distance of $\sim 1/3c$. The refinement of two basis Pb(1) and Pb(2) atoms converged with the satisfactory R factor. The Na atom, the O(1) atom of the hydroxyl group (involved in the coordination environment only about the Pb(1) and Pb(2) atoms), two C atoms, and the O(2) and O(3) atoms forming the triangular coordination environments about the C atoms were localized from the difference electron-density syntheses by the method of successive approximations. The resulting formula $\text{NaPb}_2(\text{CO}_3)_2(\text{OH})$ (**I**) is electrically neutral. The structure model was refined with allowance for anomalous absorption of the Mo radiation by lead atoms using only isotropic thermal parameters. Attempts at anisotropic refinement failed because of the pronounced pseudosymmetry of the structure in the space group $P\bar{3}1c$, which is seen from the analysis of the atomic

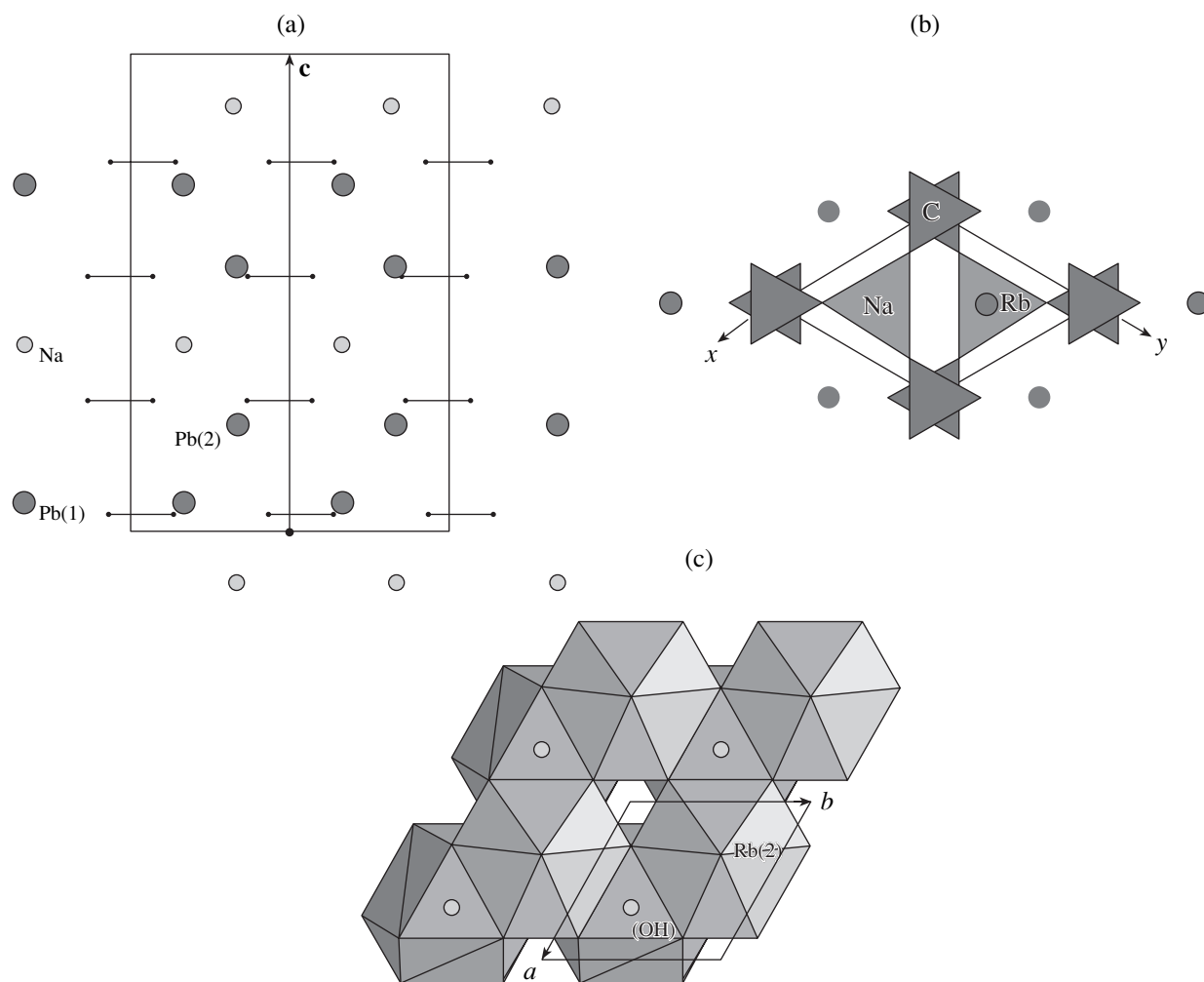


Fig. 2. Crystal structure of $\text{NaPb}_2(\text{CO}_3)_2(\text{OH})$: (a) the side diagonal projection onto the (110) plane (CO_3 -triangles are shown by solid lines and Na and Pb atoms are represented by circles); (b) the projection onto the (001) plane (CO_3 groups are shown by triangles and Na and Pb atoms are represented by prisms and circles, respectively); (c) the projection onto the (001) plane (the Pb(2)-polyhedra are visible; OH groups are represented by circles).

coordinates. A singular point on the pseudoaxis $\bar{3}$ (an inversion pseudocenter) is located at a height $z = 0.14$ (and 0.64). Two positions of Pb atoms in the sp. gr. $P31c$ are related by this pseudocenter, which corresponds to one independent Pb atom in the position $4f$ of the supergroup $P\bar{3}1c$. In this supergroup, a Na atom (with the z coordinate rounded to $1/4$) occupies the $2c$ position, a Cl atom is located in the $4e$ position, the O(1) atom (with the z coordinate also rounded to $\sim 1/4$) occupies the $2d$ position, and the O(2) and O(3) atoms merging into one atom are located in the general position $12i$. The refinement of this model within the sp. gr. $P\bar{3}1c$ did not allow us to reduce the R factor below 0.087. The supergroup was rejected because of the violation of two principal structural criteria—(1) the isotropic thermal parameter ($B = 4.42 \text{ \AA}^2$) for the O atom with the coordinates corresponding to the position $12i$

in the supergroup was too high and (2) the Pb–O interatomic distance (1.908 \AA ; the ionic radius of Pb^{2+} is 1.20 \AA) and the too long Na–O interatomic distance (3.04 \AA ; the ionic radius of Na^+ is 0.97 \AA) were too short. The splitting of the position $12i$ of the oxygen atom into two positions, O(2) and O(3), substantially improved the Pb–O (2.62 – 2.74 \AA) and Na–O (2.38 – 2.59 \AA) distances, reduced the difference in the lengths of the bonds between the Pb(1) and Pb(2) atoms and the common O(1) atom of the hydroxyl group, and lowered the symmetry (the loss of the inversion center), which is in agreement with the IR spectral data. At the final stage of the refinement, the correction for absorption, too high despite the small size of the sample, was applied using the DIFABS program [4]. The atomic coordinates and interatomic distances are given in Tables 2 and 3, respectively.

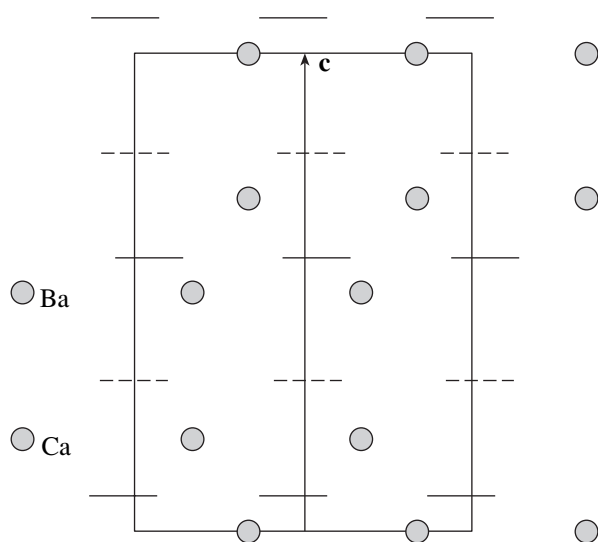


Fig. 3. Crystal structure of ewaldite projected onto the (110) plane; Ca and Ba atoms are represented by circles, CO_3 -triangles are shown by solid lines, and unlocalized CO_3 groups are indicated by dashed lines.

Study by Method of the Second Harmonic Generation

The nonlinear-optical activity of carbonate **I** was examined using powdered samples obtained by grinding. A sample with 100 to 150- μm particles was prepared by isolating the coarse-ground fraction with the use of sieves. A sample of the finely dispersed fraction with 3 to 5- μm grains was obtained by 20-min precipitation of an alcoholic suspension. The temperature dependence of the second harmonic generation (SHG) was obtained on the samples placed into an electric furnace. The test for the second harmonic generation was performed in the reflection mode using a YAG : Nd laser according to the procedure described in our earlier studies [5]. At room temperature, the second-harmonic intensity with respect to that of the reference sample of crystalline quartz with a dispersity of 3 μm were 1.2 and 0.7 for the coarse- and finely-dispersed samples,

Table 2. Coordinates of basis atoms and isotropic thermal parameters for the $\text{NaPb}_2(\text{CO}_3)_2(\text{OH})$ structure

Atom	x/a	y/b	z/c	B_j
Na	2/3	1/3	0.8927(11)	1.59(6)
Pb(1)	2/3	1/3	0.5570	0.85(4)
Pb(2)	2/3	1/3	0.2258(1)	0.90(4)
C(1)	0	0	0.035(3)	0.44(6)
C(2)	0	0	0.276(3)	0.32(6)
O(1)	2/3	1/3	0.388(4)	1.47(6)
O(2)	0.151(7)	0.288(8)	0.536(2)	1.20(6)
O(3)	0.276(7)	0.141(7)	0.755(2)	0.83(6)

respectively. The low SHG signal and an insignificant increase in its intensity for the coarse-ground sample indicate that carbonate **I** exhibits rather weak optical nonlinearity and, probably, possesses no phase synchronism with the neodymium laser radiation and its second harmonic. According to Kurts [6], crystals **I** should be related to the nonlinear-optical class *D*.

A rise in the temperature to 220–250°C resulted in no substantial changes in the nonlinear-optical properties. In the temperature range from 250 to 300°C, the intensity of the second-harmonic signal rapidly decreased and finally became zero. Subsequent cooling did not restore the nonlinear-optical activity of the samples, which proves the irreversibility of the structural change occurred. X-ray diffraction analysis and IR spectroscopy data show that, upon thermal treatment, carbonate **I** lost the quadratic optical nonlinearity which can be associated with the removal of the OH group from the sample.

RESULTS AND DISCUSSION

In the structure of new carbonate **I** (Figs. 2a, 2b), the CO_3 -triangle has the symmetry 3, which is consistent with the results of IR spectroscopy. The plane of the CO_3 -triangle is parallel to the *ab*-plane of the unit cell. The C–O distances are slightly different (Table 3) but range within the corresponding values known for a number of minerals. The C–O distances in dawsonite $\text{NaAl}(\text{OH})_2\text{CO}_3$ [7] are 1.25 and 1.308 Å (two distances); in fairchildite $\text{K}_2\text{Ca}(\text{CO}_3)_2$ [8], 1.284 (two distances) and 1.288 Å; in paralstonite $\text{BaCa}(\text{CO}_3)_2$ [9], 1.279, 1.289, and 1.285 Å; and in barytoalcite $\text{BaCa}(\text{CO}_3)_2$ [10], they range from 1.15 to 1.43 Å. The average C–O distance for two triangles in carbonate **I** is identical to that in dolomite $\text{CaMg}(\text{CO}_3)_2$ [11] (C–O = 1.285 Å). The Pb atoms in the minerals phosgenite $\text{Pb}_2(\text{CO}_3)\text{Cl}_2$ [12], cerussite PbCO_3 [13], and hydrocerussite $\text{Pb}_3(\text{CO}_3)_2(\text{OH})_2$ [14] with known structures adopt high coordination numbers (9 or 10). If seven O atoms located at distances up to ~2.7 Å (Table 3) are included into the coordination sphere of Pb atoms, the polyhedra remain open, like those in hydrocerussite; however, the addition of three more O atoms located at distances larger than 3 Å complements the coordination of the Pb(1) and Pb(2) atoms to ten-vertex polyhedra (because of the pseudosymmetry). These polyhedra can be described by hexahedral “boxes” with flat bottoms and caps ended with shared hydroxyl groups closest to the Pb(1) and Pb(2) atoms (Fig. 2c). The distances in these polyhedra around lead atoms in phosgenite (from 2.36 to 3.34 Å), cerussite (from 2.59 and 2.76 Å), and hydrocerussite (from 2.75 to 3.10 Å) are quite consistent with the Pb–O distances in carbonate **I** refined within the acentric space group. The coordination polyhedra around Na atoms are almost regular trigonal prisms.

The metrics of the axes in the structures of carbonate **I** and ewaldite $\text{BaCa}(\text{CO}_3)_2$ ($a = 5.284$ Å, $c = 12.78$ Å,

sp. gr. $P6_3mc$ [15]) are virtually identical. The replacement of Ba^{2+} by Na^+ leads to a necessary increase in the number of large cations in the formula of carbonate **I**. One of the CO_3 -triangles in the ewaldite structure has not been localized as yet [15]. Comparing the side diagonal projections of these structures (Figs. 2a, 3), we see that the positions of Ba and Ca atoms in ewaldite are identical to the positions of Na and Pb(1) atoms in carbonate **I**. By analogy, it can be assumed that a CO_3 group not revealed in the ewaldite structure should be located between the Ca- and Ba-layers (dashed lines in Fig. 3) at the height z identical to the height observed for an additional Pb(2) cation in structure **I**.

The mineral paralstonite of the aragonite group with the formula $BaCa(CO_3)_2$ identical to that of ewaldite belongs to the trigonal system (sp. gr. $P321$) [9]. The c -parameter of paralstonite (6.148 Å) is half as large as that of carbonate **I**, whereas the $a(b)$ parameter (8.692 Å) is close to the length of the unit-cell diagonal of carbonate **I**. The close $a(b)$ parameters were also found in phosgenite and hydrocerussite. The cationic motifs in ewaldite and carbonate **I** are complicated by an additional layer built into it and increasing in the c -parameter. The unit cell of the minimum volume (sp. gr. $P312$) is observed in lead- and oxygen-deficient borate $Pb_{0.75}[BO_{2.25}]$ studied recently. The $a(b)$ parameters of the latter (~ 5 Å) are close to those of aragonite, fairchildite, dolomite, and cerussite, whereas its c parameter is equal to that of ewaldite. This borate was found to be structurally close to carbonates, and, first of all, to aragonite.

In the search for compounds structurally close to carbonate **I**, we revealed, quite surprisingly, diorthosilicate $NaBa_3[Si_2O_7](OH)$ [16] (**II**), whose unit-cell parameters ($a = 5.79$ Å, $c = 14.74$ Å, sp. gr. $P6_3/mmc$) are very close to those of **I** (despite the differences between these compounds). The coordination polyhedron around Ba(2) in **II** is identical to Pb-polyhedra in **I** (within the symmetry of the position). This polyhedron was described as the combination of a hexagonal pyramid and a half of the Archimedean cuboctahedron, whose triangular base is formed by a triangular face of the tetrahedron of a linear diortho group. In **II**, Ba(2)-polyhedra are linked in pairs via the shared vertices of

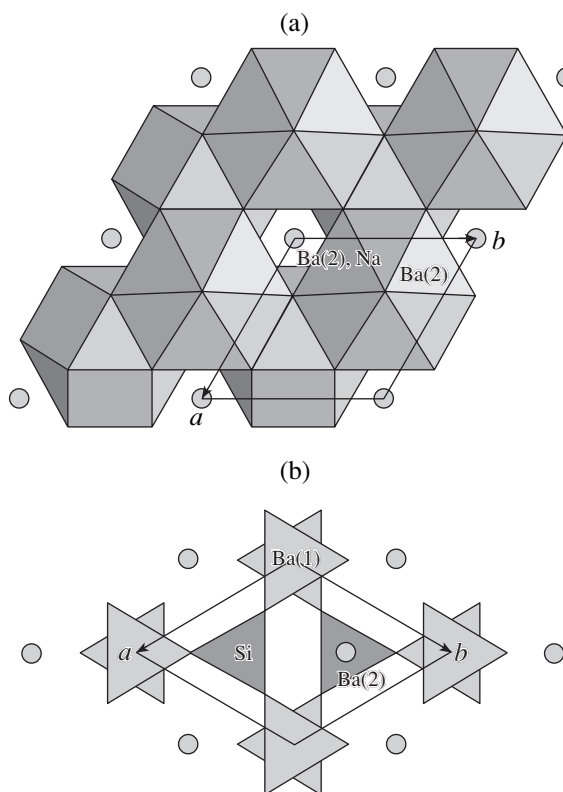


Fig. 4. Crystal structure of $NaBa_3[Si_2O_7](OH)$ (a) projected onto the (001) plane (Ba(2)-polyhedra are seen; Ba(1) and Na atoms are represented by overlapping circles); and (b) projected onto the (001) plane (Ba(1)-prisms and the Si diortho groups are seen; Ba(2) atoms are represented by circles).

the pyramid occupied by OH groups with shortened Ba–OH distances (Fig. 4a) (as in the structure of carbonate **I**). In carbonate **I**, Na-prisms are observed instead of diortho $[Si_2O_7]$ groups in **II** (which link Ba(2)-polyhedra into columns), with the Na atoms in the prisms occupying the central position of the bridging O atom of a diortho group in **II**. The columns of the second type in **II** along the c -axis consist of Na-octahedra and Ba(1)-trigonal prisms (Fig. 4b). In carbonate **I**, these columns are replaced by CO_3 -triangles (Fig. 2b)

Table 3. Principal interatomic distances (Å) in the $NaPb_2(CO_3)_2(OH)$ structure

Pb(1)-polyhedron		Pb(2)-polyhedron		Na-polyhedron	
Pb(1)–O(1)	2.28(5)	Pb(2)–O(1)	2.18(5)	Na–O(3)	$2.38(4) \times 3$
Pb(1)–O(2)	$2.62(4) \times 3$	Pb(2)–O(3)	$2.72(4) \times 2$	Na–O(2)	$2.59(4) \times 3$
Pb(1)–O(3)	$2.70(4) \times 3$	Pb(2)–O(3)	$2.74(4) \times 3$		
Pb(1)–O(3)	$3.44(5) \times 3$	Pb(2)–O(2)	$3.09(5) \times 3$		
C(1)-triangle		C(2)-triangle			
C(1)–O(2)	$1.31(4) \times 3$	C(2)–O(3)	$1.26(4) \times 3$		
O(2)–O(2)	$2.28(5) \times 3$	O(3)–O(3)	$2.18(5) \times 3$		

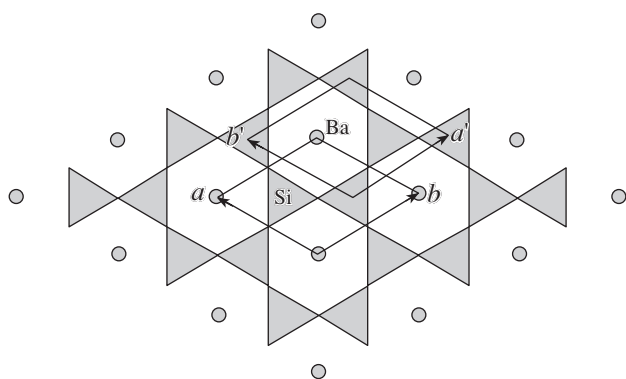


Fig. 5. Crystal structure of $\text{Ba}[\text{AlSiO}_4]_2$ projected onto the (001) plane; Si-tetrahedra are seen; Ba atoms are shown by circles. The a' and b' axes are shown to facilitate the comparison of the structures.

(the shared bases of the octahedra and prisms in **II**). In carbonate **I**, all the distances between the triangles along the c -axis are equivalent (Fig. 2a), whereas the corresponding distances in **II** have different values due to the differences in the heights at which the Na-octahedron and the Ba(1)-prism are located. Similar to the shared bases of the octahedra and prisms in **II** (Fig. 4b), the pairs of CO_3 -triangles in the structure of **I** (Fig. 4b) are rotated with respect to one another by 60° . The $\text{NaBa}_3[\text{Si}_2\text{O}_7](\text{OH})$ silicate is structurally similar to the $\text{NaPb}_2(\text{CO}_3)_2(\text{OH})$ carbonate because the ratio of the ionic radii of the pair Pb^{2+} and C^{4+} is similar to the ratio of the pair Ba^{2+} and Si^{4+} . The fragments of these structures shown in Figs. 2b and 4b are rather similar within the framework of the above-considered topology (Na-prism–Si-tetrahedron, CO_3 -triangle–Ba(1)-prism, and Pb–Ba(1)) and can be approximated by an idealized silicon–oxygen double layer built by the simplest mica $[\text{Si}_4\text{O}_{10}]$ layers linked by shared apical vertices. Such a layer was found in the $\text{Ba}[\text{Al}_2\text{Si}_2\text{O}_8]$ structure [17] (Fig. 5). These layers are translated and, thus, the c -parameter in the latter structure (7.79 \AA) is half as large as that in the structures under consideration. In this layer, the diortho groups can be replaced either by trigonal prisms (of Ba or Na) or other anionic tetrahedral or triangular (CO_3) groups, with the latter replacing the triangular bases of the SiO_4 -tetrahedra. This fact opens new possibilities for crystallochemical analysis and the prediction of new structures. It should be noted that N.V. Belov was the first to analyze the structural

analogy between diorthosilicates and minerals with triangular anions [18].

ACKNOWLEDGMENTS

We are grateful to E.A. Guseva (the Department of Petrography of the Faculty of Geology of Moscow State University) for performing the X-ray spectral analysis.

REFERENCES

1. I. Kostov, *Mineralogy* (Oliver and Boyd, Edinburgh, 1968; Mir, Moscow, 1971).
2. *The Infrared Spectra of Minerals*, Ed. by V. C. Farmer (Mineralogical Society, London, 1974), p. 206.
3. V. A. Strel'tsov and V. E. Zavodnik, *Kristallografiya* **34**, 1369 (1989) [*Sov. Phys. Crystallogr.* **34**, 824 (1989)].
4. N. Walker and D. Stuart, *Acta Crystallogr., Sect. A: Found. Crystallogr.* **A39** (1), 158 (1983).
5. S. Yu. Stefanovich, in *Extended Abstracts of European Conference on Lasers and Electro-Optics (CLEO-Europe'94)*, Amsterdam, 1994, p. 249.
6. S. K. Kurts and T. T. Pery, *J. Appl. Phys.* **39** (8), 3798 (1968).
7. E. Corazza, C. Sabelli, and S. Vannucci, *Neues Jahrb. Mineral., Monatsh.*, 381 (1977).
8. F. Pertlik, *Z. Kristallogr.* **157**, 199 (1981).
9. H. Effenberger, *Neues Jahrb. Mineral., Monatsh.*, 353 (1980).
10. K. F. Alm, *Ark. Mineral. Geol.* **2**, 399 (1960).
11. H. Effenberger and K. Mereiter, *Z. Kristallogr.* **156**, 233 (1981).
12. G. Giuseppetti and C. Tadini, *TMPM, Tscherma's Mineral. Petrogr. Mitt.* **21**, 101 (1974).
13. G. Chevrier, G. Giester, G. Heger, *et al.*, *Z. Kristallogr.* **199**, 67 (1992).
14. J. M. Cowley, *Acta Crystallogr.* **9**, 391 (1956).
15. G. Donnay and H. Preston, *TMPM, Tscherma's Mineral. Petrogr. Mitt.* **15**, 201 (1971).
16. O. S. Filipenko, E. A. Pobedinskaya, V. I. Ponomarev, and N. V. Belov, *Dokl. Akad. Nauk SSSR* **200**, 591 (1971) [*Sov. Phys. Dokl.* **16**, 703 (1972)].
17. Y. Takeuchi, *Mineral. J.* **2**, 311 (1958).
18. N. V. Belov, *Essays on Structural Mineralogy* (Nedra, Moscow, 1976).

Translated by T. Safonova

STRUCTURE OF INORGANIC COMPOUNDS

Crystal Structures of Two Ancylite Modifications

Yu. V. Belovitskaya*, I. V. Pekov*, E. R. Gobechiya*, N. A. Yamnova*,
Yu. K. Kabalov*, N. V. Chukanov**, and J. Schneider***

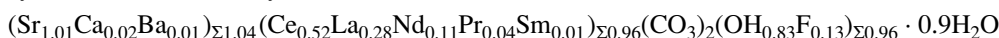
* *Geology Faculty, Moscow State University, Vorob'evy gory, Moscow, 119899 Russia*
e-mail: mineral@geol.msu.ru

** *Institute of Problems of Chemical Physics, Russian Academy of Sciences,
Chernogolovka, Moscow oblast, 142432 Russia*

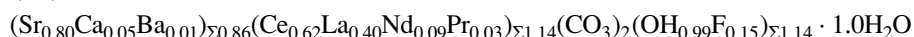
*** *Institut für Kristallografie und Mineralogie, University of Munich, München, D-80-333 Germany*

Received July 6, 2000

Abstract—The crystal structures of two ancylite specimens from Khibiny massif (the Kola Peninsula, Russia)—ancylite-(Ce) from alkali hydrothermalites



and ancylite-(Ce) from carbonatites—have



been refined by the Rietveld method. A focusing STOE-STADIP diffractometer with a bent Ge(111) primary monochromator was used ($\lambda\text{MoK}_{\alpha 1}$ radiation, $2.16^\circ < 2\theta < 54.98^\circ$; reflection number 237–437). All the computations for ancylite from alkali hydrothermalites were performed within the sp. gr. $Pmc2_1$, $a = 5.0634(1) \text{ \AA}$, $b = 8.5898(1) \text{ \AA}$, $c = 7.2781(1) \text{ \AA}$, $V = 316.55(1) \text{ \AA}^3$, $R_{wp} = 1.90$; the computations for ancylite from carbonatites were performed within the sp. gr. $Pm\bar{c}n$, $a = 5.0577(1) \text{ \AA}$, $b = 8.5665(2) \text{ \AA}$, $c = 7.3151(2) \text{ \AA}$, $V = 316.94(1) \text{ \AA}^3$, $R_{wp} = 2.38$ in the anisotropic approximation of thermal vibrations of cations and oxygen atoms. © 2002 MAIK “Nauka/Interperiodica”.

INTRODUCTION

Ancylite-(Ce) described by the formula $(\text{Sr,Ca})_{2-x}\text{REE}_x(\text{CO}_3)_2(\text{OH,F})_x \cdot n\text{H}_2\text{O}$ (with $x \approx 1.0$ – 1.5 , $n \approx 1$) is one of the rare earth carbonates occurring in many alkaline massifs (the Khibiny, Sebljavr, the Kola peninsula, Vuorijarvi, Sallanlatva, and Northern Karelia (Russia), Mont Saint-Hilaire (Canada), Narssarsuk (Greenland), etc.). It is also characteristic of late low-alkali hydrothermal formations associated with apaitic rocks and carbonatites.

The ancylite family consists of five minerals described by the general formula $M_{2-x}^{2+}\text{REE}_x(\text{CO}_3)_2(\text{OH})_x \cdot n\text{H}_2\text{O}$, namely, ancylite-(Ce) and ancylite-(La) with $M^{2+} = \text{Sr}$ [1], calcioancylite-(Ce) [2] and calcioancylite-(Nd) [3] with $M^{2+} = \text{Ca}$, and gysinite-(Nd) [4] with $M^{2+} = \text{Pb}$. The crystal structure of ancylite-(Ce) was first determined within the sp. gr. $Pm\bar{c}n$ in 1975 [5]. The metal atoms in the structure are located in ten-vertex polyhedra forming a three-dimensional framework (Fig. 1).

We studied crystal structures of two ancylite-(Ce) modifications found in specimens from Khibiny massif (the Kola Peninsula): the ancylite-(Ce) from alkali hydrothermalites (the Lovchorrite Mine, the Hackman Valley) described by the formula $(\text{Sr}_{1.01}\text{Ca}_{0.02}\text{Ba}_{0.01})_{\Sigma 1.04} \cdot (\text{Ce}_{0.52}\text{La}_{0.28}\text{Nd}_{0.11}\text{Pr}_{0.04}\text{Sm}_{0.01})_{\Sigma 0.96}(\text{CO}_3)_2(\text{OH}_{0.83}\text{F}_{0.13})_{\Sigma 0.96} \cdot 0.9\text{H}_2\text{O}$ (sp. gr. $Pmc2_1$) (specimen 52) and ancylite-(Ce) from carbonatites (the region of the

Tulilukht Bay) described by the formula $(\text{Sr}_{0.80}\text{Ca}_{0.05}\text{Ba}_{0.01})_{\Sigma 0.86}(\text{Ce}_{0.62}\text{La}_{0.40}\text{Nd}_{0.09}\text{Pr}_{0.03})_{\Sigma 1.14} \cdot (\text{CO}_3)_2(\text{OH}_{0.99}\text{F}_{0.15})_{\Sigma 1.14} \cdot 1.0\text{H}_2\text{O}$ (sp. gr. $Pm\bar{c}n$) (specimen 54). Since the IR spectra obtained from these two

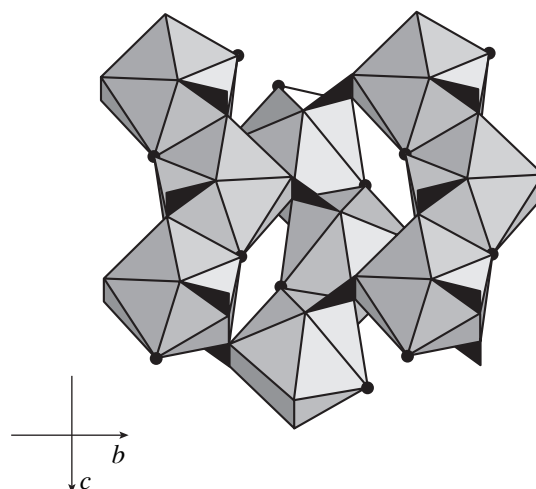


Fig. 1. Projection of an ideal ancylite structure onto the (100) plane. The CO_3^{2-} groups are indicated by black triangles. The black circles indicate the O(3) position in the structure of ancylite from carbonatites (specimen 54) corresponding to the O(31) and O(32) positions in the structure of ancylite from alkali hydrothermalites (specimen 52).

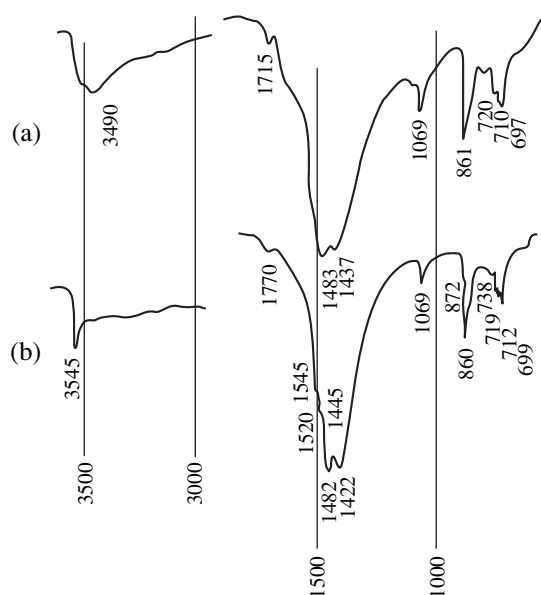


Fig. 2. IR spectra of ancyllites from (a) alkali hydrothermalites and (b) carbonatites. The numbers indicate frequencies in cm^{-1} .

specimens (Fig. 2) were essentially different, we undertook their structural investigation.

EXPERIMENTAL

Ancylite-(Ce) from alkali hydrothermalites from the Hackman Valley (specimen 52) forms bright yellow aggregates of split platelike crystals with a thickness of up to 0.5 mm forming, in turn, cellular pseudomorph after the hexagonal prismatic mineral (probably burbankite) in association with feldspar, natrolite, eudialyte, aegirine, astrophyllite, and apatite. Ancylite-(Ce) from calcite carbonatites from the region of the Tululukht Bay (specimen 54) is an aggregate of white split

isometric crystals up to 0.3 mm in length forming together with strontianite a cavernous pseudomorph after burbankite.

The chemical compositions of the specimens (cations, fluorine, Table 1) was studied by electron microprobe analysis (Camebax SX 50, analyst N.N. Kononkova, Moscow State University).

The powder specimens were prepared from the specially selected homogeneous ancylite grains. The X-ray diffraction spectra were obtained on a focusing STOE-STADIP diffractometer with bent Ge(111) primary monochromator $\lambda\text{MoK}\alpha_1$ radiation, $2.16^\circ < 2\theta < 54.98^\circ$, with a total number of reflections of 437 (specimen 52); $5.00^\circ < 2\theta < 44.98^\circ$, with a total number of reflections of 237 (specimen 54). All the computations were made by the WYRIET program, version 3.3 [6] within the sp. gr. $Pmc2_1$ (specimen 52) and the sp. gr. $Pm\bar{c}n$ (specimen 54). The initial structure model refined within the sp. gr. $Pm\bar{c}n$ was the model suggested by Dal Negro, Rossi, and Tazzoli [5]. The model refined within the sp. gr. $Pmc2_1$ was also based on the structure of highly symmetric ancylite but with due regard for the absence of the plane n .

Specimen 54 showed the presence of strontianite impurity (4.2%) and, therefore, the refinement was performed for two phases simultaneously—ancylite and strontianite as the second phase.

We used ionic scattering curves. The profile peak was approximated according to the Pearson-VII function at 6FWHM . The asymmetry was refined at $2\theta < 40^\circ$. The refinement was performed with gradual inclusion into the process of new parameters to be refined and constant automatic modeling of the background until the attainment of a stable R factor. Upon the refinement in the isotropic approximation, the reliability factor R_{wp} was 2.87% (specimen 52) and 2.67% (specimen 54).

Some parameters of the data acquisition and the results of the structure refinement of ancylites in the

Table 1. Chemical composition (wt %) and the formulas of studied ancylites

Components	Specimen 52	Specimen 54	Components	Specimen 52	Specimen 54
CaO	0.34	0.68	Sm ₂ O ₃	0.31	0.09
SrO	27.65	21.24	F	0.64	0.73
BaO	0.46	0.36	CO ₂	(23.28)	(22.44)
La ₂ O ₃	12.10	16.64	(H ₂ O)1	(1.98)	(2.27)
Ce ₂ O ₃	22.50	25.53	(H ₂ O)2	(4.32)	(4.92)
Pr ₂ O ₃	1.76	1.37	–O=F ₂	0.27	0.31
Nd ₂ O ₃	4.93	4.03	Total	(100.00)	(100.00)

Note: 1. Specimen 52 is ancylite from alkali hydrothermalites from Lovchorrite Mine and Hackman Valley of the compositions $(\text{Sr}_{1.01}\text{Ca}_{0.02}\text{Ba}_{0.01})_{\Sigma 1.04}(\text{Ce}_{0.52}\text{La}_{0.28}\text{Nd}_{0.11}\text{Pr}_{0.04}\text{Sm}_{0.01})_{\Sigma 0.96}(\text{CO}_3)_2(\text{OH}_{0.83}\text{F}_{0.13})_{\Sigma 0.96} \cdot 0.9\text{H}_2\text{O}$. Specimen 54 is ancylite from carbonatites from the region of Tululukht Bay $(\text{Sr}_{0.80}\text{Ca}_{0.05}\text{Ba}_{0.01})_{\Sigma 0.86}(\text{Ce}_{0.62}\text{La}_{0.40}\text{Nd}_{0.09}\text{Pr}_{0.03})_{\Sigma 1.14}(\text{CO}_3)_2(\text{OH}_{0.99}\text{F}_{0.15})_{\Sigma 1.14} \cdot 1.0\text{H}_2\text{O}$. 2. The calculated values are given in parentheses; the number of OH-groups (to which the (H₂O)1 value corresponds) was calculated from the stoichiometry; the number of water molecules (H₂O)2 was calculated from the difference of the total.

Table 2. Unit-cell parameters and the refined data for crystal structures of two ancylite specimens

Characteristic	Specimen 52	Specimen 54	Characteristic	Specimen 52	Specimen 54
a , Å	5.0634(1)	5.0577(1)	R_p	1.45	1.87
b , Å	8.5898(1)	8.5665(2)	R_{wp}	1.90	2.38
c , Å	7.2781(1)	7.3151(2)	R_{exp}	1.83	2.87
V , Å ³	316.55	316.94	R_B	1.53	1.34
Sp. gr.	$Pmc2_1$	$Pm\bar{c}n$	R_F	1.43	1.63
2 θ -range, deg	2.16–54.98	5.00–44.98	s^*	1.04	0.83
Number of reflections	437	237	DWD^{**}	0.81	1.04
Number of refined parameters	90	50	σ_x^{***}	1.660	1.587

* $s = R_{wp}/R_{exp}$, R_{exp} is the expected value of R_{wp} .

** Durbin–Watson statistics [8].

*** Factor used for calculating standard deviations [9].

Table 3. Atomic coordinates, isotropic temperature parameters (Å²), and occupancies of the positions in ancylite-(Ce) from alkali hydrothermalites (specimen 52), sp. gr. $Pmc2_1$

Atom	Characteristic	Value	Atom	Characteristic	Value
$M(1)$	x	0	O(11)	x	0
	y	0.0977(5)		y	0.418(4)
	z	0.6437(5)		z	0.271(3)
	B_j	0.48(5)	O(12)	B_j	2.1(8)
	q (Sr)*	0.486(2)		x	0.5
	q (RE + Ba)**	0.486(2)		y	0.919(4)
	q (Ca)	0.016(6)		z	0.244(2)
$M(2)$	x	0.5	O(21)	B_j	1.4(8)
	y	0.5897(5)		x	0.277(2)
	z	0.8475(5)		y	0.122(2)
	B_j	0.66(5)	z	0.352(2)	
	q (Sr)	0.498(2)	O(22)	B_j	1.3(5)
	q (RE)**	0.498(2)		x	0.223(2)
	C(1)	x		0	y
y		0.554(6)		z	0.151(2)
z		0.191(2)	O(31)	B_j	1.5(5)
B_j		1.9(9)		x	0
C(2)	x	0.5		y	0.204(3)
	y	0.056(6)	z	0.992(3)	
	z	0.308(2)	O(32)	B_j	1.4(9)
	B_j	1.8(9)		x	0.5
				y	0.660(3)
			z	0.516(3)	
			B_j	1.0(8)	

Notes: 1. Refinement was made for the composition $(\text{Sr}_{0.49}\text{RE}_{0.48}\text{Ca}_{0.02}\text{Ba}_{0.01})_{\Sigma 1.00}(\text{Sr}_{0.50}\text{RE}_{0.50})_{\Sigma 1.00}(\text{CO}_3)_2(\text{OH, F})_{0.98} \cdot 0.9\text{H}_2\text{O}$. The number of OH-groups was calculated from the stoichiometry; the number of water molecules was calculated from the difference of the total.

2. The refinement for RE was made with the use of the f -curve of cerium.

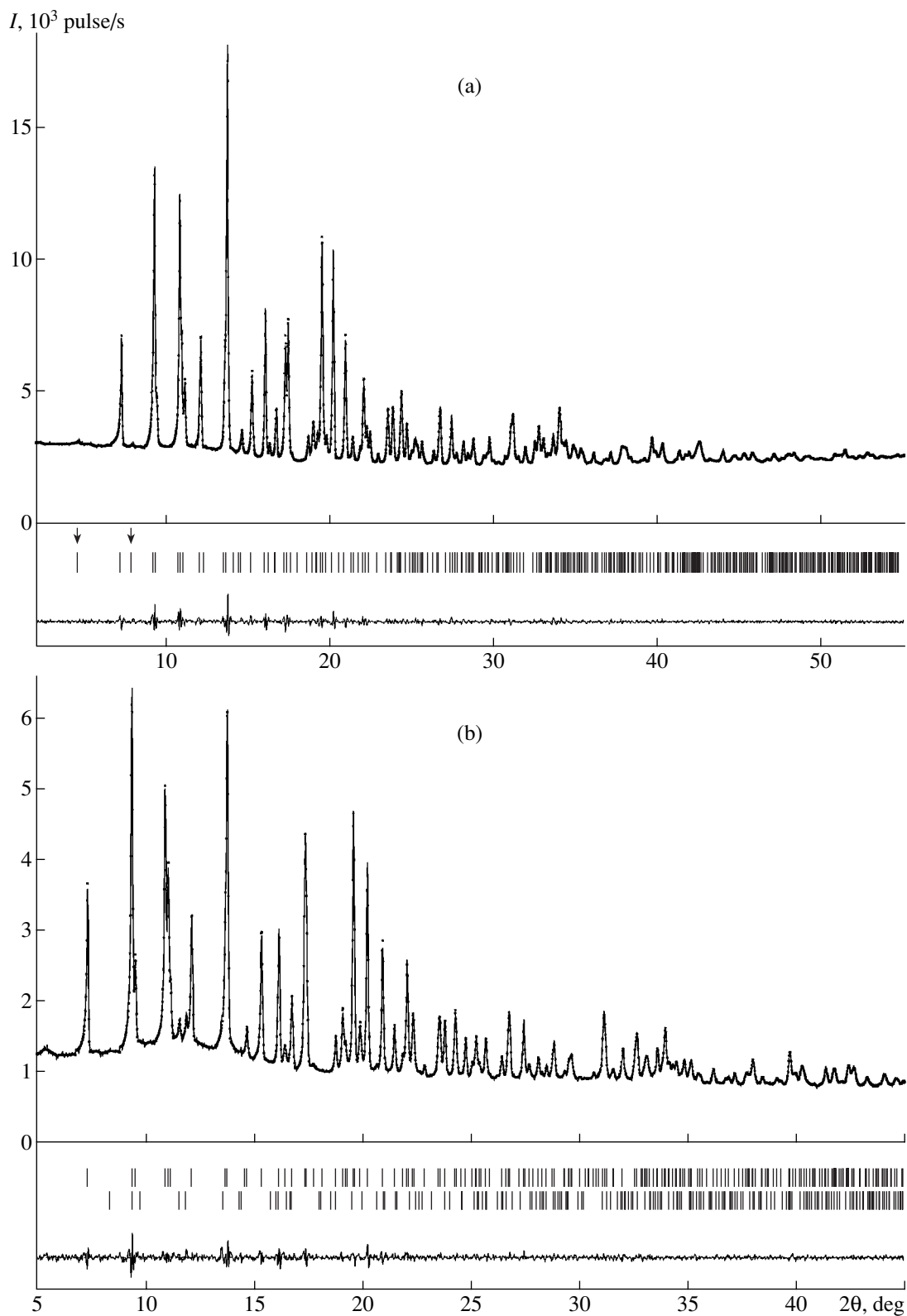


Fig. 3. Experimental (solid line) and calculated (dots) X-ray diffraction spectra from ancyrites (a) specimen 52 and (b) specimen 54. Arrows indicate the additional reflections in the spectrum from ancyrite from alkali hydrothermalites ($2\theta = 4.739^\circ$, $d = 8.579 \text{ \AA}$, $hkl = 010$ and $2\theta = 8.020^\circ$, $d = 5.072 \text{ \AA}$, $hkl = 100$) which violate the law of systematic absences for the sp. gr. *Pmcn*. The specimen from carbonatites has a strontialite impurity (the lower line diagram).

Table 4. Atomic coordinates and isotropic temperature parameters (\AA^2) and occupancies of the positions in ancylite-(Ce) from carbonatites (specimen 54), sp. gr. *Pmcn*

Atom	Characteristic	Value	Atom	Characteristic	Value
<i>M</i>	<i>x</i>	1/4	O(1)	<i>x</i>	3/4
	<i>y</i>	0.3409(3)		<i>y</i>	0.3286(2)
	<i>z</i>	0.6482(3)		<i>z</i>	0.7336(2)
	B_j	0.96(2)	O(2)	B_j	2.7(5)
	q (RE + Ba)*	1.153(3)		<i>x</i>	0.5266(2)
	q (Sr)	0.798(4)		<i>y</i>	0.1223(1)
	q (Ca)	0.056(8)		<i>z</i>	0.8525(2)
C	<i>x</i>	3/4	O(3)	B_j	1.2(3)
	<i>y</i>	0.1961(4)		<i>x</i>	1/4
	<i>z</i>	0.8154(5)		<i>y</i>	0.4183(2)
	B_j	3.7(9)		<i>z</i>	0.9736(2)
				B_j	2.7(5)

Notes: 1. Refinement was made for the composition $(RE_{1.13}Sr_{0.80}Ca_{0.06}Ba_{0.02})_{\Sigma 2.01}(CO_3)_2[(OH, F)_{1.15}(H_2O)_{1.0}]_{\Sigma 2.15}$. The number of OH-groups was calculated from the stoichiometry; the number of water molecules was calculated from the difference of the total.
2. The refinement for RE was made with the use of the *f*-curve of cerium.

anisotropic (metal and oxygen atoms) and isotropic (carbon atoms) approximations are listed in Table 2. Figure 3 shows the experimental (solid line) and the calculated (dots) X-ray diffraction spectra of ancylites. The coordinates and the isotropic temperature corrections for atoms and the position occupancies are indicated in Tables 3 and 4.

The IR spectra of ancylites prepared in the shape of tablets with KBr were obtained on a Specord 75 IR spectrophotometer.

DISCUSSION

The crystal structure of ancylite-(Ce) was first solved within the sp. gr. *Pmcn* as a derivative of the aragonite structure in 1975 [5]. Our results obtained for ancylite-(Ce) from carbonatites (specimen 54) agree well with the data of this first structure determination [5]. Divalent Sr, Ca, Ba cations and rare earth elements in ancylite are located in ten-vertex polyhedra formed by O(1), O(2), and O(3) oxygen atoms. Ten-vertex polyhedra share triangular O(1)–O(3)–O(2) faces and form chains along the *c*-axis. In turn, these chains form a three-dimensional framework via (CO_3) -triangles, with each triangle being surrounded with three *M*-polyhedra sharing their edges (Fig. 1).

The average distances in the polyhedra are *M*–O 2.63, C–O 1.31 Å (specimen 54) and *M*(1)–O 2.69, *M*(2)–O 2.62, C(1)–O 1.29, and C(2)–O 1.29 Å (specimen 52).

Unlike the X-ray diffraction pattern from ancylite from carbonatites (Fig. 3b), the X-ray diffraction pattern from ancylite from alkali hydrothermalites (Fig. 3a) has some additional reflections ($2\theta = 4.739^\circ$, $d = 8.579$ Å,

$hkl = 010$ and $2\theta = 8.020^\circ$, $d = 5.072$ Å, $hkl = 100$), which violate the law of systematic absences for the sp. gr. *Pmcn*. Therefore, the structure of this mineral was refined within the less symmetric group *Pmc2*₁ in which the cations (Sr, Ca, Ba, and RE) are located in two crystallographically nonequivalent positions *M*(1) and *M*(2). Since the ratio of the number of divalent cations to the total number of rare earth elements in this specimen was close to 1 : 1, we first assumed that *M*²⁺ and RE occupy two separate positions and that the lowering of the symmetry is caused by cationic ordering. However, the structure refinement showed that both these positions are occupied statistically (Table 3) and the lowering of the symmetry in the structure of this ancylite modification is caused by the displacement of atoms from the special positions to the general ones. The disappearance of the plane *n* is associated with the split of each position in the above structure into two nonequivalent positions (Tables 3 and 4), with the differences in the coordinates of each pair of atoms being much more pronounced than the accuracy of the determination of these coordinates.

The calculation of the local balance by the method suggested in [7] and the allowance for possible hydrogen bonds allowed us to single out O atoms, (OH)[–] groups, and H₂O molecules in the anionic part of the structure. In the structure of ancylite from carbonatites (specimen 54), the O(1) and O(2) positions are occupied by O atoms, whereas the O(3) position is statistically filled with (OH)[–]-groups and H₂O-molecules. In the structure of low-symmetric ancylite from alkali hydrothermalites (specimen 52), the OH[–]-groups and H₂O molecules are orderly distributed over the O(32) and O(31) positions, respectively.

The IR spectrum of ancylite from alkali hydrothermalites (specimen 52) (Fig. 2a) has a band at 3480–3490 cm^{-1} corresponding to the stretching vibrations of OH^- groups forming relatively weak hydrogen bonds. Sometimes, we also observed a shoulder at 3530–3540 cm^{-1} , which is attributed to free OH^- groups whose number is considerably less than the number of these groups linked by hydrogen bonds. The water molecules form rather strong hydrogen bonds, which manifest themselves in the IR spectrum as a broad band with the maximum at 2900–3000 cm^{-1} . The triply degenerate band of bending vibrations of CO_3^{2-} anions is split into four to six components, which indicates the presence of CO_3 -groups of at least two kinds. At the same time, the presence of an unsplit band due to fully symmetric stretching vibrations of CO_3^{2-} groups at 1068 cm^{-1} indicates a considerable violation of the local symmetry of carbonate anions only for one kind of CO_3^{2-} groups.

The IR spectrum of ancylite from carbonatites (specimen 54) considerably differs from that of ancylite from alkali hydrothermalites in that it has a narrow intense band at 3540–3545 cm^{-1} and a narrow band at 739 cm^{-1} (Fig. 2b) attributed to the stretching and bending vibrations of OH^- anions forming no hydrogen bonds, whereas no hydroxyl groups linked by a hydrogen bond are present at all (the absence of the band at 3480–3490 cm^{-1}).

Thus, we can state that there exist two ancylite modifications which are crystallized in two different space groups of the orthorhombic system and have essentially different X-ray and IR-spectroscopic characteristics. Taking into account the corresponding crystallochemical data, these modifications should be described by

different formulas (Tables 3 and 4). The representative sampling of IR spectra of ancylites from numerous alkaline massifs over the entire world allows us to state that both ancylite modifications occur widely in nature.

ACKNOWLEDGMENTS

This study was supported by the Russian Foundation for Basic Research, project no. 99-05-39019 and the National Scientific Foundation of China (NSDC).

REFERENCES

1. V. N. Yakovenchuk, Yu. P. Men'shikov, Ya. A. Pakhomovskii, and G. Yu. Ivanyuk, *Zap. Vseross. Mineral. O-va.* **126** (1), 96 (1997).
2. I. V. Pekov, O. V. Petersen, and A. V. Voloshin, *Neues Jahrb. Mineral., Abh.* **171** (3), 309 (1997).
3. P. Orlandi, M. Pasero, and G. Vezzalini, *Eur. J. Mineral.* **2**, 413 (1990).
4. H. Sarp and J. Bertrand, *Am. Mineral.* **70** (11–12), 1314 (1985).
5. A. Dal Negro, G. Rossi, and V. Tazzoli, *Am. Mineral.* **60**, 280 (1975).
6. J. Schneider, in *Profile Refinement on IBM-PC's: Proceedings of the IUCr. International Workshop on the Rietveld Method, Petten, 1989*, p. 71.
7. Yu. A. Pyatenko, A. A. Voronkov, and Z. V. Pudovkina, *Mineralogical Crystal Chemistry of Titanium* (Nauka, Moscow, 1976), p. 155.
8. R. Hill and H. Flack, *J. Appl. Crystallogr.* **20**, 356 (1987).
9. J.-F. Berar and P. Lelann, *J. Appl. Crystallogr.* **24**, 1 (1991).

Translated by L. Man

STRUCTURE OF INORGANIC COMPOUNDS

Structural Characteristics of a New Cation-Deficient Representative of the Labuntsovite Group

K. A. Rozenberg*, R. K. Rastsvetaeva**, I. V. Pekov*, and N. V. Chukanov***

* Faculty of Geology, Moscow State University,
Vorob'evy gory, Moscow, 119899 Russia

** Shubnikov Institute of Crystallography, Russian Academy of Sciences,
Leninskii pr. 59, Moscow, 117333 Russia

e-mail: rast@ns.crys.ras.ru

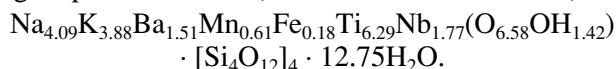
*** Institute of Problems of Chemical Physics in Chernogolovka,
Russian Academy of Sciences, Chernogolovka, Moscow oblast, 142432 Russia

Received June 6, 2001

Abstract—The crystal structure of a new representative of the labuntsovite group from the Khibiny massif (the Kola Peninsula) has been refined. The unit-cell parameters are $a = 14.298(7)$ Å, $b = 13.816(7)$ Å, $c = 7.792(3)$ Å, $\beta = 116.85(5)^\circ$, $V = 1373.3$ Å³, sp. gr. $C2/m$, $R_{\text{aniso}} = 0.047$, 1084 reflections with $F > 4\sigma(F)$. The mineral differs from lemmleinite-Ba and other members of the group by the predominance of the vacancies in two key cationic positions—C position is occupied by Ba cations (37%) and D position is occupied mainly by Mn cations (47%). © 2002 MAIK “Nauka/Interperiodica”.

The minerals of the labuntsovite group are characterized by wide-range compositional heterovalent isomorphism, which should necessarily be taken into account when predicting the ion-exchange properties of micro- and mesoporous materials based on the minerals of this structure type. Ten representatives of this group have been structurally characterized. In this study, we established the structure of a new specimen from the Gakman valley (the Khibiny massif, the Kola Peninsula).

The mineral was discovered in pegmatitic bulges of the natrolite–microcline composition embedded in gneissous nepheline syenites in the form of orange short-prismatic crystals up to 5 mm in length. The mineral occurs in association with aegirine, catapleite, barylite, fluorite, and galenite. The chemical composition of the new mineral was established using seven points by electron microprobe analysis (the water content was not determined) and corresponds to the following empirical formula (calculated for 16 Si atoms):

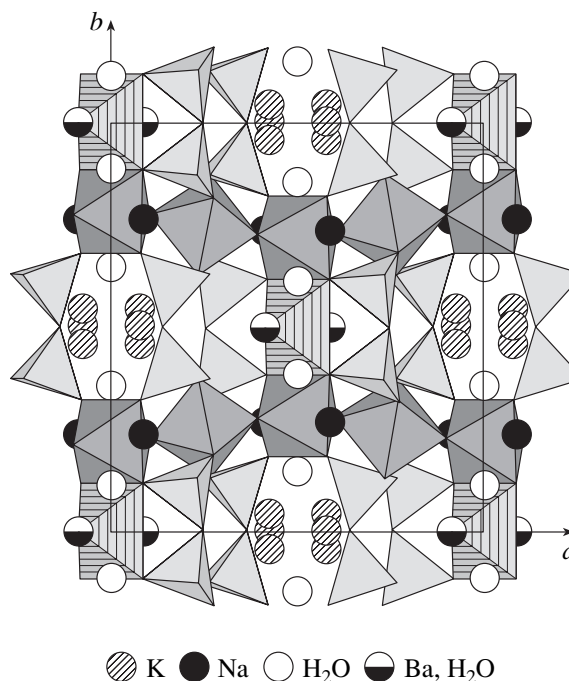


The principal characteristics of the crystal and the details of the X-ray data collection are given in Table 1.

Proceeding from the chemical composition, we assumed that the new mineral is structurally similar to lemmleinite-Ba and used the coordinates of the framework atoms of the latter [1] as the starting model. The difference electron density synthesis calculated upon the refinement of the structure revealed the split K(1) and K(2) positions with incomplete occupancies. The final atomic coordinates are given in Table 2. The crys-

tallochemical formula of the mineral can be written as $\text{Na}_{3.5}\text{K}_4[\text{Ba}_{1.5}(\text{Mn},\text{Fe})_{0.9}(\text{H}_2\text{O})_{1.8}][\text{Ti}_{7.8}\text{Nb}_{0.2}(\text{O},\text{OH})_8] \cdot [\text{Si}_4\text{O}_{12}]_4 \cdot 5.4\text{H}_2\text{O}$.

The structure of the new mineral (figure) has a mixed framework typical of labuntsovites consisting of



Crystal structure of the mineral projected onto the (001) plane. The Mn-octahedra are hatched. Circles of different types represent large cations and water molecules.

Table 1. Structural data and details of collection of the X-ray data

Characteristic	Parameter	Characteristic	Parameter
Parameters of monoclinic unit cell, Å, deg	$a = 14.298(7)$ $b = 13.816(7)$ $c = 7.792(3)$ $\beta = 116.85(5)^\circ$	Ranges of the indices of measured reflections	$-16 < h < 14;$ $-15 < k < 16;$ $0 < l < 9$
Volume of monoclinic unit cell, Å ³	1373.3	$\sin\theta/\lambda$	< 0.58
Sp. gr.; <i>Z</i>	<i>C2/m</i> ; 8	Total number of reflections	1235
Radiation; λ , Å	CuK α ; 1.5411	Number of independent reflections	1084 $F > 4\sigma(F)$
Density, g/cm ³	2.9	<i>R</i> -factor upon anisotropic refinement	0.047
Crystal dimensions, mm	0.15 × 0.1 × 0.25	Program used for the refinement	AREN [2]
Diffractionmeter	SYNTEX P2 ₁	Program used for introduction of the absorption correction	DIFABS [3]

Table 2. Atomic coordinates, equivalent thermal parameters, multiplicities, and occupancies of the positions

Atom	<i>x/a</i>	<i>y/b</i>	<i>z/c</i>	<i>Q q</i>	<i>B</i> _{eq} , Å ²
Si(1)	0.2082 (1)	0.1102 (1)	0.8035 (1)	8 1	1.18 (7)
Si(2)	0.3199 (1)	0.1111 (1)	0.2493 (1)	8 1	1.25 (7)
Ti(1)	0	0.2276 (1)	0.5	4 1	1.55 (6)
Ti(2)	0.25	0.25	0.5	4 1	1.66 (6)
<i>D</i>	0	0	0.5	2 0.47(1)	1.6 (1)
<i>C</i>	0.873 (1)	0	0.3422 (1)	4 0.83(1)	2.16 (3)
K(1)	0.4207 (1)	0	0.7033 (3)	4 0.69(1)	2.7 (1)
K(2)	0.4246 (8)	0.0444 (8)	0.713 (2)	8 0.15(1)	4.5 (3)
Na	0.4130 (4)	0.2643 (3)	0.0077 (9)	8 0.44(1)	3.4 (2)
O(1)	0.2336 (2)	0.1278 (2)	0.272 (4)	8 1	1.8 (2)
O(2)	0.2736 (2)	0.1823 (2)	0.7377 (4)	8 1	1.8 (2)
O(3)	0.2461 (3)	0	0.7847 (7)	4 1	1.8 (3)
O(4)	0.4204 (2)	0.1802 (2)	0.3028 (4)	8 1	1.9 (2)
O(5)	0.2649 (2)	0.1260 (2)	0.3864 (4)	8 1	1.6 (2)
O(6)	0.3640 (3)	0	0.2708 (6)	4 1	1.7 (3)
O(7)	0.832 (2)	0.1169 (2)	0.6741 (4)	8 1	1.7 (2)
O, OH	0.1014 (2)	0.2255 (2)	0.3974 (4)	8 1	1.7 (2)
H ₂ O (1)	0.5	0.1468 (8)	0	4 0.68(2)	8.5 (3)
H ₂ O (2)	0	0.1125 (6)	0	4 0.68(2)	5.2 (2)

Note: *D* = Mn_{0.75} + Fe_{0.25}; *C* = Ba_{0.45} + (H₂O)_{0.55}; Ti(2) = Ti_{0.95} + Nb_{0.05}.

columns of vertex-sharing [TiO₆]-octahedra linked by four-membered rings of [SiO₄]-tetrahedra. The channels in the structure are occupied by Na, K, and Ba atoms and water molecules. The chemical composition and the structure of the new specimen make it similar to lemmleinite-Ba; however, there are also some differences. Like other labuntsovites, the H₂O(1) and H₂O(2) molecules in the new mineral are in the coordination spheres of Na atoms, with each water molecule being bound to one of the large cations. The third H₂O mole-

cule and a Ba atom occupy the mixed *C*-position due to which the coordination polyhedron of a Mn atom is complemented to an octahedron, as opposed to the structure of lemmleinite-Ba, in which H₂O molecules and Ba atoms occupy different although close positions. Whereas in the structure of lemmleinite-Ba, K atoms are located in one position. In the structure of the specimen studied, these atoms occupy two positions spaced by a distances of 0.61(1) Å, with the position K(2) being occupied by 15%.

According to the nomenclature of the Commission on New Minerals and Mineral Names of the International Mineralogical Association, four positions in the channels of the crystal structure are group-forming ones in the minerals under consideration. Two of these positions, namely, the *D* position occupied by medium-sized cations and the *C* position occupied by large cations (in some earlier studies, these positions were indicated as M^{II} and A^{III} , respectively) complement each other statistically. In the structure of the new mineral, the *D* position is occupied mainly by Mn atoms (47%), whereas the *C* position is occupied by Ba-atoms (37%) and water molecules (47%). Hence, the cationic vacancies prevail in both positions, which distinguishes the new mineral from other representatives of this group.

ACKNOWLEDGMENTS

This study was supported by the Russian Foundation for Basic Research, project no. 99-05-65035.

REFERENCES

1. R. K. Rastsvetaeva, N. V. Chukanov, and I. V. Pekov, Dokl. Akad. Nauk **357** (1), 64 (1997).
2. V. I. Andrianov, Kristallografiya **32**, 228 (1987) [Sov. Phys. Crystallogr. **32**, 130 (1987)].
3. N. Walker and D. Stuart, Acta Crystallogr., Sect. A: Found. Crystallogr. **A39** (2), 158 (1983).

Translated by T. Safonova

STRUCTURE OF INORGANIC COMPOUNDS

Structural Characteristics of Na,Fe-Decationated Eudialyte with the Symmetry $R\bar{3}$

R. K. Rastsvetaeva* and A. P. Khomyakov**

* Shubnikov Institute of Crystallography, Russian Academy of Sciences,
Leninskii pr. 59, Moscow, 117333 Russia
e-mail: rast@ns.crys.ras.ru

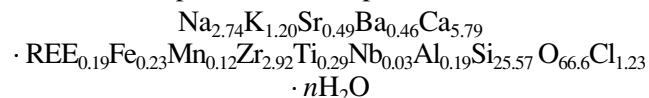
** Institute of Mineralogy, Geochemistry, and Crystal Chemistry of Rare Elements,
ul. Veresaeva 15, Moscow, 121357 Russia

Received March 15, 2001

Abstract—The crystal structure of a new highly decationated representative of the eudialyte group has been established ($R = 0.055$, 1734 $|F|$). The mineral is described by the simplified formula $(\text{H}_3\text{O})_9\text{Na}_2(\text{K},\text{Ba},\text{Sr})_2\text{Ca}_6\text{Zr}_3[\text{Si}_{26}\text{O}_{66}(\text{OH})_6](\text{OH})_3\text{Cl} \cdot \text{H}_2\text{O}$ ($Z = 3$). The unit-cell parameters are $a = 14.078(3)$ Å, $c = 31.24(1)$ Å; $V = 5362$ Å³; sp. gr. $R\bar{3}$. Being chemically and structurally related to the hydrated analogues studied previously (in particular, to potassium oxonium eudialyte), the new mineral differs from its analogues in that it has a higher degree of Na- and Fe-cation depletion. The replacement of 3/4 of Na cations by loose and mobile H_3O groups results in structure destabilization, which is seen from the high values of the thermal parameters of the atoms and the loss of the symmetry plane. © 2002 MAIK “Nauka/Interperiodica”.

The properties of zeolite-like zirconosilicate eudialyte as a potential ion exchanger are clearly seen from the existence of its decationated analogues characterized by high degrees of hydration. Earlier, we established the structures of two such specimens containing up to 7 wt % of water, which were found in the Lovozero and Khibiny massifs [1, 2]. In this study, we examined the eudialyte-like mineral found in syenite pegmatites from the Inaglinskii massif (South Yakutia). This mineral is characterized by a higher degree of hydration (up to 10 wt % of H_2O) and by a very low (about 3.5 wt %) total content of Na and Fe oxides. According to Efimov *et al.* [3], this fact is responsible for the pale-pink color of the mineral, which is rather rare for widely occurring eudialytes, the low density (2.62 g/cm³), and the low values of the refractive indices (1.567–1.572).

The results of microprobe analysis together with the data on the water content determined by the Penfield method corresponds to the empirical formula ($Z = 3$)



(where n is ~16).

X-ray diffraction data were collected from an isometric single crystal. The characteristics of the single crystal and the details of the X-ray diffraction study are given in Table 1.

Based on the similarity of the compositions of the mineral under study and potassium oxonium eudialyte [1], we assumed that they are structurally similar and used the coordinates of the positions of the framework atoms of this analogue as the starting model. The posi-

tions of all framework atoms of the mineral were revealed from a series of Fourier syntheses. At the final stage, the positions with low occupancies were localized from difference electron density synthesis. The inclusion of the impurity atoms with the use of mixed atomic scattering curves led to a sufficiently low R fac-

Table 1. Structural data and details of X-ray diffraction study of the crystal

Unit-cell parameters, Å	$a = 14.078(3), c = 31.24(1)$
Unit-cell volume, Å ³	$V = 5362$
Density, g/cm ³ : ρ_{calcd} ; ρ_{obs}	2.7; 2.62
Sp. gr., Z	$R\bar{3}$; 3 (for the simplified formula)
Radiation, λ , Å	$\text{MoK}\alpha$; 0.71073
Crystal dimensions, mm	$0.15 \times 0.25 \times 0.2$
Diffractometer	Enraf-Nonius
$\sin\theta/\lambda$	< 0.7
Ranges of the indices of measured reflections	$-19 < h < 17, 0 < k < 19, 0 < l < 42$
R_{av} or equivalent reflections	0.029
Total number of reflections	2790 $I > 2\sigma(I)$
Number of independent reflections	1734 $ F > 4\sigma(F)$
Program for calculations	AREN[4]
Program for absorption correction	DIFABS [5]
Number of independent positions	60
R factor upon anisotropic refinement	0.055

tor. However, the thermal parameters of all the atoms were too high. Although the refinement within the sp. gr. *R3* did not lead to a substantial improvement in the *R* factor, it gave reliable thermal parameters. The lowering of the symmetry compared to the sp. gr. *R3m*, characteristic of a number of structures of the eudialyte group, is most often associated with the ordering of the Ca atoms and of some elements replacing these atoms in the positions of the six-membered rings. In the mineral under study, the Ca and (Ca,Ce) atoms are ordered. Apparently, the lowering of the symmetry is associated mainly with the destabilization of the structure caused by the replacement of Na atoms by oxonium groups, which results in systematic displacements of the atoms from the vertical plane *m* exceeding the experimental error. The most substantial displacements are observed for the oxonium groups characterized by the highest mobility and located in their own subpositions with occupancies less than 100%.

The final atomic coordinates are given in Tables 2 and 3. Some characteristics of the polyhedra are indicated in Table 4.

The principal characteristics of the composition and the structure of hydrated eudialyte are described by its crystallochemical formula ($Z = 1$) $Zr_9(Ca_{17.64}Ce_{0.36})[Si_{72}O_{198.7}(OH)_{17.3}][Si_3][Si_{1.5}Ti_{0.75}^{[VI]}(Al_{0.65}Nb_{0.1})^{[VI]}][(H_3O)_{4.4}Na_{2.2}^{[IV]}(Fe,Mn)_{1.0}^{[VI]}][(H_3O)_{20.9}Na_{6.5}K_{3.6}Ba_{1.6}Sr_{1.31}Ce_{0.2}][(OH)_{9.6}Cl_{3.9}(H_2O)_{2.16}(SO_4)_{0.6}]$, where the compositions of the key structural fragments are indicated in brackets and the coordination numbers of the cations are given by Roman numerals in brackets. The sulfate group established by the X-ray diffraction analysis replaces the Cl atom or the H₂O molecule occupying the corresponding position on a threefold axis in a number of other minerals of the eudialyte group.¹

The simplified formula of the mineral is $(H_3O)_9Na_2(K,Ba,Sr)_2Ca_6Zr_3[Si_{26}O_{66}(OH)_6](OH)_3Cl \cdot H_2O$ ($Z = 3$).

The mineral is characterized by a high oxonium content. The X-ray diffraction analysis provided only indirect evidence of the presence of oxonium groups, because only O atoms were localized in the Na positions from electron density maps. We assigned these O atoms to (H₃O)⁺ ions. Taking into account a substantial deficiency in positive charges, these groups cannot be interpreted as neutral H₂O molecules. The presence of oxonium groups was also confirmed by the IR spectra of hydrated eudialytes [2]. Compared to other oxonium-containing minerals [1, 2], this specimen has the maximum amount of H₃O groups. In addition to three Na positions, in which oxonium groups were revealed earlier, we established the Na(2) position and two positions in the plane of the Ca-rings (figure). In high-alka-

Table 2. Coordinates and equivalent (B_{eq}) thermal parameters of the framework atoms

Atom	<i>x/a</i>	<i>y/b</i>	<i>z/c</i>	$B_{eq}, \text{\AA}^2$
Zr	0.3352(2)	0.1681(2)	0.1669(1)	2.48(3)
Ca	0.4018(2)	0.3312(2)	0.3330(1)	2.25(5)
Ca'	0.4011(2)	0.0702(2)	0.3332(1)	2.45(5)
Si(1)	0.5236(2)	0.2616(2)	0.2529(1)	1.4(1)
Si(2)	-0.0088(3)	0.6029(3)	0.1014(1)	3.1(1)
Si(2)'	-0.0097(3)	0.3880(3)	0.1006(1)	2.4(1)
Si(3)	0.2033(3)	0.4077(3)	0.0790(1)	2.9(1)
Si(4)	0.0828(3)	0.5411(3)	0.2595(1)	2.3(1)
Si(5)	0.0511(3)	0.3223(4)	0.2360(1)	2.5(1)
Si(5)'	0.2726(3)	0.3233(4)	0.2354(1)	3.2(1)
Si(6)	0.1411(3)	0.0709(3)	0.0816(1)	2.1(1)
O(1)	0.4596(9)	0.2336(11)	0.2079(4)	3.2(3)
O(2)	0.2491(10)	0.0218(10)	0.2022(4)	3.2(4)
O(2)'	0.2547(10)	0.2267(8)	0.2050(4)	3.2(3)
O(3)	0.4082(10)	0.3108(10)	0.1339(4)	3.5(3)
O(3)'	0.4121(8)	0.0962(9)	0.1362(3)	2.6(3)
O(4)	0.6064(8)	0.3966(8)	0.2512(5)	3.7(3)
O(5)	0.4542(9)	0.2253(10)	0.2961(4)	3.3(3)
O(6)	0.4015(14)	0.0570(16)	0.0520(5)	5.7(4)
O(6)'	0.3974(10)	0.3470(11)	0.0532(4)	4.4(4)
O(7)	0.0990(9)	0.3736(10)	0.1063(4)	3.2(3)
O(7)'	0.2773(6)	0.3722(6)	0.1062(3)	1.6(2)
O(8)	0.0215(9)	0.5123(8)	0.1071(4)	2.9(3)
O(9)	0.2710(10)	0.5480(8)	0.0739(5)	4.0(3)
O(10)	0.1850(10)	0.3584(10)	0.0265(4)	3.7(3)
O(11)	0.0242(10)	0.5171(8)	0.3024(4)	3.2(3)
O(12)	0.1817(10)	0.3616(10)	0.2205(4)	3.3(4)
O(13)	0.0370(16)	0.2918(16)	0.2866(5)	5.7(4)
O(13)'	0.2589(11)	0.2909(12)	0.2835(4)	5.3(4)
O(14)	0.3904(10)	0.4279(11)	0.2302(5)	3.9(4)
O(14)'	0.3946(15)	-0.0381(17)	0.2293(6)	6.5(3)
O(15)	0.3978(14)	0.6073(14)	0.2557(5)	5.1(1)
O(16)	0.0625(9)	0.1262(8)	0.0817(4)	2.8(2)
O(17)	0.2006(9)	0.1038(9)	0.1247(3)	2.9(2)
O(18)	0.2158(10)	0.1052(10)	0.0424(3)	3.1(3)

Note: The atoms related by the pseudosymmetry plane *m* are primed.

¹ Sulfur was not detected in the grains studied by the microprobe analysis.

Table 3. Coordinates and equivalent thermal parameters (B_{eq}) of the extraframework atoms, multiplicities (Q), and occupancies (q) of the positions

Atom	x/a	y/b	z/c	Q	q	$B_{\text{eq}}, \text{\AA}^2$
Si(7a)	0.3333	0.6667	0.2773(6)	3	0.55(3)	5.6(4)
Si(7b)	0.3333	0.6667	0.2449(5)	3	0.45(3)	2.45(3)
Si(8)	0.3333	0.6667	0.0600(6)	3	0.50(2)	2.5(3)
Ti	0.3333	0.6667	0.1009(9)	3	0.25(1)	3.7(5)
Al	0.3333	0.6667	0.044(2)	3	0.25(2)	6.3(5)
S	0.6667	0.3333	0.040(3)	3	0.20(4)	6.9(5)
M	0.492(1)	0.510(1)	-0.0004(7)	9	0.35(1)	3.0(3)
A(1)	0.1153(7)	0.2265(8)	0.1519(3)	9	1.0	2.2(3)
A(2a)	0.5631(3)	0.4360(3)	0.1792(1)	9	0.71(1)	2.7(1)
A(2b)	0.565(3)	0.436(3)	0.1648(9)	9	0.29(4)	7.5(7)
A(3a)	0.192(1)	0.096(2)	0.2942(6)	9	0.60(1)	6.7(3)
A(3b)	0.158(1)	0.079(1)	0.2805(4)	9	0.40(4)	5.5(3)
A(4a)	0.464(2)	0.232(2)	0.0501(4)	9	0.30(4)	5.7(4)
A(4b)	0.534(2)	0.266(2)	0.045(1)	9	0.70(1)	8.0(5)
A(5a)	0.224(3)	0.464(5)	0.322(1)	9	0.32(4)	4.2(5)
A(5b)	0.416(3)	0.596(2)	0.005(1)	9	0.39(4)	3.8(8)
OH(1)	0.3333	0.6667	0.187(1)	3	0.67(6)	3.5(6)
OH(2)	0.222(4)	0.604(4)	0.162(1)	9	0.27(4)	5.6(6)
OH(3)	0.3333	0.6667	0.331(1)	3	0.55(9)	7.9(5)
OH(4)	0.3333	0.6667	0.005(1)	3	0.50(3)	8.5(6)
Cl(1)	0	0	0.197(1)	3	0.50(3)	6.7(6)
Cl(2a)	0.6667	0.3333	0.1424(4)	3	0.59(5)	4.4(4)
Cl(2b)	0.6667	0.3333	0.098(2)	3	0.20(3)	6.9(5)
H ₂ O	0.631(5)	0.380(5)	0.132(2)	9	0.24(4)	6.1(7)

Note: Hereafter, M denotes the position in the center of the "square"; A(1–5) are the cationic positions corresponding to the Na(1–5) positions in the structures of high-sodium eudialytes.

line analogues of eudialyte, the latter positions are occupied either by Na [6] or K [7]. The distance between the positions of these cations correlates with the cation sizes and increases from the minimum value (2.8 Å) in alluaivite [6] to the maximum value (3.8 Å) in the new mineral. In the structure under consideration, the Na(1) position is fully occupied by the oxonium groups (as in the specimen found in Khibiny); the remaining Na positions, except for Na(2), are also occupied predominantly by oxonium groups.

In all three structures, the cavities between the rings are filled with hydroxyl groups forming a tetrahedral and octahedral environment around the cations located on threefold axes. The octahedra located on the axes are oriented in the direction of the cavities. Such an orientation is characteristic only of hydrated specimens and is associated with the absence of Na atoms in these cavities. Indeed, in the new mineral, the Ti-octahedron is oriented in the direction of the cavity, whereas in the

other two minerals, the Na-, and Zr-octahedra are oriented toward the cavities [1, 2].

It can be assumed that the presence of oxonium ions in the Ca layer is responsible for the noticeable elongation of the structure in the direction of the threefold axis. Thus, the c -parameter of the unit-cell (31.24 Å) considerably exceeds the c -parameter in typical eudialytes where it varies from 29.96 to 30.35 Å [8]. The lower density of the mineral is most likely associated with the more flexible Ca-containing layers and not with the rigidly fixed fragments (Zr,Si-containing layers), in particular, with the absence of the Fe atoms in the former layers. This assumption was confirmed by the distortion of the "square." The edges of the Ca-octahedra forming two opposite sides of the square (3.32 and 3.42 Å) are substantially longer than those found earlier (2.79–3.24 Å). The elongation of the Ca-octahedra along the z -axis is accompanied by their contraction in the perpendicular direction, which provides the minimum value of the a -parameter of the unit-cell (14.08 Å)

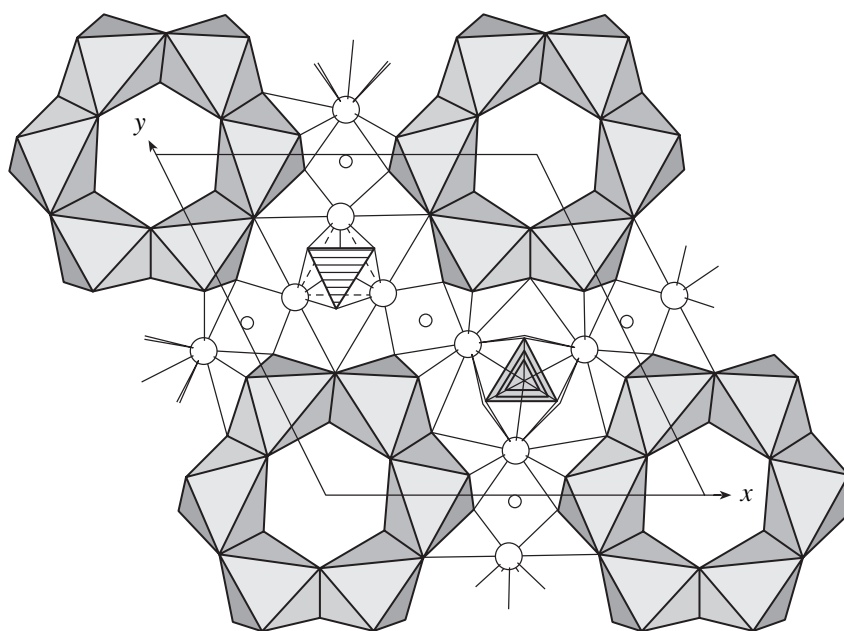
Table 4. Characteristics of the coordination polyhedra

Position	Composition, Z = 1	Coordination number	Cation–anion distances	
			limiting	average
Zr	9Zr	6	1.98–2.11	2.06
Ca	9Ca	6	2.25–2.40	2.33
Ca'	8.64Ca + 0.36Ce	6	2.24–2.46	2.35
Si(7a)	1.65Si	4	1.64–1.68	1.65
Si(7b)	1.35Si	4	1.55–1.80	1.61
Si(8)	1.5Si	4	1.51–1.72	1.55
Ti	0.75Ti	6	1.67–2.34	2.01
Al	0.65Al + 0.1Nb	6	1.72–2.23	1.97
S	0.6S	4	1.31–1.62	1.54
<i>M</i>	2.2Na + 1.0(Fe, Mn)	4	2.11–2.60	2.39
		6	1.85–2.60	2.23
A(1)	9H ₃ O	9	2.49–3.10	2.67
A(2a)	4.7Na + 1.6Ba	9	2.37–2.88	2.66
A(2b)	2.5H ₃ O + 0.2Ce	7	2.14–2.88	2.59
A(3a)	4.9H ₃ O + 0.5Sr	9	2.44–3.28	2.78
A(3b)	3.6K	9	2.58–3.22	2.85
A(4a)	1.8Na + 0.81Sr	8	2.16–3.17	2.80
A(4b)	4.5H ₃ O	9	2.19–3.20	2.85
A(5a)	1.9H ₃ O + 1.0OH	9	2.49–3.31	2.89
A(5b)	2.5H ₃ O + 1.0OH	7	2.58–3.36	2.91

Note: The Si(1–6)-tetrahedra involved in the silicon–oxygen rings of the framework are not indicated.

with a simultaneous increase in the distance between the rings (the lengths of the two other sides of the square are 3.58 and 3.13 Å; the corresponding values in other known eudialytes are in the range 2.80–3.04 and 2.91–3.25 Å, respectively).

Therefore, the new mineral is related, both chemically and structurally, to the hydrated analogues studied earlier (and, in particular, is similar to potassium oxonium eudialyte) and is characterized by the highest degree of depletion of Na- and Fe-cations. The struc-



A layer of the decationated eudialyte structure projected onto the (001) plane; Si-tetrahedra are hatched with solid lines; Na atoms and oxonium cations are indicated by small and large circles, respectively.

ture of the new mineral is less stable because of the replacement of 3/4 of the Na atoms by looser and mobile H₃O groups. This is seen from the high thermal parameters of the atoms, the loss of the symmetry plane, the distortion of the coordination polyhedra, and the shortening of some interatomic distances. In the new mineral, the characteristic splitting of positions of the extraframework atoms into partly occupied subpositions characterized by isomorphous replacement is most pronounced.

ACKNOWLEDGMENTS

This study was supported by the Russian Foundation for Basic Research, project no. 99-05-65035.

REFERENCES

1. R. K. Rastsvetaeva, M. N. Sokolova, and B. E. Borutskii, *Kristallografiya* **35** (6), 1381 (1990) [*Sov. Phys. Crystallogr.* **35**, 814 (1990)].
2. I. A. Ekimenkova, R. K. Rastsvetaeva, and N. V. Chukanov, *Dokl. Akad. Nauk* **371** (5), 625 (2000).
3. A. F. Efimov, S. M. Kravchenko, and E. V. Vlasova, *Tr. IMGRÉ* **16**, 141 (1963).
4. V. I. Andrianov, *Kristallografiya* **32** (1), 228 (1987) [*Sov. Phys. Crystallogr.* **32**, 130 (1987)].
5. N. Walker and D. Stuart, *Acta Crystallogr., Sect. A: Found. Crystallogr.* **A39** (2), 158 (1983).
6. R. K. Rastsvetaeva, A. P. Khomyakov, V. I. Andrianov, and A. I. Gusev, *Dokl. Akad. Nauk SSSR* **312** (6), 1379 (1990) [*Sov. Phys. Dokl.* **35**, 492 (1990)].
7. R. K. Rastsvetaeva and A. P. Khomyakov, *Kristallografiya* **46** (4), 715 (2001) [*Crystallogr. Rep.* **46**, 647 (2001)].
8. O. Johnsen and J. D. Grice, *Can. Mineral.* **37** (4), 865 (1999).

Translated by T. Safonova

STRUCTURE
OF INORGANIC COMPOUNDS

Structure Studies of Solid Solutions of Oxygen in Electrolytic Niobium

A. V. Arakcheeva*, V. V. Grinevich*, G. Chapuis**, and V. F. Shamraï*

* *Baikov Institute of Metallurgy and Materials Technology, Russian Academy of Sciences,
Leninskii pr. 49, Moscow, 117334 Russia*

e-mail: arakchee@ultra.imet.ac.ru

** *Institute of Crystallography, University of Lausanne, BSP,
Lausanne, 1015 Switzerland*

Received April 17, 2001

Abstract—The crystal structures (cubic system, sp. gr. $Im\bar{3}m$) of solid solutions of oxygen in niobium of the compositions $NbO_{x < 0.01}$ (**I**), $NbO_{0.150(6)}$ (**II**) and $NbO_{0.107(5)}$ (**III**) were studied for the first time by single-crystal X-ray diffraction analysis (Syntex *P1* diffractometer, λMoK_{α} radiation). Crystals **I** ($a = 3.2969(8)$ Å) and **II** ($a = 3.3082(6)$ Å) were prepared by the electrolysis of salt melts. Crystal **III** ($a = 3.3114(4)$ Å) was obtained after partial dissolution of crystal **I** in a solution of HNO_3 , HCl , and HF resulting in its saturation with oxygen. The residual electron density maps for crystal **I** revealed no O atoms. Localization of the O atoms in the tetrahedral cavities of crystal **II** and in the tetrahedral and octahedral cavities of crystal **III** indicates that the arrangement of the interstitial positions of oxygen atoms depends on the procedure of preparing solid solutions. In crystals **II** and **III**, the amplitudes of thermal vibrations of the Nb atoms are smaller and the anharmonicity of these vibrations is higher than those in crystal **I** virtually devoid of oxygen. The reasons for the substantially higher oxygen content (up to 17 at. %) in cubic crystals of the solid solutions of O in Nb prepared by the electrolytic method than in the analogous phase obtained upon heating (lower than 7 at. %) are discussed. © 2002 MAIK “Nauka/Interperiodica”.

INTRODUCTION

Interactions of oxygen with niobium metal are being extensively studied in connection with the problem of the corrosion resistance of metal at high temperatures and the influence of oxygen on the mechanical properties of niobium [1]. Interest in these studies stems from the fact that niobium saturated with oxygen is used as a collector in thermionic energy converters [2, 3]. It was established [1–8] that the first stage of the reaction of oxygen with niobium gives rise to solid solutions with an increased cubic unit-cell parameter, followed by the formation of the suboxide phases Nb_6O and Nb_4O characterized by the tetragonal distortion of the cubic unit cell, after which stoichiometric oxides are generated. It should be noted that the tetragonal suboxide phase, which has been initially identified as Nb_2O [9], was demonstrated to be stoichiometric oxide Nb_4O_5 [10] possessing a unique structure [11]. It was shown [12] that the formation of solid solutions of oxygen in niobium substantially affects the physical properties of lower oxides. In particular, two lower oxides with NaCl-type structures were described [12], among them the well-known NbO phase with the narrow homogeneity region and the $NbO_{1.2}$ phase possessing high hardness. The characteristic features of the oxygen arrangement in the lattice of niobium metal were discussed in several studies [12–14]. According to the results of

quantum-mechanical analysis, the tetrahedral and octahedral cavities in the body-centered cubic (bcc) structure of Nb were considered as positions occupied by oxygen atoms [13, 14]. The dependence of the mechanisms of incorporation of oxygen atoms into the structure of niobium metal on the mode of preparation of the solid solution was considered in the study of Nb samples, which were saturated with oxygen either in the course of gas-phase reactions or by thermal diffusion saturation [12]. However, the preparation of homogeneous samples of cubic solid solutions of oxygen in niobium in the case of a low oxygen content in equilibrium phases (0.7 at. % at 700°C and 5.2 at. % at 1500°C [8]; lower than 1 at. % at 550°C and ~7 at. % at 1700°C [15]) presented difficulties, because they were formed as thin interlayers between oxides and the metal upon heating of niobium in air. As a result, the positions of the oxygen atoms were impossible to localize by X-ray diffraction methods. We prepared well-faceted homogeneous single crystals of cubic solid solutions with oxygen contents up to $NbO_{0.17}$ by electrolytic crystallization from salt melts and then saturated these single crystals with oxygen upon etching in a ($HNO_3 + HCl + HF$) solution, which allowed us to localize O atoms in the Nb structure by single-crystal X-ray diffraction methods. Below, we present the results of this study.

PREPARATION OF SAMPLES

Samples of niobium with a controlled oxygen content were prepared by electrolysis of a salt melt of composition $\text{KCl} + \text{NaCl} + \text{K}_2\text{NbF}_7$ (20 wt %) using a soluble niobium-monoxide anode and a molybdenum cathode.

Recrystallized potassium heptafluoroniobate and alkali-metal chlorides of special purity grade were used as components of the electrolyte. The niobium-monoxide anode was prepared by arc melting pressed pellets using a permanent electrode. The pellets were made from a mixture of highly pure electrolytic niobium prepared according to a known procedure [16] and Nb_2O_5 taken in a molar ratio of 3 : 1.

A cylindrical molybdenum crucible with a cylindrical perforated molybdenum diaphragm inside the crucible was used as the electrolytic cell. The anodic material (NbO pieces of size 3–8 mm) was charged into the circular space between the diaphragm and the walls of the crucible. A molybdenum rod with diameter 5 mm, which was fixed coaxially in the center of the cell, served as the cathode. The cell was placed in a heat-resistant steel container, in which a highly pure atmosphere of argon was maintained. The electrolytic cell was heated externally in a shaft furnace with silicon-carbide heaters.

Electrolysis was carried out in the galvanostatic mode with the cathode-current density of 0.2 A/cm^2 at 750°C . In each cycle, a direct current of 1.5 A h was passed through the electrolytic cell.

The cathode with a precipitate grown on its surface during one cycle of electrolysis was cooled to room temperature in a water-cooled magazine of the container cover. The crystalline precipitate of the electrolysis product was separated from the cathode rod, washed off from the salt electrolyte, which was captured from the electrolytic cell, with 10% hydrochloric acid, washed repeatedly with distilled water and then with rectified ethanol, and dried in air at $30\text{--}40^\circ\text{C}$.

The electrochemical and chemical (due to interactions with the NbF_7^{2-} ions) dissolution of NbO in a melt gave rise to complex oxofluoride ions NbOF_4^- and NbOF_6^{3-} [17], whose concentrations in the electrolyte increased with the increasing total quantity of the direct current passed through the electrolytic cell. Since the strict correlation between the O : Nb molar ratio in the molten electrolyte and the oxygen content in the cathodic product was observed in the electrolysis of fluoride-chloride melts [18], cathodic precipitates obtained in successive cycles of electrolysis contained increasing concentrations of oxygen.

The concentration of oxygen in each cathodic precipitate was determined from the increase in the weight of the starting sample after its complete high-temperature oxidation in air to Nb_2O_5 . A series of NbO_x samples with $0 < x < 1.32$ were prepared in successive

cycles of electrolysis. Samples with $x < 0.17$ were obtained as well-faceted crystals with an approximately cubic habit. X-ray phase analysis (DRON-3M diffractometer, λMoK_α radiation) showed that the samples were single-phase and demonstrated that they have the cubic symmetry (sp. gr. $Im\bar{3}m$) typical of the body-centered cubic structure of Nb.

Single crystals with the minimum and maximum oxygen contents of compositions $\text{NbO}_{x < 0.01}$ (**I**) and $\text{NbO}_{0.17(1)}$ (**II**), respectively, were studied by X-ray diffraction analysis. Several crystals **I** were soaked in a dilute aqueous solution (1 : 1 v/v) of $\text{HNO}_3 + \text{HCl} + \text{HF}$ for four hours to reduce their rather large sizes ($\sim 0.3 \text{ mm}$) by partial dissolution. Due to the presence of the strong oxidizer, the crystals were not only decreased in size, but also enriched with oxygen, and the resulting samples (**III**) were also studied by X-ray analysis. As a result, we obtained data on the structure of the solid solution of O in Nb, which was prepared by the "chemical" method.

X-RAY DIFFRACTION STUDY

Single crystals **I**, **II**, and **III** selected for X-ray diffraction study had the shapes of isometric parallelepipeds with virtually perfect mirror-reflecting rectangular faces. The a parameters of the cubic unit cells were measured on a Syntex P1 diffractometer (λMoK_α radiation) based on 15 high-angle reflections of the $\langle 224 \rangle$ type lying in the 2θ angle range corresponding to $\lambda\text{MoK}_{\alpha 1} = 0.70926 \text{ \AA}$ (Table 1). In none of the three crystals were significant deviations from the cubic metric revealed. The a parameter of crystal **I** ($a = 3.2969(8) \text{ \AA}$) agrees well with the tabulated value for Nb ($a = 3.2986 \text{ \AA}$) [19] and is in the range $3.294\text{--}3.300 \text{ \AA}$ corresponding to the cubic unit-cell parameters for Nb containing no oxygen [1–9, 12–14]. The largest parameter $a = 3.3114(4) \text{ \AA}$ was found for crystal **III**. This fact indicates that crystal **III**, which was obtained from the sample with the lowest oxygen content by partial dissolution in a solution of HNO_3 , HCl , and HF , was substantially saturated with oxygen. Since we had only a few such crystals with an edge size of $\sim 0.1 \text{ mm}$ at our disposal, we did not determine the oxygen content in crystals **III** by high-temperature oxidation.

The principal details of the X-ray diffraction studies and the characteristics of the crystals are given in Table 2. For all three crystals, the experimental integrated intensities of X-ray diffraction reflections ($2\theta/\theta$ scanning technique) were measured within a hemisphere of the reciprocal space. All experimental reflections were characterized by sharp profiles, which is indicative of the high quality of the single crystals. All reciprocal-lattice vectors involved in the measured region were scanned. The intensities of all the reflections allowed within the space group $Im\bar{3}m$ were higher than $3\sigma(I)$. All the reflections were consistent with this

Table 1. Compositions, unit-cell parameters (*a*), and positions of the oxygen atoms in NbO_x crystals **I**, **II**, and **III** (sp. gr. *Im3m*)

Crystal	I	II	III
Composition determined by the oxidation method	NbO _{x < 0.01}	NbO _{0.17(1)}	Was not determined
from the results of the refinement	Nb	NbO _{0.150(6)}	NbO _{0.107(5)}
2θ angle range (deg) for λMo K _{α1} for the ⟨224⟩ reflections used in the refinement of the <i>a</i> parameter	63.58–63.65	63.34–63.37	63.27–63.30
<i>a</i> , Å	3.2969(8)	3.3082(6)	3.3114(4)
Wyckoff position and configurations of the cavities occupied by O atoms	O atoms were not found	12 <i>d</i> , tetrahedron	12 <i>d</i> , tetrahedron; 6 <i>b</i> octahedron

Table 2. Details of X-ray diffraction studies and results of the refinement of the Nb (**I**) and NbO_x (**II** and **III**) structures within the space group *Im3m*

Crystal	I	II	III
Composition	Nb	NbO _{0.150(6)}	NbO _{0.107(5)}
Dimensions, mm	0.25 × 0.25 × 0.20	0.20 × 0.20 × 0.22	0.10 × 0.12 × 0.12
Diffractometer; radiation		Syntex P1; MoK _α	
<i>N</i> _{obs} ; <i>N</i> _{indep} (sin θ/λ < 1.07); <i>N</i> _{indep} (0.7 < sin θ/λ < 1.07)		429; 31; 20	
Absorption	Integration with respect to the real habit of the crystal		
<i>R</i> _{int} for equivalent reflections	0.033	0.025	0.022
Refinement with isotropic thermal parameters of Nb atoms [<i>2a</i> : (000)]			
Nb: <i>B</i> _{iso} , Å ²	0.89(1)	0.289(1)	0.306(7)
<i>R</i> _F ; <i>wR</i> _F (0 < sin θ/λ < 1.07)	0.0188; 0.0054	0.0122; 0.0093	0.0125; 0.0067
<i>R</i> _F ; <i>wR</i> _F (0.7 < sin θ/λ < 1.07)	0.0296; 0.0286	0.0083; 0.0074	0.0092; 0.0077
Δρ _{max} ; Δρ _{min} or deformation electron density, e/Å ³	3.07; –1.76	0.94; –0.52	1.06; –0.48
Refinement of thermal parameters of Nb atoms in the anharmonic approximation			
Nb: <i>B</i> _{eq} , Å ²	0.54(1)	0.224(3)	0.262(6)
<i>B</i> ₁₁	0.01237(1)	0.0051(1)	0.0060(2)
<i>D</i> ₁₁₁₁ × 10 ⁴	–0.002(1)	–0.20(2)	–0.027(3)
<i>D</i> ₁₁₂₂ × 10 ⁴	–0.0031(7)	–0.0069(7)	–0.006(1)
<i>F</i> ₁₁₁₁₁₁ × 10 ⁶	–0.010(3)	–0.027(3)	–0.035(5)
<i>F</i> ₁₁₁₁₂₂ × 10 ⁶	0.0008(8)	–0.0046(6)	–0.004(1)
<i>F</i> ₁₁₂₂₃₃ × 10 ⁶	0.001(1)	–0.0014(4)	0.0000(7)
<i>R</i> _F ; <i>wR</i> _F	0.0092; 0.0049	0.0087; 0.0086	0.0083; 0.0055
Δρ _{max} ; Δρ _{min} , e/Å ³	0.61; –0.60	0.69; –0.61	0.80; –0.60
Localization of O atoms			
O(1) [12 <i>d</i> : (0.5 0.25 0)]: <i>B</i> _{iso} , Å ²	–	2.2(2)	0.49(8)
<i>q</i>		0.025(1)	0.0089(3)
O(2) [6 <i>b</i> : (0.5 0.5 0)]: <i>B</i> _{iso} , Å ²	–		2.1(7)
<i>q</i>			0.018(1)
<i>R</i> _F ; <i>wR</i> _F		0.0072; 0.0041	0.0061; 0.0031
Δρ _{max} ; Δρ _{min} , e/Å ³		0.35; –0.48	0.30; –0.35

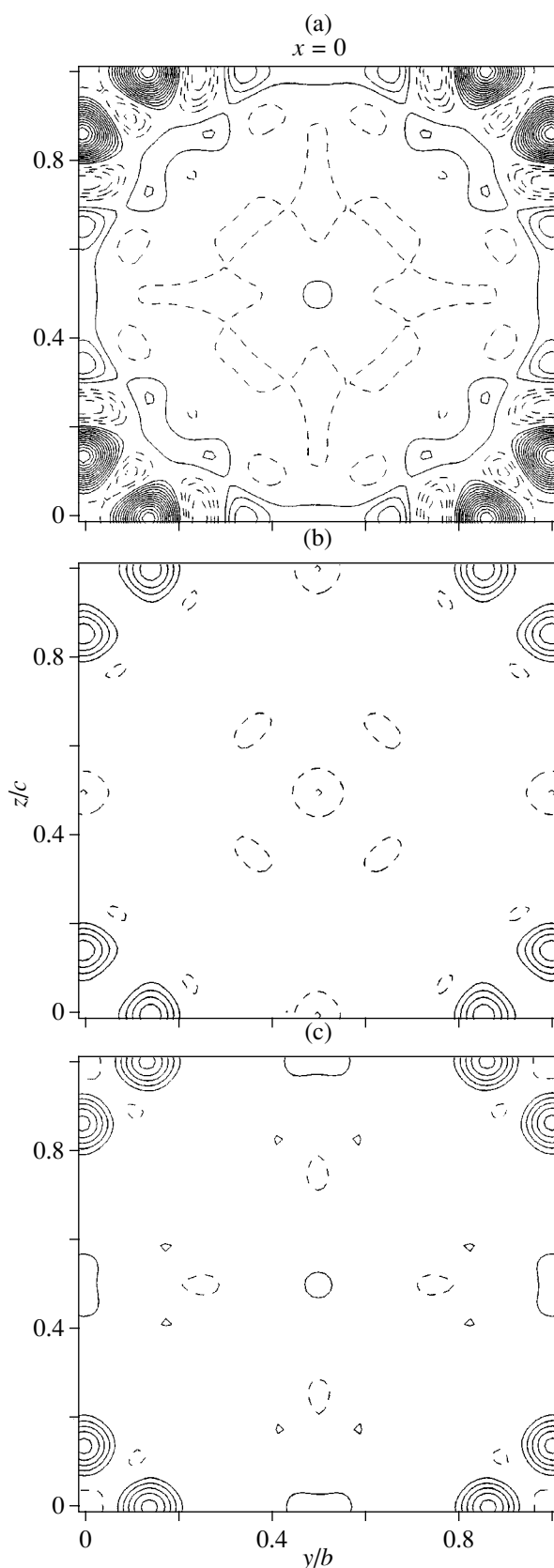


Fig. 1. The (100) sections of the deformation electron density for crystals (a) **I** (Nb), (b) **II** ($\text{NbO}_{0.15}$), and (c) **III** ($\text{NbO}_{0.107}$). The isolines are spaced by $0.2 \text{ e}/\text{\AA}^3$.

space group that characterized the bcc structure of niobium metal.

All calculations were carried out with the use of the JANA98 program package. The structure characteristics for all three crystals were determined and refined according to the same scheme. The absorption corrections were applied by numerical integration with respect to the real habit of the crystals. Then the intensities of X-ray reflections were converted into structure factors taking into account the Lorentz and polarization factors. The parameters of each structure were refined using the same number of structure factors (31), which were obtained by averaging the equivalent reflections of the same hkl set. Cycles of the refinement by the full-matrix least-squares method based on $|F|$ were alternated with cycles of the refinement based on F^2 . The scale factor and the isotropic thermal parameter of the Nb atom were refined using all independent reflections with $0 < \sin\theta/\lambda < 1.07$. Then, B_{iso} of the Nb atom was refined based on high-angle reflections with $0.7 < \sin\theta/\lambda < 1.07$. The deformation electron density maps, which were constructed based on the refined data (Fig. 1), revealed substantial dynamic (anharmonicity) or static (splitting of the position) thermal displacements of the Nb atoms along the coordination axes. This effect was adequately parametrized using the sixth-order Gram-Charlier expansion in series for the anharmonicity of thermal atomic displacements (4.43 reflections per parameter to be refined). Each probability density function for the displacements of the Nb atoms (Fig. 2) has one maximum elongated along the coordination axes. A comparative analysis of the difference electron density maps for crystals **I**, **II**, and **III** (Fig. 3) revealed information about the positions of the oxygen atoms in crystals **II** and **I** and provided evidence that crystals **I** contained no oxygen. For each oxygen position, the isotropic thermal parameter B_{iso} and the occupancy q were determined by minimizing the R factor as a function of these two correlating parameters. The R values were obtained by refining the occupancies q at fixed values of the B_{iso} parameter, which was varied from 0.2 to 3.0 with a step of 0.1. Thereafter, the residual electron density maps were constructed for crystals **II** and **III** (Fig. 4). All numerical characteristics of the refinement obtained at each stage for crystals **I**, **II**, and **III** are given in Table 2. (All results were obtained using all independent reflections, except for the results of the refinement based on high-angle reflections, which are presented in the individual line.) Let us consider the characteristic features of each crystal in more detail.

Compared to crystals **II** and **III**, crystal **I** (Table 2) is characterized by the maximum size ($V_{\text{cryst}} = 0.0125 \text{ mm}^3$) and the highest R factor of averaging of the symmetrically equivalent reflections ($R_{\text{int}} = 0.033$), which is, apparently, responsible both for the highest final R factors ($R_F = 0.0092$ and $wR_F = 0.0049$) and the highest maxima of the residual electron density ($\Delta\rho = 0.6 \text{ e}/\text{\AA}^3$). These maxima are located at a distance of

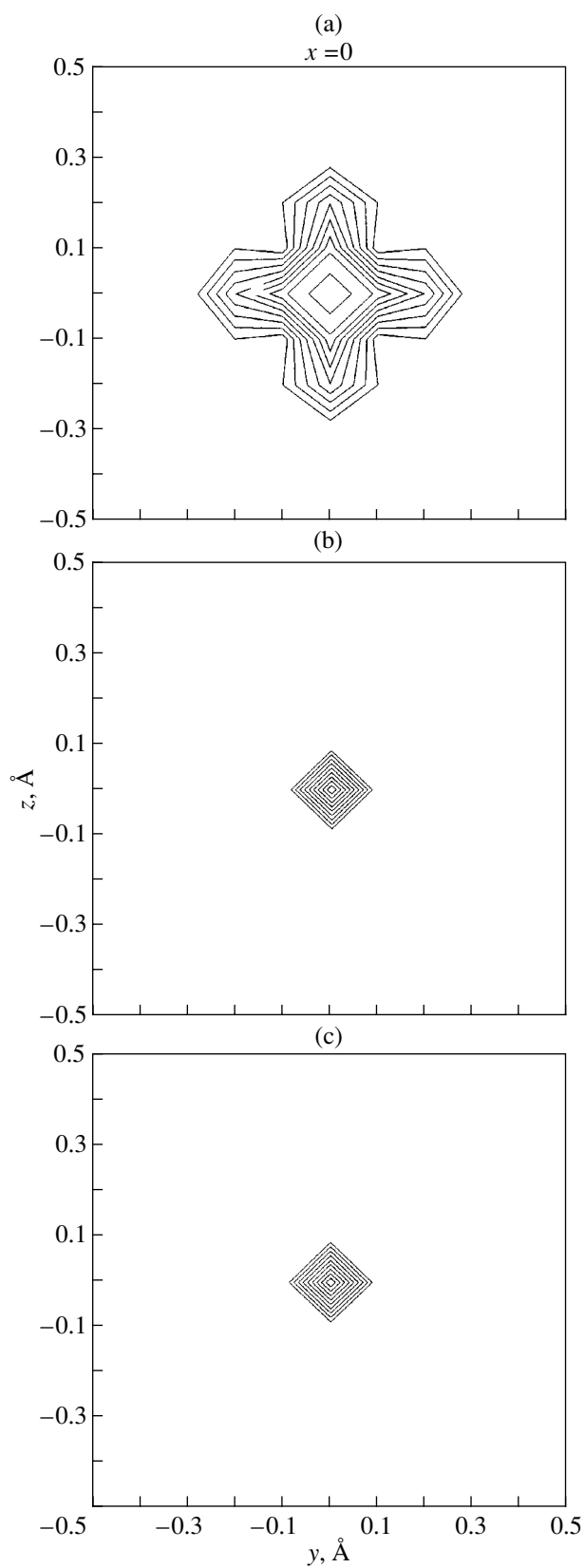


Fig. 2. The (100) sections of the probability density functions for displacements of Nb atoms in crystals (a) **I**, (b) **II**, and (c) **III**.

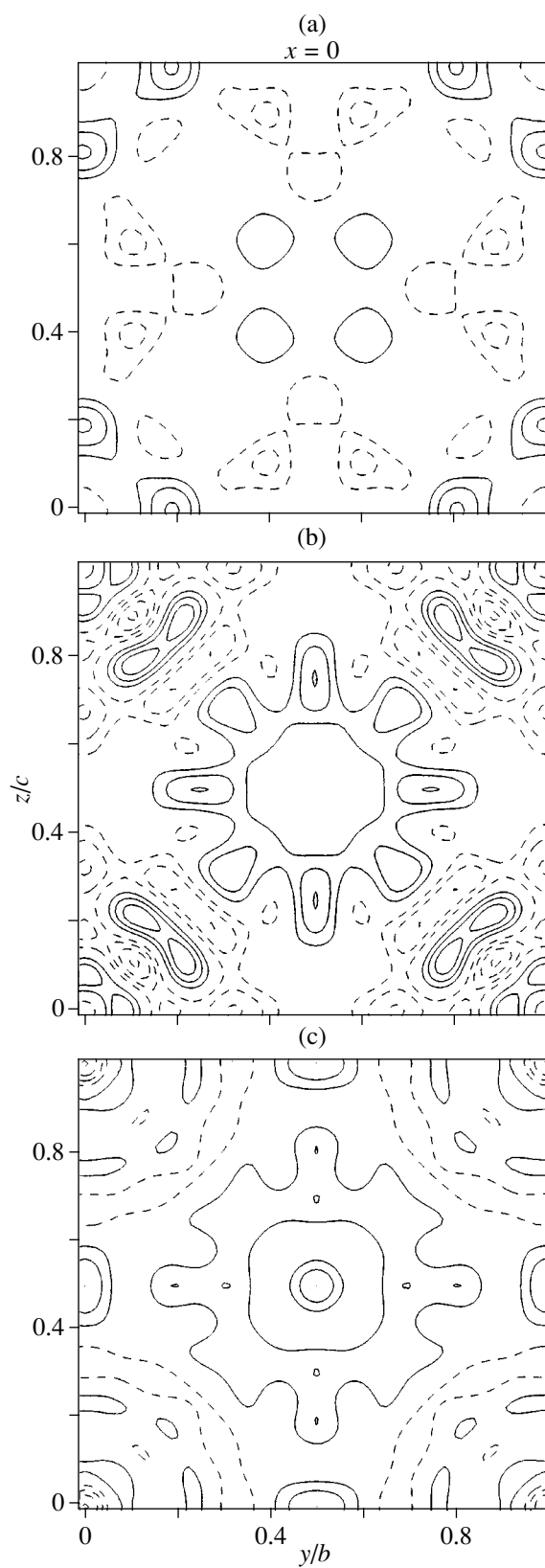


Fig. 3. The (100) sections of the difference electron density maps for crystals (a) **I**, (b) **II**, and (c) **III**. The isolines are spaced by $0.2 e/\text{\AA}^3$. For crystal **I**, the difference synthesis was simultaneously residual.

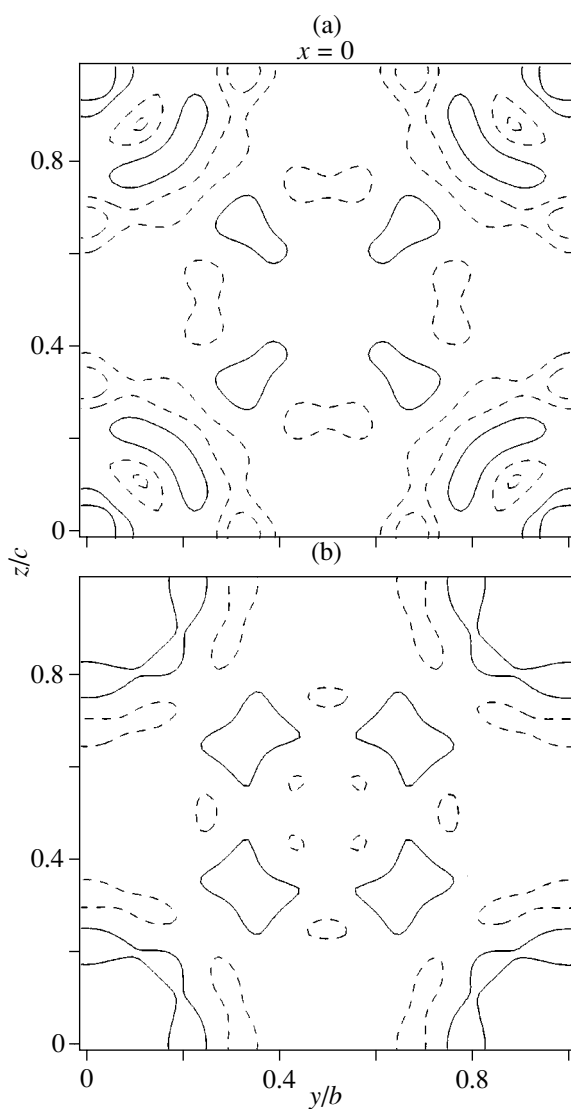


Fig. 4. The (100) sections of the residual difference electron density maps for crystals (a) **II** and (b) **III**. The isolines are spaced by $0.2 \text{ e}/\text{\AA}^3$.

0.65 \AA from the Nb atom in the $\{100\}$ directions (Fig. 3a). No other significant maxima that could be identified as O atoms were revealed in this map. This is in good agreement with the fact that crystal **I** was taken from the sample of the cathodic precipitate with the minimum oxygen content ($\text{NbO}_{x < 0.01}$), and its unit-cell parameter ($a = 3.2969 \text{ \AA}$) is close to the tabulated value for oxygen-free Nb (Table 1). This crystal, which is virtually devoid of oxygen, is characterized by the maximum amplitudes of thermal vibrations of the Nb atom (Table 2) and by the substantially higher probability of its thermal displacement compared to those observed in oxygen-containing crystals **II** and **III**.

The volume of crystal **II** ($V_{\text{cryst}} = 0.0088 \text{ mm}^3$) is 30% smaller than that of crystal **I**. In addition, crystal **II** is characterized by a better R factor for averaging equiva-

lent reflections ($R_{\text{int}} = 0.025$) and, consequently, by lower final R factors ($R_F = 0.0072$ and $wR_F = 0.0041$). The maximum $\Delta\rho$ value ($0.69 \text{ e}/\text{\AA}^3$) in the difference electron density map is observed in the position $12d$: $(0.5 \ 0.25 \ 0)$ (Fig. 3b), which corresponds to the tetrahedral cavity in the bcc Nb structure. Based on the fact that the corresponding map for crystal **I** has no maximum in this position (Fig. 3a), whereas other characteristics of the maps for crystal **I** are close to those for crystal **II**, we localized the O atoms in the tetrahedral cavities, whose centers are separated from the four nearest Nb atoms by distances of $\sim 1.85 \text{ \AA}$. The lowest R factor was obtained for the thermal parameter $B_{\text{iso}} = 2.2(2) \text{ \AA}^2$ and the occupancy of the oxygen position $q = 0.025(1)$, which corresponds to the composition $\text{NbO}_{0.150(6)}$. This composition agrees satisfactorily with that of the corresponding cathodic product ($\text{NbO}_{0.17(1)}$) determined by high-temperature oxidation (Table 1). The residual electron density map for crystal **II** (Fig. 4a) contains no additional significant maxima compared to the corresponding map for crystal **I** (Fig. 3a). In spite of the large parameters of anharmonicity of the Nb atoms in crystal **II** compared to those in crystal **I**, the amplitudes of the thermal displacements of Nb in crystal **II** are half as large as those in crystal **I** (Table 2; Figs. 1, 2).

The lowest final R factors ($R_F = 0.0061$ and $wR_F = 0.0031$) and the smallest maxima in the residual electron density map ($\Delta\rho = 0.30 \text{ e}/\text{\AA}^3$) for crystal **III** correlate with the fact that it has the smallest volume ($V_{\text{cr}} = 0.0012 \text{ mm}^3$) and is characterized by the lowest R factor for averaging equivalent reflections ($R_{\text{int}} = 0.022$). In the difference electron density map for crystal **III**, the highest peaks ($\Delta\rho = 0.80 \text{ e}/\text{\AA}^3$) correspond to the octahedral cavity in the Nb structure, i.e., to the position $6b$: $(0.5 \ 0.5 \ 0)$ (Fig. 3c). No high $\Delta\rho$ values corresponding to this position are observed in the maps for crystals **I** and **II** (Figs. 3a and 3b, respectively). The distances from the center of the octahedral cavity to the two nearest Nb atoms and the four more remote Nb atoms are 1.66 \AA and 2.34 \AA , respectively. The second highest maximum ($\Delta\rho = 0.4 \text{ e}/\text{\AA}^3$) corresponds to the position $12d$: $(0.5 \ 0.25 \ 0)$, like that observed in the map for crystal **II** (Fig. 3). The successive localization of the O atoms in both these positions led to the minimum R factors for $q_{\text{oct}} = 0.018(1)$ ($B_{\text{iso}} = 2.1(7) \text{ \AA}^2$) and $q_{\text{tet}} = 0.0089(3)$ ($B_{\text{iso}} = 0.49(8) \text{ \AA}^2$). Based on the results of the refinement, crystal **III** has the composition $\text{NbO}_{0.107(5)}$. The residual electron density map for crystal **III** (Fig. 4b) is very similar to that for crystal **II** (Fig. 4a) and contains no significant maxima. The character of the thermal displacements of the Nb atoms in **III** is identical to that in **II** (Table 2; Figs. 1b, 1c, 2b, 2c).

RESULTS AND DISCUSSION

The positions of the O atoms in the structures of cubic solid solutions of composition NbO_x were localized based on comparison of their difference electron density maps with those for the structure of oxygen-free Nb. All maps were constructed using identical sets of structure factors, which were obtained under the same experimental conditions from crystals characterized by virtually identical habit and perfection, which allowed us to reveal essential differences in the crystal structures without resorting to analysis of the details of the difference electron density maps associated with the conditions of X-ray data collections. The difference electron density maps for NbO_x differ essentially from the map calculated for Nb in that the former maps have maximum $\Delta\rho$ values corresponding to the centers of the tetrahedral and octahedral cavities in the bcc Nb structure, which were identified as oxygen positions. The fact that the residual electron density for NbO_x is similar to that for Nb confirmed the validity of the determination and the numerical characteristics of the oxygen positions. The positions of the O atoms in the Nb structure were revealed for the first time by direct X-ray diffraction methods. As mentioned above, the theoretical studies performed earlier provided evidence that oxygen atoms can occupy both octahedral [13] and tetrahedral [14] cavities in the bcc Nb structure.

The results of our study also demonstrated that the arrangement of the O atoms depends on the mode of preparation of the cubic solid solution of NbO_x . In the case of electrochemical precipitation on the cathode, which was used for the preparation of crystals **II**, both Nb and O atoms present in the melt were involved in the formation of the crystal structure, and the oxygen atoms in the crystal occupied the tetrahedral cavities in the Nb structure. Upon surface oxidation of Nb crystals in a solution of acids, O atoms occupy predominantly the octahedral cavities (the occupancy of the octahedral cavities is twice as large as that of the tetrahedral cavities, see Table 2). Taking into account that O atoms in electrolytically prepared crystals **II** occupy only the tetrahedral cavities of the body-centered cubic structure of Nb, we believe that O atoms in crystal **III** also occupied the tetrahedral cavities in the course of formation of the crystal on the cathode, whereas the octahedral cavities were filled with O atoms upon its subsequent surface oxidation in the solution of acids. The assumption that the arrangement of oxygen atoms in the Nb structure depends on the mode of preparation of the solid solution has been made in [12] based on the comparison of the characteristic features of the preparation of oxygen-containing niobium compounds by gas-phase reactions with those using thermal surface oxidation of crystals in air according to the mechanism of chemisorption (the latter has been described in detail [5]). The authors of the cited study [12] also believed that the crystal structure of the solid phase is formed in the course of gas-phase reactions with the simultaneous participation

of the O and Nb atoms, whereas O atoms are inserted into the already existing structure of Nb upon surface oxidation. Hence, the results of our study provide experimental evidence for the earlier assumption [12] that the positions that are occupied by oxygen atoms depend on the mode of formation of the NbO_x crystal. We demonstrated that NbO_x crystals prepared by electrochemical crystallization and surface oxidation contained oxygen atoms in the tetrahedral and octahedral cavities, respectively, of the bcc Nb structure.

When comparing the amounts of oxygen dissolved in the bcc Nb structure and the cubic unit-cell parameters for crystals **II** and **III** (Table 1), it can be concluded that the arrangement of O atoms in the octahedral cavities of the structure (crystal **III**) leads to a sharper increase in the a unit-cell parameter compared to crystals in which oxygen atoms occupy tetrahedral cavities (crystal **II**). The lower oxygen content in crystal **III** corresponds to the larger a parameter. This fact is attributable to the presence of two Nb–O distances (~ 1.66 Å) that are too short in the octahedra along the [100] direction. The tendency of Nb atoms to move apart along this direction leads to an increase in the unit-cell parameter.

As mentioned above, the amplitudes of thermal displacements of the Nb atoms in crystal **I**, which is virtually devoid of oxygen, are twice as large as those in solid solutions of composition NbO_x (crystals **II** and **III**). This fact is indicative of the substantial influence of oxygen on the dynamics of the crystal lattice of niobium metal. On the whole, an increase in the numerical parameters of the anharmonicity tensor for NbO_x compared to those for oxygen-free Nb (Table 2) is consistent with the statement that the insertion of additional atoms into the initial structure leads to an increase in the anharmonicity.

CONCLUSIONS

It is very interesting that the maximum concentration of oxygen in cubic solid solutions of composition NbO_x , which were prepared by the electrolysis of salt melts (up to 17 at. %, i.e., up to the composition $\text{NbO}_{x=0.17}$), is many times higher than all known concentrations for solid solutions obtained by heating Nb in air (0.5–1.5 at. % at 700–800°C and no higher than 7 at. % at 1700°C) [8, 15, 20, 21]. Apparently, the external pressure should increase the solubility of O in Nb, and it can be concluded that electrolytic crystallization of NbO_x solid solutions on the cathode exerts an effect analogous to that which appears under high external pressure. This conclusion is supported by the results of our investigation. Thus, oxygen atoms in crystals **II** prepared by the electrolytic method are located in the tetrahedral cavities of the bcc Nb structure, whose volume is four times smaller than the volume of the octahedral cavities occupied by oxygen upon surface oxidation. In addition, the volume of the cubic unit cell of crystal **II** of composition $\text{NbO}_{x=0.15}$, which was pre-

pared by the electrolytic method, (36.2 \AA^3) is 4.3% smaller than the volume of the tetragonally distorted unit cell of suboxide Nb_6O (37.78 \AA^3) of virtually the same composition ($\text{NbO}_{0.143}$) [4] and is 0.3% smaller than the volume of the unit cell of crystal **III**, which was prepared by surface oxidation and contained a smaller amount of oxygen ($\text{NbO}_{x=0.107}$). Earlier [22], we drew the conclusion that electrochemical crystallization on the cathode exerts an effect analogous to the rise in the external pressure based on an analysis of the characteristic features of the tetragonal modification of β -Ta. This modification is generated only by electrolysis and is absent in the known T - P phase diagrams for Ta. The structural defects caused by the replacement of K atoms by Ta-Ta dumbbells were observed in the cubic structure of $\text{KTa}_{1+z}\text{O}_3$ bronze, which was also prepared by the electrolysis of a salt melt [23]. These defects are indicative of the presence of local centers with a higher density in this perovskite-like structure, which can be interpreted as the manifestation of the effect analogous to that of external pressure. The synthesis of diamond and diamond-like nucleation centers (nanosized) upon electrolysis of alcoholic solutions [24–27] also confirms the above assumptions.

ACKNOWLEDGMENTS

This study was supported by the Russian Foundation for Basic Research. A.V. Arakcheeva acknowledges the financial support of the Herbert Foundation of the University of Lausanne (Switzerland).

REFERENCES

1. N. P. Lyakishev, N. A. Tulin, and Yu. L. Pliner, *Doped Alloys and Steels with Niobium* (Metallurgiya, Moscow, 1981).
2. B. Gunter, D. Lieb, C. Richmond, and F. Rufeh, *Summary Report on Oxygen Additives* (Waltham, Mass., 1974).
3. I. G. Gverdsiteli, N. E. Menabde, L. M. Tsakadze, and V. K. Tskhakaya, in *Thermionic Conversion of Heat Energy to Electric Energy* (Fiziko-Energeticheskiĭ Inst., Obninsk, 1980), p. 160.
4. G. Brauer, H. Muller, and G. Kuhner, *J. Less-Common Met.* **4** (6), 533 (1962).
5. F. Fairbrother, *The Chemistry of Niobium and Tantalum* (Elsevier, Amsterdam, 1967; Khimiya, Moscow, 1972).
6. R. P. Elliott, *Constitution of Binary Alloys* (McGraw-Hill, New York, 1965; Metallurgiya, Moscow, 1970), Vols. 1, 2.
7. O. P. Kolchin and I. V. Sumarokova, *At. Energ.* **45**, 293 (1978).
8. J. D. Fast, *Interaction of Metals and Gases* (Academic, New York, 1965).
9. T. Hurlen, *J. Inst. Met.* **89**, 273 (1961).
10. V. V. Grinevich, M. S. Model', A. V. Arakcheeva, *et al.*, *Dokl. Akad. Nauk SSSR* **319** (2), 389 (1991).
11. A. V. Arakcheeva, *Kristallografiya* **37**, 589 (1992) [*Sov. Phys. Crystallogr.* **37**, 306 (1992)].
12. V. I. Kobayakov and V. N. Taranovskaya, *Kristallografiya* **44**, 1017 (1999) [*Crystallogr. Rep.* **44**, 948 (1999)].
13. V. K. Grigorovich and E. N. Sheftel', *Dispersion Hardening of Refractory Metals* (Nauka, Moscow, 1980).
14. B. M. Zykov and A. M. Sabel'nikov, *Poverkhnost*, No. 10, 61 (1988).
15. *Binary Alloy Phase Diagrams*, Ed. by Th. B. Massalski (American Society for Metals, Metals Park, 1987, 2nd ed.), Vol. 2.
16. V. V. Grinevich, V. A. Reznichenko, G. A. Menyailova, and Yu. I. Bykovskaya, in *Electrolytic Dissolution of Niobium in Molten Salts* (Nauka, Moscow, 1975), p. 220.
17. V. V. Grinevich, V. A. Reznichenko, M. S. Model', *et al.*, *J. Appl. Electrochem.* **29**, 693 (1999).
18. V. V. Grinevich, A. V. Arakcheeva, E. G. Polyakov, *et al.*, in *Proceedings of the International Symposium on Molten Salt XI* (The Electrochemical Society, Pennington, 1998), p. 84.
19. J. Emsley, *The Elements* (Clarendon, Oxford, 1991; Mir, Moscow, 1993).
20. C. J. Altstetter, *Bull. Alloy Phase Diagrams* **5** (6), 543 (1984).
21. E. Fromm and E. Gebhardt, *Gase und Kohlenstoff in Metallen* (Springer-Verlag, Berlin, 1976; Metallurgiya, Moscow, 1980).
22. A. V. Arakcheeva, G. Chapuis, and V. Grinevich, *Acta Crystallogr., Sect. B: Struct. Sci.* **B58**, 1 (2002).
23. A. V. Arakcheeva, G. Chapuis, V. Grinevich, and V. F. Shamray, *Acta Crystallogr., Sect. B: Struct. Sci.* **B7**, 157 (2001).
24. Z. Sun, X. Wang, and Y. Sun, *Mater. Sci. Eng. B* **65**, 194 (1999).
25. Y. Namba, *J. Vac. Sci. Technol. A* **10**, 3368 (1992).
26. H. Wang, M. R. Shen, Z. Y. Ning, *et al.*, *Appl. Phys. Lett.* **69**, 1074 (1996).
27. M. C. Tosin, A. C. Peterlevitz, G. L. Surdutovich, and V. Baranauskas, *Appl. Surf. Sci.* **144–145**, 260 (1999).

Translated by T. Safonova

STRUCTURE OF COORDINATION COMPOUNDS

Structures of Mixed-Ligand Manganese(II) Compounds [Mn(Heida)(Phen)]₂ · 7H₂O and [Mn₂(Edta)(Phen)] · 4H₂O

I. N. Polyakova*, V. S. Sergienko*, and A. L. Poznyak**

* Kurnakov Institute of General and Inorganic Chemistry, Russian Academy of Sciences,
Leninskii pr. 31, Moscow, 119991 Russia
e-mail: sokol@igic.ras.ru

** Institute of Molecular and Atomic Physics, Belarussian Academy of Sciences,
pr. F. Skoriny 70, Minsk, 220072 Belarus

Received June 5, 2001

Abstract—The crystal structures of [Mn(Heida)(Phen)]₂ · 7H₂O (**I**) and [Mn₂(Edta)(Phen)] · 4H₂O (**II**) are studied by X-ray diffraction [$R_1 = 0.0375$ (0.0283) and $wR_2 = 0.0954$ (0.0662) for 5449 (3176) observed reflections in **I** (**II**), respectively]. Structure **I** contains mononuclear mixed-ligand complexes [Mn(Heida)(Phen)] and [Mn(Heida)(Phen)(H₂O)]. In structure **II**, the [Mn(Edta)]²⁻ anionic complexes and the [Mn(Phen)(H₂O)₂]²⁺ cationic complexes are linked by the bridging carboxyl groups into the tetramers with C₂ symmetry. In both compounds, two independent Mn atoms have different coordination numbers (6 and 7). © 2002 MAIK “Nauka/Interperiodica”.

INTRODUCTION

Continuing our studies of the transition-metal mixed-ligand compounds with aminocarboxylic acids and *N*-heterocyclic ligands, we determined the crystal structures of [Mn(Heida)(Phen)]₂ · 7H₂O (**I**) and [Mn₂(Edta)(Phen)] · 4H₂O (**II**), where H₂Heida is hydroxyethyliminodiacetic acid, H₄Edta is ethylenediaminetetraacetic acid, and Phen is 1,10-phenanthroline.

EXPERIMENTAL

Crystals **I** and **II** were prepared by slow evaporation of aqueous solutions containing the monoligand compound [Mn(Heida) · 2H₂O or Mn₃(HEdta)₂ · 10H₂O] and Phen in equimolar amounts.

X-ray diffraction study. The main crystal data and characteristics of the experiment and refinement for **I** and **II** are summarized in Table 1. The experimental sets of the $I(hkl)$ intensities for crystals **I** and **II** were obtained on an Enraf–Nonius CAD4 automated diffractometer (λ MoK $_{\alpha}$, graphite monochromator, ω scan mode).

Structures **I** and **II** were solved by the direct method (SHELXS86 [1]). All the H atoms were located from difference Fourier syntheses and refined isotropically. The non-hydrogen atoms were refined in the anisotropic approximation. For both crystals, the data were corrected for absorption according to the azimuthal-scan technique. The refinement was performed with the SHELXL97 program [2].

The atomic coordinates and thermal parameters are listed in Table 2. In structure **II**, the positions of the w_3 and w_5 water molecules, which are located in the vicin-

ity of the twofold rotation axis and the center of symmetry, are populated by half. The oxygen atom of the w_4 water molecule is disordered over two equally populated positions (*A* and *B*) so that the O(4*wB*) (*x*, *y*, *z*) position is occupied in combination with O(5*w*) (*x*, *y*, *z*).

RESULTS AND DISCUSSION

Structure of crystals I. Crystals **I** are built of monomeric mixed-ligand complexes of two types, [Mn(1)(Heida)(Phen)(H₂O)] and [Mn(2)(Heida)(Phen)] (Fig. 1), and molecules of crystallization water. The coordination of both Mn atoms includes three O atoms and the N atom of the Heida²⁻ tetradentate ligand and two N atoms of the Phen molecules. The Mn(1) atom is additionally coordinated by the O(1*w*) atom of the water molecule. Thus, the Mn(1) and Mn(2) atoms have different coordination numbers (7 and 6, respectively). The Mn(2) polyhedron is a distorted trigonal prism. Triangular bases of the prism, namely, N(2A)N(3A)O(3A) and O(5A)O(1A)N(1A), form an angle of 7.6°. In the projection onto the N(2A)N(3A)O(3A) plane, the Mn(2)–O(1A) bond coincides with the Mn(2)–N(3A) bond, whereas two other pairs of bonds diverge noticeably: the N(1A)Mn(2)O(3A) and O(5A)Mn(2)N(2A) pseudoangles that characterize this divergence are 15° and 50°, respectively. The Mn(1) polyhedron is a similar trigonal prism with the N(2)N(3)O(3) and O(5)O(1)N(1) bases, but the O(1)O(5)N(2)N(3) face is centered by the O(1*w*) atom. The angle between the planes of the triangular bases is 5.5°. In the projection onto the N(2)N(3)O(3) plane, the Mn(1)–N(1) bond coincides with the Mn(1)–O(3) bond, whereas two other pairs of

Table 1. Main crystal data and parameters of data collection and refinement for structures **I** and **II**

Parameter	I	II
Empirical formula	C ₁₈ H ₂₄ MnN ₃ O _{8.5}	C ₂₂ H ₂₈ Mn ₂ N ₄ O ₁₂
<i>M</i>	473.34	650.36
Space group	<i>P</i> $\bar{1}$	<i>C2/c</i>
<i>a</i> , Å	10.276(2)	18.887(4)
<i>b</i> , Å	13.675(3)	14.584(3)
<i>c</i> , Å	14.989(3)	20.085(4)
α , deg	77.61(3)	90
β , deg	82.72(3)	108.45(3)
γ , deg	89.91(3)	90
<i>V</i> , Å ³	2040.0(7)	5248(1)
<i>Z</i>	4	8
ρ (calcd), g/cm ³	1.541	1.646
Crystal size, mm	0.12 × 0.21 × 0.75	0.09 × 0.21 × 0.33
μ_{Mo} , mm ⁻¹	0.701	1.033
θ_{max} , deg	27	28
Number of reflections:		
measured	8220	5435
unique (<i>N</i> ₁) [<i>R</i> _{int}]	7812 [0.0169]	5281 [0.0256]
with <i>I</i> > 2 σ (<i>I</i>), (<i>N</i> ₂)	5449	3176
<i>R</i> ₁ , <i>wR</i> ₂ for <i>N</i> ₁	0.0693, 0.1082	0.0889, 0.0787
<i>R</i> ₁ , <i>wR</i> ₂ for <i>N</i> ₂	0.0375, 0.0954	0.0283, 0.0662
<i>GOOF</i>	0.998	0.981
$\Delta\rho_{\text{min}}$ and $\Delta\rho_{\text{max}}$, e Å ⁻³	-0.681 and 0.538	-0.519 and 0.303

bonds diverge to an even larger degree than those in the Mn(2) polyhedron: the N(2)Mn(1)O(5) and N(3)Mn(1)O(1) pseudoangles are 38° and 57°, respectively.

The *w*(1) water molecule “pushes” the O(1), N(2), and N(3) atoms in the coordination sphere of the Mn(1) atom. The angles involving these atoms change most of all in the Mn(1) polyhedron as compared to the corresponding angles in the Mn(2) polyhedron: O(1)MnO(3), 97.51(7)° and 140.89(8)°; O(1)MnO(5), 122.54(8)° and 88.51(8)°; O(1)MnN(2), 155.87(8)° and 120.44(8)°; O(3)MnN(2), 80.56(7)° and 96.16(8)°; N(1)MnN(3), 142.14(8)° and 126.82(8)°; and N(1)MnN(2), 130.86(8)° and 155.91(8)° for Mn(1) and Mn(2), respectively. The bonds with the *Heida*²⁻ and *Phen* ligands in the seven-coordinate complex of Mn(1) are substantially elongated in comparison with the corresponding bonds in the Mn(2) complex [Mn–O, 2.201(2)–2.292(2) and 2.124(2)–2.239(2) Å; Mn–N(1), 2.427(2) and 2.314(2) Å; Mn–N(2), 2.303(2) and 2.241(2) Å; and Mn–N(3), 2.365(2) and 2.246(2) Å in the Mn(1) and Mn(2) complexes, respectively].

The crystals of the initial compound Mn(*Heida*) · 2H₂O have a chain structure [3]. In addition

to the N + 3O atoms of the *Heida* ligand, the coordination of the Mn atom includes the water molecule and the carbonyl O atom of the neighboring complex in the *trans* positions with respect to the oxygen atom of the hydroxyethyl group and the nitrogen atom, respectively. In the [Mn(*Heida*)(*Phen*)] complex of compound **I**, the N(2A) and N(3A) atoms of the *Phen* molecule are situated *trans* relative to N(1A) and the carboxyl O(1A) atom. This indicates that, when interacting with *Phen* in a solution, the initial monoligand complex undergoes a transformation.

In crystal **I**, ligands of the same type (both *Heida* and *Phen*) are packed into separate layers, which are parallel to the *xy* plane and alternate in the direction of the *z*-axis. The water molecules are situated inside the hydrophilic *Heida* layer and, together with the OH groups of the hydroxyethyl branches, form an extensive system of hydrogen bonds (Table 3). The *Phen* molecules from different complexes [Mn(1) and Mn(2)] are approximately parallel to each other (the dihedral angle between their mean planes is 8.6°) and to the *xz* plane. The *Phen* molecules of the identical complexes form centrosymmetric pairs with interplanar spacings equal to 3.40 and 3.35 Å. These pairs are arranged in such a way that, in the projection onto their own plane, each

Table 2. Coordinates and parameters of thermal vibrations U_{eq} of the non-hydrogen atoms in structures **I** and **II**

Atom	<i>x</i>	<i>y</i>	<i>z</i>	$U_{eq}, \text{\AA}^2$	Atom	<i>x</i>	<i>y</i>	<i>z</i>	$U_{eq}, \text{\AA}^2$
I									
Mn(1)	0.57101(4)	0.11702(3)	0.75551(2)	0.0271(1)	O(4A)	0.9226(2)	0.9153(1)	0.7553(2)	0.0446(5)
O(1)	0.4090(2)	0.1099(2)	0.8719(1)	0.0451(5)	O(5A)	0.6229(2)	0.5940(2)	0.7609(1)	0.0434(5)
O(2)	0.3539(2)	0.1012(2)	1.0214(1)	0.0396(4)	N(1A)	0.8058(2)	0.6634(2)	0.8605(1)	0.0315(5)
O(3)	0.5638(2)	0.2784(1)	0.6956(1)	0.0342(4)	N(2A)	0.7883(2)	0.6316(2)	0.5723(1)	0.0300(5)
O(4)	0.5323(2)	0.4322(1)	0.7175(1)	0.0397(4)	N(3A)	1.0289(2)	0.6173(2)	0.6292(1)	0.0322(5)
O(5)	0.7837(2)	0.0814(2)	0.7788(2)	0.0422(5)	C(1A)	0.8472(4)	0.5766(2)	0.9279(2)	0.0406(7)
N(1)	0.6358(2)	0.2072(2)	0.8665(1)	0.0285(4)	C(2A)	0.8759(3)	0.4851(2)	0.8878(2)	0.0335(6)
N(2)	0.6633(2)	0.1183(2)	0.6025(1)	0.0327(5)	C(3A)	0.8802(3)	0.7563(2)	0.8561(2)	0.0407(7)
N(3)	0.4035(2)	0.1015(2)	0.6705(1)	0.0330(5)	C(4A)	0.8901(3)	0.8263(2)	0.7607(2)	0.0338(6)
C(1)	0.5735(3)	0.1522(2)	0.9566(2)	0.0327(6)	C(5A)	0.6636(3)	0.6805(2)	0.8761(2)	0.0449(7)
C(2)	0.4346(3)	0.1188(2)	0.9498(2)	0.0322(6)	C(6A)	0.5840(3)	0.5986(3)	0.8547(2)	0.0498(8)
C(3)	0.5835(3)	0.3080(2)	0.8446(2)	0.0367(6)	C(7A)	0.6705(3)	0.6383(2)	0.5435(2)	0.0372(6)
C(4)	0.5588(2)	0.3416(2)	0.7446(2)	0.0284(5)	C(8A)	0.6509(3)	0.6475(2)	0.4522(2)	0.0429(7)
C(5)	0.7795(3)	0.2109(2)	0.8603(2)	0.0350(6)	C(9A)	0.7570(3)	0.6486(2)	0.3878(2)	0.0425(7)
C(6)	0.8368(3)	0.1122(2)	0.8514(2)	0.0382(6)	C(10A)	0.8838(3)	0.6395(2)	0.4141(2)	0.0345(6)
C(7)	0.7880(3)	0.1257(2)	0.5682(2)	0.0412(6)	C(11A)	0.9983(3)	0.6348(2)	0.3517(2)	0.0438(7)
C(8)	0.8341(4)	0.1392(2)	0.4745(2)	0.0491(8)	C(12A)	1.1163(3)	0.6236(2)	0.3804(2)	0.0442(7)
C(9)	0.7448(4)	0.1448(2)	0.4135(2)	0.0489(8)	C(13A)	1.1330(3)	0.6183(2)	0.4748(2)	0.0361(6)
C(10)	0.6109(3)	0.1372(2)	0.4464(2)	0.0405(7)	C(14A)	1.2545(3)	0.6072(2)	0.5081(2)	0.0441(7)
C(11)	0.5109(4)	0.1413(2)	0.3871(2)	0.0501(8)	C(15A)	1.2603(3)	0.6000(2)	0.5995(2)	0.0477(7)
C(12)	0.3836(4)	0.1304(2)	0.4208(2)	0.0493(8)	C(16A)	1.1463(3)	0.6060(2)	0.6581(2)	0.0422(7)
C(13)	0.3421(3)	0.1162(2)	0.5177(2)	0.0402(7)	C(17A)	1.0223(3)	0.6229(2)	0.5386(2)	0.0289(5)
C(14)	0.2102(3)	0.1049(2)	0.5564(2)	0.0493(8)	C(18A)	0.8939(3)	0.6324(2)	0.5083(2)	0.0282(5)
C(15)	0.1777(3)	0.0915(3)	0.6488(3)	0.0542(8)	O(1w)	0.5608(2)	-0.0512(2)	0.8062(2)	0.0399(5)
C(16)	0.2776(3)	0.0908(2)	0.7043(2)	0.0421(7)	O(2w)	0.6975(3)	0.5340(2)	0.1633(2)	0.0691(8)
C(17)	0.4372(3)	0.1138(2)	0.5780(2)	0.0303(5)	O(3w)	1.0793(2)	-0.0650(2)	-0.1095(2)	0.0501(5)
C(18)	0.5733(3)	0.1235(2)	0.5426(2)	0.0322(6)	O(4w)	1.1130(2)	0.1106(2)	-0.0456(2)	0.0464(5)
Mn(2)	0.83664(4)	0.62937(3)	0.71467(2)	0.0292(1)	O(5w)	0.8863(3)	0.6836(2)	0.1376(2)	0.0613(7)
O(1A)	0.8791(2)	0.4925(1)	0.8025(1)	0.0452(5)	O(6w)	0.6836(3)	0.1547(2)	0.1698(2)	0.0567(6)
O(2A)	0.8973(2)	0.4061(2)	0.9430(1)	0.0481(5)	O(7w)	0.7789(3)	0.3534(2)	0.1226(2)	0.0727(8)
O(3A)	0.8704(2)	0.7885(1)	0.6940(1)	0.0399(4)					
II									
Mn(1)	0.08620(2)	0.09652(3)	0.22297(2)	0.0215(1)	C(8)	0.1783(2)	0.2668(2)	0.2636(2)	0.0349(7)
Mn(2)	0.00082(2)	0.17946(3)	0.02785(2)	0.0243(1)	C(9)	0.2311(2)	-0.0142(2)	0.3097(2)	0.0284(6)
O(1)	0.0357(1)	0.0950(1)	0.3188(1)	0.0260(4)	C(10)	0.2609(2)	0.0763(2)	0.2933(2)	0.0316(7)
O(2)	0.0770(1)	0.1076(1)	0.4354(1)	0.0307(4)	C(11)	0.1249(2)	0.2617(3)	-0.0355(2)	0.053(1)
O(3)	0.0769(1)	-0.0454(1)	0.1799(1)	0.0303(4)	C(12)	0.1691(2)	0.3275(3)	-0.0516(2)	0.068(1)
O(4)	0.0868(1)	-0.1952(1)	0.2013(1)	0.0385(5)	C(13)	0.1682(2)	0.4144(3)	-0.0282(2)	0.059(1)
O(5)	0.0939(1)	0.1186(1)	0.1098(1)	0.0269(4)	C(14)	0.1234(2)	0.4361(2)	0.0136(2)	0.0407(8)
O(6)	0.1548(1)	0.0480(2)	0.0452(1)	0.0422(5)	C(15)	0.1168(2)	0.5260(2)	0.0398(2)	0.050(1)
O(7)	0.1193(1)	0.2292(1)	0.2670(1)	0.0405(5)	C(16)	0.0759(2)	0.5412(2)	0.0819(2)	0.048(1)
O(8)	0.2023(1)	0.3431(2)	0.2885(1)	0.0529(6)	C(17)	0.0358(2)	0.4688(2)	0.1023(2)	0.0383(8)
N(1)	0.1545(1)	-0.0036(1)	0.3138(1)	0.0233(5)	C(18)	-0.0077(2)	0.4822(2)	0.1467(2)	0.0506(9)
N(2)	0.2107(1)	0.1151(1)	0.2267(1)	0.0252(5)	C(19)	-0.0470(2)	0.4099(3)	0.1604(2)	0.0525(9)
N(3)	0.0820(1)	0.2780(2)	0.0041(1)	0.0353(6)	C(20)	-0.0429(2)	0.3248(2)	0.1300(2)	0.0424(8)
N(4)	-0.0021(1)	0.3095(2)	0.0886(1)	0.0317(5)	C(21)	0.0380(2)	0.3806(2)	0.0751(1)	0.0313(7)
C(1)	0.1552(2)	0.0339(2)	0.3817(1)	0.0255(6)	C(22)	0.0820(2)	0.3641(2)	0.0299(1)	0.0307(6)
C(2)	0.0830(1)	0.0826(2)	0.3781(1)	0.0225(5)	O(1w)	0.0156(1)	0.0836(2)	-0.0478(1)	0.0407(6)
C(3)	0.1157(2)	-0.0923(2)	0.2991(1)	0.0256(6)	O(2w)	-0.0912(2)	0.2296(2)	-0.0638(1)	0.0403(6)
C(4)	0.0917(2)	-0.1139(2)	0.2204(1)	0.0267(6)	O(3w)*	0.009(2)	0.6743(5)	0.261(2)	0.134(8)
C(5)	0.2192(2)	0.0676(2)	0.1658(1)	0.0293(6)	O(4wA)*	0.7267(4)	0.3667(5)	0.0681(4)	0.049(2)
C(6)	0.1508(2)	0.0788(2)	0.1012(1)	0.0264(6)	O(4wB)*	0.7594(4)	0.3913(5)	0.0702(5)	0.051(2)
C(7)	0.2224(2)	0.2149(2)	0.2242(2)	0.0339(7)	O(5w)*	0.7220(3)	0.2115(4)	0.0383(3)	0.057(1)

* Site occupancy is 0.5.

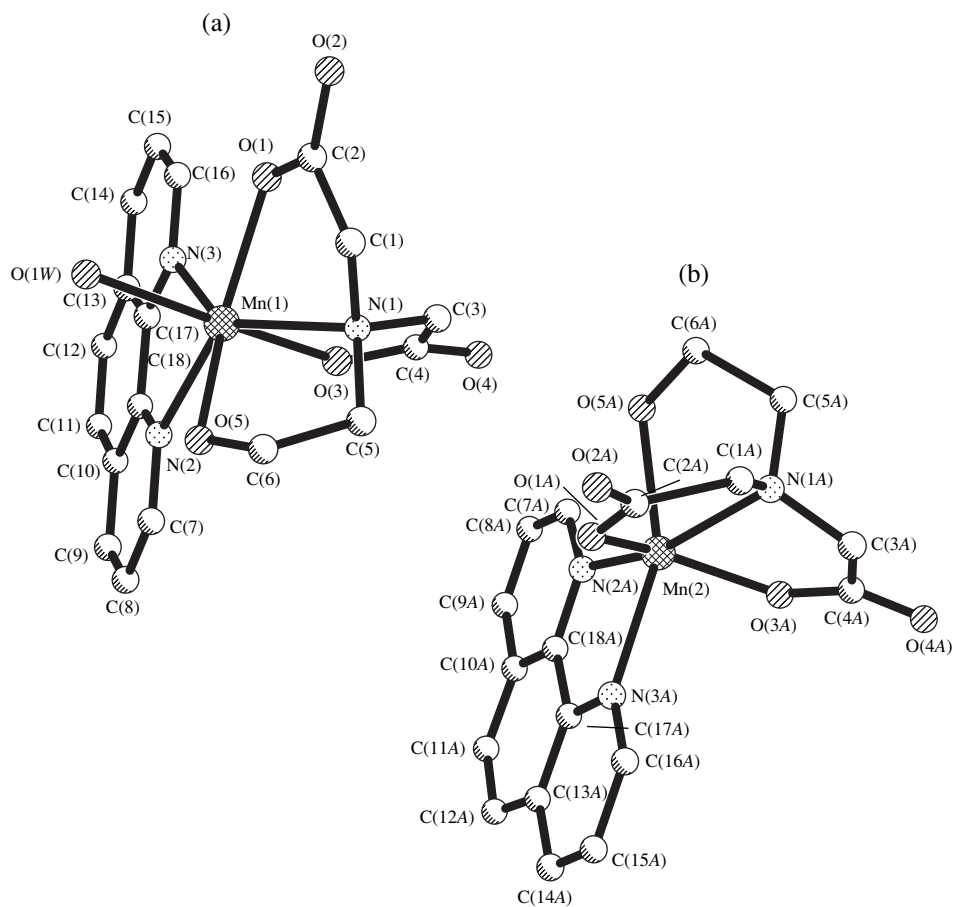


Fig. 1. Structure of (a) $[\text{Mn}(\text{Heida})(\text{Phen})(\text{H}_2\text{O})]$ and (b) $[\text{Mn}(\text{Heida})(\text{Phen})]$ complexes in **I**. The H atoms are omitted.

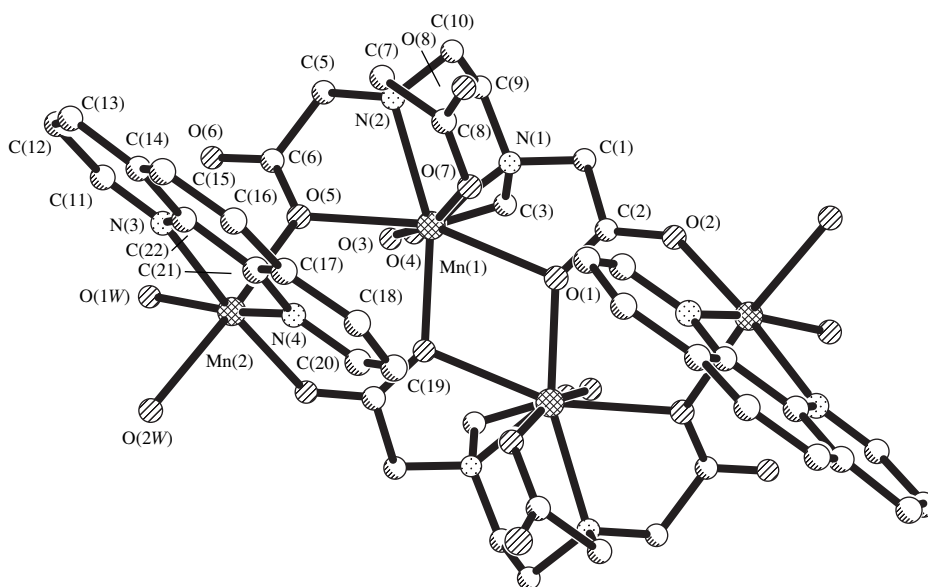


Fig. 2. Structure of the $\{[\text{Mn}(\text{Edta})][\text{Mn}(\text{Phen})(\text{H}_2\text{O})_2]\}_2$ tetramer in **II**. The H atoms are omitted.

Table 3. Characteristics of hydrogen bonds in structures **I** and **II**

X–H...Y	Symmetry transformation for the Y atom	Distance, Å		X–H...Y angle, deg
		X...Y	H...Y	
I				
O(1w)–H(1w1)···O(6w)	$1 - x, -y, 1 - z$	2.829(4)	2.02(4)	174(4)
O(1w)–H(2w1)···O(2)	$1 - x, -y, 2 - z$	2.779(3)	2.02(4)	174(4)
O(2w)–H(1w2)···O(4)	$1 - x, 1 - y, 1 - z$	2.875(4)	2.12(4)	158(3)
O(2w)–H(2w2)···O(5w)	x, y, z	2.754(5)	1.94(4)	174(4)
O(3w)–H(1w3)···O(4A)	$x, y - 1, z - 1$	2.799(3)	1.97(4)	167(4)
O(3w)–H(2w3)···O(4w)	$2 - x, y, z$	2.813(4)	1.90(6)	178(6)
O(4w)–H(1w4)···O(2)	$1 + x, y, z - 1$	2.780(3)	2.08(4)	175(4)
O(4w)–H(2w4)···O(3w)	x, y, z	2.806(3)	1.70(7)	169(5)
O(5w)–H(1w5)···O(2A)	$2 - x, 1 - y, 1 - z$	2.803(4)	2.01(4)	164(6)
O(5w)–H(2w5)···O(4w)	$2 - x, 1 - y, -z$	2.857(4)	2.07(5)	173(5)
O(6w)–H(1w6)···O(7w)	x, y, z	2.802(4)	1.94(4)	168(4)
O(6w)–H(2w6)···O(3w)	$2 - x, -y, -z$	2.857(4)	2.14(5)	161(5)
O(7w)–H(1w7)···O(2A)	$x, y, z - 1$	2.755(4)	1.88(5)	175(5)
O(7w)–H(2w7)···O(2w)	x, y, z	2.772(4)	1.88(5)	177(4)
O(5)–H(5O)···O(4A)	$x, y - 1, z$	2.743(3)	1.99(4)	170(4)
O(5A)–H(5OA)···O(4)	x, y, z	2.639(3)	1.79(3)	170(3)
II				
O(1w)–H(1w1)···O(3)	$-x, -y, -z$	2.732(3)	1.85(4)	172(4)
O(1w)–H(2w1)···O(2)	$x, -y, z - 0.5$	3.079(3)	2.43(4)	139(4)
O(1w)–H(2w1)···O(6)	x, y, z	2.750(3)	2.14(4)	132(4)
O(2w)–H(1w2)···O(4)	$-x, -y, -z$	2.834(3)	2.12(4)	174(4)
O(2w)–H(2w2)···O(5w)	$0.5 - x, 0.5 - y, -z$	2.812(7)	2.18(5)	154(4)
O(2w)–H(2w2)···O(4wA)	$0.5 - x, 0.5 - y, -z$	2.897(8)	2.33(5)	142(5)
O(3w)–H(1w3)···O(4)	$x, 1 + y, z$	2.89(3)	2.23(8)	149(8)
O(3w)–H(1w3)···O(4)	$-x, 1 + y, 0.5 - z$	2.89(3)	2.23(8)	149(8)
O(4wA)–H(1w4)···O(8)	$1 - x, y, 0.5 - z$	2.787(8)	1.93(4)	163(4)
O(4wA)–H(2w4)···O(6)	$0.5 + x, 0.5 + y, z$	2.942(8)	2.01(5)	172(4)
O(4wB)–H(1w4)···O(8)	$1 - x, y, 0.5 - z$	2.788(9)	1.93(4)	163(4)
O(4wB)–H(2w4)···O(6)	$1 - x, y, 0.5 - z$	2.958(8)	2.01(5)	147(4)
O(5w)–H(1w5)···O(4wA)	$1.5 - x, 0.5 - y, -z$	2.85(1)	1.98(7)	159(6)
O(5w)–H(2w5)···O(4wB)	x, y, z	2.739(9)	1.89(9)	154(7)
C(18)–H(18)···O(3w)	$-x, y, 0.5 - z$	3.37(2)	2.36(4)	170(3)
C(13)–H(13)···O(4wB)	$1 - x, 1 - y, -z$	3.368(9)	2.47(4)	164(3)
C(20)–H(20)···O(7)	$-x, y, 0.5 - z$	3.193(4)	2.42(3)	141(2)
C(15)–H(15)···O(5w)	$x - 0.5, 0.5 + y, z$	3.363(7)	2.47(3)	157(3)
C(16)–H(16)···O(2w)	$-x, 1 - y, -z$	3.385(4)	2.65(3)	136(2)

molecule overlaps with two other *Phen* molecules, which results in the formation of the layer. The shortest intermolecular C...C distances in the layer are 3.292–3.536 Å.

Structure of crystals II. Structure **II** is built of the $\{[\text{Mn}(1)(\text{Edta})][\text{Mn}(2)(\text{Phen})(\text{H}_2\text{O})_2]\}_2$ associates with

the C_2 symmetry (Fig. 2) and molecules of crystallization water. The Mn(1) atom is coordinated by the N(1), N(2), O(1), O(3), O(5), and O(7) atoms of the *Edta*⁴⁻ ligand and the O(1)' atom of the neighboring complex that is related to the reference one by the twofold rotation axis. Thus, two anionic complexes are linked by

the O(1) and O(1)' bridging atoms into the dimer. The Mn(1)–O(1)–Mn(1)'–O(1)' four-membered ring is almost planar: the angle of folding along the O(1)–O(1)' segment is 1.4°. The Mn(1)–O(1)–Mn(1)' bridge has an asymmetric structure [2.403(2) and 2.187(2) Å]. The Mn(2) atom is coordinated by the N(3) and N(4) atoms of the *Phen* molecule, the O(1 w) and O(2 w) atoms of water molecules, and the O(5) and O(2)' atoms of the *Edta* ligands from the two moieties of the dimer. The coordination numbers of the Mn(1) and Mn(2) are 7 and 6, respectively.

Note that, in the crystals of the initial compound Mn₃(*HEdta*)₂ · 10H₂O, the Mn atoms also form complexes of two types, namely, the anionic complexes [Mn(*HEdta*)(H₂O)][−] and the cationic complexes [Mn(H₂O)₄]²⁺, which are linked by the bridging carboxyl groups into the centrosymmetric trinuclear associates [4, 5].

A similar division of the Mn²⁺ ions into the anionic and cationic complexes with coordination numbers 7 and 6 is observed in the [Mn(H₂O)₄][Mn(*Edta*)(H₂O)] · 4H₂O compound (**III**) [6]. In the anionic moiety, in contrast to **II**, the seventh vertex in the Mn environment is occupied by the water molecule. In the cationic moiety, the Mn octahedron consists of four O atoms of water molecules and two O atoms of the carboxyl groups of two neighboring anionic complexes. Thus, the cationic and anionic complexes alternate to form the chains.

In the series of Mn²⁺ ethylenediaminetetraacetates with different cations, the structure of the complex remains the same: the Mn atom is coordinated by the hexadentate *Edta*^{4−} ligand and the water molecule. Some of these compounds (Cat = Li⁺ [7], Na⁺, Rb⁺ [6], and Nd³⁺ [8]), like **III**, have polymeric structures, and others (Cat = NH₄⁺ and Mg²⁺ [6]) contain isolated anionic complexes. The tetranuclear structure found in compound **II** has not been observed earlier among the Mn²⁺ complexes with *Edta*^{4−}.

The Mn(1) polyhedron in **II** is a distorted monocapped trigonal prism with the N(1)O(1)O(3) and N(2)O(5)O(7) triangular bases and the O(1)' atom centering the O(1)O(3)O(5)O(7) face. The bases of the prism are almost parallel (the dihedral angle is 2.5°) but are twisted by an angle of ~20°. In structure **III**, the seven-vertex polyhedron of the Mn atom is also described as a monocapped trigonal prism with the N and O atoms of the *Edta*^{4−} ligand at the vertices of the bases and the H₂O molecule in the “cap.”

Although the seven-coordinate manganese complexes in **II** and **III** are similar in structure, their Mn–*Lig* bond lengths differ significantly. In **II**, the Mn–N bonds [2.345(2) and 2.374(2) Å] are shorter and the spread of the Mn–O bond lengths [2.137(2)–2.403(2) Å]

is larger than that in **III** [2.386(9) and 2.430(9); 2.16(2)–2.25(2) Å, respectively]. These differences are at least in part attributed to the difference in the functions of the carboxyl groups in the two structures.

The O–H...O hydrogen bonds involving the $w1$, $w2$, and $w4$ water molecules link the tetramers into the three-dimensional framework (Table 3). The *Phen* molecules contribute to the stabilization of the structure through the formation of the C–H...O hydrogen bonds. In addition, the stacking interactions link the *Phen* molecules into the centrosymmetric pairs with the interplanar spacing equal to 3.32 Å and the shortest intermolecular C...C distances equal to 3.355–3.478 Å.

Thus, the addition of phenanthroline to aqueous solutions of the monoligand Mn²⁺ complexes with *Heida*^{2−} and *HEdta*^{3−} results, in the former case, in the formation of the mixed-ligand [Mn(*Heida*)(*Phen*)] and [Mn(*Heida*)(*Phen*)(H₂O)] complexes in which each metal atom is chelated by both ligands and, in the latter case, in the formation of the separate chelate complexes [Mn(*Edta*)]^{2−} and [Mn(*Phen*)(H₂O)₂]²⁺ which are linked by the bridging carboxyl groups into the tetramers.

ACKNOWLEDGMENTS

We acknowledge the support of the Russian Foundation for Basic Research in the payment of the license for using the Cambridge Structural Database, project no. 99-07-90133.

REFERENCES

1. G. M. Sheldrick, *Acta Crystallogr., Sect. A: Found. Crystallogr.* **A46** (6), 467 (1990).
2. G. M. Sheldrick, *SHELXL97: Program for the Refinement of Crystal Structures* (Univ. of Göttingen, Göttingen, 1997).
3. N. N. Anan'eva, T. N. Polynova, and M. A. Poraï-Koshits, *Koord. Khim.* **7** (10), 1556 (1981).
4. S. Richards, B. Pedersen, J. V. Silverton, and J. L. Hoard, *Inorg. Chem.* **3** (1), 27 (1964).
5. I. N. Polyakova, A. L. Poznyak, V. S. Sergienko, and L. V. Stopolyanskaya, *Kristallografiya* **46** (1), 47 (2001) [*Crystallogr. Rep.* **46**, 40 (2001)].
6. X. Solans, S. Gali, M. Font-Altaba, *et al.*, *Afinidad* **45**, 243 (1988).
7. N. N. Anan'eva, T. N. Polynova, and M. A. Poraï-Koshits, *Zh. Strukt. Khim.* **15** (2), 261 (1974).
8. Tao Yi, Song Gao, and Biaoguo Li, *Polyhedron* **17**, 2243 (1998).

Translated by I. Polyakova

STRUCTURE
OF ORGANIC COMPOUNDS

Supramolecular Architecture of Two Charge-Transfer
Complexes Based
on 2,7-(X,X)-4,5-Dinitro-9-Dicyanomethylenefluorenes
(X = NO₂ or CN) and Tetrathiafulvalene

L. G. Kuz'mina*, I. F. Perepichka**, D. F. Perepichka**,
J. A. K. Howard***, and M. R. Bryce***

* Kurnakov Institute of General and Inorganic Chemistry, Russian Academy of Sciences,
Leninskii pr. 31, Moscow, 119991 Russia

** Litvinenko Institute of Physicoorganic and Coal Chemistry, National Academy of Sciences of Ukraine,
ul. R. Lyuksemburg, Donetsk, 84114 Ukraine

*** Chemistry Department, Durham University, Durham DH1 3LE, England
e-mail: kuzmina@igic.ras.ru

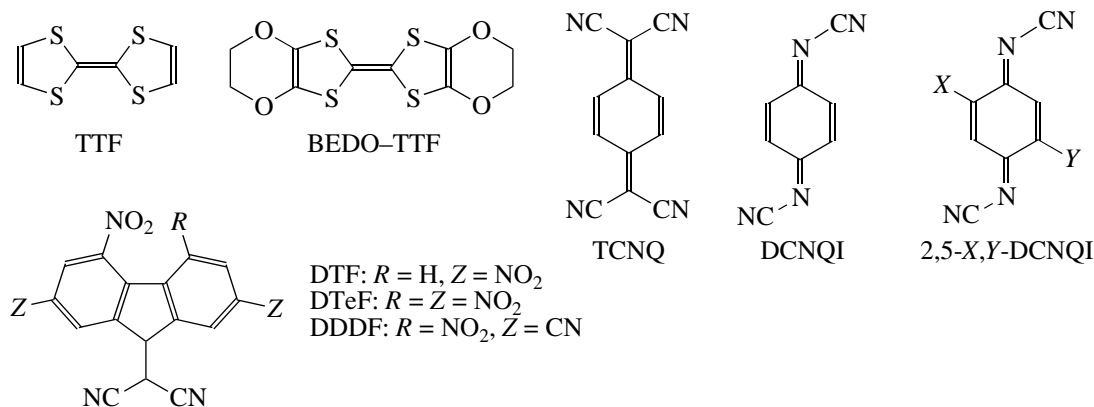
Received March 29, 2001

Abstract—The crystal packings of two charge-transfer complexes based on tetrathiafulvalene and substituted fluorenes—2,4,5,7-tetranitro-9-dicyanomethylenefluorene (in complex **I**) or 2,7-dicyano-4,5-dinitro-9-dicyanomethylenefluorene (in complex **II**)—are analyzed. Crystals of complex **II** involve a third component, namely, C₆H₅Cl solvate molecules. Crystals of both complexes are characterized by the formation of stacks composed of alternating donor and acceptor molecules and sheets in which the molecules are linked through different-type weak interactions. In structure **II**, chlorobenzene molecules occupy cavities that are formed in stacks in the vicinity of the tetrathiafulvalene molecules due to the larger difference in size of the donor and acceptor molecules in complex **II** as compared to that in complex **I**. The chlorobenzene molecules provide a close packing. These molecules are involved in the system of weak interactions to form the Cl...N and C–H...N secondary bonds with the CN groups of the acceptor molecules in the sheets. © 2002 MAIK “Nauka/Interperiodica”.

INTRODUCTION

Molecular organic conductors have been studied extensively over the last two decades [1]. After the discovery of the first stable charge-transfer complex with a metallic conductivity, namely, the complex of

tetrathiafulvalene (TTF) with 7,7,8,8-tetracyanoquinodimethane (TCNQ) [2], a great number of donors—tetrathiafulvalene derivatives—have been synthesized [1–4]. The chemical diagrams of the corresponding compounds are shown in Scheme I.



Scheme I.

However, the structure of acceptors has not been adequately investigated. There had been only a few

works dealing with charge-transfer complexes and radical ion salts that contained acceptors other than TCNQ

molecules [5] until the discovery of the new type of acceptors, namely, *N,N'*-dicyano-1,4-quinodiiimines (DCNQI) [6–9]. Radical ion salts 2,5-*X,Y*-DCNQI with Li, Na, K, Tl, and Ag possess the properties of metallic semiconductors, whereas the radical ion salts with Cu have an extremely high metallic (three-dimensional) conductivity [10].

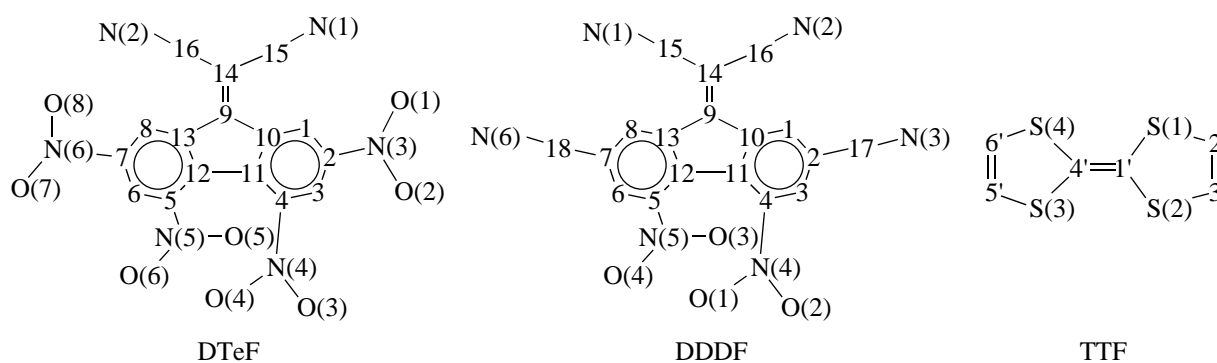
The use of substituted fluorenes with different substituents in the 2- and 7-positions (and in the 4- and 5-positions) as acceptors in charge-transfer complexes makes it possible to change substantially the size and the shape of acceptor molecules, thus affecting the packing of the donor and acceptor molecules in crystals. The electrical conductivity of these charge-transfer complexes can vary by six orders of magnitude [7–10]. Undoubtedly, the electrical conductivity should be governed by the specific features of the supramolecular structure (crystal packing) of charge-transfer complexes. The elucidation of the regularities in the architecture of their crystals is important for the modeling of the structure of charge-transfer complexes with the highest conductivity. Recent investigations into the supramolecular architecture revealed the interrelation between the structure of crystals and their properties [11–16].

In the present work, we analyzed how the replacement of the substituent in the electron-acceptor component of the charge-transfer complex affects its crystal packing by using the example of two fluorene charge-transfer complexes with the same tetrathiafulvalene molecule as a donor component. The properties of these and related charge-transfer complexes either have already been understood or are being investigated intensively. In particular, it was established that the electronic properties of fluorene acceptors are comparable to those of TCNQ and DCNQI derivatives. The fluorene acceptors readily form the charge-transfer complexes with aromatic electron donors [17, 18]. These complexes often possess semiconductor proper-

ties and photoconductivity [17, 19–21]. Recently, Horiuchi *et al.* [22] revealed a metallic conductivity in charge-transfer complexes of bis(ethylene-dioxy)tetrathiafulvalene (BEDO-TTF) with fluorene electron acceptors such as 2,4,7-trinitro-9-dicyanomethylene-fluorene (DTF) and 2,4,5,7-tetranitro-9-dicyanomethylene-fluorene (DTeF): $\sigma = 65 \text{ S cm}^{-1}$ at 298 K and $\sigma = 390 \text{ S cm}^{-1}$ at 8 K for BEDO-TTF : DTF = 2 : 1 and $\sigma = 18 \text{ S cm}^{-1}$ at 298 K and $\sigma = 32 \text{ S cm}^{-1}$ at 94 K for BEDO-TTF : DTeF = 2 : 1 (pressed pellets).

In this work, we investigated the crystal structures of two charge-transfer complexes based on substituted fluorenes and tetrathiafulvalene. Compound **I** is the tetrathiafulvalene complex with 2,4,5,7-tetranitro-9-dicyanomethylene-fluorene (TTF : DTeF = 1 : 1). Compound **II** is the tetrathiafulvalene complex with 2,7-dicyano-4,5-dinitro-9-dicyanomethylene-fluorene (DDDF) and chlorobenzene (*Sol*) $\text{C}_6\text{H}_5\text{Cl}$ (TTF : DDDF : *Sol* = 1 : 1 : 1). These charge-transfer complexes differ in degrees of misfit in the shape and size of the donor (*D*) and acceptor (*A*) molecules. Moreover, different substituents (NO_2 and CN groups) in the 2- and 7-positions of the acceptor molecules impose different geometric constraints on the formation of intermolecular secondary bonds that are responsible for the specific features of the molecular packing motif in crystals. At the same time, the DTeF and DDDF fluorene acceptors are closely similar in electron-acceptor properties (the electron affinities are 2.71 and 2.77 eV, respectively) [23]. Therefore, the differences in crystal packings of compounds **I** and **II** can be determined only by the aforementioned factors (different sizes and geometric constraints on the formation of intermolecular secondary bonds).

The synthesis, properties, and X-ray molecular structures of these charge-transfer complexes were described in our earlier work [23]. The donor and acceptor components of the studied complexes with the atomic numbering are shown in Scheme II.



Scheme II.

STACKING MOTIFS IN STRUCTURES **I** AND **II**

Two crystallographically independent solvent molecules in structure **II** are located at the centers of sym-

metry and, hence, are disordered over two positions with the same occupancy. These molecules occupy the centers of symmetry of two different systems (*i* and *j*) and exhibit different types of disordering. The type of

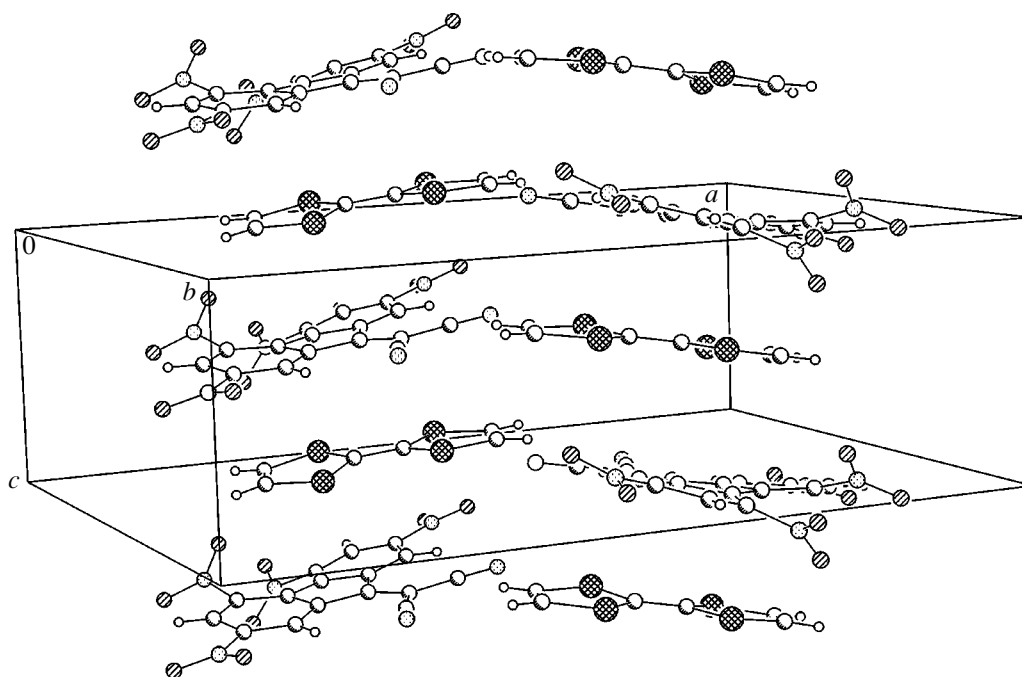
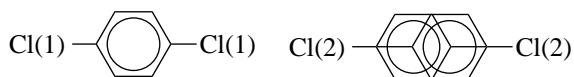


Fig. 1. Stacking structure of charge-transfer complex I.

disordering of the solvent molecules is depicted in Scheme III.



Scheme III.

The molecule at the left is disordered with respect to the symmetry center of the system *i*. This center of symmetry coincides with the center of the benzene ring. The centers of the benzene rings of two disordered components of the molecule at the right are displaced from the symmetry center of the system *j* in opposite directions.

Crystals **I** and **II** are characterized by the same stacking motif of alternating donor and acceptor molecules (Figs. 1, 2), which is typical of charge-transfer complexes. In both crystals, the stacks are aligned along the shortest unit-cell dimension. The nearest-neighbor like molecules inside each stack are related by the translation. The replacement of two NO₂ groups in the 2- and 7-positions of fluorene (in molecule **I**) by the CN groups (molecule **II**) leads to an increase in the linear size of the acceptor molecule. Therefore, in order to provide a close crystal packing, an additional structural block, namely, the solvent molecule, should be introduced into the crystal lattice of compound **II**. The chlorobenzene solvate molecules that belong to the symmetry center system *i* fill part of the free intrastack space and partially occupy cavities between the stacks (Fig. 2). The solvate molecules belonging to the symmetry center system *j* occupy the interstack space and are

arranged at a small angle with respect to the *a* axis in the crystal. However, the structural function of these molecules is not confined only to ensuring a close crystal packing.

In both structures, the mean planes of the donor and acceptor molecules are not strictly parallel to each other. The table presents the short intermolecular distances in the stacking triad with the tetrathiafulvalene molecule sandwiched between two acceptor molecules ("above" and "below"). The mutual orientations of molecules in these triads are shown in Figs. 3 and 4 in projections onto the mean plane of one of the fluorene fragments. It can be seen from these figures that the stacking structures of complexes **I** and **II** differ qualitatively. The acceptor molecules with the tetrathiafulvalene molecule in between are displaced relative to each other in their own planes in structure **II** to a greater extent than in structure **I**. In structures **I** and **II**, the central tetrathiafulvalene molecules are differently located with respect to the fluorene fragments. In structure **I**, the double bond between heterocycles is actually projected outside the tricyclic system. In structure **II**, the double bond predominantly lies between the fluorene tricycles of the upper and lower molecules, even though the chlorobenzene molecule is also located between the two acceptor molecules. This means that the stacking interaction between the donor and acceptor molecules only slightly depends, at least within certain limits, on their mutual displacements and rotations in parallel planes. The data presented in the table also indicate differences in mutual packings of molecules in the stack:

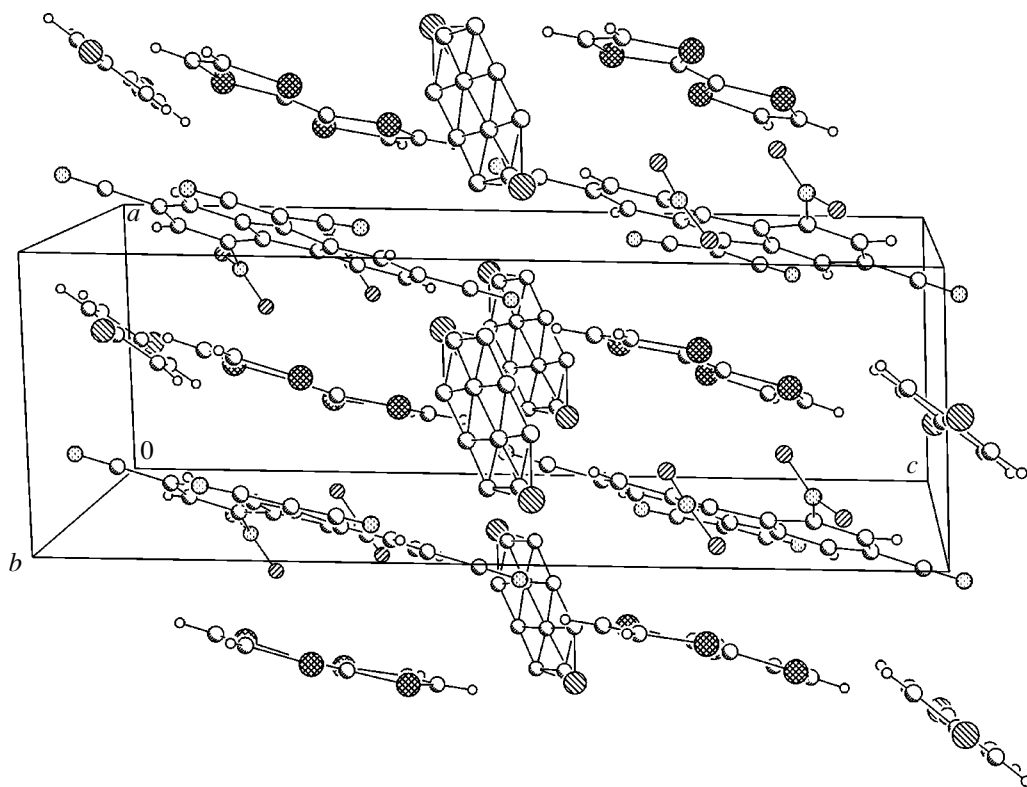


Fig. 2. Stacking structure of charge-transfer complex **II** and location of solvate molecules of both types.

the short intrastack intermolecular contacts in structures **I** and **II** are different.

Compounds **I** and **II** have a common feature in their stacking structure—the intermolecular contacts of the tetrathiafulvalene molecule with one acceptor molecule are generally shorter than those with the other acceptor molecule. This implies that the pair donor–acceptor π – π interactions contribute substantially to the stacking motif of crystal packing.

The described (qualitative and quantitative) differences in the stacking motifs of structures **I** and **II** can be associated with the formation of different systems of intermolecular secondary bonds in the crystals. These bonds are accomplished through different electron–electron interactions (n – σ^* , n – π^* , and p – π^*) with the participation of functional groups of the acceptor and donor molecules. These interactions can change the ratio between the highest occupied and lowest unoccupied molecular orbital levels in the donor and acceptor molecules and, hence, can influence the ability of these molecules to transfer electrons; i.e., these interactions can affect the properties of the charge-transfer complex. In this respect, there is a need to examine the systems of directional secondary bonds and the structural units formed in the crystals as a result of these interactions.

TWO-DIMENSIONAL MOTIFS IN STRUCTURES **I** AND **II**

The crystal structures of both compounds, apart from the stacks, involve infinite sheets of molecules linked through weak interactions. These sheets in structures **I** and **II** differ in appearance and geometry.

Figure 5 shows the puckered sheet of the acceptor and donor molecules linked through different-type secondary interactions in crystal **I**. Each donor molecule forms five short contacts containing three sulfur atoms and two C–H fragments involved in the hydrogen bonds with the CN and NO₂ groups of the neighboring acceptor molecules. Each acceptor molecule is involved in five weak interactions with the neighboring donor molecules through the oxygen atoms of the NO₂ groups and the CN group. The contacts S(1)···O(3) (3.10 Å), S(2)···O(8) (3.20 Å), and S(4)···O(5) (3.24 Å) are somewhat shorter than or comparable to the sum of the van der Waals radii. The O(3) and O(8) oxygen atoms are virtually aligned with one of the S–C bonds of the relevant sulfur atom: the O(3)···S(1)–C(1') angle is equal to 162.8° and the O(8)···S(2)–C(1') angle is 162.2°. The observed geometry of the short contacts is typical [24, 25] and corresponds to the n – σ^* interaction with the participation of the sp^2 orbital of the lone electron pair of the oxygen atom in the NO₂ group and the σ^* orbital of the S–C bond. This geometry is in agreement with the n – π^* interaction involving the p orbital

Short intrastack contacts (Å) between the tetrathiafulvalene molecule and two substituted fluorene molecules located above (molecule *A*) and below (molecule *B*) in structures **I** and **II**

I				II			
TTF-DTeF(<i>A</i>)		TTF-DTeF(<i>B</i>)		TTF-DDDF(<i>A</i>)		TTF-DDDF(<i>B</i>)	
S(1)–C(8)	3.32	S(1)–C(9)	3.63	S(1)–C(4)	3.61	S(1)–C(11)	3.37
S(2)–C(11)	3.22	S(1)–C(13)	3.60	S(2)–C(2)	3.47	S(1)–C(12)	3.42
S(2)–C(12)	3.39	S(2)–C(10)	3.67	S(2)–C(17)	3.55	S(2)–C(10)	3.45
S(2)–O(4)	3.12	S(2)–C(11)	3.66	S(3)–C(10)	3.86	S(2)–C(1)	3.40
S(4)–C(14)	3.20	S(3)–C(1)	3.64	S(3)–C(1)	3.87	S(2)–C(9)	3.73
S(4)–C(16)	3.42	S(3)–O(1)	3.44	S(4)–C(11)	3.72	S(3)–C(14)	3.22
S(4)–C(15)	3.36	S(4)–C(15)	3.64	S(4)–C(12)	3.46	S(3)–C(15)	3.25
C(1')–C(9)	3.29	S(4)–N(1)	3.78	S(4)–C(13)	3.65	S(4)–C(8)	3.25
C(1')–C(13)	3.31	C(1')–C(9)	3.66	C(1')–C(2)	3.75	S(4)–C(13)	3.60
C(1')–C(10)	3.60	C(1')–C(10)	3.63	C(1')–C(3)	3.74	C(1')–C(9)	3.26
C(2')–C(7)	3.52	C(2')–C(13)	3.59	C(1')–C(4)	3.79	C(1')–C(10)	3.38
C(2')–C(6)	3.67	C(2')–C(12)	3.54	C(1')–C(11)	3.84	C(1')–C(13)	3.48
C(3')–C(5)	3.51	C(2')–C(13)	3.59	C(4')–C(10)	3.55	C(2')–C(4)	3.45
C(3')–C(12)	3.45	C(3')–C(11)	3.76	C(4')–C(1)	3.82	C(2')–C(11)	3.63
C(4')–C(9)	3.27	C(3')–C(12)	3.52	C(4')–C(11)	3.72	C(3')–C(1)	3.68
C(4')–C(14)	3.42	C(6')–N(1)	3.50	C(5)–C(14)	3.64	C(3')–C(2)	3.63
C(6')–N(1)	3.38			C(6')–C(9)	3.69	C(4')–C(13)	3.39
				C(6')–C(13)	3.62	C(4')–C(9)	3.29
				C(4')–C(14)	3.48		
				C(5')–C(15)	3.39		

of the lone electron pair of the sulfur atom and the π^* orbital of the NO_2 group. The $\text{O}(5)\cdots\text{S}(4)\text{--C}(4')$ and $\text{O}(5)\cdots\text{S}(4)\text{--C}(6')$ angles are equal to 123.0° and 137.8° , respectively. However, it is evident that one lone electron pair of the $\text{O}(5)$ atom is oriented toward the line aligned with the $\text{S}(4)\text{--C}(6')$ bond.

One further weak interaction with the participation of the donor and acceptor molecules is the $\text{C}\text{--H}\cdots\text{NC}$ hydrogen bond. The $\text{N}\cdots\text{H}$ distance (2.47 \AA) and the angles $\text{H}(3')\cdots\text{N}(2)\text{--C}(16)$ (150.7°) and $\text{N}(2)\cdots\text{H}(3')\text{--C}(3')$ (163.5°) have standard values for hydrogen bonds of this type [26]. It is quite probable that there exists one more hydrogen bond, namely, the $\text{C}(2')\text{--H}(2')\cdots\text{O}(3)$ hydrogen bond with the $\text{H}(2')\cdots\text{O}(3)$ distance equal to 2.53 \AA . However, the short contact between these atoms can be governed by the geometric constraints on the system of weak interactions.

The weak interactions described above are responsible for the formation of zigzag ribbons in the crystal. The ribbons are linked together into puckered sheets due to the $\text{O}\cdots\text{O}$ interactions between the $\text{O}(1)$ and $\text{O}(7)$ oxygen atoms of the NO_2 groups in the adjacent ribbons. The $\text{O}\cdots\text{O}$ distance (2.87 \AA) most likely corre-

sponds to a very weak interaction with a geometry such that the $\text{O}\cdots\text{O}$ line appears to be nearly perpendicular to the planes of both NO_2 groups (with angles of 85.2° and 85.6°). This geometry is most consistent with the $\pi\text{--}\pi^*$ interactions between these groups.

No other specific interactions, except for the aforementioned $\pi\text{--}\pi^*$ interactions, participate in bonding the puckered sheets. The stacking of these sheets results in the formation of the parallel alternating stacks *...ADADAD...*

The system of secondary bonds in structure **II** differs essentially from that in structure **I**. Figure 6 depicts the sheet in structure **II**. The tracery ribbons formed by conjugate centrosymmetric macrocycles involving two pairs of unlike molecules can be distinguished in the sheet of the crystal. It can be seen that macrocycles of two types alternate in the ribbon. A macrocycle of the first type is formed through secondary bonds and has a large cavity that contains the *j*-type solvent molecule. The minimum size of this cavity (i.e., the distance between the acceptor hydrogen atoms oriented toward the interior of the macrocycle) is equal to 6.75 \AA . The cavity is large enough to house the solvent molecule (see Fig. 6). The macrocycle is formed by secondary

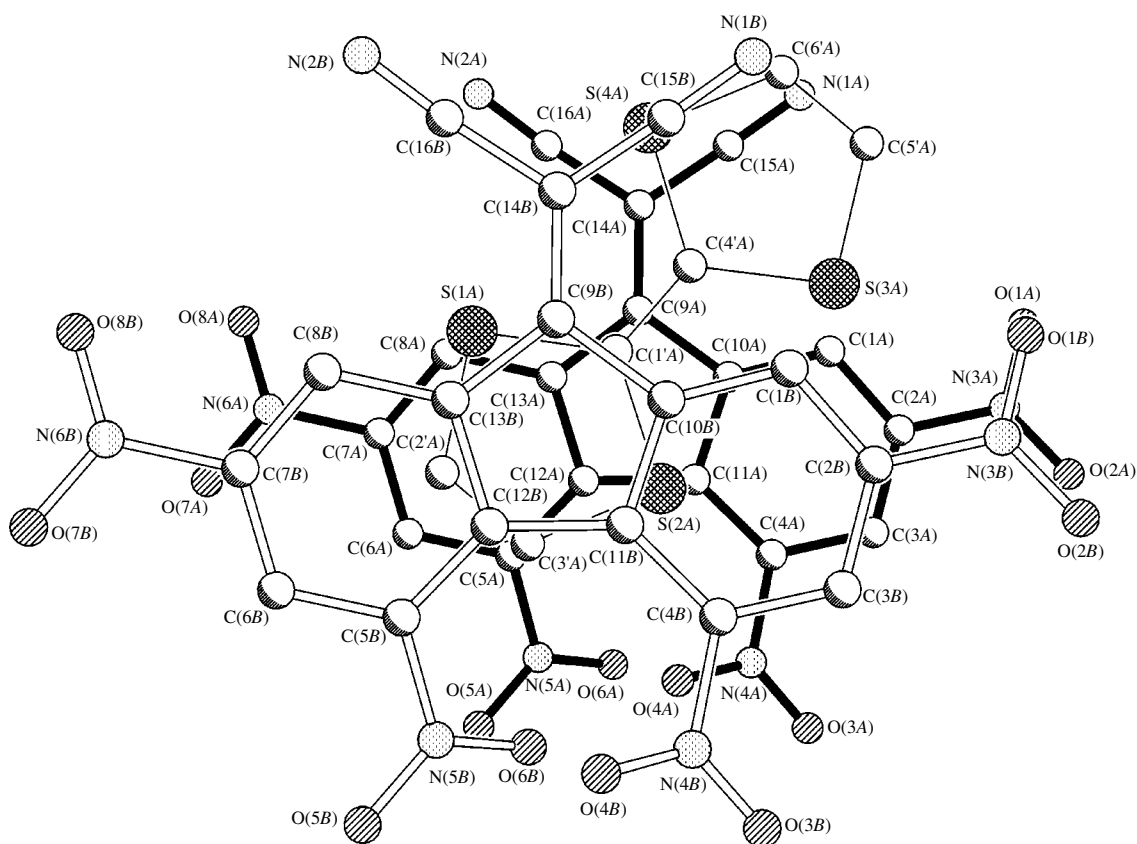


Fig. 3. Mutual arrangement of molecules in the DTef-TTF-DTef triad in a stack of structure I. In atomic numbering, the letter A indicates the basis molecules and B refers to the acceptor molecule related to the basis molecule by the translation z .

bonds of the O...S and N...S types with the participation of the S(3) and S(2) atoms of the tetrathiafulvalene molecules, the O(2) atom of the NO₂ group, and the N(3) atom of the CN group of the acceptor molecules. The S...O and S...N distances are equal to 3.04 and 3.08 Å, respectively. The O(2)...S(3)-C(4'), N(3)...S(2)-C(1'), S(3)...O(2)-N(4), and S(2)...N(3)-C(17) angles are 172.8°, 168.3°, 130.7°, and 173.8°. These parameters are geometrically favorable for the $n-\sigma^*$ and $n-\pi^*$ interactions.

Each tetrathiafulvalene molecule is involved in one more weak interaction: the CH group participates in the formation of the hydrogen bond with the CN group of the acceptor molecule that belongs to the adjacent four-component macrocycle of the second type. The N(6)...H(6') distance is equal to 2.45 Å, and the N(6)...H(6')-C(6') and H(6')...N(6)-C(18) angles are 162.5° and 161.2°, which is typical of hydrogen bonds involving nitrile groups. This macrocycle contains no cavity large enough to house the solvent molecule. Solvent molecules of the *i* type are located outside the ribbons. Each of these molecules participates in the sheet formation through the C-H...NC hydrogen bonds of two centrosymmetrically related acceptor molecules belonging to the adjacent ribbons. These hydrogen bonds have a conventional geometry: the angles at the

H and N atoms are equal to 162.4° and 170.7°, and the N(1)...H(3') distance is 2.49 Å. Moreover, the Cl atom of the chlorobenzene molecule is involved in the secondary interaction with the fluorene molecule. This interaction is rather strong: the Cl...N distance is 3.14 Å, the angle at the Cl atom is 159.5°, and the angle at the N(6) atom is 105.7°. Since the Cl atom in this molecule is disordered over two positions, several alternative descriptions of the crystal structure become possible. For example, one view holds that the Cl atom is statistically disordered over two positions in each sheet. According to other variants, the packing is characterized by different types of local ordering within either ribbons, or sheets, or domains. The crystal packing has defied adequate description only on the basis of X-ray diffraction experiment. However, this is of no fundamental importance, because even the aforementioned hydrogen bonds will suffice to link the ribbons into sheets.

Apart from the weak interaction within the sheet, the Cl atom is involved in the intersheet weak interaction with the N atom of the CN group in the 7-position (see Fig. 7). The Cl(1A)...N(6C) distance is 3.29 Å, and the C(1'A)-Cl(1A)...N(6C) and Cl(1A)...N(6C)-C(18C) angles are equal to 93.9° and 94.4°, respectively. Figure 7 also shows the intersheet short contacts

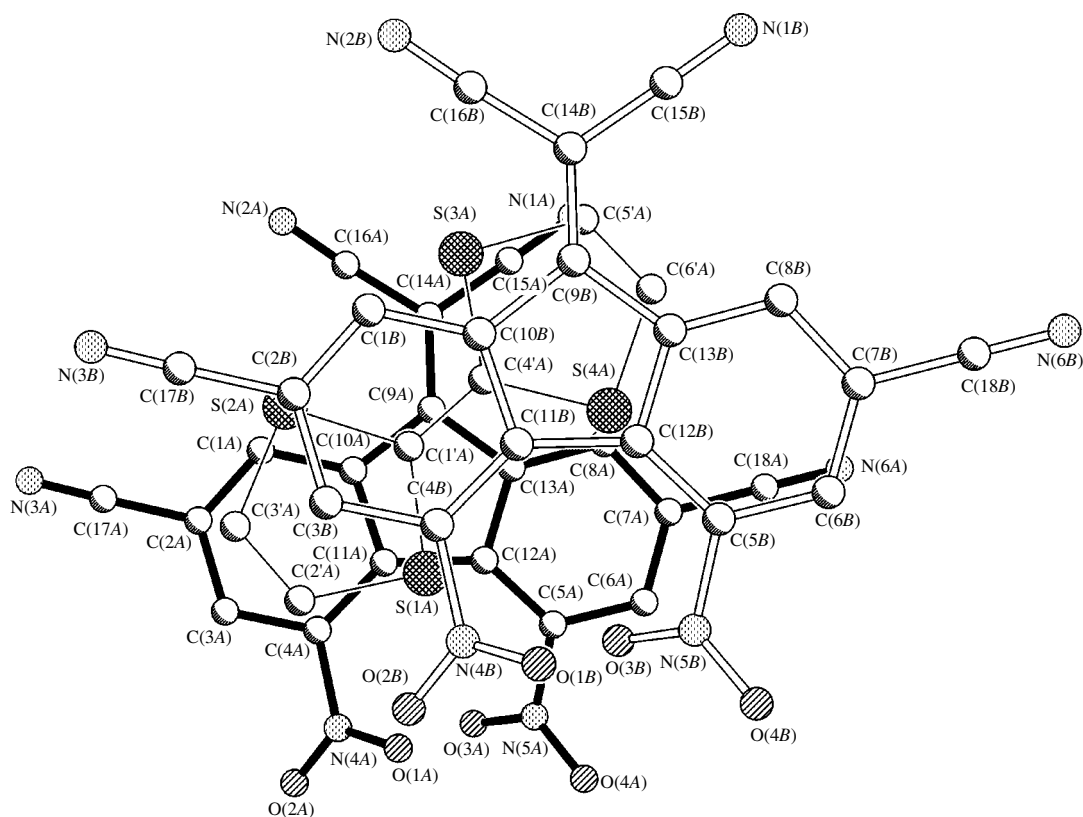
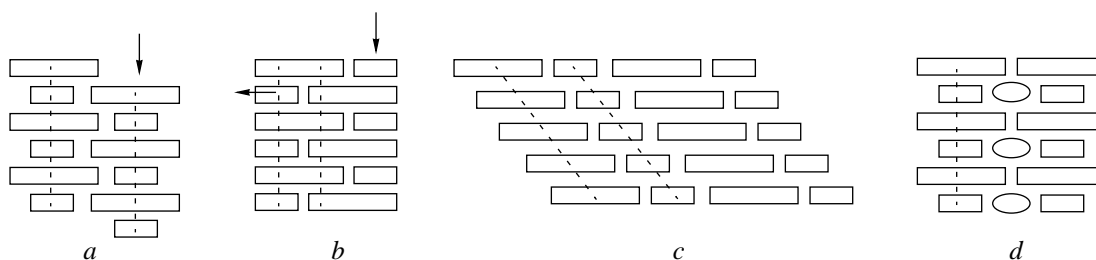


Fig. 4. Mutual arrangement of molecules in the DDDF-TTF-DDDF triad in a stack of structure **II**. In atomic numbering, the letter *A* indicates the basis molecules and *B* refers to the acceptor molecule related to the basis molecule by the translation *x*.

of the *j*-type solvate molecule, whose role is not confined only to filling the macrocycle cavity. The Cl(2A)⋯N(2A) and Cl(2B)⋯N(2B) distances are 3.16 Å, and the angles at the Cl and N atoms are equal to 154.1° and 129.3°, respectively. For these intersheet secondary bonds, there can also arise different-type crystal packings due to the disordering of the Cl atoms. If the Cl atoms of both solvate molecules are statistically disordered, the sheets are cross-linked at random into a three-dimensional framework. In the case when the elements of local ordering of the Cl atoms are present in the structure, there can arise double sheets or a rather ordered cross-linking of the sheets. However, the elucidation of the actual situation calls for further X-ray structure investigation with crystals grown using solvents such as *p*-dichlorobenzene or toluene.

SCHEMATIC REPRESENTATION OF THE STRUCTURE TYPES OF CHARGE-TRANSFER COMPLEXES

As follows from the above analysis of the crystal packing in structures **I** and **II**, the stack ...ADADAD..., which is composed of the alternating donor and acceptor molecules, is a typical structural motif of the charge-transfer complexes under consideration. The ...ADADAD... stacks built up of the acceptor and donor molecules of different sizes can form several genetically related packings. Scheme IV represents four variants of the supramolecular architecture of alternating stacks in the structure of charge-transfer complexes (the large and small rectangles stand for the large-sized acceptor and small-sized donor molecules, respectively; ovals symbolize the molecules of the third component; and dashed lines show the stack orientation).



Scheme IV.

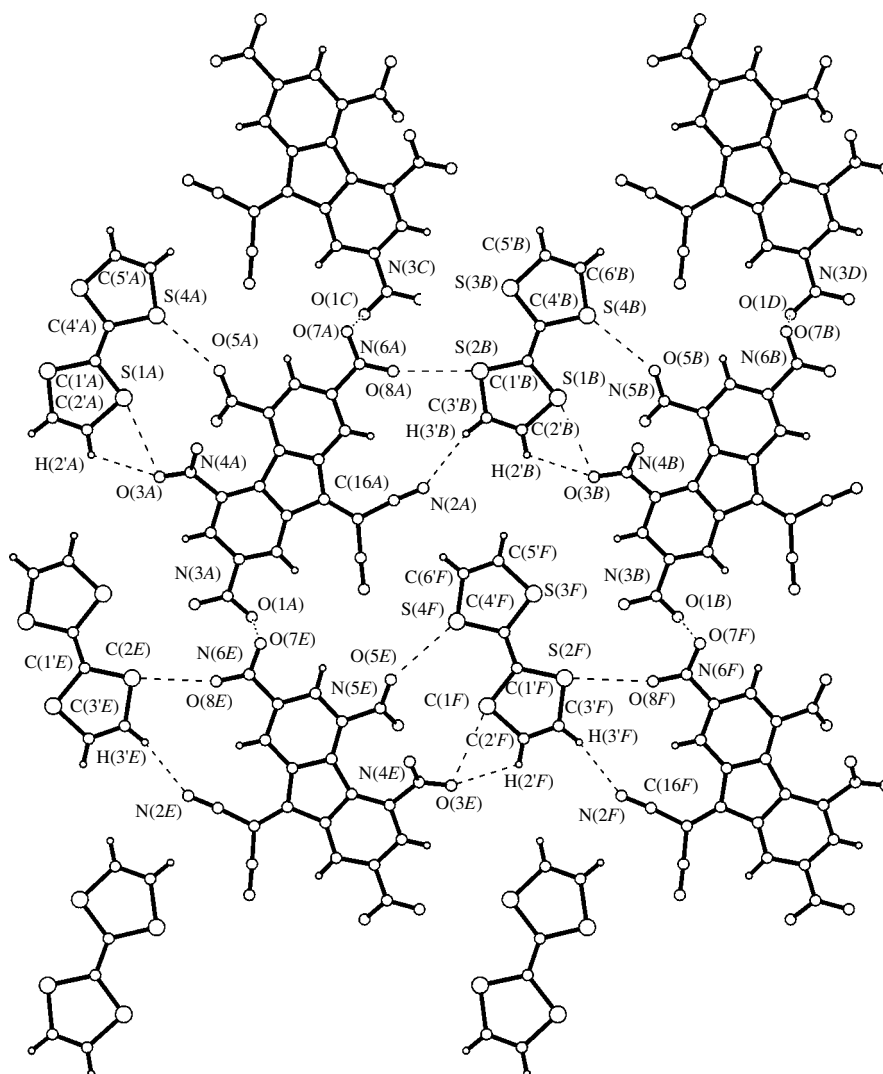


Fig. 5. A sheet of the molecules linked through weak interactions in structure **I**. Letters in atomic numbering indicate different symmetry-related molecules.

In the close packing *a*, one stack is shifted relative to the other stack so that the large-sized acceptor molecules partially fill the interstack space in the vicinity of the small molecule in the adjacent stack. It is this supramolecular architecture that is observed in the charge-transfer complex **I**. As was shown above, the displacement of the small molecules with respect to the large molecules in parallel planes does not affect the π interaction between the acceptor and donor molecules. However, this displacement can result in packing *b*, which is characterized by stacking not only of the type ...ADADAD... but also of the type ...AAA..., i.e., the stacking of large-sized acceptor molecules. It is expected that, in the limit, at a certain size ratio of the acceptor and donor molecules, packing *b* will transform into packing *c* with separate molecular stacks ...AAAA... and ...DDDD... . Packing *c* is especially desirable because it corresponds to the highest (i.e.,

metallic) conductivity [27]. Thus, the description of the packings in the structure of charge-transfer complexes with the use of the graphs considered has revealed their genetic relationship and directed the way to the controlled modification of the supramolecular architecture of these complexes. This can be achieved either by varying the size and shape of the acceptor and donor molecules or by substituting the particular functional groups for the other groups with different geometric constraints on the formation of secondary bonds.

The crystal lattice with packing *d* involves the third component. This packing is characteristic of the structure of complex **II** when solvent molecules of the *j* type are disregarded. Actually, these molecules have no effect on the stacking motif of the crystal, because they are arranged at large angles with respect to the sheets considered above.

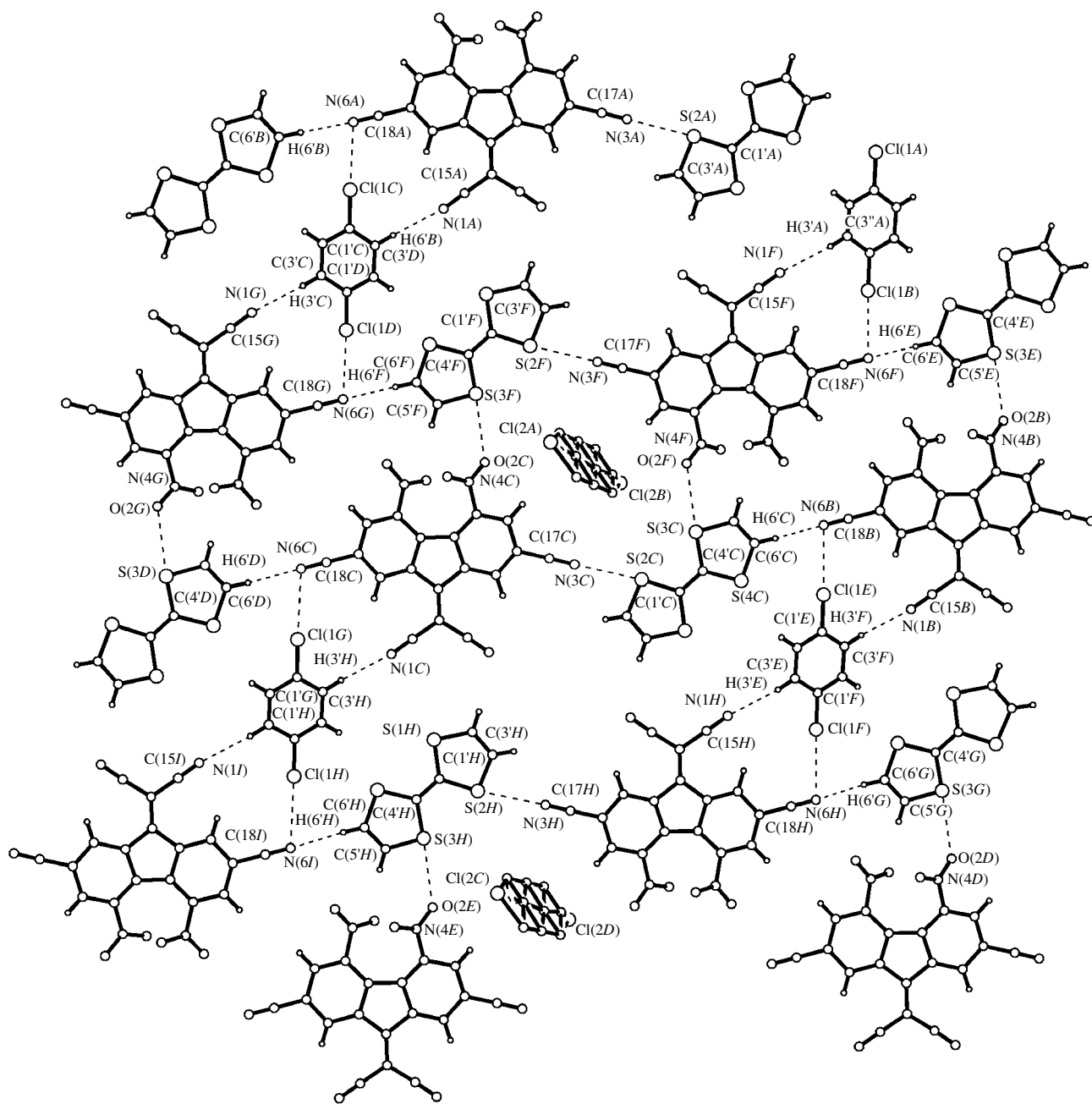


Fig. 6. A sheet of the molecules linked through weak interactions in structure **II**. Letters in atomic numbering indicate the different symmetry-related molecules.

Note that the presence of the *i*-type solvate molecules in the stacks of complex **II** can hardly affect the intrastack π - π interaction, because these molecules possess weak acceptor properties and enter into the stack only around its periphery. However, the inference can be made that, in the case when a molecule similar in size and shape to the chlorobenzene molecule but with the donor or acceptor properties is introduced into the lattice, the properties of the charge-transfer complex can be modified significantly with no change in the general packing motif. This opens up one more way to

the controlled modification of the supramolecular architecture of charge-transfer complexes through the proper choice of the third component.

In principle, other variants of the supramolecular architecture can also be proposed for charge-transfer complexes with a stoichiometry differing from 1 : 1. For example, the structure of complexes with the stoichiometry $A : D = 1 : 2$ can be characterized by packing *d*, in which the second donor molecule plays the role of the third component. It should be noted that

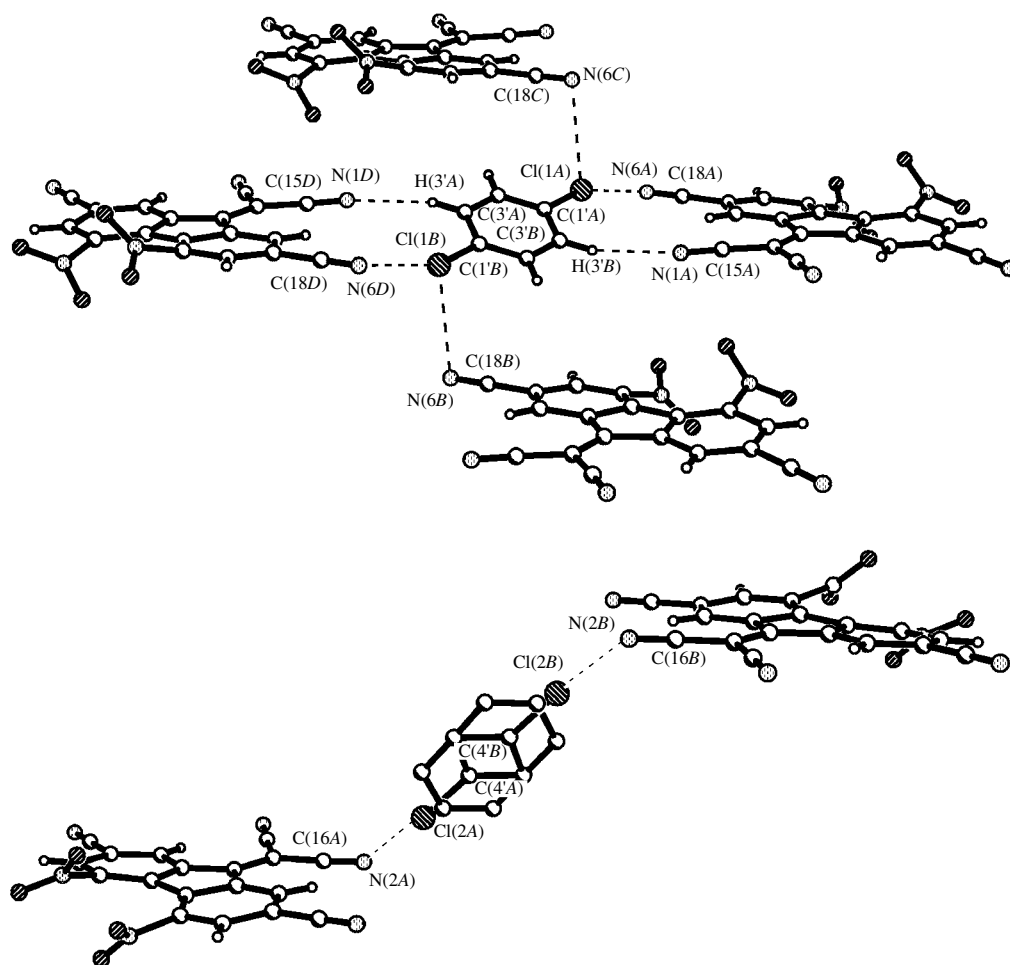


Fig. 7. Weak interactions of the C_6H_5Cl molecules involved in the *i* and *j* systems.

there can also occur more complicated situations, which will be discussed in separate works.

ACKNOWLEDGMENTS

This work was supported by the Russian Foundation for Basic Research (project no. 01-03-32474) and the Royal Society.

REFERENCES

1. V. Khodorhovsky and J. Y. Becker, in *Organic Conductors: Fundamentals and Applications*, Ed. by J.-P. Farges (Marcel Dekker, New York, 1995).
2. J. Ferraris, D. O. Cowan, V. V. Walatka, and J. H. Perlstein, *J. Am. Chem. Soc.* **95**, 948 (1973).
3. M. R. Bryce, *Chem. Soc. Rev.* **20**, 355 (1991).
4. A. Krief, *Tetrahedron* **42**, 1209 (1986).
5. K. Kobayashi and Y. Mazaki, *J. Synth. Org. Chem. (Jpn.)* **46**, 639 (1988).
6. A. Aumüller and S. Hünig, *Angew. Chem., Int. Ed. Engl.* **23**, 447 (1984).
7. S. Hünig, *Pure Appl. Chem.* **62**, 395 (1990).
8. P. Erk, H. Meixner, T. Metzenthin, *et al.*, *Adv. Mater.* **3**, 311 (1991).
9. K. Sinzger, S. Hünig, M. Jopp, *et al.*, *J. Am. Chem. Soc.* **115**, 7696 (1993).
10. S. Hünig, *J. Mater. Chem.* **10**, 1469 (1995).
11. G. R. Desiraju, *Chem. Commun.*, 1475 (1997).
12. G. R. Desiraju, *Angew. Chem., Int. Ed. Engl.* **34**, 2311 (1995).
13. G. R. Desiraju, in *Comprehensive Supramolecular Chemistry*, Ed. by D. D. MacNicol, F. Toda, and R. Bishop (Pergamon, New York, 1996), Vol. 6, pp. 1–22.
14. G. R. Desiraju, *Curr. Opin. Solid State Mater. Sci.*, 451 (1997).
15. J. D. Dunitz, in *The Crystal as a Supramolecular Entity*, Ed. by G. R. Desiraju (Wiley, Chichester, 1996), pp. 1–30.
16. G. R. Desiraju, *Crystal Engineering: The Design of Organic Solids* (Elsevier, Amsterdam, 1989).
17. D. D. Mysyk, I. F. Perepichka, and N. I. Sokolov, *J. Chem. Soc., Perkin Trans. 2*, 537 (1997).

18. D. D. Mysyk, N. M. Sivchenkova, V. É. Kampar, and O. Ya. Neĭland, *Izv. Akad. Nauk Latv. SSR, Ser. Khim.*, 621 (1987).
19. I. F. Perepichka, D. D. Mysyk, and N. I. Sokolov, in *Current Trends in Polymer Photochemistry*, Ed. by N. S. Allen, I. R. Bellobono, M. Edge, and E. Selli (Ellis Horwood, London, 1995), pp. 318–327.
20. Yu. P. Getmanchuk and N. I. Sokolov, in *Fundamentals of Optical Memory and Media* (Vishcha Shkola, Kiev, 1983), issue 14, p. 11.
21. P. Strohriegl and J. V. Grazulevicius, in *Handbook of Organic Conductive Molecules and Polymers*, Ed. by H. S. Nalwa (Wiley, Chichester, 1997), Vol. 1, p. 553.
22. S. Horiuchi, H. Yamochi, G. Saito, *et al.*, *J. Am. Chem. Soc.* **118**, 8604 (1996).
23. I. F. Perepichka, L. G. Kuz'mina, D. F. Perepichka, *et al.*, *J. Org. Chem.* **63**, 6484 (1998).
24. L. G. Kuz'mina, *Koord. Khim.* **25** (9), 643 (1999).
25. A. Ellern, J. Bernstein, J. Y. Becker, *et al.*, *Chem. Mater.* **6**, 1378 (1994).
26. W. F. Cooper, J. W. Edmonds, F. Wudl, and P. Coppens, *Cryst. Struct. Commun.* **3**, 23 (1974).
27. F. Vögtle, in *Supramolecular Chemistry: An Introduction* (Wiley, Chichester, 1991), pp. 290–312.

Translated by O. Borovik-Romanova

STRUCTURE
OF ORGANIC COMPOUNDS

Molecular Structure of Diantipyrylphenylmethane
and Its Complex with Neodymium Nitrate

K. A. Lysenko*, M. L. Kuznetsov**, Yu. N. Medvedev**, and B. E. Zaitsev***

* Nesmeyanov Institute of Organoelement Compounds, Russian Academy of Sciences,
ul. Vavilova 28, Moscow, 117813 Russia

** Moscow State Pedagogical University, ul. Malaya Pirogovskaya 1, Moscow, 119882 Russia

*** Russian University of Peoples' Friendship, ul. Miklukho-Maklaya 6, Moscow, 117198 Russia

Received December 13, 2000

Abstract—The structures of diantipyrylphenylmethane (DAPM) and its complex with neodymium nitrate $[\text{Nd}(\text{NO}_3)_3 \cdot \text{DAPM} \cdot \text{CH}_3\text{OH}] \cdot 2\text{CH}_3\text{OH}$ are determined by X-ray diffraction. The free ligand adopts a *trans* conformation with the opposite orientation of the oxygen atoms of the carbonyl groups. In the complex, diantipyrylphenylmethane acts as a bidentate ligand and coordinates the Nd atom through the carbonyl oxygen atoms, thus forming the eight-membered metallocycle. The coordination number of neodymium is nine (six O atoms of the bidentate nitrate groups, two O atoms of diantipyrylphenylmethane, and one O atom of the methanol molecule). © 2002 MAIK "Nauka/Interperiodica".

INTRODUCTION

It is well known that pyrazolone-5 derivatives (specifically diantipyrylphenylmethane and its substituted derivatives) and their complexes with *d* and *f* elements are widely used in pharmacology, analytical chemistry [1], and dye chemistry [2]. Earlier [3], we reported the preparation and spectral properties of the diantipyrylphenylmethane (DAPM) complexes with anhydrous lanthanide nitrates. It was concluded from the IR spectroscopic data that the ligand bidentately coordinates a lanthanide atom through the oxygen atoms of the carbonyl groups. However, analysis of the vibrational spectra cannot provide answers to questions as to which conformation is adopted by the ligand in the complex and which structure (mononuclear or bridging) is formed.

Moreover, the structural data on diantipyrylphenylmethane derivatives and their complexes are few in number [4–6]. In this respect, the aim of the present work was to investigate the molecular structures of diantipyrylphenylmethane (**I**) and its complex with neodymium nitrate (**II**) and to analyze the structural changes in the ligand upon its coordination.

EXPERIMENTAL

Single crystals **I** suitable for the X-ray diffraction study were prepared by recrystallization of DAPM from absolute methanol at room temperature. Complex **II** was synthesized by the reaction between methanol solutions of $\text{Nd}(\text{NO}_3)_3$ (0.3 M) and of the ligand (4×10^{-2} M) in a 1 : 1 stoichiometric ratio [3]. The evaporation of the solution at room temperature in a dry box (P_2O_5 served as a drying agent) for three days resulted

in the precipitation of the single crystals suitable for X-ray structure analysis. The crystal sample used for data collection was sealed in a glass capillary. The crystal data and main refinement parameters for compounds **I** and **II** are summarized in Table 1. Both structures were solved by the direct method, and the non-hydrogen atoms were refined first in the isotropic approximation and then in the anisotropic approximation with the full-matrix least-squares procedure. In structure **I**, the hydrogen atoms were located from the electron-density difference syntheses and refined isotropically. In structure **II**, the positions of the hydrogen atoms were calculated from geometric considerations and refined within the riding model. The hydrogen atoms of the coordinated and solvate methanol molecules in structure **II** could not be included in the refinement, because they were not located. The absolute structure of **II** was determined by the refinement of the Flack parameter [8], whose value was equal to $-0.04(3)$. All the calculations were performed with the SHELXTL PLUS 5 program package [9] on a personal computer. The atomic coordinates for structures **I** and **II** are listed in Tables 2 and 3, respectively.

RESULTS AND DISCUSSION

General views of molecules **I** and **II** with atomic numbering are shown in Figs. 1 and 2, respectively.

The bond lengths and angles in molecule **I** are close to the corresponding parameters in the other pyrazolone-5 derivatives [10, 11]. In the crystal, the molecule adopts a *trans* conformation (Fig. 1) with the opposite orientation of the carbonyl groups with respect to the plane of the C(2)–C(4)–C(6) fragment. This orientation is characterized by the O(1)C(1)C(5)O(2)

Table 1. Crystal data and refinement parameters for structures **I** and **II**

Compound	I	II
Formula	C ₂₉ H ₂₈ N ₄ O ₂	C ₃₂ H ₃₁ N ₇ O ₁₄ Nd
Molecular weight	464.55	881.88
Space group	<i>P</i> 2 ₁ / <i>c</i>	<i>P</i> 2 ₁ 2 ₁ 2 ₁
<i>a</i> , Å	18.152(4)	10.899(3)
<i>b</i> , Å	9.665(2)	13.031(3)
<i>c</i> , Å	14.361(3)	27.377(6)
β, deg	101.71(3)	
<i>V</i> , Å ³	2467.0(9)	3888(2)
<i>Z</i>	4	4
<i>F</i> (000)	984	1776
ρ _{calcd} , g cm ⁻³	1.251	1.506
Diffractometer	CAD-4 Enraf-Nonius	Siemens P3
Radiation	MoK _α (λ = 0.71073 Å)	MoK _α (λ = 0.71073 Å)
μ, cm ⁻¹	0.8	99.00
Absorption correction	None	DIFABS [7]
<i>T</i> _{min} / <i>T</i> _{max}		0.776/0.845
Temperature, K	293(2)	293(2)
Scan mode	θ/5/3θ	θ/2θ
2θ _{max} , deg	50	52
Number of unique reflections	3530	4095
<i>R</i> ₁ [on <i>F</i> for reflections with <i>I</i> > 2σ(<i>I</i>)]	0.0364 (2193 reflections)	0.0425 (3177 reflections)
<i>wR</i> ₂ (on <i>F</i> ₂ for all reflections)	0.1253 (3480 reflections)	0.1447 (4045 reflections)
Number of parameters refined	429	487

pseudotorsion angle equal to 158.3°. The angle between the planes of two pyrazolone rings in molecule **I** is 66.1°. The bond lengths in two antipyrine fragments [C(1)C(2)C(3)N(1)N(2) and C(5)C(6)C(7)N(3)N(4)] of the DAPM molecule have close values (Table 4).

The nitrogen atoms in molecule **I** have the pyramidal environment. The phenyl and methyl substituents at the nitrogen atoms are located on opposite sides of the plane of the pyrazolone ring; the C(9)N(1)N(2)C(12) and C(11)N(3)N(4)C(18) torsion angles are equal to -72.1° and -55.8°, respectively. Note that, for the N(1) and N(3) nitrogen atoms, the mean deviation (0.37 Å) from the plane passing through the atoms bound to N(1) and N(3) is slightly larger than the mean deviation for the N(2) and N(4) atoms (0.19 Å). The flattening of the atomic coordination observed for the N(2) and N(4) atoms is possibly due to their participation in the conjugation with the carbonyl groups. The N–N bond length in both heterocycles is virtually the same and averages 1.411 Å, which is smaller than the standard N_{pyramidal}–N_{pyramidal} bond length (1.45 Å [12]). The dihedral angles between the planes of the phenyl and pyrazole rings in molecule **I** are 35° and 50.3°. For comparison, in the antipyrine molecule, the corresponding angle is equal to -52.1° [10], and in the amidopyrine

molecule, these angles are 37.7° and 40.1° [11]. The N(2)–C(12) and N(4)–C(18) bond lengths [1.424(3) and 1.420(3) Å, respectively] are close to the standard value for the C_{ar}–N_{sp³} bond (1.42 Å [12]). This also indicates the lack of substantial conjugation between the phenyl and pyrazolone rings.

Note that the bond lengths in two C=C–C(O)–N(*Ph*) fragments of the *N*-phenyl substituted antipyrine rings differ slightly from one another. For example, the C(1)–O(1) bond [1.225(3) Å] is slightly shorter than the C(5)–O(2) bond [1.236(3) Å], and the N(4)–C(5) bond [1.388(3) Å] is slightly shorter than the N(2)–C(1) [1.399(3) Å]. The C(2)–C(3) and C(6)–C(7) bond lengths in the two rings are equal to each other [1.350(3) Å]. Therefore, the splitting of the ν(CO) absorption band in the IR spectrum of **I** (1664 and 1644 cm⁻¹) [3] can be attributed to the nonequivalence of the C=O groups in the DAPM molecule.

The C–C–C angles at the C(4) atom are slightly larger than the tetrahedral angle (112.1°–115.7°), and the C(2)C(4)C(24)C(25) and C(6)C(4)C(24)C(25) torsion angles are equal to -146.7° and -12.9°, respectively.

Table 2. Coordinates ($\times 10^4$) and equivalent isotropic thermal parameters (U_{eq} , $\text{\AA}^2 \times 10^3$) of the non-hydrogen atoms in structure **I**

Atom	<i>x</i>	<i>y</i>	<i>z</i>	U_{eq}	Atom	<i>x</i>	<i>y</i>	<i>z</i>	U_{eq}
O(1)	6070(1)	3495(2)	5745(1)	55(1)	C(13)	4405(1)	3061(3)	5159(2)	47(1)
O(2)	8463(1)	-119(2)	7796(1)	45(1)	C(14)	3765(2)	2968(3)	4459(2)	57(1)
N(1)	5472(1)	900(2)	7086(2)	45(1)	C(15)	3388(2)	1730(3)	4279(2)	63(1)
N(2)	5333(1)	1986(2)	6415(2)	42(1)	C(16)	3662(2)	568(3)	4785(2)	56(1)
N(3)	8395(1)	880(2)	5456(1)	41(1)	C(17)	4308(1)	636(3)	5476(2)	47(1)
N(4)	8695(1)	93(2)	6271(2)	41(1)	C(18)	9056(1)	-1183(2)	6160(2)	42(1)
C(1)	6014(1)	2608(2)	6337(2)	38(1)	C(19)	9685(1)	-1556(3)	6816(2)	52(1)
C(2)	6582(1)	1955(2)	7064(2)	35(1)	C(20)	10040(2)	-2794(3)	6716(3)	65(1)
C(3)	6237(1)	974(2)	7493(2)	40(1)	C(21)	9777(2)	-3638(3)	5964(3)	70(1)
C(4)	7415(1)	2307(2)	7299(2)	32(1)	C(22)	9155(2)	-3271(3)	5297(3)	72(1)
C(5)	8355(1)	469(2)	7016(2)	34(1)	C(23)	8778(2)	-2047(3)	5400(2)	59(1)
C(6)	7875(1)	1624(2)	6660(2)	32(1)	C(24)	7552(1)	3865(2)	7472(2)	32(1)
C(7)	7939(1)	1862(2)	5754(2)	36(1)	C(25)	8158(1)	4539(3)	7229(2)	48(1)
C(8)	6547(2)	-15(3)	8286(3)	56(1)	C(26)	8295(2)	5930(3)	7452(2)	56(1)
C(9)	4949(2)	902(5)	7754(3)	68(1)	C(27)	7835(2)	6656(3)	7918(2)	50(1)
C(10)	7605(2)	2963(3)	5077(3)	52(1)	C(28)	7237(1)	5989(2)	8179(2)	49(1)
C(11)	8925(2)	1236(4)	4854(3)	65(1)	C(29)	7097(1)	4614(2)	7951(2)	41(1)
C(12)	4679(1)	1893(2)	5678(2)	39(1)					

The positions of the carbonyl groups allow the participation of the oxygen atoms in the weak intramolecular C–H...O contacts: the O(2) atom approaches the H(4) atom attached to C(4) [O(2)...H(4), 2.49(2) Å; O(2)...C(4), 2.463(3) Å; and the C(4)–H(4)...O(2) angle, 76(1)°], which results in the formation of the planar H-bonded five-membered ring; and the O(1) atom

approaches the H(10a) atom [O(1)...H(10a), 2.26 Å; C(10)...O(1), 3.167(3) Å; and the C(10)–H(10a)...O(1) angle, 141(1)°].

According to the X-ray structure analysis, the composition of complex **II** is represented by the formula [Nd(NO₃)₃ · DAPM · CH₃OH] · 2CH₃OH. The coordination sphere of the metal atom (the coordination num-

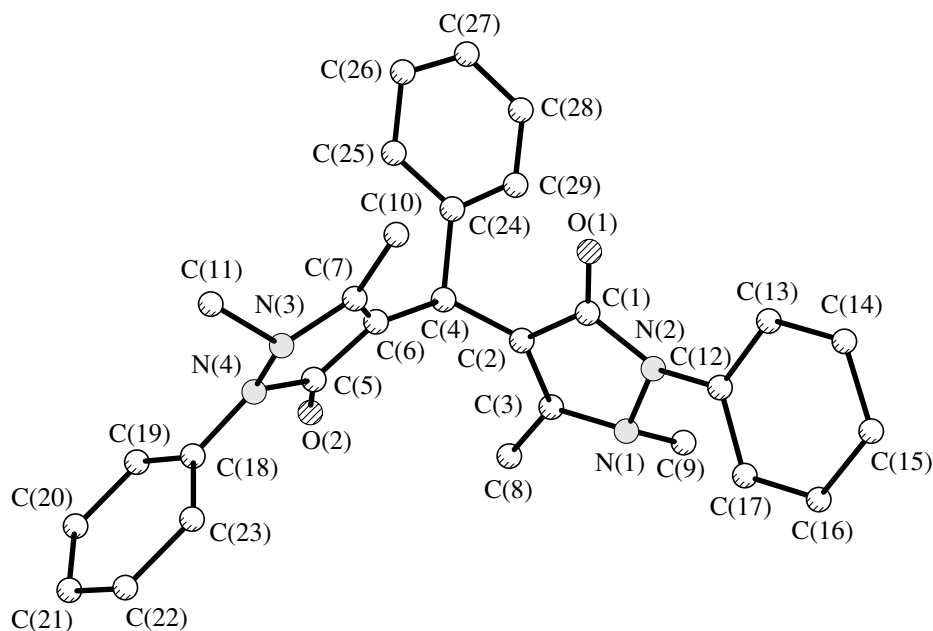
**Fig. 1.** A general view and the atomic numbering in molecule **I**.

Table 3. Coordinates ($\times 10^4$) and equivalent isotropic thermal parameters (U_{eq} , $\text{\AA}^2 \times 10^3$) of the non-hydrogen atoms in structure **II**

Atom	<i>x</i>	<i>y</i>	<i>z</i>	U_{eq}	Atom	<i>x</i>	<i>y</i>	<i>z</i>	U_{eq}
Nd	6260(1)	9770(1)	1228(1)	34(1)	C(8)	10807(9)	12153(9)	38(4)	55(3)
O(1)	6917(5)	11297(4)	856(2)	38(1)	C(9)	10086(11)	13772(8)	785(4)	70(3)
O(2)	7816(6)	8981(5)	777(2)	46(2)	C(10)	11045(8)	9511(7)	-463(3)	51(2)
O(3)	5509(7)	10790(6)	1921(2)	64(2)	C(11)	11431(12)	7553(10)	113(5)	80(4)
O(4)	5612(9)	7912(6)	1119(3)	83(3)	C(12)	8060(8)	12984(7)	1401(3)	37(2)
O(5)	4482(9)	8775(7)	1588(4)	102(4)	C(13)	8881(11)	12995(8)	1787(3)	61(3)
O(6)	4007(12)	7214(8)	1428(5)	146(5)	C(14)	8480(13)	13392(10)	2232(4)	74(4)
O(7)	7301(9)	8930(7)	1950(3)	83(3)	C(15)	7302(16)	13791(11)	2275(5)	92(5)
O(8)	8235(7)	10229(8)	1674(3)	75(2)	C(16)	6537(12)	13741(11)	1900(5)	85(4)
O(9)	9070(10)	9365(11)	2253(4)	142(5)	C(17)	6897(11)	13354(9)	1449(4)	62(3)
O(10)	4283(7)	10637(7)	938(3)	71(2)	C(18)	9775(10)	7496(7)	968(3)	48(2)
O(11)	5150(8)	9685(7)	401(3)	77(2)	C(19)	10785(10)	7552(9)	1272(4)	66(3)
O(12)	3473(8)	10500(10)	222(4)	113(4)	C(20)	10891(17)	6860(11)	1652(5)	93(5)
N(1)	9563(7)	12739(6)	738(3)	42(2)	C(21)	9993(16)	6159(12)	1742(5)	92(5)
N(2)	8425(6)	12548(6)	942(2)	38(2)	C(22)	8994(15)	6118(10)	1434(5)	89(4)
N(3)	10589(7)	8379(6)	245(3)	44(2)	C(23)	8870(13)	6793(8)	1051(4)	67(3)
N(4)	9674(7)	8210(6)	573(3)	44(2)	C(24)	8401(7)	10768(7)	-558(3)	35(2)
N(5)	4666(10)	7952(8)	1380(4)	72(3)	C(25)	8172(9)	9973(6)	-877(3)	49(2)
N(6)	8207(10)	9517(10)	1958(4)	78(3)	C(26)	8033(11)	10129(9)	-1369(3)	60(3)
N(7)	4295(8)	10289(9)	521(4)	70(3)	C(27)	8158(11)	11112(10)	-1555(3)	65(3)
C(1)	7910(7)	11700(6)	716(3)	32(2)	C(28)	8363(9)	11934(7)	-1237(4)	55(2)
C(2)	8718(9)	11433(6)	324(3)	34(2)	C(29)	8464(8)	11744(7)	-739(3)	40(2)
C(3)	9685(8)	12089(7)	349(3)	39(2)	C(30)	6116(18)	11096(12)	2365(5)	112(6)
C(4)	8432(6)	10528(6)	3(3)	29(2)	C(1S)	1113(16)	10523(14)	1239(4)	113(5)
C(5)	8788(9)	8947(6)	516(3)	34(2)	O(1S)	1108(12)	10452(14)	1727(5)	182(7)
C(6)	9162(7)	9587(6)	128(3)	31(2)	C(2S)	3197(10)	11131(8)	2133(3)	100(3)
C(7)	10265(8)	9218(7)	-39(3)	42(2)	O(2S)	2893(21)	11825(16)	2518(7)	141(8)

ber is nine) is formed by three bidentate nitrate groups, two oxygen atoms of the carbonyl groups of DAPM, whose coordination results in the closure of the eight-membered metalocycle, and the methanol molecule (Fig. 2). Thus, our earlier conclusion concerning the bidentate coordination of DAPM in lanthanide complexes, which was made based on the analysis of the IR spectra [3], is confirmed by the X-ray diffraction study.

It should be noted that the lanthanide complexes with bidentate nitrate groups are characterized by the largest coordination numbers, which, apparently, can be explained by the forced shortening of the O...O distance in the nitrate group to 2.14 Å [13]. If the bidentate nitrate groups are treated as pseudomonodentate ligands, the coordination polyhedron of the neodymium atom can be described as a severely distorted octahedron.

The Nd–O distances vary in the range 2.335(6)–2.569(7) Å: the Nd–O_{DAPM} distances are the shortest among them [2.335(6) and 2.348(6) Å], whereas the

Nd–O_{NO₃} bonds are longer [2.528(8)–2.569(7) Å]. A similar situation is observed for many of the nitrate complexes [14, 15]. The structure parameters of the nitrate groups, which form virtually planar chelate rings with the neodymium atom, are similar to those described in [13–15]. The Nd–O_{MeOH} bond length is 2.357(7) Å.

The coordination of DAPM results in considerable structural changes in the ligand. First, the DAPM molecule undergoes a conformational transformation: the molecule changes over from the *trans* conformation in the free ligand to the *cis* conformation with the O(1)C(1)C(5)O(2) pseudotorsion angle equal to -13.8°. The angle between the planes of two pyrazolone rings in the coordinated DAPM molecule decreases only slightly (from 61.6° in the free ligand to 56.0° in the complex). The bond lengths in the C(1)C(2)C(3)N(1)N(2) and C(5)C(6)C(7)N(3)N(4) antipyrine fragments of complex **II** differ insignificantly, as is the case in the uncoordinated ligand.

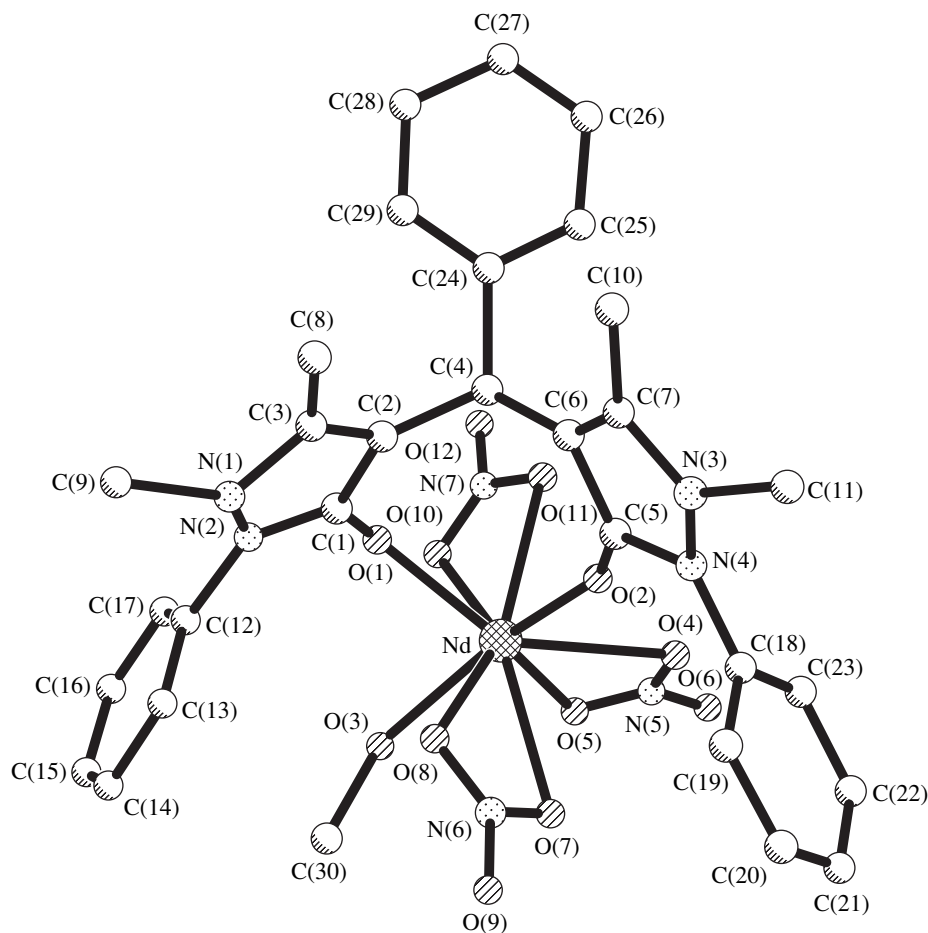


Fig. 2. A general view and the atomic numbering in molecule II.

Table 4. Selected bond lengths d (Å) and angles ω (deg) in structure I

Atoms	d	Atoms	d
O(1)–C(1)	1.225(3)	N(3)–C(11)	1.459(4)
O(2)–C(5)	1.236(3)	N(4)–C(5)	1.388(3)
N(1)–C(3)	1.396(3)	N(4)–C(18)	1.420(3)
N(1)–N(2)	1.413(3)	C(1)–C(2)	1.455(3)
N(1)–C(9)	1.479(4)	C(2)–C(3)	1.350(3)
N(2)–C(1)	1.399(3)	C(2)–C(4)	1.521(3)
N(2)–C(12)	1.424(3)	C(4)–C(6)	1.512(3)
N(3)–C(7)	1.383(3)	C(5)–C(6)	1.445(3)
N(3)–N(4)	1.409(3)	C(6)–C(7)	1.350(3)
Atoms	ω	Atoms	ω
C(3)–N(1)–N(2)	105.8(2)	C(7)–N(3)–N(4)	105.6(2)
C(3)–N(1)–C(9)	116.3(2)	C(7)–N(3)–C(11)	122.0(2)
N(2)–N(1)–C(9)	113.1(2)	N(4)–N(3)–C(11)	115.4(2)
C(1)–N(2)–N(1)	109.6(2)	C(5)–N(4)–N(3)	109.9(2)
C(1)–N(2)–C(12)	125.7(2)	C(5)–N(4)–C(18)	126.9(2)
N(1)–N(2)–C(12)	117.9(2)	N(3)–N(4)–C(18)	119.0(2)

The coordination of the Nd atom in DAPM leads to a lengthening of the C–O carbonyl bonds [C(1)–O(1), 1.26(1) Å and C(5)–O(2), 1.28(1) Å] and a significant shortening of the N–N bonds [N(1)–N(2), 1.38(1) Å and N(3)–N(4), 1.36(1) Å]. Note that, despite the difference in the C(1)–O(1) and C(5)–O(2) bond lengths in the coordinated ligand, the IR spectrum of this complex exhibits a single $\nu(\text{CO})$ band with a maximum at 1611 cm^{-1} . It is possible that the splitting of the band is not observed because of the considerable width of this band.

The coordination of the DAPM molecule results also in a significant flattening of the configuration of the bonds involving the nitrogen atoms. The deviations of the N(1) and N(2) atoms from the planes passing through the adjacent atoms are 0.12 and 0.22 Å, respectively. The corresponding deviations of the N(3) and N(4) atoms are 0.17 and 0.06 Å, respectively. Note that, similar to the uncoordinated ligand, the phenyl and methyl substituents in both substituted antipyrine fragments are located on opposite sides of the pyrazolone ring. The C(9)N(1)N(2)C(12) and C(11)N(3)N(4)C(18) torsion angles are -38.2° and 31.4° , respectively. A comparison of the bond length

distributions in the pyrazolone heterocycles of the free and coordinated DAPM molecules suggests that the coordination of the DAPM molecule enhances the conjugation of the nitrogen atoms with the C=C–C=O fragment. This leads to a flattening of the environment of the nitrogen atoms, a shortening of the N–C bonds (1.37–1.39 Å), and an additional lengthening of the C=C [1.36(1) and 1.37(1) Å] and C=O bonds.

The lengths of the N–C bonds between the pyrazolone and phenyl rings and the C–C bonds at the C(4) atom change insignificantly. This indicates that, in the DAPM molecule involved in the complex, there occurs virtually no conjugation between the pyrazolone rings nor between the phenyl and pyrazolone rings. The angles between the planes of the phenyl and pyrazolone rings in the complex (52.8° and 57.0°) are smaller than those in the free ligand.

ACKNOWLEDGMENTS

This study was supported by the Russian Foundation for Basic Research (project no. 00-03-32807) and the State Program of Support for Leading Scientific Schools of the Russian Federation (project no. 00-15-97359).

REFERENCES

1. *Diantipyrylphenylmethane and Its Homologs as Analytical Reagents*, Ed. by S. I. Gusev (Permsk. Univ., Perm, 1974).
2. N. V. Trofimov, N. A. Kanaev, and A. I. Busev, *Zh. Obshch. Khim.* **45** (2), 385 (1975).
3. M. L. Kuznetsov, Yu. N. Medvedev, B. E. Zaitsev, *et al.*, *Zh. Neorg. Khim.* **40** (2), 259 (1995).
4. V. K. Bel'skiĭ, D. I. Semenishin, V. I. Yarovets, and O. I. Kunt'yĭ, *Kristallografiya* **32** (4), 1029 (1987) [*Sov. Phys. Crystallogr.* **32**, 605 (1987)].
5. Yu. N. Mikhaĭlov, G. M. Lobanova, A. S. Kanishcheva, *et al.*, *Zh. Neorg. Khim.* **28** (8), 2056 (1983).
6. E. Akgun and U. Pindur, *Arch. Pharm. (Weinheim)* **317** (9), 737 (1984).
7. N. Walker and D. Stuart, *Acta Crystallogr., Sect. A: Found. Crystallogr.* **A39**, 158 (1983).
8. H. D. Flack, *Acta Crystallogr., Sect. A: Found. Crystallogr.* **A39**, 876 (1983).
9. G. M. Sheldrick, *SHELXTL, Version 5: Software Reference Manual* (Siemens Industrial Automation Inc., Madison, 1994).
10. T. P. Singh and M. Vijayan, *Acta Crystallogr., Sect. B: Struct. Crystallogr. Cryst. Chem.* **B29** (4), 714 (1973).
11. T. P. Singh and M. Vijayan, *Acta Crystallogr., Sect. B: Struct. Crystallogr. Cryst. Chem.* **B32** (8), 2432 (1976).
12. F. H. Allen, O. Kennard, D. G. Watson, *et al.*, *J. Chem. Soc., Perkin Trans. 2*, S1 (1987).
13. A. Wells, *Structural Inorganic Chemistry* (Clarendon, Oxford, 1984; Mir, Moscow, 1987), Vol. 2.
14. L. A. Aslanov, L. I. Soleva, M. A. Poraĭ-Koshits, and S. S. Goukhberg, *Zh. Strukt. Khim.* **13** (4), 655 (1972).
15. W. T. Carnall, S. Sigel, and J. R. Ferraro, *Inorg. Chem.* **12**, 560 (1973).

Translated by I. Polyakova

CRYSTAL
CHEMISTRY

General Structural Features of Centric and Acentric Polymorphic Pairs of Organic Molecular Crystals: I. Polymorphic Pairs $P2_1/c-P2_12_12_1$

L. N. Kuleshova and M. Yu. Antipin

Nesmeyanov Institute of Organoelement Compounds, Russian Academy of Sciences,
ul. Vavilova 28, Moscow, GSP-1, 117813 Russia

e-mail: lukul.@xrlab.ineos.ac.ru

Received June 27, 2001

Abstract—A systematic investigation into the general structural features of centric and acentric polymorphic pairs of organic molecular crystals is performed using the data available in the Cambridge Structural Database. The main regularities of the formation of these modifications are revealed. The inference is made that the intermolecular association plays an important role in the formation of crystal packing. © 2002 MAIK “Nauka/Interperiodica”.

INTRODUCTION

Investigation into the general structural features of crystalline materials is one of the most important directions of the engineering of organic molecular crystals [1]. This field of research involves the design of organic crystalline materials with a specified molecular arrangement responsible for many physical solid-state characteristics, such as electromagnetic and nonlinear optical properties, electronic and ionic conductivities, etc. Manifestation of certain properties (for example, nonlinear optical properties) requires a noncentrosymmetric arrangement of molecules in the condensed phase [2]. Among the nonlinear optical materials known to date, organic crystals, as before, remain the most interesting objects of investigation.

As a rule, the search for new organic optical nonlinear materials involves a combination of two key stages. The first stage includes the design and synthesis of stable chromophore molecules with high molecular hyperpolarizability (molecular nonlinear optical engineering). The second stage consists in preparing noncentrosymmetric crystals of chromophores with an optimum molecular orientation required to achieve the maximum macroscopic nonlinear optical effect (nonlinear optical engineering of crystals). Currently available techniques of molecular nonlinear optical engineering have been worked out in sufficient detail [2–7]. However, actual approaches to control over the molecular packing in crystals of potentially important compounds are still being developed. The basic problems concerning the prediction and formation of optimum crystal packing are associated with the great diversity of possible molecular orientations that are characterized by minimum differences in free energies in the crystal. It is this circumstance that, in the framework of

the thermodynamic approach, provides an explanation of the existence of different polymorphic systems. In the case when the above differences in free energies increase, the possibility of forming polymorphic modifications decreases. At the same time, the real crystal structure does not necessarily possess a minimum energy, and, in some cases, another polymorphic modification can be obtained only through the change in crystallization conditions. In 1965, McCrone [8] stated that the number of polymorphic modifications of a particular compound is in direct proportion to the time and money spent on their search. Ignoring this circumstance can lead to an underestimate of many promising but centrosymmetric materials, merely because nobody has made an attempt to obtain another (possibly, noncentrosymmetric) modification of the compound under investigation.

It should be noted that the existence of polymorphic modifications is governed not only by the minimum free energy of the crystalline phases but also by the kinetic processes of crystal nucleation and growth. Hence, there is a need to use an approach that makes it possible to evaluate how the crystallization conditions affect the formation of the crystal structure. One way of obtaining this estimate is to treat the crystallization process as a supramolecular synthesis in which the change in the physicochemical conditions brings about the formation of different packings. Within this approach, analysis of possible polymorphism is of crucial importance in designing new promising materials with a specified crystalline architecture. Among the most interesting works in the field of nonlinear optics, special mention should be made of research into the polymorphism of *N*-(2-acetamido-4-nitrophenyl)pyrrolidine, 2-furaldehyde-5-nitro-*N*-benzoylhydrazone, and 2-(4-methoxyphenyl)-5-(4-nitrophenyl)pyrazolidin-5-ene

[9]; 8-(4'-acetylphenyl)-1,4-dioxo-8-azaspiro[4,5]decane [10]; 5-nitro-2-thiophenecarboxaldehyde-4-methylphenylhydrazone [11]; and 2-adamantylamino-5-nitropyridine [12]. However, similar works are still few in number. In this respect, it is of interest to reveal and analyze the general structural features of polymorphic modifications for all currently known compounds that are capable of forming both centric and acentric crystalline modifications. In the future, this information can be useful in designing crystalline materials with a specified molecular arrangement.

First attempts to analyze the data accumulated in the Cambridge Structural Database on compounds with centric and acentric modifications were made by Brock *et al.* [13] in 1991 and led the researchers to a number of important conclusions. First, the universally accepted concept that centrosymmetric (racemic) crystals, as a rule, should possess higher densities and, hence, should be more energetically favorable was disproved. Second, the statistical analysis of the thermodynamic characteristics for polymorphic modifications existing at room temperature [14] revealed that the formation of centrosymmetric crystals are not thermodynamically preferable. On the one hand, the aforementioned conclusions should lend impetus to researchers' efforts to obtain acentric crystalline modifications. On the other hand, these inferences have failed to explain the predominance of centrosymmetric crystals among the structures collected in the Cambridge Structural Database.

In the present work, we undertook a systematic investigation into the structure of polymorphic (centric and acentric) modifications with the aim of revealing the general structural features that are essential to the understanding of the mechanisms of formation of the crystal structure. Moreover, the available data on the conditions and procedures of preparing polymorphs were used to elucidate how these factors affect the formation of crystals. In our opinion, the results of our investigation provide a better insight into the mechanisms of crystallization processes and can be useful in solving many problems of crystal engineering, including important problems concerning the design of acentric crystalline modifications with nonlinear optical properties.

THE CHOICE OF OBJECTS

Theoretically, centric and acentric crystalline modifications of the same compound can be formed upon crystallization either from a racemic mixture of enantiomers containing an asymmetric atom or from a solution containing achiral molecules or molecules with a low barrier to racemization. The former enantiomers are referred to as resolved enantiomers and can have different refcodes in the Cambridge Structural Database. The latter enantiomers are termed unresolved (or rapidly inverted) enantiomers and, as a rule, are described by identical literal refcodes but with a differ-

ent numbering in the Cambridge Structural Database. According to McCrone [8], polymorphic modifications are the crystals capable of forming the same compound upon melting or dissolving. In the strict sense, polymorphic modifications are the crystals that belong only to the latter group of molecules. Since the potential nonlinear optically active molecules of interest fall in this group, we have restricted ourselves to the search for polymorphic modifications with identical literal refcodes. Furthermore, we considered only the most commonly encountered space groups [15], namely, the centrosymmetric space groups $P\bar{1}$, $P2_1/c$, and $Pbca$; the chiral space groups $P2_12_12_1$,¹ $P2_1$, and $P1$; and the racemic but noncentrosymmetric space groups Pc , $Pna2_1$, and $Pca2_1$. For each of these space groups, we created a file containing the refcodes of all the compounds specified by the attribute "form" in the qualifier. All the possible settings (including nonstandard settings) for these groups were taken into consideration. Then, for the purpose of revealing different structures with the same literal refcode, the files of centrosymmetric space groups were compared with the files of noncentrosymmetric space groups by using the specially developed program REFCOMP. A total of 128 pairs of centric and acentric modifications were found in the Cambridge Structural Database (Version 2000). It should be noted that the pairs in which a crystal with the space group $P2_1/c$ serves as a centrosymmetric counterpart are considerably more frequent (101 pairs) in the Cambridge Structural Database as compared to those with the space groups $P\bar{1}$ (19 pairs) or $Pbca$ (8 pairs). Possibly, this stems from the fact that the $P2_1/c$ group is most often encountered in organic compounds. For the refcodes obtained in such a manner, all the data available in the Cambridge Structural Database were extracted through the database query QUEST3D. A number of polymorphic modifications were rejected, because the available data were either incomplete or invalid: errors in the determination of the space group and atomic coordinates, the absence of atomic coordinates, etc.

A preliminary analysis of the composition and structure of the compounds found in the Cambridge Structural Database demonstrated that, as would be expected, the majority of these compounds belong to planar conjugate or aromatic systems in which the chirality arises as the result of insignificant rotations of the functional groups with respect to each other. The nonlinear optical activity is characteristic of eleven compounds, namely, MABZNA, MNPHOL, DEF DAN, BANGOM, FOVYOE, HAMNEO, CLBZNT, BAAANL, TALJIZ, NMBYAN, and SESHUT. The pairs of polymorphic modifications whose molecules belong to the group of resolved enantiomers are also encountered but considerably more

¹ This is the sole noncentrosymmetric space group in which the antiparallel orientation of molecular dipoles excludes manifestations of the nonlinear optical effect.

Table 1. Total number of pairs of centric and acentric modifications available in the Cambridge Structural Database

$P2_1/c-P2_12_12_1$	41	$P\bar{1}-P2_12_12_1$	9	$Pbca-P2_12_12_1$	2
$P2_1/c-P2_1$	17	$P\bar{1}-P2_1$	4	$Pbca-P2_1$	2
$P2_1/c-Pna2_1$	16	$P\bar{1}-Pna2_1$	2	$Pbca-Pna2_1$	2
$P2_1/c-Pca2_1$	3	$P\bar{1}-Pca2_1$	2	$Pbca-Pca2_1$	2
$P2_1/c-Pc$	11	$P\bar{1}-Pc$	2	$Pbca-Pc$	–
$P2_1/c-P1$	4	$P\bar{1}-P1$	3	$Pbca-P1$	–

rarely. For the most part, these modifications are found to occur in the $P2_1/c-P2_12_12_1$ pair. In the present work, we analyzed the general structural features of the $P2_1/c-P2_12_12_1$ pairs of polymorphic modifications. The other pairs listed in Table 1 will be considered in a separate work.

THE $P2_1/c-P2_12_12_1$ POLYMORPHIC PAIRS

As was noted above, the most frequently encountered pair of polymorphic modifications embraces 41 compounds with different chemical compositions. After rejecting the refcodes with incomplete data, we obtained 27 compounds (Table 2). Eighteen compounds that fall in the group of unresolved enantiomers are presented in the first part of Table 2, and nine compounds that belong to the group of resolved enantiomers, organometallic compounds, and complexes are given in the second part of Table 2. Our main concern in the present work is with the former group of compounds, because this group includes the majority of potential organic nonlinear optical materials. However, before proceeding further, we will dwell briefly on the most pronounced structural features of polymorphic modifications belonging to the latter group of compounds.

Polymorphic Pairs of Resolved Enantiomers

The centric and acentric modifications, which belong to the group of resolved enantiomers (nine compounds), were synthesized under the same conditions (one pot polymorphism) in more than half of these cases (JAMLUE, FESKAP, CUMTAF, BARWUM, BUNKOK, and VISSOF). Hereafter, these polymorphic modifications will be referred to as concomitant modifications. Under these conditions, the formation of racemic crystals is accompanied by the spontaneous separation of the enantiomers. Such a high percentage of spontaneously separated enantiomers among the compounds under investigation can be a consequence of the procedure of their choice. Indeed, identical ref-

codes are assigned to the polymorphs formed simultaneously. Otherwise, as was already mentioned, these polymorphs could be specified by different refcodes in the Cambridge Structural Database and they would not be included in the groups of compounds which we chose in this work. Polymorphic modifications of CHAPEP, BIGTIU, and SECZAB precipitated from different solvents (see Table 2). For the most part, the molecules belonging to unresolved enantiomers are rather bulky and do not form intermolecular hydrogen bonds. Therefore, the distinctive structural feature of polymorphic modifications of this group is that the racemic pair of molecules and the pure enantiomer, as a rule, form topologically quite different structures in which identical structural motifs are absent. The unit cell parameters of these polymorphic modifications differ noticeably; however, the unit cell volumes and densities of the polymorphs are found to be rather close in magnitude in the majority of the cases under consideration.

Polymorphic modifications of JAMLUE (Fig. 1) whose molecules contain a hydroxyl group merit more detailed consideration. For this compound, a quite different situation takes place. A system of van der Waals contacts and hydrogen bonds that arise between molecules of the same chirality through interactions of bridging iodide anions brings about the formation of distinct chiral layers. These layers form crystals of two types, namely, the noncentrosymmetric crystals with the $P2_12_12_1$ space group (congruent stacking of molecular layers of the same chirality) and the centrosymmetric crystals with the $P2_1/c$ space group (stacking of molecular layers of different chiralities). In this case, the unit cell parameters prove to be close in magnitude² and the packing densities are also very close in magnitude and differ by only 0.01 g/cm³.

²The unit cell parameters are considered to be close in magnitude in the case when they differ by no more than 5–10%. The same is also true for the angle of monoclinicity, which, as a rule, is close to 90°. The unit cell parameters are multiples when the asymmetric part of the unit cell in one of the modifications under consideration involves several molecules ($Z' > 1$).

Table 2. Polymorphic pairs $P2_1/c$ - $P2_12_12_1$

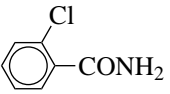
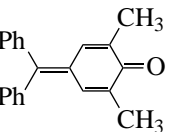
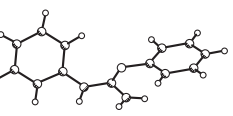
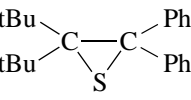
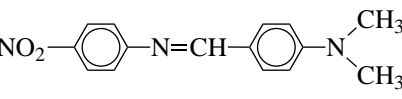
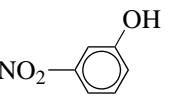
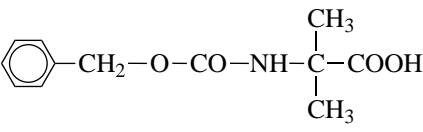
Compound	REFCODE (ΔD)	Space group	Z'	$V, \text{\AA}^3$	$D, \text{g/cm}^3$	Unit cell parameters	Packing fragments	Molecular geometry	Solvent	Comments
Concomitant polymorphic modifications of unresolved enantiomers and chiral molecules										
	CLBZAM (-0.016)	$P2_1/n$ $P2_12_12_1$	1 1	1340.8 1291.6	1.640 1.702	Close	Close	Close	Both from water	Identical systems of hydrogen bonds
	DMFUSC (-0.07)	$P2_1/c$ $P2_12_12_1$	1 1	1596.5 1587.5	1.191 1.198	Close	Close	Close	Both from benzene and cyclohexane	Phase transition $P2_1/c \rightarrow P2_12_12_1$
	DPGUAN (-0.002)	$P2_1/c$ $P2_12_12_1$	2 2	2329.3 2324.5	1.205 1.207	Close	Dif-ferent	Close	Both from ethanol	Different systems of hydrogen bonds
	DTBPTP (+0.048)	$P2_1/c$ $P2_12_12_1$	1 1	1854.5 1933.6	1.162 1.114	Close	Close	Close	Both through evaporation of <i>n</i> -propanol	$T_m = 102^\circ\text{C}; T_{ex} = 140^\circ\text{C}$ $T_m = 114^\circ\text{C}; T_{ex} = 25^\circ\text{C}$
	MABZNA (-0.007)	$P2_1/c$ $P2_12_12_1$	1 4	1347.5 5362.9	1.327 1.334	Mul-tiple	Close	Dif-ferent	Both from the reaction mixture	Phase transition (heating) Nonlinear optical material (potential)
	MNPHOL (-0.064)	$P2_1/c$ $P2_12_12_1$	1 1	625.3 599.1	1.478 1.542	Close	Close	Close	Both from benzene	$T_{ex} = 295 \text{ K}$ $T_{ex} = 22 \text{ K}$, nonlinear optical material (potential)
Nimodipine*	VAWWEV (-0.029)	$P2_1/c$ $P2_12_12_1$	1 1	2194.8 2144.8	1.266 1.295	Close	Close	Dif-ferent	Both from the mother solution, spontaneously	Different positions of methoxy groups
	FIKFIO (+0.071)	$P2_1/c$ $P2_12_12_1$	1 2	1231.1 2607.6	1.279 1.208	Dif-ferent	Dif-ferent	Dif-ferent	Both from the ethyl acetate-petroleum ether mixture	$T_m = 73-74^\circ\text{C}$ $T_m = 84-85^\circ\text{C}$

Table 2. (Contd.)

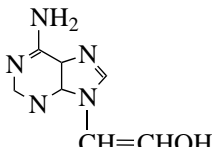
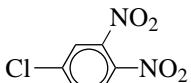
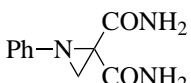
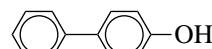
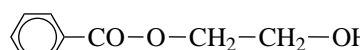
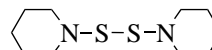
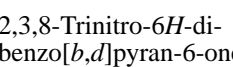
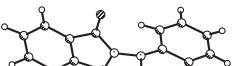
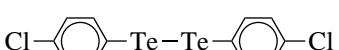
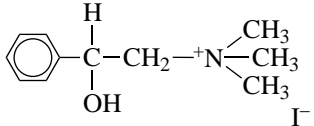
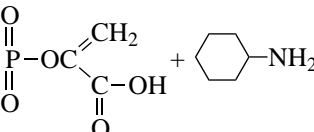
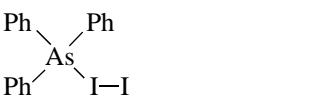
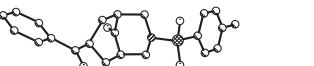
Compound	REFCODE (ΔD)	Space group	Z'	V, Å ³	D, g/cm ³	Unit cell parameters	Packing fragments	Molecular geometry	Solvent	Comments
Polymorphic modifications of unresolved enantiomers prepared from the same solvent under different conditions										
	FABFUJ	$P2_1/c$	3	2450.2	1.457	Multiple	Close	Close	Aqueous solutions, different kinetics	Identical systems of hydrogen bonds
	(-0.008)	$P2_12_12_1$	2	1624.0	1.465					
	(+0.012)	$P2_12_12_1$	1	823.6	1.445					
	DEFDUN	$P2_1/c$	1	625.3	1.478	Different	Different	Different	Hot ethanol	$T_m = 310^\circ\text{C}$
	(-0.064)	$P2_12_12_1$	1	599.1	1.542				Ethanol at room temperature	$T_m = 313^\circ\text{C}$, nonlinear optical material (potential) Phase transition $P2_1/c \rightarrow P2_12_12_1$ Different systems of hydrogen bonds
	COYMOS	$P2_1/n$	1	990.2	1.376	Different	Different	Close	Diluted ethanol	Different systems of hydrogen bonds
	(+0.007)	$P2_12_12_1$	1	995.3	1.369				Concentrated ethanol	
Polymorphic modifications of unresolved enantiomers prepared from different solvents										
	BOPSAA	$P2_1/c$	1	876.1	1.289	Multiple	Close	Close	Sublimation	Identical systems of hydrogen bonds
	(-0.008)	$P2_12_12_1$	2	1743.1	1.297				Acetone, ethanol	
	HETPAL	$P2_1/c$	1/2	1192.6	1.415	Close	Close	Close	Benzene, methanol	Identical systems of hydrogen bonds
	(-0.015)	$P2_12_12_1$	1	1180.7	1.430				Ethyl acetate	
	DPIPDS	$P2_1/c$	1/2	1278.2	1.207	Close	Different	Close	Petroleum ether	
	(+0.001)	$P2_12_12_1$	1	1279.7	1.206				Ethanol	
	CIVTUM	$P2_1/n$	1	1340.8	1.640	Different	Different	Different	Acetone	$T_m = 237-238^\circ\text{C}$
	(-0.062)	$P2_12_12_1$	1	1291.6	1.702				Acetic acid	$T_m = 239-240^\circ\text{C}$
	NOSWAR	$P2_1/n$	2	2353.5	1.345				-	
	PUMVIC	$P2_1/c$	3	3491.2	1.497	Different	Different	Close	-	Charge-transfer complex
	(+0.018)	$P2_12_12_1$	1	1177.9	1.479					
	CLPHTE	$P2_1/c$	1	1371.9	2.315	Different	Different	Different	Dichloroethane	
	(-0.049)	$P2_12_12_1$	1	1343.4	2.364				Petroleum ether-benzene	

Table 2. (Contd.)

Compound	REFCODE (ΔD)	Space group	Z'	V, Å ³	D, g/cm ³	Unit cell parameters	Packing fragments	Molecular geometry	Solvent	Comments
Polymorphic pairs of resolved enantiomers, organometallic compounds, and complexes										
	JAMLUE (+0.010)	$P2_1/c$ $P2_12_12_1$	1 1	1285.0 1293.6	1.587 1.577	Close	Close	Close	Both from the reaction mixture	Identical systems of hydrogen bonds
		CHAPEP (-0.003)	$P2_1/c$ $P2_12_12_1$	1 1	1307.1 1304.6	1.357 1.360	Different	Different	Different	Methyl ethyl ether Water
	FESKAP (-0.041)	$P2_1/c$ $P2_12_12_1$	1 1	1888.4 1850.0	1.969 2.010	Different	Different	Different	Both from the reaction mixture	
		CUMTAF (+0.018)	$P2_1/c$ $P2_12_12_1$	1 1	2603.5 2032.6	1.317 1.298	Different	Different	Different	Both from the reaction mixture upon cooling
Haloxazolam**	BUNKOK	$P2_1/c$	1	1531.0	1.636	Different	Different	Different	From cooled methanol, spontaneously	
***	BARWUM (+0.053)	$P2_12_12_1$ $P2_1/c$	1 2	1590.1 3274.1	1.575 1.471	Different	Different	Different	From the mother solution, spontaneously	$T_m = 103^\circ\text{C}$
****	BIGTIU (-0.004)	$P2_12_12_1$ $P2_1/c$	1 1	1696.5 1808.9	1.418 1.422	Different	Different	Different	CS ₂ <i>m</i> -Xylene	$T_m = 84^\circ\text{C}$
Diethyl-dibenzoberrelene-11,12-dicarboxylate	VISSOF (+0.010)	$P2_12_12_1$ $P2_1/c$	1 2	1806.0 3622.9	1.424 1.277	Different	Different	Different	From ethanol, spontaneously	
4,4-Diphenylcyclohexa-2-en-1-one	SECZAB (+0.010)	$P2_12_12_1$ $P2_1/c$	1 1	1826.0 1372.1	1.267 1.202	Different	Different	Different		
	(-0.048)	$P2_12_12_1$	1	1319.7	1.250					

* Nimodipine is isopropyl-2-methoxyethyl-2,6-dimethyl-4-(3-nitrophenyl)-1,4-dihydro-3,5-pyridinedicarboxylate.

** Haloxazolam is 10-bromo-11*b*(2-fluorophenyl)-2,3,7,11*b*-tetrahydrooxazolo[3,2-*d*][1,4]dibenzodiazepin-6(5*H*)-one.*** 1,3,3,5,5-penta(1-aziridinyl)-1- λ^6 -2,4,6,3,5-thio-triazadiphosphorine-1-oxide.

**** 2,2,4,4,6,6-hexakis(1-aziridinyl)-cyclotri(phosphazene).

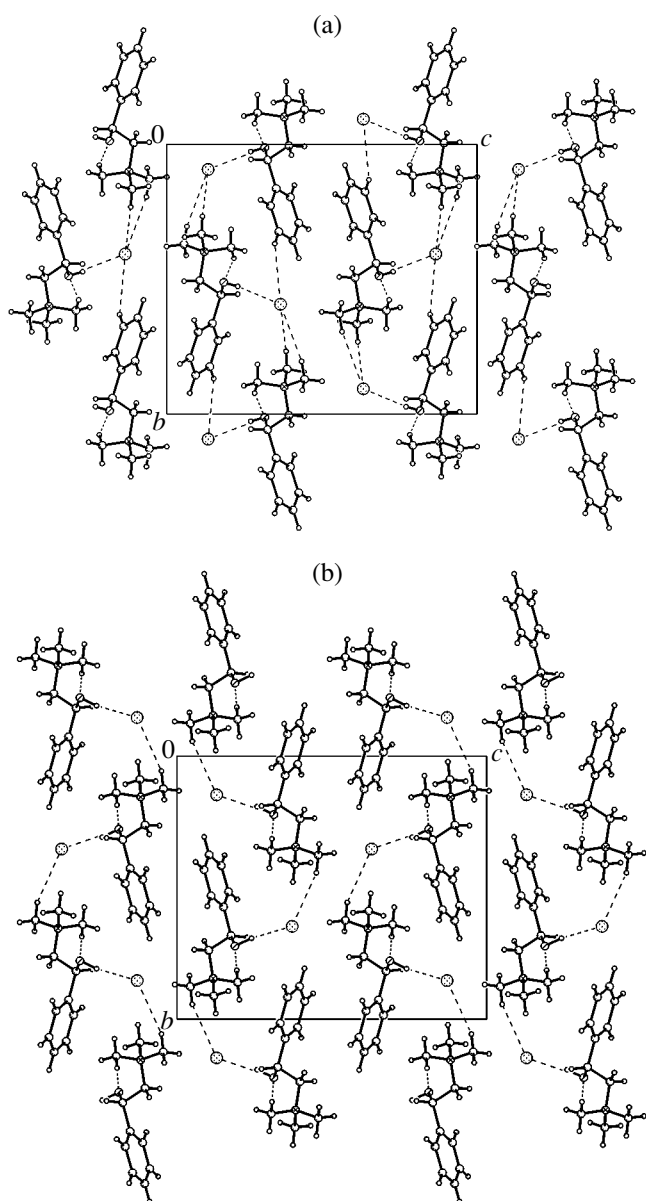


Fig. 1. Packings of identical chiral layers in the (a) $P2_12_12_1$ and (b) $P2_1/c$ modifications of JAMLUE. The layers are arranged in the (110) plane.

Polymorphic Modifications of Unresolved Enantiomers

The centric and acentric modifications, which belong to the group of unresolved enantiomers, are also frequently formed simultaneously (CLBZAM, DMFUSC, DPGUAN, DTBPTP, MABZNA, MNPHOL, FIKFIO, and VAWWEV). (The thermodynamic aspect of the concomitant polymorphism was discussed in detail in the review by Bernstein *et al.* [16].) In three other cases (FABFUJ, DEFUN, and COYMOS), different modifications were prepared through crystallization from the same solvent but under different kinetic conditions by varying the initial con-

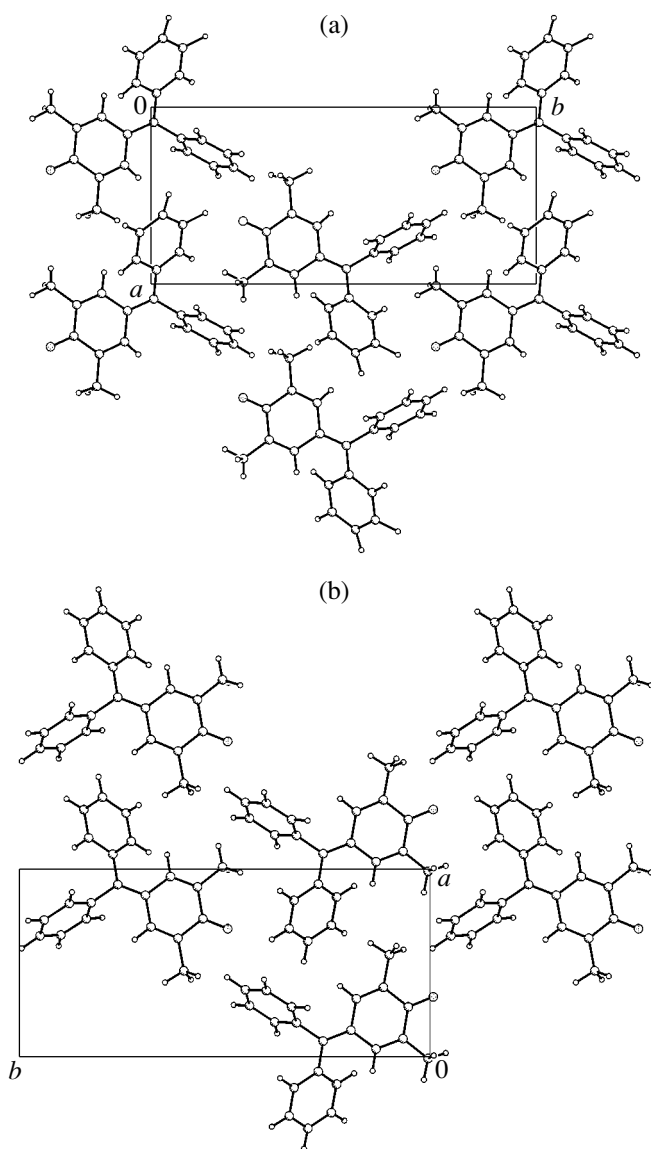


Fig. 2. Projections of identical chiral layers in the (a) $P2_12_12_1$ and (b) $P2_1/c$ modifications of DMFUSC onto the xy plane.

centration, temperature, and crystallization rate. Polymorphic modifications of BOPSAA, HETPAL, DPIPDS, CIVTUM, and CLPHTE were synthesized from different solvents.

The majority of the molecules involved in this group are planar, conjugate, and small in size. The chirality of these molecules stems from insignificant rotations of the functional groups with respect to each other without appreciable expenditure of energy. It is worth noting that different polymorphic modifications of these compounds exhibit an even more pronounced tendency for the unit cell parameters (and, correspondingly, the densities of crystals) to retain the close values, provided that packing fragments remain unchanged.

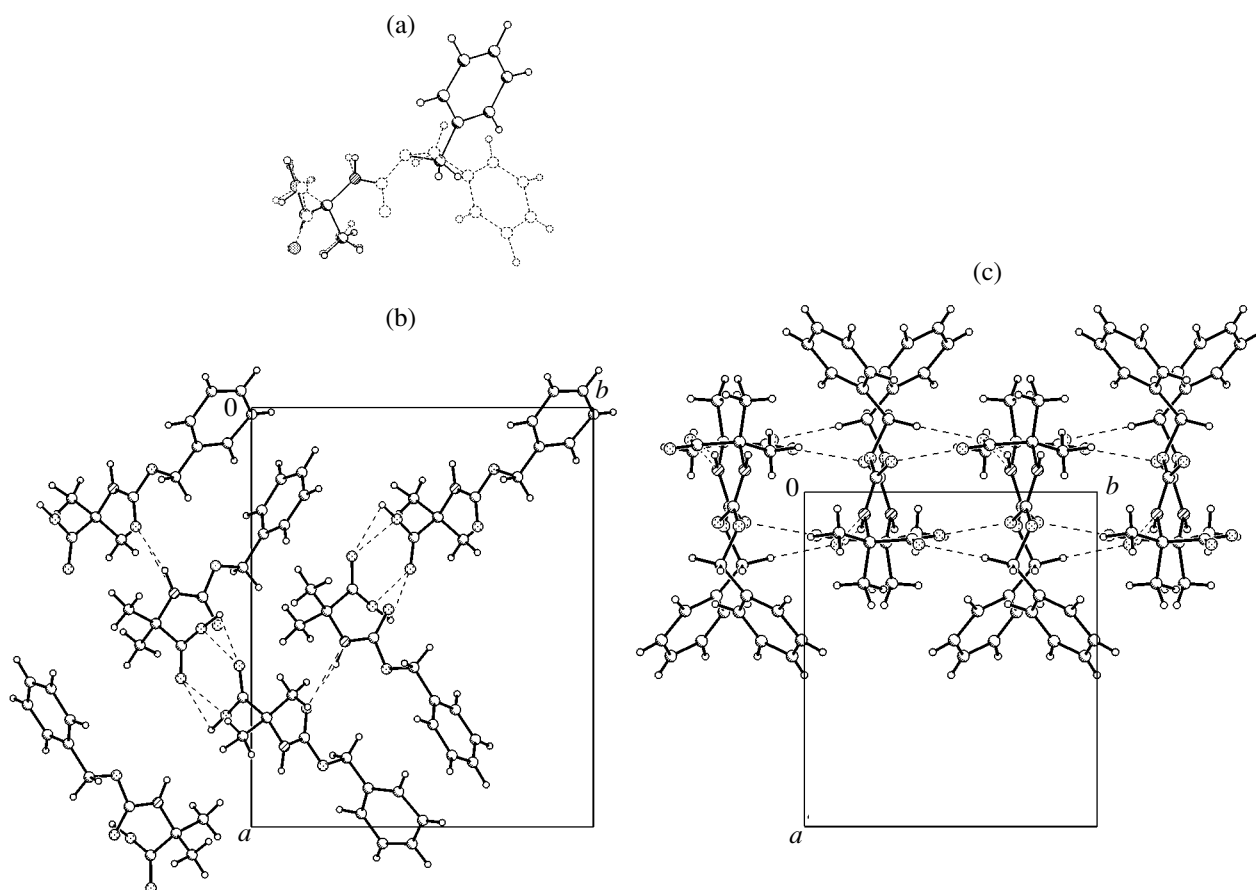


Fig. 3. Modifications of FIKFIO: (a) molecular geometries and molecular packings in the (b) $P2_12_12_1$ and (c) $P2_1/c$ modifications.

Concomitant polymorphic modifications. Identical chiral packing fragments are most frequently observed in concomitant polymorphic modifications. For example, the CLBZAM polymorphs are characterized by identical chiral layers formed at the expense of the intermolecular hydrogen bonds $\text{NH}\cdots\text{O}$. Although the DMFUSC polymorphic modifications contain no hydrogen bonds and the crystals are formed through pure van der Waals interactions, these structures are also built up of identical chiral layers (Fig. 2). The structures of DMFUSC polymorphic modifications differ in their layer stacking: congruent stacking with a shift is observed in the acentric modification and antiparallel stacking with inversion occurs in the centric modification. The polymorphic structural phase transition $\alpha(P2_1/c, Z' = 1) \rightarrow 383 \text{ K} \rightarrow \beta(P2_12_12_1, Z' = 1)$ between the α and β modifications of DMFUSC is observed at a temperature of 383 K. The phase transformation is accompanied by the mutual cooperative rotation of the layers with respect to each other by 30° and the inversion of each second layer. A similar situation arises with polymorphic modifications of VAWWEV. In these compounds, chains containing molecules of the same chirality are formed through hydrogen bonds. The chains of the same chirality form a noncentrosym-

metric crystal, whereas the chains of different chiralities are linked together to form a centrosymmetric structure with unit cell parameters that are close in magnitude. Identical stable chiral fragments are revealed in other concomitant modifications of this group. The sole exception is represented by the FIKFIO polymorphic modifications (Fig. 3). These modifications involve different molecular associates and, hence, are characterized by different packing densities and different lattice parameters. In this case, the formation of different supramolecular fragments can be explained by the fact that molecules with different conformations already coexist in a solution of this compound.

A very interesting example of different packings formed by identical molecular associates is provided by the DPGUAN modifications. Both crystalline forms are characterized by $Z' = 2$; i.e., they are polysystem crystals. In both modifications, the chains with a similar structure (Fig. 4) are composed of crystallographically different molecules. Note that both chains are pseudocentrosymmetric. In the noncentrosymmetric crystal, molecules in the chain are related by an approximate glide-reflection plane along the c -axis. In the centrosymmetric crystal, molecules in the chain are related by the glide-reflection pseudoplane a , which approximately

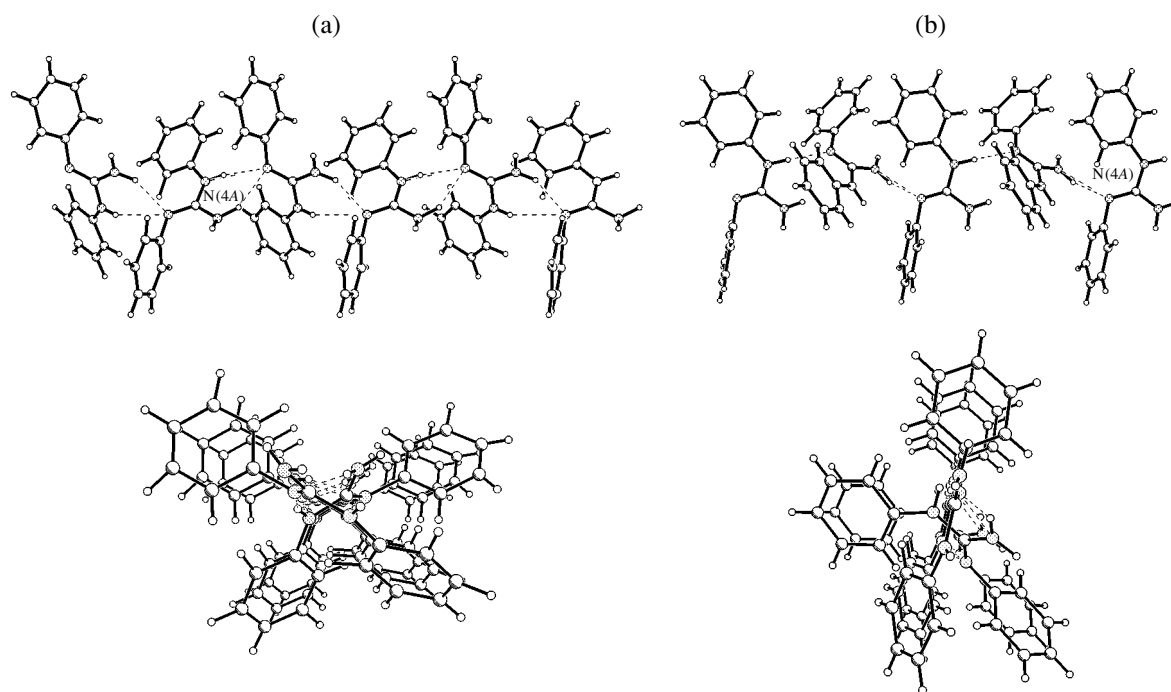


Fig. 4. Structures of chains formed by independent molecules in the (a) $P2_12_12_1$ and (b) $P2_1/c$ modifications of DPGUAN in the projections parallel and perpendicular to the chain.

coincides with the (1 1 0) plane. A detailed analysis of the molecular packing in these crystals according to the scheme proposed in our earlier work [17] revealed that both pseudosymmetric crystals can be treated as the same hypothetical crystal with the pseudogroup of higher symmetry: $[(P2_12_12_1, Z' = 2) + c(1, 0.25, 1)] \rightarrow (Pbca, Z' = 1) \leftarrow [(P2_1/c, Z' = 2) + a(110)]$. However, no real crystal with this symmetry was found.

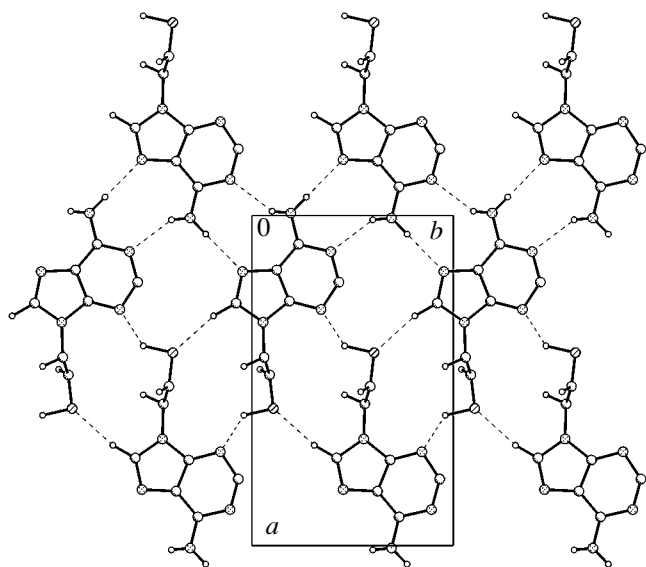


Fig. 5. Structure of a chiral layer in the FABFUJ modification.

Polymorphic modifications prepared from the same solvent under different conditions. Identical and stable supramolecular fragments can be formed not only in concomitant modifications but also in polymorphs precipitated from the same solvent under different conditions by varying the concentration, temperature, or crystallization rate. An example of the kinetic polymorphism is represented by the FABFUJ polymorphic modifications. The main crystallographic parameters of these modifications and the conditions of their preparation are given in Table 3. Modifications **II** and **III** belong to polysystem crystals and exhibit a pseudosymmetry (the pseudosymmetry was thoroughly considered in our recent work [17]). All three polymorphic modifications presented in Table 3 are built up of identical chiral layers (Fig. 5), which, in turn, are formed through hydrogen bonds. Note that these modifications differ only in the type of layer packing. A rapid cooling of the saturated solution leads to the formation of crystals with antiparallel packing and inversion, whereas the structure of crystals grown through evaporation from diluted solutions is characterized by congruent packing (Fig. 6). It is worth noting that modification **II** grown under virtually equilibrium conditions has the highest density and is completely ordered, whereas modifications **I** and **III** are partially disordered along the c -axis.

In some cases, especially when molecules are not involved in strong intermolecular hydrogen bonds, a change in the crystallization temperature can bring about a change in the orientation of substituents and,

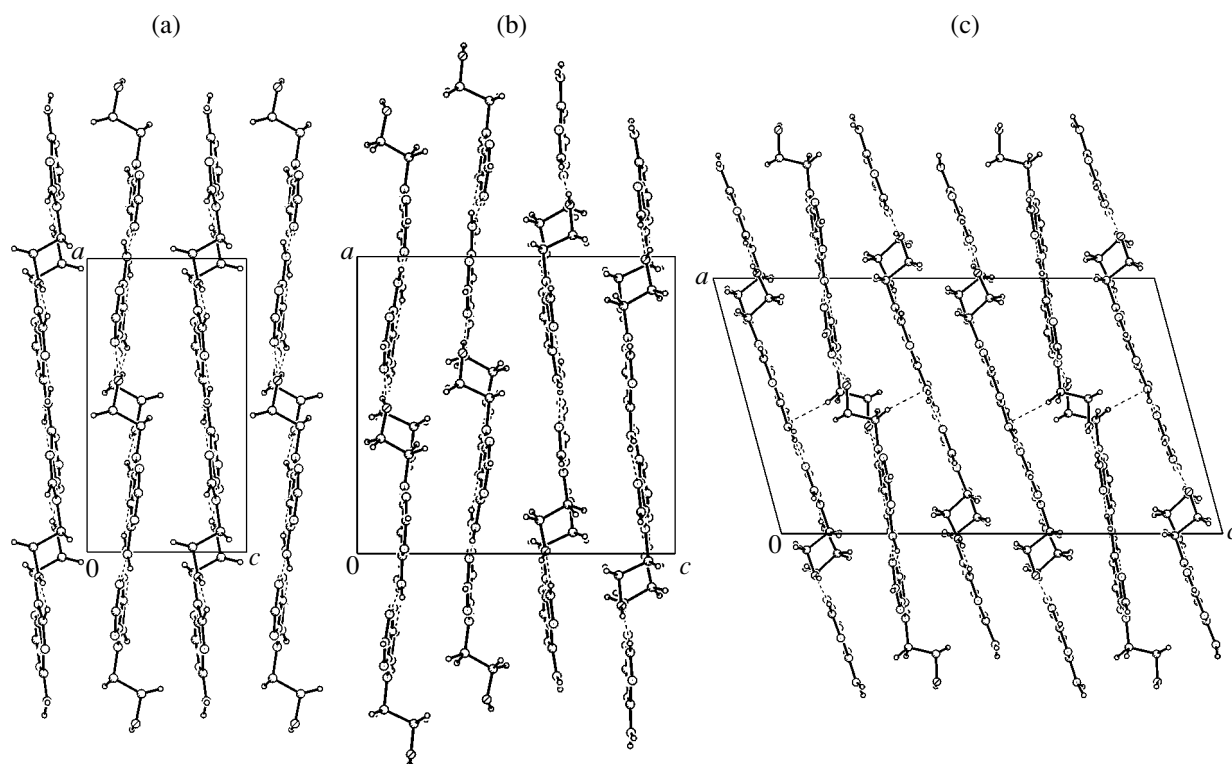


Fig. 6. Packings of chiral layers in the (a) $P2_12_12_1$ ($Z' = 1$), (b) $P2_12_12_1$ ($Z' = 2$), and (c) $P2_1/c$ ($Z' = 3$) modifications of FABFUJ.

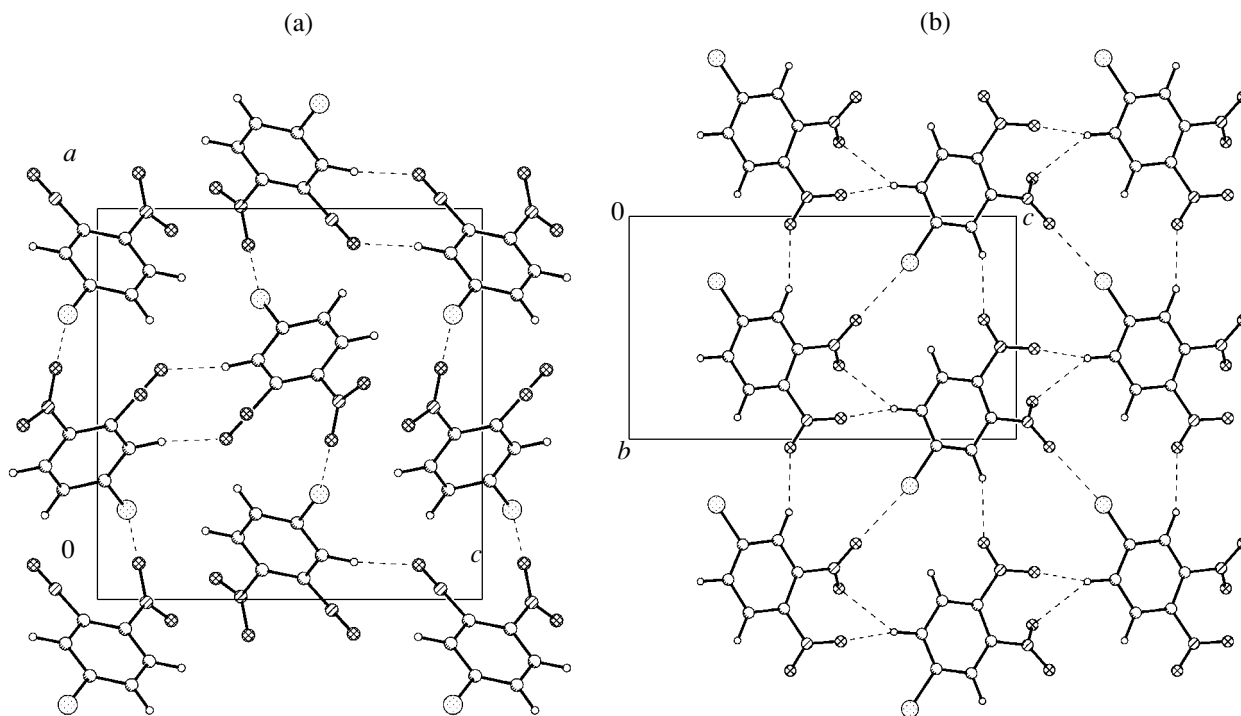


Fig. 7. Molecular packings in the (a) $P2_12_12_1$ and (b) $P2_1/c$ modifications of DEFDUN in the projections parallel and perpendicular to the chain.

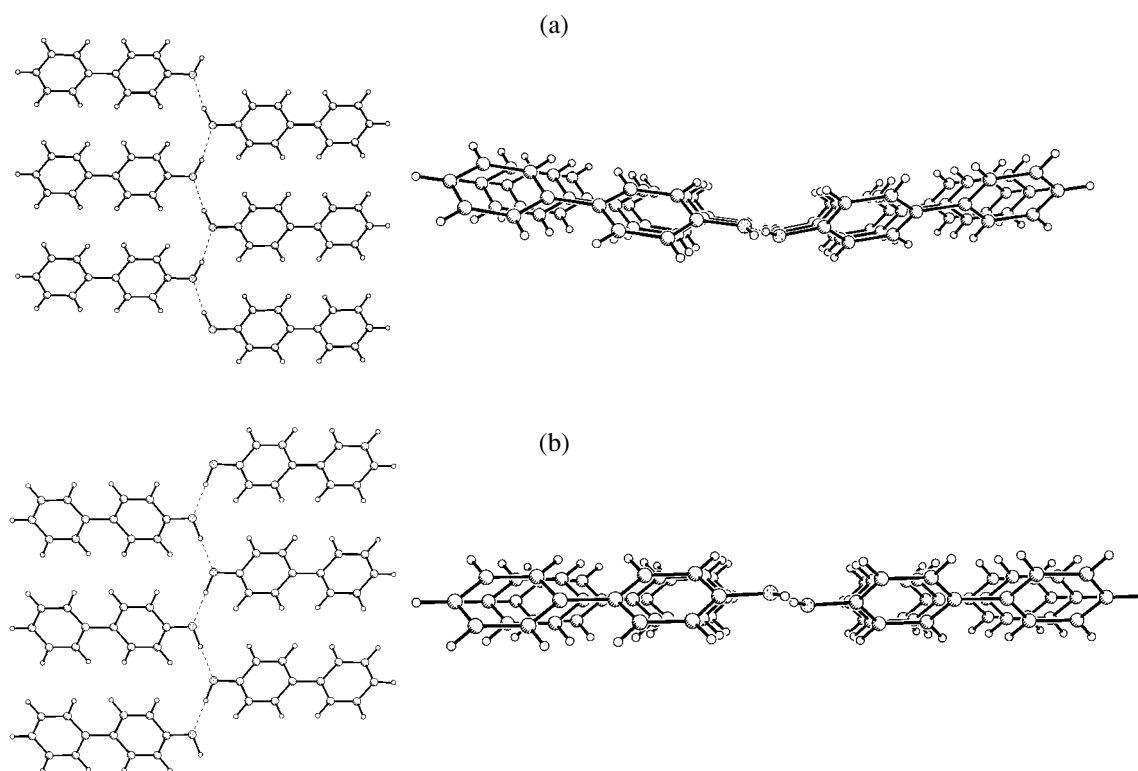


Fig. 8. Structures of chains in the (a) $P2_12_12_1$ and (b) $P2_1/c$ modifications of BOPSAA.

hence, in the type of supramolecular associate. For example, thermodynamic polymorphism occurs in the DEFUN modifications. The orientation of the nitro groups with respect to the central benzene ring in molecules of the centric modification, which was prepared in a hot supersaturated ethanol solution, differs from that of the acentric modification synthesized at room temperature. As a consequence, different systems of short contacts stabilizing the structure (Fig. 7) are formed in these crystals. However, it can be seen from Fig. 7 that the mutual arrangements of molecules in the layer differ only slightly and the layers themselves are composed of molecules of the same chirality. The cen-

tric form is unstable at room temperature and, with time, undergoes the phase transition $P2_1/c$ ($Z' = 1$) \rightarrow $P2_12_12_1$ ($Z' = 1$). This transition is attended by a change in the orientation of the nitro groups with inversion and insignificant rotations (by $\sim 35^\circ$) of the molecules about their centers of gravity. In turn, this leads to a transformation of the system of short contacts.

Polymorphic modifications synthesized in different solvents. Identical supramolecular fragments (and, correspondingly, close values of unit cell parameters) are also observed in the polymorphic modifications produced from different solvents under different conditions. This situation occurs, for the most part, when the

Table 3. Crystallographic parameters for polymorphic modifications of FABFUJ

Modification	I	II	III
Space group	$P2_12_12_1$	$P2_12_12_1$	$P2_1/c$
Z'	1	2	3
a	13.556	13.572	13.543
b	8.271	8.248	8.290
c	7.340	14.508	22.591
β	90	90	104.97
D_{calcd} , g/cm ³	1.445	1.466	1.457
Crystallization conditions	Evaporation of unsaturated aqueous solution	Slow evaporation of diluted aqueous solution	Rapid cooling of saturated aqueous solution

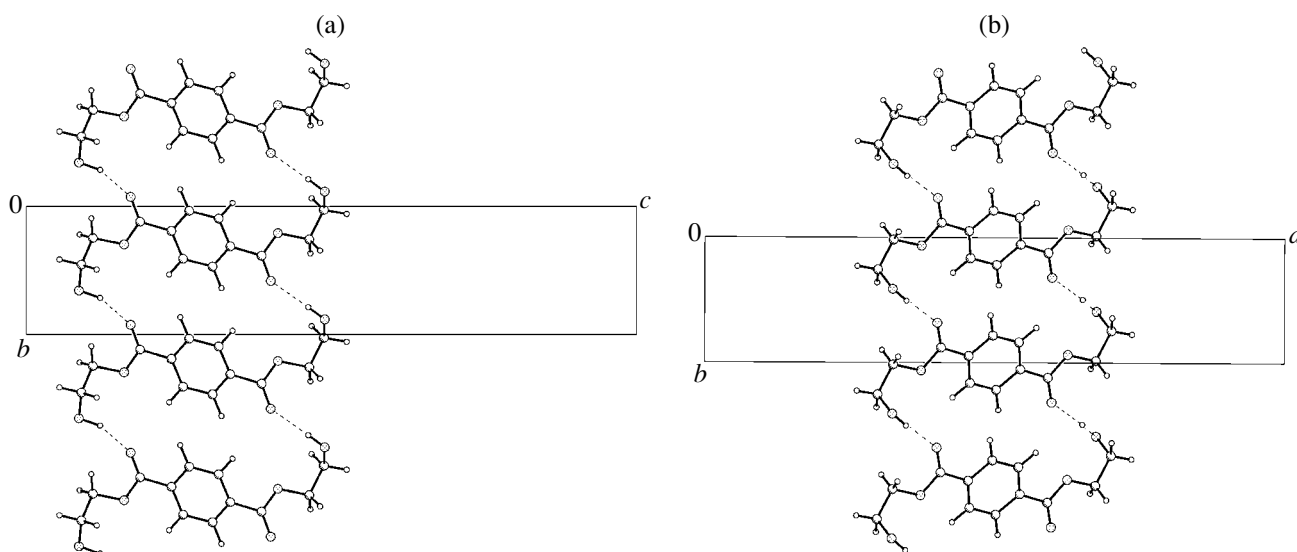


Fig. 9. Molecular packings in the (a) $P2_12_12_1$ and (b) $P2_1/c$ modifications of HETPAL.

supramolecular fragment is formed through sufficiently strong intermolecular hydrogen bonds, which are retained irrespective of the solvent type. The polymorphic modifications of BOPSAA (Fig. 8) and HETPAL (Fig. 9) can serve as examples. However, we cannot rule out the possibility that earlier attempts to choose

an appropriate solvent for crystallization of these modifications were unsuccessful or that the second modification was simply overlooked. For example, the first data on the polymorphism in MNPHOL were reported 120 years ago. However, the acentric form (in addition to the well-known centric modification) was found among the MNPHOL crystals precipitated from benzene only in 1996. Molecules of all the other pairs of polymorphic modifications listed in Table 2 are incapable of forming strong intermolecular hydrogen bonds. In the case of different solvents, these molecules adopt different geometries; the molecular topology and unit cell parameters in polymorphic modifications are also different. The difference between the densities of centric and acentric modifications has a standard value, i.e., does not exceed 3–4%.

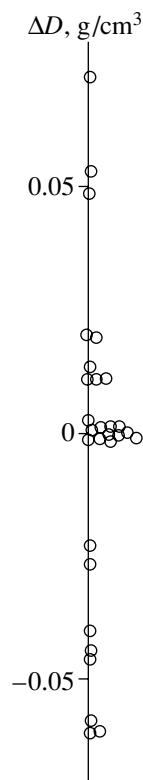


Fig. 10. Distribution of the ΔD values (ΔD is the difference between the densities of centric and acentric modification).

Although the main objective of the present work was to analyze the general structural features of polymorphic modifications, brief mention should be made of the relative density of centric and acentric modifications. Figure 10 displays the differences ΔD between the densities of centric and acentric modifications. The values of ΔD are equal, on average, to ~ 1 –2% for the majority of the modifications under investigation and do not exceed 3–4% even for the largest differences that correspond to the polymorphic modifications of DTBPTP and MNPHOL, for which the densities were measured at different temperatures (see Table 2). The only exception is provided by the FIKFIO modifications whose densities differ by almost 6%. The close densities of different polymorphic modifications imply that their free energies are also rather close in magnitude. By and large, this confirms the inferences made earlier by Brock *et al.* [13]: compared to the acentric crystals, the centric crystals have a lower density and, hence, are less energetically favorable. Moreover, it

should be noted that, in the pair of polymorphic modifications under consideration, the acentric crystals with a higher density are encountered even more frequently. This is especially true in regard to concomitant polymorphic modifications with close lattice parameters.

CONCLUSIONS

In summary, we can draw the conclusion that, in all cases when the polymorphs are built up of identical stable supramolecular fragments, the unit cell parameters are either close in magnitude or multiples irrespective of the technique used for preparing the crystals. The examples considered above confirm the inferences made in [17] that the intermolecular association plays an important role in the formation of crystal packing. In the case when molecules form stable associates through hydrogen bonds, the crystal structure is composed not of individual molecules but of larger-sized supramolecular fragments. The displacement of these fragments with respect to each other can lead both to a lowering of the symmetry of the real crystal and the appearance of a pseudosymmetry and to the formation of different crystalline modifications. When molecules form stable chiral associates, there arise centric and acentric polymorphic modifications. This inference is in complete agreement with the results obtained by Bernstein *et al.* [18], who performed a numerical simulation of the possible crystal packings of achiral planar molecules of aromatic hydrocarbons. In [18], it was demonstrated that a simple displacement of identical planar achiral layers by half the translation can readily result in the transformation from the centrosymmetric group $P2_1/c$ to the chiral group $P2_12_12_1$, and vice versa. In our opinion, these arguments are also true for molecules with a low racemization barrier. It is not improbable that the above simplicity of the transformation also plays a role in the occurrence of this pair of centric and acentric modifications.

ACKNOWLEDGMENTS

We are grateful to A.I. Yanovskii for the development of the REFCOMP program and his assistance with the Cambridge Structural Database and to V.N. Khrustalev and G.G. Andreev for their help in preparing the manuscript.

This work was supported by the Russian Foundation for Basic Research, project nos. 00-03-32840a and 99-07-90133.

REFERENCES

1. L. N. Kuleshova and M. Yu. Antipin, *Usp. Khim.* **68**, 3 (1999).
2. *Nonlinear Optical Properties of Organic Molecules and Crystals*, Ed. by D. S. Chemla and J. Zyss (Academic, New York, 1987), Vols. 1, 2.
3. S. R. Marder and J. W. Perry, *Science* **263**, 1706 (1994).
4. C. B. Gorman and S. R. Marder, *Proc. Natl. Acad. Sci. USA* **90**, 11 297 (1993).
5. G. Bourhill, L.-T. Cheng, G. Lee, *et al.*, *Mater. Res. Soc. Symp. Proc.* **328**, 625 (1994).
6. S. R. Marder, C. B. Gorman, F. Meyers, *et al.*, *Science* **265**, 632 (1994).
7. C. B. Gorman and S. R. Marder, *Chem. Mater.* **7**, 215 (1995).
8. W. C. McCrone, in *Physics and Chemistry of the Organic Solid State*, Ed. by D. Fox, M. M. Labes, and A. Weissberger (Interscience, New York, 1965), Vol. 2, p. 725.
9. S. R. Hal, P. V. Kolinsky, R. Jones, *et al.*, *J. Cryst. Growth* **79**, 745 (1986).
10. H. Kagawa, M. Sagawa, T. Hamada, *et al.*, *Chem. Mater.* **8**, 2622 (1996).
11. F. Pan, C. Bosshard, M. S. Wong, *et al.*, *Chem. Mater.* **9**, 1328 (1997).
12. M. Yu. Antipin, T. V. Timofeeva, R. D. Clark, *et al.*, *J. Mater. Chem.* **11**, 351 (2001).
13. C. P. Brock, W. B. Schweizer, and J. D. Dunitz, *J. Am. Chem. Soc.* **113**, 9811 (1991).
14. A. Gavezzotti and G. Filippini, *J. Am. Chem. Soc.* **117**, 12 299 (1995).
15. C. P. Brock and J. D. Dunitz, *Chem. Mater.* **6**, 1118 (1994).
16. J. Bernstein, R. D. Davey, and J.-O. Henc, *Angew. Chem. Int. Ed. Engl.* **38**, 3440 (1999).
17. L. N. Kuleshova, V. N. Khrustalev, and M. Yu. Antipin, *Kristallografiya* **45**, 1034 (2000) [*Crystallogr. Rep.* **45**, 953 (2000)].
18. J. Bernstein, J. A. Sarma, and A. Gavezzotti, *Chem. Phys. Lett.* **174**, 361 (1990).

Translated by O. Borovik-Romanova

CRYSTAL
CHEMISTRY

On Polymorphism and Morphotropism of Rare Earth Sesquioxides

P. P. Fedorov, M. V. Nazarkin, and R. M. Zakalyukin

Shubnikov Institute of Crystallography, Russian Academy of Sciences,
Leninskiĭ pr. 59, Moscow, 117333 Russia

Received March 28, 2001

Abstract—The data on the phase transitions in the series of rare earth sesquioxides are considered in terms of the thermodynamic theory of morphotropism. It is shown that the scheme of polymorphism and morphotropism suggested by V.V. Glushkova is the most adequate. The derivatographic dehydration of lanthanum and neodymium oxide hydrates is performed. The transition of the cubic *C* modification into the hexagonal *A* modification of neodymium oxide is accompanied by the removal of volatile impurities and, thus, is not a polymorphic transition proper. © 2002 MAIK “Nauka/Interperiodica”.

INTRODUCTION

Polymorphism, morphotropism, and crystal structures of rare earth (RE) sesquioxides of the composition R_2O_3 in oxidation degree III have been studied in [1–13]. Three main structure types in which these compounds are crystallized at room temperature have been known since the studies of Goldschmidt: hexagonal *A*-type, the monoclinic *B*-type close to *A*, and the cubic *C*-type. At temperatures exceeding 2000°C, there exist two more modifications denoted as *H* and *X*.

At present, two main schemes of polymorphism and morphotropism in the R_2O_3 series (Figs. 1a, 1b) are known. In the scheme suggested by Foex and Traverse (Fig. 1a), the existence range of the *B* modifications in the temperature–cationic radius diagram has a lenslike shape and is limited from below by the existence range of the cubic *C*-phases. Moreover, it is also assumed that there exist low-temperature *C*-modifications of cerium oxides crystallizing in the *A*-type ($R = \text{La–Nd}$). The low-temperature phase transitions with the participation of *C*-modifications are indicated in accordance with data [1]. In the Glushkova scheme (Fig. 1b), the boundaries between the fields of the *A*- and *B*- and between the *B*- and *C*-modifications are almost vertical in the low-temperature region. The reversible $B \rightleftharpoons C$ transitions take place only for the Tb, Dy, and Ho oxides. The low-temperature *C*-modifications of the La–Gd oxides are interpreted as nonequilibrium ones.

The canonical scheme suggested in [9, 11, 12] is widely used; however, it is somewhat erroneous.

The use of the thermodynamic theory of morphotropism [14, 15] allows one to solve the problem, which has been discussed for the last 75-odd years [2, 4, 12, and the references there], of the possible existence of stable low-temperature cubic *C*-modifications in Ce sesquioxides reversibly transforming into *A*- or *B*-modifications during heating. It was shown [14] that, if the

thermodynamic function of a compound is a smooth function of ionic radius r [which is the necessary and sufficient condition for the description of the corresponding dependences of the phase-transition temperatures $T(r)$ (e.g., melting) by smooth functions], then the curve separating the regions of the thermodynamic stability of the phases having different structures in the T – r coordinates should have a vertical tangent with the approach to the temperature of absolute zero. If the Debye model is applicable to both modifications, then, in the low temperature range, this curve is described by the limiting equation

$$T = a|r_0 - r|^n,$$

where a and r_0 are the parameters and $n = 0.25$. For trifluorides RF_3 , the experimental data yield $n = 0.284$ [15]. The aim of the present study is to consider the polymorphism of RE oxides in terms of the thermodynamic theory of morphotropism.

THERMAL DECOMPOSITION OF LANTHANUM AND NEODYMIUM HYDROXIDES

There are numerous data on the stabilization of the cubic *C*-modifications of RE oxides by various impurities and, first of all, by water [2, 4, 5]. We studied here the dehydration of lanthanum and neodymium oxide hydrates by the derivatographic method (a Q -1500 derivatograph, platinum crucibles, heating rate 10°C/min). The starting materials were chemically pure La_2O_3 and Nd_2O_3 reagents kept in air for not less than twenty years.

The X-ray phase analysis of the specimens was performed on an HZG-4 diffractometer (Carl Zeiss, Jena, Germany), CuK_α radiation, Ni-filter, and Si external standard. The initial specimen was preliminarily

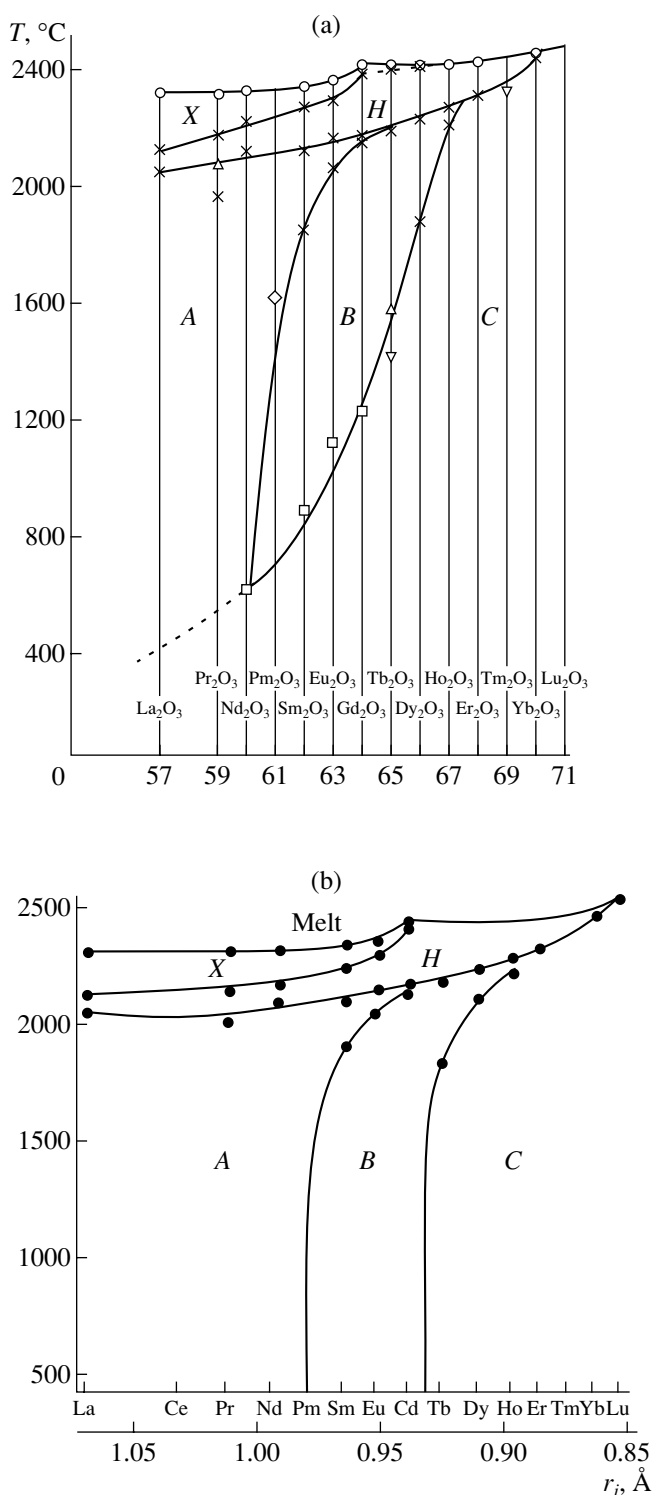


Fig. 1. Phase transition in the R_2O_3 series: (a) according to DTA data [6]: \odot solidification points, \times transformation points; X-ray phase analysis data [1]: \triangle transformation point during temperature increase, ∇ transformation point during lowering of the temperature according to data [1]; \square transformation points according to data [13]; \diamond transformation points of Pm_2O_3 as functions of the nucleus charge of an N -cation; (b) according to data [4] with no allowance for the metastable states dependent on the ionic radius R^{3+} .

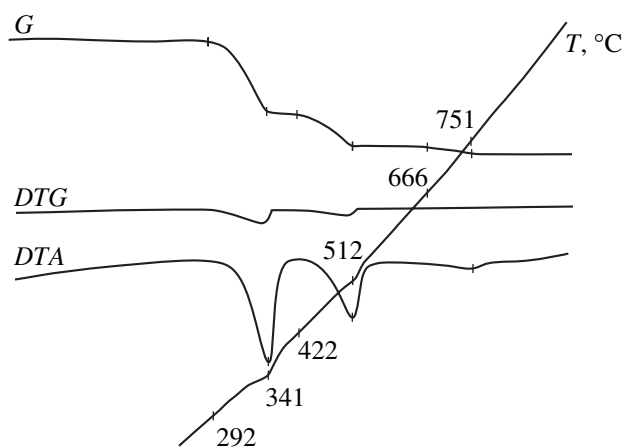


Fig. 2. Derivatogram of thermal decomposition of hydrated lanthanum oxide.

ground in a jasper mortar. The angular range was 10° – 60° ; the recording rate was $2^{\circ}/\text{min}$.

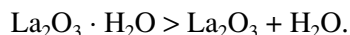
The positions and intensities of the diffraction peaks were calculated by the *Profit* and *Powder2* programs with allowance for both $CuK\alpha_1$ and $CuK\alpha_2$ lines. Substance identification was done by comparing the experimental data with the data of the JCPDS Powder Data Base (1997). The indexing of diffraction patterns and calculation of the lattice parameters were done by the LS method within the *Powder 2* program.

The X-ray diffraction patterns obtained from the starting materials were essentially different from those of La_2O_3 and Nd_2O_3 . Their comparison with the Data Base data showed that these lines corresponded to $La(OH)_3$ and $Nd(OH)_3$, sp. gr. $P6_3/m$ (JCPDS no. 36-1481, $a = 6.528 \text{ \AA}$ and $c = 3.858 \text{ \AA}$ and no. 06-0601, $a = 6.421 \text{ \AA}$ and $c = 3.74 \text{ \AA}$, respectively).

As is seen from Fig. 2, the decomposition of hydrated lanthanum oxide proceeds in three stages. The weight losses correspond to the following reactions: at the first stage at $T = 292^{\circ}C$,



and at the second and third stages ($T = 422^{\circ}C$),



The above temperatures correspond to the beginning of the decomposition processes on the curve of the weight loss (G). These equations were confirmed by the diffraction patterns of the samples heated to certain temperatures corresponding to the processes that were fixed on derivatograms (Fig. 3).

The X-ray diffraction pattern of $La_2O_3 \cdot H_2O$ (Fig. 3b) is similar to that of $LaO(OH)$: monoclinic system, sp. gr. $P2_1/m$, $a = 4.417 \text{ \AA}$, $b = 3.929 \text{ \AA}$, $c = 6.572 \text{ \AA}$, $\beta = 112.5^{\circ}$ [15] (JCPDS no. 19-0656). However the lattice parameters of $La_2O_3 \cdot H_2O$ are essentially different from those of $LaO(OH)$ (according to our data, $a =$

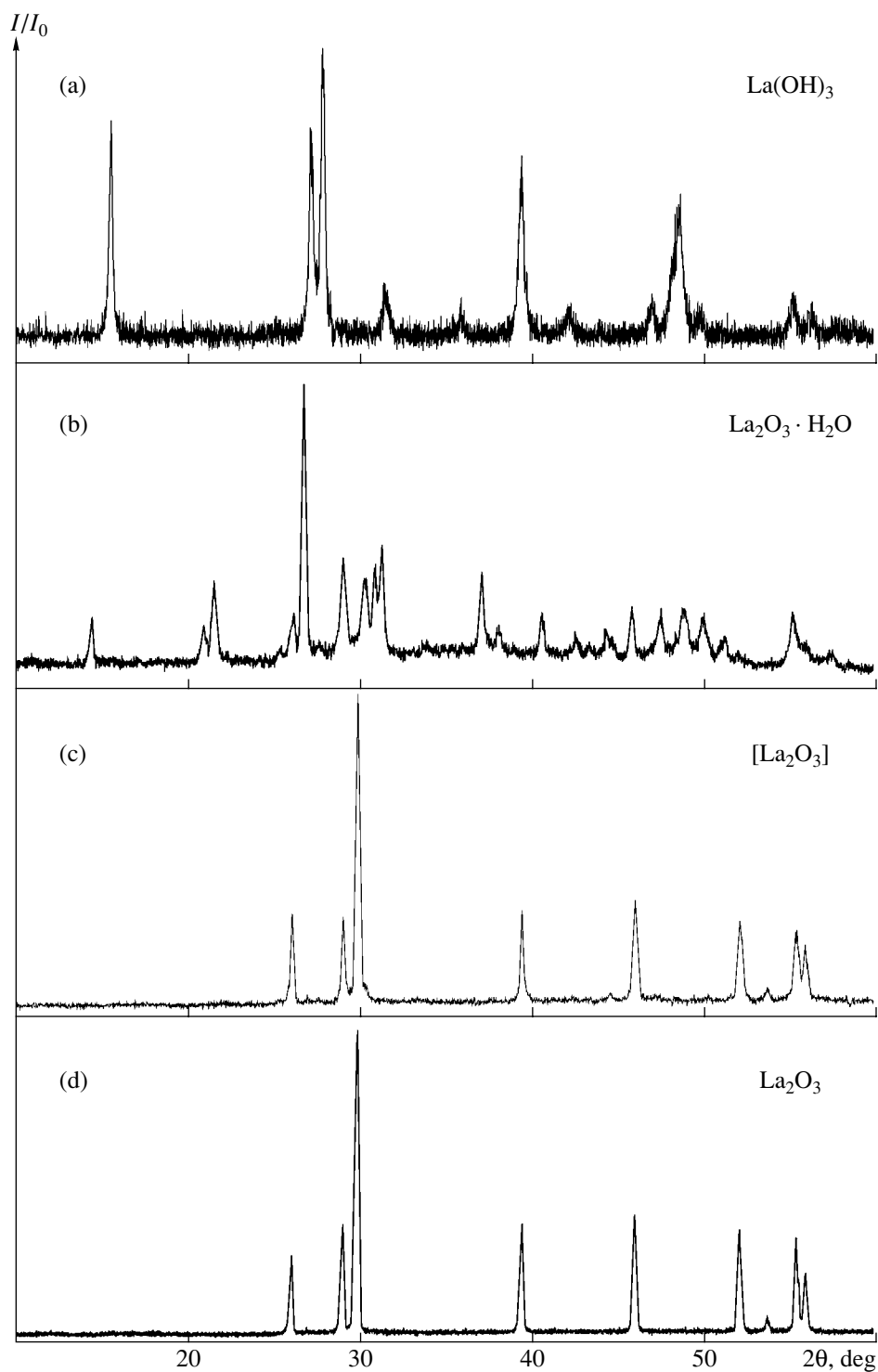


Fig. 3. X-ray diffraction patterns from dehydrated lanthanum oxide at different stages of dehydration; (a) initial sample; heating to (b) 360, (c) 600, and (d) 1000°C.

4.436 Å, $b = 3.930$ Å, $c = 6.619$ Å, $\beta = 112.12^\circ$). The diffraction pattern taken upon the second stage of decomposition (Fig. 3c) was almost identical to that of completely dehydrated oxide. The unit-cell parameters of the trigonal lattice were determined as $a = 3.923$ Å, $c = 6.124$ Å and $a = 3.935$ Å, $c = 6.127$ Å upon the sec-

ond and third stages of decomposition, respectively. The Data Base indicates for La_2O_3 (JCPDS no. 05-0602) the sp. gr. $P\bar{3}m1$, $a = 3.937$ Å, $c = 6.129$ Å. The analysis of the additional weak reflections on the diffraction pattern observed upon the second stage of decomposi-

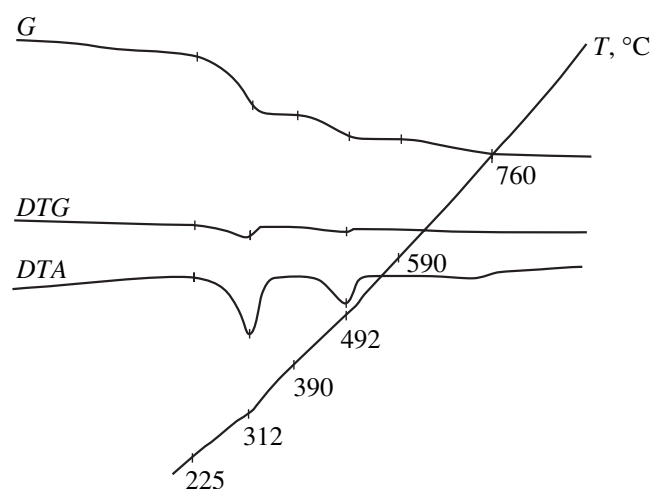
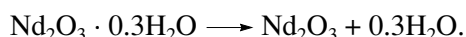


Fig. 4. Derivatogram of thermal decomposition of hydrated neodymium oxide.

tion and disappearing upon the third stage (Fig. 3c) indicates the presence of several percent of lanthanum oxycarbonate $\text{La}_2\text{O}_2\text{CO}_3$ (JCPDS no. 37-0804). These reflection disappeared upon the third stage of decomposition (Fig. 3d).

The decomposition of $\text{Nd}(\text{OH})_3$ (Fig. 4) proceeds in three stages. The calculation of the weight losses corresponds to the following reactions at $T = 225, 390, 590^\circ\text{C}$:



The X-ray diffraction pattern of the sample upon the first stage of water loss corresponded to the formula $\text{NdO}(\text{OH})$ and was similar to the X-ray diffraction pat-

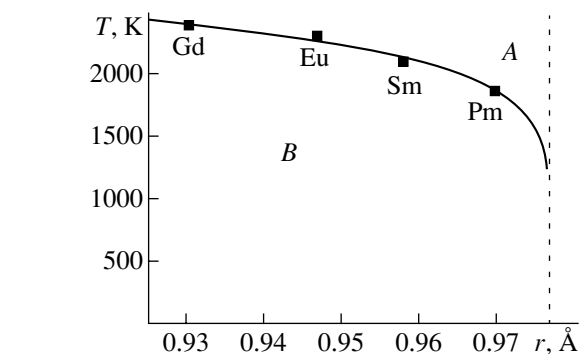


Fig. 5. Approximation of the data on the temperatures of $A \rightarrow B$ phase transitions [6, 13]. Solid line describes the equation $T = 3607(0.977 - r)^{0.1323}$, dash line ($r = 0.977 \text{ \AA}$) is the boundary of the morphotropic transformation. The ionic radii were taken at c.n. 6 [19].

tern from $\text{LaO}(\text{OH})$. It was indexed in the monoclinic system $a = 4.388 \text{ \AA}$, $b = 3.870 \text{ \AA}$, $c = 6.392 \text{ \AA}$, $\beta = 112.2^\circ$ (Table 1), which is consistent with [16], where it was stated that all the RE oxyhydroxides are isostructural. The Data Base provides no indexing of these patterns (JCPDS no. 13-0167).

Upon the second phase of decomposition, the C-phase of neodymium oxide was detected (cubic face centered lattice, $a = 11.078 \text{ \AA}$), which, in actual fact, is a hydrate of the composition $\text{Nd}_2\text{O}_3 \cdot 0.3\text{H}_2\text{O}$. In the temperature range $590\text{--}760^\circ\text{C}$, the Nd hydrate, $\text{Nd}_2\text{O}_3 \cdot 0.3\text{H}_2\text{O}$, decomposes to the Nd_2O_3 of the A type corresponding to JCPDS no. 06-0408 ($P\bar{3}m1$, trigonal system, $a = 3.831 \text{ \AA}$ and $c = 5.999 \text{ \AA}$).

Table 1. Indexing of X-ray diffraction pattern of NdOOH

2θ , deg	d (obs), \AA	$10^4/d^2$ (obs)	I/I_0	hkl	$10^4/d^2$ (calc)	$\Delta 10^4/d^2$
14.900	5.9409	283.3	17	0 0 1	285.6	-2.30
21.320	4.1642	576.7	42	-1 0 1	577.0	-0.32
21.709	4.0905	597.6	52	1 0 0	606.1	-8.51
27.679	3.2203	964.3	100	0 1 1	953.3	11.01
29.871	2.9888	1119.5	47	-1 0 2	1119.1	0.35
31.089	2.8744	1210.3	18	1 0 1	1206.6	3.75
31.918	2.8016	1274.1	58	-1 1 1	1259.1	15.00
38.339	2.3459	1817.1	26	0 1 2	1810.2	6.93
41.165	2.1911	2082.9	20	-2 0 1	2080.7	2.24
43.424	2.0822	2306.5	14	-2 0 2	2308.1	-1.50
45.944	1.9737	2567.1	18	0 0 3	2570.7	-3.62
47.372	1.9175	Nd_2O_3	20	Nd_2O_3	Nd_2O_3	Nd_2O_3
50.742	1.7978	3093.9	22	2 1 0	3092.3	1.67
57.285	1.6070	3872.3	22	1 2 1	3877.2	-4.90

Table 2. Parameters of the equation $T = a|r_0 - r|^n$ which describe the upper temperature boundary of stability of various families of phases

Compound	$r_0, \text{\AA}$	$a, \text{K/\AA}$	n	Correlation coefficient	Reference
$\text{Pb}_4\text{R}_3\text{F}_{17}$	1.230*	1430	0.091	0.9989	20
$\text{Ca}_8\text{R}_5\text{F}_{31}$	1.165*	1800	0.136	0.9994	20
Ca_2RF_7	1.171*	2030	0.192	0.9997	20
$\text{RF}_3(\beta\text{-YF}_3)$	$1.226 \pm 0.005^*$	3160	0.284	0.960	15
$B\text{-R}_2\text{O}_3$	$0.977 \pm 0.014^{**}$	3600 ± 950	0.132 ± 0.093	0.9893	Present study

* Ionic radii of fluorides at c.n. 8 [19].

** Ionic radii of oxygen at c.n. 6 [19].

DISCUSSION OF RESULTS

The results obtained in our study confirm and supplement the X-ray diffraction data [4, 5] on the transition of the cubic *C*-modification of neodymium oxide to the trigonal *A*-modification accompanied by the removal of volatile impurities. Therefore, this transformation cannot be considered as a polymorphic transition proper. The stages and the hydration temperatures observed in this study agree with the data in [4, 5, 16, 17]. The inconsistencies can be explained by the different methods used for preparing the initial hydrated forms.

According to our data, the dehydration of neodymium oxide is completed at a rather high temperature, 760°C. It seems that the presence of strongly bound (residual) water explains the error made by Warshaw and Roy, who described the reversible transitions in the R_2O_3 oxides of the cerium group in the presence of H_2O [1]. They considered water only as a means for accelerating the phase transition but not affecting the chemical composition (i.e., as a catalyst). However, in actual fact, a small amount of residual water in the substance changes the pattern of polymorphism and morphotropism.

The structural changes occurring in R_2O_3 in the transition from the *C*- to the *A*-modification can be described by the mechanism of crystallographic shear [5, 10, 11, 18].

Thus, of two alternative schemes of polymorphism and morphotropism in the series of RE sesquioxides, the scheme in Fig. 1b seems to be more adequate. Proceeding from the changes in the melting points in the series of RE oxides with due regard for the "gadolinium kink," the whole series can be divided into two groups—cerium and yttrium. The model of an ideal morphotropic series can be applied to both of these groups [14]. This situation corresponds to RE fluorides [15]. Figure 5 shows the results of the LS procedure applied to data [6, 13] on the temperatures of the $A \rightleftharpoons B$ polymorphic transformations in accordance with the limiting thermodynamic equation $T = a|r_0 - r|^n$, where $a = 3600 \pm 950$, $r_0 = (0.977 \pm 0.014) \text{\AA}$, and $n = 0.132 \pm 0.093$. The ionic radii (tabulated to the third decimal place) were taken from the system suggested in [19]

at c.n. 6. The approximation obtained is characterized by a high value of the correlation coefficient.

Table 2 lists the parameters of this equation, which describe the stability boundaries of various phases. The deviation of n from the value 0.25 can be explained by the fact that the transition temperatures are rather far from the temperature of absolute zero. The value $r_0 = 0.977 \text{\AA}$ lying between the ionic radii of Pm and Nd sets the boundary of the morphotropic $A \rightleftharpoons B$ transformation in R_2O_3 oxides. The data on the $B \rightleftharpoons C$ polymorphic transitions for R_2O_3 have not been processed quantitatively because of the insufficient number of points.

In [7], some additions to the scheme of polymorphism and morphotropism in R_2O_3 series were made which concerned high-temperature polymorphism in yttrium oxides (the existence of the *A*- and *B*-modifications in the narrow temperature intervals). The conclusions drawn are based on the data for samples containing 10 mol % of heterovalent impurities (Sr and Ca oxides but not Mg and Ba oxides). We believe that such an approach is erroneous because it ignores the possible stabilization of unstable crystalline modifications by impurities [4] accompanied by the formation of individual berthollide phases separated from the ordinate of the corresponding component [15, 21].

ACKNOWLEDGMENTS

The authors are grateful to Kh.S. Bagdasarov, Yu.V. Pisarevskii, and F.M. Spiridonov for their interest in this study and discussion of the results.

REFERENCES

1. J. Warshaw and R. Roy, *J. Phys. Chem.* **65**, 2048 (1961).
2. G. Brauer and R. Muller, *Z. Anorg. Allg. Chem.* **321** (5–6), 234 (1963).
3. M. Foex and J.-P. Traverse, *C. R. Seances Acad. Sci.* **262**, 636 (1966).
4. V. B. Glushkova, *Polymorphism of Rare-Earth Oxides* (Nauka, Leningrad, 1967).
5. V. S. Rudenko and A. G. Bogdanov, *Izv. Akad. Nauk SSSR, Neorg. Mater.* **6** (12), 2158 (1970).

6. J.-P. Traverse, *Contribution au developpement de méthodes d' experimentation a temperature élevée. Application a l'étude du polymorphisme des sesquioxides de terres rares et des changements de phases dans les systems zircone–chaux et zircone–oxyde de strontium*, Thèse (L'Université Scientifique et Medicale de Grenoble, Grenoble, 1971).
7. L. M. Lopato, F. V. Shevchenko, A. E. Kushchevskii, and S. G. Tresvyatskii, *Izv. Akad. Nauk SSSR, Neorg. Mater.* **10** (8), 1481 (1974).
8. P. Duran, *Bull. Soc. Fr. Ceram.*, No. 102, 47 (1974).
9. J. Coutures, A. Rouanet, R. Verges, and M. Foex, *J. Solid State Chem.* **17** (1/2), 171 (1976).
10. O. Greis, *J. Solid State Chem.* **34** (1), 39 (1980).
11. C. Boulesteix, *Handbook on the Physics and Chemistry of Rare Earth*, Ed. by K. A. Gschneidner and L. Eyring (North-Holland, Amsterdam, 1982), Chap. 44, p. 321.
12. B. I. Pokrovskii and F. M. Spiridonov, in *Compounds of Rare-Earth Elements. Systems with Oxides of Elements from Groups I–III*, Ed. by I. V. Tananaev (Nauka, Moscow, 1983), p. 17.
13. F. Weigel and U. Scherer, *Radiochim. Acta* **4**, 197 (1965).
14. P. P. Fedorov, *Kristallografiya* **40**, 308 (1995) [*Crystallogr. Rep.* **40**, 278 (1995)].
15. P. P. Fedorov and B. P. Sobolev, *Kristallografiya* **40**, 315 (1995).
16. V. P. Klevtsov and L. P. Sheina, *Izv. Akad. Nauk SSSR, Neorg. Mater.* **1** (12), 2219 (1965).
17. B. N. Rybakov, A. F. Moskvicheva, and G. D. Beregovaya, *Zh. Neorg. Khim.* **14** (11), 2904 (1969).
18. B. G. Hyde, *Acta Crystallogr., Sect. A: Cryst. Phys., Diffr., Theor. Gen. Crystallogr.* **A27** (6), 617 (1971).
19. R. D. Shannon, *Acta Crystallogr., Sect. A: Cryst. Phys., Diffr., Theor. Gen. Crystallogr.* **A32** (5), 751 (1976).
20. P. P. Fedorov, L. V. Medvedeva, and B. P. Sobolev, *Zh. Fiz. Khim.* **67** (5), 1073 (1993).
21. P. P. Fedorov, P. I. Fedorov, and B. P. Sobolev, *Zh. Neorg. Khim.* **18** (12), 3319 (1973).

Translated by L. Man

PHASE
TRANSITIONS

Structural Phase Transitions in Heteroepitaxial Ferroelectric Films

I. N. Zakharchenko, P. N. Timonin, E. V. Sviridov, and V. A. Aleshin

Research Institute of Physics, Rostov State University, pr. Stachki 8, Rostov-on-Don, 344090 Russia

Received October 18, 1999; in final form, March 7, 2001

Abstract—The changes in the structural–deformational characteristics occurring during the phase transitions in the crystal lattice of epitaxially grown thin (Ba,Sr)TiO₃ films on the (001) cleavage of MgO crystals have been studied. It is shown that microdeformations along the surface normal of the wall of a *c*-domain film increase with the temperature and attain maximum values in the vicinity of the phase transition. No decrease in the dimensions of the coherent-scattering regions was observed. The comparison of the deformation of the “average” lattice and microdeformations led to the assumption that the transition from the paraelectric to the ferroelectric phase is accompanied by the dislocation-induced formation of a dipole-glass-type intermediate phase at the temperatures exceeding that of the phase transition. © 2002 MAIK “Nauka/Interperiodica”.

INTRODUCTION

In recent decades, intensive studies of the physical properties of thin ferroelectric films and phase transitions occurring in these films have been performed. The properties of these films often differ from the properties of bulk specimens of the same compositions: in particular, phase transitions in the films are often diffuse and are similar to those observed in ferroelectrics–relaxors [1, 2].

Studying thin epitaxial (Ba,Sr)TiO₃ films grown on the (001) surface of MgO crystals, we established that the degree of phase-transition diffusion depends on the perfection of the crystal structure characterized by the dimension of the coherent-scattering region, *D*, and the value of the average microdeformation $\tilde{\epsilon}_3 = \sqrt{\langle(\Delta d/d)^2\rangle}$ along the [001] direction (where *d* is the corresponding interplanar spacing) [3]. The $\tilde{\epsilon}_3$ values of various films at room temperature are about 10^{−3}–10^{−4}, whereas the *D* values exceed 1000 Å; the degree of phase-transition diffusion is higher for films with higher $\tilde{\epsilon}_3$ values [3], i.e., depends on the presence of linear defects (dislocations). It is also shown that the ferroelectric phase transition occurs at temperatures higher than in the bulk specimens of the same compositions because of the compressive thermoelectric stresses caused by the difference in the thermal expansion coefficients of the film and the substrate [4].

In some instances, the values of the lattice parameters *c* were higher and the values of the *a* parameters, lower than the corresponding values for the bulk specimen. Also, at temperatures *T* exceeding the phase-transition temperature *T*_C, the unit cell remains tetragonal

but becomes nonpolar—the etching figures of domains observed in an electron microscope disappeared [3, 4]. These anomalies were explained by the effect of thermoelastic stresses and the anisotropic distribution of point defects in the films associated with the technology of film formation (high-frequency cathode sputtering).

The above results allow one to assume that the restructuring of the crystal lattice of the films during phase transitions is characteristic of both ferroelectrics and ferroelectrics–relaxors and, thus, should reflect the elastic interaction between the film and the substrate.

The diffusion of phase transitions in ferroelectrics–relaxors is associated with the formation of an intermediate dipole-glass phase prior to the transition from the paraelectric to the ferroelectric phase. Crystal restructuring is studied in most detail for lead magnesium niobate and its solid solution with lead titanate [5, 6]. The specific features of diffuse scattering and the changes in the widths and the intensities of Bragg reflections are interpreted as the result of the formation of mesoscopic polar clusters in the nonpolar cubic matrix whose dimensions increase with lowering of the temperature. In turn, macroscopic regions with nonuniform spontaneous deformation provide the formation of a dipole-glass phase [5]. By measuring the broadening of the Bragg reflections, we determined the average microdeformation of the crystal lattice along the directions corresponding to the reflection indices and, thus, evaluated the degree of structure disorder in both dipole-glass and other phases.

The first-order phase transition in the (Ba,Sr)TiO₃ films [7] is accompanied by the nucleation of a new phase, with both phases being coexistent within a certain temperature interval [8]. As a result, the dimen-

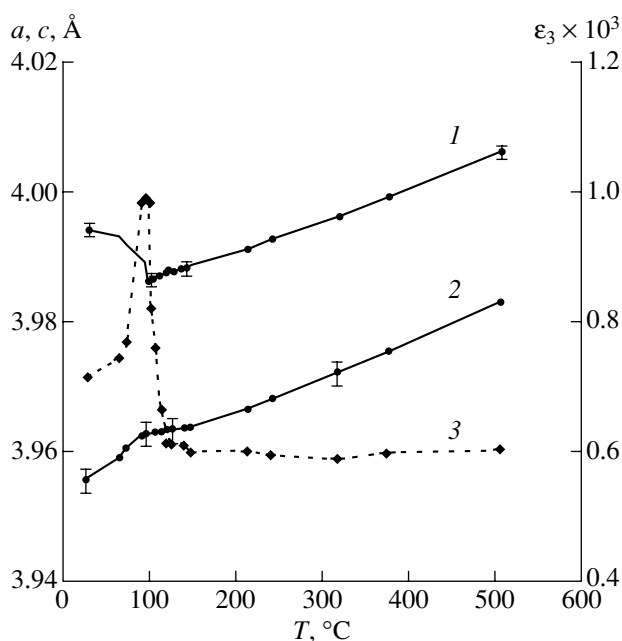


Fig. 1. Temperature dependence of the parameters of the average unit cell: (1) $c(T)$, (2) $a(T)$, and (3) the average microdeformation along the [001] direction, $\tilde{\epsilon}_3(T)$.

sions of the blocks of the crystal lattice decreased [9]. Kenzig [10] observed the broadening of reflections which could be associated with a decrease in the dimensions of coherent-scattering regions.

The present study is dedicated to structural phase transitions in heteroepitaxial ferroelectric films. We studied the temperature dependence of the unit-cell parameters and the changes in the structural–deformational characteristics, such as the average microdeformation and the dimension of the coherent-scattering regions during phase transitions. The temperature dependence of the “average” unit-cell deformation [11] was compared with the temperature dependence of the average microdeformation during phase transitions.

It would be interesting to compare the results of the traditional studies of the temperature dependence of the dielectric constant obtained earlier [12–14] (not considered here) with the structural data. It was shown both experimentally and theoretically (within the frameworks of the thermodynamic approach) that the biaxial compressive stresses usually observed in epitaxial $(\text{Ba,Sr})\text{TiO}_3/\text{MgO}$ films suppress the formation of the maximum for the ϵ_{11} component of the dielectric-constant tensor in the temperature range corresponding to the transition from the tetragonal to the cubic phase. In this case, the main components $\epsilon_{11} = \epsilon_{22}$ of the dielectric-constant tensor readily measured in epitaxial films on flat dielectric substrates provide no additional information.

EXPERIMENTAL

The $(\text{Ba}_{0.7}, \text{Sr}_{0.3})\text{TiO}_3$ films were grown by high-frequency sputtering of polycrystal line targets of stoichiometric composition [15] in an oxygen atmosphere under a pressure of 93 Pa. The films were deposited onto as-cleaved MgO (001) surfaces. The substrates were preliminarily heated up to 450°C by a resistive heater and then bombarded with the plasma particles of a high-frequency discharge, which heated the substrate up to 850°C. The power of the high-frequency discharge was 25 W/cm², the deposition rate was 130 Å/min. Upon the attainment of the desired film thickness (0.5–2.0 μm), the high-frequency discharge was switched off, and the film was spontaneously cooled to ~250°C. The high heat capacity of the heater provided sufficient inertial cooling at an average rate of 5°C/min. In the temperature range from 250°C to room temperature, the average cooling rate was maintained at a level of about 1°C/min, which resulted in the formation of the equilibrium domain structure in the film.

The X-ray diffraction studies were made on a DRON-3 diffractometer (filtered CuK_α radiation). The specimens were placed into a special chamber fixed on a goniometer, which allowed one to record the reflections within the temperature range 20–550°C. The phase transitions were recorded during the cooling of the specimen preliminarily heated up to 500°C. The $\tilde{\epsilon}$ and D values were obtained by the approximation method [6]. The reflection profiles were approximated by Gaussians.

RESULTS AND DISCUSSION

According to the X-ray diffraction data, the (001) planes and the [100] and [010] directions in the films and in the substrates were parallel. The c -axis of the film was normal to the surface (the “ c -domain films”). The method used in our study is described elsewhere [17].

The changes in the structural–deformational characteristics during phase transitions were studied on the films with a rather high degree of structural perfection.

Figure 1 (curves 1 and 2) shows the temperature dependence of the lattice parameters for a 0.6-μm-thick film, whose average microdeformation along the direction normal to the film surface was $\epsilon_3 = 7.7 \times 10^{-4}$ at $D > 1000$ Å at room temperature. As was indicated earlier, the kink in the temperature curve of the c - and a -parameters, indicating the occurrence of the phase transition, is observed at a considerably higher temperature than the phase-transition temperature in the bulk specimen (35°C [18]). At $T > T_c$, the unit-cell symmetry remained tetragonal. The c -parameter was determined using the 004 reflection, whereas the a -parameter was determined from the angular positions of the 004 and 224 reflections.

No decrease in the dimensions of the coherent-scattering regions along the [001] direction (characteristic of ferroelectric films undergoing the first-order phase transition) was observed in the whole temperature range studied. The broadening ratio β_1/β_2 for the $00l_1$ and $00l_2$ reflections was equal to the tangent ratio of the corresponding Bragg angles: in other words, reflection broadening was caused by microdeformations alone.

Figure 1 (curve 3) shows the temperature dependence of $\tilde{\varepsilon}_3$ whose squared value is, in fact, the S_{33} component of the tensor of averaged random microdeformations $S_{ij} = \langle \varepsilon_i \varepsilon_j \rangle$ with $i, j = 1, 2, \dots, 6$ [19]. The maximum $(S_{33})^{1/2} = \varepsilon_3 \sim 10^{-3}$ values were observed in the vicinity of the phase transition.

The range of the angular block misorientation with respect to the film normal determined by the 1θ -scanning at a narrow slit of the static counter remained constant.

Analyzing the data obtained, we compared the temperature dependences of uniform volume (ε_v) and shear (ε_t) deformations of the average unit cell with the temperature dependences of the average volume ($\tilde{\varepsilon}_v$) and shear ($\tilde{\varepsilon}_t$) microdeformations. The ε_v and ε_t values were determined from the following equations:

$$\varepsilon_v = 2\langle \varepsilon_1 \rangle + \langle \varepsilon_3 \rangle,$$

$$\varepsilon_t = \langle \varepsilon_3 \rangle - \langle \varepsilon_1 \rangle,$$

where

$$\langle \varepsilon_1 \rangle = (a_T - a_0)/a_0,$$

$$\langle \varepsilon_3 \rangle = (c_T - c_0)/c_0,$$

and a_T and c_T are the average unit-cell parameters at the temperature T . The $\langle \varepsilon_1 \rangle$ and $\langle \varepsilon_3 \rangle$ deformations were calculated with respect to the unit-cell parameters a_0 and c_0 measured at the maximum temperature from which the films were cooled.

The $\tilde{\varepsilon}_v$ and $\tilde{\varepsilon}_t$ values were determined from the equations relating reflection broadening and the components of the tensor of averaged random microdeformation, S_{ij} [19]. Since the tetragonality of the unit cell in the temperature range studied was low ($c/a < 1.01$), we used the well-known relationships for the cubic crystal $S_{11} = S_{22} = S_{33}$ and $S_{12} = S_{13} = S_{23}$. Then, reflection broadening during $\theta/2\theta$ scanning along the scattering vector is given by the equations

$$\beta_{00l}^2 = 16S_{11} \tan^2 \theta_{00l},$$

$$\beta_{l/2l}^2 = 16/3(S_{11} + S_{12}) \tan^2 \theta_{l/2l},$$

whence, using the measured β_{004} and β_{224} values and the calculated S_{11} and S_{12} values, we obtain

$$\tilde{\varepsilon}_v = \sqrt{\langle (\varepsilon_1 + \varepsilon_2 + \varepsilon_3)^2 \rangle} = \sqrt{3(S_{11} + 2S_{12})},$$

$$\tilde{\varepsilon}_t = \sqrt{\langle (\varepsilon_1 - \varepsilon_3)^2 \rangle} = \sqrt{2(S_{11} - S_{12})}.$$

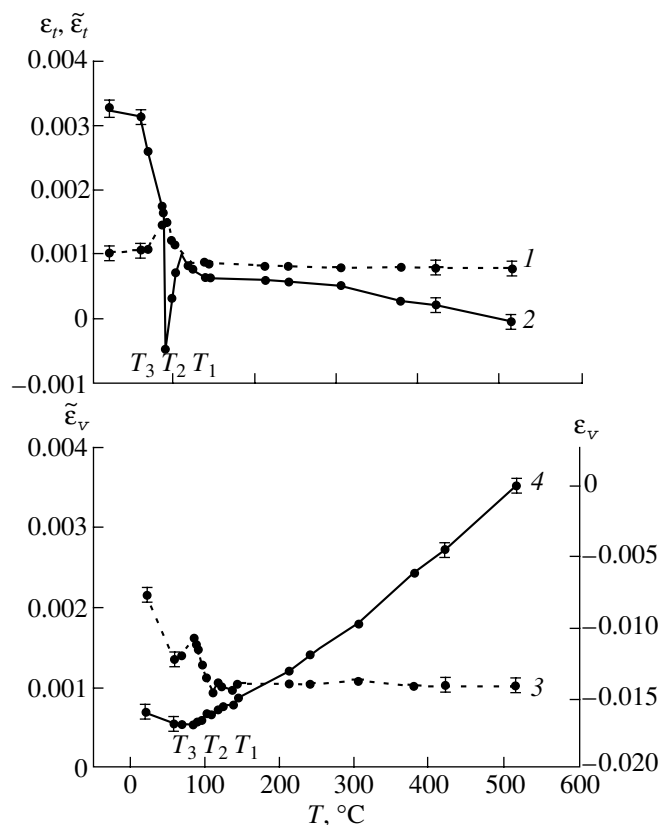


Fig. 2. Temperature dependence of the deformation of the average unit cell and microdeformation: (1) average shear microdeformation $\tilde{\varepsilon}_t$, (2) shear deformation of the average unit cell ε_t , (3) average volume microdeformation $\tilde{\varepsilon}_v$, and (4) volume deformation of the average unit cell ε_v .

Figure 2 illustrates these dependences. During cooling, the first kink on the $\tilde{\varepsilon}_t(T)$ plot (curve 1) is observed at $T_1 \approx 110^\circ\text{C}$. An increase in ε_t recorded at this temperature is accompanied by a drastic decrease in the uniform shear deformations ε_t in the averaged unit cell (curve 2). In a ferroelectric undergoing a phase transition, the dependence of the c - and a -parameters at further cooling provides an increase in ε_t [8]. An increase in ε_t on curve 2 begins only at $T < T_2 \approx 91^\circ\text{C}$ upon the ε_t jump at $T = T_2$ (where T_2 corresponds to the kink on the curves $c(T)$ and $a(T)$ (Fig. 1, curves 1, 2)). At temperatures lower than T_2 , the behavior of the shear microdeformations is changed and $\tilde{\varepsilon}_t$ starts decreasing. Finally, at $T < T_3 \approx 63^\circ\text{C}$, both ε_t and $\tilde{\varepsilon}_t$ become temperature-independent.

The ε_t and $\tilde{\varepsilon}_t$ dependences observed lead to the assumption that, in the temperature range $T_2 < T < T_1$, an intermediate dislocation-induced dipole-glass phase should exist [20]. Indeed, an increase in $\tilde{\varepsilon}_t$ at T_1 indicates the appearance of spontaneous random displace-

ments giving rise to lattice disordering because $\tilde{\epsilon}_t > \epsilon_t$. At T_2 , the averaged lattice becomes polar, and the shear deformations of the average unit cell drastically increase and start exceeding $\tilde{\epsilon}_t$, which also indicates the formation of macroscopic regions of rather uniform polarization. At $T_3 < T < T_2$, a mixed phase is observed in which the average polar lattice coexists with the regions of the dipole-glass phase in which the directions of local dipole moments are disordered. At $T < T_3$, the random shear microdeformations $\tilde{\epsilon}_t$ decrease to the values approximately equal to those observed in the paraelectric phase at $T > T_1$, whereas ϵ_t considerably exceeds $\tilde{\epsilon}_t$. Thus, below T_3 , only the macroscopically homogeneous ferroelectric phase exists.

It should be emphasized that the dependences of the volume microdeformations also have anomalies at temperatures T_1 , T_2 , and T_3 (curve 3 in Fig. 2), which is consistent with the conclusion regarding the formation of intermediate phases. At the same time, the dependence of the volume deformation of the average unit cell corresponds to the behavior of a conventional ferroelectric crystal (Fig. 2, curve 4).

It seems that the elastic interaction between the film and the substrate increases the phase-transition temperature and causes the tetragonal distortion of the cubic unit cell in the paraelectric phase.

CONCLUSION

In the films studied, the ferroelectric tetragonal phase is formed in the tetragonal and not in the cubic matrix. At $T > T_C$, dislocations break the lattice periodicity and give rise to microdeformations; they are also sources of fluctuations in the local electric fields. This, in turn, leads to the diffusion of the phase transition and the formation of intermediate phases during such transformations. During the restructuring of the crystal lattice, some blocks that have undergone phase transitions at a higher temperature do not form individual coherent-scattering regions and can promote only higher microdeformations.

ACKNOWLEDGMENTS

This study was supported by the Russian Foundation for Basic Research, project no. 98-02-18069.

REFERENCES

1. Z. Surovyak, A. M. Margolin, I. N. Zakharchenko, *et al.*, *Thin Solid Films* **176**, 227 (1989).
2. I. N. Zakharchenko, E. V. Sviridov, V. A. Alyoshin, and L. A. Sapozhnikov, in *Abstracts of the Second International Seminar in Relaxor Ferroelectrics, Dubna, 1998*, p. 112.
3. Z. Surovyak, A. E. Panich, and V. P. Dudkevich, *Thin Ferroelectric Films* (Rostovskii Pedagog. Univ., Rostov-on-Don, 1994).
4. V. M. Mukhortov, Yu. I. Golovko, V. A. Aleshin, *et al.*, *Phys. Status Solidi A* **77** (1), K37 (1983).
5. O. A. Bunina, I. N. Zakharchenko, P. N. Timonin, and V. P. Sakhnenko, *Kristallografiya* **40** (4), 708 (1995) [*Crystallogr. Rep.* **40**, 655 (1995)].
6. S. B. Vakhrushev, Author's Abstract of Doctoral Dissertation in Physics and Mathematics (St. Petersburg, 1998).
7. L. A. Shebanov, *Uch. Zap. Latv. Univ. im. Petra Stuchki* **189**, 150 (1974).
8. G. A. Smolenskiĭ, V. A. Bokov, V. A. Isupov, *et al.*, *The Physics of Ferroelectric Phenomena*, Ed. by G. A. Smolenskiĭ (Nauka, Leningrad, 1985).
9. Yu. V. Zvirgzde and Ya. Ya. Kruchan, *Izv. Akad. Nauk Latv. SSR, Ser. Fiz. Tekh. Nauk*, No. 5, 57 (1976).
10. W. Kenzig, *Helv. Phys. Acta* **24** (2), 175 (1951).
11. M. A. Krivoglaz, *Theory of X-ray and Thermal Neutron Scattering by Real Crystals* (Nauka, Moscow, 1967; Plenum, New York, 1969).
12. I. N. Zakharchenko, Ya. S. Nikitin, V. M. Mukhortov, *et al.*, *Phys. Status Solidi A* **114**, 559 (1989).
13. S. Desu, Z. J. Chen, P. V. Dudkevich, *et al.*, *Mater. Res. Soc. Symp. Proc.* **401**, 195 (1996).
14. Z. Surowiak, V. M. Mukhortov, and V. P. Dudkevich, *Ferroelectrics* **133**, 1 (1993).
15. V. M. Mukhortov, Yu. I. Golovko, V. I. Mukhortov, *et al.*, *Pis'ma Zh. Tekh. Fiz.* **5**, 1175 (1979) [*Sov. Tech. Phys. Lett.* **5**, 492 (1979)].
16. V. I. Iveronova and G. P. Revkevich, *Theory of X-ray Scattering* (Mosk. Gos. Univ., Moscow, 1972).
17. M. G. Radchenko, E. V. Sviridov, E. I. Bondarenko, *et al.*, Available from VINITI No. 6268-84 (Rostovs. Univ., Rostov-on-Don, 1984).
18. V. A. Bokov, *Zh. Tekh. Fiz.* **27** (8), 1784 (1957) [*Sov. Phys. Tech. Phys.* **2**, 1657 (1958)].
19. P. N. Timonin, I. N. Zakharchenko, O. A. Bunina, and V. P. Sakhnenko, *Phys. Rev. B* **58** (6), 3015 (1998).
20. P. N. Timonin, *Zh. Éksp. Teor. Fiz.* **116** (3), 986 (1999) [*JETP* **89**, 525 (1999)].

Translated by L. Man

PHASE
TRANSITIONS

Polymorphous Transformations of the *B1–B2* Type in Crystals of Finite Dimensions

S. V. Karpenko, A. Kh. Kyarov, A. I. Temrokov, and D. L. Vinokurskii

Research Institute of Applied Mathematics and Automation, Kabardino-Balkar Research Center,
ul. Shortanova 89a, Nalchik, 260000 Russia

Kabardino-Balkar State University, ul. Chernyshevskogo 142, Nalchik, 360004 Russia

Received January 10, 2001; in final form, May 16, 2001

Abstract—High-pressure-induced structural phase transitions in alkali halide crystals have been studied. The pressure of the *B1–B2* phase transition in crystals of finite dimensions is studied with the use of pair-interaction potentials within the theory of inhomogeneous electron gas. It is shown that the pressure of polymorphous transformation depends on the initial crystal dimensions. The anomalous dependence of the transition pressure on the dimensions of crystalline grains in lithium fluoride is considered and interpreted. Some structural and surface characteristics of the *B1* and *B2* modifications of a number of alkali halide crystals are calculated in the approximation of seven coordination spheres. © 2002 MAIK “Nauka/Interperiodica”.

INTRODUCTION

The phase transition between the *B1*-type (sodium chloride structure) and the *B2* (cesium chloride structure) phases of alkali halide crystals is being studied both experimentally and theoretically. The experimental study is performed by two main methods—specimen compression by a shock wave and the creation of static pressure in a diamond cell. Bridgman [1] used the method of static compression and observed the phase transitions in KCl and KBr crystals in the pressure range 20–30 kbar. Later, Al'tshler [2, 3] studied shock-wave induced compression in some alkali halide crystals. His experimental results confirmed the Bridgman data for potassium chloride and bromide, and thus proved the possibility of a polymorphous transformation in these compounds in the vicinity of 20 kbar. The first detailed theoretical study of the *B1–B2* phase transition was made by Jacobs [4] using the short-range Born–Mayer potential with due regard for the interactions only between the nearest neighbors [5]. Despite the fact that the pressures of polymorphous transformations obtained in [5] only approximately corresponded to the experimental data, Jacobs determined some important characteristics of this transition: the change in the crystal volume ΔV_i under the pressure of the phase transition and the jump in the lattice constant. Born and Huang [6] and Tosi [7] used the refined Born–Mayer approximation to determine the phase transition pressure and the cohesion energy of the *B1* and *B2* phases.

Later, Gordon and Kim used the model of an inhomogeneous electron gas [8] to calculate the cohesion energy of the *B1* and *B2* phases and the pressure of the polymorphous transformations in the crystals of lithium, potassium, and sodium bromides, fluorides, and

chlorides. The best agreement with the experimental data was attained for the cohesion energy of the *B1* phase and under the transition pressure. Later Cohen and Gordon [9] studied these phases in more detail—the short-range potentials also took into account the quantum corrections for inhomogeneity of kinetic energy; they also made an attempt to consider the effect of the second and the third nearest neighbors. However, the allowance for the contributions from the ions of the second and third coordination spheres often deteriorated the agreement between the theory and the experiment.

It should be noted that all the above investigations were made for infinite crystals. In [10], the effect of the surface contribution to the thermodynamic potential of a crystal on the properties of the *B1–B2* phase transition was studied for a number of alkali halide crystals.

In recent years, the development of the high-pressure methods triggered studies of the properties of polymorphous transformations in crystalline substances [11–15]. However, despite the considerable progress in the experimental and theoretical studies of polymorphous transformations, many problems still remain to be solved. Thus, while the structure and properties of high-pressure phases have been insufficiently studied, the polymorphous transformations in crystals of finite dimensions have been hardly studied at all.

The present investigation is dedicated to the characteristics of polymorphous transformations in ionic crystals of finite dimensions. Special consideration is given to the calculation of the elastic characteristics of crystals and their dependence on the pressure applied. The knowledge of these values is necessary for understanding the nature of the binding forces in ionic crystals. All

the calculations were performed in the approximation of the zero absolute temperature.

SIZE EFFECT IN THE *B1*–*B2* TRANSITION IN SMALL CRYSTALS

Proceeding to polymorphous phase transitions in alkali halide crystals of finite dimensions, we have to modify the thermodynamic potential of the crystal under the conditions of hydrostatic pressure [16] by adding a new term, which describes the surface energy of the crystal. To simplify the model, we assume that the surface of a crystal of the *B1* phase is (100)-faceted, whereas a crystal of the *B2* phase is (110)-faceted, because, under zero external pressure and absolute-zero temperature, these faces possess minimum surface energies. Thus, the thermodynamic potential of such a crystal, with due regard for the surface contribution, can be written in the form

$$G_{B1} = \sum_{k=1}^7 N_k^{(i)} U_k^{(i)} (a_k^{(i)} R^{(i)}) - V^{(i)} \frac{\partial}{\partial V^{(i)}} \left[\sum_{k=1}^7 N_k^{(i)} U_k^{(i)} (a_k^{(i)} R^{(i)}) \right] - \alpha_{\mu}^{(i)} / R^{(i)} + 4\pi r^2 k \sigma, \quad (1)$$

where $\alpha_{\mu 1} = 1.747558$ and $\alpha_{\mu 2} = 1.76268$ are the Madelung constants of the *B1* and *B2* structures, R_1 and R_2 are the distances between the nearest neighbors in these modifications, $V_1 = 2R_1^3$ and $V_2 = (8/3\sqrt{3})R_2^3$ are the unit volumes of the *B1* and *B2* phases, $U_{B1}(R_1)$ and $U_{B2}(R_2)$ are the pair-interaction potentials, $a_k = R_k/R_0$ is the ratio of the radius of the k th coordination sphere to the radius of the first one, and N_k is the coordination number. The subscript i enumerates both *B1* and *B2* phases. It should be noted that we used numerical values of the pair potentials obtained by the self-consistent method [17] within the theory of inhomogeneous electron gas, with r being the initial radius of the crystal, σ , the surface energy, and k , the numerical coefficient taking into account the deviation of the crystal shape from spherical. Since the thermodynamic potentials of both phases are equal at the transition point, Eq. (1) determines the implicit dependence of the polymorphous-transformation pressure on crystal dimensions [10].

The surface energy $\sigma(hkl)$ was calculated in the zeroth approximation, i.e., with no allowance for surface distortions of the interionic distances. In accordance with the definition of the surface energy [18], we have at 0 K

$$\sigma(hkl) = \sum_i \sum_{j=0}^{\infty} (W_j^{(i)} - W_{\infty}^{(i)}) n_j(hkl), \quad (2)$$

where $\sigma(hkl)$ is the surface energy of the (hkl) face, $W_j^{(i)}$ is the energy of a particle in the j th layer provided by the i th type of the interacting forces, $W_{\infty}^{(i)}$ is the same in the crystal bulk, and $n_j(hkl)$ is the number of particles in the j th plane per unit area. In the zeroth approximation used, Eq. (2) acquires the form [19]

$$\sigma(hkl) = n_0(hkl) \sum_i (W_0^{(i)} - W_{\infty}^{(i)}). \quad (3)$$

Now, consider a plane net inside an infinite solid. Obviously, for a perfect (undistorted) crystal, we have

$$W_{\infty}^{(i)} = W_S^{(i)} + 2W_{v/2}^{(i)}, \quad (4)$$

where $W_S^{(i)}$ is the energy of a particle on the net provided by the i th type of interaction with all the remaining particles in this plane, and $W_{v/2}^{(i)}$ is the energy of the same particle determined by its interaction with all the other particles in the planes above and below the plane under consideration. Thus, the particle energy in the surface plane of an undistorted crystal is

$$W_0^{(i)} = W_S^{(i)} + W_{v/2}^{(i)}. \quad (5)$$

Eliminating $W_{v/2}^{(i)}$ from Eqs. (4) and (5) and substituting the result into Eq. (3), we obtain

$$\sigma(hkl) = (1/2)n_0(hkl) \sum_i (\beta^{(i)} - 1) W_{\infty}^{(i)}, \quad (6)$$

where $\beta^{(i)} = \frac{W_S^{(i)}}{W_{\infty}^{(i)}} = \frac{A_S^{(i)}}{A_V^{(i)}}$ is the ratio of the sums over the

infinite plane net to the sum over the infinite lattice for the i th type of the interionic forces. In particular, for Coulomb forces, β is the ratio of the Madelung constant for the plane net to the Madelung constant for the three-dimensional lattice. For other forces, β is the ratio of the rapidly converging series whose summation presents no difficulties.

Surface tension can be calculated by using the formula relating the surface-tension tensor and surface energy [19] in the form

$$\sigma = \frac{\int \alpha_{im} dU_{im} dS}{dS} - S \frac{\partial \sigma}{\partial S} + \mu_j \Gamma_j, \quad (7)$$

where dU_{im} is the deformation-tensor differential, S is the surface area, and μ_j and Γ_j are the chemical potential and adsorption of the j th component (over the doubly repeating subscripts $i, m = 1, 2$, and $j = 1, 2, \dots, k$ is the number of the components in the system over which the summation is performed). For an isotropic surface and

Table 1. Surface energy and surface tension for alkali halide crystals

Crystal	$\sigma \times 10^{-3}, \text{J/m}^2$					$\alpha \times 10^{-3}, \text{N/m}$				
	B1 phase			B2 phase		B1 phase			B2 phase	
	1 [20]	2 [21]	3	4 [22]	5	6 [20]	7 [21]	8	9 [22]	10
LiF	465	289	392	461	537	1491	1978	1250	2131	1997
LiCl	–	230	271	332	318	–	1711	1500	1510	1481
LiBr	–	207	244	301	309	–	1637	1119	1150	1107
NaF	287	266	279	356	337	521	1214	637	708	691
NaCl	280	211	260	337	318	462	641	553	621	602
NaBr	189	192	174	220	231	267	534	306	376	384
KF	233	226	257	313	320	489	719	669	720	718
KCl	177	175	185	234	228	316	404	381	444	420
KBr	170	159	162	210	211	299	341	376	428	436
RbF	224	213	237	320	308	381	600	665	712	725
RbCl	275	166	191	227	224	316	549	531	600	613
RbBr	178	150	140	215	202	286	282	271	341	350

Note: The results of the present study are listed in columns nos. 3, 5, 8, and 10.

for the surface with a rotational symmetry not lower than of the third order, Eq. (7) takes the form

$$\sigma = \alpha - S \frac{\partial \sigma}{\partial S} + \mu_j \Gamma_j. \quad (8)$$

For the one-component system, the third term in the right-hand side of Eq. (8) goes to zero if one uses the Gibbs equimolar interface ($\Gamma = 0$). For such a choice of interface, we have

$$\sigma = \alpha + S \frac{\partial \sigma}{\partial S}.$$

If the distance between the particles is R , then $dS = 2RdR$, and, therefore,

$$\alpha = \sigma + \left. \frac{R \partial \sigma}{2 \partial R} \right|_{R=R_0}. \quad (9)$$

Substituting equations of the surface energy of an undistorted crystal into Eq. (9), we arrive at

$$\alpha(hkl) = \frac{1}{2} n_0(hkl) \sum_i (\beta^{(i)} - 1) W_\infty^{(i)} + \left. \frac{R \partial \sigma}{2 \partial R} \right|_{R=R_0}. \quad (10)$$

Table 1 lists the surface energy and the surface tension calculated by Eqs. (6) and (10) for a number of alkali halide crystals. Upon the determination of the surface contribution to the thermodynamic potential of the crystal, one can also calculate the pressure of the polymorphous $B1$ – $B2$ transformation by the equations of potentials G_{B1} and G_{B2} for both crystalline modifications [10]. This calculation shows that the transition pressure is strongly dependent on the crystal dimensions. Table 2 lists the calculated dependences $p_0(r)$ for a number of alkali halide crystals.

Table 2 shows that, for all the alkali halide crystals (except for lithium fluoride), the pressure of polymorphous transformation increases with the reduction of the initial crystal dimensions. For a nonspherical crystal ($k = 2$), the transition pressure is on average 6–8% higher than for an ideal spherical crystal ($k = 1$). For a lithium fluoride crystal, the situation is opposite—with a decrease in the crystal size the pressure of the $B1$ – $B2$ transition also decreases. This is explained by the different cohesion energies of the crystal, which for lithium fluoride is considerably higher than for other halides. This, in turn, gives rise to a higher pressure of polymorphous transformation for an infinitely large LiF crystal. However, the calculation of the surface energies of ionic crystals under high pressures show [22] that the surface energy of lithium fluoride under these conditions is lower in the $B2$ phase than in the $B1$ phase and, therefore, the surface contribution to the thermodynamic potential *accelerates* the phase transition by reducing the transition pressure. For the remaining alkali halide crystals, the size effect results in an increase in the pressure of the $B1$ – $B2$ phase transition with a decrease in the crystal dimensions.

ELASTIC CONSTANTS OF THE $B1$ MODIFICATIONS OF ALKALI HALIDE CRYSTALS

The occurrence of the structural phase transitions makes it necessary to study the elastic properties of crystals in the high- and low-pressure ranges. The calculations of the elasticity moduli $C_{\alpha\beta}$ and their dependence on pressure provide important information on the nature of binding forces in the high- and low-pressure

Table 2. Pressure of polymorphous transformation (kbar) as a function of the crystal dimensions

Crystal		$R_0 \times 10^{-10}$, m							
		25	50	75	100	125	150	200	250
LiF	1	151	202	221	230	236	250	258	264
	2	166	224	235	246	254	260	268	271
LiCl	1	220	198	182	176	172	171	170	169
	2	231	215	202	188	182	178	176	174
LiBr	1	158	142	130	123	119	117	115	113
	2	160	147	134	130	124	120	118	116
NaF	1	296	250	219	198	182	170	164	160
	2	310	260	225	204	187	175	170	168
NaCl	1	174	161	144	143	142.8	142.6	142.3	142
	2	183	170	151	146	145.5	145	144.7	144.5
NaBr	1	61	50	48	46	45	44.6	44.4	44
	2	67	58	54	53	52.5	52	51.5	51.4
KF	1	134	120	110	108	106	104	101	100
	2	140	127	116	114	113	112.7	112.5	112
KCl	1	43	39	36	34	33.5	33	32.3	32
	2	51	46	41	37	36.5	36	35.7	35
KBr	1	46	40	38	37	36	35	34.5	34
	2	50	44	40	38	37	36	35	34.8
RbF	1	48	44	41	39	38	37.8	37.3	37
	2	51	46	43	41	40	39.5	39.2	39
RbCl	1	25	23	22	21	20.8	20.6	20.4	20.3
	2	27	25	24	23.8	23.6	23.4	23.2	23
RbBr	1	20	19	18	17.5	17	16.5	16.2	16
	2	22	20	19	18.5	18	17.8	17.6	17.5

Note: 1 indicates that the crystal has a spherical shape ($k = 1$); 2 indicates that $k = 2$.

phases ($B2$ and $B1$, respectively) of the crystals studied and also allow one to draw some conclusions about the reasons for the loss of lattice stability upon compression. Thus, a decrease in C_{44} upon crystal compression indicates that the resistance to the shear deformation decreases, i.e., the lattice loses its stability under hydrostatic compression precisely because of the loss of its resistance to shear deformation.

Important information on the nature of binding forces in the $B1$ phase of alkali halides can be obtained by studying elastic constants C_{11} , C_{12} , and C_{44} . Since these constants depend on the first and second derivatives of the short-range potential $U(R)$, allowing for higher coordination spheres can considerably change the calculated data. The elastic constants were calculated under zero pressure at $T = 0$ K. These calculations are very important, because, experimentally, the elastic constants are usually determined by the ultrasonic method [23], which often yields dubious results, and, thus, only some experiments can be extrapolated to the region of the absolute zero.

When calculating the elastic constant, one has to separate the contributions from the Coulomb and short-range forces,

$$C_{11} = C_{11}^{\text{Coul}} + C_{11}^{\text{sh}}. \quad (11)$$

The same is true for the constants C_{12} and C_{44} . The Coulomb contribution is determined by summing up the interactions between all the lattice ions, whereas the short-range contribution is limited only to seven coordination spheres. Blackman [24] obtained the following relationships for the elastic constants of cubic ionic crystals

$$C_{11} = \frac{1}{V} \sum_i [Q(x^i)^4 + P(x^i)^2], \quad (12)$$

$$C_{12} = \frac{1}{V} \sum_i [Q(x^i)^2 (y^i)^2 - P(x^i)^2], \quad (13)$$

$$C_{44}^* = \frac{1}{V} \sum_i [Q(x^i)^2 (y^i)^2 + P(x^i)^2], \quad (14)$$

$$C_{44} = C_{44}^* - \frac{c^2}{D}, \quad (15)$$

$$c = \frac{1}{V} \sum_i x^i y^i z^i Q, \quad (16)$$

$$D = \frac{1}{V} \sum_i [Q(x^i)^2 + P(x^i)], \quad (17)$$

where V is the unit-cell volume ($2R^3$ for the $B1$ phase) and $(x/R, y/R, z/R)$ are the crystallographic coordinates. Summation is performed over all the lattice ions. The quantities P and Q in Eqs. (12)–(17) are determined as follows

$$P = \left(\frac{1}{r} \frac{d}{dr} U_{B1}^i(r) \right) \Big|_R, \quad (18)$$

$$Q = \left[\frac{1}{r} \frac{d}{dr} \left(\frac{1}{r} \frac{dU_{B1}^i(r)}{dr} \right) \right] \Big|_R, \quad (19)$$

where R is the equilibrium interionic distance. To calculate the Coulomb components of elastic constants, one has to sum up the rapidly converging series described in detail by Tosi [7]. Below, we present the data calculated by the Tosi scheme:

$$C_{11}^{\text{Coul}} = -2.55604/2R^4, \quad C_{12}^{\text{Coul}} = 0.11298/2R^4, \quad (20a)$$

$$C_{44}^{\text{Coul}} = 1.24802/2R^4, \quad D^{\text{Coul}} = -4.189/2R^6. \quad (20b)$$

In the calculations of the non-Coulomb components of the elastic constants, the pair potentials were approximated by a smooth continuous function together with its derivatives up to the second order. Table 3 lists the elastic constants for alkali halide crystals in the $B1$ phase. The modulus of hydrostatic compression B was calculated as

$$B = \frac{1}{3}(C_{11} + 2C_{12}).$$

Our calculations show that, under high pressures, the properties of the $B1$ – $B2$ phase transition for most alkali halides can be considered in the approximation of pair-additive interactions between ions, with the multiparticle effects being ignored. The latter can be estimated by calculating the deviation from the equality for the Cauchy relationship $C_{11} = C_{44}$. In cubic crystals, where in the absence of external pressure the ions are the centers of inversion, the neglect of the zero vibrations makes the Cauchy relationship valid. Of course, our model satisfies these requirements, which is reflected in Table 3—the relationship is satisfied for all the crystals studied. It is rather difficult to take into

Table 3. Elastic constants of the $B1$ modification of alkali halide crystals (Pa)

Crystal		$C_{11} \times 10^{10}$	$C_{12} \times 10^{10}$	$C_{44} \times 10^{10}$	$B \times 10^{10}$
LiF	1	9.25	5.91	5.91	8.14
	2	8.17	6.50	6.50	7.06
	3	13.90	6.05	6.84	8.67
LiCl	1	5.51	2.38	2.38	3.28
	2	5.45	2.77	2.77	3.66
	3	6.07	2.27	2.69	3.54
LiBr	1	6.12	2.20	2.20	2.51
	2	5.21	2.27	2.27	3.25
	3	–	–	–	–
NaF	1	12.49	2.05	2.05	5.02
	2	8.08	2.78	2.78	4.55
	3	10.85	2.29	2.90	5.14
NaCl	1	5.31	1.30	1.30	2.11
	2	4.86	1.27	1.27	2.46
	3	6.00	1.27	1.40	2.85
NaBr	1	5.16	1.00	1.00	2.23
	2	4.56	1.03	1.03	2.21
	3	4.90	0.98	1.09	2.29
KF	1	7.61	1.50	1.50	3.38
	2	7.08	1.61	1.61	2.55
	3	7.57	1.35	–	2.58
KCl	1	3.50	0.90	0.90	1.94
	2	3.39	0.86	0.86	2.09
	3	3.68	0.58	0.93	2.02
KBr	1	4.33	0.62	0.62	1.58
	2	4.16	0.70	0.70	1.86
	3	4.30	0.55	0.57	1.80
RbF	1	7.11	1.21	1.21	2.80
	2	6.70	1.30	1.30	3.10
	3	–	–	–	–
RbCl	1	4.26	0.48	0.48	1.80
	2	4.18	0.69	0.62	1.85
	3	4.50	0.52	0.50	1.85
RbBr	1	3.90	0.47	0.47	1.45
	2	3.74	0.56	0.56	1.62
	3	3.97	0.40	0.41	1.59

Note: 1 indicates the results of the present study; 2—Cohen and Gordon results [9]; 3—experiment [23].

account the multiparticle interactions in ionic crystals within the theory of inhomogeneous electron gas. However, in many instances, the two-particle approximation yields rather accurate results.

Two difficulties can arise when comparing the theoretically calculated and the experimentally measured

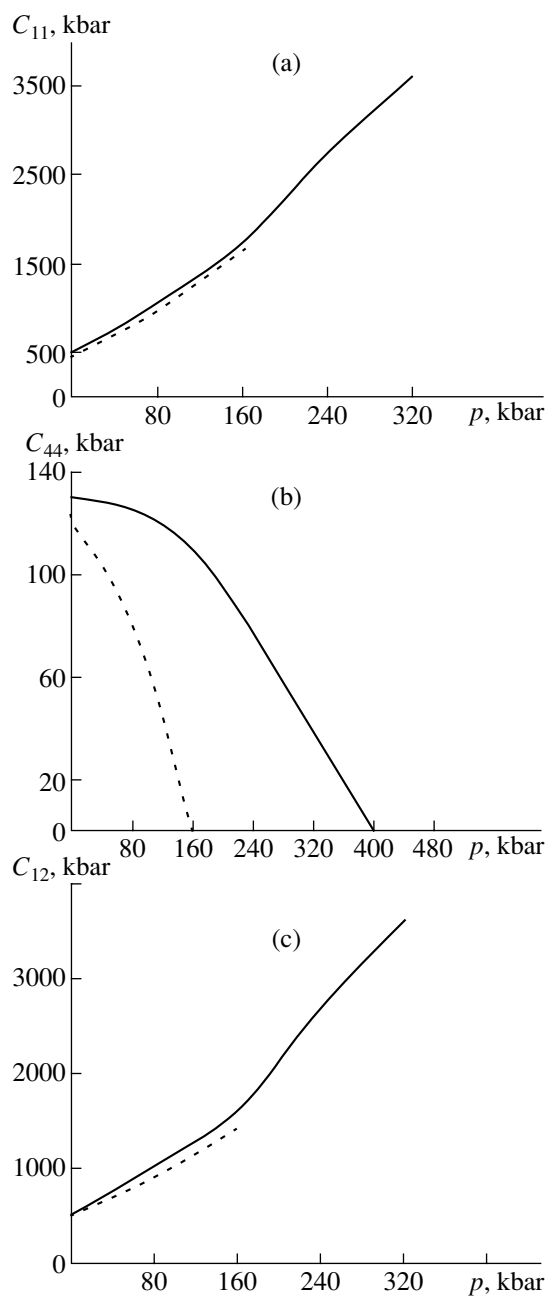


Fig. 1. Dependence of (a) C_{11} , (b) C_{44} , and (c) C_{12} on the applied pressure for the $B1$ phase of sodium chloride. Dashed line indicates the calculations for the model of nearest neighbors; solid line indicated the results of the present study.

elastic constants. First, the values of the elastic constants are somewhat ambiguous, especially that of C_{12} . The constants C_{11} and C_{44} can be determined directly by measuring the longitudinal and transverse particle displacements with respect to the $[100]$ direction, whereas C_{12} can be determined only as a linear combination of elastic constants determined, as a rule, for the $[110]$ direction. The second difficulty is more serious.

In many instances, the elastic constants calculated at 0 K are compared with the experimental data obtained at much higher temperatures. Therefore, prior to their comparison, one has to extrapolate the experimental data to the region of absolute zero, which inevitably introduces some additional errors.

Figure 1 shows the elastic constants of a sodium chloride crystal as functions of the applied pressure. To construct the curves of elasticity moduli as functions of pressure $C_{\alpha\beta}(p)$, we used the calculated dependences of the interionic distance and pair potential as functions of the external pressure calculated in the process determining the pressure of the polymorphous transformation. Minimizing the thermodynamic potential (1), we determine the interionic distance at the given pressure $r = R(p)$. The value thus obtained is then used to determine the pair potential $U(r) = U[R(p)]$, which is approximated by a smooth continuous function and its derivatives up to the second order. Using the values of R and U at a given pressure, we calculate the values of P in Eq. (18) and Q in Eq. (19), which, in turn, allows us to determine the elasticity moduli under the pressure p . Then, this procedure is repeated for the next pressure value $p' = p + \Delta p$, etc. up to the pressure of the $B1$ – $B2$ transformation.

Analyzing the curves in Fig. 1, one can see that, with an increase in the pressure, the deviation from the Cauchy relationship increases approximately by the linear law

$$C_{12} - C_{44} = \gamma p, \quad (21)$$

where p is the applied pressure and $\gamma = 2.85$. It should be noted that Cohen and Gordon [9] obtained the value $\gamma \approx 2$ in the approximation of three coordination spheres.

CONCLUSIONS

The study of the structural phase transitions in the crystals of the composition M^+X^- is based on the approximation of the pair ion interactions with the pair potential being determined by the self-consistent method within the theory of inhomogeneous electron gas. The rather good agreement between the theoretically calculated and the experimental data confirms the validity of the used pair potentials of ion interactions. To confirm the accuracy of the performed calculations, it is very important to determine the modulus of the hydrostatic compression B and elastic constants $C_{\alpha\beta}$, because these values have already been calculated by many researchers and are quite reliable. Thus, the good agreement between the elastic characteristics of twelve alkali halide crystals confirms the validity of the pairwise approximation for the description of the $B1$ phase of alkali halides. The deviation from the Cauchy relationship observed for the $B2$ phase under high pressure limits the use of two-particle description and shows that, along with pair components of the binding forces

at high pressures (about one hundred kbar) in the crystals studied, an important role is also played by nonpair (e.g., covalent) ionic interactions.

REFERENCES

1. P. W. Bridgman, Proc. Am. Acad. Arts Sci. **76**, 72 (1945).
2. L. V. Al'tshuler, L. V. Kuleshova, M. N. Pavlovskii, and G. V. Simakov, Zh. Éksp. Teor. Fiz. **47**, 61 (1964) [Sov. Phys. JETP **20**, 42 (1964)].
3. L. V. Al'tshuler, Usp. Fiz. Nauk **85** (2), 197 (1965) [Sov. Phys. Usp. **8**, 52 (1965)].
4. R. B. Jacobs, Phys. Rev. **16** (1), 837 (1938).
5. I. E. Mayer, J. Chem. Phys. **60**, 270 (1974).
6. M. Born and K. Huang, *Dynamical Theory of Crystal Lattices* (Clarendon, Oxford, 1954; Inostrannaya Literatura, Moscow, 1958).
7. M. P. Tosi, J. Phys. Chem. Solids **24**, 965 (1963).
8. R. G. Gordon and I. S. Kim, J. Chem. Phys. **56**, 3122 (1972).
9. A. J. Cohen and R. G. Gordon, Phys. Rev. B **12** (8), 3228 (1975).
10. V. F. Ukhov, R. M. Kobeleva, G. V. Dedkov, and A. I. Temrokov, *Electronic-Statistical Theory of Metals and Ionic Crystals* (Nauka, Moscow, 1982).
11. S. N. Val'kovskii, V. N. Erofeev, G. I. Peresada, and E. G. Ponyatovskii, Fiz. Tverd. Tela (St. Petersburg) **34** (2), 360 (1992) [Sov. Phys. Solid State **34**, 192 (1992)].
12. A. A. Popov, V. N. Udodov, and A. I. Potekarev, Izv. Vyssh. Uchebn. Zaved., Fiz., No. 9, 80 (1999).
13. R. S. Berry and B. M. Smirnov, Zh. Éksp. Teor. Fiz. **117** (3), 562 (2000) [JETP **90**, 491 (2000)].
14. É. I. Éstrin, Materialovedenie, No. 9, 11 (1999).
15. S. A. Kukushkin and A. V. Osipov, Zh. Éksp. Teor. Fiz. **113** (6), 2193 (1998) [JETP **86**, 1201 (1998)].
16. S. V. Karpenko, A. Kh. Kyarov, and A. I. Temrokov, in *Proceedings of the 15th International Conference "Equations of State of the Matter," Terskol, 2000*, p. 42.
17. A. Kh. Kyarov and A. I. Temrokov, Izv. Vyssh. Uchebn. Zaved., Fiz., No. 6, 3 (1994).
18. J. W. Gibbs, *The Scientific Papers*, Vol. 1: *Thermodynamics* (Longmans, Green, New York, 1906; Inostrannaya Literatura, Moscow, 1953).
19. S. N. Zadumkin and A. I. Temrokov, Izv. Vyssh. Uchebn. Zaved., Fiz., No. 9, 40 (1968).
20. G. V. Dedkov and A. I. Temrokov, Izv. Vyssh. Uchebn. Zaved., Fiz., No. 2, 19 (1979).
21. G. C. Benson and K. S. Iun, J. Chem. Phys. **42** (9), 3085 (1965).
22. L. Szasz, Z. Naturforsch. A **32**, 252 (1977).
23. G. Simmons and H. Wang, *Single Crystal Elastic Constants and Calculated Aggregate Properties* (Cambridge Univ. Press, Cambridge, 1971), p. 123.
24. M. Blackman, Proc. Phys. Soc. London, Sect. B **70**, 827 (1957).

Translated by L. Man

REAL STRUCTURE
OF CRYSTALS

Study of Polycrystalline Diamond Layers Deposited from Gas Phase

G. F. Kuznetsov*, V. G. Ral'chenko**, V. P. Varnin***, V. I. Polyakov*,
A. V. Khomich*, A. I. Rukovishnikov*, Yu. Sh. Temirov*, I. G. Teremetskaya***,
N. V. Tkal'****, and V. G. Anisimov****

* *Institute of Radio Engineering and Electronics, Russian Academy of Sciences (Fryazino Branch),
pl. Vvedenskogo 1, Fryazino, Moscow oblast, 141120 Russia
e-mail: gfk217@ire216.msk.su*

** *Center for Scientific Research, Institute of General Physics, Russian Academy of Sciences,
ul. Vavilova 38, 117942 Russia*

*** *Institute of Physical Chemistry, Russian Academy of Sciences,
Leninskii pr. 31, Moscow, 117915 Russia*

**** *Velikiĭ Novgorod State University, Velikiĭ Novgorod, Russia*

Received, April 12, 2001

Abstract—Crystallite size in polycrystalline diamond layers with a grain size exceeding 3 μm are determined by the X-ray topography method with the use of a divergent beam from a point source. For layers with thicknesses in the range 80–700 μm deposited in SHF plasma and 1–40 μm obtained by the method of a hot filament, the size distribution of crystallites is obtained. Asterism of some spots on X-ray diffraction patterns from the diamond layers with thicknesses exceeding 100 μm showed plastic deformation of individual crystallites. The parameters of deep levels in the band gap of undoped high-resistance diamond layers and the acceptor-type defects with an activation energy higher than 1 eV are determined by the method of charge relaxation spectroscopy. © 2002 MAIK “Nauka/Interperiodica”.

INTRODUCTION

Usually, the degree of perfection and the dimensions of polycrystalline diamond layers deposited from the gas phase are established by transmission and scanning electron microscopy (TEM and SEM) and atomic-resolution electron microscopy [1–3]. The standard method of studying the phase composition is Raman spectroscopy (RS) [1, 4]. The structure of diamond layers is also characterized by X-ray diffractometry [5] and X-ray topography, which provide, e.g., the study of crack formation in homoepitaxial diamond layers [6]. The diffractometric studies usually allow qualitative phase analysis which reveals, along with the phase of pure diamond, the transition layers of various carbide phases (SiC, TiC, etc.) formed due to the interaction of carbon with the substrate material. Both X-ray diffractometry and Raman spectroscopy are also used to determine internal stresses in polycrystalline diamond layers [5, 7].

This study was undertaken to determine the conditions for using an X-ray method to determine the crystallite sizes in the irradiated volume of the polycrystalline diamond layers. The methods for measuring and calculating the average crystallite size in thin layers of various polycrystalline materials, and especially of metals, is based on the determination of the number of small spots in the discrete intensity distribution over the

area of Debye rings on X-ray diffraction patterns [8]. However, in polycrystalline diamond layers, the averaging of crystallite size is inadmissible because crystallites start growing at deliberately introduced 5 nm-large nuclei so that, in 0.5–1.0 mm-thick layers, some crystallites attain a size of up to 1 mm.

We believe that it is most convenient to study crystallite size in thick ($\geq 1 \mu\text{m}$) polycrystalline diamond layers by the most informative and nondestructive X-ray topographic method, which, unlike SEM, does not require time- and labor-consuming sample thinning. SEM provides information only about the shape and size of the faces of those crystallites which emerge to the free surface or are seen on the transverse cleavage of the grown layer. However, such data are often insufficient for understanding and explaining the macroscopic characteristics of polycrystalline diamond layers. At the same time, crystallite sizes in polycrystalline diamond layers grown under nominally the same conditions determine the strength [9], the impurity concentration [10, 11], and the optical absorption [12] of these layers.

One of the authors (G.F.K.) used the X-ray methods [8] developed for high-resolution Laue diffraction patterns suggested by Guinier, Tennevin, and Fujiwara and showed [13–16] the possible use of the quantitative X-ray topographic analysis of the epitaxial layers with the use

of a divergent X-ray beam from a quasi-point source. This method was aimed at determining the sizes of blocks of mosaic and the angles of their minimum and maximum misorientation in single-crystal layers grown by the method of nonisostructural heteroepitaxy [13–16]. To study thick (40–1000 μm) polycrystalline diamond layers, the method of a divergent beam from a quasi-point source [17–19] was modified for samples in which the crystallite size exceeded 3 μm . Because of the very low absorptive power of diamond, the method of a divergent beam from a quasi-point source allows one to study polycrystalline diamond layers grown almost in the whole range of thicknesses—from several micrometers to several thousand micrometers.

EXPERIMENTAL

Methods of Growth and Study of Polycrystalline Diamond Layers

Single-crystal diamond layers with a thickness in the range 80–670 μm were grown in an ASTeX PDS-19 SHF plasmochemical reactor with a 8 kW-source with a frequency of 2.45 GHz [20]. The working gas was the $\text{CH}_4/\text{H}_2/\text{O}_2$ mixture with ratios $\text{CH}_4/\text{H}_2 = 2.5\%$ and $\text{O}/\text{C} = 0\text{--}0.7\%$. The substrates were polished single-crystal silicon wafers 60 mm in diameter. The films were deposited under a pressure of 100 torr at substrate temperature $T = 700\text{--}900^\circ\text{C}$. Then, the diamond layers were separated from the substrates and cut into about 1-cm²-large samples. The typical structure of the surface of a grown $\sim 100\text{-}\mu\text{m}$ -thick diamond layer is shown in Fig. 1. Thinner layers ($\leq 40\ \mu\text{m}$) were synthesized on silicon by the method of a hot filament with the use of the methane–acetone mixtures at the Institute of Physical Chemistry of the Russian Academy of Sciences. Diamond starts growing at numerous nucleation centers in the form of randomly oriented crystallites finally forming a polycrystalline diamond layer. As a rule, crystallites grow as columns with the transverse dimension increasing with the layer thickness.

To study the physical characteristics and the structure of polycrystalline diamond layers thus grown, we used a number of electrophysical (charge deep-layer spectroscopy) and optical (optical absorption and Raman spectroscopy) methods and also X-ray topography and diffractometry. On the basis of the method of a divergent beam from a quasi-point source [13–16], an original X-ray topographic method [17–19] for the quantitative analysis of crystallite sizes in the bulk of polycrystalline diamond layers irradiated with an X-ray beam was developed at the Institute of Radio Engineering and Electronics. This method was the main method in the present study as well. The preferable orientation of crystallites was studied by a more efficient X-ray diffractometry method [16, 19, 21] (Bragg reflection, $\text{Cu}K_{\alpha_1}$ radiation).

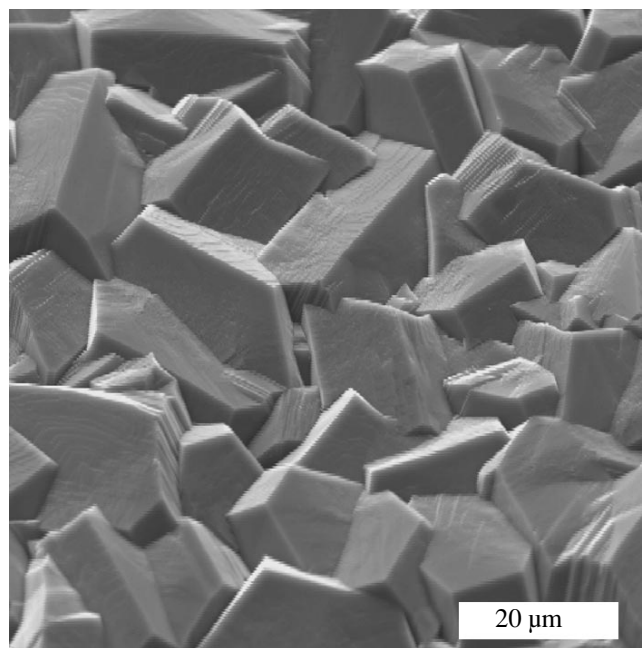


Fig. 1. Electron micrograph of a characteristic growth surface of a 110- μm -thick diamond layer grown in the SHF plasma.

Size Distribution of Crystallites in Polycrystalline Diamond Layers

The method of a convergent beam from a quasi-point source provides the linear resolution along the azimuthal direction of about 7 μm in polychromatic X-ray radiation [17–19]. In the characteristic $\text{Mo}K_{\alpha_1}$ radiation ($\lambda K_{\alpha_1} = 0.70929\ \text{\AA}$), the resolution along the Bragg direction is 3 μm [13–16]; the resolution of the photographic plates used is also about 3 μm . This signifies that X-ray topography allows one to record on a photographic plate the discrete images of reflections from individual $\geq 3\text{-}\mu\text{m}$ -large crystallites. For smaller crystallites, the reflections merge into Debye rings. Indeed, for finely grained samples with a thickness ranging from 1 to 40 μm , the topographs usually had only solid rings. However, under certain growth conditions (low rates of nucleation and secondary nucleation), some crystallites in the layers with the thickness $d \leq 40\ \mu\text{m}$ attained dimensions sufficient for the formation of a discrete intensity distribution not only on the Debye rings formed in the characteristic radiation but also on reflections formed in the polychromatic X-ray radiation.

The crystallite sizes were calculated based on their sizes determined along the azimuthal direction on topographs [17–19]. Using a projector or an optical microscope, we measured all the reflections in the 60°-large sector of a Debye ring formed in the diffraction of the $\text{Mo}K_{\alpha_{1,2}}$ and $\text{Co}K_{\alpha_{1,2}}$ radiations or the polychromatic radiation. When calculating the size of each crystallite,

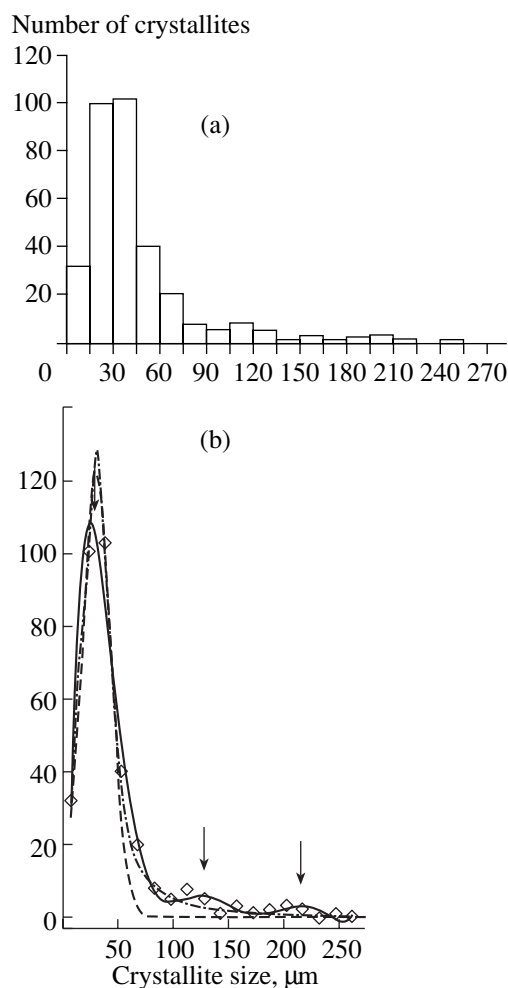


Fig. 2. (a) Histogram of the size distribution of crystallites in an 80- μm -thick diamond layer and (b) the approximation of this distribution by the Gaussian (dash-dotted line) and Lorentzian (dashed line) functions and a seventh-order polynomial (solid line).

we took into consideration the divergence of a beam from a quasi-point source and the geometry of the experiment [13–16]. In order to obtain the true crystallite size, it is sufficient to subtract from the crystallite length along the azimuthal direction the length of the image of a pointlike crystallite along the same direction in the polychromatic radiation, i.e., 7 μm . In this case, we assume that the size of each crystallite is equal to the maximum size of its azimuthal section by the system of diffracting crystallographic planes, $\{111\}$. Outside the Debye rings, some crystallites can also give rise to the formation of diffraction reflections from the $\{110\}$ and $\{331\}$ planes.

The crystallite sizes determined in an 80 μm -thick diamond layer are shown on a histogram in Fig. 2a. The maximum number of crystallites is observed in the range 15–45 μm , whereas their sizes range from 3 to 240 μm . The size distribution for crystallites in this sample was approximated by the Gaussian and Lorent-

zian functions and the n th-order polynomial (solid, dash-dotted, and dashed lines in Fig. 2b). The maximum number of crystallites have a size not exceeding 31 μm for the Gaussian distribution, 30.5 μm for the Lorentzian distribution, and 24.5 μm for the approximation by the n th-order polynomial. Thus, it is seen that all three approximations give close results. It should also be indicated that the histogram has two additional weak maxima (150 and 250 μm) for larger crystallites. These maxima are also seen on the approximation by a polynomial. The existence of crystallites two or three times larger than the thickness of the grown layer (80 μm) can be the consequence of the intergrowth of several neighboring crystallites with close orientations. Sample 3 with a thickness of 200 μm yields, in addition to the main maximum corresponding to 60 μm , also two maxima at 175 and 250 μm (Fig. 3). Some crystallites in this sample attain a size of 450 μm . For a 230 μm -thick layer grown under different conditions, the main maximum corresponds to a size of about 20 μm (Fig. 4). Moreover, there are also two additional maxima at 90 and 160 μm that show that the position of the main maximum on the size distribution of crystallites depends, to a large extent, on the growth conditions rather than on the layer thickness.

We also analyzed the layers with thicknesses of 670 and 700 μm (samples 6 and 7; sample 7 was synthesized by the method of an arc plasmatron, Norton, USA). The size distribution of crystallites in a 700- μm -thick layer is shown in Fig. 5 (approximation by a seventh-order polynomial). The Gaussian and Lorentzian approximations have the main maximum at about 35 and 38 μm , respectively. Thus, in the samples studied, the maximum on the size distribution of crystallites attains values from 5 to 40% of the layer thickness, although in layers with thicknesses of up to 200 μm , there is also a small number of crystallites two or three times larger than the layer thickness. Since the method used in our studies does not allow the detection of crystallites with sizes less than 3 μm , they are ignored in the distributions obtained.

Detection of Plastic Deformation of Crystallites

Some diffraction spots from crystallites on X-ray topographs from thick polycrystalline diamond layers (100–700 μm) show asterism [8]. Asterism manifests itself in a considerable increase in the lengths of diffraction spots from some crystallites along the Bragg direction in comparison with the lengths of the same spots along the azimuthal direction. This signifies that the conventional diffraction spots are transformed into characteristic diffraction “tails” caused by asterism. The topograph from an 80 μm -thick polycrystalline diamond layer has reflections whose sizes in the azimuthal direction are almost equal to, or slightly larger than, their sizes along the Bragg direction (Fig. 6a). However, for polycrystalline diamond layers with a thick-

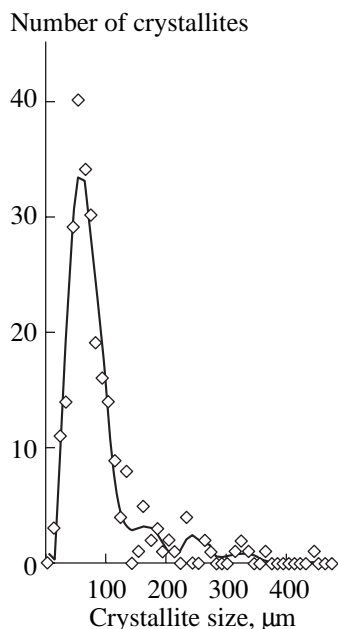


Fig. 3. Size distribution of crystallites in a 200- μm -thick layer approximated by a seventh-order polynomial.

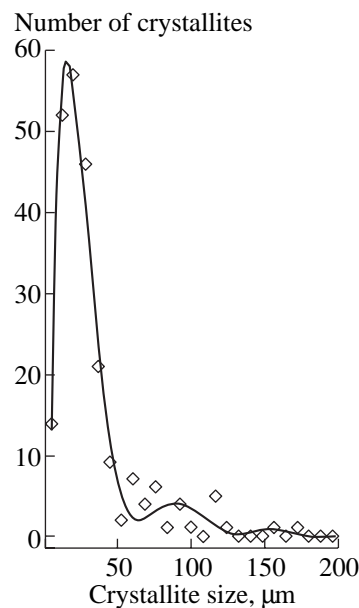


Fig. 4. Size distribution of crystallites in a 230- μm -thick layer approximated by a seventh-order polynomial.

ness $d \geq 100 \mu\text{m}$, the sizes of numerous reflections in the Bragg direction considerably exceed their “azimuthal sizes” (Fig. 6b). The pronounced asterism of diffraction spots indicates plastic deformation [8, 17, 18] in some diamond crystallites. We believe that this is direct proof of the fact that the intercrystallite pressure exceeded the high-temperature diamond strength. As a result, crystallites underwent plastic deformation during layer growth. At the same time, rather symmetric shapes (even circular, in accordance with the shape of the X-ray tube focus) of reflections indicates the non-uniform pressure distribution in the layer during its growth, and the crystallites which underwent only elastic deformation of various degrees provided the formation of symmetric reflections.

Different elastic stresses acting onto individual crystallites in the layer are explained by different contacts between neighboring crystallites (either by faces or by obtuse angles), the structure and the rigidity of the intercrystallite layers, and the crystallite sizes. The topographs show that with an increase in the thickness of a deposited polycrystalline diamond layer from 100 to 670 μm , the number of plastically deformed crystallites also increases. This shows that the polycrystalline diamond layer became more monolithic and, the intercrystallite layers became more rigid and provided better transfer of elastic stresses from one crystallite to another. As a result, an ever increasing number of crystallites undergo plastic deformation and show asterism on the topographs.

Taking into account some limitations, the length of the diffraction tails along the Bragg direction can be considered as an approximate measure of plastic deformation in individual crystallites.

Our measurements showed that the length of the spots with tails along the Bragg direction range from 10 to 170 μm and, in some instances, attains values of 0.5–1.0 mm, whereas the dimension of the point image along the Bragg direction in the monochromatic $\text{MoK}\alpha_1$ radiation is about 3 μm and, in the polychromatic radiation, 7 μm . In the wavelength units, a point of the crystal is imaged in the diffraction spot along the Bragg direction in the wavelength range $\delta\lambda \approx 7.1 \times 10^{-4} \text{ \AA}$ of the polychromatic X-ray radiation. Then the length of the tail lies within

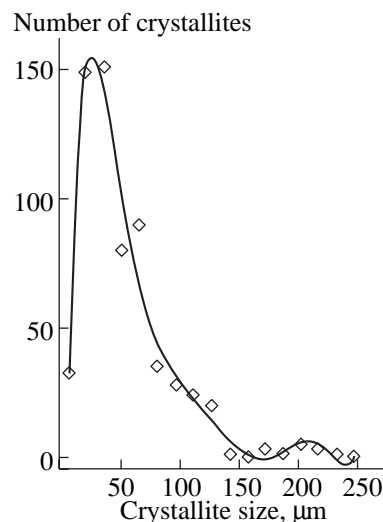


Fig. 5. Size distribution of crystallites in a 700- μm -thick polycrystalline diamond layer approximated by a seventh-order polynomial.

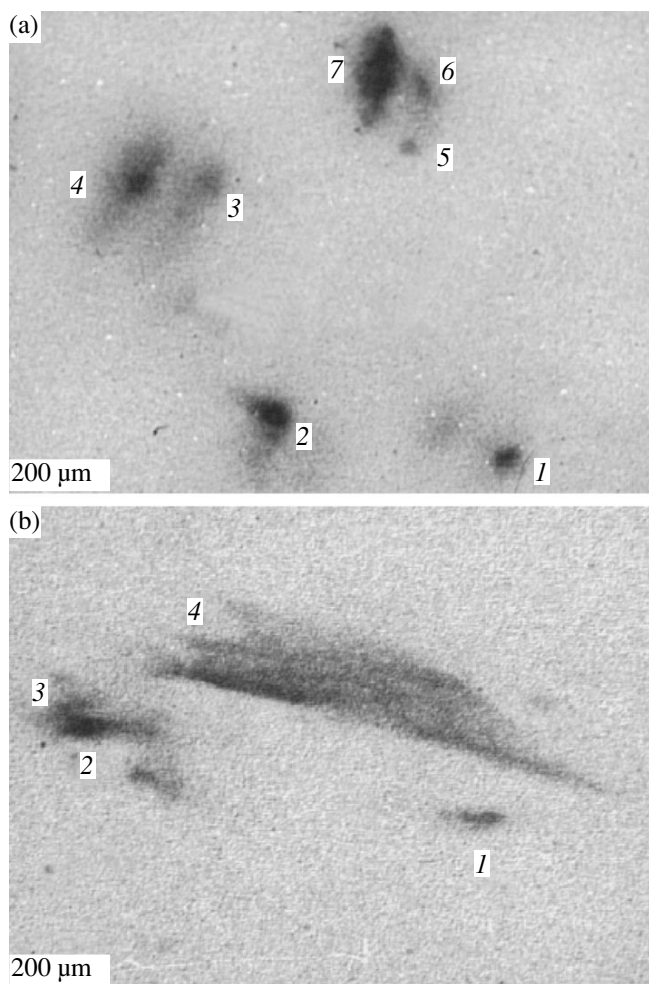


Fig. 6. X-ray topographs from crystallites in diamond layers with the thickness (a) 80 and (b) 200 μm . The crystallites corresponding to spots 1 and 5 of the thin layer and spot 2 of the thick layer have practically no asterism. Diffraction spots 2, 3, 6, 4, and 7 due to the crystallites of the thin layer and spots 1, 3, and 4 due to crystallites of the thick layer show an increasing degree of asterism.

$\delta\lambda = (1.0 \times 10^{-3}) - (17.0 \times 10^{-3}) \text{ \AA}$ and, in some instances, attains a value of $\delta\lambda_{\text{max}} = 0.1 \text{ \AA}$.

We believe that asterism is caused mainly by the misorientation of the individual parts of a crystallite that underwent shear plastic deformations. The calculation by the Bragg equation yields the minimum asterism of the order of one angular minute for weakly deformed crystallites. For strongly deformed crystallites, the misorientation attains up to $14.5''$, and, in some rare instances, even 1.5° . Using the rough model of small-angle dislocation subboundaries [22], one can calculate the residual elastic stresses in individual plastically deformed crystallites [23]. Our calculations showed that elastic stresses vary from 70 kPa for crystallites providing the minimum asterism to 20 MPa for crystallites providing pronounced asterism and attain a value of 0.7 GPa for crystallites providing the maxi-

imum asterism. The data on asterism can be treated mathematically in the same way as in the determination of the crystallite sizes. The distributions of crystallites depending on the asterism they provide on diffraction patterns (the size of the spots in micrometers) for four polycrystalline diamond layers are shown in Fig. 7. The maximum number of crystallites was determined for the first highest maxima almost identical for three samples. The asterism corresponding to these maxima is about 20 μm , which exceeds by about three times the length of the point image of a perfect crystal along the Bragg direction in the polychromatic radiation and corresponds to the wavelength interval of about $\delta\lambda_{\text{min}} = 2.1 \times 10^{-3} \text{ \AA}$. In addition, three weaker maxima with the asterism values 60, 85, and 125 μm are also formed. These maxima are especially pronounced for sample 4, with the first maximum being shifted toward the value 28 μm and the second asterism maximum being only slightly lower than the first one. The second maximum and the broad third and fourth maxima are several times higher than the corresponding maxima for other samples. In comparatively thin samples ($<100 \mu\text{m}$), only some crystallites were in conditions favorable for noticeable plastic deformation.

The ultimate strength of a natural single-crystal diamond at room temperature depends on the type of deformation (compression, extension, shear) and varies from 9 to 190 GPa [22–27]. For technical diamonds, the deformation is considerably lower—from 0.23 to 0.48 GPa [27]. The theoretical calculation and the experimental measurements yield approximately the same shear strength: 121 [22] and 132 GPa [27], respectively.

The unit-cell parameters of silicon ($a_0 = 5.4282 \text{ \AA}$) and diamond ($a_0 = 3.5676 \text{ \AA}$) considerably differ, and the lattice mismatch for this system is about 42%. It is well known that the growth of diamond on a single-crystal silicon substrate is accompanied by the formation of a silicon carbide interlayer, which slightly decreases the mismatch.

In trying to reveal the physical reasons for the formation of enormous elastic stresses giving rise to plastic deformation of individual crystallites in a growing polycrystalline diamond layer, one should not ignore possible isostructural heteroepitaxy of diamond crystallites on the single-crystal silicon substrate. Consider one of possible models.

Prior to the growth of polycrystalline diamond layers, the surface of the single-crystal silicon substrate is seeded with about 5-nm-large micronuclei most probably randomly oriented with respect to the substrate lattice. However, at the initial stage of growth, each of the micronuclei can be affected by the local mechanism of isostructural heteroepitaxy via the intermediate silicon carbide layer. Using the notions and formulas (1.5)–(1.9) from [28] for stresses in isostructural heteroepitaxy with due regard for the elastic relaxation of the system caused by bending deformation, the considerably dif-

ferent values of the Young's moduli for silicon and polycrystalline diamond aggregates ($E_1 = 176.58$ GPa and $E_2 = 1143$ GPa [26, 27]), and Poisson's ratios ($\nu_1 = 0.215$ and $\nu_2 = 0.0691$, respectively), we see that in isostructural heteroepitaxy at the substrate thickness $d_1 = 3$ mm and the polycrystalline diamond-layer thickness $d_2 = 600$ μm , the expected tensile stresses in the polycrystalline diamond layer, $\sigma_{(xx)2} \approx \sigma_{(yy)2} = 274.7$ GPa, would exceed the tensile strength $\sigma_{t2} = 190$ GPa for a natural single-crystal diamond at room temperature. For artificially grown polycrystalline diamond layers, the strength limit is lower than for a natural single-crystal diamond [26, 27].

There are indications of the direct effect of the silicon–diamond contact during deposition of diamond films and layers. Thus, it is shown [23, 24] that stress relaxation occurs via the formation mainly of planar defects (microtwins, stacking faults). However, as a rule, the formation of the pure diamond phase occurs in the transition layer containing amorphous carbon and silicon carbide [1, 24]. The internal stresses arising in thick polycrystalline diamond layers can hardly be associated only with the pronounced mismatch of the diamond and the substrate lattices; nevertheless, the lattice mismatch provides the formation of the stresses exceeding the threshold of the plastic deformation of diamond.

The internal stresses determined in polycrystalline diamond layers [23, 24] are obviously insufficient for the plastic deformation of individual crystallites. Mapping microstresses in diamond layers with the preferable $\{110\}$ crystallite orientation by the method of confocal Raman spectroscopy [7], we revealed the irregular arrangement of the regions with a length ranging from several micrometers to tens of micrometers in which the elastic stresses attained values of up to 9 GPa. Most often, these regions were observed in the vicinity of the crystallite boundaries [23, 26], which was attributed to the formation of stresses due to the appearance of incoherent crystallite boundaries in the process of formation of dislocation rows.

In plastic deformation caused by indentation of the natural faces of a diamond single crystal at room temperature, the generation of dislocations was observed [26, 27, 29, 30]. The cathodoluminescence topography provided recording of slip bands consisting of rows of linear dislocations [26] in two mutually perpendicular $\langle 110 \rangle$ directions. The generation of a single dislocation or a dislocation half-loop is an elementary event of plastic deformation. However, no attempts were made to calculate the local elastic stresses within the theory of planar dislocation pileups for diamond single crystals, despite the fact that successful attempts of this kind have already been made in conditions providing the generation of planar dislocation pileups in single crystals of the $A^{\text{III}}B^{\text{V}}$ semiconductors [31, 32].

Proceeding to textures, we should like to indicate that randomly oriented crystals formed on the surface

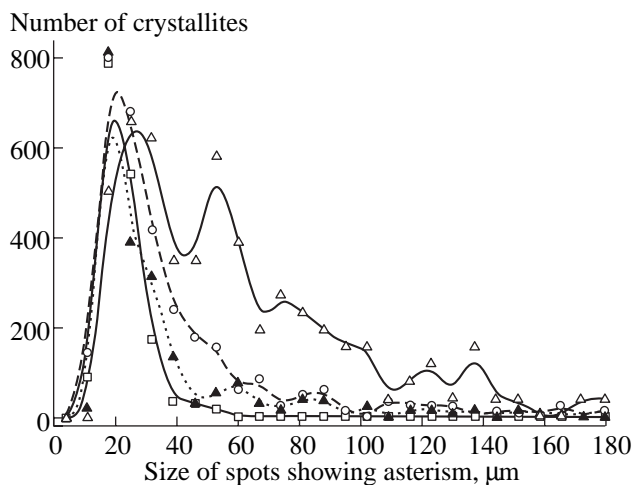


Fig. 7. Asterism distribution for crystallites in four samples of polycrystalline diamond layers with different thicknesses: (□) 40 μm , (○) 200 μm (sample 4), (△) 200 μm (sample 3), and (▲) 670 μm .

compete with one another during growth. In the final analysis, only those crystals survive in which the direction of the maximum growth rate is normal to the substrate surface. The diamond layers acquire an obvious column-like structure and the crystallite sizes gradually increase [1]. Therefore, the intensity ratios for the lines on the X-ray diffraction patterns from polycrystalline diamond layers often differ from the ratios indicated in the corresponding ASTM cards for the diamond powder. We obtained the diffraction patterns for Bragg diffraction from both surfaces of the diamond layers separated from the substrate—the lower finely grained surface adjacent to the substrate and the upper coarse-grained (growth) surface. The relative intensities of the diffraction lines obtained by the method of X-ray rocking curves [17–19, 33] are indicated in Table 1 for two

Table 1. Intensity ratios for the lines on the diffraction patterns obtained from the finely grained lower surface contacting with the substrate and freely growing coarse-grained upper surface of diamond layers with thickness d equal to 80 and 700 μm

hkl	Intensity				ASTM*
	80		700		
	lower surface	upper surface	lower surface	upper surface	
111	100	40	100	25	100
220	40	75	40	100	50
311	30	100	20	15	40
400	10	10	25	0	10
331	5	10	65	50	25

* For comparison, the ASTM data for powder diamond samples are indicated.

Table 2. Concentration of the nitrogen impurity in polycrystalline diamond layers

Sample	Thickness d , μm	Nitrogen concentration, $n \times 10^{17} \text{ cm}^{-3}$
1	80	8
2	100	9
3	200	20
4	200	25
5	230	20
6	670	26
7	700	2
8	40	60

80- and 700- μm -thick layers (samples 1 and 7). Similar to the case of powders, the intensity of the 111 lines in the lower parts of the layers is maximal. Nevertheless, for a 700- μm -thick layer, a certain texture is observed, i.e., the preferable growth of crystallites with the (331) planes parallel to the substrate surface. For an upper freely growing surface of the layer, the maximum intensity is observed either for the 220 or the 311 lines, depending on the growth conditions. The (110) texture is characteristic of films and layers of the optical quality synthesized in the SHF-discharge [7].

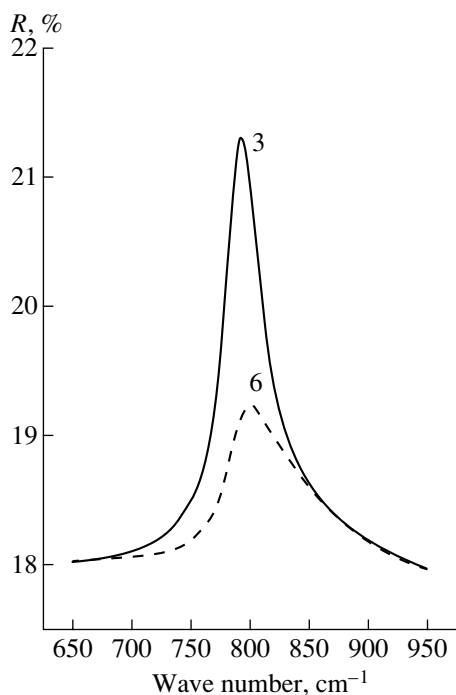


Fig. 8. Reflection spectra from the surfaces of the layers on the substrate side for samples 3 (dashed line) and 6 (solid line). The band with the maximum in the vicinity of 800 cm^{-1} is attributed to the transition SiC layer with the thicknesses 1.2 and 3.2 nm, respectively.

IMPURITIES AND DEFECTS

Nitrogen is the main “technological impurity” in synthetic diamonds, and even small amounts of nitrogen (at a level of 10^{17} cm^{-3}) considerably change the electrical, optical, thermal, and mechanical properties of the grown structures, the rate of their growth, and the morphology of a growing surface. In natural diamonds and diamonds synthesized under high pressure, the nitrogen concentration is usually determined from the light absorption coefficient at certain wavelengths in the visible IR or UV ranges [9]. The application of the well-known calibrations to diamond films obtained by the deposition from the gas phase is hindered by the fact that the nitrogen concentration in these diamond films is lower by one to two orders of magnitude and their weak characteristic bands overlap with the absorption bands due to intrinsic defects and inclusions of non-diamond carbon. We used the method of calculating the concentration of the substituted paramagnetic nitrogen suggested in [20, 34] (in the samples studied, the impurity nitrogen was in the paramagnetic state) by considering the characteristic band with the maximum lying in the vicinity of 270 nm and providing the determination of the nitrogen concentration in unpolished samples within an accuracy of fractions of *ppm* (10^{-4} at. %). The measured nitrogen concentrations in polycrystalline diamond layers grown under different conditions were in the range $(2\text{--}26) \times 10^{17} \text{ cm}^{-3}$ (Table 2).

The transmission and reflection spectra of most polycrystalline diamond layers deposited onto silicon substrates had a relatively narrow band with the maximum at 800 cm^{-1} in the IR range attributed to the SiC layer formed at the diamond–silicon interface. Figure 8 shows the reflection spectra from SiC films for two samples of polycrystalline diamond layers. The thicknesses of the transition SiC layers determined from these spectra are 1.2 and 3.2 nm, respectively, whereas for the remaining samples, the thickness of this layer ranged from 0.2 to 4.3 nm.

The electrophysical properties of polycrystalline diamond layers were studied by the method of charge-based deep-layer transient relaxation spectroscopy (Q-DLTS) [35, 36]. The method is based on the measurement of the parameters of the transient process of the charge equilibrium restoration in the sample under the action of either an electric pulse or a pulse of absorbed light. The analysis of this process provides information on the activation energy and cross section of the process, and the concentrations of various structural intrinsic or impurity-induced defects with the corresponding energy levels in the band gap of the material studied. The charge-based relaxation deep-level transient spectroscopy (Q-DTLS) differs from the well-known capacitance-based deep-level transient spectroscopy (C-DLTS) developed by Lang [29] and allows one to study not only semiconductor but also semi-insulating (high-resistivity) materials, to which undoped polycrystalline diamond layers are related. Moreover, when

obtaining Q-DLTS spectra, one also uses the time (rate) window instead of the temperature one, as in [29], which allows the use of isothermal spectroscopy, which is characterized by lower measurement errors. We obtained Q-DLTS spectra with the aid of a computer-controlled ASEC-3 system [35, 36]. The signal measured is described as $\Delta Q = Q(t_1) - Q(t_2)$, where t_1 and t_2 are the times measured from the beginning of discharge (relaxation). In order to obtain the spectrum (the separation of the contribution that comes into the charge ΔQ from the change in the charge state of various types of electrically active defects), the ΔQ value is measured as a function of the time (rate) window $\tau_m = (t_2 - t_1)/\ln(t_2/t_1)$ at the constant ratio $t_1/t_2 = \alpha$. The functional dependence $\Delta Q(\tau_m)$ has maxima all of which are associated with the change of the charge state of the corresponding electrically active defects—trapping centers. The maximum of the spectral dependence $\Delta Q(\tau_m)$ is located at

$$e_{p(n)} = \tau_m^{-1} = \sigma \Gamma_{p(n)} T^2 \exp(-E_a/kT), \quad (1)$$

where $e_{p(n)}$ is the rate of hole (electron) emission from the trapping centers of the given type, $\Gamma_{p(n)} = 2 \times 3^{1/2} (2\pi/h^2)^{3/2} k^2 m_{p(n)}^*$, σ is the capture cross section, T is the temperature, E_a is the activation energy, h and k are the Planck and the Boltzmann constants, respectively, and $m_{p(n)}^*$ is the effective mass of a hole (electron). The measured signal is related to the emission rate as

$$\Delta Q = Q_0 [\exp(-e_{p(n)} t_1) - \exp(-e_{p(n)} t_2)], \quad (2)$$

where $Q_0 = \int_0^\infty Q(t) dt$.

Using Eqs. (1) and (2), we can determine the concentration of electrically active defects, $N_t = 4\Delta Q_{\max}/qA$, where ΔQ_{\max} is the maximum value of the DLTS signal, q is the electron charge, and A is the contact area. The activation energy E_a and the cross section σ are determined from the Arrhenius dependence

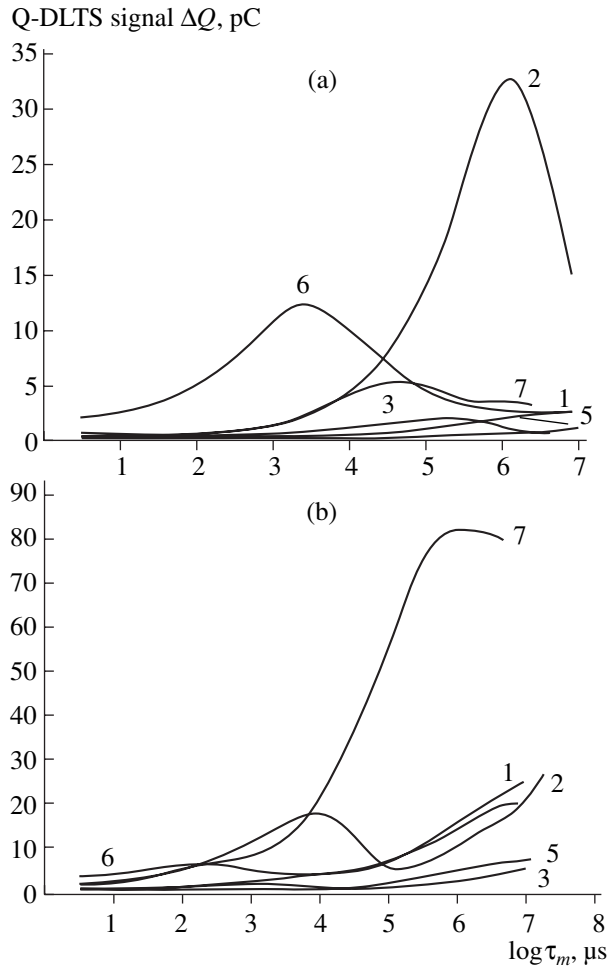


Fig. 9. Q-DLTS spectra of polycrystalline diamond layers at (a) $T = 295$ K (the region of the A peak) and (b) $T = 500$ K (the region of the B peak). The numbers of the samples are indicated at the curves.

$\ln(\tau_m^{-1} T^{-2})$ as a function of T^{-1} for each maximum or its slope in the Q-DLTS spectrum.

The sensitivity in the measurements of Q-DLTS spectra with the use of an ASEC-3 system was $\Delta Q_{\min} =$

Table 3. Electrical parameters of polycrystalline diamond layers containing electrically active defects of types A and B

Sample	Thickness $d, \mu\text{m}$	$\rho^*, \Omega \text{ cm}$	$N_{t(A)}^{**}, \text{cm}^{-3}$	$E_{a(A)}, \text{eV}$	$\sigma_{(A)}, \text{cm}^2$	$N_{t(B)}, \text{cm}^{-3}$	$E_{a(B)}^{***}, \text{eV}$	$\sigma_{(B)}^{****}, \text{cm}^2$
1	80	10^{13}	$>6 \times 10^{12}$	0.39	2×10^{-22}	$>5 \times 10^{13}$	0.49	$\sim 10^{-23}$
2	100	10^{12}	8×10^{13}	0.17	2×10^{-22}	$>10^{14}$	0.58	$\sim 10^{-20}$
3	200	1.4×10^{10}	5×10^{12}	0.24	2×10^{-22}	$>10^{13}$	0.25	$\sim 10^{-23}$
5	230	10^{14}	10^{11}	—	—	$>10^{12}$	0.64	$\sim 10^{-22}$
6	670	5×10^7	3×10^{13}	0.08	3×10^{-23}	$>6 \times 10^{13}$	1.1	$\sim 10^{-17}$
7	700	5×10^9	2×10^{13}	0.28	5×10^{-21}	2×10^{14}	1	3×10^{-17}

* Resistivity.
 ** Density of recharged defects upon the application of a 1 V/μm-electric field.
 *** Activation energy.
 **** Capture cross section.

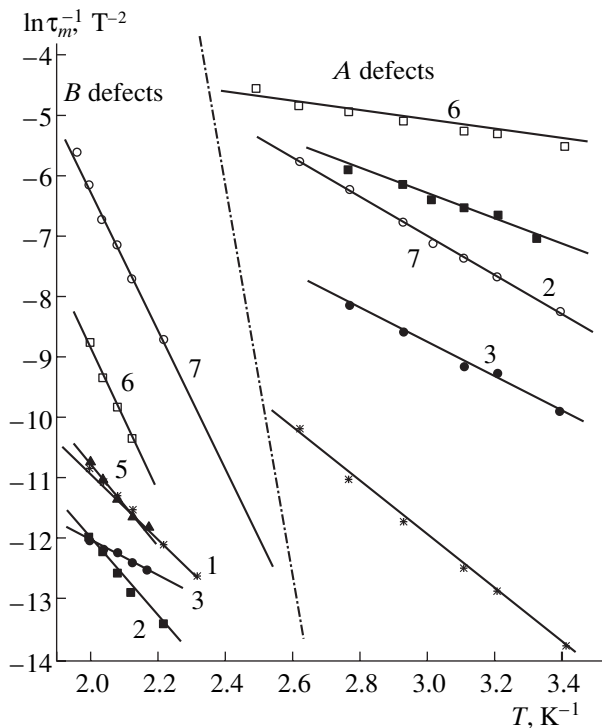


Fig. 10. Arrhenius dependences for the *A* and *B* defects in polycrystalline diamond layers and the corresponding *A* and *B* peaks in the Q-DLTS spectra. The activation energies E_a and the capture cross sections σ of these defects are indicated in Table 3.

10^{-16} K, whereas the range of the variation of the time window was $\tau_m = 2 \times 10^{-6} - 2 \times 10^2$ s.

Figure 9 shows the Q-DLTS spectra at 295 and 500 K, and Figure 10, the Arrhenius dependences. The experimentally determined and the calculated electro-physical parameters of polycrystalline diamond layers are listed in Table 3. The characteristic feature of all the samples is the pointlike electrically active defects having continuous energy spectra (the background in the Q-DLTS spectra). Most probably, these defects are located at the crystallite boundaries in the disordered intercrystallite space. The existence of a continuous spectrum of states is characteristic of amorphous, in particular, diamond-like carbon materials.

The defect concentrations are indicated in Table 3 for a certain (common for all the samples) intensity of the applied field, which allows one to estimate the relative (but not the absolute) variation of the defect concentration in the samples. All the samples are characterized by the presence of acceptor-type defects conditionally denoted here as type-*A* (the *A* peak in the Q-DLTS spectra) and type-*B* (the *B* peak or its slope in the Q-DLTS spectra) defects. The activation energy of *A*-defects is relatively low and does not exceed 0.4 eV of the valence-band ceiling. The capture cross section of these defects is low and is practically the same for all the samples. Most probably, these are point defects pro-

vided by broken carbon bonds and vacancies. The type-*B* defects are deeper and become active only during sample heating. However, their capture cross section allows one to consider them as point defects. It should also be emphasized that in the polycrystalline diamond layers studied, the concentration of acceptors is higher than that of donors, $N_A - N_D > 0$, and, thus, the samples have the hole conductivity.

The thickest layers, 6 and 7, have considerably different defect characteristics. The defects associated with peak *B* in these samples form deeper energy levels of the acceptor type with an activation energy exceeding 1 eV, their capture cross section is higher by five to six orders of magnitude than that of thinner samples, and they also have a higher concentration. Obviously, these acceptor defects should be related to a type other than *A* and *B*. It is possible that their formation is caused by the plastic deformation of crystallites revealed from the analysis of X-ray topographs from thick polycrystalline diamond layers.

As was shown by Samsonenko *et al.* [30], diamonds with considerable degree of plastic deformation possess a lower resistivity ($10^3 \Omega \text{ cm}$ for diamonds of type IIa with continuous conducting dislocation networks). At temperatures lower than 230 K, the activation energy of conductivity is 0.3 eV [30]. Our measurements of the temperature dependence of resistivity ρ of polycrystalline diamond layers yielded an activation energy of conductivity in the range 0.2–0.4 eV, with the ρ value for thicker samples (6, 7) lower by several orders of magnitude than for the remaining samples (Table 3). It should also be indicated that the temperature dependences of conductivity provide only integrated information on all the electrically active defects, whereas the DLTS method allows one to single out the contribution to the activation energy of conductivity that comes from various defects with the concentrations differing by six to seven orders of magnitude and to determine their capture cross sections.

CONCLUSION

Using the X-ray topography method providing the determination of the crystallite sizes exceeding $3 \mu\text{m}$, we analyzed quantitatively crystallites in the polycrystalline diamond layers grown from the gas phase on silicon substrates and obtained their size distributions.

The X-ray topography method developed in our study is applicable to both polycrystalline materials weakly absorbing the X-ray radiation and thin layers of strongly absorbing metals.

The X-ray topographs obtained revealed asterism of diffraction spots due to many crystallites. This phenomenon was interpreted as the first direct proof of the fact that the considerable part of the crystallites had undergone plastic deformation during the growth of polycrystalline diamond layers. The plastic deformation is assumed to be caused by the intercrystallite pressure

exceeding the high-temperature strength of diamond during the growth of thick layers.

The optical spectra confirmed the existence of a transition silicon carbide layer with a thickness of several nanometers formed during the growth of polycrystalline diamond layers on single-crystal silicon substrates. It is found that the concentration of the impurity nitrogen in the samples ranges from 2×10^{17} to $2.6 \times 10^{18} \text{ cm}^{-3}$. For the first time, the charge-based relaxation spectroscopy of defects in undoped high-resistivity polycrystalline diamond layers was used. The parameters of deep energy levels formed by defects in the band gap of diamond are determined. It is also shown that the acceptor-type defects with an activation energy exceeding 1 eV are formed.

ACKNOWLEDGMENTS

This study was supported by the Russian Foundation for Basic Research, project no. 01-02-16046.

REFERENCES

1. L. C. Nistor, J. Van Landuyt, V. G. Ralchenko, *et al.*, *Diamond Relat. Mater.* **6**, 159 (1997).
2. L. Chang, C. J. Chen, F. R. Chen, *et al.*, *Diamond Relat. Mater.* **5**, 326 (1996).
3. A. N. Stepanova, L. L. Aksenova, A. V. Kuznetsov, *et al.*, *Mater. Lett.* **22**, 285 (1995).
4. D. S. Knight and W. B. White, *J. Mater. Res.* **4**, 385 (1989).
5. D. Rats, L. Bimbault, L. Vandenbulcke, *et al.*, *J. Appl. Phys.* **78**, 4994 (1995).
6. C. K. Suzuki, A. H. Shinihara, and P. H. Godoy, *Diamond Relat. Mater.* **7**, 289 (1998).
7. I. I. Vlasov, V. G. Ralchenko, E. D. Obratsova, *et al.*, *Appl. Phys. Lett.* **71**, 1789 (1997).
8. A. Guinier, *Théorie et technique de la radiocristallographie* (Dunod, Paris, 1956; Fizmatgiz, Moscow, 1961).
9. C. S. J. Pickles, J. R. Brandon, S. E. Coe, and R. S. Sussmann, in *Proceedings of Topical Symposium IV "Diamond Films" of the 9th CIMTEC-World Ceramic Congress and Forum on New Materials, 1998* (Techna, Faenza, 1999), p. 435.
10. S. Nijhawan, S. M. Jankovsky, and B. W. Sheldon, *J. Mater. Res.* **14**, 1046 (1999).
11. S. M. Pimenov, V. V. Kononenko, V. G. Ralchenko, *et al.*, *Appl. Phys. A* **69**, 81 (1999).
12. E. Woerner, C. Wild, W. Mueller-Sebert, *et al.*, in *Proceedings of Topical Symposium IV "Diamond Films" of the 9th CIMTEC-World Ceramic Congress and Forum on New Materials, 1998* (Techna, Faenza), 1999, p. 305.
13. G. B. Bokij, G. F. Kuznetsov, V. V. Pantelev, *et al.*, in *Problems of Crystallography* (Mosk. Gos. Univ., Moscow, 1971), p. 206.
14. G. F. Kuznetsov, *Appar. Metody Rentgenovskogo Anal.* **12**, 162 (1973).
15. G. F. Kuznetsov and S. A. Semiletov, *Reviews on Electronic Technology, Series "Microelectronics"* (TsNII Élektronika, Moscow, 1975), Vol. 1, p. 280.
16. G. F. Kuznetsov, Doctoral Dissertation on Physics and Mathematics (Moscow, 1989).
17. V. G. Anisimov, L. N. Danil'chuk, G. F. Kuznetsov, *et al.*, in *Proceedings of the International Workshop "Silicon Carbide and Related Materials"* (Novgor. Gos. Univ., Novgorod, 1997), p. 64.
18. V. G. Anisimov, L. N. Danil'chuk, G. F. Kuznetsov, *et al.*, in *Scientific Works of the 1st International Seminar "Topical Problems of Strength" Dedicated to V. A. Likhachev and 33th Seminar "Topical Problems of Strength," Novgorod, 1997*, Vol. 2, Part 1, p. 186.
19. G. F. Kuznetsov, *Physics of Semiconductor Devices* (Narosa Publishing House, New Delhi, 1997), Vol. II, p. 1099.
20. A. V. Khomich, V. G. Ralchenko, A. A. Smolin, *et al.*, *Chem. Vap. Deposition* **5**, 361 (1997).
21. S. A. Semiletov, G. F. Kuznetsov, A. M. Bagamadova, *et al.*, *Kristallografiya* **23** (2), 357 (1978) [*Sov. Phys. Crystallogr.* **23**, 197 (1978)].
22. B. K. Vainshtein, V. M. Fridkin, and V. L. Indenbom, *Modern Crystallography*, Vol. 2: *Structure of Crystals*, Ed. by B. K. Vainshtein, A. A. Chernov, and L. A. Shuvalov (Nauka, Moscow, 1979; Springer-Verlag, Berlin, 1982).
23. I. Vlasov, V. Ralchenko, D. Zakharov, and N. Zakharov, *Phys. Status Solidi A* **174**, 11 (1999).
24. X. J. Guo, S. L. Sung, F. R. Chen, and H. C. Shih, in *Proceedings of Topical Symposium IV "Diamond Films" of the 9th CIMTEC-World Ceramic Congress and Forum on New Materials, 1998* (Techna, Faenza, 1999), p. 3.
25. L. C. Nistor, J. Van Landuyt, V. G. Ralchenko, *et al.*, *J. Mater. Res.* **12**, 2533 (1997).
26. E. J. Brookes, J. D. Comins, R. D. Daniel, and R. M. Erasmus, *Diamond Relat. Mater.* **9**, 1115 (2000).
27. *Natural Diamonds of Russia* (Polyaron, Moscow, 1997).
28. Yu. A. Tkhoriik and L. S. Khazan, *Plastic Deformation and Misfit Dislocations in Heteroepitaxial Structures* (Naukova Dumka, Kiev, 1983).
29. D. V. Lang, *J. Appl. Phys.* **45**, 3023 (1974).
30. N. D. Samsonenko, G. B. Bokij, V. A. Emets, and V. I. Timchenko, *Kristallografiya* **25**, 1300 (1980) [*Sov. Phys. Crystallogr.* **25**, 741 (1980)].
31. G. F. Kuznetsov, in *Physics of Semiconductor Devices* (Allied Publ., Delhi, 1999), Vol. I, p. 179.
32. G. F. Kuznetsov, *Kristallografiya* **46**, 320 (2001) [*Crystallogr. Rep.* **46**, 276 (2001)].
33. G. F. Kuznetsov, *Kristallografiya* **45**, 326 (2000) [*Crystallogr. Rep.* **45**, 294 (2000)].
34. S. V. Nistor, M. Stefan, V. I. Ralchenko, *et al.*, *J. Appl. Phys.* **87**, 8741 (2000).
35. V. I. Polyakov, A. I. Rukovichnikov, V. P. Varnin, *et al.*, *Mater. Res. Soc. Symp. Proc.* **442**, 687 (1997).
36. V. I. Polyakov, N. M. Rossukanyi, A. I. Rukovichnikov, *et al.*, *J. Appl. Phys.* **84**, 2882 (1998).

Translated by L. Man

PHYSICAL PROPERTIES
OF CRYSTALS

**Gd₃Ga₅O₁₂:Nd³⁺ Crystals for a Continuous-Wave
Diode-Pumped Laser Operating
in ⁴F_{3/2} → ⁴I_{11/2} and ⁴F_{3/2} → ⁴I_{13/2} Channels**

A. A. Kaminskii*, **A. V. Butashin***, **K. S. Aleksandrov****, **L. N. Bezmaternykh****,
V. L. Temerov**, **I. A. Gudim****, **N. V. Kravtsov*****, **V. V. Firsov*****, **D. T. Seo******,
U. Hömmerich****, **D. Temple******, and **A. Braud*******

* Shubnikov Institute of Crystallography, Russian Academy of Sciences,
Leninskii pr. 59, Moscow, 117333 Russia

e-mail: kaminalex@mail.ru

** Institute of Physics, Siberian Division, Russian Academy of Sciences, Krasnoyarsk, Russia

*** Institute of Nuclear Physics, Moscow State University, Vorob'evy gory, Moscow, 119899 Russia

**** Research Center for Optical Physics, Hampton University, Hampton, 23688 USA

***** CIRIL, rue Claude Bloch, BP 5133, Caen Cedex, 14040 France

Received October 16, 2001

Abstract—Garnet crystals of the composition Gd₃Ga₅O₁₂:Nd³⁺ (concentration series C_{Nd} = 1–10 at. %) were grown from flux. In terms of spectroscopy, these crystals, unlike those grown from melts, form a medium with a single activator center. For the first time, continuous-wave lasing was excited by diode pumping with the use of Gd₃Ga₅O₁₂:Nd³⁺ crystals at the wavelengths λ₃ = 1.3315 and λ₄ = 1.3370 μm of the ⁴F_{3/2} → ⁴I_{13/2} channel and also the simultaneous generation at two wavelengths, λ₁ = 1.0621 and λ₂ = 1.0600 μm, of the ⁴F_{3/2} → ⁴I_{11/2} channel. © 2002 MAIK “Nauka/Interperiodica”.

INTRODUCTION

The first studies of laser generation and spectroscopy of garnets were performed on flux-grown Y₃Al₅O₁₂:Nd³⁺ crystals [1–3]. The widespread use of these materials in active elements of flashlamp-pumped lasers requires the growth of large crystals 10 cm in length and 1 cm in diameter. To grow such crystals, special methods of crystallization from melts were developed such as the Czochralski method. However, the comparison of the properties of aluminum garnets Y₃Al₅O₁₂:Ln³⁺ grown from melts (*T*_m = 1930°C) and from flux (at temperatures 1100–1200°C) showed that the latter have better spectroscopic parameters corresponding most closely to the model of a single activator center [4, 5]. Furthermore, at the crystallization of Y₃Al₅O₁₂:Nd³⁺ crystals from flux, the distribution coefficient of neodymium considerably exceeds the value *K*_{Nd} = 0.18 characteristic of the crystallization from melts. In connection with the development of semiconductor diode-laser pumping in recent years, the interest in crystals grown from flux with a volume of up to 1 cm³ is renewed (including Y₃Al₅O₁₂:Nd³⁺ with an elevated activator concentration, C_{Nd} ≥ 1.5 at. %). Such crystals are used in compact laser devices providing a high quality of radiation (a narrow spectral line, single-mode lasing, low losses, and minimum beam divergence).

Below, we report on the growth of the concentration series of Nd³⁺-doped gadolinium–gallium garnet crystals, Gd₃Ga₅O₁₂:Nd³⁺ (Nd-doped GGG), the study of their lasing properties under diode-laser pumping and also compare their laser and spectroscopic data obtained with those of crystals grown by the Czochralski method from a melt [6].

The Gd₃Ga₅O₁₂:Nd³⁺ single crystals were grown from boron–barium fluxes of the composition 56 wt % (BaO + 0.62B₂O₃) + 44 wt % Gd_{3–x}Nd_xGa₅O₁₂, where *x* = 0.03, 0.1, and 0.3. The saturation temperature of the fluxes was *T*_{sat} = 1200–1230°C; the slope of its concentration dependence was *dT*_{sat}/*dn* = 15°C/wt %. The crystals were synthesized in platinum crucibles by the group method [7] on six “prismatic” seeds with square bases of 1 mm² and heights of 10–15 mm. The lateral seed faces were formed by the equilibrium (110) and (211) planes. The seeds were cut out from selected high-quality Gd₃Ga₅O₁₂ crystals.

Upon the attainment of the initial overcooling by 3–4°C (corresponding to the middle of the metastable zone), the flux temperature was decreased at a rate of *dT/dt* = 1–6°C/day (24 h), which corresponded to the growth rate of the crystals at the main stage of growth, up to 0.5 mm/day. The crystal holder was reversibly rotated with a period of 0.5–1 h. The crystallization temperature ranged from 80 to 100°C; the grown crys-

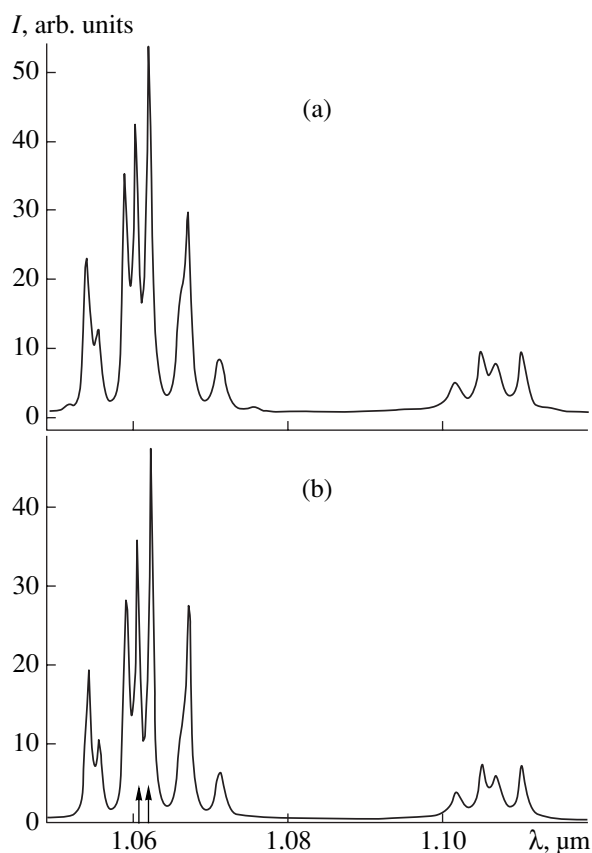


Fig. 1. Luminescence spectra of Nd³⁺ ions (concentration ~1 at. %, $^4F_{3/2} \rightarrow ^4I_{11/2}$ transitions) at 300 K from gadolinium–gallium garnet crystals grown (a) from melt and (b) from flux. Arrows indicate the lasing lines.

tals weighed 100–120 g. The unit-cell parameters of the crystals were measured on a Geigerflex (Rigaku Co.) X-ray powder diffractometer ($Co_{K\alpha}$ -radiation, 1200, 1220, and 1222 reflections).

Gd₃Ga₅O₁₂:Nd³⁺ single crystals with a volume of up to 2 cm³ were used to prepare the samples in the shape of polished plane–parallel plates parallel to the most developed faces of the (110) rhombododecahedron with a thickness of 2–4 mm and an area of up to 50 mm². This orientation of the plates reduced the undesirable effect of growth striae on the lasing characteristics. Similar samples were also prepared from garnet crystals grown from melt. The ends of the active laser elements had no antireflection coating.

The laser experiments were performed in a 20-cm-long hemispherical cavity at 300 K. The curvature radius of the spherical (exit) mirror was 100 mm. The crystal was located close to the plane selective mirror through which the end pumping was made. This mirror had a high transmission coefficient ($T \approx 80\%$) at the pumping wavelength ($\lambda_p \approx 0.81 \mu\text{m}$) and a high reflection coefficient ($R > 99.9\%$) at the lasing wavelengths.

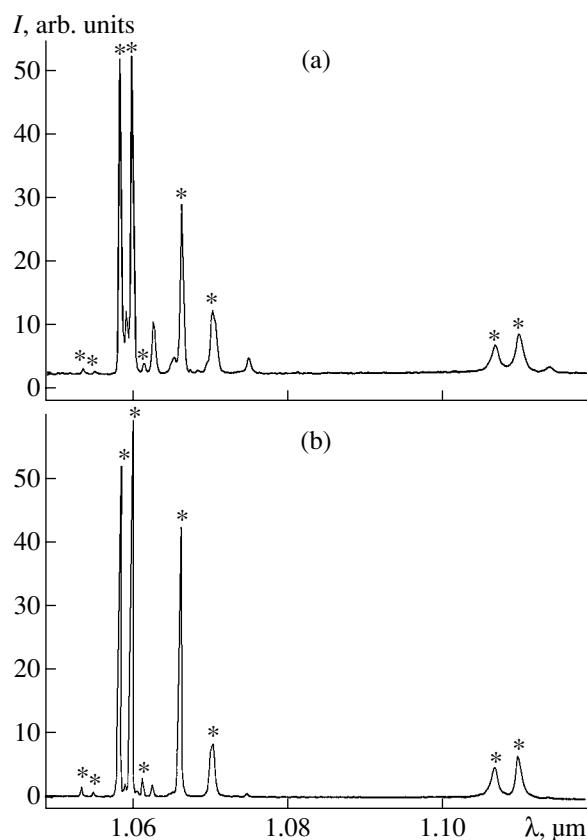


Fig. 2. Luminescence spectra of Nd³⁺ ions (concentration ~1 at. %, $^4F_{3/2} \rightarrow ^4I_{11/2}$ transitions) at 15 K in the gadolinium–gallium garnet crystals (a) grown from melt and (b) grown from flux. Asterisks indicate the lines of the principal center of Nd³⁺ ions in a Gd₃Ga₅O₁₂ crystal.

A diode-laser ATS-2440 with a nominal power of 1 W thermally stabilized to 0.1°C was used as a pumping source. Absorption and luminescence spectra of Nd³⁺-doped gadolinium–gallium garnet crystals were recorded on an AM510-M1 (Action Research Co.) diffraction spectrometer by an InSbAl detector. The temperature measurements of the spectra were made on a CSW-202 (Advanced Research Systems) double-loop close-cycle helium refrigerator in the range 15–300 K.

The examination of the absorption and luminescence spectra of the Nd³⁺-doped gadolinium–gallium garnet crystals grown from melt and from flux obtained at 300 K were practically identical. The luminescence spectra consist of homogeneously broadened lines (Fig. 1) whose positions and intensities are adequately described within the approximation of a single activator center with the scheme of crystal-field splitting suggested in [6]. At the same time, the low-temperature luminescence (Figs. 2, 3) and absorption (Fig. 4) spectra were different: the number and intensities of additional lines in comparison with those of the principal activator center Nd³⁺ for crystals grown from melt were much more pronounced.

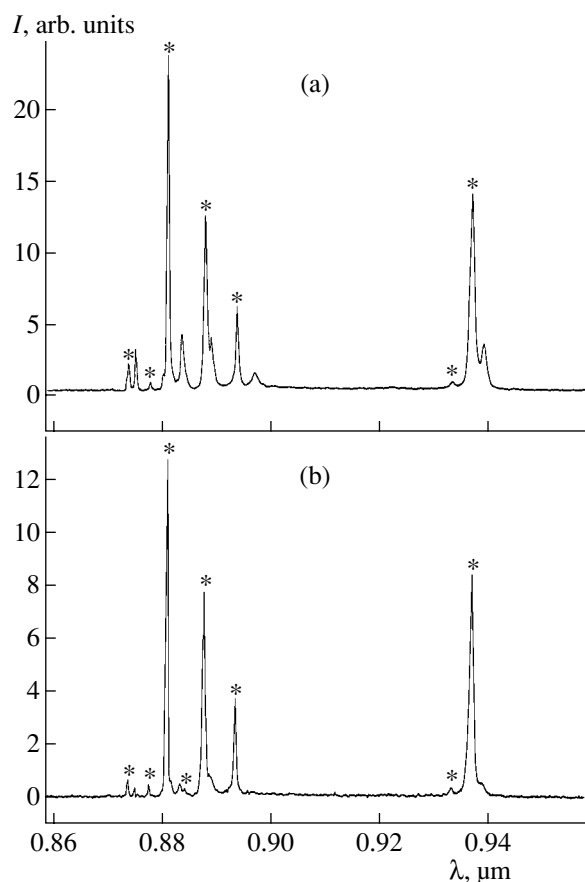


Fig. 3. Luminescence spectra of Nd^{3+} ions (concentration ~ 1 at. %, ${}^4\text{F}_{3/2} \rightarrow {}^4\text{I}_{9/2}$ transitions) at 15 K in the gadolinium–gallium garnet crystals (a) grown from melt and (b) grown from flux. Asterisks indicate the lines of the principal center of Nd^{3+} ions in $\text{Gd}_3\text{Ga}_5\text{O}_{12}$ crystal.

These differences can be interpreted based on the crystal chemistry of garnets. It is well known that in the quasi-binary Gd_2O_3 – Ga_2O_3 system, the gadolinium–gallium garnet has a range of existence of $\text{Gd}_{3+x}\text{Ga}_{5-x}\text{O}_{12}$ solid solutions enriched in gadolinium oxide (Gd_2O_3) in comparison with the stoichiometric composition $\text{Gd}_3\text{Ga}_5\text{O}_{12}$. The formation of these solid solutions is interpreted as a partial replacement of Gd^{3+} by Ga^{3+} ions in the octahedral positions of the structure [8, 9]; the unit-cell parameter of these solid solutions is described by the following formula [10]:

$$a_{s.s} = a_0 \left[1 + \left(\frac{r(\text{Gd}^{3+})}{r(\text{Ga}^{3+})} - 1 \right) \times 0.0268x \right], \quad (1)$$

where $a_0 = 12.375 \text{ \AA}$ is the unit-cell parameter of the stoichiometric garnet, $\text{Gd}_3\text{Ga}_5\text{O}_{12}$, and r are the octahedral ionic radii of the ions. The existence range of solid solutions is rather large (up to $x \approx 0.3$). The most homogeneous crystals are grown from a congruent melt of the composition $\text{Gd}_{3.05}\text{Ga}_{4.95}\text{O}_{12}$ [10].

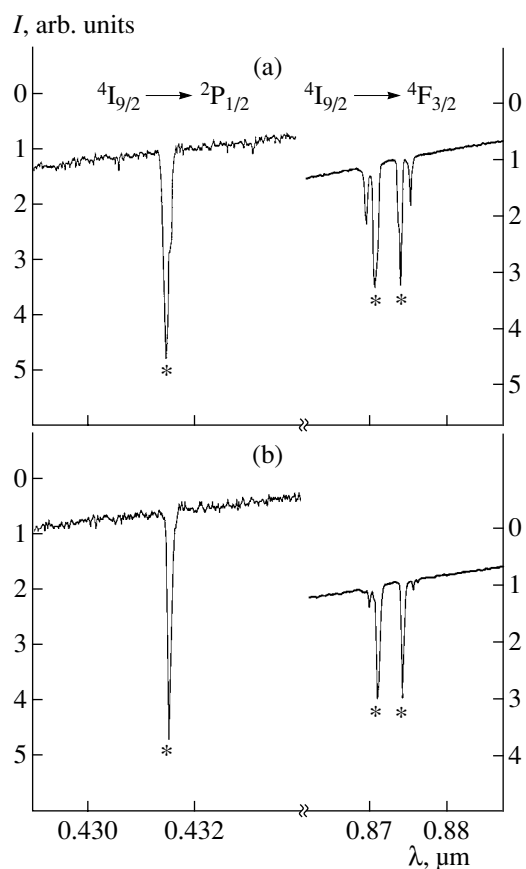


Fig. 4. Luminescence spectra of Nd^{3+} ions (concentration ~ 1 at. %, ${}^4\text{I}_{9/2} \rightarrow {}^2\text{P}_{1/2}$ and ${}^4\text{I}_{9/2} \rightarrow {}^4\text{F}_{3/2}$ transitions) at 15 K from the gadolinium–gallium garnet crystals (a) grown from melt and (b) grown from flux. Asterisks indicate the lines of the principal center of Nd^{3+} ions in $\text{Gd}_3\text{Ga}_5\text{O}_{12}$ crystal.

All the absorption and luminescence spectral lines should be attributed to the activator centers of Nd^{3+} ions replacing the Gd^{3+} ions in the c -positions of the structure (the concentration of large Nd^{3+} ions in the octahedral positions of the garnet is very low even in the $\text{Nd}_3\text{Ga}_5\text{O}_{12}$ crystals [11]). The structure of Nd^{3+} activator centers in the gadolinium–gallium garnet is determined to a large extent by the distribution of the cations from the second coordination sphere located in four distorted cubes, four octahedra, and six (2 + 4) tetrahedra sharing edges and vertices with a distorted NdO_8 cube (see table).

The principal center (type 1 in table) is formed by distorted NdO_8 cubes built by ten Ga and four Gd atoms from the second coordination sphere, which corresponds to the stoichiometric garnet of the composition $\text{Gd}_3\text{Ga}_5\text{O}_{12}$ and a low concentration of Nd^{3+} activator ions. The additional activator center (type 2) observed in the spectroscopic experiment is, most likely, formed in the case where nine Ga atoms and five Gd atoms are

within the second coordination sphere around a Nd³⁺ ion. Since the octahedral ionic radius of Gd³⁺ (0.94 Å) substantially exceeds that of Ga³⁺ (0.62 Å), this replacement strongly distorts the oxygen environment of a Nd³⁺ ion (since the NdO₈ polyhedron and the nearest octahedron share an edge). The calculation shows that in a gadolinium–gallium garnet of the congruent composition Gd_{3.05}Ga_{4.95}O₁₂ grown from melt, the centers of type 2 would comprise up to 8% of the total number of the Nd³⁺ activator centers even if one ignores possible correlations characteristic of the garnet structure (the structure with large Ln atoms in *c*-positions is stabilized by the ions larger than Ga³⁺ located in the octahedral *a*-positions, e.g., by Sc, Lu, and Yb ions [12]).

The gadolinium–gallium garnet crystals grown from melt studied have the unit-cell parameter $a_{Cz} = 12.385 \pm 0.001$ Å; their composition estimated by Eq. (1) is Gd_{3.06}Ga_{4.94}O₁₂. Our garnet crystals grown from flux have the unit-cell parameter $a_{flux} = 12.377 \pm 0.001$ Å, their composition is close to stoichiometric, Gd₃Ga₅O₁₂, which is typical of crystals grown from flux [13]. This explains a considerably lower concentration of the second activator center (type 2) in our Gd₃Ga₅O₁₂:Nd³⁺ crystals grown from flux in comparison with its concentration in the crystals grown from melt.

The pair centers (type 3)—a pair of Nd³⁺ ions in the adjacent distorted cubes—can evidently be formed in crystals grown from both melt and flux depending on the activator concentration in the crystal. However, the spectra obtained show that, at the activator content of about 1 at. % in Nd³⁺-doped gadolinium–garnet crystals, the concentration of these centers is lower than the concentration of type 2 centers.

In laser experiments, a continuous-wave lasing was excited in Gd₃Ga₅O₁₂:Nd³⁺ crystals grown from flux. With no selective elements in the cavity, lasing occurred simultaneously at the wavelengths $\lambda_1 = 1.0621$ and $\lambda_2 = 1.0600$ μm of the ⁴F_{3/2} → ⁴I_{11/2} channel. The lasing threshold for Gd₃Ga₅O₁₂:Nd³⁺ crystals grown from flux was somewhat (by ~20%) lower than that of crystals grown from melt. The use of selective mirrors with high reflection coefficients in the vicinity of 1.33 μm highly transparent in the range 1.05–1.06 μm in the cavity provided generation at the wavelengths $\lambda_3 = 1.3315$ and $\lambda_4 = 1.3370$ μm of the ⁴F_{3/2} → ⁴I_{13/2} channel. The accuracy of the photoelectric record of the lasing wavelength was ±0.0005 μm. The output power for the Gd₃Ga₅O₁₂:Nd³⁺ lasers emitting in the vicinity of 1.06 and 1.33 μm as a function of the pumping power is shown in Fig. 5. In a crystal with the concentration $C_{Nd} \approx 10\%$, lasing in both spectral ranges was also excited, which shows that one can use highly concentrated Gd₃Ga₅O₁₂:Nd³⁺ crystals to design minilasers. These high concentrations provide the com-

Cation distribution around distorted NdO₈ cubes within the second coordination sphere in Nd³⁺-doped gadolinium–gallium garnet

Type of center	<i>c</i> -positions (distorted cube)	<i>a</i> -positions (octahedron)	<i>d</i> -positions (tetrahedron)
1	4Gd	4Ga	6Ga
2	4Gd	3Ga + 1Gd	6Ga
3	3Gd + 1Nd	4Ga	6Ga

plete absorption of the pumping energy at a wavelength of the active element of about 2–3 mm.

Comparing the measured spectral and laser characteristics of the Nd³⁺-doped gadolinium–gallium garnet crystals grown from melt and from flux, we see that the latter have somewhat narrower (by 10–30%) absorption and luminescence lines (Figs. 2–4). In our opinion, the high structural disorder in crystals grown from melt is explained by the following: (1) The equilibrium concentration of point defects (vacancies and atoms in interstitial and unusual positions) is high at temperatures close to 1800°C and decreases only slightly during fast cooling upon completion of growth; (2) the presence in the melt of the component Ga₂O₃ that can be evaporated and dissociated with an increase in the temperature; and (3) the pulling rate is 1–2 mm/h, which is higher by several orders of magnitude than the rate of crystallization from flux. On the other hand, growth from flux proceeds at a temperature of about 1200°C in air, with the concentration of point defects being lower and the Ga₂O₃ component more stable. Finally, the partial filling of the octahedral positions in the gadolinium–gallium garnet structure with Gd³⁺ ions also gives rise to a certain structural disorder. (Similar

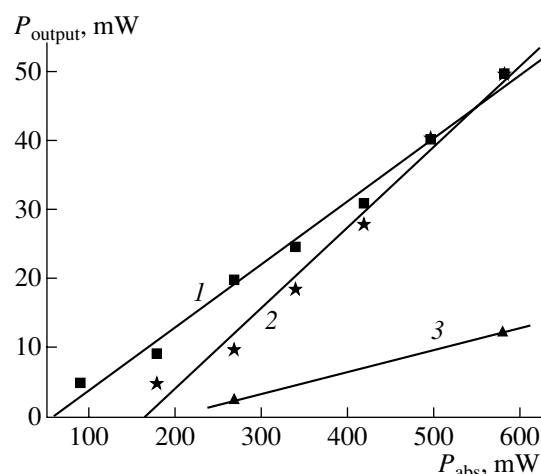


Fig. 5. The emission power (at two wavelengths) of a continuous-wave Gd₃Ga₅O₁₂:Nd³⁺ laser in the 1.06 μm range with activator concentrations (1) 3 and (2) 10 at. % and in the 1.33 μm range with activator concentration (3) 10 at. % as a function of the pumping power of a semiconductor laser ($\lambda_{pump} = 0.81$ μm).

phenomena were earlier observed when studying the crystals grown from melt in the mixed $\text{Nd}^{3+}:\text{Y}_3(\text{Ga},\text{Al})_5\text{O}_{12}$ [14] and $\text{Nd}^{3+}:\text{Y}_3(\text{Y},\text{Ga})_2\text{Ga}_3\text{O}_{12}$ [15] systems.) However, the crystallization from melt does not allow the attainment of a high degree of gadolinium–gallium garnet matrix disorder because of the substantial divergence of the solidus and liquidus curves in the instances where the composition of the melt differs from the congruent one. Therefore, the crystallization from flux seems to be more advantageous because the range of existence of the $\text{Gd}_{3+x}\text{Ga}_{5-x}\text{O}_{12}$ solid solutions is also quite large at a temperature of 1200°C [10]. Thus, varying the $\text{Gd}_2\text{O}_3/\text{Ga}_2\text{O}_3$ ratio in the flux, it is possible to grow a disordered garnet of the composition up to $\text{Gd}_{3.3}\text{Ga}_{4.7}\text{O}_{12}$.

Thus, the concentration series of the $\text{Gd}_3\text{Ga}_5\text{O}_{12}:\text{Nd}^{3+}$ garnet crystals were grown from flux. It was shown that unlike crystals grown from melt, spectroscopically, these crystals can be considered as a medium with a single activation center. For the first time, continuous-wave lasing was excited in diode-pumped $\text{Gd}_3\text{Ga}_5\text{O}_{12}:\text{Nd}^{3+}$ crystals at wavelengths $\lambda_3 = 1.3315$ and $\lambda_4 = 1.3370$ μm of the ${}^4\text{F}_{3/2} \rightarrow {}^4\text{I}_{13/2}$ channel and the simultaneous generation at two wavelengths $\lambda_1 = 1.0621$ and $\lambda_2 = 1.0600$ μm of the channel ${}^4\text{F}_{3/2} \rightarrow {}^4\text{I}_{11/2}$. The power characteristics of lasing can be essentially improved by using an antireflection coating with optimum dimensions and the activator concentration or by optimizing the cavity. In the growth experiments, an interesting problem, along with the reduction in the optical inhomogeneity (growth striae and faceting) of the $\text{Gd}_3\text{Ga}_5\text{O}_{12}:\text{Nd}^{3+}$ crystals, is also the preparation of the $\text{Gd}_{3+x}\text{Ga}_{5-x}\text{O}_{12}:\text{Nd}^{3+}$ crystals ($x \geq 0.2$) with considerable structural disorder. The media whose absorption spectra have broadened lines provide better matching with the diode pumping whose wavelength can experience temperature drift.

ACKNOWLEDGMENTS

The authors are grateful to B.V. Mill for measuring the unit-cell parameters of the crystals. The authors greatly benefited from the cooperation with the Joint Open Laboratory “Laser Crystals and Precise Laser

Systems.” The study was supported by the Russian Foundation for Basic Research, International Association for the Promotion of Cooperation of the Former Soviet Union (INTAS), project no. 99-01366; and the Programs “Fundamental Metrology,” “Fundamental Spectroscopy,” and “Laser Physics” of the Ministry of Industry, Science, and Technology of the Russian Federation.

REFERENCES

1. J. E. Geusic, H. M. Marcos, and L. G. Van Uitert, *Appl. Phys. Lett.* **4**, 182 (1964).
2. A. A. Kaminskii, *Zh. Éksp. Teor. Fiz.* **51**, 49 (1966) [*Sov. Phys. JETP* **24**, 33 (1966)].
3. G. A. Bogomolova, A. A. Kaminskii, and V. A. Timofeeva, *Phys. Status Solidi* **16**, K165 (1966).
4. V. V. Osiko, Yu. K. Voronko, and A. A. Sobol, *Crystals* (Springer-Verlag, Berlin, 1984), Vol. 10, p. 87.
5. V. Lupei, *Opt. Mater.* **16**, 137 (2001).
6. Kh. S. Bagdasarov, G. A. Bogomolova, M. M. Gritsenko, *et al.*, *Dokl. Akad. Nauk SSSR* **216** (5), 1018 (1974) [*Sov. Phys. Dokl.* **19**, 353 (1974)].
7. L. N. Bezmaternykh, I. A. Gudim, and V. L. Temerov, in *Proceedings of the 9th National Conference on Crystal Growth, Moscow, 2000*, p. 171.
8. C. D. Brandle and R. L. Barns, *J. Cryst. Growth* **26**, 169 (1974).
9. J. R. Carruthers, M. Kokta, R. L. Barns, and M. Grasso, *J. Cryst. Growth* **19**, 204 (1973).
10. M. Allibert, C. Chatillon, J. Mareschal, and F. Lissalde, *J. Cryst. Growth* **23**, 289 (1974).
11. B. V. Mill and A. V. Butashin, *Izv. Akad. Nauk SSSR, Neorg. Mater.* **18** (8), 1394 (1982).
12. B. V. Mill, *Magnetic and Crystallochemical Study of Ferrites* (Mosk. Gos. Univ., Moscow, 1971), p. 64.
13. W. Tolksdorf, G. Bartles, G. P. Espinosa, *et al.*, *J. Cryst. Growth* **17**, 322 (1972).
14. R. K. Watts and W. C. Holton, *J. Appl. Phys.* **45** (2), 873 (1974).
15. A. A. Kaminskii, K. Ueda, D. Temple, *et al.*, *Opt. Rev.* **7** (2), 101 (2000).

Translated by A. Zolot'ko

PHYSICAL PROPERTIES
OF CRYSTALS

Circular Dichroism of Uniaxial Sulfate Crystals in the Range
of Electronic Transitions of Sulfate Groups

V. I. Burkov*, Yu. V. Denisov*, and Z. B. Perekalina**

* Moscow Institute of Physics and Technology,
Institutskii per. 9, Dolgoprudnyi, Moscow oblast, 141700 Russia

** Shubnikov Institute of Crystallography, Russian Academy of Sciences,
Leninskii pr. 59, Moscow, 117333 Russia

e-mail: sper34@ns.crys.ras.ru

Received April 16, 2001; in final form, November 8, 2001

Abstract—Absorption and circular-dichroism spectra of uniaxial inactivated sulfate crystals KLiSO_4 and $[\text{C}_2\text{H}_4(\text{NH}_2) \cdot \text{H}_2\text{SO}_4]$ have low-intensity bands in the spectral range of 0.20–0.35 μm . These bands are attributed to forbidden transitions in a sulfate group. © 2002 MAIK “Nauka/Interperiodica”.

INTRODUCTION

The study of cubic double sulfates-langbeinites crystals (sp. gr. 2₁3) shows that an SO_4^{2-} -group is one of the chromophores contributing to a crystal gyrotropy (see review [1]). In the ultraviolet range of 0.18–0.30 μm , the forbidden electronic transitions in a sulfate group in these crystals manifest themselves in the absorption and circular-dichroism spectra. The main contribution to the optical rotation in the range of 0.2–0.8 μm comes from the allowed transitions of a more short-wave length range.

In this connection, the role of a sulfate group in the gyrotropy of inactivated uniaxial sulfate crystals is of great interest. The data on the gyrotropy of uniaxial KLiSO_4 , KNaSO_4 , $[\text{C}_2\text{H}_4(\text{NH}_2)_2 \cdot \text{H}_2\text{SO}_4]$ (ethylenediamine sulfate) and $\text{NiSO}_4 \cdot 6\text{H}_2\text{O}$ crystals, and biaxial $(\text{NH}_2\text{CH}_2\text{COOH})_3 \cdot \text{H}_2\text{SO}_4$ (triglycine sulfate) and MgSO_4 crystals are reviewed in [2]. Gyrotropy in these compounds manifests itself only in the crystalline state.

The effect of electronic transitions in sulfate groups on the gyrotropic properties of these crystals is of special interest because, unlike cubic langbeinites, the contribution to the circular dichroism and optical rotation in uniaxial and biaxial crystals comes not only from the $\langle pm \rangle$ but also from the $\langle pq \rangle$ modes (where $\langle p \rangle$, $\langle m \rangle$, and $\langle q \rangle$ are the matrix elements of the electric, magnetic, and quadrupole moments of the transitions, respectively [3]).

An active role of electronic transitions in sulfate groups in the gyrotropy of uniaxial crystalline sulfates is indirectly shown in [4], where the data on circular-dichroism spectra of crystalline sulfates doped with tetrahedral CrO_4^{2-} and MoO_4^{2-} -ions incorporated into the positions of sulfate groups in the crystal lattice are pre-

sented. However, there is no direct experimental evidence of the contribution of these transitions to the gyrotropic properties of these crystals.

Below, we describe the detailed study of the absorption and the circular-dichroism spectra of inactivated uniaxial potassium–lithium sulfate (KLiSO_4) **1** and ethylenediamine sulfate $[\text{C}_2\text{H}_4(\text{NH}_2)_2 \cdot \text{H}_2\text{SO}_4]$ crystals **2** and the experimental data on the involvement of electronic transitions in sulfate groups in the gyrotropic properties of these crystals.

The study of the optical-rotation dispersion in these crystals in the range 0.2–0.6 μm shows that the dispersion curves are of a conventional nature [4–6], which shows that the contribution of forbidden transitions in sulfate groups to the optical-rotation dispersion is insignificant. Hence, one can hardly expect the formation of intense bands in the range of 0.20–0.35 μm in the circular-dichroism spectra.

STRUCTURE OF KLiSO_4
AND $[\text{C}_2\text{H}_4(\text{NH}_2) \cdot \text{H}_2\text{SO}_4]$ CRYSTALS

The structure of a KLiSO_4 crystal **1** (sp. gr. $P6_3(C_6^6)$, unit-cell parameters $a = 5.15 \text{ \AA}$ and $c = 8.63 \text{ \AA}$, and $Z = 2$) is a close packing of tetrahedral sulfate ions with local symmetry C_3 (Fig. 1) [7]. Sulfur atoms are located in a tetrahedron with one face lying in the plane normal to the 6₃-axis (the optical axis of the crystal). Potassium atoms occupy the octahedral voids between the tetrahedra of sulfate groups, whereas lithium atoms are in tetrahedral voids. Potassium atoms are located on the 6₃-axis and lithium atoms, on the 3-axis. Two molecules in the unit cell related by the 6₃-axis form no helical structure of SO_4^{2-} -tetrahedra.

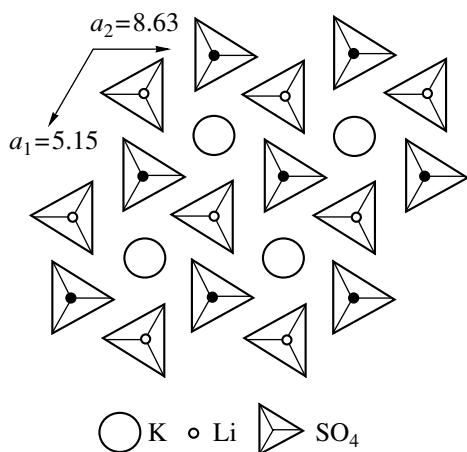


Fig. 1. Fragment of the KLiSO_4 structure.

The structure of a $[\text{C}_2\text{H}_4(\text{NH}_2)_2 \cdot \text{H}_2\text{SO}_4]$ crystal **2** (sp. gr $P4_122$ (D_4^4) or $P4_322$ (D_4^8), unit-cell parameters $a = 8.47 \text{ \AA}$ and $c = 18.03 \text{ \AA}$, and $Z = 8$) (Fig. 2) consists of layers of ethylenediamine and SO_4^{2-} -groups normal to screw axis 4_1 , which is the optical axis of the crystal [8]. The ethylenediamine (the C_2 symmetry) is located in the structure in such a way that the C–C bond is almost parallel to screw axis 4_1 of the crystal. The distorted tetrahedra of sulfate groups (the C_2 symmetry) are also located around the 4_1 -axis so that the twofold axes of the tetrahedra coincide with the twofold axes of the crystal lattice. Because the tetrahedra in the crystal

structure are distorted, the S–O bond lengths in sulfate groups differ by 0.01 \AA from the conventional length of 1.5 \AA .

It follows from the description of the structure that the chromophors responsible for the optical activity in a crystal **1** are SO_4^{2-} -groups and also K^+ - and Li^+ -ions in the positions with C_3 symmetry. In crystal **2**, in addition to sulfate groups (C_2 symmetry), a chromophor responsible for the optical activity is also ethylenediamine (C_2 symmetry). Thus, it is seen that both the symmetry and the orientation of sulfate groups relative to the optical axis in crystal **2** differ from those in crystal **1**. In other chromophors, electronic transitions lie in the range of vacuum ultraviolet and, therefore, their bands cannot be measured.

EXPERIMENTAL

The dispersion of optical rotation was studied on a spectropolarimeter. The absorption spectra were obtained on a Specord M-40 spectrophotometer and on a spectrophotometric setup with an MDR-23 monochromator. The spectra of circular dichroism were studied on a Mark-3S dichrometer. These devices were modified with the aid of the program of computerization of nonstandard optical techniques written in the Moscow Institute of Physics and Technology on the basis of Pentium computers with unique interface cards for control and data collection. This computer program not only allows one to control the operations performed by the device and obtain experimental data and their graphical mapping in real time, but also provides a

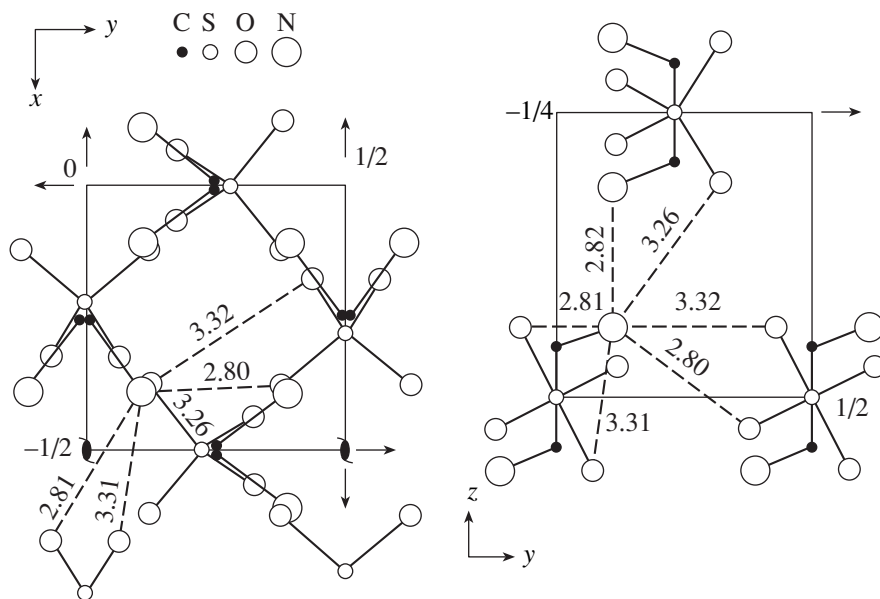


Fig. 2. Two projections of the fragment of the ethylenediamine sulfate structure.

complete set of procedures for spectra processing, including modern methods for reducing the noise components of the spectra, transformation of the spectra, and their approximation by given contours, elimination of undesirable background components, comparison of spectra, etc. Using this equipment and the program of the data processing, we managed to reveal new details of the spectra, in particular, in the range with pronounced absorption.

Ethylenediamine sulfate crystals were grown from aqueous solutions by the method of spontaneous crystallization and were of a high optical quality. The measurements were made on plates cut out parallel to the cleavage plane and oriented normally to the 4_1 -axis coinciding with the optical axis of the crystal. The KLiSO_4 crystals were grown from aqueous solutions on a seed by the method of decreasing temperature. The study of specimens in a polarization microscope showed the absence of any domain structure. The spectra were obtained from the specimens from 0.5 to 4.0 mm in thickness.

RESULTS AND DISCUSSION

The absorption spectra in the range 0.2–0.3 μm are similar for both crystals (Figs. 3 and 4, curve 1) and resemble the corresponding spectra of double sulfate crystals (langbeinites) [1]. The results obtained show that absorption in this spectral range is caused by electronic transitions in SO_4^{2-} groups. The intensity of the band with the maximum at 0.28 μm is very low, especially for crystal 2, which is typical of the transitions forbidden by the selection rules.

At the same time, the positions and intensities of the bands on the circular-dichroism spectra are different. The circular-dichroism spectra of crystal 1 (Fig. 3, curve 2) show only one low-intensity band with the maximum at $\lambda = 0.28 \mu\text{m}$ in the range of 0.25–0.30 μm , whereas the spectrum of crystal 2 has two bands at λ equal to 0.30 and 0.25 μm in this range (Fig. 4, curve 2). Moreover, the circular-dichroism spectrum of crystal 2 has the third band with the maximum at $\lambda = 0.21 \mu\text{m}$ with the intensity higher by an order of magnitude than the intensity of the two first maxima (Fig. 4, curve 2). Evidently, different gyrotropic properties of these crystals in the range of electronic transitions in sulfate groups should be explained by different orientations of these groups with respect to the optical axis along which the axial circular-dichroism spectra are measured.

Now, consider qualitatively the effect of the orientation of SO_4^{2-} ions depending on the electronic structure of sulfate groups. The electronic structure of tetrahedral sulfate groups was intensely studied in the 1960–1970s. The electronic structure of the sulfate group was first studied in [9–11]. Later, calculations of the energy of molecular orbitals were made by various computa-

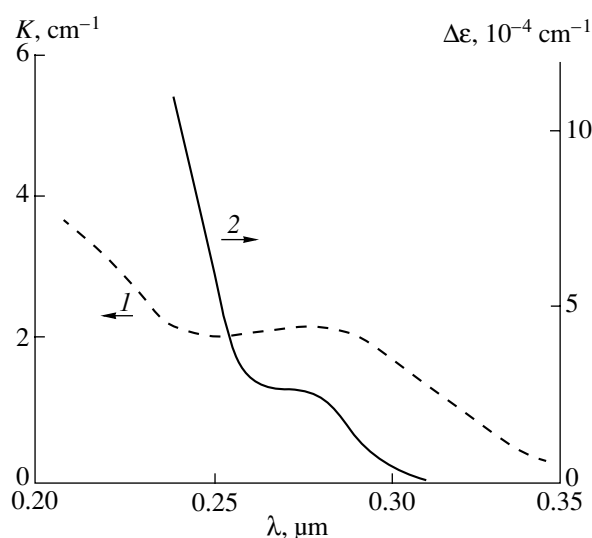


Fig. 3. (1) Absorption and (2) circular-dichroism spectra of a KLiSO_4 crystal.

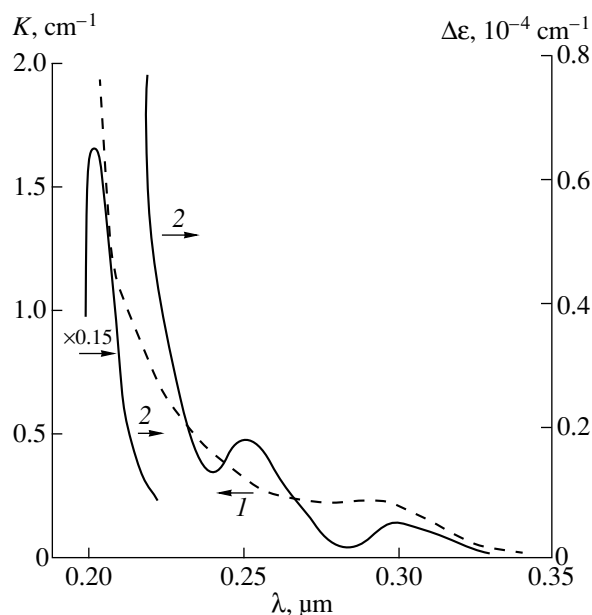


Fig. 4. (1) Absorption and (2) circular-dichroism spectra of ethylenediaminesulfate crystal [curve (2) corresponds to the data reduced by a factor of 15 along the ordinate axis].

tional methods of quantum chemistry [12–17]. At present, the following sequence of the filled orbitals is universally accepted: $(1a_1)^2, (1t_2)^6, (2a_1)^2, (2t_2)^6, (1e)^4, (3t_2)^6, (1t_1)^6$ [17] (Fig. 5). The antibinding orbital with the minimum energy has not been definitively established as yet. In a number of studies, the first empty orbital was calculated to be $(4t_2^*)$ in the sequence $(4t_2^*)(3a_1^*)(2e^*)(5t_2^*)$; in other studies, it was calculated as $(3a_1^*)$ in the sequence $(3a_1^*)(4t_2^*)(2e^*)(5t_2^*)$. In the first case, because of the interaction with a hole on the

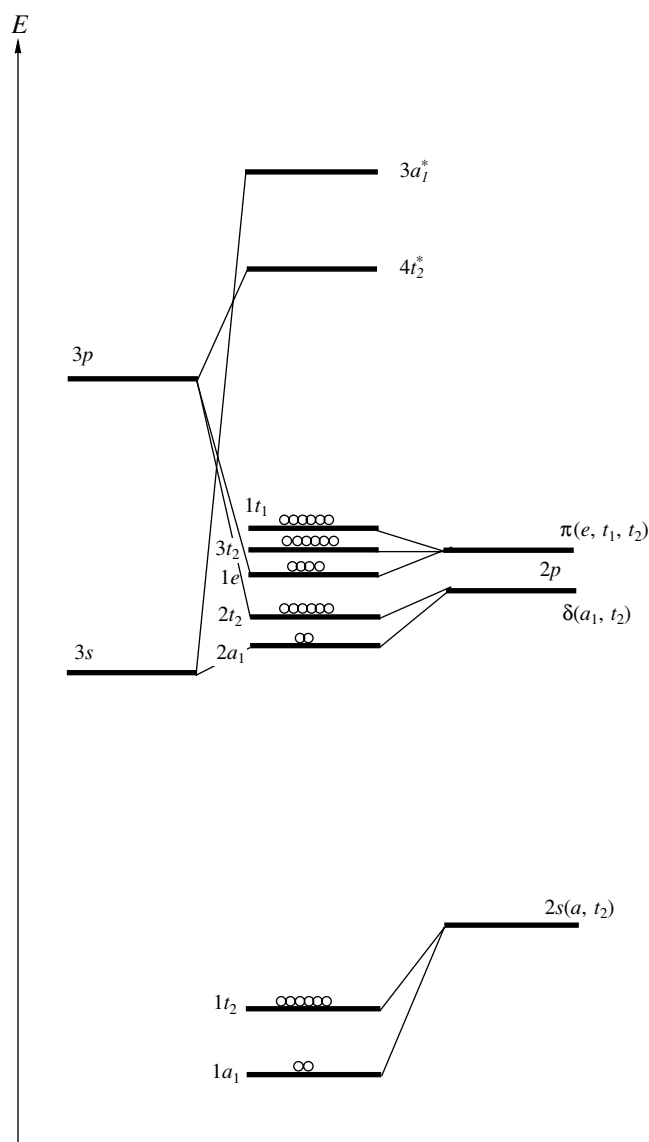


Fig. 5. Schematic of molecular orbitals of sulfate groups (open circles denote electrons on molecular orbitals).

ligand orbital, the $(1t_1)^5(4t_2^*)$ state yields the following terms: 3T_1 , 3T_2 , 1T_1 , 1T_2 , 1E , 1A_1 . In the second case, because of the above interactions, the excited configuration $(1t_1)^5(3a_1^*)^1$ yields two terms, 1T_2 and 3T_2 . Within the T_d symmetry, the 1A_1 – 1T_2 transitions are allowed in the electrical dipole approximation. Because of the spin–orbital interactions, the appearance in the absorption spectrum of the transitions to 3T_1 , 3T_2 , 1T_1 , 1E , 1A_1 forbidden in the electrical dipole approximation cannot be excluded.

It is clear that, within the T_d symmetry, SO_4^{2-} -groups do not possess any optical activity. In crystal **1**, the symmetry of sulfate groups is C_3 , and all the T -states are split into the A - and E -states. Since the threefold axis of

these groups is parallel to the optical axis of the crystal, only the A – E transitions are active in the axial circular-dichroism spectrum.

In crystal **2**, the symmetry of SO_4^{2-} groups is C_2 , and, therefore, all the T states should be split into the A - and $2B$ -states. However, the bond lengths and the bond angles show that sulfate groups in crystal **2** have a higher (D_2) symmetry. It is expedient to consider this group, because the directions of the moments of the $\langle \mu \rangle_{0i}$ and $\langle m \rangle_{i0}$ transition (where $\langle \mu \rangle_{0i}$ is the matrix element of the electrical dipole moment, $\langle m \rangle_{i0}$ is the matrix element of the magnetic dipole moment, and A , B , and B' are the excited i -states) within this group are aligned along three mutually perpendicular twofold axes. Thus, knowing the orientation of sulfate groups in crystal **2**, we can state that the projections of the moments of all the transitions onto the plane normal to the optical axis have nonzero values. Therefore, the transitions from the ground A -state to all the excited A , B , and B' states may contribute to the axial circular-dichroism spectrum. The above consideration explains different circular-dichroism spectra for crystals **1** and **2**.

Thus, the studies of the circular-dichroism spectra of uniaxial inactivated crystals of double sulfates showed that SO_4^{2-} -groups are the chromophors responsible for the optical activity. This signifies that both allowed and forbidden transitions in the SO_4^{2-} groups contribute to the optical activity of these crystals. In the spectral range under study (0.2–0.35 μm), only the forbidden transitions are active in the formation of circular-dichroism spectra dependent on the orientation of SO_4 groups, whereas the allowed transitions are responsible mainly for the dispersion of the rotation of the polarization plane at values exceeding 0.2 μm [2].

ACKNOWLEDGMENTS

The authors are grateful to A.V. Egorysheva for study of the absorption spectra.

REFERENCES

1. V. I. Burkov and Z. B. Perekalina, *Neorg. Mater.* **37** (3), 1 (2001).
2. V. A. Kizel' and V. I. Burkov, *Gypotropy of Crystals* (Nauka, Moscow, 1980).
3. F. S. Richardson and G. Hilmes, *Mol. Phys.* **30**, 237 (1975).
4. V. I. Burkov, *Neorg. Mater.* **30** (1), 12 (1994).
5. Z. B. Perekalina, A. Yu. Klimova, and L. M. Belyaev, *Kristallografiya* **23** (1), 124 (1978) [*Sov. Phys. Crystallogr.* **23**, 66 (1978)].
6. V. A. Kizel', Yu. I. Krasilov, and V. N. Shamraev, *Opt. Spektrosk.* **17**, 863 (1964).

7. M. Karppinen, J. O. Lundgren, and R. Liminga, *Acta Crystallogr., Sect. C: Cryst. Struct. Commun.* **C39**, 34 (1983).
8. K. Sakurai, *J. Phys. Soc. Jpn.* **16**, 1205 (1961).
9. D. M. Bishop, M. Randict, and J. R. Morton, *J. Chem. Phys.* **45**, 1880 (1966).
10. D. M. Bishop, *Theor. Chim. Acta* **8**, 285 (1967).
11. D. M. Bishop, *J. Chem. Phys.* **48**, 1872 (1968).
12. H. Johansen, *Theor. Chim. Acta* **32**, 273 (1974).
13. K. Taniguchi and B. L. Henke, *J. Chem. Phys.* **64**, 3021 (1976).
14. R. Manne, *J. Chem. Phys.* **46**, 4645 (1967).
15. M. Ketton and D. P. Santry, *Chem. Phys. Lett.* **7**, 105 (1970).
16. U. Gelius, B. Roos, and P. Siegbahn, *Theor. Chim. Acta* **23**, 59 (1971).
17. G. Hojer, S. Meza-Hojer, and G. Hernández De Pedrero, *Chem. Phys. Lett.* **37**, 301 (1976).

Translated by T. Dmitrieva

PHYSICAL PROPERTIES
OF CRYSTALS

Influence of X-ray Irradiation on the Optical Properties
of Chromium-Doped KLiSO₄ Crystals

Z. B. Perekalina*, K. A. Kaldybaev**, A. F. Konstantinova*,
V. P. Orekhova*, and A. D. Tynaev**

* Shubnikov Institute of Crystallography, Russian Academy of Sciences, Leninskii pr. 59, Moscow;
e-mail: afkonst@usa.net

** Issyk-Kul State University, Karakol, Kyrgyzstan

Received June 13, 2001

Abstract—The absorption and circular-dichroism spectra of chromium-activated KLiSO₄ crystals both nonirradiated and irradiated with an X-ray beam have been studied. It was established that in nonirradiated crystals chromium ions are mainly trivalent (Cr³⁺) and have octahedral coordination. In irradiated crystals, along with the centers provided by (Cr³⁺) ions, new centers are formed associated with (Cr⁴⁺) and (Cr⁵⁺) ions. © 2002 MAIK “Nauka/Interperiodica”.

Doping crystals gives rise to the formation of centers that have different local environments that manifest themselves in the absorption and circular-dichroism spectra.

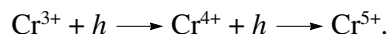
It is well known that the irradiation of crystals with an X-ray beam is usually accompanied by a change in ion valence and, as a consequence, also in the physical and chemical properties of the crystals. Circular-dichroism spectra provided by different optically active centers associated with the incorporation of impurities into a crystal are extremely sensitive to changes in their local symmetry caused by various external factors, including irradiation. In this connection, it was expedient to study the effect of the X-ray irradiation of crystals on the circular dichroism of chromium-activated KLiSO₄ crystals with well-known optical properties [1, 2].

A potassium–lithium sulfate KLiSO₄ crystal belongs to the hexagonal pyramidal symmetry class 6, sp. gr. *P*6₃ with two molecules in the unit cell. The KLiSO₄ crystals have the tetrahedral framework structure consisting of chains of distorted oxygen tetrahedra with sulfur and lithium ions located on the threefold axes and K⁺ ions located the sixfold axis in the octahedral voids formed by these tetrahedra [3, 4].

Chromium-doped KLiSO₄ crystals (KLiSO₄ : Cr) were grown from an aqueous KLiSO₄ solution with 1.5 g/l of Cr₂(SO₄)₃ · 6H₂O at the Issyk-Kul State University [1]. Well-faceted green transparent crystals were used to prepare the specimens (the crystal segments having no stresses or domains were used) [5]. The analysis of the EPR spectra of the specimens [6, 7] showed that chromium ions in KLiSO₄ crystals are trivalent and replace K⁺ ions in strongly distorted octahedral voids. The changed valence is compensated by an SO₃³⁻-radical.

The absorption spectra of undoped and chromium-activated KLiSO₄ crystals were studied on 1.85- and 0.95-mm-thick plates oriented normally to the optical axis in the spectral range from 200 to 800 nm at room temperature (Fig. 1).

Undoped KLiSO₄ crystals are transparent in the visible and ultraviolet spectral ranges (Fig. 1, curve 1). In the absorption spectra of Cr-doped KLiSO₄ crystals, three wide bands with the maxima at $\lambda = 280, 420,$ and 600 nm are observed (Fig. 1, curve 2), which are characteristic of octahedrally coordinated Cr³⁺ ions and associated with the allowed spin-quartet transitions from the ⁴A_{2g} ground state to the ⁴T_{2g}(F), ²T_{1g}(F), and ⁴T_{1g}(P) levels of the Cr³⁺ ion. The absorption spectra of irradiated chromium-doped KLiSO₄ crystals are also shown in Fig. 1 (curve 3). It is seen that upon irradiation of these crystals, the intensity of the absorption band at $\lambda \sim 600$ nm decreases, which shows that the number of Cr³⁺ ions diminish. The decrease in the intensity of this band in the spectrum of the irradiated crystal is accompanied by the formation of a new absorption band at 355 nm attributed to Cr⁵⁺ ions. Comparing the EPR and the optical-absorption spectra, we established that under the effect of X-ray irradiation, some Cr³⁺ ions in alkali metal crystals change their valence by gradually trapping two holes according to the scheme [7]



The circular-dichroism spectra of nonirradiated and irradiated chromium-doped KLiSO₄ crystals were studied in the spectral range 230–800 nm with a sensitivity of $\sim 4 \times 10^{-6}$ optical density per millimeter on a dichrometer (Fig. 2).

The circular-dichroism spectra of nonirradiated specimens (Fig. 2, curve 2) show two wide bands with

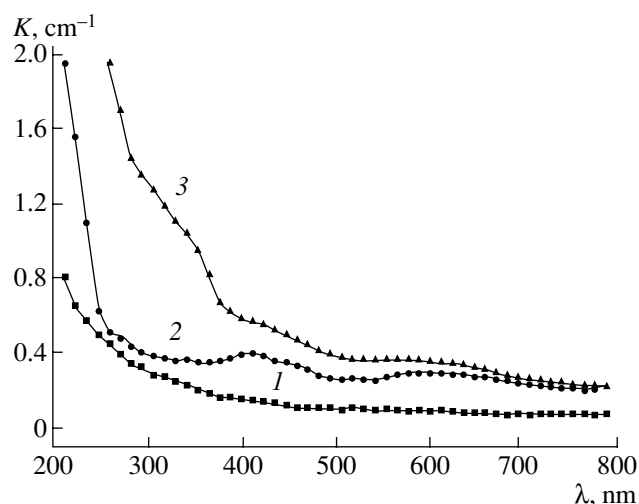


Fig. 1. Absorption spectra of undoped and chromium-activated potassium-lithium sulfate crystals; (1) KLiSO_4 ; (2) nonirradiated $\text{KLiSO}_4 : \text{Cr}$; (3) $\text{KLiSO}_4 : \text{Cr}$ crystals irradiated with an X-ray beam.

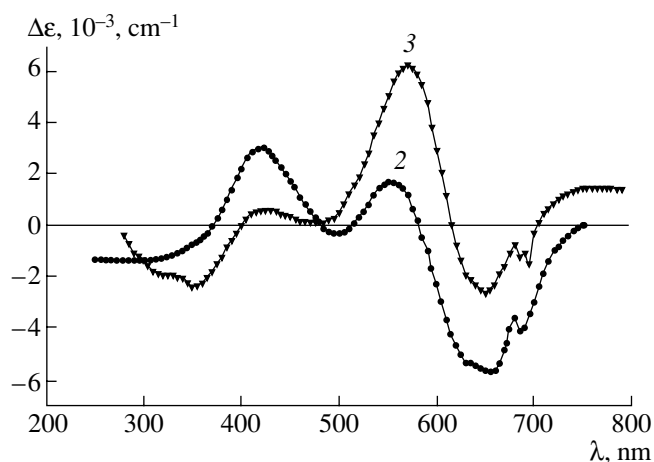


Fig. 2. Circular-dichroism spectra of potassium-lithium sulfate crystals; (2) nonirradiated $\text{KLiSO}_4 : \text{Cr}$; (3) $\text{KLiSO}_4 : \text{Cr}$ irradiated with an X-ray beam.

two maxima at 420 and 650 nm corresponding to the Cr^{3+} bands observed in the absorption spectrum. In the spectra of circular dichroism, these bands have opposite signs. The wide band with the maximum at 650 nm in the long wavelength edge has a narrow band at 685 nm which, most probably, corresponds to the ${}^4A_2 \rightarrow {}^2E$ transition [2].

In the circular-dichroism spectra, the additional bands with the maxima at 500 and 550 nm are also observed to be not associated with the Cr^{3+} ions. Presumably, these bands are caused by tetrahedrally coordinated Cr^{4+} ions [8]. The absence of these bands in the absorption spectrum of irradiated crystals seems to be explained by the low concentration of these ions in the crystal. In the ultraviolet range of the circular-dichroism spectrum (250–370 nm), a wide band, evidently combining the bands associated with chromium ions of different valences (Cr^{3+} , Cr^{4+}), SO_4 groups, and color centers [2, 7, 9], is observed.

As is seen from Fig. 2, the circular-dichroism spectra of the irradiated $\text{KLiSO}_4 : \text{Cr}$ crystal (Fig. 2, curve 3) have considerably changed because of the changes in the Cr^{3+} and Cr^{4+} ion concentrations and the appearance of Cr^{5+} ions. The intensities of the circular-dichroism bands of Cr^{3+} ions at $\lambda \sim 420$ and 650 nm decreased and a wide band with the maximum at 355 nm due to Cr^{5+} ions appeared. Moreover, the intensity of the band due to Cr^{4+} ions in the green spectral range considerably increased and the band maximum was shifted to $\lambda \approx 570$ nm. The positional changes observed for the band maxima at 650 nm in the circular-dichroism spectra can be caused by the appearance of ions having different valence and a change of the local environment of the absorption center because of irradiation.

Thus, it is shown that the X-ray irradiation of $\text{KLiSO}_4 : \text{Cr}$ crystals changes the valence and the local environment of chromium ions. The examination of the circular-dichroism spectra of crystals shows that these spectra are more informative than the absorption spectra. The study of the circular-dichroism spectra of irradiated crystals provides more detailed information on the transition of the impurity from one valent state to another.

REFERENCES

1. A. A. Alybakov, N. A. Gubanov, and K. Shaersheev, *Cryst. Res. Technol.* **43** (2), K92 (1982).
2. B. N. Grechushnikov, T. F. Veremeichik, K. A. Kaldyvaev, *et al.*, *Zh. Prikl. Spektrosk.* **54** (4), 669 (1991).
3. R. Wyckoff, *Crystal Structures* (Interscience, New York, 1960), Vol. 3, p. 112.
4. M. Karppinen, J.-O. Lundgren, and R. Liminga, *Acta Crystallogr., Sect. C: Cryst. Struct. Commun.* **C39**, 34 (1983).
5. H. Klapper, Th. Hahn, and S. J. Chung, *Acta Crystallogr., Sect. B: Struct. Sci.* **B43**, 147 (1987).
6. L. Conte and F. Holuj, *Phase Transit.* **6**, 259 (1986).
7. A. A. Alybakov and K. Shaersheev, *Izv. Akad. Nauk Kirg. SSR*, No. 3, 20 (1984).
8. P. I. Macfarlane, T. P. J. Han, B. Henderson, and A. A. Kaminskii, *Opt. Mater.*, No. 3, 15 (1994).
9. V. I. Burkov, Yu. V. Denisova, and Z. B. Perekalina, *Kristallografiya* **47** (2), 313 (2002).

Translated by T. Dmitrieva

PHYSICAL PROPERTIES OF CRYSTALS

EPR Spectra of Cr³⁺-Doped LuNbO₄ Crystals

A. G. Beda*, A. A. Bush**, A. F. Volkov**, and V. F. Meshcheryakov**

* *Institute of Theoretical and Experimental Physics,
ul. Bol'shaya Cheredushkinskaya 25, Moscow, 117259 Russia
e-mail: beda@itep.ru*

** *Moscow State Institute of Radioengineering, Electronics, and Automation (Technical University),
pr. Vernadskogo 78, Moscow, 117454 Russia*

Received April 2, 2001

Abstract—Ferroelastic LuNbO₄ single crystals containing 0.3 at. % Cr³⁺ ions have been grown by the floating zone technique, and their EPR spectra have been studied at a frequency of 9.8 GHz at room temperature. The lines on the spectra are due to the transitions caused by three paramagnetic centers formed as a result of the replacement of one isovalent position of a Lu³⁺ ion and two nonisovalent positions of Nb⁵⁺-ions by Cr³⁺-ions. As a result of twinning, the line number is doubled and four principal directions arise along which the same spectra are obtained. The spectra of these centers were described by a spin Hamiltonian with $S = 3/2$, the D and E parameters ranging from 0.024 to 0.17 cm⁻¹, and the g -factors $g_{\parallel} = 1.75$ –2.20 and $g_{\perp} = 1.90$ –2.13.
© 2002 MAIK “Nauka/Interperiodica”.

INTRODUCTION

The use of the method of dynamic orientation of the nuclei suggested in [1] requires the selection of a suitable working substance with a pronounced quadrupole splitting of the energy levels of the nucleus studied (the NQR frequency should range within several dozens of megahertz). This substance should also possess considerable splitting of levels of paramagnetic impurity (of the order of several dozens of gigahertz) in the absence of a magnetic field.

Unfortunately, we did not find any substances with known NQR and EPR frequencies of the paramagnetic dopants. Therefore, we used as a promising working material the compound LuNbO₄, in which the NQR frequency for lutetium nuclei lies in the proper range [2]. Single crystals of this compound doped with ~0.3 at. % Cr³⁺ ions were obtained, and the EPR spectra of chromium ions were studied. The calculation of the spectra allowed us to determine the types of centers formed by Cr³⁺ ions and the level splitting of a paramagnetic Cr³⁺ ion.

LuNbO₄ crystals belong to ABO₄-type compounds, where A is a rare earth element and $B = \text{Nb}$ or Ta , with the structure of fergusonite ($\text{Y}_{1-x}\text{Yb}_x\text{NbO}_4$), a mineral which crystallizes in the monoclinic space group $I2/a$ [3–10]. The structure of this mineral is derived from the scheelite (CaWO_4) structure, whose projection onto the xy plane is shown in Fig. 1 [4]. This structure has the crystallographically independent positions of Lu and Nb and two crystallographically independent positions of oxygen (O1 and O2). Lutetium is coordinated with oxygen atoms forming a distorted eight-vertex polyhedron. In contrast to the scheelite

structure in which tungsten atoms are surrounded with four oxygen atoms forming a regular tetrahedron, in the fergusonite structure, two additional oxygen anions are located close to a niobium atom. As a result, the coordination number of niobium is $(4 + 2)$. The LuO₈-polyhedra share the O(1)–O(1) and O(2)–O(2) edges and form a three-dimensional framework where each LuO₈-polyhedron is surrounded by its four nearest neighbors—similar polyhedra. The voids of the three-dimensional framework are filled with the zigzag chains of NbO₆-polyhedra sharing the O(2)–O(2) edges and, thus, forming columns. In a layer parallel to the xy plane, the LuO₈- and NbO₆-polyhedra share vertices in such a way that each LuO₈-polyhedron shares vertices with two adjacent NbO₆-polyhedra. A LuO₈-polyhedron shares two vertices and two edges with NbO₆-polyhedra from the neighboring layers.

The above crystals possess ferroelastic properties [7–9]; with an increase in temperature they undergo the ferroelastic phase transition accompanied by an increase in the symmetry to the tetragonal ($4/mF2/m$). The physical properties of the LuNbO₄ crystal are studied insufficiently because of the difficulties encountered in the growth of single crystals. Our study is dedicated to the growth of LuNbO₄ : Cr single crystals and the study of the EPR spectra of Cr³⁺ ions introduced into their lattice.

GROWTH OF SINGLE CRYSTALS

The crystals were grown by the floating zone technique on an URN-2-ZP setup using optical heating [11]. Polycrystalline rods of the composition

(Lu_{0.997}Cr_{0.003})NbO₄ synthesized using the conventional ceramic technology served as the starting material for crystallization. The rods 8 mm in diameter and 90 mm in length were fired and sintered at temperatures of 1200 and 1350°C, respectively. Zone recrystallization proceeded at a linear rate of 4.5 mm/h, with the upper ceramic rod and the lower recrystallized ingots being rotated in opposite directions with an angular velocity of 40–60 rpm.

The ingots thus obtained were boules of monoclinic LuNbO₄ single crystals ~8 mm in diameter and 20 mm in length. The crystal layers up to ~1 mm in thickness were transparent and had a light yellow–green color and possessed a pronounced cleavage along the (010) planes. The studies of the platelike crystals with the (010) basal plane in an MMP-2 polarization microscope showed that they consist of polysynthetic twins seen as alternating light and dark bands.

The X-ray diffraction studies were performed on a DRON-4 diffractometer (CuK α -radiation). It is established that the powder X-ray diffraction pattern is well consistent with the known data on LuNbO₄ crystals [3–10] and can be indexed on the basis of the monoclinic unit-cell with the parameters $a = 5.229(4)$ Å, $b = 10.8211(3)$ Å, $c = 5.030(8)$ Å, $\beta = 94.5(6)^\circ$ (the unit-cell parameters were calculated for the base-centered sp. gr. $C2/c$ often used for fergusonite crystal, a non-conventional version of the sp. gr. $I2/a$ [3–10]).

EPR SPECTRA

The EPR spectra were studied at a frequency of 9.80 GHz on a Bruker ER-200tt spectrometer at room temperature. The specimen was a 1 × 3 × 6-mm single-crystal LuNbO₄ : Cr plate with the {130} basal and {010} lateral faces. The crystal was glued with different faces to a quartz rod of the spectrometer with BF-2 glue. During measurements, the rod could be rotated around its axis, thus changing the crystal orientation in the applied magnetic field. At an arbitrary orientation of the crystal in the magnetic fields with an intensity of up to 9 kOe, the EPR spectrum consisted of more than 30 lines. The number, position, and intensity of the lines changed depending on the magnetic-field orientation. If the magnetic field was oriented along the monoclinic b -axis, the spectrum was considerably simplified (Fig. 2a). There are four mutually perpendicular directions normal to the b -axis in the ac plane; the spectra obtained along these directions are considerably simplified and are identical (Fig. 2b). In this case, the lines corresponding to the transitions in one center degenerated, and the lines corresponding to the transitions in other centers doubled, whereas within an interval of ~1.5°, the situation was reversed. These data allow one to determine the misorientation angle of the symmetry axes of the local environment for different

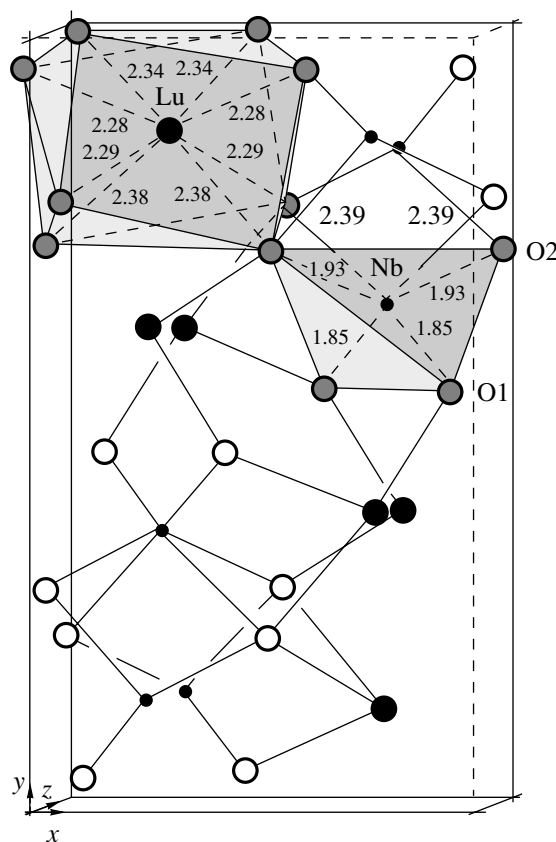


Fig. 1. Projection of the LuNbO₄ structure onto the xy plane. The coordination polyhedra of Lu³⁺ and Nb⁵⁺ ions are hatched.

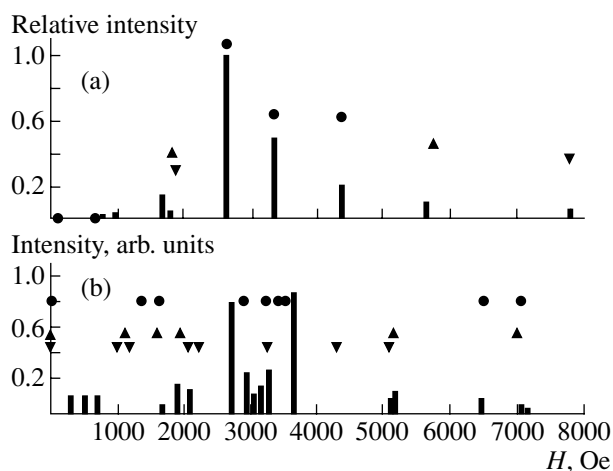


Fig. 2. EPR spectra of Cr³⁺ ions in LuNbO₄ at a frequency of 9.80 GHz at room temperature. Vertical bars indicate the positions of the resonance lines and their intensities; filled circles indicate the positions of the EPR lines due to Cr³⁺ ions located in the lutetium sites; filled triangles indicate the positions of the Cr³⁺-resonance lines in the niobium sites O1; inverted filled triangles, the positions of the Cr³⁺-resonance lines in the niobium sites O2. (a) External magnetic field is parallel to the C_2 -axis. The calculation was performed at the parameter values listed in the table. (b) External magnetic field is oriented along four directions with the minimum spectrum multiplicity which are normal to the C_2 -axis. Only the positions of the resonance lines are calculated.

types of centers. The minimal linewidth on the EPR spectrum was 10 Oe.

The spectra observed are attributed to Cr³⁺ paramagnetic centers. As was indicated above, the structure has two crystallographically independent positions for Lu and Nb atoms and two crystallographically independent positions for oxygen atoms, O1 and O2. Since the ionic radii of Cr³⁺ and Nb⁵⁺ are close [12], the Cr³⁺ cations introduced into the LuNbO₄ structure in low concentrations can replace not only the Lu³⁺-positions but also the Nb⁵⁺-positions. The filling of the niobium positions gives rise to an oxygen deficit either in the O1 or in the O2 position. The existence of four mutually orthogonal directions perpendicular to the twofold axis C₂, along which the spectra are identical, can be explained by the twinning characteristic of ferroelastic crystals because of phase transition. As a result, along these directions, one can simultaneously observe two spectra formed corresponding to two mutually perpendicular directions of the nearest environment of paramagnetic center, which can be transformed into one another by rotation through 90°. Thus, in this compound, one paramagnetic isovalent center can be formed in the Lu³⁺ position and two oxygen-deficient paramagnetic centers can be formed in the Nb⁵⁺ position.

The spectra were identified and the parameters of the spin Hamiltonian were determined by comparing the observed and the calculated line positions. At the parallel orientation (the magnetic field applied along the twofold symmetry axis), the spectra were identified by both the positions and the intensities of the EPR lines. To describe the spectrum at the monoclinic symmetry of the nearest environment of chromium ions with S = 3/2, the following spin Hamiltonian [13] was used:

$$\hat{H}_S = g_{\parallel}\beta\hat{H}_z\hat{S}_z + g_{\perp}\beta(\hat{H}_x\hat{S}_x + \hat{H}_y\hat{S}_y) + D[\hat{S}_z^2 - S(S+1)] + E(\hat{S}_x^2 - \hat{S}_y^2), \quad (1)$$

where β is the Bohr magneton, g_∥ and g_⊥ are the g-factors, and D and E are the constants that describe anisotropy along the monoclinic C₂ axis and in the plane normal to it, respectively. If the magnetic field is applied along the z-axis, the energy levels take the values

$$E_{1,2} = (1/2)g_{\parallel}\beta H_z \pm \sqrt{(g_{\parallel}\beta H_z + D)^2 + 3E^2}, \quad (2)$$

$$E_{3,4} = -(1/2)g_{\parallel}\beta H_z \pm \sqrt{(g_{\parallel}\beta H_z - D)^2 + 3E^2},$$

and the eigenfunctions are

$$\psi_{1,2} = a_{1,2}|3/2\rangle + b_{1,2}|-1/2\rangle, \quad (3)$$

$$\psi_{3,4} = a_{3,4}|1/2\rangle + b_{3,4}|-3/2\rangle,$$

where

$$a_{1,2}^2 = \frac{-D - g_{\parallel}\beta H_z/2 - E_{1,2}}{g_{\parallel}\beta H_z - 2E_{1,2}},$$

$$b_{1,2}^2 = \frac{D + 3g_{\parallel}\beta H_z/2 - E_{1,2}}{g_{\parallel}\beta H_z - 2E_{1,2}},$$

$$a_{3,4}^2 = \frac{D - 3g_{\parallel}\beta H_z/2 - E_{3,4}}{-g_{\parallel}\beta H_z - 2E_{3,4}},$$

$$b_{3,4}^2 = \frac{-D + g_{\parallel}\beta H_z/2 - E_{3,4}}{-g_{\parallel}\beta H_z - 2E_{3,4}}. \quad (4)$$

Since the eigenstates at E = 0 are ψ₁ → |3/2⟩, ψ₂ → |-1/2⟩, ψ₃ → |1/2⟩, and ψ₄ → |-3/2⟩, this notation is also convenient at E ≠ 0, but one has to keep in mind their conventional sense. In this orientation, the probabilities of transitions are determined by the expressions

$$W_{1/2 \rightarrow 3/2} \propto \left[a_3 \left(\frac{\sqrt{3}}{2} a_1 + b_1 \right) + \frac{\sqrt{3}}{2} b_1 b_3 \right]^2,$$

$$W_{-3/2 \rightarrow 3/2} \propto \left[a_4 \left(\frac{\sqrt{3}}{2} a_1 + b_1 \right) + \frac{\sqrt{3}}{2} b_1 b_4 \right]^2,$$

$$W_{-1/2 \rightarrow 1/2} \propto \left[\frac{\sqrt{3}}{2} a_2 a_3 + b_2 \left(a_3 + \frac{\sqrt{3}}{2} b_3 \right) \right]^2, \quad (5)$$

$$W_{-3/2 \rightarrow -1/2} \propto \left[a_4 \left(\frac{\sqrt{3}}{2} a_2 + b_2 \right) + \frac{\sqrt{3}}{2} b_2 b_4 \right]^2,$$

$$W_{-1/2 \rightarrow 3/2} = 0, \quad W_{1/2 \rightarrow -3/2} = 0.$$

It is seen from Eqs. (3)–(5) that the orthorhombic component of the crystal field leads to a mixing of the states |3/2⟩ and |-1/2⟩ as well as |1/2⟩ and |-3/2⟩, and the occurrence of the additional transition |-3/2⟩ → |3/2⟩ with W_{-3/2 → 3/2} ≠ 0, which was forbidden earlier.

Using the above formulae, we calculated the EPR spectrum in the case where the magnetic field was applied along the C₂-axis. The calculated lines and the experimental spectrum are shown in Fig. 2. Both positions and intensities of the lines observed in the parallel orientation at H = 2623, 3371, and 4360 Oe are well described by the Hamiltonian at the parameter values listed in table. We attribute these three lines to isovalent Cr³⁺ centers formed by the replacement of Lu³⁺ by Cr³⁺ ions. The calculated positions and relative intensities of the resonance lines are shown by circles in Fig. 2a. The lines denoted by upward-directed filled triangles (for one center) and downward-directed filled triangles (for another center) should be attributed to two non-equivalent Cr³⁺ centers occupying the Nb⁵⁺ positions. The parameters of the spin Hamiltonians that describe the spectra of these centers are listed in the table.

The energy-level values and the positions of the resonance lines for the perpendicular direction can be

Parameters of EPR spectra of Cr³⁺ ions in LuNbO₄

Type of center	g_{\parallel}	g_{\perp}	D , cm ⁻¹	E , cm ⁻¹	ν_0 , GHz
Lu ³⁺	1.82 ± 0.01	1.90 ± 0.02	0.024	0.093	9.7
The first Nb ⁵⁺ ion	1.75 ± 0.01	2.05 ± 0.02	0.17	0.14	17.7
The second Nb ⁵⁺ ion	2.2 ± 0.1	2.13 ± 0.05	0.084	0.11	13.4

obtained only numerically by solving the secular equation corresponding to Hamiltonian (1). In this case, only the g_{\perp} -value of the g -factor was used as a fitting parameter. Therefore, in Fig. 2b the line positions are indicated for $H_x \neq 0, H_y = 0$ and $H_x = 0, H_y \neq 0$. The agreement between the calculated and observed spectra is satisfactory; however, in order to describe the spectrum in more detail and with a higher accuracy, the measurements should also be made at another frequency.

CONCLUSIONS

Thus, large LuNbO₄ ferroelastic single crystals containing 0.3 at. % of Cr³⁺ ions are grown for the first time by the floating zone technique ~1 cm³ in volume, and their EPR spectra are studied. The spectrum lines are caused by the transitions from three paramagnetic centers formed by the replacement of an isovalent Lu³⁺ and two nonisovalent Nb⁵⁺ ions by Cr³⁺ ions. Twinning revealed in the crystals leads to a doubling of the number of lines and the formation of four principal directions normal to the twofold axis C_2 of the crystal, with the spectra along these directions being the same. The spectra of these centers are described within the framework of the spin Hamiltonian with $S = 3/2$, the D and E parameters ranging from 0.024 to 0.170 cm⁻¹, and the g -factors $g_{\parallel} = 1.75$ –2.20 and $g_{\perp} = 1.90$ –2.13.

The EPR frequencies of the Cr³⁺ ions in the zero magnetic field (9.7, 13.4, and 17.7 GHz) lie in the ultrahigh frequency range, which allows one to use lutetium

niobate single crystals in experiments on the dynamic orientation of the nuclei.

REFERENCES

1. V. A. Atsarkin, A. L. Barabanov, A. G. Beda, and M. V. Novitsky, Nucl. Instrum. Methods Phys. Res. A **440**, 626 (2000).
2. A. F. Volkov, L. A. Ivanova, Yu. N. Venevtsev, and L. L. Rappoport, Zh. Fiz. Khim. **56**, 1002 (1982).
3. *Minerals. Compound Oxides, Titanates, Niobates, Antimonates, and Hydroxides (Handbook)*, Ed. by F. V. Chukhrov and É. M. Bonshtedt-Kupletskaya (Nauka, Moscow, 1967), Vol. II, issue 3, p. 248.
4. P. A. Arsen'ev, V. B. Glushkova, A. A. Evdokimov, et al., *Rare Earth Compounds. Zirconates, Hafnates, Niobates, Tantalates, and Antimonates* (Nauka, Moscow, 1985).
5. L. A. Ivanova, E. B. Perova, and Yu. N. Venevtsev, *Synthesis, Structure, and Properties of Stibiotantalites and Fergusonites*, in *Series Scientific and Technological Prognosis in Catalysis, Corrosion, and Synthesis of Ferroelectric Materials* (NIITÉKhIM, Moscow, 1977).
6. *X-ray Powder Data File* (American Society for Testing and Materials, Philadelphia, 1981), Card Index ASTM, File 23-1207.
7. W. Jeischko, A. W. Sleight, W. R. McCellan, and J. F. Weiher, Acta Crystallogr., Sect. B: Struct. Crystallogr. Cryst. Chem. **B32**, 1163 (1976).
8. L. H. Brixner, J. F. Whitney, F. C. Zumsteg, and G. A. Jones, Mater. Res. Bull. **12**, 17 (1977).
9. A. T. Aldred, Mater. Lett. **1**, 197 (1983).
10. A. I. Kondrat'eva, S. K. Filatov, L. V. Andrianova, and A. M. Korovkin, Izv. Akad. Nauk SSSR, Neorg. Mater. **25**, 1710 (1989).
11. A. M. Balbashov and S. K. Egorov, J. Cryst. Growth **52**, 498 (1981).
12. R. D. Shannon, Acta Crystallogr., Sect. A: Cryst. Phys., Diffr., Theor. Gen. Crystallogr. **A32**, 751 (1976).
13. S. A. Al'tshuler and B. M. Kozyrev, *Electron Paramagnetic Resonance* (Fizmatgiz, Moscow, 1961; Academic, New York, 1964).

Translated by T. Dmitrieva

PHYSICAL PROPERTIES
OF CRYSTALS

Comparative Analysis of Methods for Studying
Internal Stresses in Crystals

V. S. Chudakov

Shubnikov Institute of Crystallography, Russian Academy of Sciences,
Leninskii pr. 59, Moscow, 117333 Russia

Received July 19, 2001

Abstract—The possibilities provided by the main polarization optical methods of studying internal stresses in differently oriented plates prepared from cubic crystals are compared. A promising method for obtaining exhaustive information on the stressed state of an object, including the trajectories and the values of the principal stresses, is described. © 2002 MAIK “Nauka/Interperiodica”.

Most of the dielectric and semiconductor cubic crystals are transparent in the near IR range of the spectrum. This allows us to efficiently study their stressed states in polarized light. Such studies give valuable information on the quality of the growth apparatus, shortcomings of the technologies used, and, based on the defect concentration, also provide a preliminary certification of the crystal quality affecting the mechanical, optical, and electrophysical properties of future details and devices.

Internal stresses in transparent solids induce artificial optical anisotropy and, in particular, they locally transform isotropic crystals into uniaxial (classes $\bar{4}3m$, 432 , and $m3m$) or biaxial (classes 23 and $m3$) ones [1]. The patterns of birefringence distribution caused by induced anisotropy and observed in polarized light are essentially dependent on the orientation of the principal stresses with respect to the principal symmetry axes and the direction of observation. Such a dependence predetermines essential differences in the observed patterns in the analysis of differently oriented plates despite the same distribution of the internal stresses.

For arbitrarily oriented plates, the value of the induced difference in the principal refractive indices Δn (birefringence) depends on the refractive index n_0 of an unstressed crystal, the values of the principal stresses σ_{ij} and the differences between them, and the piezo-optic coefficients π_{ij} and their combinations in a rather complicated way. In most occasions, one uses in practice thin (111)- and (100)- and sometimes also (110)-oriented plates prepared from crystals of the classes $m3m$ and $\bar{4}3m$. To describe the stressed state revealed with the aid of induced optic anisotropy, one uses the piezo-optic coefficient π_{44} and the difference $(\pi_{11} - \pi_{12})$. If the stressed state of the crystal is provided by microstresses, one can assume that the plane stressed state is studied for thin plates related to the induced birefrin-

gence in differently oriented plates in the following way: for the (111)-oriented plates

$$\Delta n = n_0^3(\sigma_2 - \sigma_1)(\pi_{11} - \pi_{12} + 2\pi_{44})/6, \quad (1a)$$

$$\alpha_0 = \beta; \quad (1b)$$

for the (100)-oriented plates

$$\Delta n = 0.5n_0^3(\sigma_2 - \sigma_1) \quad (2a)$$

$$\times [(\pi_{11} - \pi_{12})^2 \cos^2 2\beta + \pi_{44}^2 \sin^2 2\beta]^{1/2},$$

$$\tan 2\alpha_0 = (\pi_{11} - \pi_{12}) \tan 2\beta / \pi_{44}; \quad (2b)$$

and for the (110)-oriented plates

$$\Delta n = 0.5n_0^3 \{ [0.5(\pi_{11} - \pi_{12} + \pi_{44})(\sigma_1 \cos^2 2\beta + \sigma_2 \sin^2 \beta - (\pi_{11} - \pi_{12})(\sigma_1 \sin^2 \beta + \sigma_2 \cos^2 2\beta))]^2 + [\pi_{44}(\sigma_2 - \sigma_1) \sin^2 \beta]^2 \}^{1/2}, \quad (3a)$$

$$\tan 2\alpha_0 = \pi_{44}(\sigma_2 - \sigma_1) \sin 2\beta / [0.5(\pi_{11} - \pi_{12} + \pi_{44}) \times (\sigma_1 \cos^2 \beta + \sigma_2 \sin^2 \beta)] \quad (3b)$$

$$- (\pi_{11} - \pi_{12})(\sigma_1 \sin^2 \beta + \sigma_2 \cos^2 \beta)],$$

where α_0 is the azimuth of the fast axis of the optical indicatrix at the point of observation measured from the direction of the maximum transmission of the polarizer, and β is the azimuth of the principal stress σ_1 measured from the [100] axis.

The transition from the stresses in the plates to the volume stresses in the initial Czochralski-grown silicon crystal is described in [2].

As follows from the above relationships, the exhaustive study of a plate depends on its orientation. It is most convenient to study the (111)-oriented plates because they provide a direct relation between the measured Δn and α_0 values and the $(\sigma_2 - \sigma_1)$ and β values.

This allows us to directly record stress diagrams by certain methods. In (100)- and (111)-oriented plates, all the orthogonal directions are equivalent, but the principal axes of the stress tensor do not coincide with the principal axes of the indicatrix, i.e., $\alpha_0 \neq \beta$; the only exception are the points at which the principal stresses act along the [100]- and [110]-axes. In this case, $\alpha_0 = \beta$ and

$$\Delta n_{[100]} = n_0^3(\pi_{11} - \pi_{12})(\sigma_2 - \sigma_1)/2, \quad (4)$$

$$\Delta n_{[110]} = n_0^3\pi_{44}(\sigma_2 - \sigma_1)/2. \quad (5)$$

In the general case, in order to determine Δn in the plate of the (100)-cut, one first has to calculate the β value.

In the plate of the (110)-cut, not all the orthogonal directions are equivalent, which complicates the form of Eqs. (3a) and (3b). An analysis of these relationships shows that it is impossible to study the internal stresses in the (110)-plates. An exception is the four points located at the plate edge. At two of these points, the tangents to the plate edge are parallel to [100], whereas at two other points they are parallel to [110]. At the edge points of an arbitrarily oriented plate, only the uniaxial stresses σ_τ tangential to the plate edge exist. If these stresses in the (110) plate coincide with the [100]- and [110]-directions, we have

$$\Delta n_{[100]} = n_0^3(\pi_{11} - \pi_{12})\sigma_\tau/2, \quad (6)$$

$$\Delta n_{[110]} = n_0^3(\pi_{11} - \pi_{12} + \pi_{44})\sigma_\tau/4. \quad (7)$$

To determine the parameters of the stressed state of an object, one has to know the Δn and α_0 values, which are determined with the use of various polariscopes. The values of Δn and α_0 in polariscopes with visual observation and in those supplied with infrared image transformers are determined by the Senarmont method [2] or with the aid of various compensators [3] providing the determination of the phase difference δ_0 or the path difference Γ . These parameters are related to the averaged Δn values as follows: $\delta_0 = 2\pi\Delta n d/\lambda$ and $\Gamma = \Delta n d$, where d is the plate thickness and λ is the wavelength of the radiation used. It should be remembered that for thick plates the average Δn value can considerably differ from the maximum and, thus, can distort the information on the critical values of the internal stresses. This method is inapplicable to the analysis of microstresses because it requires the knowledge of the stress distributions around the defects with due regard for their shapes and dimensions.

The probing radiation transmitted by a stressed object in scanning polariscopes with a rotating element [4] (an analyzer, a polarizer, or a phase plate) undergoes amplitude-phase modulation and is recorded by a photodetector. The parameters of the modulated part of the signal contain information on both Δn and α_0 in the amplitude and the signal phase. The method of the amplitude-phase modulation of the radiation does not

allow the visual observation of the induced birefringence.

The reliability of the pattern reflecting the stressed state of the crystal in the polarized light depends on the wavelength of the probing radiation, the type of polarization, the degree of optical homogeneity of the object, and on the observation method. This is explained by the fact that the image is an interference pattern dependent on the above factors and, therefore, is often inconsistent with the stress distribution.

The most serious distortion of the information on the stress distribution is characteristic of a linear crossed polariscope in which the brightening level I depends on both Δn and α_0 :

$$I \sim \tau \sin^2(\delta_0/2) \sin^2 2\alpha_0, \quad (8)$$

where τ is the optical transmission of the object. At points where $\alpha_0 = 0^\circ$ and 90° , the maximum darkening is observed, which is limited by the quality of the polarization elements. The set of points with the maximum darkening forms isoclines moving along the object during its rotation. Similar darkening is also observed at points where $\Gamma = \lambda$. To identify these points, one has to use radiation with a different wavelength. It follows from (9) that the inconsistency of the brightness and the stress level is explained by the term $\sin^2 \delta_0/2$.

In a circular polariscope with two crossed quarter-wave plates, the distortions introduced by the azimuth of the object with respect to the polarizer are removed because

$$I \sim \tau \sin^2(\delta_0/2). \quad (9)$$

In polariscopes with a rotating polarization element and a rotating half-wave phase plate, information on the stress distribution is distorted much less, because the following expressions are valid:

$$I_{(\omega)} \sim \tau \sin \delta_0 \sin 2(\omega t - \alpha_0), \quad (10)$$

$$I_{(\omega)} \sim \tau \sin \delta_0 \sin 2(2\omega t - \alpha_0), \quad (11)$$

where ω is the circular frequency of the element rotation. For a rotating phase plate, the frequency of the probing-radiation modulation is twice as high as that for a rotating polarization element. Also, at $\delta_0 < 30^\circ$, one can assume, within the admissible accuracy, that the amplitude of the modulated signals is proportional to δ_0 . For (111)-plates, this allows us to record the stress diagrams in the automatic mode without any corrections. If the software used takes into account the signal phase, the stress diagrams can be recorded also for the (100)- plates and at $\delta_0 > 30^\circ$.

Of special interest are the points at which birefringence is not observed in the plane stressed state irrespective of the stress value. As follows from (1a) and (2a), birefringence in the (111)- and (100)-plates is not observed at points where $\sigma_1 = \sigma_2$. In other plates with nonequivalent orthogonal directions, birefringence is

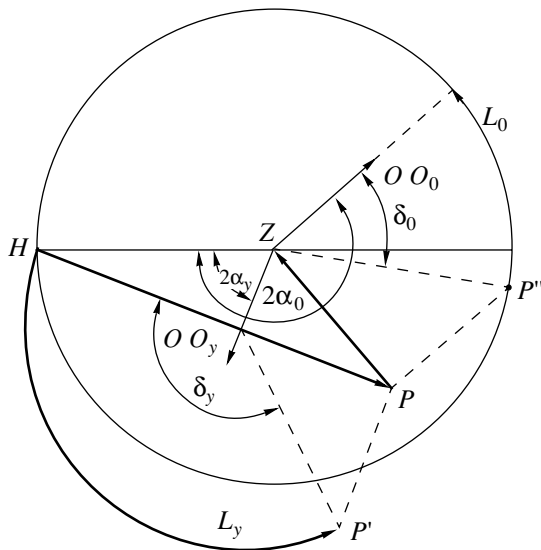


Fig. 1. Illustrating the transformation of the initial linearly polarized radiation into circularly polarized radiation with the use of a tunable crystalloptical device and an arbitrarily oriented object; *H* is the point on the sphere equator which denotes the initial linearly polarized radiation, *Z* is the sphere pole, *P* is the point which denotes the elliptically polarized radiation at the entrance of the object, *L_y* and *L₀* are the arcs of the transformation, and *HP* and *PZ* are their projections onto the equatorial plane of the sphere; δ_y and δ_0 are the phase differences introduced by the device at the azimuths of the fast axes α_y and α_0 , the points *P'* and *P''* are the projections of the point *P* onto the planes containing the arcs *L_y* and *L₀*, respectively, and *OO₀* and *OO_y* are the directions of the optical axes of the object and the device, respectively.

not observed at the points with other stress ratios. Thus, at points with zero birefringence in the (110)-plates, the principal stresses act along the two- and fourfold axes with the stress ratios

$$\sigma_1/\sigma_2 = 2(\pi_{11} - \pi_{12})/(\pi_{11} - \pi_{12} + \pi_{44})$$

or

$$\sigma_1/\sigma_2 = 2[1 + \pi_{44}/(\pi_{11} - \pi_{12})]. \tag{12}$$

As was indicated above, the visual information on the birefringence distribution, irrespective of the method of its observation, is distorted by nonuniform transmission. Birefringence in optically inhomogeneous objects can be quantitatively evaluated with the use of compensators. However, calculations show that it is more convenient to use a crystalloptical device with a variable path difference and methods using a rotating element, although for different purposes than in a compensator. Such a device is placed immediately behind a polarizer and transforms the linearly polarized radiation into elliptically polarized radiation with the parameters providing its transformation, upon the transmission through the object into a circularly polarized radiation. Like natural radiation, the circularly polarized radiation is not modulated by a rotating ele-

ment, which allows the determination of the moment of the attainment of this polarization with a high accuracy, even if the polarization elements are of insufficiently high quality. The device parameters allow the determination of the parameters of birefringence at any point of the object without changing its azimuthal position with respect to the polarizer (as is necessary in a linear polariscope) by using special software or a programmed calculator.

To determine the relationship between the birefringence parameters of the device and the object at the moment of the zero modulated signal, we can use the Poincaré sphere method [5]. Figure 1 shows the horizontal projection of this sphere. The initial linearly polarized radiation is indicated by the point *H* on the sphere equator. In a device with the parameters δ_y and α_y , the linearly polarized radiation *H* is transformed into the elliptically polarized one along the arc *L_y*. The projection of the arc *L_y* onto the equatorial plane is *HP*. If necessary, the ellipticity parameters can be determined proceeding from the coordinates of the point *P* [5]; however, it is not necessary for the solution of our problem. After the elliptically polarized light is transmitted by an object with the parameters δ_0 and α_0 , it is transformed into circularly polarized light along the arc *L₀* (point *Z*). The point *Z* is the sphere pole and *PZ* is the projection of the arc *L₀*. The solution of the problem allows one to establish the relation between the parameters of the object and the device. First, δ_0 is determined as

$$\delta_0 = \arccos(\sin \delta_y \sin 2\alpha_y). \tag{13}$$

Then, using the data on δ_0 , the azimuth α_0 is calculated from

$$2\alpha_0 = \pi/2 + 2\alpha_y - \arcsin(\cos \delta_y \sin 2\alpha_y / \sin \delta_0). \tag{14}$$

It is assumed in Eqs. (13) and (14) that the calibrated scales of the device have zero readings of δ_y and α_y . However, at initial parameters of zero, both the polariscope with a rotating element and the linear polariscope are insensitive to the stressed regions of the object in which the principal stresses are either parallel or orthogonal to the direction of the maximum transmission. Therefore, technologically, it is more convenient to use a crystalloptical device with the zero setting corresponding to the conditions $\delta_y = \pi/2$ and $\alpha_y = \pi/4$. A device with such parameters is equivalent to a quarter-wave plate located along the diagonal to the direction of the maximum transmission. In this setting, the device has maximum sensitivity to internal stresses irrespective of the object azimuth. The use of the scales with the changed zero reading is characterized by different relation between the parameters δ_y and α_y and the parameters of the object δ_0 , and α_0 :

$$\delta_0 = \arccos(\cos \delta'_y \cos 2\alpha'_y), \tag{15}$$

$$2\alpha_0 = \pi - 2\alpha'_y - \arcsin(\sin\delta'_y \cos 2\alpha'_y / \sin\delta_0), \quad (16)$$

where $\delta'_y = \pi/2 - \delta_y$ and $\alpha'_y = \pi/4 - \alpha_y$.

The corresponding software provides the use of a simple device consisting of two identical plates with natural birefringence transforming the polarization, e.g., thin mica sheets which can be rotated in the azimuthal direction with respect to one another [6]. The path difference of one plate should exceed $\lambda/4$.

The characteristics of a polariscope with a rotating phase plate studied with the aid of Muller matrices [5] show that the influence of nonuniform transmission on information about the distribution of induced birefringence at the two-channel recording of the modulated signals can be eliminated. To implement the corresponding system, it is necessary to use a rotating phase

plate which has a phase difference greater than 90° but less than 180° . Let a rotating phase plate differ from a 180° -plate by the value δ' . Then, the complete spectrum of the photodetector signal has three components—one constant and two modulated at different frequencies (at a double and at a fourfold rotation frequency of the phase plate, respectively):

$$U \sim \tau[(1 - \sin\delta_0 \sin 2\alpha_0 \sin^2(\delta'/2)) + \cos\delta_0 \sin\delta' \sin 2\omega t + \sin\delta_0 \cos^2(\delta'/2) \sin(4\omega t - 2\alpha_0)]. \quad (17)$$

To exclude the dependence of U on τ , only two modulated components are recorded simultaneously along two different channels calibrated prior to measurements; τ is excluded during the signal separation. The true value of δ_0 is calculated by the formula

$$\delta_0 = \arctan\{[2U_k(4\omega)U_0(4\omega)\tan(\delta'/2)]/U_k(2\omega)U_0(2\omega)\}, \quad (18)$$

where $U_0(4\omega)$ and $U_0(2\omega)$ are the signals from the points of the object and $U_k(4\omega)$ and $U_k(2\omega)$ are the calibration levels of the signals. The channels are calibrated in an unusual way—in the absence of the object. In this case, the value of $U_k(4\omega)$ is measured for a linearly polarized radiation, whereas $U_k(2\omega)$, for a circularly polarized one. To transform the radiation, a special tunable crystalloptical device is placed immediately after the polarizer. The linear polarization is attained at $\delta_y = 0^\circ$, whereas the circular one, at $\delta_y = 90^\circ$ and $\alpha_y = 45^\circ$. The information about the azimuth α_0 of the fast axis is contained in the signal phase at the fourfold modulation frequency. Thus, modern automation methods provide the successful implementation of the above algorithm for studying internal stresses during the scanning process, even for optically inhomogeneous objects.

The studies showed some other advantages of polariscopes with a rotating phase plate. Figure 2 shows the curves recorded during scanning of a plate prepared from a single crystal of neodymium-doped yttrium-aluminum garnet. Curve 1 was recorded for a rotating analyzer and curve 2, for a rotating phase plate. Earlier, using the method described in [7], we determined the local inclusions in this plate with a noticeable polarizability, especially well pronounced at the plate edges. It is seen from these curves that the presence of polarizing defects considerably distorted the information on the induced birefringence in the case of a rotating analyzer. The absorbing and the polarizing defects differently distort the information on birefringence distribution. The absorbing defects always reduce the birefringence values, whereas the polarizing ones can either considerably increase or decrease these values.

Important information on the stressed state of an object is provided by the trajectories of the principal

stresses, at any point of which the direction of one of the principal stresses coincides with the tangential direction. In addition to the information on the directions of the principal stresses, the set of these trajectories demonstrates, similarly to a topographic map, the sites of stress concentration. Moreover, the trajectories of the principal stresses provide the separate measurements of the principal stresses.

It is impossible to record all the families of the trajectories of principal stresses without the invocation of modern means of automation and computerization. It is especially important for crystals. One of the most promising methods for recording the trajectories of the principal stresses is the controlled motion of the stage. If necessary, the stage motion is synchronized with a two-coordinate plotter so that it can move in any direction by the command of the automated system. These commands are worked out by a computer on the basis of the information on the azimuth of the fast axis with the subsequent determination of the azimuth of the principal stress. Depending on the operation speed of the system, the table moves along the trajectories of the principal stresses either in the stepwise or in continuous modes.

A more complicated stepwise scanning of an object along the trajectory of the principal stress provides the measurement of the principal stresses. The solution of this complicated problem is based on the Lamé-Maxwell theorem [8], according to which the equation of the equilibrium state at point i of the stressed object in the integral form is

$$\sigma_{i1} = \sigma_{01} - \int_0^i [(\sigma_2 - \sigma_1)/\rho_2] dS_1, \quad (19)$$

where σ_{01} and σ_{i1} are the known and the sought stresses at the points O and i located on one trajectory, respec-

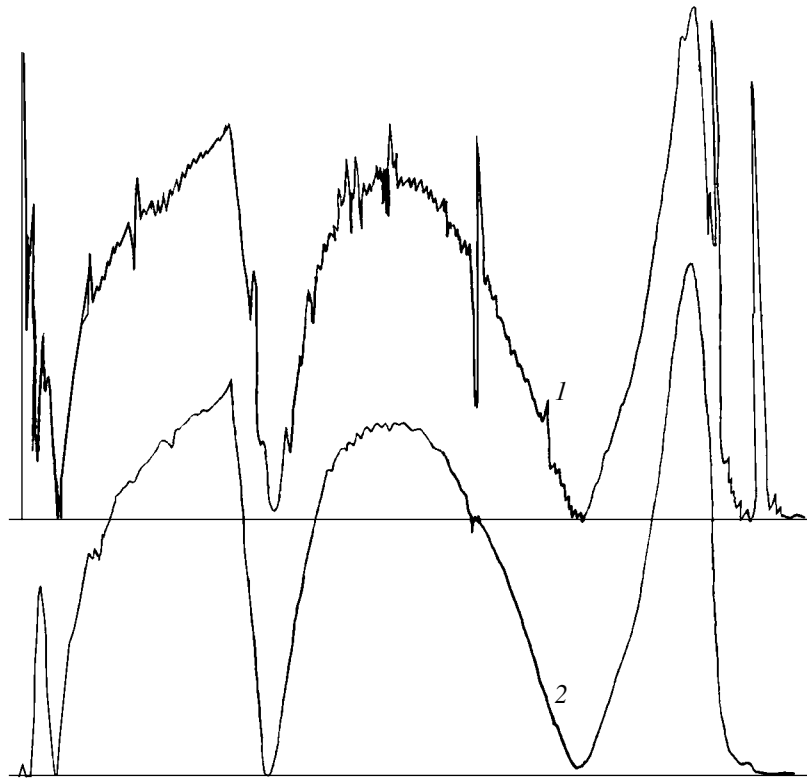


Fig. 2. Automatic records of induced birefringence in a plate cut out from a neodymium-doped yttrium-aluminum garnet single crystal with polarizing defects. Curve 1 is obtained at the rotating analyzer and curve 2, at the rotating phase plate providing the elimination of the effect of polarization.

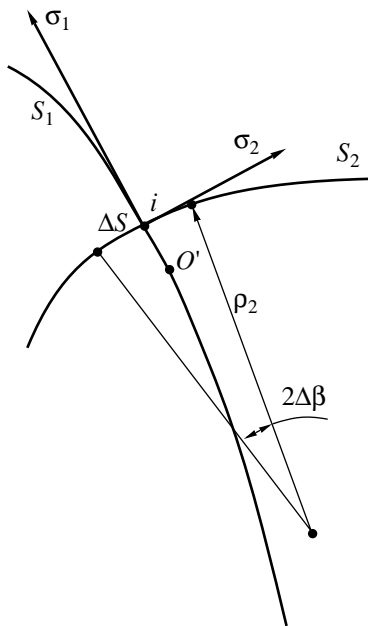


Fig. 3. Parameters used in the calculation of the principal stresses σ_1 and σ_2 . The trajectories of the principal stresses S_1 and S_2 are intersected at the point i , O' is the point with the known parameters, ΔS is the scanning step, ρ_2 is the curvature radius of S_2 at the point i , and $\Delta\beta$ is the change in the azimuth of the point i in the orthogonal displacement from this point by one step.

tively. The difference $(\sigma_2 - \sigma_1)$ and the radius ρ_2 of the orthogonal trajectory are measured at the point i . Figure 3 shows a fragment of the intersection of two trajectories of the principal stresses with an indication of all the parameters necessary for calculating σ_1 . The object is studied along the trajectory with the index S_1 .

The value of ρ_2 is determined by the method based on the use of the data on the change $\Delta\beta$ of the azimuth of the principal stress σ_1 in the vicinity of the point i on the line coinciding with the direction of σ_2 . At a small step ΔS in the α measurements on both sides of S_1 , it is possible to put, with a high degree of accuracy, that $\rho_2 = 2\Delta S/\Delta\beta$. The above assumptions provide the determination of the principal stresses in the form

$$\sigma_{i1} = \sigma_{01} - (\sigma_{i2} - \sigma_{i1})\Delta\beta/2. \quad (20)$$

As was indicated above, the points where the principal stresses can readily be determined, are located at the edge of the plate. Therefore, the study of the object should be started exactly at these points.

The analysis performed shows that the solution of the particular and the general problems associated with the study of internal stresses and the use of methods with a rotating polarization element or a rotating phase plate are much more efficient than other methods. This advantage manifests itself in a higher sensitivity and

operation speed and in the possibility of using modern means of automation and computerization in the studies of crystals. Moreover, the method allows the investigation of various defects in crystals by considering their polarizabilities [8], the changes in the refractive indices or the absorption power [10] using photoelectric apparatus conventionally used for the studies of the stressed state of objects, and the differences in their spectral characteristics [9].

REFERENCES

1. J. F. Nye, *Physical Properties of Crystals: Their Representation by Tensors and Matrices* (Clarendon, Oxford, 1957; Inostrannaya Literatura, Moscow, 1960).
2. V. L. Indenbom and V. I. Nikitenko, in *Stresses and Dislocations in Semiconductors: Collection of Articles*, Ed. by M. V. Klassen-Neklyudova (Akad. Nauk SSSR, Moscow, 1962), p. 8.
3. M. Born and E. Wolf, *Principles of Optics* (Pergamon, Oxford, 1969; Nauka, Moscow, 1973).
4. V. S. Chudakov, Prib. Tekh. Éksp., No. 5, 210 (1977).
5. W. A. Shurcliff, *Polarized Light: Production and Use* (Harvard Univ. Press, Cambridge, 1962; Mir, Moscow, 1965).
6. B. N. Grechushnikov, A. I. Vislobokov, E. A. Evdishchenko, *et al.*, *Kristallografiya* **38** (2), 55 (1993) [*Crystallogr. Rep.* **38**, 164 (1993)].
7. V. S. Chudakov and B. N. Grechushnikov, Prib. Tekh. Éksp., No. 5, 195 (1975).
8. M. M. Frocht, *Photoelasticity* (Wiley, New York, 1941; GITTL, Moscow, 1950).
9. V. S. Chudakov and B. N. Grechushnikov, *Opt.-Mekh. Prom-st'*, No. 7, 49 (1977).
10. V. S. Chudakov, *Kristallografiya* **46**, 328 (2001) [*Crystallogr. Rep.* **46**, 284 (2001)].

Translated by L. Man

PHYSICAL PROPERTIES
OF CRYSTALS

Second-Harmonic Generation in Vinylidene
Fluoride–Trifluoroethylene Copolymers Doped
with Donor–Acceptor Molecules

K. A. Verkhovskaya*, A. D. Grishina**, N. I. Kuznetsova*, L. Ya. Pereshivko**,
T. V. Krivenko**, and V. V. Savel'ev**

* Shubnikov Institute of Crystallography, Russian Academy of Sciences,
Leninskiĭ pr. 59, Moscow, 117333 Russia

** Frumkin Institute of Electrochemistry, Russian Academy of Sciences,
Leninskiĭ pr. 31, Moscow, 117071 Russia

Received June 5, 2001

Abstract—The temperature dependence of the second-harmonic generation in a vinylidene fluoride–trifluoroethylene ferroelectric copolymer doped with 5 wt % of a noncentrosymmetric 4-anilino-4'-nitroazobenzene chromophore is analyzed. The second-order susceptibility $\chi^{(2)}$ in the ferroelectric phase of these copolymers appears to be twice as high as in the poly(methyl methacrylate) with the same chromophore content. The effect is attributed to the presence in ferroelectrics of a local electric field associated with the spontaneous polarization. The intensity of the second-harmonic generation in both ferroelectric and paraelectric phases correlates with the variation of the surface potential. © 2002 MAIK “Nauka/Interperiodica”.

INTRODUCTION

The generation of the second harmonic of laser radiation is provided by nonlinear properties of noncentrosymmetric polar media. Nonlinear optical properties arise in polymer media involving chromophores possessing donor–acceptor properties giving rise to the formation of the polar structure (the arrows in Figs. 1a and 1b indicate the direction from a donor to an acceptor). The second harmonic can be generated only in a noncentrosymmetric medium, where donor and acceptor molecules are distributed not randomly but have the preferred orientation in the polymer bulk. The chromophores are oriented in the polymer bulk by applying a potential difference U inducing a constant orienting field $E_0 = U/d$, where d is the layer thickness. Figures 1a and 1b show the random distribution of the dipole moments of chromophores in the absence of the field E_0 and upon their orientation in the field E_0 , respectively. The electric-field vector $E(\omega)$ of a laser radiation wave polarizes a chromophore, i.e., induces an additional intramolecular charge transport in a donor–acceptor molecule. The charge transfer from a donor to an acceptor considerably exceeds the transfer in the opposite direction. As is shown in Fig. 1c, upon the orientation of chromophores in the field E_0 , the volume polarization P induced by the electric field $E(\omega)$ has the nonzero value. As a result of the effect of the strong field of a light wave, the total induced polarization includes the contribution that is nonlinear with respect to the field and can be represented as a sum of the Fourier components of the frequencies of ω , 2ω , etc., i.e., $P = P(0) +$

$P(\omega) + P(2\omega)$ (Fig. 1c). In this case, the radiation intensity of the second harmonic $[I(-2\omega)]$ is related to the polarization as $[I(2\omega)]^{0.5} \propto P(2\omega) = [\chi^{(2)}E(\omega)E(\omega)]$, where $\chi^{(2)}$ is the second-order volume susceptibility. Upon switching-off of the field E_0 , the time of the orientational relaxation of dipoles (transition from the oriented state of dipoles in Fig. 1b to the state shown in Fig. 1a) is determined by the structural properties of the polymer matrix and, primarily, by the relation between the chromophore dimensions and the free volume of the polymer [1].

The present study deals with generation of the second harmonic of a laser radiation by ferroelectric polymers doped with a noncentrosymmetric chromophore. The use of a ferroelectric polymer as a matrix can promote an increase in the polar order.

Hill *et al.* [2] observed the generation of the second harmonic in nonlinear molecules introduced into a ferroelectric polyvinylidene fluoride–trifluoroethylene matrix (a host–guest composite system). The 8- μm -thick films contained 10 wt % of nonlinear molecules (4-(4'-cyanophenylazo)-NN-bis-(methoxycarbonylmethyl)-aniline). The effect was observed at room temperature ($d_{33} = 2.6 \text{ pm/V}$). A linear dependence of the coefficient d_{33} on the concentration of nonlinear molecules was established.

EXPERIMENTAL RESULTS
AND DISCUSSION

The ferroelectric matrix used consisted of a vinylidene fluoride–trifluoroethylene copolymer

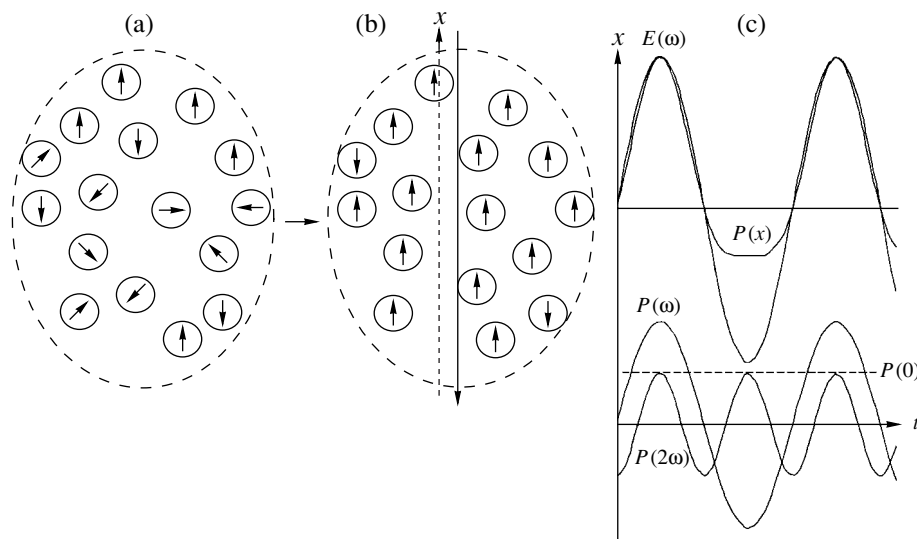


Fig. 1. Distribution of donor–acceptor molecules (a) without and (b) with the field E_0 . (c) Upper panel: the time dependence of the volume polarization $P(x)$ induced by the electric field $E(\omega)$ of a light wave along the x -axis. Lower panel: the Fourier components $P(0)$, $P(\omega)$, and $P(2\omega)$ of the anharmonic $P(x)$ function.

(PVDF–TrFE), $-(\text{CH}_2-\text{CF}_2)_n-(\text{CHF}-\text{CF}_2)_m-$, doped with 5 wt % of a noncentrosymmetric chromophore, 4-anilino-4'-nitroazobenzene (DO-3 dispersion orange dye). The DO-3 content corresponded to a concentration of 0.17 mol/dm^3 . The PVDF–TrFE polymer films are polycrystals consisting of crystalline lamellas mixed with the amorphous phase. The structural $-\text{CH}_2-\text{CF}_2$ unit of vinylidene fluoride possesses the dipole moment of $7 \times 10^{-30} \text{ C m}$ (near 2D) similar to conventional ferroelectrics. Ferroelectric switching in vinylidene fluoride and its copolymers is usually discussed within the model of nucleation and growth of antiparallel domains [3, 4]. The process of switching of spontaneous polarization is usually associated with the rotation of a polymer link about of the molecular chain and the propagation of such a defect (kink) along this chain. The films were obtained using copolymer grains with a relative content of vinylidene fluoride–trifluoroethylene of 70–30 and 60–40 mol % (Atochem, France). According to Furukawa [5], the heated 70–30 and 60–40 films undergo the transition from the ferroelectric to the paraelectric phase at $T_1 = 110$ and 90°C , respectively. The films of such compositions are characterized by a pronounced temperature hysteresis corresponding to a first-order phase transition. On cooling from the paraelectric phase, the phase transition to the ferroelectric state in these two films occurs at the temperatures $T_0 = 75$ and 70°C , respectively.

Figure 2 shows the block diagram of a setup for measuring second-harmonic generation where 1 is an Nd:YAG laser with the fundamental wavelength $\lambda = 1064 \text{ nm}$, power of 50 mJ per pulse, and a pulse duration of 10 ns. A laser beam passes through the polymer layer 2 obtained by solution casting onto a glass substrate 3 with a deposited transparent $\text{In}_2\text{O}_3/\text{SnO}_2$ elec-

trode. A fraction of the beam separated by plane 8 is directed to a test channel containing inorganic crystal 4 with nonlinear optical properties. In both channels, the second harmonic is separated by interference light filters 5 and 5' transmitting in the range of $532 \pm 10 \text{ nm}$. The second-harmonic intensities, $I(2\omega)$, are measured by digital voltmeters 7 and 7' simultaneously in both channels by photomultipliers 6 and 6'. Negatively charged particles formed as a result of air ionization due to the corona discharge arising at the application of a high voltage to needle 9 from voltage source 10 are deposited on the surface of the polymer layer. The resulting surface potential U is measured by a ring electrode connected with electrometer 11. The sample temperature was varied with the use of thermal blower 12.

As was mentioned above, the square root of the second-harmonic intensity, $I^{0.5}(2\omega)$, is proportional to the second-order volume susceptibility $\chi^{(2)}$ dependent on the density N of chromophore molecules, their orienta-

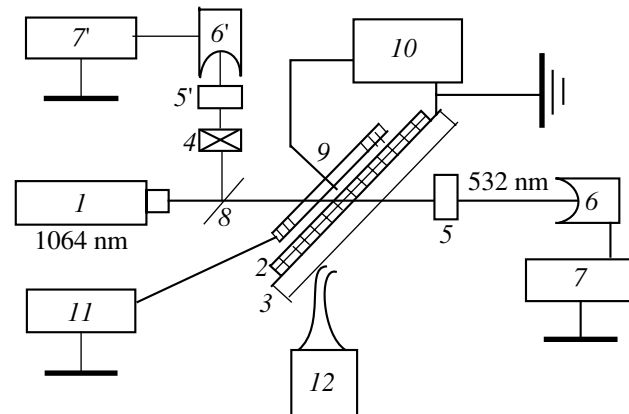


Fig. 2. Block diagram of the setup for measurements (for notation see the text).

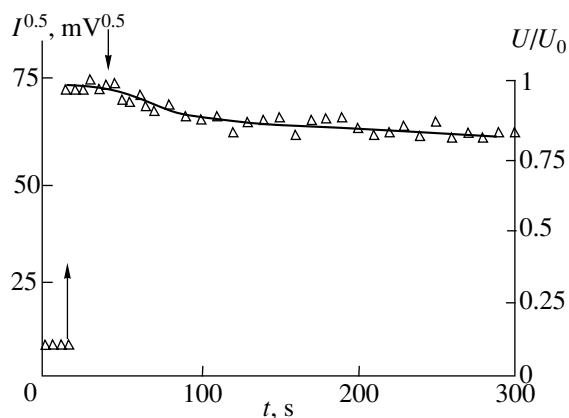


Fig. 3. The time dependences of $I^{0.5}(2\omega)$ (open triangles, left-hand ordinate axis) and U/U_0 (solid line, right-hand ordinate axis) in an as-prepared PVDF–TrFE (60–40) sample containing 5 wt % of DO-3 chromophore at room temperature. The up and down arrows indicate the instants of corona discharge switching on and off, respectively.

tion, and the second-order susceptibility (polarizability) β of an individual chromophore:

$$I^{0.5}(2\omega) \propto \chi^{(2)} \propto N\beta \langle \cos^3 \theta \rangle, \quad (1)$$

where $N = CN_A$, C is the concentration measured in mol/dm³, N_A is the Avogadro number, and θ is the angle formed by the dipole moment μ_0 of the ground state of the chromophore and the constant orienting field E_0 . The mean value $\langle \cos^3 \theta \rangle$ is determined in terms of the Langevin function,

$$\langle \cos^3 \theta \rangle = \mu_0 f_0 E_0 / 5kT, \quad (2)$$

where $f_0 E_0 = F_0$ is the local internal electric field, $f_0 = \varepsilon(n^2 + 2)/(2\varepsilon + n^2)$, where ε is the dielectric constant and n is the refractive index [$f_0 \approx 1.44$ for the poly(methyl methacrylate)]. For the ferroelectric PVDF–TrFE (70–30) polymer, the local electric field provided by spontaneous polarization is estimated as [6]

$$E_{\text{loc, theor}} = (P_{\text{ind}} + P_{\text{spont}})/3\varepsilon_0 = 2.5 \times 10^9 \text{ V/m}, \quad (3)$$

where P_{ind} and P_{spont} are the induced and spontaneous polarizations, respectively. For the 70–30 copolymer, we have $P_{\text{ind}} \ll P_{\text{spont}} = 0.065 \text{ C/m}^2$.

A strong local field in a ferroelectric partly orients the dipole molecules of the dyes. A resulting polar order can be specified by the quantities $\langle \cos \theta \rangle$ and $\langle \cos^3 \theta \rangle$ proportional to E_{loc} given by Eq. (3). In accordance with Eq. (3), the effect of the local field in the paraelectric ($P_{\text{spont}} = 0$) and ferroelectric ($P_{\text{spont}} \neq 0$) phases is different.

Figure 3 shows the appearance and the decrease in the second harmonic measured in an as-prepared PVDF–TrFE (60–40) sample containing DO-3 upon switching on and off of the corona discharge. Prior to

the switching on of the corona discharge, the generation of the second harmonic in the sample is weak, $I^{0.5}(2\omega) \sim 8 \text{ mV}^{0.5}$. We examined polydomain samples. The effect of the second-harmonic generation in an unpolarized sample is associated with a finite number of domains in the studied sample region. The switching on of the corona discharge resulted in an increase in $I^{0.5}(2\omega)$ up to $74 \text{ mV}^{0.5}$ (Fig. 3). The surface potential was found to be $U_0 \sim 40 \text{ V}$ at room temperature, which corresponds to the field $E_0 = U_0/d \approx 9 \times 10^6 \text{ V/m}$ for the layer thickness $d = 4.5 \mu\text{m}$. According to [7], the volume susceptibility is $\chi^{(2)} (= 2d_{33}) = 11.6 \text{ pm/V}$ at the DO-3 density $N = 2.3 \times 10^{20} \text{ cm}^{-3}$ ($C = 0.38 \text{ mol/dm}^3$) in poly(methyl methacrylate). In poly(methyl methacrylate) with the same DO-3 concentration, a signal of $I^{0.5}(2\omega) = 72 \text{ mV}^{0.5}$ was detected.

The DO-3 chromophore was introduced at a concentration of 0.17 mol/dm^3 or at $N = 1 \times 10^{20} \text{ cm}^{-3}$. Therefore, according to Eq. (1), one would expect that $I^{0.5}(2\omega) = 32.2 \text{ mV}^{0.5}$, which corresponds to the susceptibility $\chi^{(2)}$ of about 5.2 pm/V . However, as is seen from Fig. 3, in a ferroelectric with the DO-3 concentration of 0.17 mol/dm^3 $I^{0.5}(2\omega) = 74 \text{ mV}^{0.5}$, and, hence, $\chi^{(2)} = 12 \text{ pm/V}$, which is twice as high as the value measured in a poly(methyl methacrylate) matrix.

The measurements made under the conditions of a corona discharge indicate weak second-harmonic generation ($I^{0.5} \approx 8 \text{ mV}^{0.5}$) in PVDF–TrFE copolymers without DO-3. A comparable effect was observed earlier in polyvinylidene fluorine ferroelectric polymers [2, 8].

The excessive $\chi^{(2)}$ value in ferroelectric polymers in comparison with the value measured in a poly(methyl methacrylate) matrix may be interpreted as follows. Polarization provides the alignment of the dipoles of a PVDF–TrFE copolymer in crystalline regions along the film normal. In this case, the dye molecules are also reoriented. The investigation of the Stark effect for dye molecules introduced into a ferroelectric matrix [9] provided the estimation of both the polar order parameter of dye molecules for a polarized polymer and the electric-field intensity E_{loc} at the site of location of dye molecules. The static electric field stabilizing the induced polar order attains the value of $E_{\text{loc}} = 3 \times 10^8 \text{ V/m}$, i.e., is more intense than $f_0 E_0 = 1.3 \times 10^7 \text{ V/m}$ for poly(methyl methacrylate) by a factor of 20 [see Eq. (2)]. This can explain a much higher $\chi^{(2)}$ value in comparison with the value measured for a poly(methyl methacrylate) matrix. The above E_{loc} value is less by an order of magnitude than the local-field intensity calculated theoretically according to the Lorentz model (3). This seems to be associated with the fact that the averaging in the experiment made by Blinov *et al.* [9] was performed for both dye molecules in ferroelectric domains differently oriented with respect to the film normal and in the amorphous phase of the polymer.

Figure 3 shows that, upon switching-off of the corona discharge, the relaxation curve for the second harmonic coincides with the decreasing curve of the surface potential.

The temperature dependence of the surface potential U_0 during corona discharge measured as a function of a decreasing temperature of a PVDF-TrFE (70–30) sample, which was in the paraelectric phase at $T = 120^\circ\text{C}$, is shown in Fig. 4. It is seen that the curve abruptly changes at 73°C , the temperature close to the temperature of the phase transition from the paraelectric to the ferroelectric phase. This change is caused by a decrease in conductivity σ of the polymer with the lowering of the temperature in this range. Indeed, the potential U_0 is related to σ as [1, 10]

$$U_0 = V_c(V_c - V_0)/[V_c + \sigma/A], \quad (4)$$

where the potential V_c applied to needle 9 (Fig. 2) is constant in all the measurements, V_0 is the threshold potential for the corona discharge in air, and A is a constant. It follows from Eq. (4) that U_0 is almost independent of σ in polymers with low conductivity; i.e., at $1 \gg \sigma/(AV_c)$. At the same time, if $1 \ll \sigma/(AV_c)$ in polymer matrices, the σ -dependence of U_0 can be represented as $U_0 = B/\sigma$, where, in accordance with Eq. (4), $B = AV_c(V_c - V_0)$. Since conductivity depends on temperature as $\sigma = \sigma_0 \exp(-\Delta E/kT)$, where ΔE is the activation energy and k is the Boltzmann constant, we have

$$\ln(U_0) = \text{const} + \Delta E/kT.$$

The activation energy for the paraelectric phase of the copolymer estimated from the data in Fig. 4 is $\Delta E = 4.1$ eV. Thus, the kink in the temperature dependence of the surface potential U_0 and its dramatic increase with the lowering of the temperature in the paraelectric phase also indicates the corresponding decrease in the sample conductivity.

Figure 5 shows the time dependence of $I^{0.5}(2\omega)$ in an as-prepared PVDF-TrFE (70–30) sample with 5 wt % of the DO-3 chromophore obtained under switching on and off of the corona discharge and the varying sample temperature. The range a between solid vertical straight lines corresponds to the paraelectric state of the polymer. It is seen that the weak second harmonic is observed in the absence of an orienting field at the beginning of the measurements at room temperature and also in the PVDF-TrFE (60–40) copolymer (see Fig. 3); then, its intensity increases up to the maximum value immediately after the switching on of the corona discharge, and slowly decreases after its switching off. With an increase in the temperature, the second harmonic drops if the corona discharge is switched off at the temperature of the copolymer transition from the ferroelectric to the paraelectric phase (about 110°C). It is seen that switching on the corona discharge at 120°C (paraelectric phase) increases the intensity of the second harmonic, whereas its switching off abruptly decreases it (compare with the slow drop at 20°C). It is

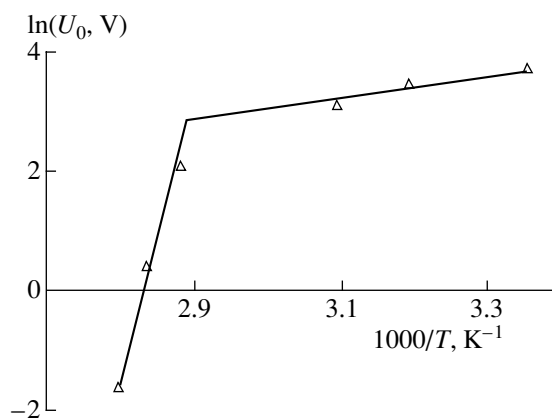


Fig. 4. The temperature dependence of the surface potential during corona discharge measured during lowering of the temperature of the PVDF-TrFE (70–30) copolymer with 5 wt % of the DO-3 chromophore.

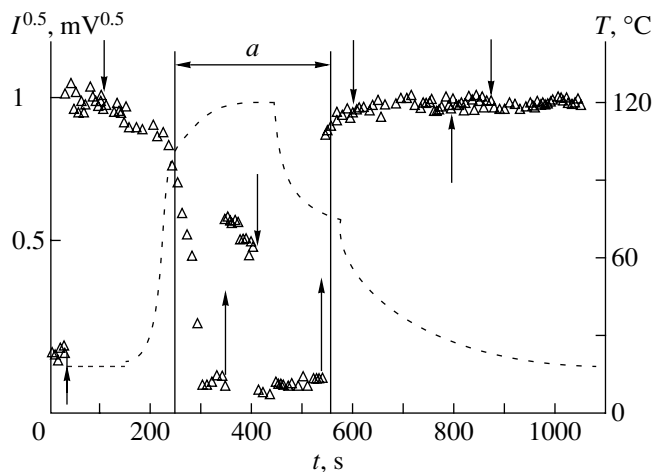


Fig. 5. The time dependence of $I^{0.5}(2\omega)$ (open triangles, left-hand ordinate axis) and (dashed line, right-hand ordinate axis) temperature of an as-prepared PVDF-TrFE (70–30) sample containing 5 wt % of the DO-3 chromophore. The up and down arrows indicate the instants of corona discharge switching on and off, respectively. The solid vertical straight lines indicate the range a corresponding to the temperature range 110 – 75°C , within which the polymer is in the paraelectric phase.

shown that the second-harmonic intensity at 120°C is lower than at room temperature. When the corona discharge is switched on once again during cooling in the range of the transition to the ferroelectric state, the second-harmonic intensity, first, reaches a value somewhat lower than the maximum one and, then, continues increasing gradually and, finally, upon the transition of the copolymer into the ferroelectric state, returns to the initial value; i.e., $(I/I_0)^{0.5} = 1$. The above changes in the second harmonic correspond to an increase in the surface potential with the lowering of the temperature in

the range of the paraelectric phase in Fig. 4. Thus, similar to the case of the ferroelectric phase (Fig. 3), the change in the second-harmonic intensity in the paraelectric phase correlates with the varying surface potential. Figure 5 also shows that, upon the restoration of the ferroelectric phase after switching off the corona discharge at $t = 600$ s, the generation of the second harmonic is retained; i.e., the copolymer remains to be polarized whereas chromophores preserve their oriented state.

CONCLUSIONS

Thus, in a ferroelectric PVDF–TrFE copolymer doped with a noncentrosymmetric chromophore (the DO-3 dye), the second-order susceptibility $\chi^{(2)}$ is twice as high as in poly(methyl methacrylate) at the same chromophore concentration. The effect is explained by a considerably more intense local orienting electric field associated with spontaneous polarization of the ferroelectric.

ACKNOWLEDGMENTS

This study was supported by the Russian Foundation for Basic Research, project nos. 99-03-32111 and

01-02-16081, and by the International Science and Technology Center, project nos. 872-98 and PP-2207.

REFERENCES

1. A. D. Grishina, L. Ya. Pereshivko, T. V. Krivenko, *et al.*, *Polymer* **42** (11), 4837 (2001).
2. J. R. Hill, P. L. Dunn, G. J. Davies, *et al.*, *Electron. Lett.* **23** (13), 700 (1987).
3. T. Furukawa, M. Date, and G. E. Johnson, *J. Appl. Phys.* **54**, 1540 (1983).
4. T. Furukawa and G. E. Johnson, *Appl. Phys. Lett.* **38** (12), 1027 (1981).
5. T. Furukawa, *Phase Transit.* **18**, 143 (1989).
6. L. M. Blinov, K. A. Verkhovskaya, S. P. Palto, *et al.*, *Kristallografiya* **41**, 328 (1996) [*Crystallogr. Rep.* **41**, 310 (1996)].
7. D. M. Burland, R. D. Miller, and C. A. Walsh, *Chem. Rev.* **94** (1), 31 (1994).
8. A. Wicker, B. Berge, T. Lajzerowicz, and J. F. Legrand, *J. Appl. Phys.* **66** (1), 342 (1989).
9. L. M. Blinov, K. A. Verkhovskaya, S. P. Palto, *et al.*, *Izv. Akad. Nauk, Ser. Fiz.* **60** (10), 171 (1996).
10. M. Scharfe, *Electrophotography Principles and Optimization* (Wiley, New York, 1984).

Translated by R. Tyapaev

CRYSTAL GROWTH

Growth and Morphological Study of Copper Oxide Single Crystals

A. A. Bush*, V. Ya. Shkuratov*, A. B. Kuz'menko**, and E. A. Tishchenko**

* Moscow State Institute of Radioengineering, Electronics, and Automation (Technical University),
pr. Vernadskogo 78, Moscow, 117454 Russia
e-mail: bush@cc.nifhi.ac.ru

** Kapitza Institute for Physical Problems, Russian Academy of Sciences,
ul. Kosygina 2, Moscow, 117973 Russia

Received February 21, 2000; in final form, July 27, 2001

Abstract—Experiments on the growth of CuO single crystals by crystallization from flux in the CuO–Bi₂O₃–PbO–PbF₂, CuO–Bi₂O₃–Li₂O, CuO–Bi₂O₃–B₂O₃, CuO–BaO–Y₂O₃, and CuO–MO_x systems ($M = \text{P, V, or Mo}$) have been performed. The best results were obtained in crystallization in the CuO–Bi₂O₃–PbF₂ system: prismatic single crystals of platelet- and needlelike or isometric habit with dimensions up to $1 \times 10 \times 10$, $1 \times 1 \times 20$, or $6 \times 6 \times 8$ mm, respectively, have been grown. The CuO crystals show polysynthetic twinning in the form of numerous alternating light and dark bands bound by systems of parallel straight lines on the {110} and {111} faces. A possible model of twinning associated with the Cu₂O → CuO transformation is considered. © 2002 MAIK “Nauka/Interperiodica”.

INTRODUCTION

Recently, copper oxide (II) (CuO) crystals corresponding to the natural mineral tenorite [1] have attracted considerable attention because of their unusual magnetic properties and possible high- T_c superconductivity (HTSC) [2–9]. Copper oxide exhibits the properties of low-dimensional antiferromagnets (AFM) with two points of magnetic transitions: the transition from the paramagnetic phase to AFM with incommensurate modulations of the magnetic structure at $T_{N1} = 230(2)$ K and the transition to the commensurate AFM phase at $T_{N2} = 213(1)$ K. The temperature dependence of the magnetic susceptibility shows small jumps along the b - and c -axes at T_{N2} . Above T_{N1} , the susceptibility continues increasing to form a broad maximum at $\sim 550^\circ\text{C}$ rather than decreases according to the Curie–Weiss law, which indicates the preservation of the magnetic short-range order above T_{N1} . The magnetic properties of CuO are similar to those of the YBa₂Cu₃O₆ HTSC phase [4, 9]. Moreover, CuO is a component of almost all known mixed-oxide compounds exhibiting HTSC associated with the existence of Cu–O planes [9]. Thus, the comprehensive study of the structure and the properties of CuO are of interest and importance for clarifying the nature of high-temperature superconductivity.

The known CuO crystals [3, 4, 10–17] do not fully satisfy the requirements of size and quality, which hinders their further study. In this connection, the studies aimed at synthesis of large high-quality copper oxide single crystals are very important. Below, we describe the synthesis of CuO single crystals and their X-ray diffraction and morphological studies.

CRYSTAL GROWTH

Since the reversible CuO → Cu₂O phase transition occurs at 1026°C [18], it is very difficult to grow CuO crystals from the native melt under normal pressure. Therefore, we grew these crystals by crystallization from fluxes of various compositions.

When choosing the starting compositions for crystallization, we took into account the characteristic features of the phase diagrams of the CuO systems with Bi₂O₃, SrO, BaO, YBa₂Cu₃O₆, R₂O₃ ($R = \text{Y, Eu, or Dy}$), etc. [14, 15, 18–23] and the other known data on crystal growth of CuO. These data showed that it is expedient to use the Bi₂O₃ flux. However, these data are incomplete and do not provide unique information on the compositions of the melts. Therefore, to choose the optimum systems, we had to perform the trial experiments on crystallization in the CuO–Bi₂O₃, CuO–Bi₂O₃–MO_x ($M = \text{PbO, PbF}_2, \text{Li}_2\text{O, or B}_2\text{O}_3$), CuO–PbO, CuO–PbO–PbF₂, CuO–MO_x ($M = \text{Li, P, V, or Mo}$), and CuO–BaO–Y₂O₃ systems.

The initial components were oxides, carbonates, and fluorides of the corresponding metals of the analytical-purity grade. The acetone-homogenated mixtures of the starting components were heated in alundum crucibles up to temperatures exceeding their melting points ($\sim 1060^\circ\text{C}$), were kept at the maximum temperatures for 1–3 h, and then cooled, first, to subsolidus temperatures ($\sim 600^\circ\text{C}$) at a rate of 5 K/h, and then to room temperature in the switched-off furnace.

The best results were obtained upon crystallization of the following compositions: CuO 0.8–0.7; Bi₂O₃

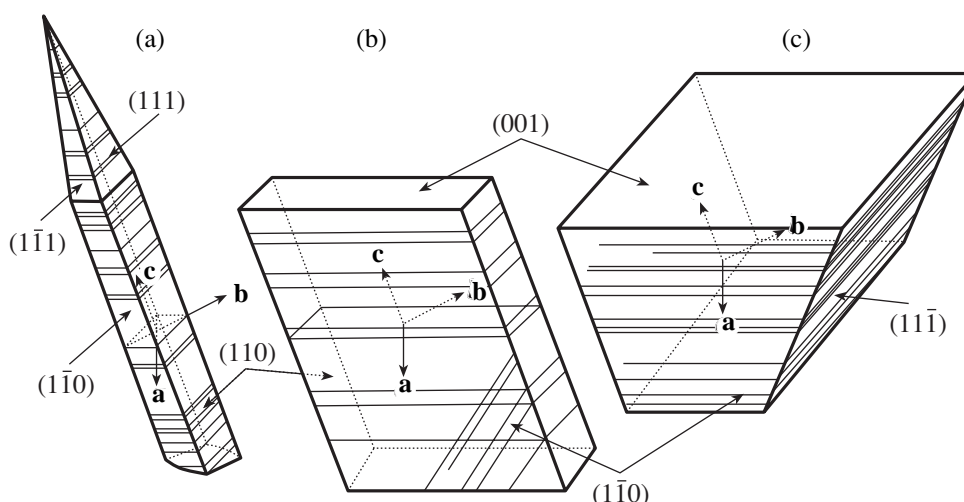


Fig. 1. Habit of (a) needle-like, (b) platelet-like, and (c) isometric CuO crystals (the horizontal and the diagonal hatchings indicate the polysynthetic twins in systems 1 and 2, respectively; **a**, **b**, and **c** indicate the orientations of the crystallographic axes).

0.2–0.3; and $x\text{PbF}_2$ ($x = 0\text{--}0.30$). The surfaces of the crystallized melts had platelet-like CuO crystals with a $10 \times 20\text{-mm}$ basal plane, and the plate thickness was up to 1 mm. These crystals contained single crystals of CuO in a needle-like form (elongated in the *c*-axis) and $1 \times 1 \times 10$ and $6 \times 6 \times 8$ mm isometric prisms (Fig. 1). Black crystals exhibited cleavage along the (110) and (001) planes and had the characteristic {110}, {111}, and {001} growth forms (Fig. 1). The crystals also showed polysynthetic twinning which manifested itself in the presence of alternating light and dark bands on the crystal faces.

Another characteristic defect of CuO crystals are the various inclusions. The surfaces of natural and polished faces had Bi_2O_3 , PbO, and Al_2O_3 inclusions inherited from the flux and the remaining polishing paste. The dimension of these inclusions attains a value of 0.5 mm.

The X-ray diffraction pattern of powdered crystals obtained on a DRON-4 diffractometer (filtered $\lambda\text{CuK}\alpha$ radiation) corresponds to the ASTM data for CuO [24]. Based on these data and the results obtained in [1, 4, 5, 8, 11, 16, 17, 23, 25, and 26] we indexed the X-ray pattern within the monoclinic unit cell with the parameters $a = 4.688(5)$ Å, $b = 3.420(5)$ Å, $c = 5.132(3)$ Å, $\beta = 99.5(1)^\circ$. An examination of platelet-like CuO crystals revealed no pyroelectric effect in the temperature range of 80–300 K, which indicated the absence of phase transitions with the lowering of the symmetry down to polar in this temperature range.

POLYSYNTHETIC TWINNING

Polysynthetic twins were observed on the {110} and {111} faces in the form of numerous alternating light and dark bands limited by the systems of parallel straight lines (Figs. 1–3). In the most widespread system 1 (Fig. 2), these bands are parallel to the (001)

plane. In the different parts of the crystal, the distances between the neighboring bands vary from several microns to several millimeters. In most cases, the width of light bands considerably exceeds the width of dark ones. These bands are also clearly seen in the reflected light in the optical and metallurgical microscopes. These bands are also visible to the naked eye when studying the natural faces at different angles. Investigation of the crystals during heating demonstrates that the above-described twin structure remained practically unchanged up to $\sim 1000^\circ\text{C}$.

The angles between the crystal faces were measured on an RGNS-2 goniometer. The angle between the (110) planes of the adjacent regions of the faces separated by the straight lines equals 11.2° . This fact and the X-ray diffraction patterns measured from different crystal faces indicate that the twins of system 1 are adjacent along the (001) planes. The adjacent twins are characterized by the parallel orientation of their **a**- and **b**-axes, whereas the unit cell changes its orientation in such a way that the angle between the **c**-axis and the (001) plane decreases from 99.5° to 80.5° when crossing the twin boundary [the (001) plane] (Fig. 3). Thus, the crystal structures of the adjacent twins in system 1 are related by the mirror-reflection (001) plane.

An examination of some crystals revealed, along with the above-described system of bands on the {110} faces, analogous systems of straight bands which intersect the first system at a certain angle. The most common system is system 2 (Fig. 2). The bands of system 2 form an angle of 120° with the bands of system 1 in the (010) plane. The existence of various band systems shows the complex character of CuO twinning.

Twinning in natural CuO minerals was first reported in [1]. Polysynthetic twinning of CuO microcrystals was observed in [27–29]. Apparently, the twin formation is not associated with the growth conditions of

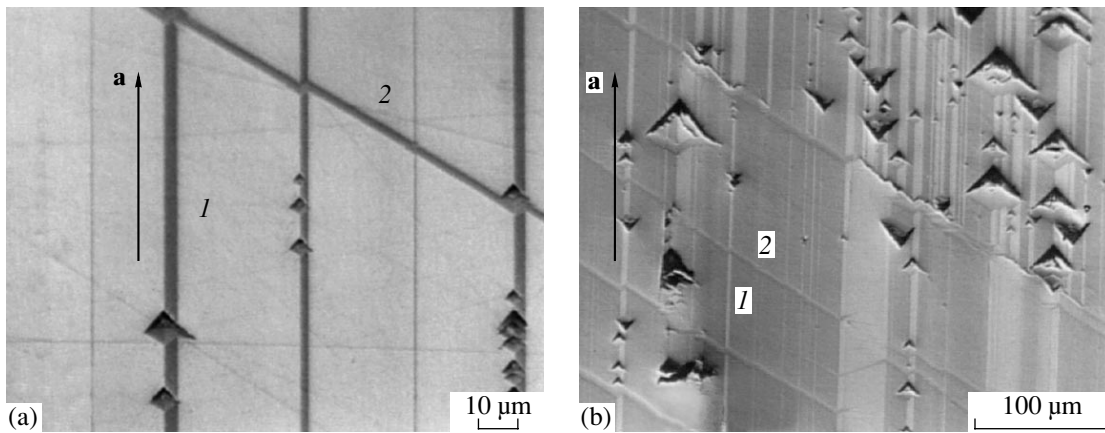


Fig. 2. Polysynthetic twinning observed on the {010} faces of CuO crystals in a metallurgical microscope; 1 and 2 indicate two different systems of polysynthetic twins.

CuO single crystals. Twinning is inherent in the CuO phase. Evidently, twinning of CuO crystals produces a strong effect on their physical properties and, therefore, should be taken into account when interpreting the crystal properties.

POSSIBLE TWINNING MODELS

Usually, polysynthetic twinning is associated with phase transitions of the distorting (non-reconstructive) type [30, 31]. On cooling a high-temperature high-symmetry (prototype) phase, the cooperative atomic displacements occur at the phase-transition point. These displacements can be differently oriented with respect to the initial crystal lattice in different regions of the crystal and can give rise to polysynthetic twinning in the crystals in the low-temperature phase. The local regions of the crystal, which undergo different transformations, become twins with respect to each other.

The measurements of the temperature dependence of the unit-cell parameters showed that CuO undergoes no phase transitions in the temperature range of 20–1000°C [25]. The $\text{CuO} \longleftrightarrow \text{Cu}_2\text{O}$ transformation at 1026°C accompanied by the change in the symmetry ($C2/c \longleftrightarrow Pn3m$) is the only known transformation taking place during the heating of CuO crystals [1, 8, 18]. This transformation is of a reconstructive nature and is accompanied by considerable changes in the unit-cell parameters ($a = b = c = 4.26 \text{ \AA} \longleftrightarrow a = 4.69 \text{ \AA}, b = 3.42 \text{ \AA}, c = 5.13 \text{ \AA}; \alpha = \beta = \gamma = 90^\circ \longleftrightarrow \alpha = \gamma = 90^\circ, \beta = 99.5^\circ$) and by chemical reactions of oxygen evolution–absorption. Apparently, this transformation should result in crystal destruction, and, hence, at first glance, Cu_2O cannot be the prototype phase for CuO.

Possibly, the CuO crystals are related to the prototype phase with a high temperature of transition to the prototype phase and which decompose prior to the attainment of this temperature. In these cases, the hypo-

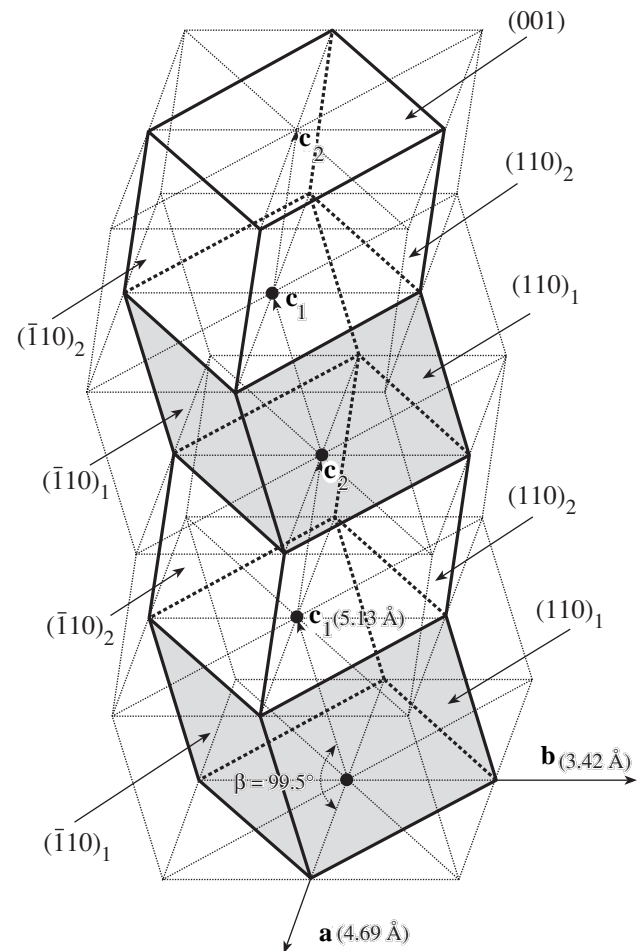


Fig. 3. Schematic representation of polysynthetic twinning along the (001) planes of a CuO crystal; the angles between the $(110)_1$ and $(110)_2$, $(110)_2$ and $(110)_1$, (001) and $(110)_1$, (001) and $(110)_2$, and (110) and $(\bar{1}10)$ faces are 11.3° , 168.7° , 84.4° , 95.6° , and 73.1° , respectively.

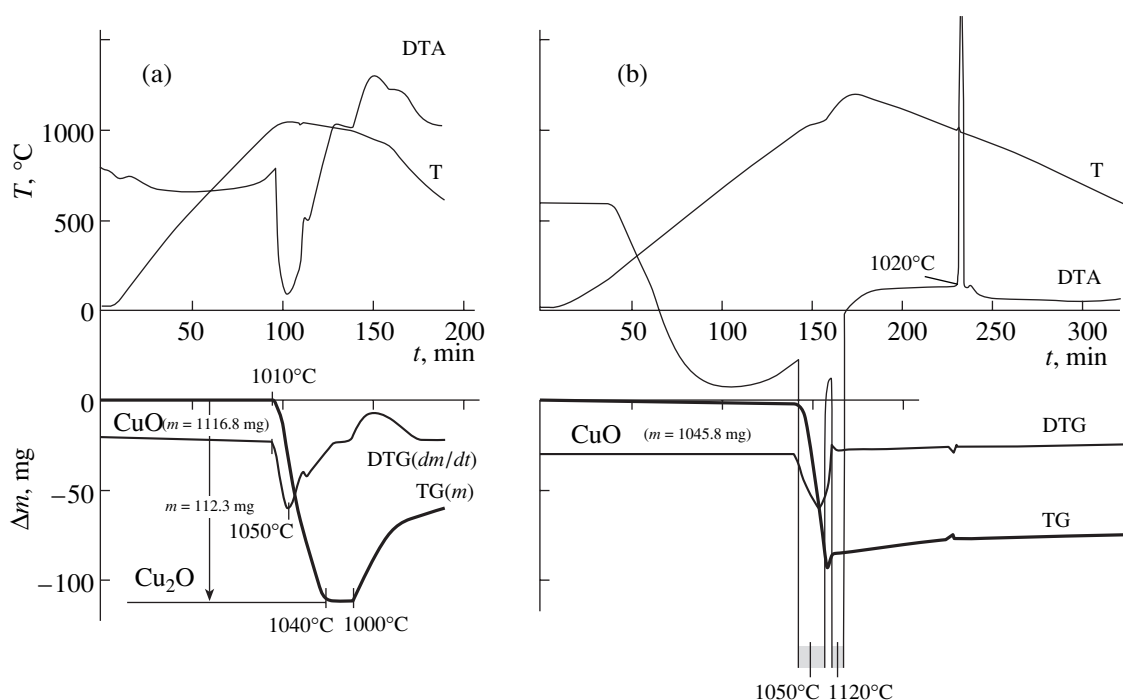


Fig. 4. Derivatograms of a high-purity grade CuO powder measured in air at the maximum heating temperatures (a) 1060°C and (b) 1200°C; T, TG, DTA, and DTG are the curves of thermal, thermal gravimetric, differential thermal, and differential-thermal gravimetric analyses, respectively; m is the initial weight of the specimen.

thetical symmetry of the prototype phase should be determined by the symmetry of the low-symmetry phase and by the orientation of the domain structure of the latter. In the case of CuO, the untwining of polysynthetic twins of system I is accompanied by an increase in the crystal symmetry from monoclinic to at least orthorhombic ($\beta \rightarrow 90^\circ$). The presence of other systems of polysynthetic twinning in the CuO crystals indicates a higher symmetry of the prototype phase. These results, along with the analysis of the CuO behavior during heating and crystallization (Fig. 4) [1, 8, 14, 18, 19, 21, 23, 25, 28], give grounds to consider the cubic Cu₂O phase as the prototype high-symmetry phase of CuO crystals. According to [28], the thermal treatment of CuO single crystals under the moderately reductive conditions at 400°C leads to the evolution of oxygen from CuO and its transformation into Cu₂O accompanied by the disappearance of twinning. The crystal structures of CuO and Cu₂O are characterized by different distortions of the crystal lattice and positions of the oxygen atoms; however, the copper atoms occupy analogous positions in these crystals [1, 8, 18]. It should also be noted that polysynthetic twinning appearing in the phase transformation, which is accompanied by a change in the oxygen content in the unit cell, was observed in the crystals of the Y-123 HTSC phase [29].

Apparently, the ability of the crystal lattice to rearrange without destruction of the crystal in the Cu₂O \rightarrow CuO transformation is associated with the

complex kinetics of this transformation and the existence of a number of intermediate Cu_{1-2x}²⁺Cu_{2x}¹⁺O_{1-x} states. Derivatograms obtained from CuO on a Paulik-Erdey derivatograph (Fig. 4) show that the Cu₂O \rightarrow CuO transformation occurs within a long temporal and temperature ranges sufficient for the crystal lattice to be rearranged without destruction of the crystal.

According to [31], the symmetry change from $Pn3m$ to $C2/c$ in the transition from Cu₂O to CuO indicates that CuO belongs to the $m3mF2/m$ class of ferroelastics characterized by 12 possible orientational states of domains and a large number of various planes that can play the role of domain boundaries [32].

ACKNOWLEDGMENTS

We are grateful to H. Bron (Materials Science Group of the Department of Applied Physics at the University of Groningen, the Netherlands) for his help in processing the crystal surfaces and obtaining their images.

This study was supported by the Russian Foundation for Basic Research, project no. 99-02-17752.

REFERENCES

1. *Minerals. Simple Oxides. Handbook*, Ed. by F. V. Chukhrov (Nauka, Moscow, 1965), Vol. II, issue 2, p. 41.

2. B. X. Yang, J. M. Tranquada, G. Shirane, *et al.*, Phys. Rev. B **38** (1), 174 (1988).
3. O. Rondo, M. Ono, E. Sugiura, *et al.*, J. Phys. Soc. Jpn. **57** (10), 3293 (1988).
4. T. A. Arbutova, A. A. Samokhvalov, I. B. Smolyak, *et al.*, Pis'ma Zh. Éksp. Teor. Fiz. **50** (1), 29 (1989) [JETP Lett. **50**, 34 (1989)].
5. T. A. Arbutova, A. A. Samorokov, I. B. Smolyak, *et al.*, J. Magn. Magn. Mater. **95**, 168 (1991).
6. U. Kobler and T. Chattopadhyay, Z. Phys. B **82** (3), 383 (1991).
7. P. J. Brown, T. Chattopadhyay, J. B. Forsyth, *et al.*, J. Phys.: Condens. Matter **3**, 4281 (1991).
8. E. Gmelin, Indian J. Pure Appl. Phys. **30**, 596 (1992).
9. *Chemistry of High-Temperature Superconductors*, Ed. by D. L. Nelson, W. S. Whittingham, and Th. F. George (Am. Chemical Society, Washington, 1987; Mir, Moscow, 1988).
10. B. M. Wanklyn and D. J. Garrard, J. Mater. Sci. Lett. **2**, 285 (1983).
11. A. A. Samokhvalov, N. N. Loshkareva, Yu. P. Sukhorukov, *et al.*, Pis'ma Zh. Éksp. Teor. Fiz. **49** (8), 456 (1989) [JETP Lett. **49**, 523 (1989)].
12. B. A. Gizhevskii, A. A. Samokhvalov, N. M. Chebotaev, *et al.*, Sverkhprovodimost: Fiz., Khim., Tekh. **4** (4), 827 (1991).
13. Yu. S. Ponosov, G. A. Bolotin, N. M. Chebotaev, *et al.*, Sverkhprovodimost: Fiz., Khim., Tekh. **4** (7), 1422 (1991).
14. C. Chen, Y. Hu, B. M. Wanklyn, *et al.*, J. Mater. Sci. **28**, 5045 (1993).
15. C. Chen, Y. Hu, B. M. Wanklyn, *et al.*, J. Cryst. Growth **129**, 239 (1993).
16. T. Ito, H. Yamaguchi, K. Okabe, and T. Masumi, J. Mater. Sci. **33**, 3555 (1998).
17. X. G. Zheng, M. Suzuki, and C. N. Xu, Mater. Res. Bull. **33** (4), 695 (1998).
18. *Minerals. Handbook*, Ed. by F. V. Chukhrov *et al.* (Nauka, Moscow, 1974), nos. 1, 2.
19. A. A. Zhokhov, Zh. D. Sokolovskaya, G. K. Baranova, and I. I. Zver'kova, Sverkhprovodimost: Fiz., Khim., Tekh. **3** (12), 161 (1990).
20. J. Sestak, J. Therm. Anal. **36**, 1639 (1990).
21. M. P. Kulakov and D. Ya. Lenchinko, Thermochim. Acta **188**, 129 (1991).
22. B.-J. Lee and D. N. Lee, J. Am. Ceram. Soc. **74** (1), 78 (1991).
23. A. A. Fotiev, B. V. Slobodin, and V. A. Fotiev, *Chemistry and Technology of High-Temperature Superconductors* (Ural'skoe Otd. Ross. Akad. Nauk, Yekaterinburg, 1994).
24. ASTM, file No. 5-661.
25. M. I. Domnina, S. K. Filatov, I. I. Zyuzukina, and L. P. Vergasova, Izv. Akad. Nauk SSSR, Neorg. Mater. **22** (12), 1992 (1986).
26. J. B. Forsyth and S. Hull, J. Phys.: Condens. Matter **3**, 5257 (1991).
27. G. N. Kryukova, V. I. Zaikovskii, V. A. Sadykov, *et al.*, J. Solid State Chem. **73**, 191 (1988).
28. V. A. Sadykov, S. F. Tikhov, G. N. Kryukova, *et al.*, J. Solid State Chem. **73**, 200 (1988).
29. H. Schmid, E. Burkhardt, E. Brixel, *et al.*, Z. Phys. C **72**, 305 (1988).
30. R. W. Cahn, Adv. Phys. **3** (12), 363 (1954).
31. K. Aizu, J. Phys. Soc. Jpn. **27** (2), 387 (1969).
32. J. Sapriel, Phys. Rev. B **12**, 5128 (1975).

Translated by T. Safonova

Effect of Growth Conditions on Formation of Grain Boundaries in Epitaxial Silicon Layers

G. S. Konstantinova and V. N. Lozovskii

Novocherkassk State Technical University,
ul. Prosveshcheniya 132, Novocherkassk, 346400 Russia

Received January 20, 2000

Abstract—The formation of grain boundaries of the general type, along with small- and large-angle symmetric grain boundaries with the $\langle 110 \rangle$ axis in the epitaxial layers grown onto bicrystal substrates by the method of thermal migration has been studied. The solvent was aluminum. It is shown that if the grain boundaries in the epitaxial layer are tilted to the crystallization front or if there is a temperature gradient tangential to this front, their orientation differs from their orientation in the substrate. The large-angle symmetric boundaries are more stable than the boundaries of the general type. The grain-boundary energy and rotation moment of large-angle symmetric boundaries are evaluated. © 2002 MAIK “Nauka/Interperiodica”.

INTRODUCTION

The formation and development of small- and large-angle symmetric grain boundaries in epitaxial silicon layers grown by the thermally-induced migration method under conditions where the grain boundaries are normal to the crystallization front have been studied elsewhere [1]. It was shown that many large-angle boundaries with the $\langle 110 \rangle$ axis are split, and that the splitting reactions can be used to evaluate grain-boundary energies. Below, we describe the study of grain-boundary formation in epitaxial layers under conditions where the grain boundaries are tilted to the crystallization front and when there is a tangential temperature gradient. The results obtained enable us to perform not only relative evaluations, but also provide the evaluation of grain-boundary energies and the rotation moments that cause the deviation of the grain boundary from its initial position toward the orientation with the minimum energy.

CALCULATION OF THE POSITION OF THE GRAIN-BOUNDARY IN THE EPITAXIAL LAYER

Let a grain boundary GB between grain 1 and grain 2 (Fig. 1a) in the substrate be normal to the initial crystallization front CF_0 . During the process of thermally-induced migration, a plane liquid layer of flux is moving from the substrate through the crystal-source along the direction of the temperature gradient. The epitaxial layer is left behind the crystallization front (CF). The grain boundary intersects the crystallization front and forms a groove, which can be treated as a liquid linear inclusion on the crystallization-front surface. The melt in the groove volume is in contact with solid phases I and II. If these phases are thermodynamically equivalent, no driving force giving rise to tangential displace-

ment of the groove arises, and a grain boundary in the epitaxial layer is formed normally to the initial crystallization front CF_0 .

If the substrate dictates the formation of the grain boundary at an angle α to the normal (Fig. 1b), the groove shape becomes asymmetric. The tangential diffusion flows can arise in the groove, which provide a balance between the surface tension of grain boundary and the interface. The additional tangential diffusion flow of atoms of the substance to be crystallized can also be caused by the applied temperature gradient G_t , which is tangential to the crystallization front. The additional diffusion flows give rise to additional displacement of the groove along the crystallization front in the direction opposite to that of the diffusion flow

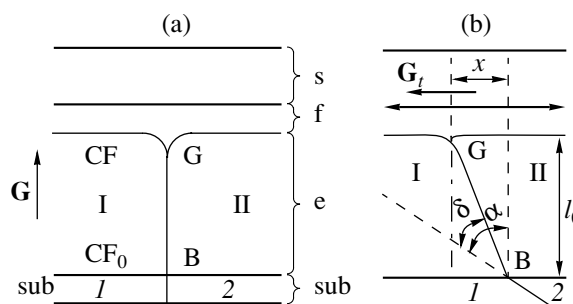


Fig. 1. Schematic cross section of the sample illustrating the process of thermally-induced migration: (1, 2) adjacent grains in the substrate; (e) epitaxial layer; (s) crystal-source; (f) flux; (sub) substrate; (CF) the crystallization front; (CF_0) the initial crystallization front; (B) grain boundary in epitaxial layer; (G) the groove on the crystallization front; (G) and (G_t) normal and tangential temperature gradients, respectively. (a) the grain boundary in the epitaxial layer is normal to the crystallization front; (b) the grain boundary is tilted to the crystallization front.

(the displacement mechanism is similar to the mechanism of thermally-induced migration). As a result, the grain boundary in the epitaxial layer starts deviating from the orientation dictated by the substrate.

In our experiments, the coherent $\{111\}\Sigma = 3$ grain boundaries with a low specific surface energy σ (~ 0.05 J/m²) produced no visible grooves on the crystallization front.¹

In all the epitaxial layers irrespective of the α -value in the presence of G_t , such boundaries showed no deviations from the crystallographic orientation. Grain boundaries of the general types (with high values of σ and the absence of the orientation dependence of σ) were formed normally to the crystallization front [2]. To a number of large-angle grain boundaries with low σ values (the so-called special grain boundaries) there corresponds a deep minimum on the orientational dependence of σ . These grain boundaries deviated from the initial orientation at the angle δ (see Fig. 1b). The energy gain owing to a decrease in the grain-boundary area during its deviation from the normal is compensated with an increase in σ .

Assuming that the grain-boundary length in the direction normal to the drawing plane in Fig. 1 equals unity, we can state that the equilibrium value of the angle $(\alpha - \delta)$ is determined by the condition $dE = \sigma dl + ld\sigma = 0$, where $E = \sigma l$ is the grain-boundary energy,

$l = \frac{l_0}{\cos(\alpha - \delta)}$ is the grain-boundary length, and $d\sigma = \frac{d\sigma}{d\delta} d\delta$. Substituting l , dl , and $d\sigma$ into the initial expression for dE , we have

$$\tan(\alpha - \delta) = \frac{1}{\sigma} \frac{d\sigma}{d\delta}, \quad (1)$$

where $\frac{d\sigma}{d\delta}$ is the rotation moment applied to the surface

unit of the grain boundary and $(\frac{1}{\sigma} \frac{d\sigma}{d\delta})$ is the normalized

rotation moment. Since neither σ nor $\frac{d\sigma}{d\delta}$ are dependent

on α , the deviation δ should increase with an increase in α . In the presence of the tangential temperature gradient G_t , the equilibrium position of the boundary is determined by the condition

$$dE - F_t dx = 0, \quad (2)$$

where $x = l_0 \tan(\alpha - \delta)$ and F_t is the thermodynamic force per groove-length unit provided by the temperature gradient G_t .

¹ $\Sigma = \frac{V^L}{V^{\text{CSL}}}$, where V^{CSL} and V^L are the unit-cell volumes of the coincidence-site lattice of two neighboring grains and the unit-cell volume of the initial crystal lattice, respectively.

$$\begin{aligned} F_t &= \frac{d\mu}{dx} N = \frac{RT}{C} \frac{dC}{dx} N \\ &= \frac{RT}{C} \frac{dC}{dT} \frac{dT}{dx} N = \frac{RT}{C} \frac{dC}{dT} G_t \frac{S}{V_m}, \end{aligned} \quad (3)$$

where μ and C are the chemical potential and the solubility of silicon in the liquid phase, respectively; $\frac{dC}{dT}$ is

the slope of the liquidus line for the binary Si–Al phase diagram at the process temperature, N is the number of mole of silicon per groove-length unit, S is the area of the groove cross section, and V_m is the molar volume of silicon in the liquid phase. In accordance with Eqs. (2) and (3), the position of the grain boundary GB in the presence of G_t is determined by the condition

$$F_t - \sigma \sin(\alpha - \delta) + \frac{d\sigma}{d\delta} \cos(\alpha - \delta) = 0. \quad (4)$$

EXPERIMENTAL RESULTS AND DISCUSSION

As in [1], the process of thermally-induced migration continued for 1.0–1.3 h at $T = 1100^\circ\text{C}$ and $G = 10$ K/cm with the use of an aluminum solvent. The preparation of bicrystal substrates is described elsewhere [1]; the scheme of the substrate and the transverse cross section of the specimen with grain boundaries in the epitaxial layer are also considered in [1]. The angles between the grain boundary plane and the normal were measured in an optical microscope an accuracy of 1.0° – 1.5° . The experiments were repeated from three to five times for each type of substrate. We studied grain boundaries of the general type, along with small- and large-scale symmetric (special) grain boundaries with the $[1\bar{1}0]$ axis.

Grain Boundaries of the General Type

Four different variants of misorientated grains were used to prepare the substrates. In the absence of G_t , the grain boundaries in the epitaxial layer were normal to the initial crystallization front. If $G_t = 5^\circ\text{C}/\text{cm}$, the grain boundaries in the epitaxial layer systematically deviated toward G_t . The deviation angles δ_i for four types of substrates were 17° – 29° , 7° – 10.5° , 8° – 15° , and 10° – 34° , respectively. According to Eq. (4), we obtain at $\alpha = 0$,

$$\frac{d\sigma}{d\delta} = 0, \text{ and } \delta = -\delta_i$$

$$\sigma = \frac{F_t}{\sin \delta_i}. \quad (5)$$

Substituting $C = 0.53$, $\frac{dC}{dT} = 1.06 \times 10^{-3} \text{ K}^{-1}$ (from the phase diagram of the Si–Al system at 1100°C), $V_m = 11 \text{ cm}^3/\text{mol}$, and also the average value of the groove

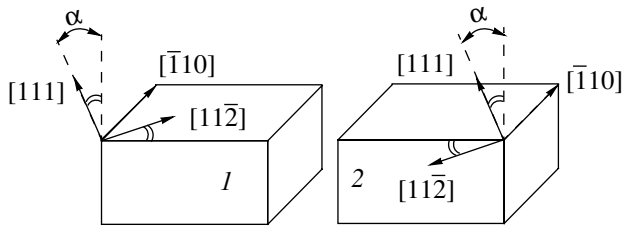


Fig. 2. Orientations of grains intergrown during the preparation of the substrates and determining the formation of the $(11\bar{2})\Sigma^* = 3$ grain boundary in the epitaxial layer at the angle α to the normal.

cross section $S = 150 \times 10^{-12} \text{ m}^2$, we obtain $F_t = 0.16 \text{ J/m}^2$. Substituting F_t and the average values δ_t into Eq. (5), we obtain the specific surface energies $\sigma = 0.41, 1.06, 0.68,$ and 0.45 J/m^2 , for the four grain boundary types respectively. These data are in good agreement within an order of magnitude with the data reported earlier [2, 3]. Because of the pronounced scatter in the δ_t and S values, the σ -values obtained above should be considered as rough estimates.

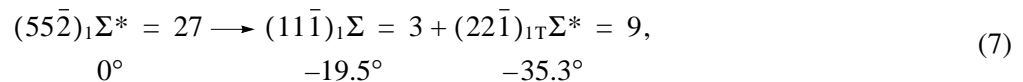
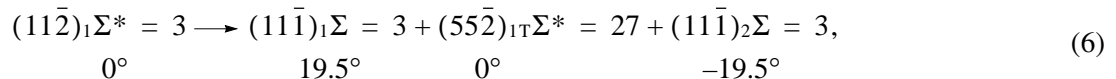
Small-Angle Boundaries

We used two types of bicrystal substrates prepared by the diffusion welding of two slightly misoriented grains ($\sim 1^\circ$): The grain-boundary (111) plane normal to the substrate $(1\bar{1}0)$ surface and the grain-boundary $(1\bar{1}0)$

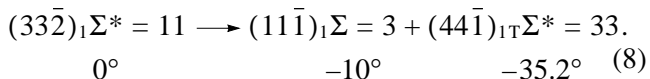
plane normal to the substrate (111) surface. In both cases, the grain boundaries in the epitaxial layers were found to be normal to the initial crystallization front $G_t = 0$. Under the temperature gradient $G_t = 5^\circ\text{C/cm}$, the grain boundaries of both types in epitaxial layers deviated from the normal toward G_t by angles $\delta_t = 18^\circ\text{--}26^\circ$ and $19^\circ\text{--}32^\circ$, respectively. For small-angle grain boundaries, σ depends on orientation [1], therefore, σ for small-angle grain boundaries are lower than for grain boundaries of the general type. It is hardly possible to evaluate σ for small-angle grain boundaries because the form of the $\sigma(\delta)$ dependence for these boundaries is unknown.

Symmetric Grain Boundaries with the $[110]$ Axis

The orientations of all the grain boundaries studied are indicated in the table as well as Σ -values and the orientations of the planes normal to the grain boundaries (the initial crystallization front). We studied incoherent grain boundaries, because we prepared the substrates by intergrowing the grains only slightly ($\sim 1^\circ$) deviating from the misorientations indicated in the table. Grain boundaries 1 and 2 do not split in epitaxial layers, whereas other grain boundaries are split with the formation of coherent $\{111\}\Sigma = 3$ boundaries and other incoherent special boundaries [1]. In the latter case, we studied grain boundaries formed during splitting, e.g., $\{55\bar{2}\}\Sigma^* = 27$ and $\{22\bar{1}\}\Sigma^* = 9$ formed by following reactions [1]:



and also grain boundary $\{441\}\Sigma^* = 33$ formed by the reaction



In reactions (6)–(8), below the symbols of grain boundaries, we also indicate the angles they form with the normal to the initial crystallization front. The signs “+”

and “–” indicate the counter- and the clockwise measurements from the normal. The asterisks indicate incoherent grain boundaries, the subscripts “1,” “1T,” and “2” relate to grain 1, its twin [the twinning plane $(11\bar{1})_1$], and grain 2, respectively. The tilt of the grain boundary in the epitaxial layer was set during the substrate preparation. Thus, in order to obtain grain boundary 4 in the epitaxial layer forming an angle α with the normal, we had to intergrow the grains shown in Fig. 2. The splitting reactions (6) at angles $\alpha = 0^\circ$ and $\alpha = 19.5^\circ$ are shown in Fig. 3a and in Fig. 3b, respectively. The KD_1 and KD_2 are coherent $\{111\}\Sigma = 3$ boundaries, while KD is an incoherent $(55\bar{2})_{1T}\Sigma^* = 27$ boundary. The substrate structure is described in detail in [1]. The positions of the coherent grain boundaries correspond to the crystallographic position, whereas the incoherent grain boundary deviates from it toward the normal. The reac-

The orientations of large-angle symmetric grain boundaries and the planes normal to these boundaries (CF_\perp)

No.	1	2	3	4	5	6
GB	$11\bar{1}$	$11\bar{3}$	$22\bar{1}$	$55\bar{2}$	$44\bar{1}$	$11\bar{4}$
Σ	3	11	9	27	33	9
CF_\perp	112	332	114	115	118	221

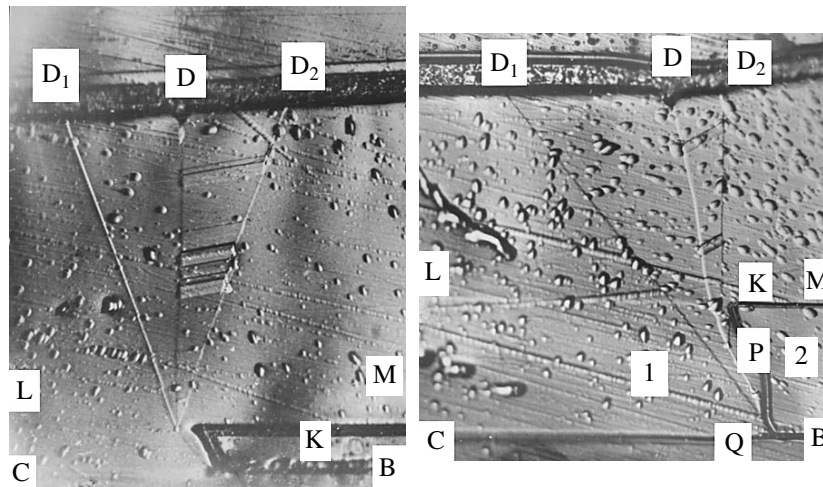


Fig. 3. Splitting reaction (6) on the transverse $(\bar{1}10)$ CLKMB cross section of the substrate. The epitaxial layers start growing from the LKM surface (a) the substrate surface has the (111) orientation; splitting starts at the point K; (b) the substrate surface forms an angle of 19.5° with the (111) plane; splitting started at the points P and Q of the substrate.

tions of all types resulted in the appearance in the epitaxial layers of coherent $\{111\}\Sigma = 3$ grain boundaries and forming no visible grooves, in accordance with the crystallographic conditions, at arbitrary angles α with the normal. The incoherent special grain boundaries deviated toward the normal. The deviation angles δ increased with α and were different for different types of grain boundaries. For instance, at $\alpha = 20^\circ$, the average values of the angle δ for grain boundaries 2, 3, 4, and 5 were 9.5° , 3.4° , 5.5° , and 6.2° , respectively (see table). In accordance with Eq. (1) for the δ values given above, the values of normalized rotation moments $\frac{1}{\sigma} \frac{d\sigma}{d\delta}$ are equal to 0.19, 0.30, 0.25, and 0.26, respectively.

For the grain boundary $(22\bar{1})\Sigma^* = 9$ at $\alpha = 35.3^\circ$, the deviation is $\delta = 5.2^\circ$, which yields $\frac{1}{\sigma} \frac{d\sigma}{d\delta} \Big|_{\alpha=5^\circ} = 0.58$. For the grain boundary $(44\bar{1})\Sigma^* = 33$, the normalized rotation moment $\frac{1}{\sigma} \frac{d\sigma}{d\delta} \Big|_{\delta=6^\circ} = 0.26$ has a much lower value than for the previous grain boundary. It should be indicated that no splitting (7) occurs if the grain boundary $(22\bar{1})\Sigma^* = 9$ forms an angle α with the normal such that $|\alpha| > 45^\circ$. Splitting by Eq. (8) is terminated for the boundary $(44\bar{1})\Sigma^* = 33$ at $|\alpha| > 25^\circ$.

For the grain boundary 1 (see table) at the set tilt angles in the range $\alpha = 10^\circ - 35^\circ$, the coherent $\{111\}\Sigma = 3$ and small-angle grain boundaries were formed at angles α in the epitaxial layers instead of the coherent boundaries. Small-angle boundaries were inclined toward the normal.

The same situation was also observed for grain boundary 6. For the (221) substrate plane tilted to the

initial crystallization front, the splitting of grain boundary 6 in the epitaxial layers corresponded to the following reaction: $(11\bar{4})_1\Sigma^*(9) \rightarrow (11\bar{1})_1\Sigma = 3 + (11\bar{1})_2\Sigma = 3$. One of the boundaries obtained should be incoherent, since the initial grain boundary is incoherent. However, in fact, a small-angle grain boundary was split from the incoherent $\{111\}\Sigma^* = 3$ boundary. As a result, two coherent $\{111\}\Sigma = 3$ boundaries were formed in the epitaxial layer (which had crystallographic orientation) and one small-angle grain boundary forming an angle with the normal.

Effect of the Tangential Temperature Gradient

The temperature gradient $G_t = 5^\circ\text{C}/\text{cm}$ directed as is shown in Fig. 1b compensated (partly or completely) for the deviation of the tilt large-angle boundaries with respect to normal. For example, the $\{113\}\Sigma^* = 11$ grain boundary at $\alpha = 15^\circ$ did not deviate from its position toward the normal within the accuracy. The grain boundary $\{552\}\Sigma^* = 27$ at $\alpha = 15^\circ$ was formed at an angle of $\alpha = 17^\circ$. Splitting according to reaction (8) proceeded under the conditions where the formed $\{441\}\Sigma^* = 33$ grain boundary formed angles $\alpha = 25^\circ$ and $\alpha = 35^\circ$ with the normal. (As was mentioned above, under these conditions and in the absence of G_t no splitting reaction occurred.)

If the grain boundary in the epitaxial layer is normal to the crystallization front, then $\alpha = 0$, and the equilibrium condition (4) for small angles δ acquires the form:

$$F_t - \sigma\delta_t - \frac{d\sigma}{d\delta} = 0. \quad (9)$$

The deviations from the normal under the action of G_t for the $\{552\}\Sigma^* = 27$, $\{113\}\Sigma^* = 11$, and $\{221\}\Sigma^* = 9$ grain boundaries were within the accu-

racy. Hence, the rotation moments for these boundaries are $\frac{d\sigma}{d\delta} \geq F_t = 0.16 \text{ J/m}^2$.

For the $\{441\}\Sigma^* = 33$ grain boundary, the average deviation angle equals $\delta_t = 7^\circ$. Invoking Eq. (9) and the above value $\left. \frac{1}{\sigma} \frac{d\sigma}{d\delta} \right|_{\alpha = 6^\circ} = 0.26$, we obtain that, given a deviation of the grain boundary from the exact orientation $\{441\}\Sigma = 33$ by an angle of 6° , its surface energy has the value $\sigma = 0.43 \text{ J/m}^2$ and its rotation moment becomes equal to $\frac{d\sigma}{d\delta} = 0.11 \text{ J/m}^2$. However, these values are only rough estimates because of the considerable scatter in δ_t values.

CONCLUSIONS

The results obtained show that the appearance of grain boundaries forming a groove when intersecting the crystallization front during epitaxial growth is essentially dependent on the growth conditions, namely, on the angle formed by the boundary with the normal to the crystallization front and the existence of a tangential temperature gradient. Diffusion flows in the groove volume arising due to the above factors lead to its displacement along the crystallization front. This process

can be interpreted as a variant of thermally induced migration. The groove displacement results in the deviation of the grain boundary in the epitaxial layer from its initial orientation dictated by the substrate.

Incoherent large-angle symmetric boundaries (or special boundaries) with corresponding sharp minima on the orientational dependence of the surface energy are more stable in comparison with small-angle and general boundaries.

The effect of grain boundary deviation from the orientations set by the substrate allows one to estimate both the grain-boundary energy and the rotation moment which "tries" to return the grain boundary to the orientation with the minimum energy.

REFERENCES

1. G. S. Konstantinova and V. N. Lozovskii, *Kristallografiya* **44**, 698 (1999) [*Crystallogr. Rep.* **44**, 649 (1999)].
2. Ch. V. Kopetskiĭ, A. N. Orlov, and L. K. Fionova, *Grain Boundaries in Elemental Materials* (Nauka, Moscow, 1987).
3. A. V. Andreeva and L. K. Fionova, *Fiz. Met. Metalloved.* **52** (3), 593 (1981).

Translated by V. Semenov

INFORMATION

Report on the Results of the 2001 Struchkov Prize Competition for Young Scientists and Announcement of the 2002 Competition

The Struchkov Prize has been awarded annually since 1997 for the best scientific study in crystal chemistry and the application of X-ray structure analysis to the solution of chemical problems. Researchers who are residents of the Commonwealth of Independent States or the Baltic states and are under 36 years of age at the time of the presentation of their documents are invited to participate in the competition. Each scientific study is presented on behalf of a single author, and each author is allowed to present only one work a year. The results presented to the competition should be published or submitted for publication in a refereed journal. The winner of the competition is decided by a special competition jury that is formed by the leaders of the Center of X-ray Structure Studies and consists of leading Russian scientists in crystal chemistry and X-ray structure analysis. The decision of the jury will be announced not later than November 1 this year.

Sixteen young scientists from Moscow, Chernogolovka, Novosibirsk, Kazan, Tashkent, and Chisinau took part in the 2001 competition.

In 2001, two Struchkov Prizes were awarded. The winners are

M.A. Zakharov, a postgraduate from the Department of General Chemistry, Faculty of Chemistry, Moscow State University, for his study entitled "Synthesis and Crystal Structure of Acid Selenates"; and

Ya.V. Zubavichus, a researcher from the Laboratory of the Structural Studies of Polymers, Nesmeyanov Institute of Organoelement Compounds, Russian Academy of Sciences, for his study entitled "Structural Characterization of Partially Ordered Layered Nanocomposites Based on Molybdenum Disulfide."

The winners of the competition received diplomas and monetary awards. In addition, nine incentive prizes were awarded to the following researchers: S.B. Artemkina (Novosibirsk), A.V. Churakov (Moscow), K.K. Turgunov (Tashkent), Yu.K. Gubina (Moscow), E.V. Karpova (Moscow), Yu.V. Torubaev (Moscow), I.S. Neretin (Moscow), O.N. Kazheva (Chernogolovka), and O.A. Lodochnikova (Kazan).

Since 2000, the competition has been sponsored by the Struchkov Prize Society, which is the International Crystallographic Association of former students and colleagues of Yu.T. Struchkov. The 2001 prizes amounted to 24000 roubles, and the incentive prizes

amounted to 3000 roubles each. Any winner of the incentive prize is allowed to participate in future competitions.

To take part in the 2002 competition, a competitor should present to the Center of X-ray Structure Studies no later than June 1, 2002 the following documents:

1. A completed competitor form including his/her:

(a) full name;

(b) title of the scientific study presented to the competition;

(c) date of birth;

(d) scientific degree and post;

(e) affiliation;

(f) postal address of the institution;

(g) office telephone;

(h) e-mail;

(i) full name of the supervisor (for those who have supervisors).

2. An abstract of the study (prepared accurately and not exceeding three pages printed with a line spacing of one and a half, 38 lines to a page, and 65 characters to a line) containing a clear explanation of the competitor's contribution to the study.

3. A list of papers published or submitted for publication relating to the subject of the study presented to the competition.

4. Reprints or photocopies of all or some of these papers (at the author's discretion).

The documents should be sent to the Center of X-ray Structure Studies, Nesmeyanov Institute of Organoelement Compounds, Russian Academy of Sciences, ul. Vavilova 28, Moscow, 117813 Russia.

The data indicated in paragraphs 1–3 should be presented to the jury as MS DOS ASCII files. The files can be sent by post on a diskette or by e-mail: premiya@xrlab.ineos.ac.ru. For further information, contact the Center by tel. (095) 135-9271 or e-mail: star@xrpent.ineos.ac.ru or lukul@xray.ineos.ac.ru.

Translated by I. Polyakova